

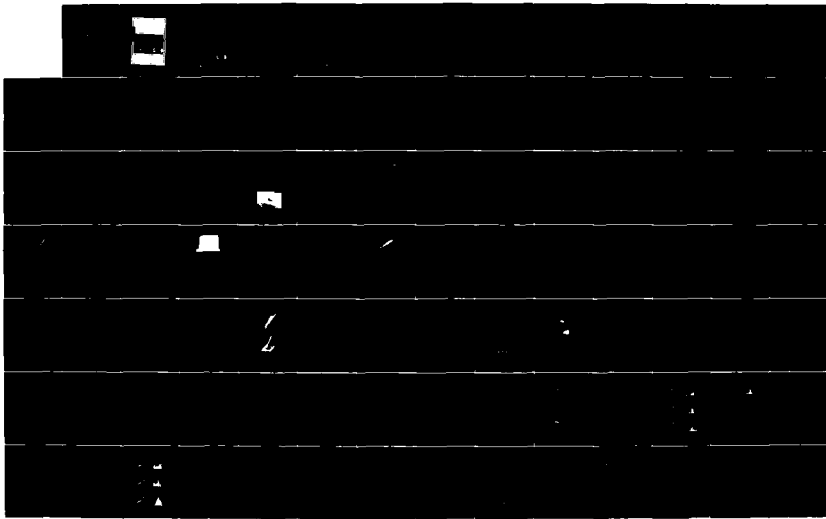
AD-A182 635

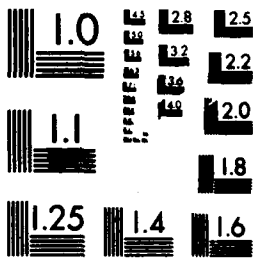
ENGINE RESPONSE TO DISTORTED INFLOW CONDITIONS:
CONFERENCE PROCEEDINGS OF (U) ADVISORY GROUP FOR
AEROSPACE RESEARCH AND DEVELOPMENT NEUILLY, MAR 87
AGARD-CP-400 F/G 20/4

1/44

UNCLASSIFIED

NL





MICROCOPY RESOLUTION TEST CHART
NATIONAL BUREAU OF STANDARDS-1963-A

2

DTIC FILE COPY

AGARD-CP-400

AGARD-CP-400

AGARD

ADVISORY GROUP FOR AEROSPACE RESEARCH & DEVELOPMENT

TRIPLE ALPHABETIC ORDER BY SUBJECT SUBJECT TRACK

AD-A182 635

AGARD CONFERENCE PROCEEDINGS No.400

Engine Response to Distorted Inflow Conditions

DISTRIBUTION STATEMENT A
Approved for public release
Distribution Unlimited

DTIC
ELECTE
MAY 06 1987
S D D

NORTH ATLANTIC TREATY ORGANIZATION



DISTRIBUTION AND AVAILABILITY
ON BACK COVER

400043 CL

87 5 5 021

COMPONENT PART NOTICE

THIS PAPER IS A COMPONENT PART OF THE FOLLOWING COMPILATION REPORT:

TITLE: Engine Response to Distorted Inflow Conditions: Conference Proceedings
of the Propulsion and Energetics Specialists' Meeting (68th) Held
in Munich, Germany on 8-9 September 1986.

TO ORDER THE COMPLETE COMPILATION REPORT, USE AD-A182 635.

THE COMPONENT PART IS PROVIDED HERE TO ALLOW USERS ACCESS TO INDIVIDUALLY AUTHORED SECTIONS OF PROCEEDING, ANNALS, SYMPOSIA, ETC. HOWEVER, THE COMPONENT SHOULD BE CONSIDERED WITHIN THE CONTEXT OF THE OVERALL COMPILATION REPORT AND NOT AS A STAND-ALONE TECHNICAL REPORT.

THE FOLLOWING COMPONENT PART NUMBERS COMPRISE THE COMPILATION REPORT:

AD#: P005 462 thru P005 473 AD#: _____
AD#: _____ AD#: _____
AD#: _____ AD#: _____

| | |
|--------------------|-------------------------------------|
| Accession For | |
| NTIS GRA&I | <input checked="" type="checkbox"/> |
| DTIC TAB | <input type="checkbox"/> |
| Unannounced | <input type="checkbox"/> |
| Justification | |
| By _____ | |
| Distribution/ | |
| Availability Codes | |
| Dist | Avail and/or Special |
| A-1 | |

S DTIC
ELECTE
JUL 31 1987
D
E

DTIC FORM 463
MAR 85

This document has been approved
for public release and sale; its
distribution is unlimited.

OPI: DTIC-TID

AGARD-CP-400

NORTH ATLANTIC TREATY ORGANIZATION
ADVISORY GROUP FOR AEROSPACE RESEARCH AND DEVELOPMENT
(ORGANISATION DU TRAITE DE L'ATLANTIQUE NORD)

AGARD Conference Proceedings No.400
ENGINE RESPONSE TO DISTORTED INFLOW CONDITIONS

Papers presented at the Propulsion and Energetics 68th (A) Specialists' Meeting,
held in Munich, Germany, 8—9 September 1986.

THE MISSION OF AGARD

The mission of AGARD is to bring together the leading personalities of the NATO nations in the fields of science and technology relating to aerospace for the following purposes:

- Exchanging of scientific and technical information;
- Continuously stimulating advances in the aerospace sciences relevant to strengthening the common defence posture;
- Improving the co-operation among member nations in aerospace research and development;
- Providing scientific and technical advice and assistance to the Military Committee in the field of aerospace research and development (with particular regard to its military application);
- Rendering scientific and technical assistance, as requested, to other NATO bodies and to member nations in connection with research and development problems in the aerospace field;
- Providing assistance to member nations for the purpose of increasing their scientific and technical potential;
- Recommending effective ways for the member nations to use their research and development capabilities for the common benefit of the NATO community.

The highest authority within AGARD is the National Delegates Board consisting of officially appointed senior representatives from each member nation. The mission of AGARD is carried out through the Panels which are composed of experts appointed by the National Delegates, the Consultant and Exchange Programme and the Aerospace Applications Studies Programme. The results of AGARD work are reported to the member nations and the NATO Authorities through the AGARD series of publications of which this is one.

Participation in AGARD activities is by invitation only and is normally limited to citizens of the NATO nations.

The content of this publication has been reproduced directly from material supplied by AGARD or the authors.

Published March 1987

Copyright © AGARD 1987
All Rights Reserved

ISBN 92-835-0412-7



Printed by Specialised Printing Services Limited
40 Chigwell Lane, Loughon, Essex IG10 3TZ

RECENT PUBLICATIONS OF THE PROPULSION AND ENERGETICS PANEL

Conference Proceedings

Testing and Measurement Techniques in Heat Transfer and Combustion
AGARD Conference Proceedings No.281, 55th A Meeting, May 1980

Centrifugal Compressors, Flow Phenomena and Performance
AGARD Conference Proceedings No.282, 55th B Meeting, May 1980

Turbine Engine Testing
AGARD Conference Proceedings No.293, 56th Meeting, Sep/October 1980

Helicopter Propulsion Systems
AGARD Conference Proceedings No.302, 57th Meeting, May 1981

Ramjets and Ramrockets for Military Applications
AGARD Conference Proceedings No.307, 58th Meeting, October 1981

Problems in Bearings and Lubrication
AGARD Conference Proceedings No.323, 59th Meeting, May/June 1982

Engine Handling
AGARD Conference Proceedings No.324, 60th Meeting, October 1982

Viscous Effects in Turbomachines
AGARD Conference Proceedings No.351, 61st A Meeting, June 1983

Auxiliary Power Systems
AGARD Conference Proceedings 352, 61st B Meeting, May 1983

Combustion Problems in Turbine Engines
AGARD Conference Proceedings 353, 62nd Meeting, October 1983

Hazard Studies for Solid Propellant Rocket Motors
AGARD Conference Proceedings 367, 63rd A Meeting, May/June 1984

Engine Cyclic Durability by Analysis and Testing
AGARD Conference Proceedings No.368, 63rd B Meeting, May/June 1984

Gears and Power Transmission Systems for Helicopters and Turboprops
AGARD Conference Proceedings No.369, 64th Meeting October 1984

Heat Transfer and Cooling in Gas Turbines
AGARD Conference Proceedings No.390, 65th Meeting, May 1985

Smokeless Propellants
AGARD Conference Proceedings No.391, 66th A Meeting, September 1985

Interior Ballistics of Guns
AGARD Conference Proceedings No.392, 66th B Meeting, September 1985

Advanced Instrumentation for Aero Engine Components
AGARD Conference Proceeding No.399, 67th Meeting, May 1986

Transonic and Supersonic Phenomena in Turbomachines
AGARD Conference Proceedings No.401, 68th B Meeting, September 1986



| | |
|--------------------|-------------------------------------|
| Accession For | |
| NTIS CRA&I | <input checked="" type="checkbox"/> |
| DTIC TAB | <input type="checkbox"/> |
| Unannounced | <input type="checkbox"/> |
| Justification | |
| By | |
| Distribution / | |
| Availability Codes | |
| Dist | Avail and/or Special |
| A-1 | |

Working Group Reports

Aircraft Fire Safety
AGARD Advisory Report 132, Vol.1 and Vol.2. Results of WG11 (September and November 1979)

Turbulent Transport Phenomena (in English and French)
AGARD Advisory Report 150. Results of WG 09 (February 1980)

Through Flow Calculations in Axial Turbomachines
AGARD Advisory Report 175. Results of WG 12 (October 1981)

Alternative Jet Engine Fuels
AGARD Advisory Report 181. Vol.1 and Vol.2. Results of WG 13 (July 1982)

Suitable Averaging Techniques in Non-Uniform Internal Flows
AGARD Advisory Report 182 (in English and French). Results of WG 14 (June/August 1983)

Producibility and Cost Studies of Aviation Kerosines
AGARD Advisory Report 227. Results of WG 16 (June 1985)

Performance of Rocket Motors with Metallized Propellants
AGARD Advisory Report 230. Results of WG 17 (September 1986)

Lecture Series

Non-Destructive Inspection Methods for Propulsion Systems and Components
AGARD LS 103 (April 1979)

The Application of Design to Cost and Life Cycle Cost to Aircraft Engines
AGARD LS 107 (May 1980)

Microcomputer Applications in Power and Propulsion Systems
AGARD LS 113 (April 1981)

Aircraft Fire Safety
AGARD LS 123 (June 1982)

Operation and Performance Measurement of Engines in Sea Level Test Facilities
AGARD LS 132 (April 1984)

Ramjet and Ramrocket Propulsion Systems for Missiles
AGARD LS 136 (September 1984)

3-D Computation Techniques Applied to Internal Flows in Propulsion Systems
AGARD LS 140 (June 1985)

Engine Airframe Integration for Rotorcraft
AGARD LS 148 (June 1986)

Other Publications

Airbreathing Engine Test Facility Register
AGARD AG 269 (July 1981)

THEME

This meeting provided research scientists and development engineers with a broad information on acceptable inflow distortion parameters to be applied to airframe intake integration, computation technique for engine/compressor performance predictions of distorted inflow, distortion inflow detection and experimental investigation of engine instability and response to flow distortion, extending to the present-state-of-the-art, methods and data reported in previous Symposia, and particularly in the 46th PEP Meeting (September 1975) on 'Unsteady Phenomena in Turbomachinery', and the AGARD Lecture Series No.72 (November 1964) on 'Distortion Induced Engine Instability'.

Particular attention of the meeting was also focused on: matching inlet and engine designs; aeromechanical response of turbo-engine to time-variant total pressure and temperature distribution; test techniques for simulating the effects of dynamic distortion on engine stability.

* * * * *

Cette réunion a donné aux scientifiques et aux ingénieurs de développement une grande quantité d'informations sur les paramètres acceptables de distorsion de l'entrée d'air à appliquer à l'intégration de l'admission de la cellule, sur les techniques de calcul pour prévoir l'influence de la distorsion d'entrée d'air sur les performances des moteurs et des compresseurs, sur la détection de la distorsion d'entrée d'air et sur les études expérimentales de l'instabilité des moteurs et de leurs réponses à la distorsion de l'écoulement; ces informations actualiseront, en tenant compte du niveau actuel de la technique, les méthodes et les données signalées dans les Symposiums précédents et en particulier dans la 46ème Réunion du PEP (Septembre 1975) sur 'Les phénomènes transitoires dans les turbomachines', et dans le Cycle de Conférences AGARD No.72 (Novembre 1984) sur 'L'instabilité des moteurs provoquée par le distorsion'.

Cette réunion a étudié plus particulièrement les sujets suivants: adaptation de la conception de l'entrée d'air à la conception du moteur; réponse aérodynamique d'une turbomachine à la distribution de pression et de température en fonction du temps; technique d'essais pour simuler les effets de la distorsion dynamique sur la stabilité des moteurs.

PROPULSION AND ENERGETICS PANEL

Chairman: Professor H.Wittenberg
Delft University of Technology
Dept. of Aerospace Engineering
Kluyverweg 1
2629 HS Delft, Netherlands

Deputy Chairman: Dr W.L.MacMillan
EMF Communication Satellite
Defence Research Establishment
Ottawa
Ontario, Canada K1A 0ZA

PROGRAMME COMMITTEE

Professor D.Dini (Chairman)
Universita degli Studi, Istituto di Macchine
Via Diotalvi 3, 56100 Pisa, Italy

M. l'Ing. Princ. de l'Arm. P.Ramette
Direction des Recherches, Etudes et Techniques
26 Boulevard Victor
75996 Paris Armées, France

Professor R.Jacques
Ecole Royale Militaire
30 Avenue de la Renaissance
1040 Bruxelles, Belgium

Professor H.I.H.Saravanamuttoo
Chairman, Mechanical and Aeronautical
Engineering — Carleton University
Ottawa, Ontario K1S 5B5, Canada

Mr A.A.Martino
Manager, Systems Development and
Evaluation Group — Code PE 2
Naval Air Propulsion Center, PO Box 7176
Trenton, New Jersey 08628, US

Ir. J.P.K.Vieghert
National Aerospace Laboratory
PO Box 90502, Anthony Fokkerweg 2
1006 BM Amsterdam, Netherlands

Mr N.A.Mitchell
Rolls Royce Ltd., PO Box 3
Filton, Bristol BS12 7QE, UK

Professor G.Winterfeld
DFVLR — Institut für Antriebstechnik
Postfach 906058; 500 Köln 90, Germany

HOST NATION COORDINATOR

Professor L.Fottner
Universität der Bundeswehr, Institut für Strahlantriebe
Werner Heisenbergweg 39, 8014 Neubiberg, Germany

PANEL EXECUTIVE

Dr E. Riester
AGARD-NATO
7 rue Ancelle
92200 Neuilly sur Seine
France

ACKNOWLEDGEMENT

The Propulsion and Energetics Panel wishes to express its thanks to the National Delegates from the Federal Republic of Germany for the invitation to hold this meeting in Munich, and for the facilities and personnel which made the meeting possible.

CONTENTS

| | Page |
|--|-----------|
| RECENT PUBLICATIONS OF PEP | iii |
| THEME | v |
| PROPULSION AND ENERGETICS PANEL | vi |
| TECHNICAL EVALUATION REPORT by D.D.Williams | ix |
| | Reference |
| REVIEW OF CURRENT KNOWLEDGE ON ENGINE RESPONSE TO DISTORTED INFLOW CONDITIONS by D.D.Williams | 1 |
| <u>SESSION I – UNSTEADY FLOW AND VALIDATION OF EMPIRICAL DISTORTION PARAMETERS</u> | |
| COMPATIBILITE ENTRE D'AIR-MOTEUR: IMPACT DES METHODES THEORIQUES ET EXPERIMENTALES par M.Goutines et H.Joubert | 2 |
| NEW TRENDS IN INTAKE/ENGINE COMPATIBILITY ASSESSMENT by F.Aulehla and D.M.Schmitz | 3 |
| EFFECT OF STEADY STATE INLET TEMPERATURE DISTORTION ON THE ENGINE COMPRESSOR FLOW by W.Koschel, H.Künkler and H.Tönskötter | 4 |
| <u>SESSION II – COMPUTATION TECHNIQUE FOR ENGINE/COMPRESSOR PERFORMANCE PREDICTIONS OF DISTORTED INFLOW</u> | |
| VISCOUS ANALYSES FOR FLOW THROUGH SUBSONIC AND SUPERSONIC INTAKES by L.A.Povinelli and C.E.Towne | 5 |
| Paper 6 withdrawn | |
| CALCULATIONS OF INLET DISTORTION INDUCED COMPRESSOR FLOWFIELD INSTABILITY by T.P.Hynes, R.Chue, E.M.Greitzer and C.S.Tan | 7 |
| ETUDE NUMERIQUE DE LA TRANSMISSION D'UNE DISTORSION DANS UN COMPRESSEUR AXIAL par G.Billet, P.Chevalier et P.Laval | 8 |
| CALCUL DU COMPORTEMENT D'UNE GRILLE D'AUBES EN REGIME DE DECROCHAGE DYNAMIQUE par P.Gillant, P.Sagnes et J.P.Ollier | 9 |
| IMPROVEMENT OF THE PARALLEL COMPRESSOR MODEL BY CONSIDERATION OF UNSTEADY BLADE AERODYNAMICS by M.Lecht | 10 |
| <u>SESSION III – DISTORTED INFLOW DETECTION</u> | |
| Paper 11 withdrawn | |
| TURBOFAN ENGINE POST-INSTABILITY BEHAVIOR – COMPUTER SIMULATION, TEST VALIDATION, AND APPLICATION OF SIMULATIONS by W.G.Steenken | 12 |

| | Reference |
|--|------------------|
| TRANSMISSION OF INLET DISTORTION THROUGH A FAN by J.E.Flitcroft, J.Dunham and W.A.Abbott | 13 |
| EXPERIMENTAL INVESTIGATION ON SMALL TURBOPROP BEHAVIOUR UNDER COMPRESSOR ROTATING STALL FOR DIFFERENT INLET FLOW CONDITIONS by S.Colantuoni and G.Liotti | 14 |
| SUMMARY OF INVESTIGATIONS OF ENGINE RESPONSE TO DISTORTED INLET CONDITIONS by T.J.Biesiadny, W.M.Braithwaite, R.H.Soeder, and M.Abdelwahab | 15 |
| <u>SESSION IV – EXPERIMENTAL INVESTIGATIONS OF ENGINE INSTABILITY AND RESPONSE TO FLOW DISTORTION</u> | |
| UNSTEADY INLET DISTORTION CHARACTERISTICS WITH THE B-1B by C.J.MacMiller and W.R.Haagenson | 16 |
| DETERMINATION EXPERIMENTALE DES LOIS DE TRANSFERT DE PERTURBATIONS A LA TRAVERSEE D'UN COMPRESSEUR AXIAL par J.Huard | 17 |
| DEVELOPMENT OF INTAKE SWIRL GENERATORS FOR TURBO JET ENGINE TESTING by H.P.Genssler, W.Meyer and L.Fottner | 18 |

TECHNICAL EVALUATION REPORT

by

D.D. Williams
Rolls-Royce plc
PO Box 3
Filton
Bristol BS12 7QE
UK

SUMMARY

The 68th (A) Specialist Meeting of the PEP was held to debate state-of-the-art developments in engine response to intake distortion. The meeting was well attended and the principal objectives were met. Aeromechanical aspects of intake/engine compatibility were not covered.

Recommendations for specific technical work items arising from the presentations and discussions held at this meeting and from the subsequent oral evaluation are made (Section 3). Four follow-up PEP Specialist meetings to take place notionally in a five- to ten-year period can be considered. These cover:-

- Intake Flow Numerical Computation
- Compressor Aeromechanical Response
- Engine Stability Computer Modelling
- Statistical Aspects of Surge and Post-Stall Modelling

The last proposal has wide ramifications, extending beyond the interface flow — distortion issue.

General observations are that liaison should be maintained with other organisations working in the distortion field, eg. the S 16 Committee of the SAE. Proposals for work on developing intake total-temperature distortion methodology have been deferred pending developments in other areas.

1. INTRODUCTION

Intake/engine aerodynamic compatibility continues to be a major interface operability consideration affecting the design and development of military aircraft propulsion systems. In the decade or so since AGARD Lecture Series 72 on "Distortion-Induced Engine Instability", held in November 1974, and the 46th Propulsion and Energetics Panel Meeting held on "Unsteady Phenomenon in Turbomachinery" in September 1975, intake flow distortion, in a variety of forms, has become increasingly a key technical and formal issue as regards its effects on turbomachinery design, performance, stability and mechanical integrity.

The principal problem remains that of engine stability or surge. As a result, it is the destabilising aspect of intake distortion that is prominent in the design specifications of the intake, engine components — notably the compressors, and the intake and engine control systems. General guidelines to engine stability assessments have been developed and great progress has been made in establishing improved empirical correlations, analytical methods and numerical computer codes. Novel forms of distortion affecting propulsion system operability have been encountered during flight development.

The increased cost of ground testing (rig, wind-tunnel, engine) and flight testing has led to a further need to improve prediction methods to provide reliable assessments of the compatibility problem and anticipate solutions earlier in the design phase of a project. The rapid increase in the power of digital computers has led to the need to better understand the important underlying physical parameters governing surge, for example, to be able to interrogate the computer and to make best practical engineering use of the large numerical data base generated and minimise its costs.

It was therefore timely that the PEP 68th (A) Specialists' Meeting had engine response to distorted inflow conditions as its theme. The meeting objectives were to review the state-of-the-art and provide research scientists and development engineers with a broad information base on:-

- Acceptable Flow Distortion Parameters
- Flow Distortion Measurement
- Computational Techniques
- Experimental Engine-Response Investigations.

It was the intention that particular attention be paid to inlet/engine matching, engine stability and aeromedical response to total-pressure and temperature distortion and to test techniques for simulating the effects of dynamic distortion on engine stability.

This report summarises the papers presented (Section 2) and assesses them against the above aims using as a basis the presentation and discussion material together with the results of the oral evaluation. The main conclusions and recommendations for further work are presented with suggestions for future distortion-related PEP Specialists' Meetings (Section 3).

2. CONTENT OF MEETING

The two-day meeting was organised in four sessions covering 16 papers. There were approximately 163 officially-registered attendees from a number of universities, research establishments, industry (airframe, engine) and government bodies. Attendance was excellent at all sessions.

2.1 Introduction

The introductory overview of the state of the art discussed total-pressure distortion and other forms of intake disturbance such as planar-wave distortion, swirl and total-temperature distortion, concentrating on developments in time-variant total-pressure methodology in the context of engine stability. Attention was drawn to the comprehensive guidelines covering the empirical approach to distortion description (parameter formulation), data acquisition and processing, performance and surge correlation and assessment procedures provided in SAE publications ARP 1420 and AIR 1419. Semi-analytic dynamic distortion response, spool-coupling aspects of engine distortion response and statistical aspects of surge were stressed.

Principal conclusions were that good progress has been made since AGARD Lecture Series 72 in a number of key areas covered in the session papers. Extensions of methods to the new compact, high-duty engines for use in high-capability military aircraft are needed, particularly in the development of analytical and computer methods having improved instability onset criteria. The relevance of other forms of intake distortion to a specific propulsion system development needs to be identified earlier.

2.2 Technical Presentations

Session I — Unsteady Flow and Validation of Empirical Distortion Parameters

M.Goutines (SNECMA, Fr) reported work carried out at SNECMA to develop clean-flow surge line predictions and numerical distortion-response codes. The experimental work described a state-of-the-art, time-variant total-pressure data acquisition system and a simple means of generating and simulating dynamic pressure distortion.

It was concluded from parametric studies that compressor inlet guide vanes, low-aspect-ratio blades and small blade-row gaps increase stall margin and reduce compressor distortion sensitivities.

F.Aulehla (MBB, Ge) discussed low-cost methods for synthesising time-variant total-pressure distortion and the effects of intake swirl on surge and blade/disc vibration. Some aspects of temperature distortion due to VSTOL hot-gas reingestion were reported.

It was recommended that synthesis methods or steady-state correlation methods be considered as a basis for estimating time-variant total-pressure distortion for preliminary design work, albeit with increased uncertainty and need for greater margins.

The effectiveness of fences/baffles as simple, effective solutions to swirl problems was pointed out in the paper and during the ensuing discussion.

H.Künkler (IABG, Ge) described a steady-state temperature distortion prediction model, extending the two-compressors-in-parallel method, together with results from tests on a single-spool jet engine with total-pressure and temperature distortion.

Session II — Computation Techniques for Engine/Compressor Performance Predictions of Distorted Flow

L.A.Povinelli (NASA LeRC, US) dealt with the important topic of modelling intake flow. His paper presented the results of applying a parabolised Navier-Stokes (PNS) code to various subsonic curved inlet ducts and a 2-D hypersonic mixed-compression Mach 5 inlet. Total-pressure and secondary-flow predictions, including effects of vortex generators, were compared favourably with experimental data.

The importance of total boundary layer development on all walls was stressed. The model is thought to be capable of predicting swirl development in S-shaped ducts provided that one-sided flow separation at diffuser entry can be specified adequately. Experimental confirmation of entry conditions would be difficult. The limitations of the PNS model in regions of strongly-separated flow were discussed. Further work in this area is desirable.

T.P.Hynes (Camb U, UK) introduced a fundamental 2-D fluid-dynamic stability analysis, extending that presented by Greitzer and Hynes at the 1984 Winter Annual Meeting of ASME. The eigenvalue model predicts flow instability onset in low-speed multistage axial compressors for long-wavelength circumferentially-distorted inlet flow. Main conclusions were

that an "integrated-mean-slope" instability-onset criterion may be used for distorted flow wherever the dynamics of the compressor can be regarded as independent of the operating environment. This is valid except when system-dependent surge and compressor stall-cell frequencies coincide, when the tendency to instability increases.

The analysis provides estimates of compressor sensitivity (rate of loss of surge pressure ratio with pressure distortion level). It enables the validity of the two-compressors-in-parallel method to be examined in terms of compressor design variables.

P.Laval (ONERA, Fr) gave a comprehensive mathematical description of a major numerical code for predicting compressible 3-D flow development through turbomachinery. Numerical results obtained from a CRAY-1S, operated in the vector mode, were compared favourably with experimental data obtained from tests of a single-stage low-speed compressor operating with a steady, mixed circumferential/radial total-pressure distortion at entry. Developments of the code are in process.

A film was shown to illustrate the numerical convergence of the program to an asymptotic solution.

J.P.Ollier (Soc Bertin, Fr) provided an overview of a singularity method coupled with an unsteady boundary-layer calculation for modelling unsteady subsonic cascade flow in unstalled and dynamic-stall regimes. The short-term aim of the work is to provide a method for assessing the distortion sensitivity of multistage axial compressors.

Good numerical results have been obtained for steady flow and unsteady attached flow but quantitative validation is proving difficult due to the paucity of relevant experimental data. For dynamic stall, the studies have shown the importance of correct modelling of the flow in the neighbourhood of the separation point.

M.Lecht (DFVLR, Ge) has studied ways of improving the compressors-in-parallel model for surge-line-loss prediction due to circumferential total-pressure distortion using a simple rotor dynamic-response model based on Melick and Simkin, together with a $C_{L,max}$ overshoot formulation. Comparisons with experiment for single-stage compressors show that distorted-flow performance predictions can be substantially improved though some beyond-stall extrapolation difficulties arise.

Session III — Distorted Inflow Detection

W.G.Steenken (GE, US) addressed the important question of engine post-stall behaviour. The results of a whole-engine, low-frequency (order 50 Hz) computer model of a mixed-flow augmented turbofan engine were described briefly in relation to engine test validation. Circumstances typifying the development of cyclic surge or stagnation stall were described.

J.E.Flittcroft (RAE, UK) presented the results of research tests on a three-stage, axial-flow fan performed to investigate the effects of total-pressure distortion and inlet bulk swirl on fan distortion tolerance and its distortion-transfer characteristics. The results showed that fan contra-rotational swirl caused a severe increase in unsteady distortion at the hub of the fan at exit, particularly when associated with a steady circumferential total-pressure distortion at inlet, due to the development of rotating stall in the hub region. Theoretical modelling met with only limited success.

S.Colantuoni (Alfa Romeo, It) dealt with an experimental investigation of compressor rotating stall development and noise in the A 318 turboprop engine.

T.J.Biesiadny (NASA LeRC, US) reviewed the wide-ranging experimental and modelling work carried out by NASA on engine total-pressure and temperature distortion response. Descriptions of the LeRC hydrogen burner for generating steady-state and transient total-temperature distortions and of the air-jet generator for producing total-pressure distortion were described. Experimental results for spatial temperature distortion and temperature ramps; for spatial, rotating and pulsed total-pressure distortion and for combined pressure and temperature distortion were presented in terms of compressor sensitivities and distortion transfer. The results from refined parallel-compressor models were described as successful in accounting for the important features of the test results.

Session IV — Experimental Investigations of Engine Instability and Response to Flow Distortion

C.J.MacMiller (Rockwell, US) summarised the results of extensive investigations conducted to determine the B1-B aircraft intake performance and distortion characteristics. Planar-wave total-pressure distortions at discrete frequencies were encountered as a result of intake duct and ECS pre-cooler resonances and nose-gear wake ingestion. Several general observations were made:

- Every effort should be made to identify novel forms of distortion and their impact on engine stability and structures prior to flight development.
- The problem of engine response to combined planar and spatial time-variant distortion is not well understood and needs to be addressed. Analytical methods need to be developed.
- The engine-face acoustic termination should be simulated in small-scale intake model testing where significant planar-wave and duct resonances are anticipated to occur. (Means for accomplishing this have been identified.)

J.Huard (ONERA, Fr) dealt with experimental work on the distortion transfer through a single stage. The work is aimed at establishing a data base using Fourier analysis of the distortion profiles for the development of an unsteady semi-actuator disc model.

H.P.Genssler (MBP, Ge) described methods for generating bulk- and twin-swirl for future Larzac engine testing. Swirl pattern results from small-scale development tests show good agreement with design goals.

2.3 Discussion

The meeting content reflected well the progress that has been made in developing intake/engine distortion technology. It succeeded in achieving its principal objectives and provided a good forum for the exchange of views. Turbomachinery distortion-response aspects were well covered with the exception of aeromechanical questions such as compressor rotor-blade forced vibration and flutter.

The material can be grouped into four main categories: Intake Distortion Sources, Compressor and Engine Response (Prediction, Experimental), Test Techniques and Distortion Consequences. A grouping is shown in Table 1.

The coverage of intake distortion sources was good. The four contributions dealt with time-variant spatial total-pressure distortion (state of the art) and new approximate methods of treatment. More importantly, new forms of distortion: planar-wave total-pressure fluctuations and swirl were reported, pointing up the need to develop methods for anticipating these early enough to avoid encountering them in flight development. More attention needs to be paid to the question of engine simulation during small-scale intake wind-tunnel tests and to the development of appropriate intake distortion simulators at full scale.

The discussion of interface distortion parameters was somewhat disappointing, being limited to the reporting, without commentary, of established spatial total-pressure distortion guidelines described in SAE Aerospace Recommended Practice, ARP 1420, and Air Information Report, AIR 1419. Little progress appears to have been made in the three to eight years since these publications and, clearly, there is a need to consider the application of these recommendations and address mixed forms of intake distortion. Again, very little progress appears to have been made in developing temperature-distortion parameters and establishing and validating compressor temperature-distortion sensitivities. This represents a technology void which is surprising, recalling that HP compressors operate in the mixed pressure and temperature distortion field delivered by the LP compressor. The problem is being addressed currently by the S 16 Committee of SAE.

There was a strong emphasis on engine distortion response via fifteen relevant contributions. These were about equally divided between prediction and experimental topics, several authors contributing to both.

In the test-techniques section, methods for total-pressure, swirl and total-temperature distortion simulation were addressed. The latter is particularly relevant to the hot-gas-reingestion problem of STOL and ASTOVL aircraft and further work in this area should be encouraged. The two papers dealing with the consequences of instability reviewed the important subject of post-stall engine modelling (surge, stagnation stall) and a particular turboprop rotating stall experience.

A welcome feature was the emphasis on the development of theoretical, semi-analytic and numerical codes and their validation. Major and impressive progress has been made since the last AGARD review in the development and application of methods to the distortion problem, on both intake and engine sides of the interface. The development of prediction methods is important to anticipate problems earlier in propulsion system design, prior to component testing, to allow effective design action to be taken and reduce intake wind tunnel, compressor rig, and engine bench and ATF test costs. Developments may be expected to be very rapid so there is a near-term need to provide practical focii for intake/engine aerodynamic compatibility aspects of the work through clear problem statements. Priorities need to be stated if best use is to be made of the enormous computer data output that will result. As examples, intake Navier-Stokes codes need to be capable of dealing with separation and estimating time-variant total-pressure distortion patterns and parameters, swirl distortions in S-shaped ducts and axial-mode acoustic resonance. Turbomachinery codes need to address stage, compressor and system instabilities by means of soundly-based criteria for predicting instability onset. Much work needs to be done to ensure that the numerical stability limit is a true estimate of the aerodynamic instability.

An excellent start from fundamental principles has been made for low-speed, high hub-tip-ratio compressors in the 2-D incompressible analysis of Hynes and Greitzer. This approach needs to be extended to compressible flow and, as anticipated by the authors, to multiple components and the overall system. Clearly, a "3-D version" is required. It is still not clear how the Greitzer B parameter is to be used to help assess the stability of a military turbofan compression system. A related issue is that of the flow coupling between the spools of a multispool engine. This subject has not received sufficient attention despite the fact that it has for some time now been recognised that compressor behaviour, in particular its distortion response, is strongly dependent on the system in which it operates, when close-coupled to other components within that system.

A refreshing aspect was the attempts by several contributors to develop clearer physical insight and develop simpler, approximate theories for surge prediction, in particular to extend the two-compressors-in-parallel (2CLL) model through the inclusion of rotor unsteady response terms. Two approaches were evidenced involving blade-row channel inertia modelling and aerofoil unsteady response. These approaches need to be reconciled. This work again emphasised the need to pay careful attention to compressor boundary conditions.

There was very little discussion of structural and mechanical integrity aspects of propulsion system development, either from the intake stressing viewpoint, eg, response to engine surge loads, or compressor aeromechanical response, as may be expected perhaps from a meeting of this nature and the time constraints. Intake/engine interface distortion parameters to describe compressor rotor-blade forced vibration and flutter differ from those appropriate to surge and performance in having a strong Fourier-harmonic content. The blade-row modelling discussed at some length at the meeting was restricted to rigid blades and is not appropriate. Engine aeromechanical problems are encountered in propulsion system development and it is recommended that a separate forum be held to review this aspect of compatibility.

The meeting was reminded of statistical aspects of the surge problem and the implications for assessment procedures and design. The overall engine stability question depends on many potentially destabilising effects, other than intake distortion. Such effects include for example compressor surge margin loss due to power off-take and Reynolds number. Some of the effects are random in nature and the arithmetic summation of all effects leads to large, often unrealistic, surge margin requirements. More work is needed in this area.

The consequences of exceeding the engine stall limit (surge, stagnation stall) can now be modelled and procedures should be evolved through such whole-engine codes to estimate the wider operational implications of stall. Conclusions from such studies may well influence intake/engine compatibility considerations and design decisions.

3. CONCLUSIONS AND RECOMMENDATIONS

A number of specific recommendations for further work can be considered as an outcome of this specialist meeting.

Intakes

Develop numerical flow-prediction methods for sub- and supersonic intake diffusers capable of modelling separation, swirl development and acoustic resonances. Codes should aim to calculate distortion parameters.

Pursue simplified, time-variant, total-pressure, spatial-distortion measurement methods for use in the early stages of propulsion system design and development.

Develop temperature-distortion technology with improved full-scale simulation techniques and model/full-scale scaling rules.

Investigate the need for and means of simulating the presence of the engine during small-scale intake wind-tunnel tests.

Turbomachinery

Pursue 2-D flow stability analyses and extend to compressible flow. Applicability and limitations to low-hub-tip-ratio compressors (2-D/3-D aspects).

Consolidate circumferential-distortion, dynamic-response estimation methods and reconcile alternative channel/blade approaches.

Develop numerical codes with improved instability onset criteria.

Develop spool-coupling methodology in overall engine distortion-tolerance assessments.

Model planar-wave distortion with coupled time-variant spatial distortion.

Develop models to account for the destabilising effects of intake swirl in the presence of total-pressure distortion.

Pursue statistical aspects of surge.

Develop whole-engine models to estimate post-stall engine behaviour and evaluate control strategies.

Address aeromechanical response technology: develop relevant distortion parameters; methods for the prediction and correlation of compressor rotor blade (blade/disc) forced vibration and flutter.

It is anticipated that the above topics provide, variously, tasks appropriate to the range of AGARD participating organisations over a notional five to ten-year time span. Ongoing research and project-related efforts within this time period will mature and it is important to maintain liaison with appropriate bodies, for example the S 16 Committee of the SAE.

Recommendations for four follow-up PEP specialist meetings are suggested:-

1. Intake Flow Numerical Computation
2. Compressor Aeromechanical Response
3. Engine Stability Computer Modelling
4. Statistical Aspects of Surge and Post-Stall Computer Modelling.

The rationale underlying these suggestions is the need to assemble a wider range of informed opinion on specific aspects of the inlet/engine compatibility problem to provide a better appreciation of technological capability and prospects in the various specialist fields. Pre-requisite is the need to maintain communication across the interface. Sufficient information was generated at this specialist meeting to set appropriate guidelines.

| GROUP | | PAPER NUMBERS | AUTHORS |
|---|--|--|--|
| INTAKE DISTORTION SOURCES | | 1 3 5 16 | WILLIAMS (RR) AULEHLA - SCHMITZ (MBB) POVINELLI (NASA) MACMILLER (ROCKWELL) |
| COMPRESSOR AND ENGINE RESPONSE | | | |
| | PREDICTION (Analytic/ Numerical) | 1 2 4 7 8 9 10 | WILLIAMS (RR) GOUTINES - JOUBERT (SNECMA) KÖSCHEL - KÜNKLER - TÖNSKOTTER (RWTH, IABG) HYNES - CHUE - GREIZER - TAN (CAMP' U, MIT) LAVAL - BILLET (ONERA) GILLANT - OLLIER - SAGNES (SOC' BERTIN) LECHT (DFVLR) |
| | EXPERIMENTAL | 1 2 4 8 10 13 15 17 | WILLIAMS (RR) GOUTINES - JOUBERT (SNECMA) KÖSCHEL - KÜNKLER - TÖNSKOTTER (RWTH, IABG) LAVAL - BILLET (ONERA) LECHT (DFVLR) DUNHAM - FLITCROFT BIESIADNY (NASA) HUARD (ONERA) |
| TEST TECHNIQUES | | 2 15 18 | GOUTINES - JOUBERT (SNECMA) BIESIADNY (NASA) MEYER - FOTTNER - GENSSLER (UNIV' B, MBB) |
| DISTORTION CONSEQUENCES (MISCELLANEOUS) | | 12 14 | STEENKEN (GE) COLANTUONI (ALFA ROMEO) |

DISCUSSION

Ph. Ramette, Fr

What are the possible limitations of the next generation of computers on our ability to carry out the intake computational work?

Author's Reply:

I am not qualified to answer the question. The computer may be expected to have a powerful role in future compatibility work provided the right problems are put to it. We have to be selective in what we do and how we cope with the information generated.

F. Aulehla, Ge

1. I suggest that we should concentrate on developing simplified time-variant total-pressure distortion methods, starting perhaps from the steady half-lambda correlation and distinguishing unseparated and separated flow cases.
2. I cannot see how we can readily simulate the engine during intake model tests. Would not a mini-engine, for example CMAPS, be unrepresentative of later engines?

Author's Reply

It would be difficult to simulate a particular engine, especially over the range of throttle settings. One should consider provisioning means to simulate the acoustic termination when there is reason to believe duct resonance could be a problem.

AD-P005 462

REVIEW OF CURRENT KNOWLEDGE ON ENGINE RESPONSE TO DISTORTED INFLOW CONDITIONS

by

D D WILLIAMS
CHIEF OF INSTALLATION TECHNOLOGY
ROLLS-ROYCE plc
PO BOX 3
FILTOW
BRISTOL BS12 7QE

↓
This paper

SUMMARY

The purpose of this paper is to provide an introductory overview to the 68th PEP Specialist Meeting. It reviews some current aspects of time-variant, spatial total-pressure distortion and other forms such as swirl, static-pressure distortion, planar-wave perturbations of total pressure, and total temperature distortion. Engine response considerations include the influence of engine spool coupling on stability, developments in the modelling of total-pressure circumferential extent effects, and swirl/total-pressure interactions. Guidelines for the formulation of distortion descriptors and performance/stability assessments are reviewed.

LIST OF SYMBOLS

| | |
|---------------|--|
| a | Constant |
| AIP | Aerodynamic Interface Plane |
| Ap | Total-Pressure Distortion Attenuation Ratio |
| APD | Amplitude Probability Density |
| b | Constant |
| bx | Blade Chord |
| CN | Coupling Number |
| Cp | Static Pressure Coefficient |
| DC(60), DC(θ) | Circumferential Total-Pressure Distortion Coefficients |
| E | Extent |
| HGR | Hot Gas Reingestion |
| HPC | High-Pressure Compressor |
| H/T | Compressor Hub: Tip Ratio |
| JPT | Engine Jet-Pipe Temperature |
| K | Compressor Sensitivity |
| LPC | Low Pressure Compressor |
| M | Mach Number |
| n | Harmonic Number |
| N | Compressor RPM |
| l | Non-Dimensional Length, x/\bar{r} |
| P | Static Pressure |
| P | Total Pressure |
| r | Radius |
| R | Compressor Pressure Ratio |
| U | Compressor Wheel Speed |
| S | Compressor Sensitivity |
| t | Time |
| T | Total Temperature |

| | |
|--------------------------------|--|
| TC(120), TC(0) | Temperature Distortion Coefficients |
| W, WA | Compressor Airflow |
| x | Axial Length |
| 2CLL | Two Compressors In Parallel |
| Superscripts | |
| ($\bar{\quad}$) | Average |
| ($\bar{\quad}$) ⁻ | Low Total-Pressure Sector |
| ($\bar{\quad}$) ['] | Perturbation |
| Subscripts | |
| av | Average |
| c | Circumferential |
| Clean | Undistorted, Steady-State Flow Conditions |
| CRIT | Critical Sector Angle |
| INST | Instability Onset Value |
| L | Low-Pressure Compressor |
| m | Maximum |
| M | Constant Corrected Mass Flow |
| N | Constant RPM |
| op | Operating Value |
| R | Radial |
| Su | Surge Value |
| T,t | Total Conditions |
| Greek | |
| γ | Blade Stagger Angle |
| Δ | A Change |
| η | Intake Total-Pressure Recovery Factor |
| θ | Angular Extent or Relative Total Temperature |
| λ | Blade Unsteady Response Parameter |
| ρ | Gas Density |
| σ | Standard Deviation |
| τ | Blade Row Unsteady Parameter |
| ϕ | Axial-Velocity/Wheel Speed Ratio |
| ψ | Non-dimensional Compressor Pressure Rise |

1. INTRODUCTION

In the decade or so following AGARD Lecture Series 72 on Distortion-Induced Engine Instability, held in 1974, and the 46th PEP meeting on Unsteady Phenomena in Turbomachinery in 1975 (Refs 1,2), a great deal of progress has been made on technical, procedural and organisational aspects of the intake/engine flow compatibility problem. This is reflected in some seven relevant papers presented at the 60th PEP Symposium held in 1982. (Ref.3).

A consensus has been reached on the elements needed to formulate empirical total-pressure distortion parameters or descriptors at the Intake/Engine Interface Plane (AIP). A methodology for the treatment of time-variant, spatial distortion has been consolidated into general, practical, engineering guidelines, (Refs 4,5). Other forms of intake flow distortion, such as swirl and so-called static-pressure distortion have been identified

and treated. The problems of planar wave or "in-phase" total-pressure and total-temperature distortions have received attention, as has that of time-variant, spatial total-temperature distortion at the AIP - an important topic for future ASTOVL or VSTOL aircraft. Mathematical and computer modelling of intake flows and the distortion response of engine compression system components and the engine itself have advanced in several major respects and are being extended into the post-stall regime; these developments emphasising system unsteady dynamics. The importance of assessing the effects on engine stability of flow coupling between the spools of a multi-spool engine has been recognised and a methodology developed to account for it. A further development has been the implementation of statistical surge-margin budgeting methods.

The distortion effort continues to be driven by engine performance and, predominantly, stability aspects of the compatibility problem, dealt with here. Aeromechanical issues such as rotor-blade forced response and distortion effects on flutter boundaries appear to have received less attention so that a consensus, state-of-the-art methodology has yet to emerge. (Discussions of distortion-induced blade vibration and the effects of intake conditions on supersonic unstalled flutter in turbofan engines are provided in Refs 6 and 7).

Most significant has been the formulation of procedural guidelines to aid the construction of intake and engine design and development programmes and of performance/stability assessments appropriate to an engineering development. Practical recommendations for intake/engine interface instrumentation, test and distortion-data management exist (Refs 4,5).

Not least important is the improvement that has taken place in the organisation of the effort on compatibility. Closer collaboration between airframer, engine manufacturer, research establishments and procurement agencies has taken place - in some cases through the formation of project compatibility groups, increased international exchanges through standing committees, such as S16 of SAE, and symposia. A valuable development has been the increased involvement of the Universities and Technology Institutions in aerospace engineering problem solving, complementing fundamental research.

A result of the technology and managerial developments has been the progressive elevation of intake flow distortion to be an active consideration in propulsion system risk assessment in the early design phases of a project. It is the purpose of this paper to provide an overview of some of these developments, as best they are perceived by the author.

2. TOTAL-PRESSURE DISTORTION

A significant development in the technology of intake/engine compatibility has been the establishment of general guidelines for assessing the effects of time-variant, spatial P-distortion. With the publication of SAE Air Information Report, AIR 1419, in May 1983, supplementing Aerospace Recommended Practice, ARP 1420, published earlier, a definitive engineering methodology is available. This describes AIP distortion descriptors, methods for assessing engine performance and stability changes, and methods for conducting experimental programmes. Data acquisition, processing and management guidelines are provided.

2.1 DISTORTION DESCRIPTION

Intake steady-state and time-variant total-pressure measurements are used to define engine-face, average total pressure (recovery factor) for performance assessment and spatial-distortion components for correlating the effects of distortion on performance and stability. As the performance question is predominantly a time-average one, it is still engineering practice to use steady-state measurements to describe it. The additional dynamic measurements are used in the stability context.

The evolution of distortion descriptors and their components from those reviewed in LS 72 has stemmed from an engineering consensus derived from a thorough co-operative effort involving a lot of applications experience. Whilst no universal parameter has emerged or is thought possible for the general distortion case, agreement has been reached on the elements of a general parameter defined from pressure-probe measurements in the intake. Typical full-scale rake arrangements are shown in Figures 1 and 2.

Four basic elements have been recommended (Figure 3): Circumferential Intensity, Extent and Multiple-Per-Rev elements, defined at constant radius (per ring) and a Radial Intensity Element. These are used for two purposes:-

- (i) to complement the conventional, total-pressure contour map by an element histogram displaying information related to engine performance and stability response (Figure 4).
- (ii) to construct fan and compressor surge-pressure-ratio loss (Δ PRS) correlations.

Figure 5 shows the ARP 1420 general Δ PRS-correlation format where K_c and K_r , here applied flexibly on a ring basis, represent rates of loss of surge pressure ratio with circumferential and radial distortion and the circumferential-extent and NPR elements are incorporated into these sensitivities. The principle of linear superposition has been adopted. Figure 6 provides an example of an algebraic formulation of an engine-face

distortion parameter appropriate to circumferential distortion in annular regions of the AIP. A typical surge correlation is shown.

The effectiveness of such empirical correlations, validating the methodology, may be judged from the comparison between predicted and measured loss of surge pressure ratio shown in Figure 7 for five compressors. Similar results, stemming from the co-operative effort alluded to earlier, apply for the J 85 compressor, F 101 fan, J58 compressor, F 100 fan, TF 41 fan and compressor, and for a research fan, and turbofan core and compressor, (Ref 5).

A central consideration is the identification of permissible levels of distortion for the avoidance of surge, ie, the specification of engine distortion tolerance. The erosion of surge margin may be expressed in terms of Δ PRS or in terms of a distortion descriptor compared with a limiting level of that descriptor.

A general algorithm for accounting engine performance changes using the distortion elements, analogous to the Δ PRS relationship for stability, has not emerged. This partly reflects the fact that engine performance is highly engine, control-sensor and control-system - specific. Steady-state distortion levels are usually small at important mission performance points.

Radial total-pressure distortion attenuates rapidly through a compressor as static-pressure perturbations give rise to spanwise gradients that act to even out the flow. A consequence is that radial distortion effects, particularly of the tip-low type, are almost exclusively limited to the LP compressor, as is now well established. Axisymmetric through-flow programs are well able to be adapted to investigate the steady-state problem, though much work still remains to be done to identify instability criteria for low hub/tip designs.

In practical installations the AIP distortion is a mixture of radial and circumferential elements for which, as stated earlier, a general empirical correlation method has been developed. A task facing the engine designer, however, is that of predicting the effects of distortion on the LPC surge line prior to rig test. An interesting result is shown in Figure 8 where a three-stage fan was tested with an intake distortion comprising a tip-low radial distortion having low and high levels of circumferential distortion. Predictions of the effect of the circumferential distortion using a modified two-compressors-in-parallel (2CELL) model operating on the radially-spoiled surge line produced tolerably good agreement with the experimental results. Figure 9 shows sensitivity presented as Δ PRS vs circumferential distortion level at design speed. Similar results were obtained in the speed range 80% to 100%.

Estimation methods for high hub/tip, HP compressor are quite well developed and are reasonably reliable for circumferential distortion.

Dynamic Aspects

Techniques for the treatment of time-variant spatial distortion are now well known and need little further elaboration here. There have been no significant developments to suggest that the description of the intake spatial distortion by low-pass filtering to a frequency of approximately one LP Compressor rotor revolution is seriously in error. Strictly, cut-off frequencies differ between the fan and HP compressor and should vary through their speed ranges.

Data Scaling

Small-scale model tests are the main source of intake distortion data. In order to apply results to full scale, turbulence data must be scaled correctly. Current practice is based on holding Strouhal Number and Mach Number invariant, Reynolds Number being held as high as possible consistent with wind-tunnel facility/model-scale constraints. Scaling of the statistical data is based on turbulence dissipation/dispersion concepts, (Ref 10). Data Scaling guidelines are shown in Table 1. Reference 11 provides results on the effects of scale and the presence of an engine on the flow distortion measured in a pod intake of a transport aircraft. The results emphasize again the importance of Reynolds number and flow-field interactions between components in close-coupled installations. Results for a long, combat-aircraft intake are given in Reference 12.

Time-Variant Distortion Synthesis

The acquisition of time-variant data is expensive and time consuming. During early screening of candidate inlet configurations it may not be appropriate to employ full, time-variant-distortion measurement methods. It is however highly desirable to ensure that the preferred inlet design is selected against a background of quantified flow unsteadiness as well as steady-state distortion. For this initial screening purpose a technology for synthesising time-variant distortion from local-probe steady-state and RMS pressure recordings using random number algorithms has been established (Refs 13 to 16). An array of low- and high-response probes may be incorporated into a rotatable-rake assembly. By this means, contour plots of stationary RMS and time-averaged total-pressure may be obtained readily at selected inlet operating points from which estimates of peak time-variant distortion can be made. Should regions of high local turbulence be fixed then the data acquisition system may be simplified further. The

minimum data sampling time required to ensure statistically stationary data needs to be compatible with wind-tunnel operating times and cost. This normally is a subject for agreement between airframe and engine manufacturers. Figure 10 shows an output distortion level and pattern from a RR distortion-synthesis program. Agreement with the measured peak time-variant pattern, obtained from comprehensive AIP instrumentation, is considered to be good. At higher levels of distortion, errors can occur due to the fact that cross-correlation of total-pressure between probes is required, (Ref 9). The need to incorporate cross-correlation is indicative of large turbulence eddies in the flow, symptomatic of undesirable, large-scale, flow separation within the intake.

Circumferential Extent

Much work has been done on compressor circumferential-distortion response, a key question being that of rotor relative dwell-time in the spoiled sector, ie, of reduced frequency. A recent analysis by Hynes and Greitzer for circumferentially-distorted incompressible flow (Ref 8) provides an important, original method for predicting the stability limit of high hub/tip multistage axial compressors. The calculations show from first principles that a wide range of distortions of varying extent, intensity and waveform can be correlated using the critical-sector-angle concept, " θ_{crit} ". Figure 11, reproduced from Ref 8, shows the predicted loss of stability margin with the DC (θ_{crit}) parameter for a critical sector angle of 125° , appropriate to the analysis. This finding confirms established experimental results, eg, those of Reid, (Ref 17).

The " θ_{crit} " concept provides a basis for correlating circumferential distortion in terms of an effective intensity and leads to a modified 2CLL model for engineering assessments of loss of surge pressure ratio, having a roughly unique sensitivity. In terms of the ARP 1420 circumferential intensity and extent elements, an approximate relation is:-

$$\left(\frac{\Delta P_{TC}}{P_r} \right)_{eff} = E(\theta) \left(\frac{\Delta P_{TC}}{P} \right)$$

$$\text{where, } E(\theta) = \frac{\theta}{\theta_{crit}} \quad \text{if } \theta < \theta_{crit}$$

$$= 1.0 \quad \text{if } \theta \geq \theta_{crit}$$

This type of relationship is embodied in the DPC parameter and correlation of Figure 6.

The circumferential dynamic response is determined by a relatively simple model of the blade-row channel flow, notably that of the rotor, by equating fluid accelerations through the rows to the unsteady pressure rises across the rows. A simple development of the method utilises the rotor-row unsteady response parameter, λ , and the (provisional) instability onset $IMS = 0$ criterion of Ref 8, in the modified pressure rise equation:-

$$\frac{P_{tot} - P_{tot,stat}}{\rho U^2} = \psi(\theta) - \lambda \frac{d\psi}{d\theta}$$

$$\text{where, } \lambda = \sum_{i=1}^n (T_i) \frac{U}{r} \quad \left(T_i = \frac{b_i}{U \cos \gamma_i} \right)$$

$$\text{and } IMS = \frac{1}{2\pi} \int_0^{2\pi} \frac{d\psi}{d\theta} d\theta$$

Parabolic fits to the overall compressor characteristic in stalled and unstalled regimes yield a simple semi-analytic solution for critical semi-angle in terms of the intensity and unsteady parameters:

$$\frac{P_{tot,max} - P_{tot,min}}{\rho U^2 \psi_m} \quad \text{and} \quad \frac{\lambda (a+b)}{2ab\psi_m}$$

where, circa the peak of the compressor characteristic:-

$$\text{Unstalled Regime } (\theta \geq \theta_m) : \psi = \psi_m - a(\theta - \theta_m)^2$$

$$\text{Stalled Regime } (\theta \leq \theta_m) : \psi = \psi_m - b(\theta - \theta_m)^2$$

Results from this analysis, applied to three high-speed multistage compressors, are presented in Figure 12. Agreement with empirically-derived values of the critical sector angle is good.

Values of the response term, λ , per stage appear to be reasonably constant for LP and HP compressors. For four low H/T LP compressors and seven H/T compressors examined:

λ LPC = 0.314 ($\pm 10\%$)
per row

λ HPC = 0.140 ($\pm 13\%$)
per row

This development represents an important advance in the methodology for the estimation of compressor circumferential distortion response and it is interesting to compare Figure 11 of Paper 5 of AGARD LS 72, some twelve years ago, with an output of the analysis - c.f. Figure 13 (Ref 18) and Figure 14, respectively. The form of the loss in stall margin is well predicted by the theory, (typical values of λ/a for the assumed symmetric characteristic of Figure 14 lie in the range 0 to 0.15). The critical sector angle locus lies in the range 0 to 180°.

Further generalisation can be made to relate the critical sector angle uniquely to a compressor design-variable group and to express surge sensitivity in terms of circumferential extent and this group or theta-critical. This extension allows the conditions for the 2CLL model to be valid to be examined.

2.2 SPOOL COUPLING

Traditional assessments of engine stability treat the constituent compressors of multispool engines as uncoupled, ie regard them as operating in isolation. Estimated or empirically-derived LP compressor and HP compressor rig distortion sensitivities and distortion transfer characteristics, appropriate to compressors having roughly constant exit static-pressure are utilised. The effect of AIP distortion on the HP compressor is assessed from the LP-compressor rig distortion transfer characteristics, accounting the loss of HP-compressor surge margin due to both total-pressure and temperature distortions. It has now been established that such assessments can produce serious errors in engine distortion tolerance estimates and in the diagnosis of the "critical" compressor when the compressors are closely coupled. It has emerged that compressors of aircraft gas turbine engines are mostly close-coupled in the inner (ID) or core-flow region, (Ref 19).

The spool coupling stems from the change in the LPC (upstream) compressor-exit boundary condition in circumferential total-pressure distortion when induced interspool static-pressure distortion acts to change the LPC distortion transfer characteristics and hence the LPC distortion sensitivity and HPC sensitivities to pressure and temperature distortion. As a result, the loss of surge margin of the LP and HP compressor differ from those assessed on an uncoupled basis. Distortion results from compressors tested alone have to be interpreted carefully in the engine context. Reference 19 presents a full theoretical analysis for both compressible and incompressible flows, suggesting a method for accounting for the coupling and comparing experimental results of flow-field measurements in vaned and vane-free interspool gaps.

Figure 15 shows how the estimated distortion tolerance of an engine varies with the degree of coupling and how the perception of the critical component alters. Results agree well with engine test results from ground and flight tests. Figure 16 show how the estimated and measured fan-inner total-pressure distortion attenuation varies for uncoupled (rig) and coupled (engine) conditions, (Ref 9).

The theoretical assessment of the interspool flow-field in the vane-free gap case utilised the Rolls-Royce LINEAR A and LINEAR B two-dimensional (x, θ) codes developed in conjunction with Cambridge University. The A and B codes use overall-compressor actuator discs and blade row semi-actuator discs, respectively. The flow-fields are regarded as linear. This assumption is discussed in Ref 8. Essentially, its validity lies in the fact that velocity perturbations associated with the relatively large-extent total-pressure distortions of interest are such that quadratic terms are much smaller than first-order terms so that they have little effect on the flow-field.

The static-pressure distortion induced in a vaneless interspool gap can be expressed in terms of the gap geometry as:-

$$\frac{(p')_{\text{down}}}{(p')_{\text{up}}} = \cosh^{-1} \left(\frac{nl}{\sqrt{1-M^2}} \right)$$

This static-pressure distortion ratio is independent of the compressor operating conditions.

A Spool Coupling Number (CN) ranging between a value of zero for no coupling to 1.0 for complete coupling can be defined to quantify the extent of the interaction in terms of geometry and compressor operating conditions. This may be extended to the case of vane interspool gaps, (Ref 19).

The stability calculation uses an adaptation of the 2CLL model developed for fixed-throttle or transiently-matched multispool compression systems that provides for spool coupling by means of the coupling factor. The code (PCPCN) assumes constant static pressure at HP compressor exit. It calculates the AIP distortion required to cause surge, spool surge-margin utilisation and the critical compression system component.

A good approximation to the Δ PRS sensitivity relationship with total-pressure attenuation factor for circumferential distortion is given by:

$S = 1 - A_p$

The circumferential distortion intensity is defined in Figure 3.

Results from the isolated 2CLL and PCPCM codes are shown in Figure 17, illustrating the approximation and the effect of spool coupling in reducing LP compressor attenuation and sensitivity.

At present, predictions are based on the assumption that the interspool gap (vaned or unvaned) is a high H/T annulus at approximately constant mean radius. Further developments of the coupling methodology are required to include radial terms, particularly for swan-neck inter-ducts with swirling flow where different types of flow disturbance are highly coupled and inherently three-dimensional, Ref 20.

2.3 PLANAR-WAVE DISTORTION

Planar Wave or "In-Phase" pressure disturbances represent time changes of average total-pressure or intake recovery at the AIP. Waveforms can be deterministic - ramps, spikes, periodic (sinusoidal, Fourier) or statistically random. Computer models for estimating compressor system and engine response are well developed for deterministic problems, appropriate models depending on the frequency range of interest.

Compressor models utilizing defined, matched operating lines and unsteady mass, momentum and energy or entropy conservation equations applied on a stage-by-stage basis enable compressor sensitivities to planar waves to be quantified over a wide range of disturbance frequency. Figure 18 shows typical outputs for a sinusoidal disturbance for a seven-stage HP compressor from both the Rolls-Royce COSMOS lumped-volume stage model and LINEAR B code in the frequency range 0 to 40 Hz. Compressor sensitivity is presented as ΔPRS per unit half-amplitude of the inlet total-pressure wave. The loss of surge line for a 10% amplitude sinusoid at 30 Hz is 2.5%. Compressor rematch due to engine control system response needs to be taken into account up to 5 or 10 Hz, or so. At low frequency, circa 10 Hz, the operating pressure ratio excursion is small, as illustrated in Figure 19. This reflects the fact that the wavelength of the axial-flow disturbance at this frequency is large in relation to compressor length. The computer models provide response estimates up to about 1KHz when sensitivity continues to increase due to the increased tendency for compressor exit pressure to remain constant, (Refs 21 to 25).

Turbulence-induced changes in AIP average total-pressure are random and in conventional compatibility analyses are judged to be sufficiently small to be neglected within the uncertainty of the assessment. In highly turbulent conditions, characteristic of intake separated flow or shockwave instability in supersonic intakes, pressure amplitudes are not small and a methodology for accounting for the distortion needs to be developed. In practical installations the planar-wave distortion is accompanied by time-variant spatial distortion so that the total compatibility problem becomes complex. No state-of-the-art consensus method yet exists for dealing with it. When spatial distortion levels are small and the planar-wave frequency range low, it is plausible to consider treating the problem on the basis that the in-phase component changes the operating line and the spatial component changes the surge line on an uncoupled basis, using superposition to sum the effects. When distortion levels are high, difficulties arise due to the need to account for the phase relationship between operating line and surge line excursions. The magnitude of the difficulty may be judged from Figure 20, representative of the analysis of Ref 26, where random changes in surge and operating pressure ratio are modelled as functions of time. Surge margin remaining is represented by the difference between the upper (surge) pressure ratio and lower (op line) pressure ratio. The key feature of the result is the need for correct phasing to account for surge.

Engine and compressor facilities for enabling tests with AIP planar total-pressure waves to be carried out have been established using arrays of programmed forwards-facing airjets (Example, Ref 27) or a system of rotating and stationary perforated disks (Example, Ref 28). In conducting planar wave experimental research it is important to ensure that the test assemblies do not produce spatial distortion.

The S 16 Committee of the SAE is engaged in reviewing the planar wave/spatial total-pressure distortion problem and methodology.

3. OTHER FORMS OF DISTORTION

Total-pressure distortion is not the sole form of intake distortion that adversely affects engine behaviour. Other forms can be equally or more important, alone or in combination with total-pressure distortion. It is important at the outset of a new project to identify all forms of relevant distortion to decide what needs to be incorporated into performance, stability and aeromechanical assessments.

3.1 SWIRL

S-shaped intakes with flow curvature can produce swirl at the AIP, usually of the solid-body type, due to secondary flow generated as a consequence of flow separation at intake entry. The imbalance between stream momentum in the total-pressure-defect region and the radial static-pressure gradient needed to support radial equilibrium causes transverse flow which develops into swirl. The combination of swirl, acting in the fan

contra-rotational sense, and circumferential total-pressure distortion can for some engine designs promote loss of stability, as reported in AGARD-CP-324 (Paper 20). Figure 21 illustrates the loss of stability, expressed in terms of loss of final nozzle operating range. Theoretical analysis of the flow through multistage LP compressors on a two-dimensional, stage-by-stage basis shows that total-pressure attenuation is changed due to contra swirl - largely because of changes in first-stage loading.

Experimental research on swirl generation in highly-curved intakes and on multistage fan response is under way. Figure 22 shows a schematic of an intake model being researched in the low-speed wind tunnel at Rolls-Royce. The model, adapted from that described in References 29 to 32, is S-shaped in plan view and has provision for the insertion of parallel extension pieces between front and rear bends. Instrumentation consists of pitots, wall statics and yawmeters at the planes indicated. Results from the tests (Figure 23) show that very severe solid-body bulk swirl up to 24° or more is generated at the AIP when the intake is operated at high incidence - causing lip separation and total-pressure distortion (DC(60)) growth. These results confirm those reported in References 33 and 34 for the Tornado intake, where the severity of the swirl was much less. An important feature of the results is the large improvement in the swirl characteristics effected by a side-wall fence, (Figure 22). Similar results were obtained with a cowl-lip fence. Such fences are highly effective - as first discovered during the testing reported in the above references. An unexpected result is the large reduction in DC(60) produced by the fence, due to enhanced mixing within the duct. This finding has important design implications for military intakes intended to operate at high incidence. It would appear that duct fences located near the front of the intake can provide an alternative to intake shielding measures and hence a prospect for greater design flexibility as to intake location.

3.2 STATIC-PRESSURE DISTORTION

Another form of curvature-related distortion, termed "static-pressure distortion" arises when the flow field is highly-curved at the AIP. Such distortion can arise in essentially isentropic conditions. Figure 24 presents isobars derived from stream-static and wall-static measurements in one half of a short, bifurcated intake, where total-pressure distortion was very low. Engine performance can be adversely affected, as illustrated in Figure 25 where thrust changes are expressed in terms of a static-pressure distortion parameter defined as a (max-min) pressure coefficient. The figure shows that thrust gains of approximately 3% can be achieved in constant corrected-speed operation and of 6% at constant jet-pipe temperature by eliminating the distortion. This may be achieved by small, straight extensions of the intake duct immediately ahead of the engine face. Engine-response analysis shows that the mechanism of the engine performance loss consists of a loss of corrected airflow at constant speed together with a loss of engine core efficiency that contributes to the increase in engine jet-pipe temperature. These effects can be correlated to provide a general prediction of engine performance sensitivity using core- and overall-AIP static-pressure-distortion indices similar to that illustrated in Figure 25. The resulting correlations apply to duct modifications where static-pressure distortion is reduced through duct wall-curvature changes without increase in duct length, as reported in Reference 35.

3.3 TEMPERATURE DISTORTION

The work previously reported in AGARD Lecture Series LS 72 and, in CP 324, appears still to be a fair summary of the broad aspects of engine response to temperature distortion. Developments that have taken place have encompassed better computer modelling (Refs 21, 36, 37 and 38) but little progress has been made as regards the technology for treating practical AIP distortion problems. It is anticipated that the UK/US intergovernment MOU on ASTOVL aircraft will provide increased incentive for work in this area.

In the UK, full-scale work on hot-gas reingestion aspects of ASTOVL using an early Pegasus engine, with plenum chamber burning (PCB), installed in a Harrier airframe is being carried out by Rolls-Royce under Ministry-of-Defence sponsorship. The arrangement at the test site at Shoeburyness (Figure 26) provides for defining hot-gas reingestion (HGR) characteristics in terms of AIP mean temperature rise and time-variant spatial distortion in dynamic landing manoeuvres. Anti-HGR configurations are investigated and engine tolerance to temperature distortion is being evaluated. An important objective of the work is the acquisition of data to help establish model HGR scaling laws. The first phase of testing with a low-pressure-ratio Pegasus 2A engine was completed in December 1984. Planning for tests with a higher pressure ratio Pegasus 11 engine is in hand.

Preliminary results from the Pegasus 2A programme indicate, not unexpectedly, that engine distortion response depends both on the time-rate-of-change of intake mean total temperature as well as spatial distortion. In this respect the nature of the AIP temperature distortion problem is somewhat different to that of pressure distortion. Mean temperature rise rates lie in the range 300 to 600°C per second with maximum local rates being in the range 1000 to 1500°C per second. Engine entry temperature increases of up to 150°C can occur transiently with maximum local temperature rises being about 200°C.

Temperature distortion in terms of the TC(120) parameter typically ranges from 5% to 10% transiently close to the ground in the absence of anti-HGR measures. A typical intake total-temperature distortion pattern during landing, occurring after 0.25 seconds from

HGR onset, at a front-nozzle PCB temperature of 1000°K is shown in Figure 27. The engine was surge free.

Figure 28 presents a correlation of temperature distortion at surge onset deduced from the results of Ref 39 and 40 for the TF 30-P-3 engine. The curves derive from tests where temperature distortion was simulated by hydrogen burners programmed to provide temperature ramps at various rates from 300 to 10,000°C/sec in spatial sectors of 90°, 180°, 270° and 360° extent. They show values of allowable spatial temperature distortion, expressed as $TC(\theta_{crit})$, for threshold values of mean temperature rise rate at the surge limit. A preliminary result for the Pegasus is superimposed. Further work is required to identify distortion descriptors and a viable methodology for quantifying loss of engine stability.

The S 16 Committee of the SAE is currently engaged in studying AIP total-temperature distortion to determine whether sufficient information exists to warrant formulating guidelines to a methodology for spatial distortion. Distortion elements analogous to those for total-pressure distortion (Section 2.1) could in principle form a basis for constructing ΔPRS -related descriptors.

4. ASSESSMENT PROCEDURES

Assessments of the effects of distortion on engine performance and stability take various forms according to the perceived severity of the problem. They evolve through the engine design and development process - predefinition, preliminary design, development, qualification and flight test, as more information becomes available and the intake/engine compatibility issues mature. A consensus methodology is fully described in SAE Report AIR 1419 for total-pressure distortion. This is consistent with SAE Aerospace Standard AS 681C and Recommended Practice ARP 1257 applicable to gas turbine steady-state and transient performance computer decks (Refs 41 and 42).

4.1 PERFORMANCE

The effect of distortion on performance is calculated on a steady-state or time-averaged basis and is minimal at important aircraft operational conditions. Its assessment forms part of the wider evaluation of installed engine performance and is conducted, as necessary, after a clean-flow assessment at a specific flight condition. Clean-flow assessments include the effect of flight condition, power offtake, bleed and intake recovery at the engine operating point.

Distortion assessment procedures consist of complementary synthesis and component/engine test analysis activities. Initial estimates for turbofans may use intake split-flow (core/bypass) recovery factors as inputs to the engine performance deck. Assessment appropriate to the engine development phase utilise distortion data from rig component tests and from engine bench and altitude cell tests with distortion screens. Various synthesis procedures use fan and HP compressor distorted-flow performance characteristics or flow and efficiency "deltas" as inputs into main deck or auxiliary programs that yield thrust, fuel consumption and airflow, or changes in these quantities from clean-flow performance, as outputs.

Assessments should include engine component rematch stemming from the effect of distortion on local control sensors in the engine gas path.

Performance changes due to signal errors can be large. Figure 29 shows results obtained from a turbofan bench test with an intake total-pressure distortion pattern simulated by means of a rotatable screen. The engine was controlled by a local HP turbine entry temperature sensor. Performance gains or losses occurred due to engine rotational speed changes: overspeed when the temperature sensor (T) was located circa 180°, resulting in a performance gain; underspeed with the sensor at 360°, resulting in a performance loss. These results reflect the fact that the sensor locations corresponded respectively to low and high temperature regions of the temperature distortion pattern generated at turbine entry due to the attenuation of total-pressure distortion through the compression system.

4.2 STABILITY

The major intake/engine compatibility concern continues to be engine distortion tolerance in the context of surge avoidance. As a result, significant progress has been made in developing better stability assessment procedures with improved accounting for the destabilising effects of total-pressure distortion. Intake compatibility considerations can with more confidence be included in the specification of design requirements, notably those for LP and HP compressors (geometry, surge margin) and the engine control system, earlier in the propulsion system design process. An important aspect of this process has been the increased emphasis on collaboration between airframe engine manufacturer and procurement agencies throughout all phases of the evolution.

Stability assessments are complex and "not amenable to standardised cookbook treatment" (Ref 5). The magnitude of the assessment task depends on the anticipated severity of the compatibility problem and the particular objectives appropriate to the development programme. The determination of distortion effects forms part of an engine overall stability audit(s), (Figure 30). The clean-flow assessment accounts the effects on compressor operating and surge lines of relevant engine control functions, geometry,

power offtake, bleed and Reynolds Number in fixed and variable-throttle (handling) operation. Intake-recovery effects are included and allowances for estimated engine clearances, variable-geometry and control scatter, engine-to-engine variations and in-service deterioration are included, as appropriate. Steady-state and transient performance decks are used to determine matched operating points. The distortion assessment evaluates LP and HP compressor sensitivities, distortion transfer, spool coupling, and control implications. The overall stability audit uses the results of both clean and distorted-flow assessments to provide estimates of engine distortion tolerance, net stability margin, the critical compression-system component, the aircraft operating risk and the need for any design action.

An example of an assessment output - engine distortion tolerance expressed as an AIP distortion parameter for an installed HP compressor, is shown in Figure 31. The permissible level of distortion for HPC surge avoidance is expressed in terms of Reynolds Number Index (RNI) for various engine corrected-flows and fixed power-offtake and bleed. The curves may be used with the distortion characteristics appropriate to the engine installation to evaluate fixed-throttle intake/engine compatibility throughout the flight and manoeuvre envelopes of the aircraft.

4.3 STATISTICAL SURGE MARGIN ACCOUNTING

An important development has been the growth in the recognition of the statistical nature of the surge limit. Some of the destabilising factors referred to in Section 4.2 are random or have random components. To sum their effects arithmetically would lead to unrealistically high assessments of surge margin utilisation and surge margin requirements. Statistical considerations apply to both operating and surge lines of the compressors. Factors such as engine-to-engine build scatter, control tolerances, and variable-stator setting tolerances can be regarded as essentially random, in some cases with a load bias. In-service stability margin deterioration can have both a non-random and random aspect. Figure 32 presents an example of HP compressor operating line scatter derived from bench calibrations of 76 engines from a production batch. A total of approximately 400 test points covering a range of speeds forms the statistical population. The two-sigma value of the pressure ratio scatter is 1.4%. Figure 33 shows that the pressure-ratio APD at constant corrected flow is Gaussian.

Figure 34 presents an illustrative example of a basic stability breakdown for an HP compressor operating at a fixed-throttle setting and flight condition. Assigned random and non-random factors are tabulated. The non-random factors are summed arithmetically to yield a 16.8% surge margin utilisation and the random effects are root-sum-squared to yield a 23.6% variation. The extreme requirement is 24.7%. If the available surge margin at this condition were 25% then the probability of surge would be zero. If the surge margin available were 20.4% there would be a risk that surge margin would be low by 4.3% giving a surge probability of about 0.2%, or one engine in 530, for this extreme case.

Statistical analysis provides a realistic approach to surge margin budgeting, accounting for the fact that the worst combination of all destabilising factors is rare. It supplies management with a tool to examine whether design action is warranted.

The above point-stability assessment is capable of considerable extension, beyond that appropriate to intake/engine compatibility, to projecting surge risk during a specified mission or over the whole of the flight and manoeuvre envelopes. Surge risk can be assessed as a rate, eg, number of surges per 1,000 aircraft flying hours. In-flight shut-down rate is another criterion.

By estimating the frequencies or proportions of time in a defined portion of the flight envelope, in manoeuvre, at a rated power setting or handling - dry or reheat, etc, the cumulative probability of encountering surge and hence the aircraft operational effectiveness can be estimated. Much work is needed to define appropriate statistical methods, provide reliable operational data and establish the statistical distributions of pertinent factors. Prerequisite is the need for a high degree of collaboration among all parties concerned.

The S16 committee of SAE is exploring this wide - ranging issue.

5. CONCLUDING REMARKS

This paper has attempted a review of some of the key developments that have taken place in the last ten years or so in our understanding of engine response to intake flow distortion and in methods for dealing with the problem. It has emphasised engineering aspects of inlet/engine compatibility, focusing on practical methods for quantifying engine response rather than on academic research aspects.

Good progress has been made since AGARD Lecture Series 72 on distortion-induced engine instability. The challenge for the future is considerable, encompassing the need for:

- o Extensions of methods to new compact, high-duty compression systems for use in future high-capability aircraft.
- o Analytical and economic computer methods that provide general insight as well as ad-hoc numerical solutions.

- o The development of improved instability criteria.
- o Increased emphasis on forms of AIP distortion other than spatial total-pressure distortion: temperature distortion, swirl and static-pressure distortion, planar-wave distortion; alone and in combination with spatial total-pressure distortion.
- o Development of the statistical aspects of stability accounting procedures.

Though not directly an AIP distortion-response concern this review would be incomplete if it did not mention the very important developments that have occurred in the modelling of post-instability engine behaviour (Refs 43 to 48).

The major task is the identification of conditions under which engines will "stagnate", "hang-up" or "lock-in" following stall. This important design and operational issue is still not well understood. The establishment of a method for predicting the chance of encountering stagnation stall would appear to form a natural extension of the statistical analyses of Section 4.3 and the formulation, prospectively, of design, control and operational strategies for dealing with it.

REFERENCES

- 1 AGARD LECTURE SERIES 72. Distortion-Induced Engine Instability, November 1974.
- 2 AGARD CONFERENCE PROCEEDING NO 177. Unsteady Phenomena in Turbomachinery, 46th Meeting of the AGARD Propulsion Energetics Panel, September 1975.
- 3 AGARD CONFERENCE PROCEEDINGS NO 324. Engine Handling. 60th Symposium of the AGARD Propulsion and Energetics Panel, October 1982.
- 4 SOCIETY OF AUTOMOTIVE ENGINEERS. Aerospace Recommended Practice, ARP 1420. Gas Turbine Engine Inlet Flow Distortion Guidelines, March 1978.
- 5 SOCIETY OF AUTOMOTIVE ENGINEERS. Aerospace Information Report, AIR 1419. Inlet Total-Pressure-Distortion Considerations for Gas Turbine Engines, May 1983.
- 6 DANFORTH C E Distortion-Induced Vibration in Fan and Compressor Blading. J Aircraft Vol 12, No.4 April 1975.
- 7 HALLIWELL D G Effect of Intake Conditions on Supersonic Unstalled Flutter in Turbofan Engines. J Aircraft Vol 17, No 5. May 1980.
- 8 HYNES T P The Effect of Circumferential Inlet Distortion on Compressor Stability. Winter Annual Meeting of ASME, New Orleans December 1984
- 9 GREITZER E M
- HERCOCK R G Effect of Inlet Flow Distortion on Engine Stability Paper 20 of AGARD CP 324 October 1982.
- 10 SHERMAN D A Experimental Evaluation of an Hypothesis for Scaling Turbulence Data. AIAA 71-669 June 1971
- MOTYCKA D L
- OATES G C
- 11 MOTYCKA D L Reynolds Number and Fan/Inlet Coupling Effects on Subsonic Transport Inlet Distortion J of Propulsion and Power Vol 1 No 3 May/June 1985
- 12 STEVENS C H F 15 Inlet/Engine Test Techniques and Distortion Methodologies Studies. Vol 1 Technical Discussions NASA CR 144866 June 1978
- SPONG E D
- HAMMOCK M S
- 13 MOTYCKA D L Determination of Maximum Expected Instantaneous Distortion Patterns from Statistical Properties of Inlet Pressure Data AIAA 76-705 July 1976
- 14 STEVENS C H Evaluation of a Statistical Method for Determining Peak Inlet Flow Distortion Using F-15 and F-18 Data AIAA-80-1109 July 1980
- SPONG E D
- OLIPHANT R C
- 15 BORG R A Synthesis Method for Estimating Maximum Inlet Distortion. Paper 19 of AGARD CP301 May 1981
- 16 SEDLOCK D Statistical Analysis Method for Prediction of Maximum Inlet Distortion J of Propulsion and Power Vol 1 No. 5 Sept/Oct 1985
- 17 REID C The Response of Axial Flow Compressors to Intake Flow Distortion ASME 69-GT-29 March 1969

18. MOKELKE 'I Prediction Techniques
Paper 5 of AGARD LS 72 November 1974
19. HAM C J Some Applications of Actuator and Semi-Actuator
WILLIAMS D D Disk Theory to the Problem of Intake/Engine Compatibility.
83-Tokyo-IGTC-50 October 1983
20. GREITZER E M Asymmetric Swirling Flows in Turbomachinery Annuli
STRAND T J of Engr for Power Vol 100 No.4 October 1978
21. DAVIES M W A Stage-by-Stage Dual-Spool Compression System Modelling
Technique.
ASME 82-GT-189 1982
22. CORBETT A G Mathematical Modelling of Compressor Stability in Steady
ELDER R L and Unsteady Flow Conditions.
Paper 12 of AGARD CP-177 September 1977
23. KINZEY W F An Analysis of the Influence of some External Disturbances
on the Aerodynamic Stability of Turbine Engine Axial Flow
Fans and Compressors.
AEDC-TR-77-80 August 1977
24. REYNOLDS G G Dynamic Digital Blade Row Compression Component Stability
STEENKEN W G Model. Model Validation and Analysis of Planar Pulse
Generator and Two-Stage Fan Test Data.
AFAPL-TR-76-76 August 1976
25. SCHUERMAN J A High Frequency Dynamic Engine Simulation
FISHER K E NASA CR 135313 July 1977
McLAUGHLIN P W
26. BURSTADT P L A Method to Account for Variation of Average Compressor
WENZEL L M Inlet Pressure during Instantaneous Distortion Analysis.
AIAA 76-70 July 1976
27. McAULAY J E Effect of Dynamic Variations in Engine-Inlet Pressure on
the Compressor System of a Twin-Spool Turbofan Engine
NASA TM X-2081 September 1970
28. REYNOLDS G G An Experimental Evaluation of Unsteady Flow Effects on an
VIER W F Axial Compressor.
COLLINS T P AFAPL-TR-73-43 July 1973
29. GUO R W The Swirl in an S-Duct of Typical Air Intake Proportions.
SEDDON J Aeronautical Quarterly May 1983
30. GUO R W Swirl Characteristics of an S-Shaped Air Intake with both
SEDDON J Horizontal and Vertical Offsets.
Aeronautical Quarterly May 1983
31. GUO R W Some Unsteady Flow Characteristics of Two S-Shaped Intake
SEDDON J Models tested at High Incidence.
Bristol University Report RWG/JS/3/82 March 1982
32. SEDDON J Understanding and Countering the Swirl in S-Ducts:
Tests on the Sensitivity of Swirl to Fences.
Bristol University Report JS/1/83 December 1983
33. STOCKS C P The Design and Development of the Tornado Air Intake.
BISSINGER N C Paper 10 of AGARD CP-30 1 May 1981
34. AULEHLA F Intake Swirl, a Major Disturbance Parameter in Engine/Intake
Compatibility.
ICAS-84-4.8.1 August 1982
35. CLARK R S Development of the AV8B Propulsion System.
VASTA S K AIAA-84-2426 October 1984
36. BAGHDADI S Compressor Stability Analysis.
LUEKE J E ASME J of Engineering Vol 104 No 2 June 1982
37. WALTER W A Predicted F100 Engine Response to Circumferential Pressure
SHAW M and Temperature Distortion.
AIAA 79-1310 June 1979
38. DAS D K A Study of the Response of a Turbojet Engine to the Inlet
SEYB N J Temperature Transients.
TRIPPI A ISABE 83-7048 June 1983

- 39 ABDELWAHAB A Effects of Temperature Transients at Fan Inlet of a Turbofan Engine.
NASA TP 1031 September 1977
- 40 ABDELWAHAB A Effects of Fan Inlet Temperature Disturbances on the Stability of a Turbofan Engine
NASA TM 82699 December 1981
- 41 SOCIETY OF AUTOMOTIVE ENGINEERS. Aerospace Standard, AS 681C Gas Turbine Engine Steady-State Performance Presentation for Digital Computer Programs. Revised 4-15-74.
- 42 SOCIETY OF AUTOMOTIVE ENGINEERS. Aerospace Recommended Practice, ARP 1257, Gas Turbine Transient Performance Presentation for Digital Computer Programs. June 1972.
- 43 HOSNY W M Turbofan Engine Non recoverable Stall Computer-Simulation Development and Validation.
BITTER S J AIAA-85-1432 July 1985
STEENKEN W G
- 44 FRENCH J V Modelling Post-Stall operation of Gas Turbine Engines
AIAA-85-1431 July 1985
- 45 BURWELL A E Dynamic Engine Behaviour During Post Surge Operation of a Turbofan Engine
PATTERSON G T AIAA-85-1430 July 1985
- 46 CHUNG K A Turbine Engine Aerodynamic Model for In-Stall Transient Simulation
LEAMY K R AIAA-85-1429 July 1985
COLLINS T P
- 47 HOPF W R Stall Recovery Control Strategy Methodology and Results
STEENKEN W G AIAA-85-1433 July 1985
- 48 MOORE F K A Theory of Post-Stall Transients in Axial Compression Systems
GREITZER E M ASME 85-GT-171 and 85-GT-172 March 1980

ACKNOWLEDGEMENTS

The author is indebted to his colleagues at Rolls-Royce, in particular Mr R G Hercock, for their help in the preparation of this paper and to Rolls-Royce for permission to present it. The work has been carried out with the support of the Procurement Executive, Ministry of Defence.

Strouhal number constant

| | | | | |
|---------------|--|---|--|--|
| FREQUENCY | f_{FS} | = | f_{MS} | $\frac{LMS}{LFS} \sqrt{\frac{TtFS}{TtMS}}$ |
| TIME DELAY | τ_{FS} | = | τ_{MS} | $\frac{LFS}{LMS} \sqrt{\frac{TtMS}{TtFS}}$ |
| POWER SPECTRA | $\left(\frac{\theta(f)}{Pt^2}\right)_{FS}$ | = | $\left(\frac{\theta(f)}{Pt^2}\right)_{MS}$ | $\frac{LFS}{LMS} \sqrt{\frac{TtMS}{TtFS}}$ |
| RMS VALUES | $\left(\frac{Pt_{RMS}}{Pt}\right)_{FS}$ | = | $\left(\frac{Pt_{RMS}}{Pt}\right)_{MS}$ | MS |
| COVARIANCES | $\left(\frac{C(\tau)}{Pt^2}\right)_{FS}$ | = | $\left(\frac{C(\tau)}{Pt^2}\right)_{MS}$ | MS |

NOTATION:

| | |
|--|------------------------------|
| f - FREQUENCY | RMS - ROOT MEAN SQUARE |
| L - LENGTH | v - VELOCITY |
| Tt - TOTAL TEMPERATURE | |
| Pt - TOTAL PRESSURE | <u>SUBSCRIPTS:</u> |
| $\frac{\theta(f)}{Pt^2}$ - POWER SPECTRA | MS - MODEL SCALE |
| $\frac{C(\tau)}{Pt^2}$ - COVARIANCES | FS - FULL SCALE |
| | STROUHAL No = $\frac{fL}{v}$ |

TABLE I - DATA SCALING GUIDELINES

8 EQUISPACED RAKES
5 PROBES/RAKE LINEARLY DISTRIBUTED
(ARRANGEMENT WITH MINIMUM RAKE ASSEMBLY CENTREBODY)

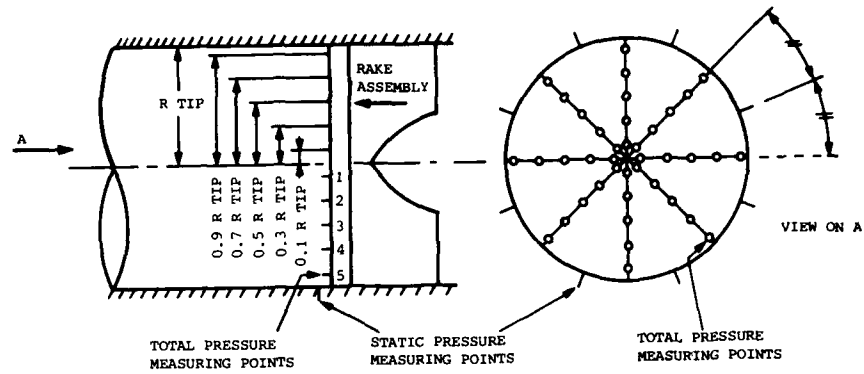


FIGURE 1 TYPICAL AIP PITOT RAKE ASSEMBLY

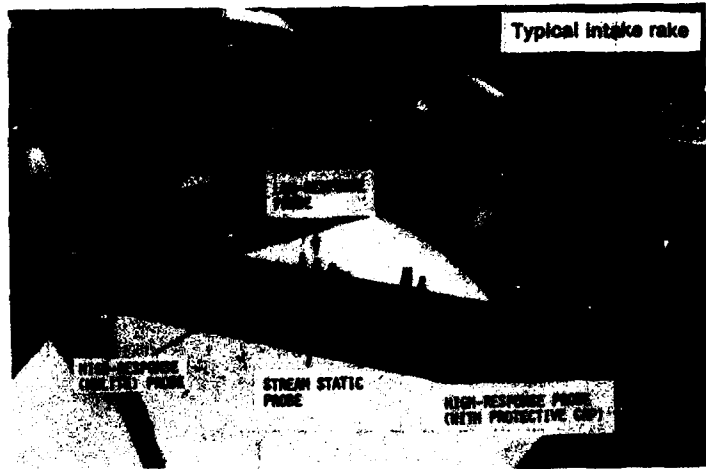


FIGURE 2 FULL SCALE RAKE ARRANGEMENT

CIRCUMFERENTIAL DISTORTION ELEMENTS, ONE-PER-REV PATTERNS

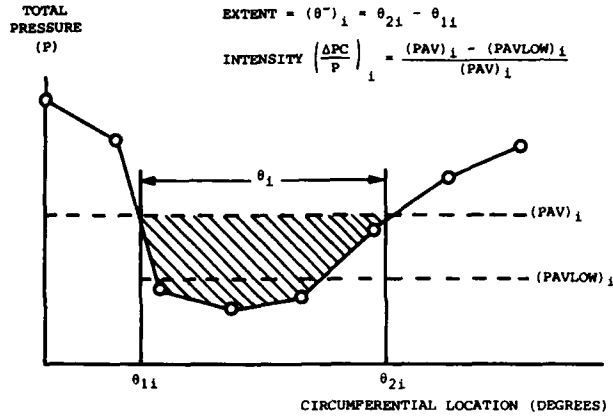


FIGURE 3a ARP1420 TOTAL PRESSURE DISTORTION ELEMENTS (1)

CIRCUMFERENTIAL DISTORTION ELEMENTS, MULTIPLE-PER-REV PATTERNS

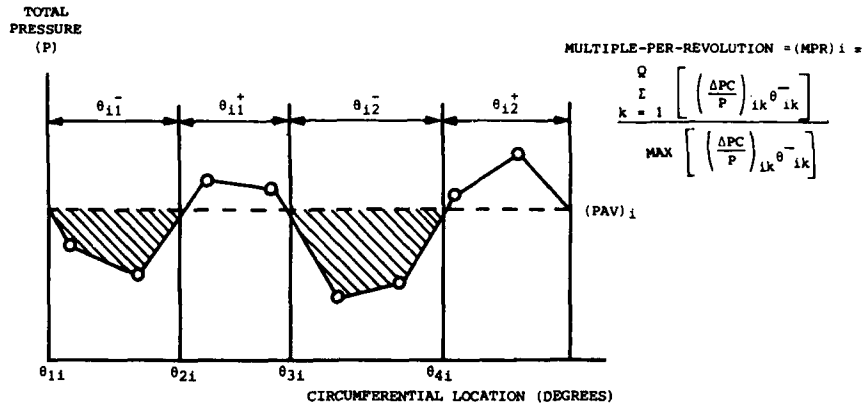


FIGURE 3b ARP1420 TOTAL PRESSURE DISTORTION ELEMENTS (2)

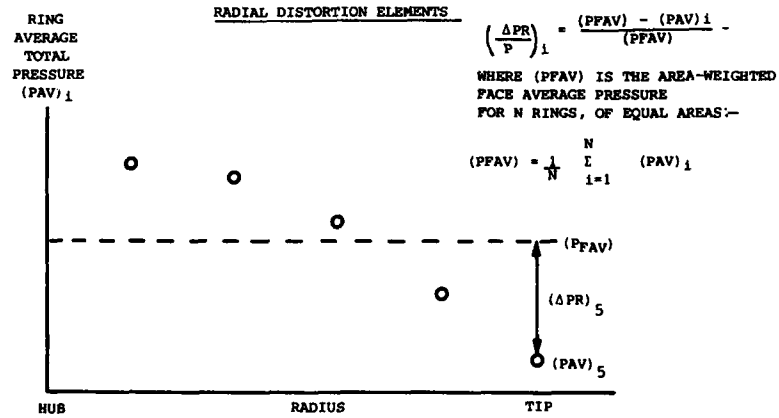


FIGURE 3c ARP1420 TOTAL PRESSURE DISTORTION ELEMENTS (3)

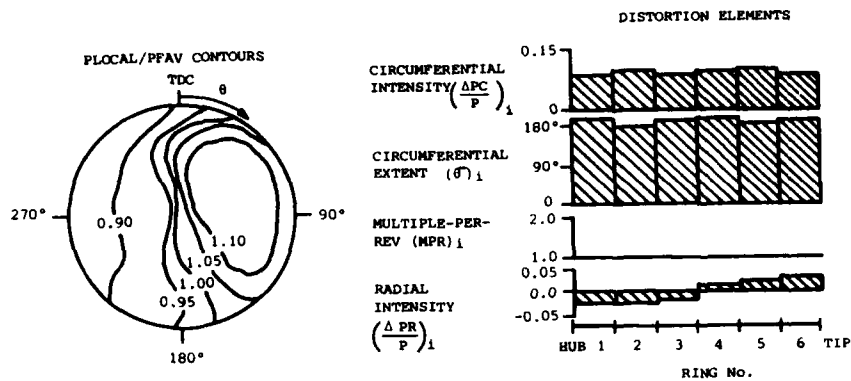
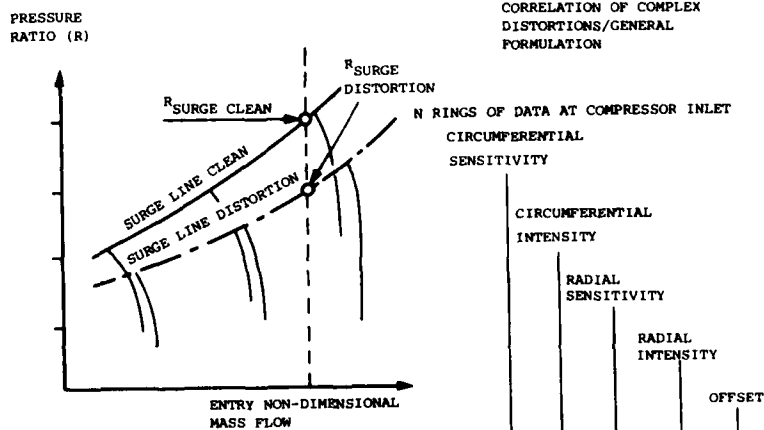


FIGURE 4 HISTOGRAM FORM OF PICTORIAL PRESENTATION

LOSS OF COMPRESSOR SURGE PRESSURE RATIO $\Delta PRS = \frac{R_{SURGE\ CLEAN} - R_{SURGE\ DISTORTION}}{R_{SURGE\ CLEAN}}$
 CONSTANT NON-DIMENSIONAL MASS FLOW



$\Delta PRS = \text{LOSS OF SURGE PRESSURE RATIO DUE TO COMPLEX DISTORTION PATTERN} = \sum_{RING\ i=1}^{RING\ N} \left[K_{C_i} \left(\frac{\Delta P_{TC}}{P_T} \right)_i + K_{R_i} \left(\frac{\Delta P_{TR}}{P_T} \right)_i + C_1 \right]$
 CIRC^L TERM + RADIAL TERM + CONSTANT

EXAMPLE FOR PURE CLASSICAL 1-REV CIRC^L DISTORTION

$\Delta PRS \rightarrow \Delta PRS_c = K_c \frac{\Delta P_{TC}}{P_T}$

FIGURE 5 SURGE PRESSURE RATIO LOSS - CORRELATION

DISTORTION PARAMETER - PIECE WISE CIRCUMFERENTIAL DISTORTION (I, J) REGION

$$DPC = \frac{1}{J} \sum_{i=1}^J \left[\left(1 - \left(\frac{\Delta PR}{P} \right)_i \right) \cdot \left(\frac{\theta_i}{\theta E} \right) \cdot f(\theta_i) \cdot \left(\frac{1}{(MPR)_i} \right)^\alpha \cdot \left(\frac{\Delta PC}{P} \right)_i \right]$$

- DC (θE) = DPC · (PFAV/q)
- $(\Delta PR/P)_i$ = RING RADIAL INTENSITY
- $(\Delta PC/P)_i$ = RING CIRCUMFERENTIAL INTENSITY
- (θ_i) = RING CIRCUMFERENTIAL EXTENT
- θE = EFFECTIVE CIRCUMFERENTIAL EXTENT
- $f(\theta_i)$ = EXTENT FACTOR
- $(MPR)_i$ = RING MULTIPLE-PER-REV ELEMENT
- α = EMPIRICAL WEIGHTING FACTOR
- PFAV = FACE AVERAGE TOTAL PRESSURE
- q = AIP DYNAMIC HEAD

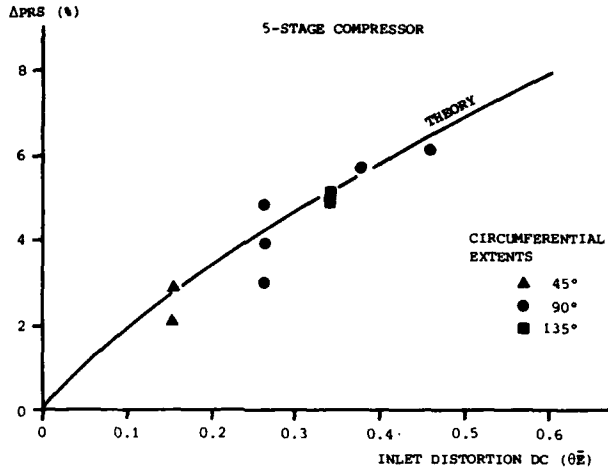


FIGURE 6 DISTORTION PARAMETER DEFINITION AND CORRELATION (EXAMPLE)

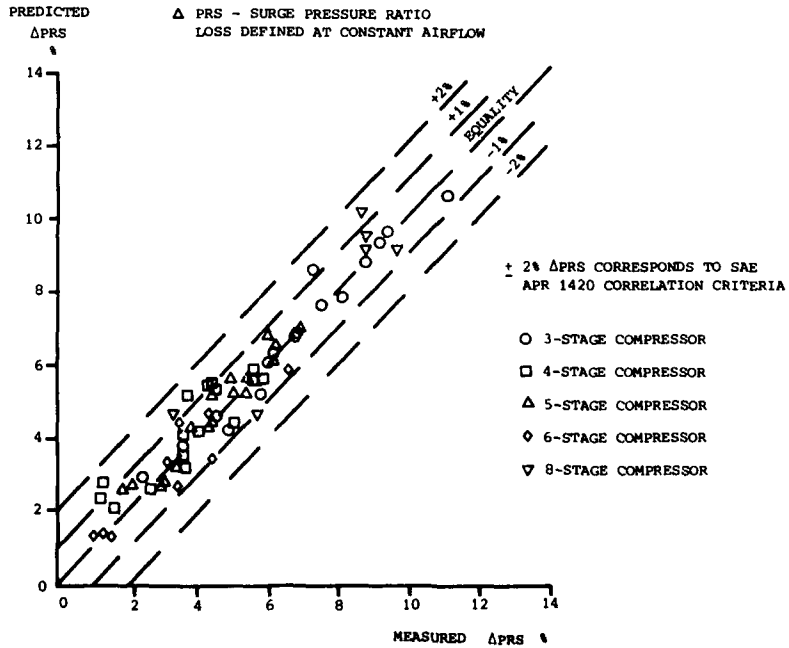


FIGURE 7 COMPARISON OF MEASURED AND PREDICTED LOSS OF COMPRESSOR PRESSURE RATIO

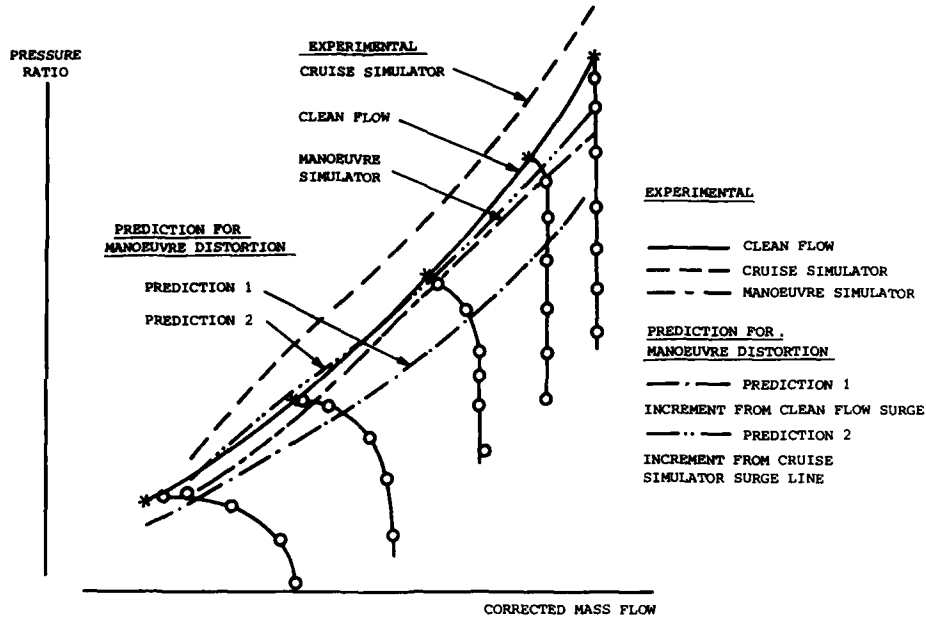


FIGURE 8 MULTISTAGE FAN RESPONSE - RADIAL AND MIXED DISTORTION
THREE-STAGE FANS

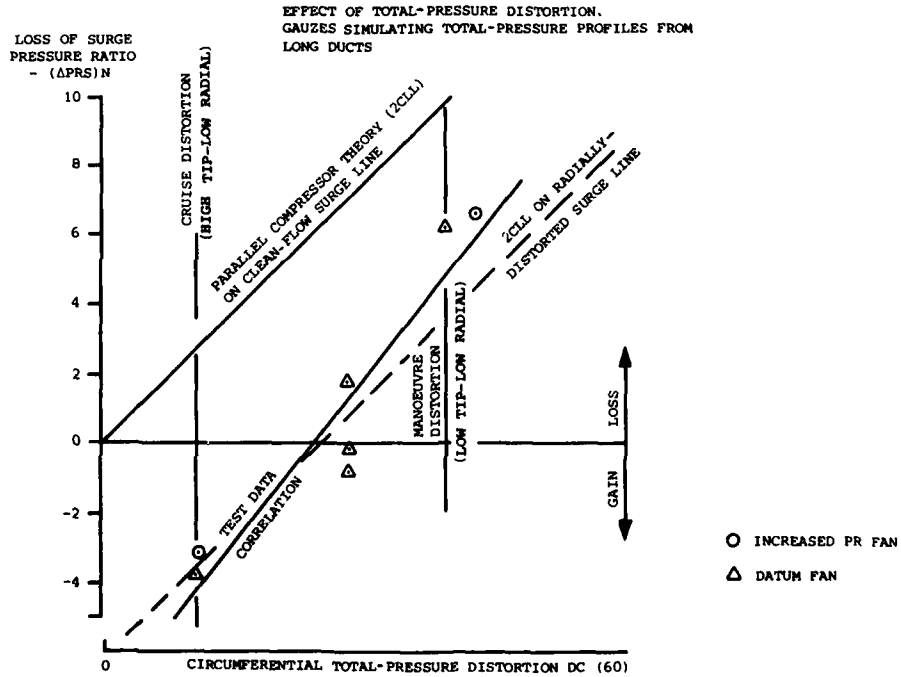


FIGURE 9 MULTISTAGE FAN RESPONSE

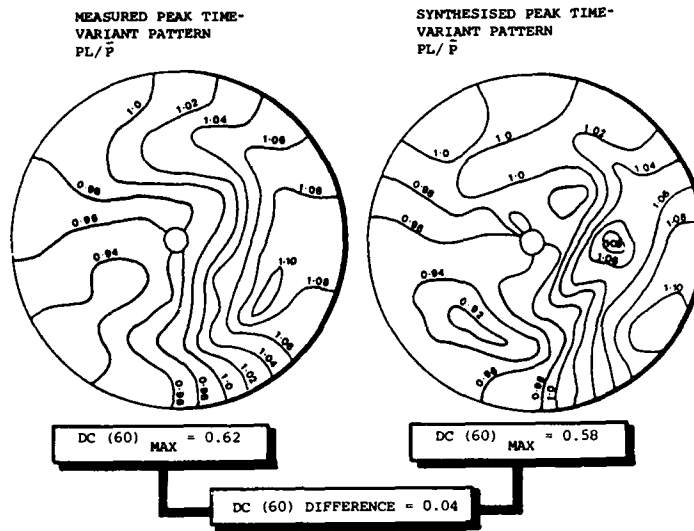


FIGURE 10 COMPARISON OF MEASURED AND SYNTHESISED PEAK TIME - VARIANT DISTORTION LEVELS AND PATTERNS

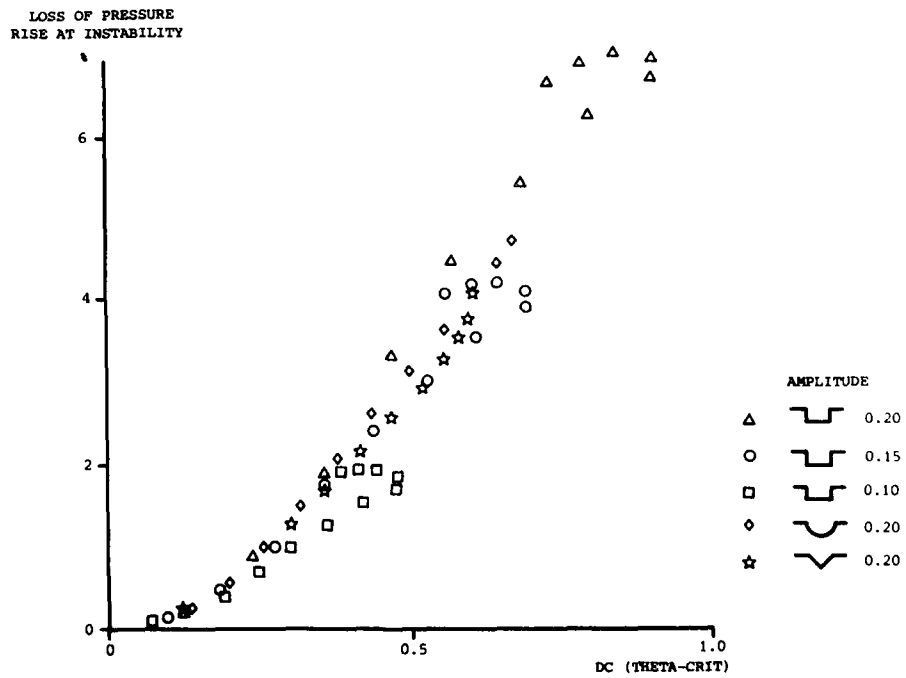


FIGURE 11 LOSS IN STABILITY MARGIN vs DC (θ_{CRIT})

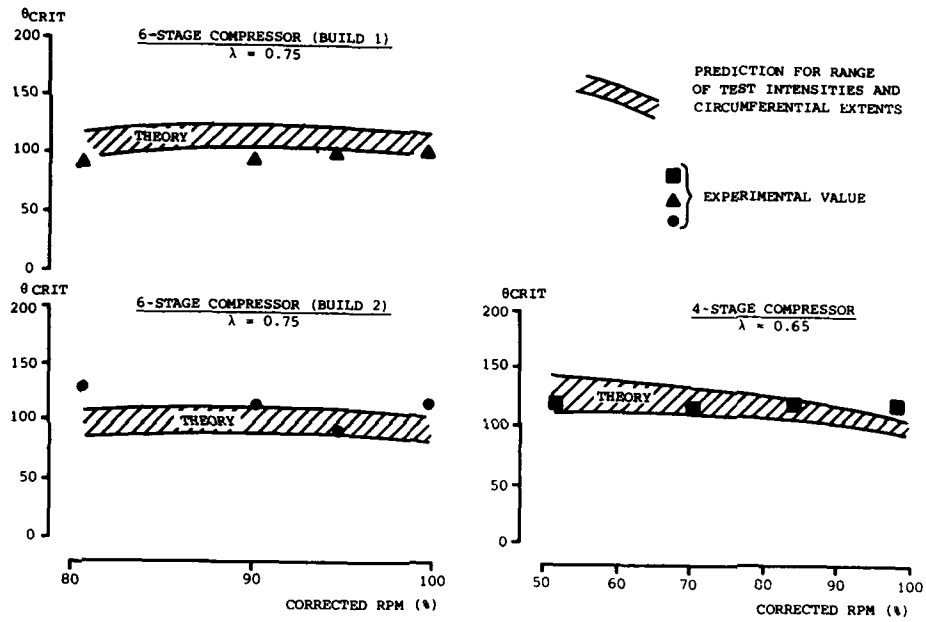


FIGURE 12 PREDICTED AND EXPERIMENTAL CRITICAL SECTOR ANGLES

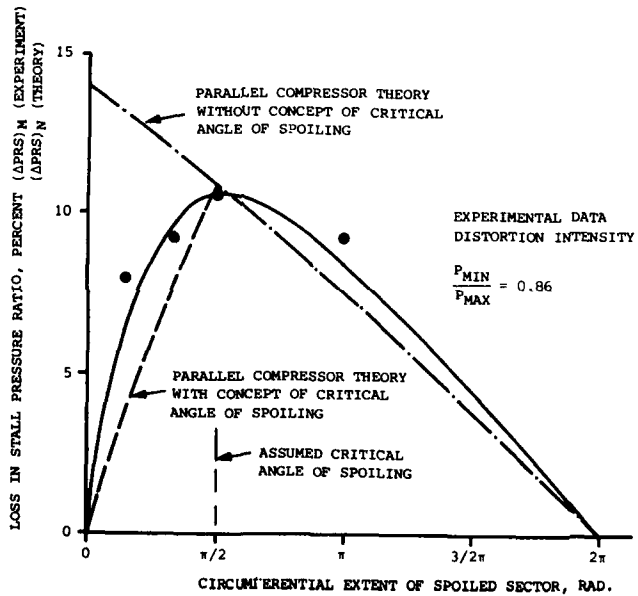
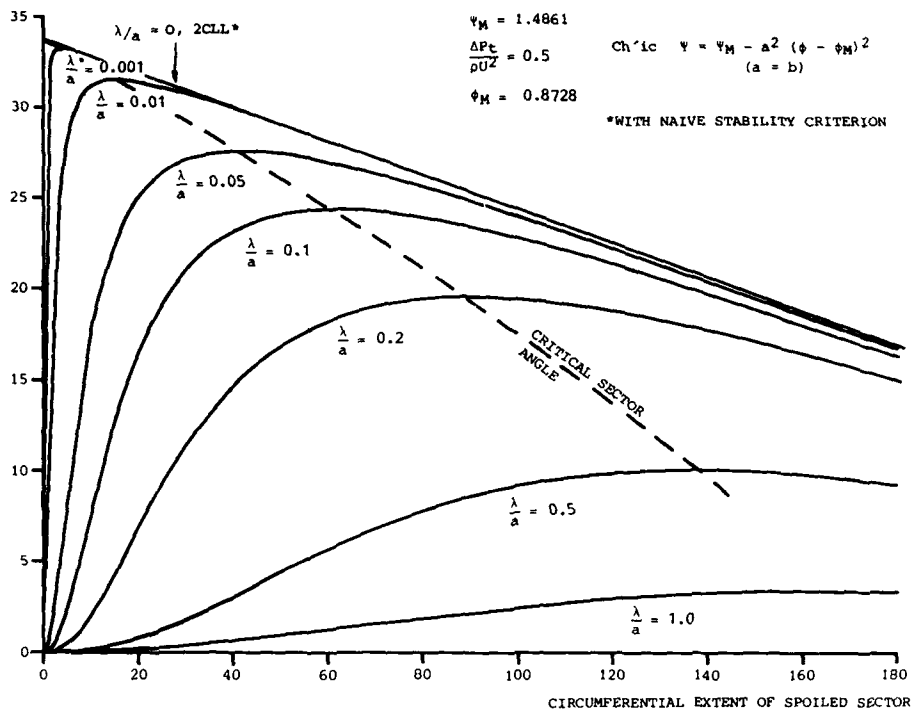


FIGURE 13 EXPERIMENTAL AND THEORETICAL LOSS IN STALL PRESSURE RATIO AS A FUNCTION OF DISTORTION ANGLE

LOSS IN PRESSURE RISE

$$\frac{\psi_M - \bar{\psi}_{INST}}{\psi_M}$$



THEORY

$$\psi_M = 1.4861$$

$$\frac{\Delta P_t}{\rho U^2} = 0.5$$

$$\phi_M = 0.8728$$

$$\text{Ch'ic } \psi = \psi_M - a^2 (\phi - \phi_M)^2$$

(a = b)

*WITH NAIVE STABILITY CRITERION

FIGURE 14 LOSS OF STABILITY MARGIN/DISTORTED SECTOR ANGLE

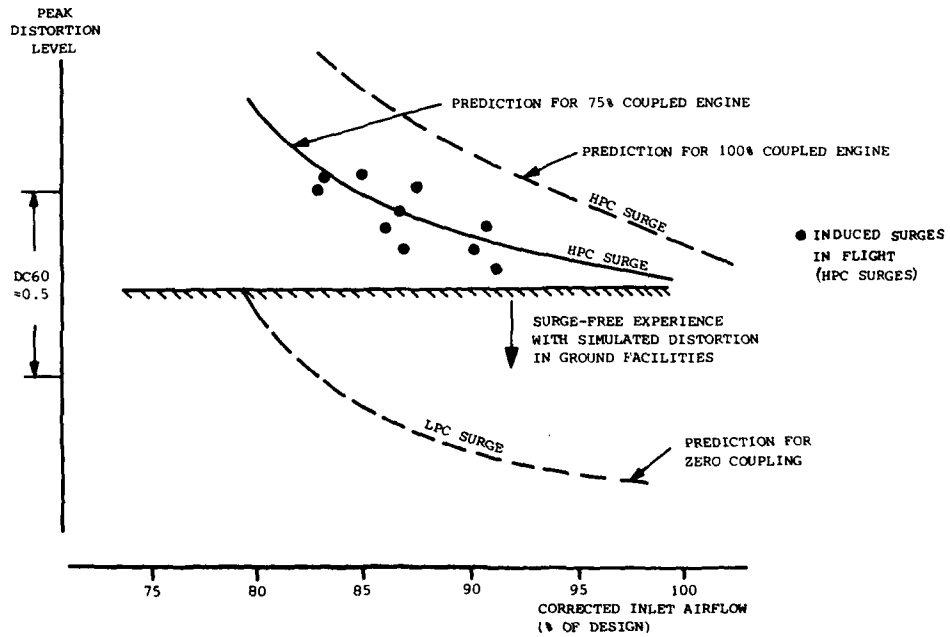


FIGURE 15 MEASURED AND PREDICTED DISTORTION TOLERANCE

$$\frac{\text{EXIT TOTAL-PRESSURE DISTORTION}}{\text{ENTRY TOTAL-PRESSURE DISTORTION}} \sim \frac{P_{t2}}{P_{t1}}$$

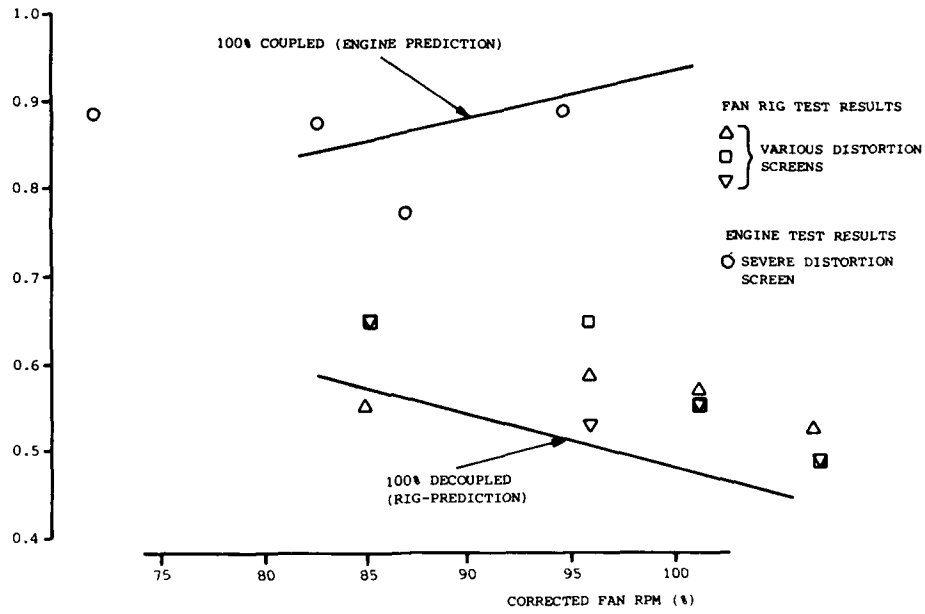


FIGURE 16 FAN TOTAL - PRESSURE DISTORTION TRANSFER

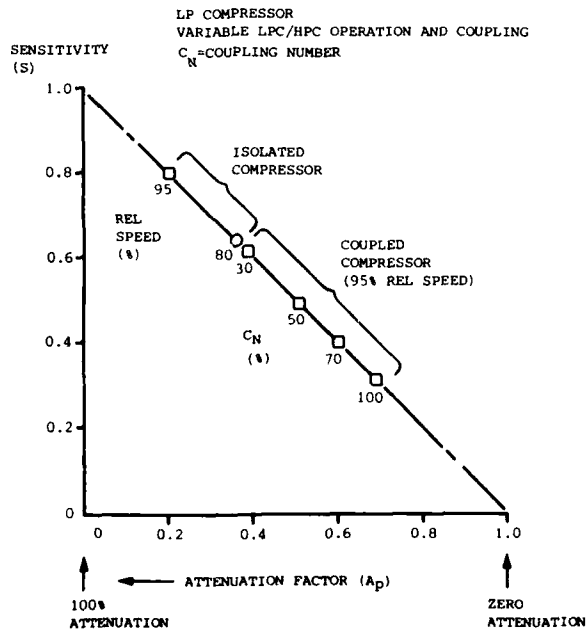


FIGURE 17 LP COMPRESSOR SENSITIVITY/ATTENUATION RELATIONSHIP

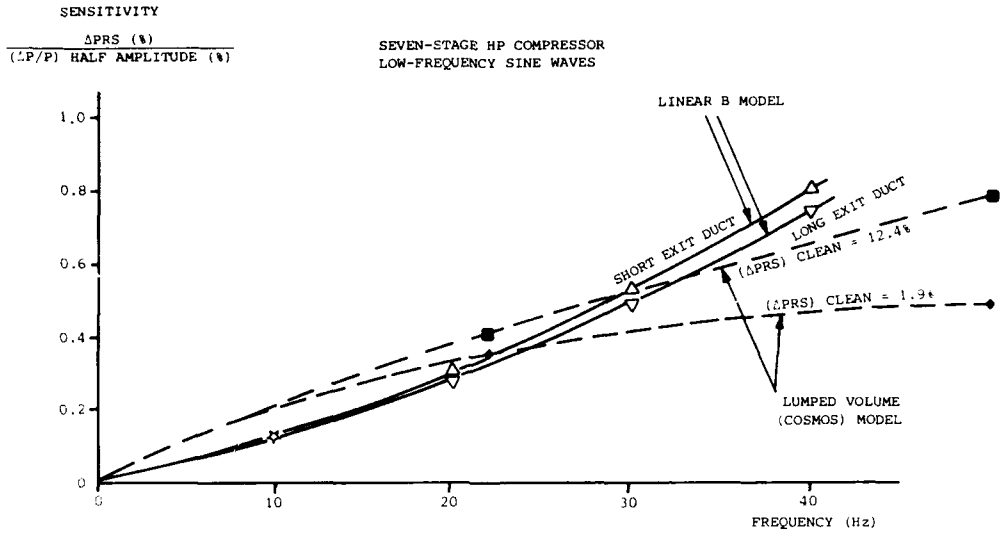


FIGURE 18 COMPRESSOR RESPONSE IN INTAKE TOTAL-PRESSURE PLANAR WAVES

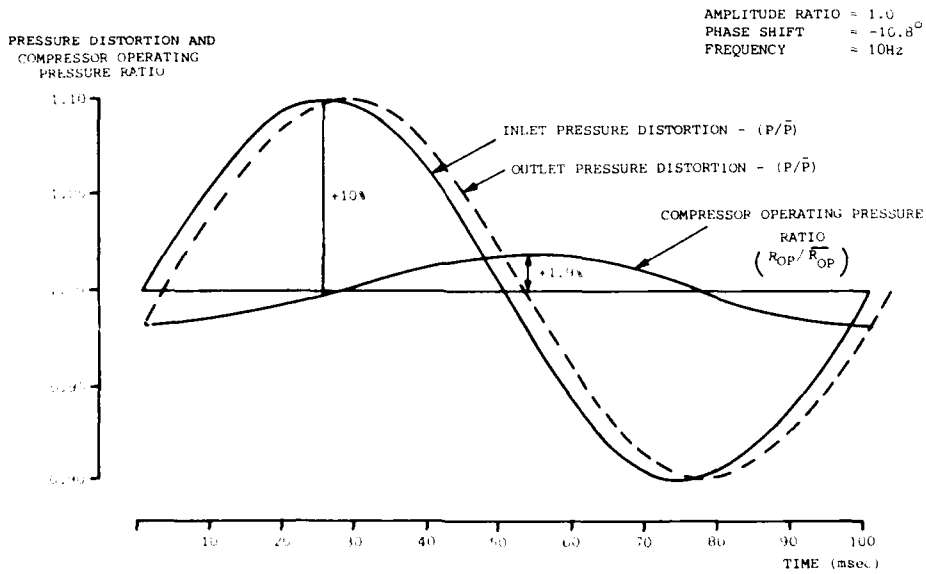


FIGURE 19 COMPRESSOR RESPONSE TO INLET PRESSURE PLANAR WAVES
COSMOS PREDICTION

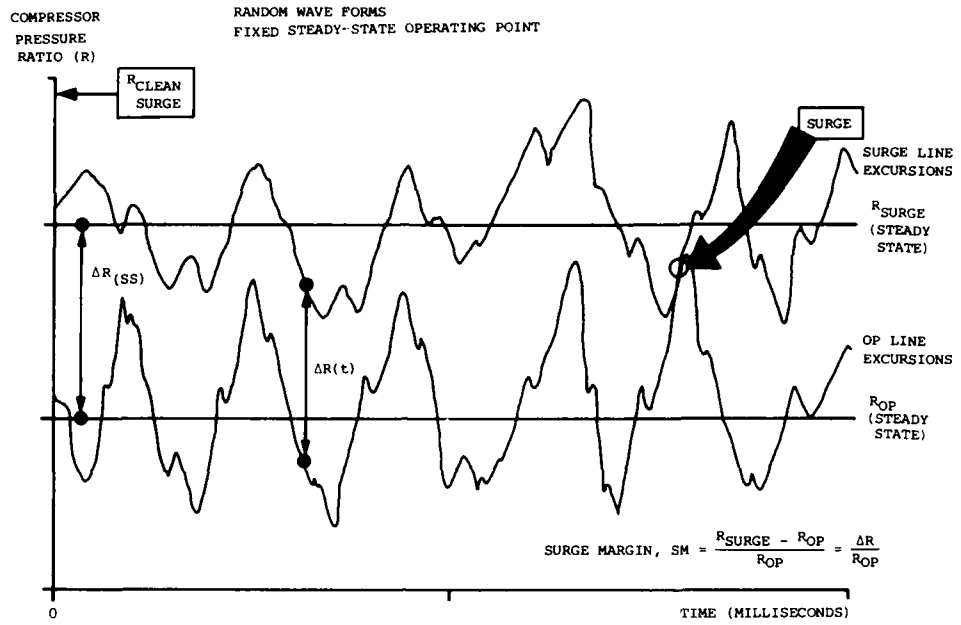


FIGURE 20 COMBINED PLANAR AND SPATIAL DISTORTION

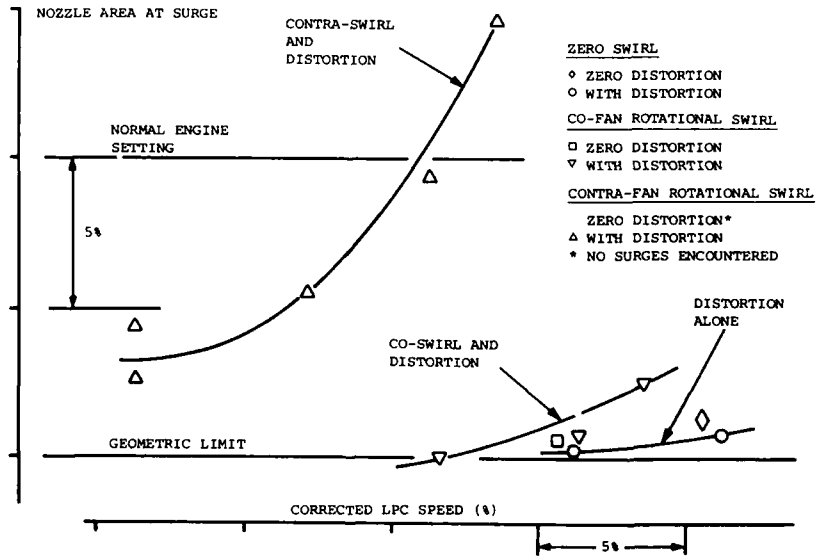


FIGURE 21 EFFECT OF INLET SWIRL AND TOTAL PRESSURE DISTORTION ON ENGINE STABILITY

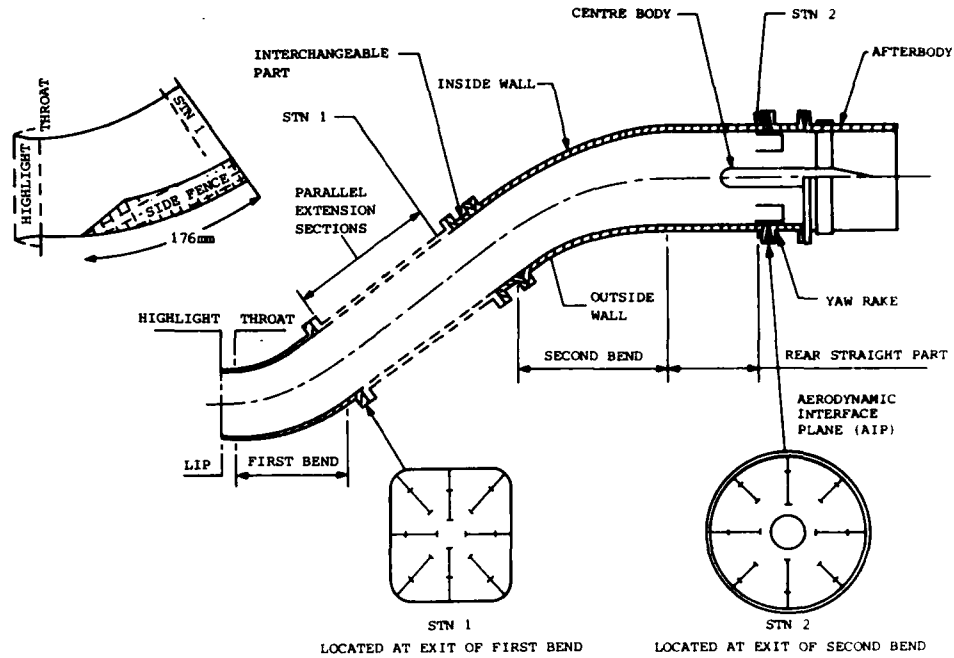


FIGURE 22 S-DUCT INTAKE RESEARCH MODEL

INTAKE MASS FLOW RATIO ≈ 0.9

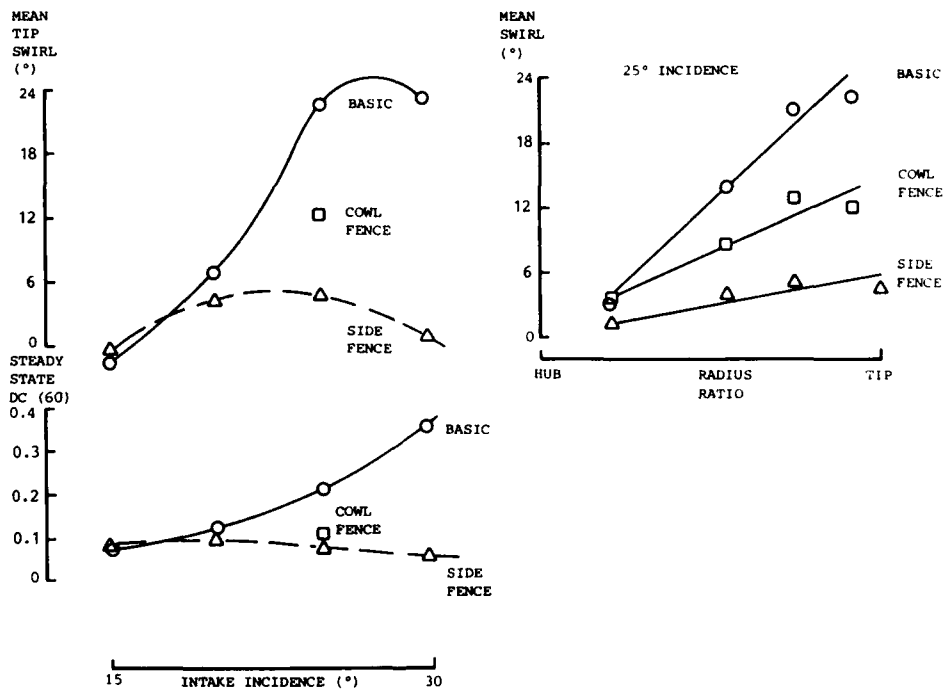


FIGURE 23 S-DUCT INTAKE MODEL TYPICAL RESULTS

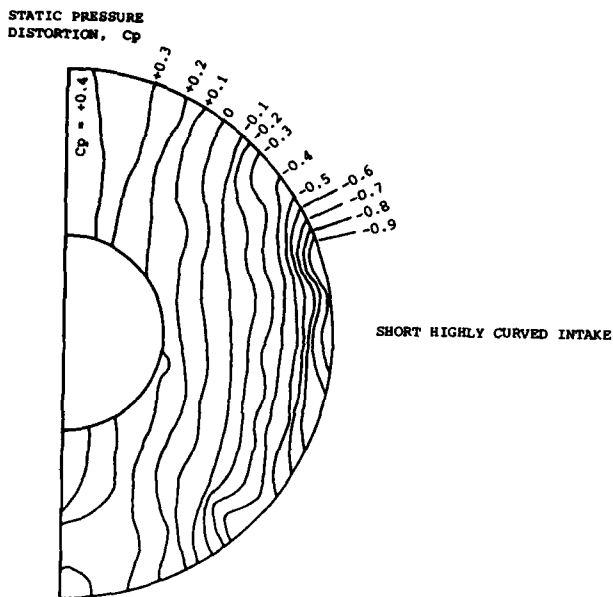


FIGURE 24 AIP VARIATION OF STATIC PRESSURE

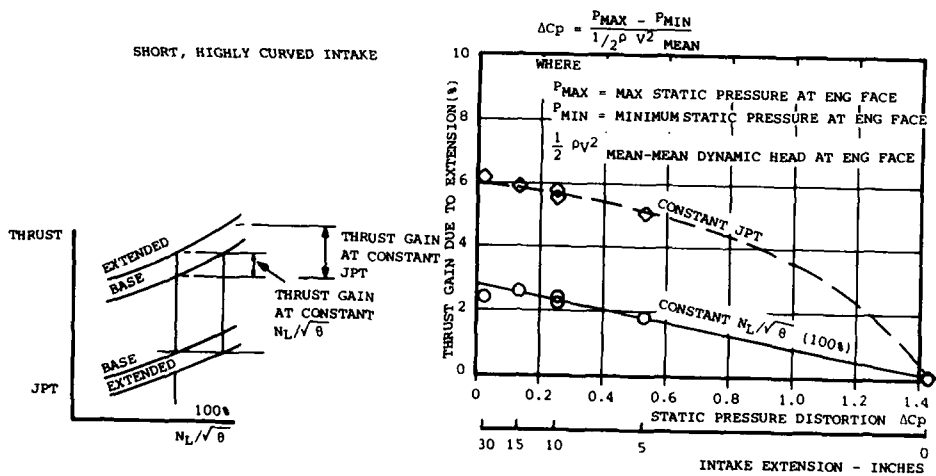


FIGURE 25 EFFECT OF STATIC PRESSURE DISTORTION ON ENGINE THRUST

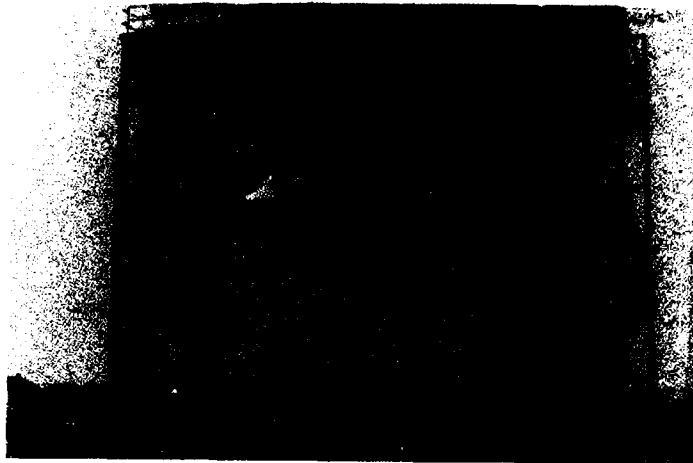
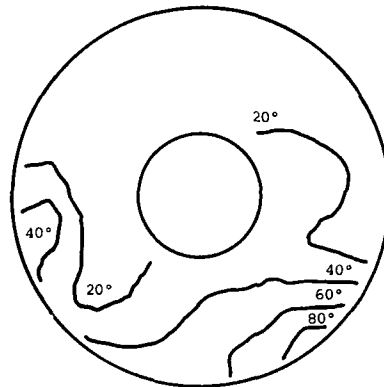


FIGURE 26 PEGASUS 2A/HARRIER AT SHOEBURYNNESS

CONTOURS OF LOCAL TEMPERATURE
RISE (°C)



SURGE FREE
NO ANTI-HGR MEASURES
HEIGHT 1.25m
TC120 = 6s
MEAN TEMP RISE 23°C
TEMP DISTORTION

$$TC120 = \frac{T_{MAX\ 120} - \bar{T}}{\bar{T}}$$

$T_{MAX\ 120}$ = AVERAGE MAX TEMP IN ANY
120° SECTOR AT THE AIP
 \bar{T} = INTAKE MEAN TEMP

FIGURE 27 TEMPERATURE DISTORTION IN VERTICAL LANDING - EXAMPLE

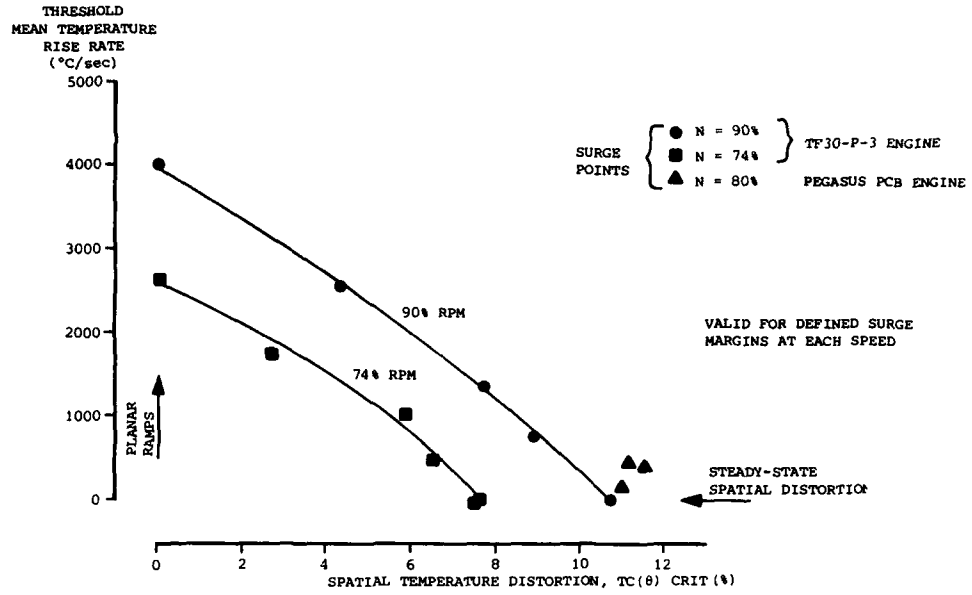


FIGURE 28 ENGINE TEMPERATURE DISTORTION TOLERANCE - EXAMPLE

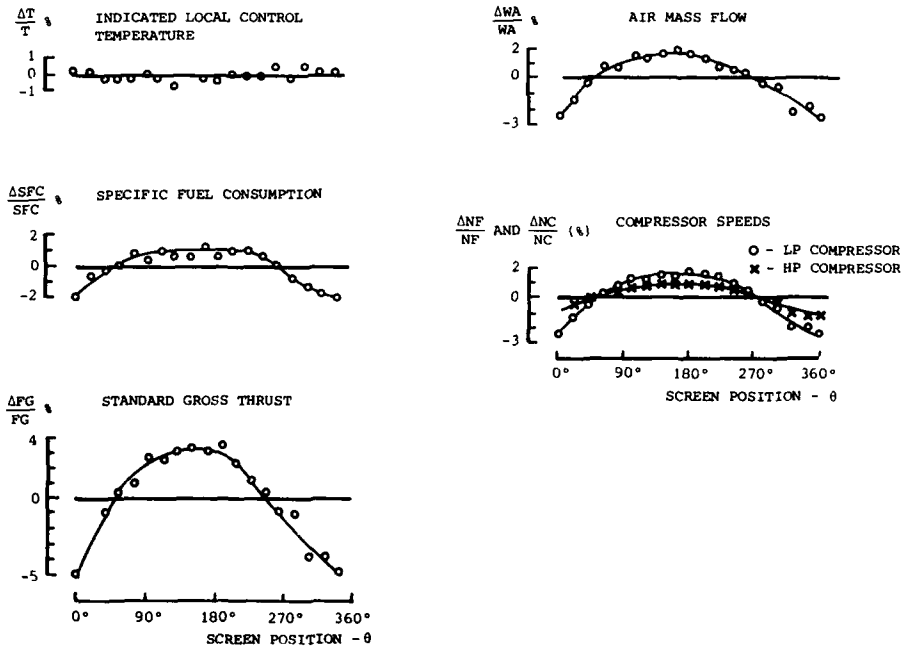


FIGURE 29 TURBOFAN ENGINE PERFORMANCE - SCREEN POSITION EFFECT

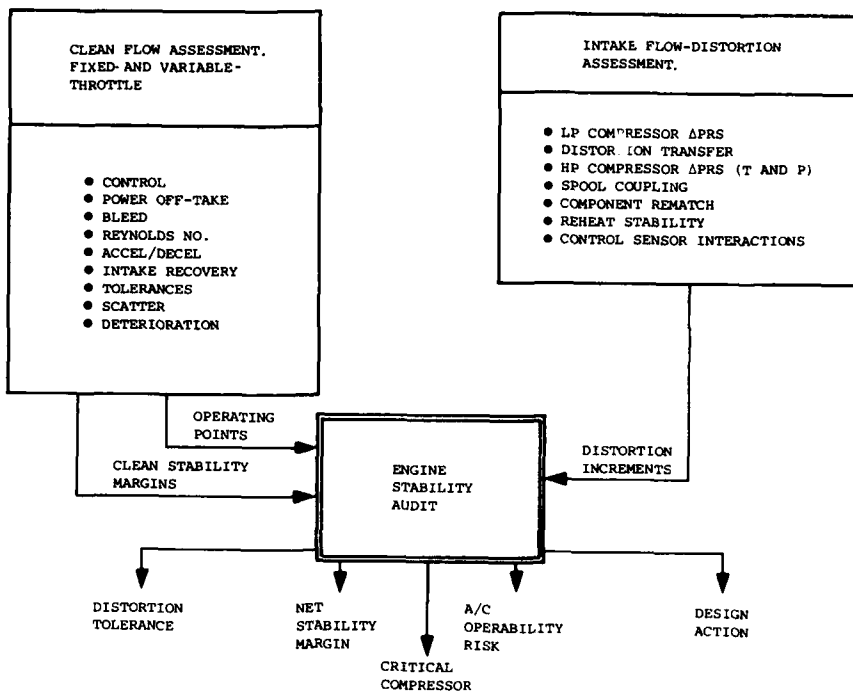


FIGURE 30 STABILITY ASSESSMENT OVERVIEW

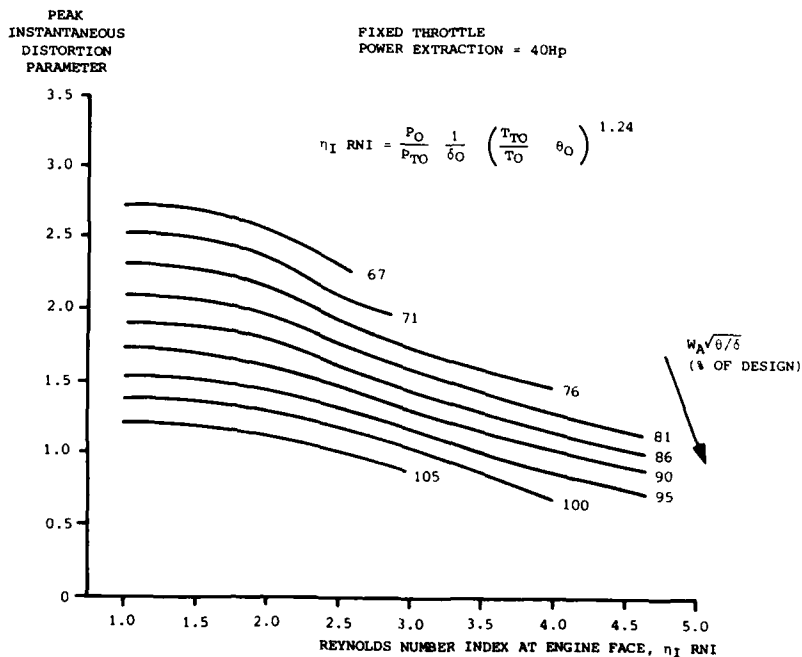


FIGURE 31 HP COMPRESSOR DISTORTION TOLERANCE

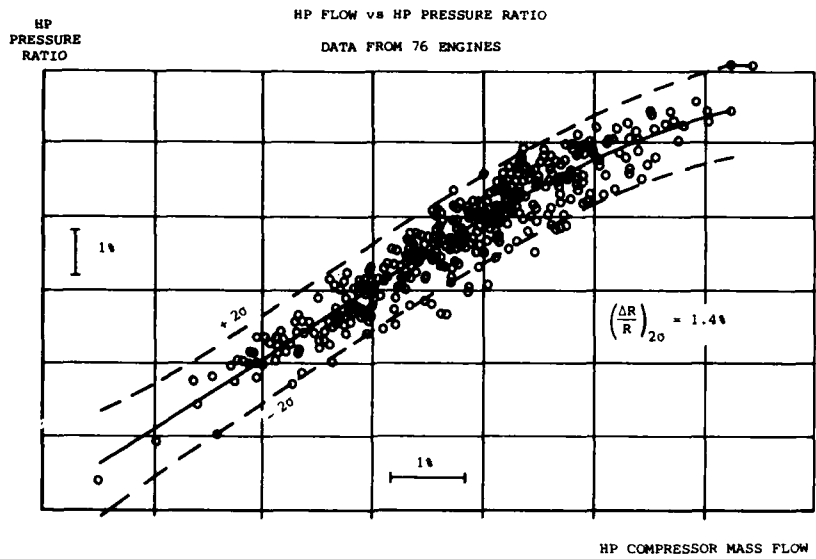


FIGURE 32 HP COMPRESSOR OPERATING LINE SCATTER

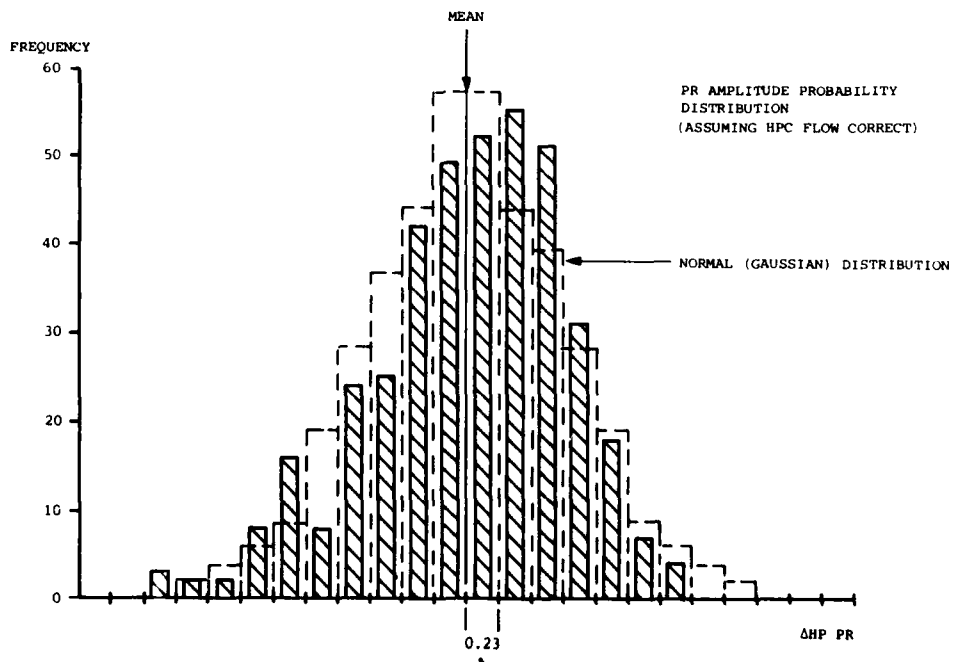


FIGURE 33 HPC PRESSURE RATIO AMPLITUDE DISTRIBUTION

HP COMPRESSOR
FIXED OPERATING POINT

| DESTABILISING FACTOR | NON-RANDOM EFFECT | RANDOM EFFECT |
|-----------------------------|-------------------|---------------|
| <u>OPERATING LINE</u> | | |
| ● INLET DISTORTION | 0 | 0 |
| ● REYNOLDS NUMBER | -4.4% | 0 |
| ● ENGINE-TO-ENGINE SCATTER | 0 | ±1.4% |
| ● CONTROL TOLERANCES | 0 | ±2% |
| ● DETERIORATION | -1.5% | ±1.5% |
| ● POWER OFF-TAKE | -3.6% | 0 |
| ● BLEED | +5.2% | 0 |
| <u>SURGE LINE</u> | | |
| ● REYNOLDS NUMBER | -4.7% | 0 |
| ● INLET DISTORTION | -6.8% | 0 |
| ● ENGINE-TO-ENGINE SCATTER | 0 | ±2.0% |
| ● DETERIORATION | -1.0% | ±1.0% |
| TOTAL SURGE MARGIN UTILISED | -16.8% | ±3.6% (RSS) |

FIGURE 34 STABILITY ASSESSMENT BREAKDOWN

DISCUSSION

Ph.Ramette, Fr

In Figure 8, how do you explain the fact that the cruise-simulator stall line is higher on the compressor map than the clean-flow stall line?

Author's Reply:

The test result applies to the effect of a tip-low total-pressure distortion on a low hub-tip-ratio multistage compressor design that has excess work capacity at the tip. Radial equilibrium is affected and span-wise changes in deviation occur. This results in an improved surge line.



COMPATIBILITE ENTREE D'AIR-MOTEUR
IMPACT DES METHODES THEORIQUES ET EXPERIMENTALES

Par

Marius GOUTINES & Hugues JOUBERT

Société Nationale d'Etude et de Construction de Moteurs d'Aviation (SNECMA)
77550 MOISSY-CRAMAYEL
FRANCE

RESUME

Pour atteindre les qualités de manoeuvre demandées aux avions militaires modernes, les turboréacteurs doivent pouvoir fonctionner avec une entrée d'air présentant d'importantes distorsions spatio-temporelles. Dans ce domaine, les objectifs principaux du concepteur de compresseurs sont l'évaluation, théorique ou expérimentale, de la marge au décrochage nécessaire et l'atténuation de la sensibilité des compresseurs aux distorsions de l'écoulement. La première partie de l'exposé décrit les méthodes de calculs théoriques utilisées. Ces méthodes nécessitent la connaissance des pertes de pression et des déviations des profils fonctionnant à forte incidence. La seconde partie traite des expériences destinées à valider les méthodes de calcul ou à démontrer la compatibilité entrée d'air-moteur : essais en vol, essais en soufflerie, création de distorsions non stationnaires sur banc d'essais au sol. La troisième partie décrit les impacts de ces études sur la conception des compresseurs.

NOTATIONS

| <u>Variables</u> | <u>Indices ou symboles</u> |
|---|---|
| a : $\bar{V}_\theta / \bar{V}_x$ | |
| A : Section de passage d'un canal inter-aubes | c : Relatif au carter |
| c : Corde d'une aube | e : Relatif à l'entrée de la grille |
| E : Energie totale par unité de volume | h : Relatif au moyeu |
| I : Rothalpie | r : Relatif à la direction radiale |
| M_v : Nombre de Mach absolu | s : Relatif à la sortie de la grille |
| M_w : Nombre de Mach relatif | x : Relatif à la direction axiale |
| P_s : Pression statique | θ : Relatif à la direction tangentielle |
| P_T : Pression totale absolue | \bar{X} : Valeur moyenne de X |
| P_T^R : Pression totale relative | X' : Perturbation de X |
| r : Constante massique des gaz parfaits | x : X'/\bar{X} |
| R : Rayon | ΔX : Variation de X |
| s : Abscisse curviligne sur une ligne de courant | X_{eff} : Valeur efficace de X |
| t : Temps | X_n^C : Coefficient de $\cos n\theta$ dans la série de Fourier de X |
| T_s : Température statique | X_n^S : Coefficient de $\sin n\theta$ dans la série de Fourier de X |
| T_T : Température totale | X_{ss} : Valeur moyenne stationnaire de X |
| U : Vitesse d'entraînement | |
| V : Vitesse absolue | |
| W : Vitesse relative | |
| x : Coordonnée axiale | |
| θ : Direction relative | |
| γ : Rapport des chaleurs spécifiques | |
| ΔSM : Variation de marge au décrochage | |
| φ : Inclinaison méridienne des tubes de courant | |
| τ : Coefficient de pertes | |
| π : Rapport de pression totale du compresseur | |
| π_s : Valeur de π au décrochage | |
| ρ : Masse volumique | |
| σ : Temps réduit ou constante de temps | |
| Ω : Vitesse de rotation | |

Les autres variables sont définies dans le texte.

1 - INTRODUCTION

Les avions de combat modernes doivent évoluer à des incidences et à des dérapages de plus en plus élevés. Les avions de transport doivent être capables d'effectuer leur service dans des conditions météorologiques de plus en plus difficiles, notamment en présence de forts vents de travers. Bien que les entrées d'air de tous les types d'avions soient sans cesse améliorées d'un point de vue aérodynamique, l'écoulement de l'air s'en trouve perturbé par des décollements non stationnaires. Dans ces conditions, les compresseurs sont alimentés par un flux hétérogène présentant d'importantes distorsions spatiales et temporelles.

La principale conséquence de cette mauvaise alimentation est une perte sensible de marge au décrochage des compresseurs. Cette perte représente environ 70 % de l'abaissement de la ligne de décrochage qui se produit, toutes causes confondues, dans les cas de fonctionnement les plus critiques des compresseurs basse pression. On observe en outre une diminution du débit aspiré par les compresseurs. Dans ce domaine, les trois principaux objectifs du motoriste sont les suivants :

- démont reravant les essais en vol, la compatibilité du moteur avec une entrée d'air donnée,
- prédire au mieux, par le calcul, les effets d'une distorsion amont pour pouvoir optimiser la conception des moteurs et évaluer notamment la marge au décrochage strictement nécessaire sur les compresseurs basse et haute pression,
- atténuer, dès le stade du projet, la sensibilité des compresseurs aux perturbations de l'entrée d'air.

Ces problèmes ont fait l'objet de très nombreuses études chez les constructeurs de turboréacteurs. En ce qui concerne les travaux de la SNECMA, il se sont intensifiés depuis 1979 (Réf 1, 2 et 3). Nous allons d'abord décrire les méthodes de calcul théoriques utilisées. La première est une méthode simplifiée. Le compresseur est divisé en plusieurs secteurs où sont appliqués des calculs monodimensionnels ; l'amont et l'aval étant traités par un calcul bidimensionnel linéarisé. En revanche, la méthode plus complète résoud les équations d'Euler de l'écoulement tridimensionnel et non permanent. La seconde partie traite des expériences destinées à valider les méthodes de calcul ou à démontrer la compatibilité entrée d'air-moteur. Enfin, la troisième partie décrit les impacts que ces études ont eu ces dernières années sur la conception des moteurs d'avions.

2 - METHODES DE CALCUL

2.1. METHODES DES SECTEURS DE COMPRESSEUR EN PARALLELE

2.1.1. Description de la méthode

Ces méthodes ont été les premières développées et ont été sans cesse perfectionnées (Réf. 4). La veine du système de compression est divisée en 4 zones (Fig. 1).

Dans la zone A et B on résoud les équations de l'écoulement bidimensionnel (x, θ) et stationnaire de fluide parfait

$$(1) \begin{cases} V_x \frac{\partial \rho}{\partial x} + \frac{V_\theta}{R} \frac{\partial \rho}{\partial \theta} + \rho \left(\frac{\partial V_x}{\partial x} + \frac{1}{R} \frac{\partial V_\theta}{\partial \theta} \right) = 0 & \text{Eq. de continuité} \\ V_x \cdot \frac{\partial V_x}{\partial x} + \frac{V_\theta}{R} \cdot \frac{\partial V_x}{\partial \theta} = -\frac{1}{\rho} \frac{\partial P_s}{\partial x} & \text{Eq. de quantité de mouvement projetée sur } x \\ V_x \cdot \frac{\partial V_\theta}{\partial x} + \frac{V_\theta}{R} \cdot \frac{\partial V_\theta}{\partial \theta} = -\frac{1}{\rho R} \frac{\partial P_s}{\partial \theta} & \text{Eq. de quantité de mouvement projetée sur } \theta \end{cases}$$

R est le rayon constant du tube de courant moyen qui est supposé cylindrique. Ces équations sont linéarisées en admettant que les perturbations dues à la distorsion circumférentielle sont petites devant les valeurs moyennées suivant θ . Les perturbations par rapport à la solution sans distorsion sont notées par le symbole (') et on introduit les variables réduites suivantes :

$$v_x = \frac{V'_x}{V_x}, \quad v_\theta = \frac{V'_\theta}{V_x}, \quad p_s = \frac{P'_s}{\rho \cdot (\overline{V_x^2} + \overline{V_\theta^2})}$$

Suivant Mokolke (Réf. 5), on suppose que l'écoulement de chaque filet fluide est isentropique et, en utilisant l'équation d'état du gaz $P_s = \rho \cdot r \cdot T_s$, les équations (1) peuvent s'écrire :

$$(2) \begin{cases} \frac{\partial v_x}{\partial x} + \frac{1}{R} \cdot \frac{\partial v_\theta}{\partial \theta} = -M_v^2 \cdot \left(\frac{\partial p_s}{\partial x} + \frac{a}{R} \cdot \frac{\partial p_s}{\partial \theta} \right) \\ \frac{\partial v_x}{\partial x} + \frac{a}{R} \cdot \frac{\partial v_x}{\partial \theta} = -(1+a^2) \cdot \frac{\partial p_s}{\partial x} \\ \frac{\partial v_\theta}{\partial x} + \frac{a}{R} \cdot \frac{\partial v_\theta}{\partial \theta} = -\left(\frac{1+a^2}{R} \right) \cdot \frac{\partial p_s}{\partial \theta} \end{cases}$$

où $a = \frac{\bar{V}_\theta}{V_x}$ et où M est le nombre de Mach moyen

La solution du système (2) est recherchée sous forme de séries de Fourier ; par exemple $V_x = \sum_{n=1}^{\infty} [V_{x_n}^c(x) \cos n\theta + V_{x_n}^s(x) \sin n\theta]$. La solution peut donc être caractérisée, pour chaque harmonique n , par les 8 fonctions ($V_x^c, V_x^s, V_\theta^c, V_\theta^s, A_n^c, A_n^s, t_n^c, t_n^s$) qui sont respectivement les coefficients des séries de Fourier de V_x, V_θ, p_T (perturbation de pression totale) et t_T (perturbation de température totale). La résolution du système (2) donne une expression analytique pour chaque fonction. Chaque expression ainsi trouvée est une fonction de x , de n et de 8 constantes qui doivent être fixées pour satisfaire aux conditions limites.

Dans la zone A, l'annulation des perturbations à l'infini amont ne laisse subsister que 2n coefficients. On suppose que la distorsion de pression et de température est engendrée, à une distance donnée du compresseur, par un dispositif au travers duquel il y a continuité du champ des vitesses. Ce dispositif, par exemple un écran, est donc caractérisé par la seule donnée de la distorsion de pression totale et de température totale qu'il impose.

Dans la zone B, les considérations physiques qui viennent d'être faites permettent d'écrire 8n relations d'où on déduit les 8n constantes qui fixent la solution. En effet, la connaissance de p_T donne 2n relations, celle de t_T donne 2n relations et la continuité de V_x et de V_θ à travers le générateur de distorsion fournit 4n relations. Finalement, le champ des vitesses dans les zones A et B ne dépend que des 2n constantes qui déterminaient l'écoulement de la zone A. Il est plus pratique de se fixer les 2n coefficients de la série de Fourier de V_x dans le plan d'entrée du compresseur (plan 3), soit $V_{x_{2n}}^c$ et $V_{x_{2n}}^s$. La connaissance de la perturbation V_x dans le plan 3 fixe donc la solution dans tout l'espace amont et en particulier fournit la perturbation V_θ dans le plan 3. Le fonctionnement de chaque secteur du compresseur peut dès lors être calculé.

Le compresseur (zone C) est divisé en plusieurs secteurs que l'on suppose fonctionner indépendamment les uns des autres. Les performances de chaque secteur sont obtenues par un calcul monodimensionnel classique sur la ligne moyenne. En particulier, l'angle relatif du flux à la sortie de chaque aubage, β_s , et le coefficient de pertes, ω , sont des fonctions connues des conditions aérodynamiques à l'entrée de l'aubage, $\beta_e = \beta_e(\beta_e, M_{we}), \omega = \omega(\beta_e, M_{we})$. On peut ainsi prendre en compte le caractère non linéaire du fonctionnement du compresseur. A ce stade du calcul, la pression statique à la sortie du compresseur, p_{s4} , est connue sur chaque secteur.

Lorsque le système de compression ne comporte pas de diffuseur de sortie, les perturbations de vitesse axiale à l'entrée du compresseur, V_{x3} , sont ajustées itérativement jusqu'à obtenir l'annulation de la perturbation de pression statique à la sortie, $p_{s4} = 0$. Si le système de compression comporte un diffuseur de sortie, l'écoulement dans la zone D est assimilé à celui d'un diffuseur plan équivalent (Réf. 6) dans lequel on résout les équations linéaires de l'écoulement stationnaire incompressible. Le processus itératif de correction de V_{x3} est alors utilisé pour satisfaire à l'annulation de la perturbation de pression statique à la sortie du diffuseur, $p_{s5} = 0$.

La modélisation est améliorée par la prise en compte des effets instationnaires dus aux mouvements des rotors à travers la distorsion stationnaire.

Nous avons utilisé l'analyse de Melick (Réf. 7). Par analogie avec un profil isolé, on admet que la grille d'aubes se comporte comme si elle était attaquée par un écoulement de direction $\beta_{e,eff}$, différente de la direction réelle instantanée β_e . Cela permet de tenir compte du temps de réponse des phénomènes visqueux. On peut simuler cet effet par l'équation suivante :

$$(3) \frac{d^2(\beta_{e,eff} - \beta_e)}{d\tau^2} + \left(\frac{1}{\tau_1} + \frac{1}{\tau_2}\right) \frac{d(\beta_{e,eff} - \beta_e)}{d\tau} + \frac{1}{\tau_1 \tau_2} (\beta_{e,eff} - \beta_e) = \frac{1}{\tau_1 \tau_2} (\beta_e - \bar{\beta}_e)$$

où τ est le temps réduit $\tau = t \cdot \frac{W_e}{c}$, τ_1 et τ_2 des constantes expérimentales. Si la perturbation $\beta_e(\theta)$ est représentée par la série de Fourier suivante :

$$\bar{\beta}_e + \sum_{n=1}^{\infty} [a_n \cos n\theta + b_n \sin n\theta], \text{ la solution de l'équation (3) est alors :}$$

$$\beta_{e,eff}(\theta) = \bar{\beta}_e + \sum_{n=1}^{\infty} F(nk) \{ a_n \cos [n\theta + \psi(nk)] + b_n \sin [n\theta + \psi(nk)] \}$$

avec :

$$F(nk) = \left[(1 + 4n^2 k^2 \tau_1^2) (1 + 4n^2 k^2 \tau_2^2) \right]^{-1/2}$$

$$\psi(nk) = 1 / \text{tg}(2nk\tau_1) + 1 / \text{tg}(2nk\tau_2) \quad k = \frac{\Omega \cdot c}{2 \cdot W_e} \text{ (fréquence réduite)}$$

En admettant que les perturbations d'incidence sont petites, on peut en déduire la correction instationnaire à apporter au rapport de pression de chaque secteur :

$$\frac{\pi_{eff} - \bar{\pi}}{\bar{\pi}} \approx \frac{\beta_{e,eff} - \bar{\beta}_e}{\beta_e - \bar{\beta}_e}$$

L'amplitude du cycle instationnaire décrit par le point représentatif dans le champ compresseur (Fig. 2) se trouve donc atténuée et son allure peut être déformée. Dans la pratique, cet effet est calculé en ne faisant intervenir que la corde de la première roue mobile.

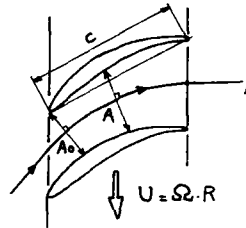
Enfin, dans le compresseur (zone C), les rotors sont alimentés par du fluide présentant des variations temporelles de température et de pression totales relatives. Les effets instationnaires qui en résultent sont approchés en schématisant l'écoulement monodimensionnel dans le canal inter-aube du rotor par l'équation suivante (Réf. 4):

$$\frac{\partial W}{\partial t} + W \cdot \frac{\partial W}{\partial A} = - \frac{1}{\rho} \frac{\partial P_s}{\partial A}$$

Cette équation permet en particulier de connaître les corrections de pression totale relative à apporter aux abaques de performances stationnaires des profils.

$$\Delta P_T^* = - K \cdot \rho_e \cdot \Omega \cdot \left[\frac{dW}{d\theta} \right]_e$$

où $K = \int_0^c \frac{A_0}{A(s)} ds$ se déduit de la géométrie des aubes.



2.1.2. Applications

Les figures 3a, 3b et 3c montrent les résultats obtenus par l'application de la méthode des secteurs de compresseurs en parallèle à un compresseur BP à 3 étages équipé d'une RDE et fonctionnant à 85 % du régime de rotation nominal. On constate une forte atténuation de la distorsion de pression totale ; le coefficient $H_p = (P_{T \max} - P_{T \min}) / P_T$ est divisé par 3 à la sortie du compresseur. Simultanément il apparaît une distorsion de température totale mesurée par le coefficient $H_T = (T_{T \max} - T_{T \min}) / T_T$.

En ce qui concerne la perte de marge au décrochage, la figure 4 montre le cycle de fonctionnement formé par l'ensemble des secteurs. On constate que les effets d'incidence fluctuante (méthode de Melick) aplatissement le cycle et procurent un très léger gain de marge au décrochage.

Les effets non stationnaires dus à la fluctuation des pressions et températures totales relatives à l'amont des rotors élargissent le cycle de fonctionnement sans avoir d'effet notable sur la marge au décrochage.

Les applications numériques se font en général en divisant le compresseur en 18 secteurs et en utilisant 20 harmoniques pour la description suivant θ . Les temps de calcul sur ordinateur sont très courts et permettent l'étude de nombreuses variantes.

2.2. METHODE DE CALCUL DE L'ÉCOULEMENT TRIDIMENSIONNEL ET NON STATIONNAIRE

2.2.1. Description sommaire de la méthode

La méthode utilisée est celle développée par MM. Laval et Billet de l'ONERA (Réf. 8). L'écoulement tridimensionnel, compressible, non stationnaire et hétérogène est obtenu en résolvant les équations d'Euler complètes dans les espaces libres d'aubages. Ce calcul est couplé avec un modèle simple représentant les rotors et les stators.

Ce modèle de grilles d'aubes est construit à l'aide des principales hypothèses suivantes :

- l'évolution radiale des surfaces de courant est imposée et provient d'un calcul axisymétrique stationnaire $V_r = V_x \cdot \tan \phi_{ss}(R, x)$
- les coefficients de pertes non stationnaires ainsi que la direction relative de sortie sont gouvernés par des équations de retard faisant intervenir des constantes de temps τ_w et τ_β

$$\tau_w \frac{\partial \omega}{\partial t} + \omega = \omega_{ss}$$

$$\tau_\beta \frac{\partial \beta_s}{\partial t} + \beta_s = \beta_{ss}$$

les variables indicées ss caractérisent les performances des aubes en écoulement stationnaire et sont des fonctions supposées connues des conditions d'entrée de l'aubage, notamment de la direction amont β_1 et du nombre de Mach relatif amont Mw_1 ,

- Le pas de l'aubage est petit devant la longueur d'onde spatiale de la distorsion.

Les hypothèses précédentes permettent d'explicitier simplement 3 relations intégrales (conservation de la masse, quantité de mouvement et énergie) qui gouvernent le fonctionnement d'un canal inter-aubes.

Dans les domaines de calcul libres d'aubage, on effectue la transformation de coordonnées suivante qui permet d'obtenir un domaine de calcul parallélépipédique

$$R + \mu = \frac{R - R_h(x)}{R_c(x) - R_h(x)}$$

Les équations d'Euler peuvent alors s'écrire sous la forme conservative suivante :

$$(4) \frac{\partial Y}{\partial t} + \frac{\partial F(Y)}{\partial x} + \frac{\partial G(Y, x, \theta, \mu)}{\partial \theta} + \frac{\partial H(Y, x, \mu)}{\partial \mu} = 0$$

$$\text{où } Y = [R_c(x) - R_h(x)] \cdot \begin{bmatrix} \rho \cdot R \\ \rho \cdot R \cdot V_x \\ \rho \cdot R (V_n \sin \theta + V_\theta \cos \theta) \\ \rho \cdot R (V_n \cos \theta - V_\theta \sin \theta) \\ E \cdot R \end{bmatrix}$$

$$E = \frac{P_s}{\delta - 1} + \frac{1}{2} \rho \cdot v^2 \text{ est l'énergie totale par unité de volume.}$$

Ce système d'équations est résolu par un schéma aux différences finies, explicite et du 2ème ordre. Il s'agit d'un schéma de désintégration qui est le produit de plusieurs opérateurs monodimensionnels. Cette technique permet d'obtenir une condition de stabilité linéaire qui pénalise le pas de temps du calcul d'une façon moindre qu'une discrétisation directe de l'opérateur tridimensionnel.

2.2.2. Applications

Nous présentons un calcul fait sur un compresseur basse pression à 3 étages avec RDE. Le maillage utilisé est formé de 93 lignes dans la direction x , 41 lignes dans la direction θ et de 11 lignes dans la direction R . Le temps de calcul est de l'ordre de 45 minutes sur l'ordinateur CRAY-1. Les figures 5a, 5b, et 5c représentent les cartes de pression totale dans les plans amont compresseur, aval rotor 1 et aval rotor 2. Comme prévu, on remarque que, dans la zone de moyeu à l'aval de la RM1, la distorsion est beaucoup moins atténuée qu'à la tête. On note un accord qualitativement satisfaisant entre les calculs tridimensionnels et les résultats d'essais présentés par les figures 12a, 12b et 12c. Un des principaux intérêts de ce calcul est de fournir les conditions de fonctionnement (angle de l'écoulement et nombre de Mach amont) de chaque profil d'aube.

2.3. METHODE DE PREDICTION DE LA STABILITE DES COMPRESSEURS ALIMENTES PAR UN ECOULEMENT HOMOGENE

La prédiction de la limite de stabilité des compresseurs alimentés par un flux homogène est un préalable nécessaire aux études spécifiques sur la distorsion. Cela apparaît, par exemple, dans la méthode décrite au paragraphe 2.1. Diverses méthodes de stabilité linéaire ont été développées (Réf. 9, 10 et 11). Nous allons décrire brièvement une méthode de calcul qui modélise le comportement du fluide sur une nappe de courant en tenant compte des effets non stationnaires dus aux volumes de chaque rangée d'aubes et aux distances qui les séparent (Réf. 12).

2.3.1. Description sommaire de la méthode

Le compresseur est divisé en plusieurs modules. Les rangées d'aubes ainsi que les espaces qui les séparent constituent chacun un module. Les principales hypothèses nécessaires sont les suivantes :

- écoulement axisymétrique
- nappes de courant tronconiques repérées par le paramètre géométrique λ (Fig. 6)
- vitesse radiale négligeable
- écoulement adiabatique
- perte et angle de sortie des aubes en fonctionnement stationnaire donnés comme fonctions des conditions d'entrée.

Chaque point d'espace est repéré par les deux coordonnées x et λ

$$R = R_e + \lambda \cdot \Delta R_e + \frac{x}{L} [R_s - R_e + \lambda (\Delta R_s - \Delta R_e)]$$

La figure 6 définit les notations employées.

Les équations de continuité, de quantité de mouvement projetée sur \vec{W} et d'énergie sont intégrées sur le volume délimité par deux tubes de courant infiniment voisins respectivement repérés par λ et $\lambda + d\lambda$ (Fig. 6). On obtient les 3 équations suivantes :

$$(5) \int_0^L R \frac{\partial R}{\partial \lambda} \frac{\partial \rho}{\partial t} dx = R_e \frac{dR_e}{d\lambda} \rho_e W_{x_e} - R_s \frac{dR_s}{d\lambda} \rho_s W_{x_s} \quad (\text{Continuité})$$

$$(6) \int_{\lambda_e}^{\lambda_s} \left(\frac{\partial W}{\partial t} + \frac{1}{W} \frac{\partial S}{\partial t} \right) d\lambda = I_e - I_s \quad (\text{quantité de mouvement projetée sur } \vec{W})$$

$$(7) \int_0^L R \frac{\partial R}{\partial \lambda} \frac{\partial}{\partial t} \left[\rho \left(E + \frac{W^2}{2} - \frac{U^2}{2} \right) \right] dx = R_e \frac{dR_e}{d\lambda} \rho_e W_{x_e} I_e - R_s \frac{dR_s}{d\lambda} \rho_s W_{x_s} I_s \quad (\text{Energie})$$

auxquelles on adjoint les deux équations supplémentaires suivantes :

- (a) En fonctionnement stationnaire, l'angle de sortie est supposé être une fonction connue des conditions d'entrée. On adopte une loi du type $\text{tg } \beta_s = b_1 \cdot \text{tg } \beta_e + b_2$ où b_1 et b_2 sont des constantes données.

En fonctionnement non stationnaire, on peut alors écrire la relation suivante :

$$(8) \quad \int_{\Delta_e}^{\Delta_s} \frac{1}{W} \cdot \frac{\partial}{\partial t} \left(\frac{W\theta}{Wx} \right) \cdot d\Delta = - \frac{W\theta_s}{Wx_s} + b_1 \cdot \frac{W\theta_e}{Wx_e} + b_2$$

Dans les modules dépourvus d'aube, (8) est remplacée par l'équation de quantité de mouvement projetée sur θ .

$$(8 \text{ bis}) \quad \int_{\Delta_e}^{\Delta_s} \frac{R}{V} \cdot \frac{\partial V\theta}{\partial t} \cdot d\Delta = R_e V\theta_e - R_s V\theta_s$$

- (b) En dehors des rangées d'aubes, les tubes de courant sont supposés isentropiques. Pour traiter les rangées d'aubes nous supposons connu le coefficient de pertes stationnaires $\bar{\omega} = \frac{P_e - P_s}{P_e - P_{se}}$ en fonction des conditions d'entrée de l'aubage.

On peut alors écrire l'équation suivante qui gouverne l'accroissement d'entropie.

$$(9) \quad \int_{\Delta_e}^{\Delta_s} \frac{1}{W} \cdot \frac{\partial S}{\partial t} \cdot d\Delta = S_e - S_s - \bar{\omega} \cdot \text{Log} \left(1 - \bar{\omega} \cdot \frac{B_e - 1}{B_s} \right)$$

où $B_e = \left(1 + \frac{W_e^2}{2 C_p T_{re}} \right)^{\frac{\gamma}{\gamma-1}}$ et $B_s = \left(1 + \frac{W_e^2 - U_e^2 + U_s^2}{2 C_p T_{re}} \right)^{\frac{\gamma}{\gamma-1}}$

Les 5 équations (5), (6), (7), (8) ou (8 bis), (9) sont ensuite linéarisées par rapport à l'état stationnaire et forment le système suivant :

$$[M] \cdot \frac{\partial}{\partial t} (\phi - \phi_{ss}) = [P] \cdot (\phi - \phi_{ss})$$

où $\phi = (\rho_e, Vx_e, V\theta_e, T_e, S_e, \rho_s, Vx_s, V\theta_s, T_s, S_s)^t$

et où [M] et [P] sont des matrices 10 x 10.

Si le compresseur se compose de n modules, on arrive à un système de 5 n équations scalaires reliant les 5n + 5 composantes du vecteur ϕ . En effet, les modules étant reliés en série, $(\rho_e)_{j+1} = (\rho_s)_j$, $(Vx_e)_{j+1} = (Vx_s)_j$, etc..., j étant le rang du module. Le nombre initial d'inconnues est donc divisé par deux, sauf pour le premier ou le dernier module. A l'entrée du premier module on impose la stationnarité des conditions génératrices et de la composante tangentielle de la vitesse $\left(\frac{\partial P_e}{\partial t} \right)_e, \left(\frac{\partial T_e}{\partial t} \right)_e, \left(\frac{\partial V\theta_e}{\partial t} \right)_e = 0$.

La sortie du dernier module est une vanne définie par sa caractéristique quasi-stationnaire. Ces conditions aux limites fournissent les 5 relations manquantes.

D'après le théorème de Lyapunov, on peut dire que la limite de stabilité du système réel est la même que celle du système linéarisé. Les instabilités apparaissent donc quand la partie réelle d'au moins une des valeurs propres de la matrice $[M]^{-1} \cdot [P]$ devient positive. Dès qu'une nappe de courant devient instable, on dit qu'il y a instabilité de fonctionnement du compresseur. Cette méthode ne peut pas différencier le décrochage total du décrochage tournant partiel.

2.3.2. Applications

La figure 7 montre les résultats de l'application du code de calcul précédemment décrit à un compresseur basse pression à 3 étages. On constate que l'accord entre le décrochage mesuré et le décrochage calculé est relativement satisfaisant. Bien entendu la prévision de la limite de décrochage est fortement dépendante de la précision avec laquelle est restitué le champ stationnaire. Les améliorations envisagées portent sur l'introduction d'une équation d'équilibre radial non stationnaire dans le système d'équations utilisées.

3 - METHODES EXPERIMENTALES

3.1. CARACTERISATIONS DES DISTORSIONS NON STATIONNAIRES

Pour assurer la compatibilité entrée d'air-moteur, il est nécessaire de connaître les distorsions auxquelles sera soumis le turboréacteur. A titre de vérification finale, ou bien s'il s'agit d'un programme d'avion expérimental, il peut être envisagé de mesurer ces distorsions au cours d'essais en vol. Il s'agit alors d'opérations coûteuses par suite des conditions difficiles de mise en oeuvre (problème de sécurité, problème d'acquisition à grande cadence à partir d'un avion de chasse, etc...). Toutefois ces méthodes d'expérimentation diffèrent peu de celles employées au cours des essais des maquettes d'entrée d'air en soufflerie.

Le but principal est l'établissement de cartes instantanées de pression totale dans un plan situé le plus près possible de l'entrée du compresseur basse pression. Ce plan est équipé de 8 peignes circonférentiellement équirépartis, chacun comportant 5 prises placées au centre de 5 anneaux fictifs d'égales sections. Chaque prise fournit la pression totale moyenne et est équipée d'un capteur à court temps de réponse qui donne la composante fluctuante de la pression totale. Les signaux sont préalablement filtrés à une fréquence proportionnelle à la vitesse de rotation du compresseur BP. Le système d'acquisition et de traitement (Fig. 8 et Réf 13) est entièrement numérique. Le dépouillement est réalisé à l'aide d'un processeur vectoriel AP120B associé à un ordinateur HP 1000. Cette chaîne, placée sur une plate-forme mobile, peut traiter 64 voies synchronisées à une fréquence d'échantillonnage maximale de 16 kHz. En temps réel, elle est capable de tracer la carte stationnaire et d'afficher les maximums de plusieurs coefficients de distorsion instantanée (K_{θ} , $K_{\theta 2}$, IDC, IDR, ...). En temps différé, des dépouillements plus complexes, tels que carte de turbulence, carte de pression totale instantanée ou étude de différents filtrages peuvent être effectués. La fig. 9 donne un aperçu des résultats qu'il est possible d'obtenir. Cette chaîne d'Acquisition et de Traitement de l'Instantané (C.A.I.I.) a été entièrement conçue et réalisée par la SNECMA.

3.2. CREATION DE DISTORSIONS NON STATIONNAIRES SUR BANC D'ESSAIS DE COMPRESSEUR

Un moyen simple de créer des distorsions non stationnaires est de créer des manches d'entrées non axisymétriques. Certains secteurs, semblables à des pavillons classiques, n'engendrent pas de perte de pression totale. D'autres secteurs présentent des arêtes vives, des diffuseurs locaux ou tout autre forme qui provoque des décollements plus ou moins intenses. Ces dispositifs sont en général mis au point à petite échelle dans une soufflerie. On recherche d'abord à reproduire la carte stationnaire de pression totale. On vérifie ensuite, à une échelle si possible plus grande, que les coefficients maximaux de la distorsion instantanée sont proches des valeurs souhaitées (Réf. 14 et 15). Les figures 10a, 10b et 10c représentent un dispositif qui a déjà été monté devant un compresseur en essais. On note que la distorsion stationnaire mesurée est très voisine de celle qui avait été relevée au cours d'essais en soufflerie sur une maquette d'entrée d'air. De tels dispositifs permettent en outre d'obtenir des distorsions dont la composante stationnaire est supérieure à celle que l'on obtient par les techniques classiques des écrans à perméabilité variable.

3.3. ESSAIS DE COMPRESSEURS OU DE MOTEURS COMPLETS

Au cours des essais de compresseurs alimentés par un dispositif créant de la distorsion, le plan amont est équipé des peignes de mesure décrits au paragraphe 3.1. Il est alors possible de relier la perte de marge au décrochage mesurée à un coefficient caractéristique de la distorsion instantanée maximale (Fig. 11). Si les essais sont suffisamment nombreux, la recherche de bonnes corrélations peut faire intervenir une fonction de plusieurs variables caractérisant la distorsion et peut nécessiter une étude fine du filtrage à effectuer.

Ces essais permettent en général de mesurer les cartes de plusieurs variables aérodynamiques (pression totale, température totale, angle absolu, etc...) dans les plans situés entre les rangées d'aubes. Les figures 12a, 12b et 12c montrent l'évolution de la distorsion de pression totale au travers d'un compresseur basse pression à 3 étages.

4 - IMPACTS DES ETUDES SUR LA CONCEPTION DES COMPRESSEURS BASSE PRESSION

4.1. ROUE DIRECTRICE D'ENTREE A L'AMONT DU COMPRESSEUR

Les résultats expérimentaux (Fig. 13) montrent qu'un compresseur muni d'une roue directrice d'entrée est moins sensible à la distorsion circonférentielle qu'un compresseur qui en est dépourvu. Le calage variable accroît l'effet bénéfique de la roue directrice d'entrée aux faibles vitesses de rotation du compresseur. Les études théoriques faites avec la méthode des compresseurs en parallèle montrent que, en annulant les perturbations circonférentielles induites de la vitesse tangentielle, la roue directrice d'entrée réduit beaucoup l'étendue du cycle décrit par le point représentatif des différents secteurs du compresseur (Fig. 14). Dans cette étude théorique la sensibilité du compresseur, exprimée par $\Delta SM/K_{\theta}$, passe de 0,28 à 0,18 par l'adjonction d'une roue directrice d'entrée n'induisant pas de circulation moyenne.

On peut donc dire qu'une roue directrice d'entrée à 3 effets bénéfiques sur le fonctionnement des compresseurs basse pression :

- elle réalise l'adaptation radiale du degré de réaction du premier étage au point de dessin,
- lorsqu'elle est à calage variable, elle permet de réadapter le compresseur aux vitesses de rotation réduite. Cela procure un important gain de marge au décrochage,
- en supprimant les perturbations circonférentielles induites de la vitesse tangentielle, elle diminue la sensibilité du compresseur à la distorsion amont.

4.2. INFLUENCE DES ALLONGEMENTS DES AUBES

Les résultats expérimentaux (Tableau 1) montrent que l'augmentation des cordes (diminution des allongements) à pas relatif fixé (diminution du nombre d'aubes) procure un gain de marge au décrochage.

| Type de compresseur | Effet de l'allongement sur la marge au pompage $\Delta \eta s / \Delta (h/c)$ |
|---------------------------|--|
| Soufflante (1 étage) | 0.046 |
| Compresseur BP (3 étages) | 0.072 |
| Compresseur à 8 étages | 0.30 |

TABLEAU 1

Influence de l'allongement moyen sur la marge au décrochage

Les résultats théoriques fournis par la méthode des compresseurs en parallèle (Fig. 15) montrent que les effets non stationnaires résultant de l'augmentation des cordes sont bénéfiques. La sensibilité à la distorsion diminue lorsque les cordes augmentent. L'adoption de grandes cordes pour le premier ou les deux premiers étages pourrait faire gagner environ 1% de marge au décrochage, uniquement par l'effet de moindre sensibilité à la distorsion circonférentielle. Nous ne possédons pas de résultats expérimentaux pour confirmer l'effet des cordes sur la sensibilité à la distorsion amont.

4.3. INFLUENCE DE L'ESPACEMENT DES RANGÉES D'AUBES

En ce qui concerne la sensibilité à la distorsion, nous ne possédons pas de résultats expérimentaux sur l'influence de l'espacement des rangées d'aubes. L'approche théorique a été faite avec un calcul bidimensionnel qui est la généralisation, à l'ensemble du compresseur, du traitement de l'espace amont exposé au paragraphe 2.1.1. Le cas d'application retenu est un compresseur à 4 étages et nous avons étudié l'influence de la distance axiale entre le rotor et le stator du premier étage et ensuite, l'influence de la distance axiale séparant les deux premiers étages (Fig. 16 et 17).

La réduction de l'espacement rotor 1 - stator 1 atténue la perturbation d'incidence sur les aubes du premier étage mais augmente la distorsion transmise aux étages suivants. La réduction de l'espacement stator 1 - rotor 2 atténue les perturbations sur le deuxième étage et les suivants mais les augmente sur le stator 1.

Pour des raisons d'encombrement et de poids, les compresseurs sont souvent conçus avec des distances entre rangées d'aubes choisies à la valeur minimum compatible avec les contraintes de dilatation des rotors et d'assemblage de la structure. Les études aérodynamiques sur la distorsion et la marge au décrochage indiquent que ce choix est bénéfique pour la stabilité aérodynamique du compresseur. Il faut toutefois indiquer que notre modèle ne tient pas compte des fortes fluctuations dues au défilement des sillages.

4.4. DISTRIBUTION DE LA CHARGE AÉRODYNAMIQUE ENTRE LES ÉTAGES

Il est évident que le premier étage des compresseurs basse pression réalise une grande partie de l'atténuation de la distorsion de pression amont et fonctionne en étant soumis aux plus fortes perturbations d'incidence. Cet étage doit donc être conçu avec des charges aérodynamiques qui ne soient pas trop élevées, notamment dans la région du moyeu. Cependant, l'obtention d'une bonne marge au décrochage aux vitesses de rotation élevées conduit à réduire la charge aérodynamique du dernier étage. Cela limite donc les possibilités de réduction de la charge aérodynamique du premier étage. Dans la pratique la conception des compresseurs basse pression fait donc toujours appel à des compromis difficiles à évaluer.

5 - CONCLUSION

Les méthodes de calcul, de la plus simple (compresseurs en parallèle) jusqu'à la plus complexe (calcul tridimensionnel non stationnaire) s'avèrent utiles pour arriver à un dessin de compresseur de moins en moins sensible à la distorsion. Parallèlement, des moyens expérimentaux ont été mis en oeuvre pour reproduire des distorsions fluctuantes existant dans les entrées d'air d'avion et démontrer ainsi la bonne compatibilité entrée d'air-moteur. Pour cela, il a été nécessaire de construire des instruments de mesure et d'analyse destinés à caractériser les cartes instantanées des variables aérodynamiques de l'écoulement.

Ces études ont montré que la présence d'une roue directrice d'entrée, l'adoption d'allongements faibles, la réduction des espaces entre les rangées d'aubes, atténuent la sensibilité du compresseur à la distorsion de pression totale et accroissent sa marge au décrochage.

REFERENCES

- 1 - B. DELAHAYE : Determination of the stable operating conditions of an axial flow compressor.
Lectures Series 1984-02
Institut Von Karman pour la Dynamique des Fluides, 20-24 Fevrier 1984.
- 2 - B. DELAHAYE, P. SAGNES : Inlet distortion and compressor behaviour. 14th Congress of the International Council of the Aeronautical Sciences - Toulouse, France 10-14 Septembre 1984.
Volume 2, paper 1.9.1., pp 996 - 1004.
- 3 - A. LARDELLIER, H. JOUBERT, P. GEYER : New engine technology
AGARD - 68th Symposium of the Flight Mechanics Panel on Improvement of Combat performances for existing and future aircraft.
Treviso, Italy, 14-17 April 1986.
- 4 - R.S. MAZZAWY : Multiple segment parallel compressor model for circumferential flow distortion
AGARD CP 177, 1976 and ASME, Journal of Engineering for Power, April 1977.
- 5 - MOKELKE : The prediction of steady, circumferential pressure and temperature distortions in multistage axial flow compressors
ASME, Paper 79 - GT - 184, 1979.
- 6 - E.M. GREITZER, H.R.C. RISWOLD : Compressor - diffusion interaction with circumferential flow distortion
Journal of Mechanical Engineering for Sciences, 1976.
- 7 - H.C. MELICK : Analysis of inlet flow distortion and turbulence effects on compressor stability.
NASA Technical Report CR 114577, March 1973.
- 8 - G. BILLET, P. LAVAL, P. CHEVALIER : Response of an axial compressor to distorted inlet flow
Conference on Computational Methods in Turbomachinery
University of Birmingham, 10 - 12 April 1984.
- 9 - J. FABRI : Growth of a perturbation in an axial flow compressor
ASME - Paper 78 GT 80, 1978.
- 10 - P. FERRAND, J. CHAUVIN : Theoretical study of flow instabilities and inlet distortion in axial compressors
ASME - Paper 81 GT 211, 1981.
- 11 - B. DELAHAYE : Study of instabilities in axial flow compressors. 6th International Symposium on Air Breathing Engines
Paris, France, June 6 - 10, 1983
Paper 7076, pp 656 - 664.
- 12 - P. GILLANT, P. SAGNES
Notes Techniques de la Société BERTIN.
- 13 - P. PERRIER, B. DELAHAYE, G. LARUELLE : Système d'acquisition et d'analyse pour essais dynamiques d'entrées d'air
Aerodynamics of Power Plant Installation
AGARD - CPP n° 301 - Paper 18.
- 14 - B. DELAHAYE, G. LARUELLE : Dispositif de simulation au banc compresseur d'une prise d'air à grande incidence
Aerodynamics of Power Plant Installation
AGARD - CPP n° 301 - Paper 17.
- 15 - J.R. BION, H. SALAUN : Qualification de l'écoulement dans les prises d'air et évaluation de la perte de marge au pompage due aux distortions à l'entrée du compresseur
15ème Congrès ICAS, 7 - 12 Septembre 1986, Londres (à paraître).

REMERCIEMENTS

Les auteurs tiennent à remercier J. BLEUZEN pour la contribution qu'il a apportée à cette étude. Ils remercient également la Direction de la SNECMA d'avoir autorisé cette publication.

Les études exposées ici n'ont été possibles que grâce au soutien actif et continu de la Délégation Générale pour l'Armement et notamment de la D.R.E.T. et du S.T.P.A.

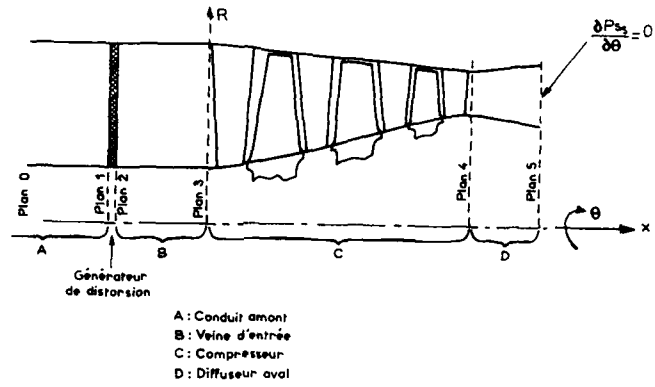


Figure 1 METHODE DES COMPRESSEURS EN PARALLELE
DIVISION DE LA VEINE DU SYSTEME DE COMPRESSION

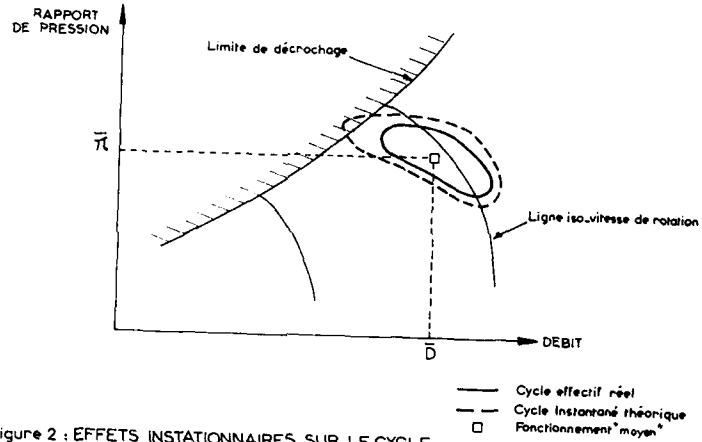


Figure 2 : EFFETS INSTATIONNAIRES SUR LE CYCLE
DE FONCTIONNEMENT DU COMPRESSEUR

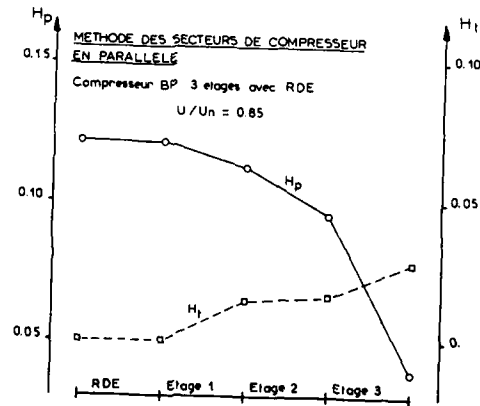
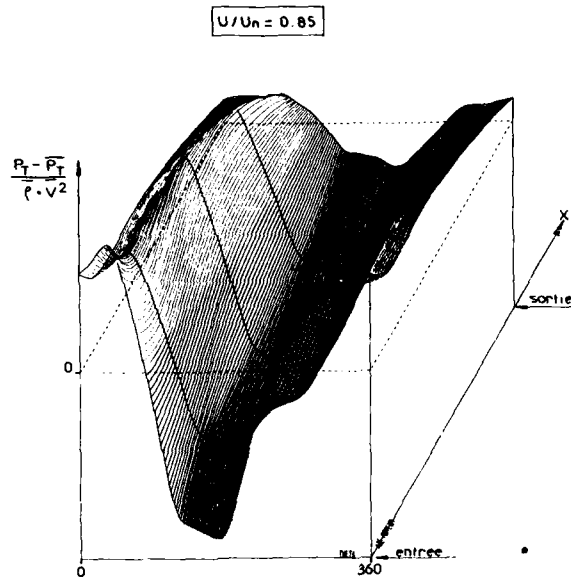
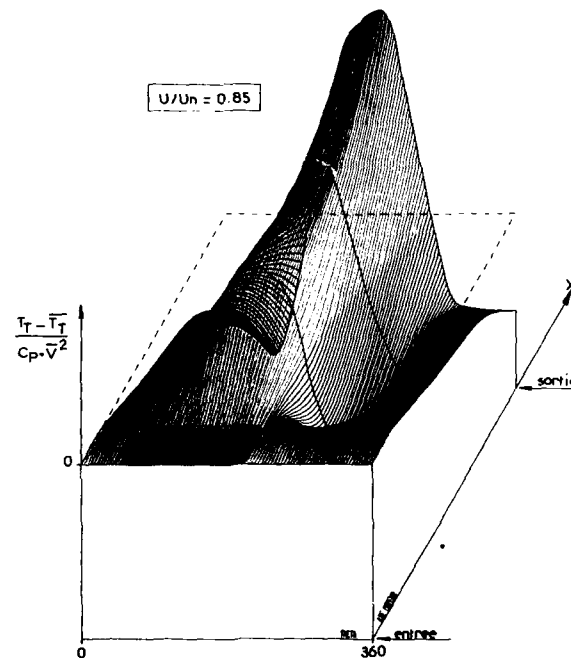


Fig 3a: EVOLUTION DE COEFFICIENTS DE DISTORSION
A LA TRAVERSE D UN COMPRESSEUR



METHODE DES SECTEURS DE COMPRESSEUR EN PARALLELE

Fig 3b: ATTENUATION DE LA DISTORSION DE PRESSION TOTALE
A TRAVERS UN COMPRESSEUR BP 3 ETAGES AVEC RDE



METHODE DES SECTEURS DE COMPRESSEUR EN PARALLELE

Fig 3c: APPARITION D'UNE DISTORSION DE TEMPERATURE TOTALE
A TRAVERS UN COMPRESSEUR BP 3 ETAGES AVEC RDE

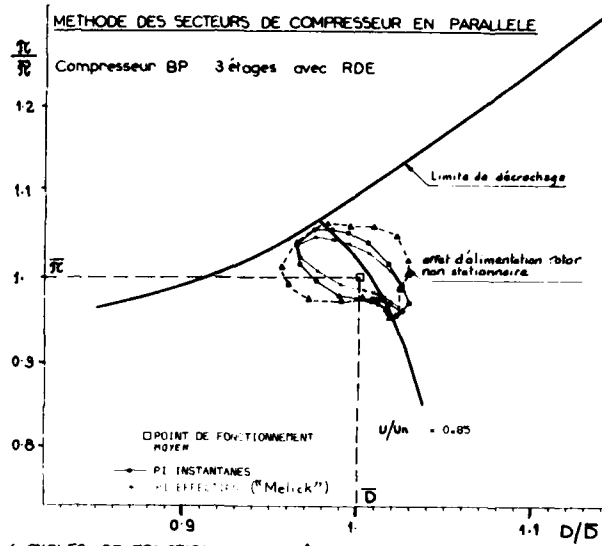


Fig 4: CYCLES DE FONCTIONNEMENT D'UN COMPRESSEUR SOUMIS A UNE DISTORSION AMONT - EFFETS NON-STATIONNAIRES

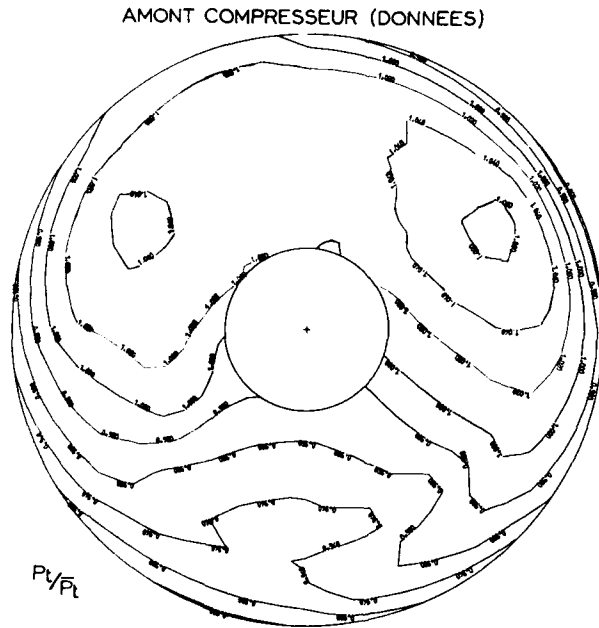


Figure 5a: CALCUL 3D NON STATIONNAIRE
CARTE DE PRESSION TOTALE ABSOLUE

AVAL ROTOR N°1

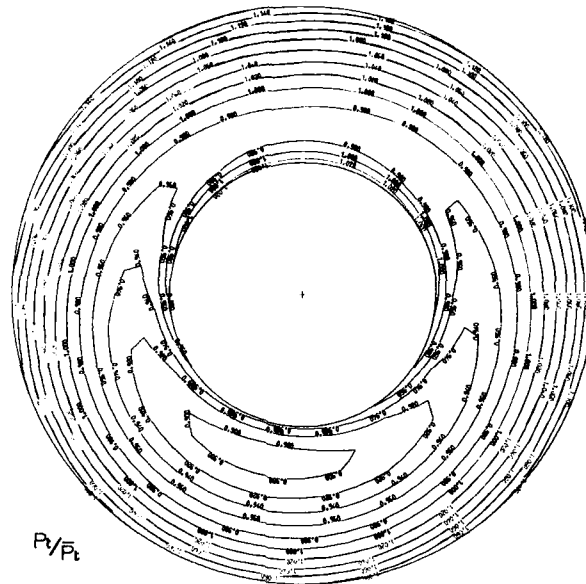


Figure 5b : CALCUL 3D NON STATIONNAIRE
CARTE DE PRESSION TOTALE ABSOLUE

AVAL ROTOR N°2

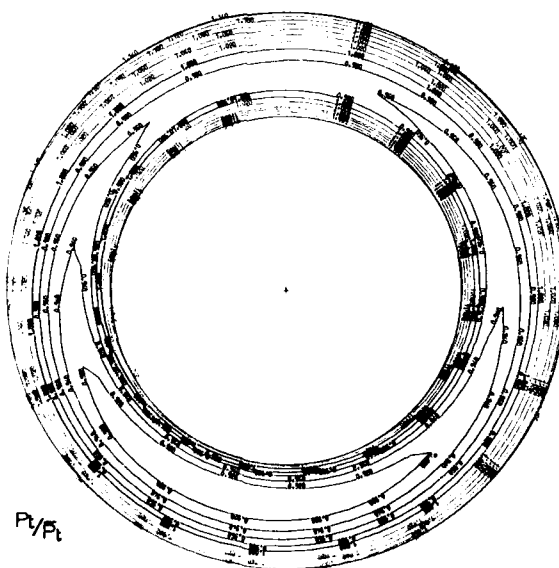


Figure 5c : CALCUL 3D NON STATIONNAIRE
CARTE DE PRESSION TOTALE ABSOLUE

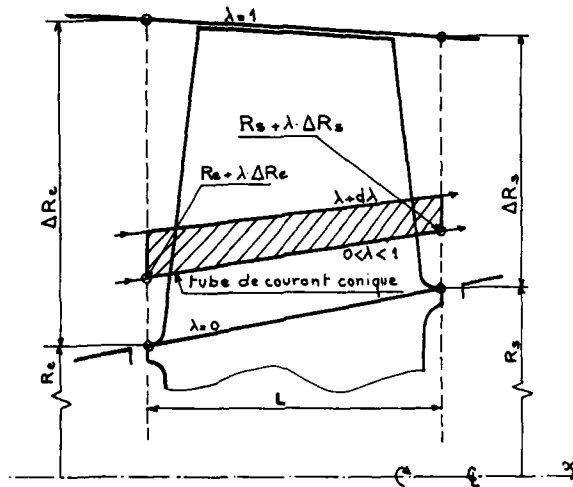


Fig 6: PARAMETRAGE DES TUBES DE COURANT
DEFINITION DES PRINCIPAUX SYMBOLES

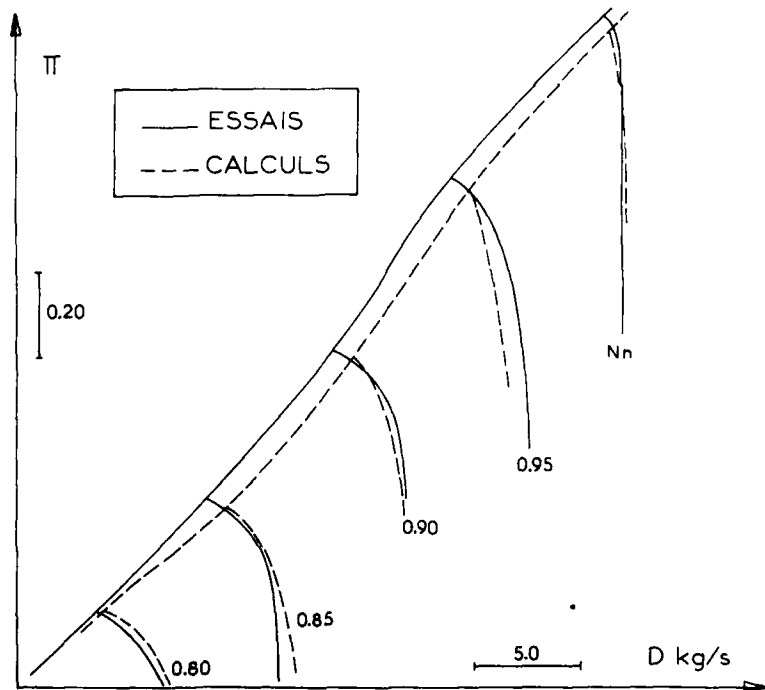


Figure 7. PREVISION DE LA LIMITE DE DECROCHAGE
COMPRESSEUR BP - 3 ETAGES - AVEC RDE -

FIGURE 8 : SCHEMA DE LA CHAINE D'ACQUISITION
ET DE TRAITEMENT INSTATIONNAIRE
*UNSTEADY DATA ACQUISITION
AND PROCESSING SYSTEM BLOCK DIAGRAM*

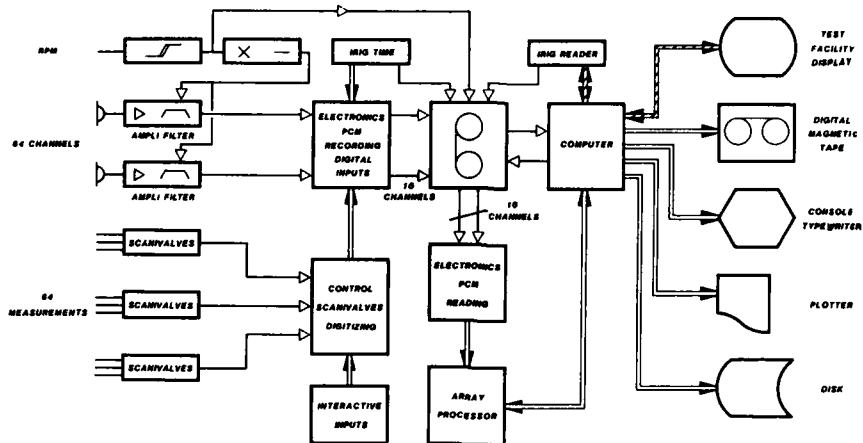
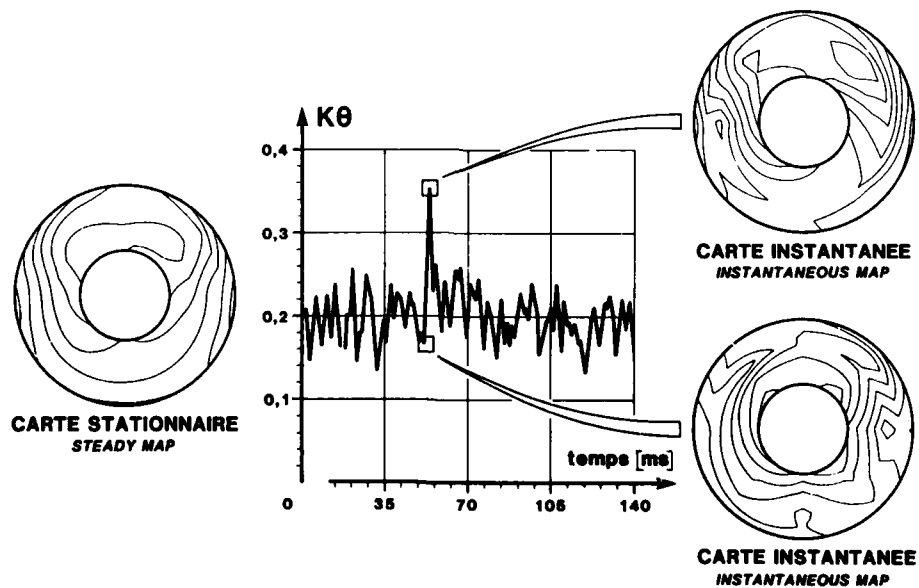
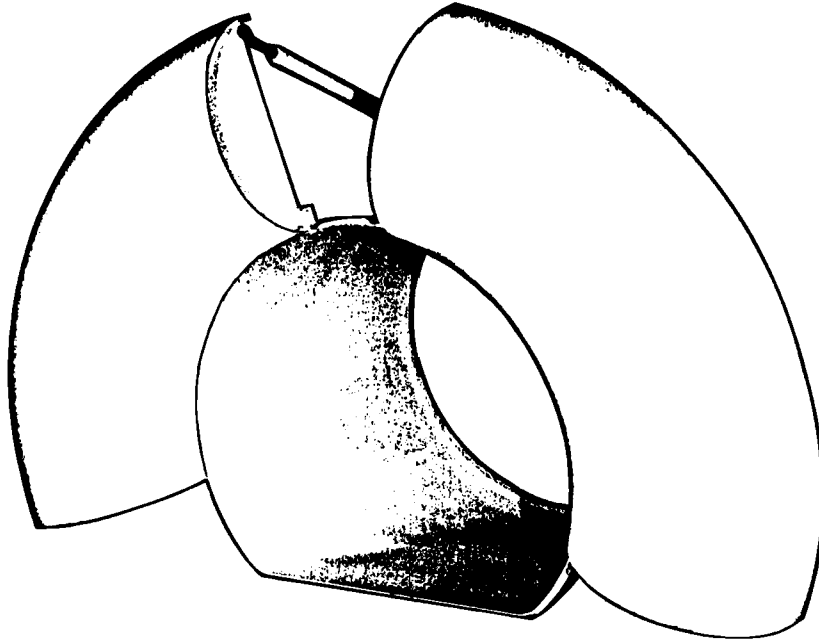


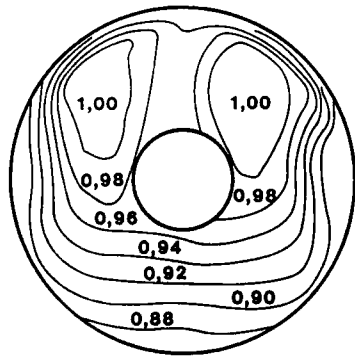
FIGURE 9 : MESURES EN SOUFFLERIE SUR MAQUETTES D'AVION
WIND-TUNNEL MEASUREMENTS ON AIRCRAFT SCALE MODEL



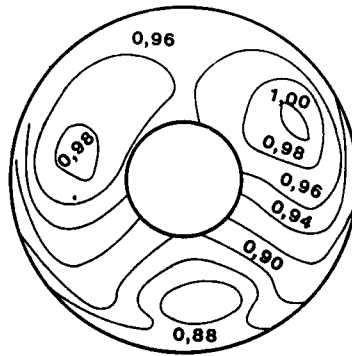
**FIGURE 10a: VUE DE LA MANCHE DE SIMULATION
SIMULATION AIR INTAKE**



**FIGURE 10b:
CARTE DE PRESSION STATIONNAIRE
DE LA MANCHE REELLE
STEADY PRESSURE MAP
OF THE ACTUAL AIR INTAKE**



**FIGURE 10c:
CARTE DE PRESSION STATIONNAIRE
DE LA MANCHE DE SIMULATION
STEADY PRESSURE MAP
OF THE SIMULATION AIR INTAKE**



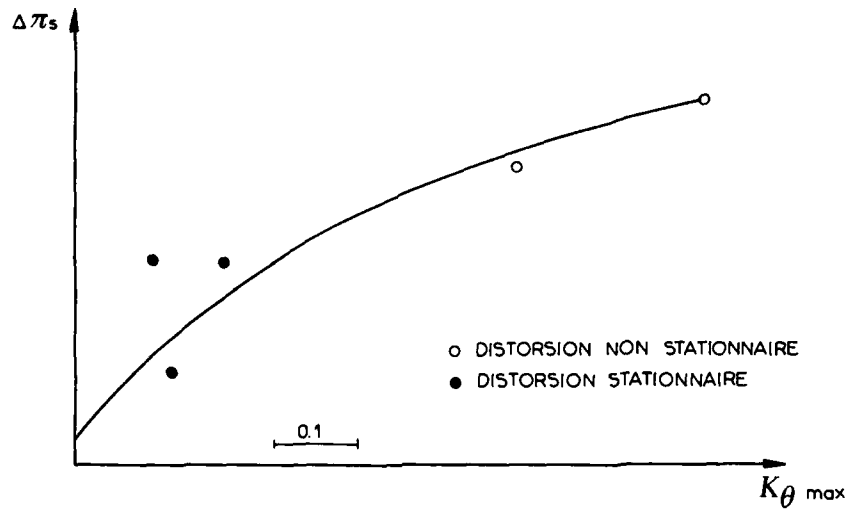


Fig: 11: SENSIBILITE D'UN COMPRESSEUR A LA DISTORSION CIRCONFERENCELLE
 VALEURS EXPERIMENTALES - REGIME DE ROTATION NOMINAL

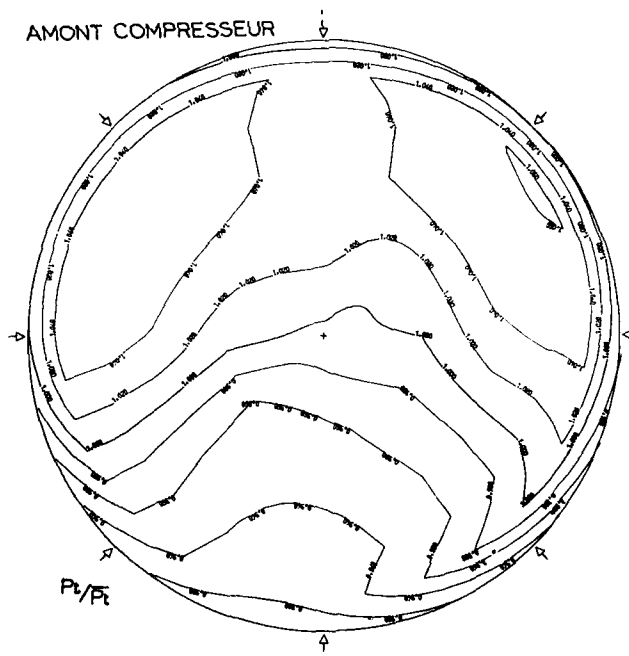


Figure 12a, ESSAI DE COMPRESSEUR BP 3 ETAGES
 CARTE DE PRESSION TOTALE ABSOLUE

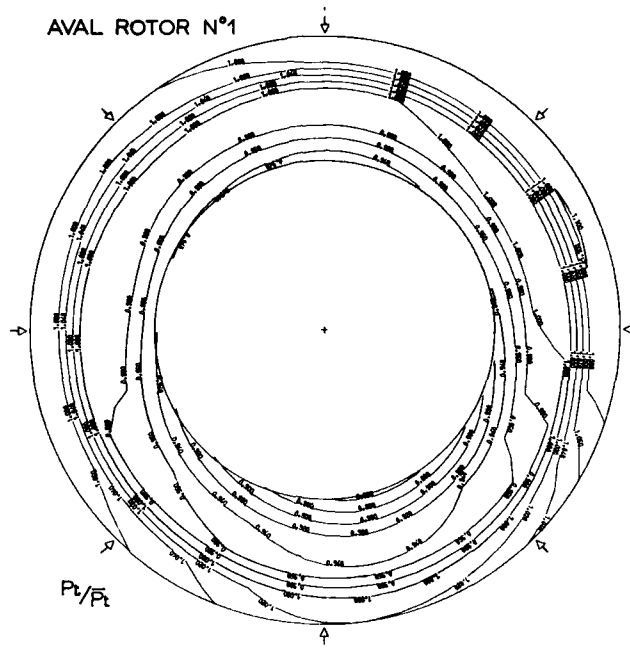


Figure 12b, ESSAI DE COMPRESSEUR BP 3 ETAGES
CARTE DE PRESSION TOTALE ABSOLUE

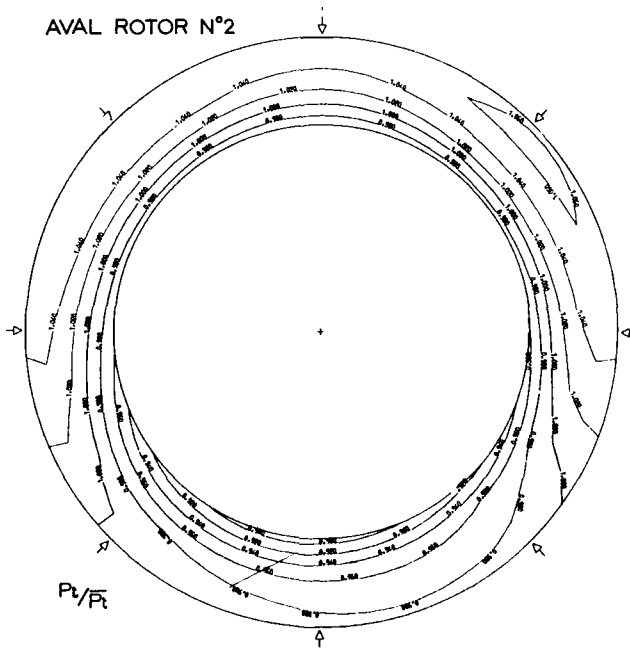


Figure 12c, ESSAI DE COMPRESSEUR BP 3 ETAGES
CARTE DE PRESSION TOTALE ABSOLUE

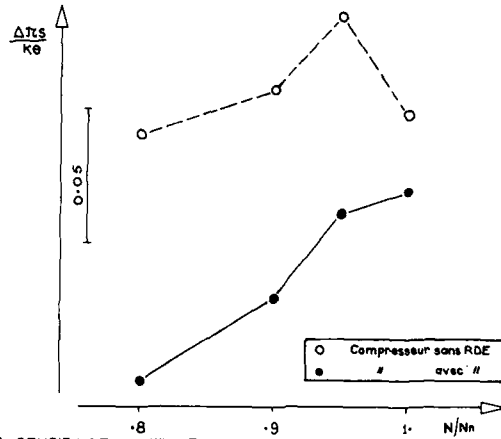


Figure 13 : SENSIBILITE EXPERIMENTALE A LA DISTORSION CIRCONFERENCELLE INFLUENCE D'UNE ROUE DIRECTRICE D'ENTREE

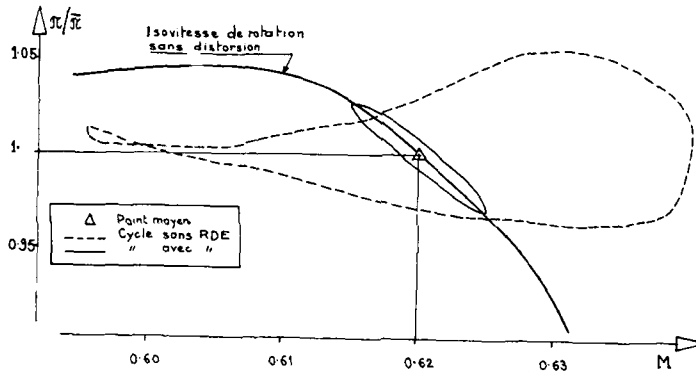


Figure 14 CYCLES DE FONCTIONNEMENT AVEC ET SANS RDE COMPRESSEUR BP 3 ETAGES - DISTORSION AMONT

METHODE DES SECTEURS DE COMPRESSEUR EN PARALLELE

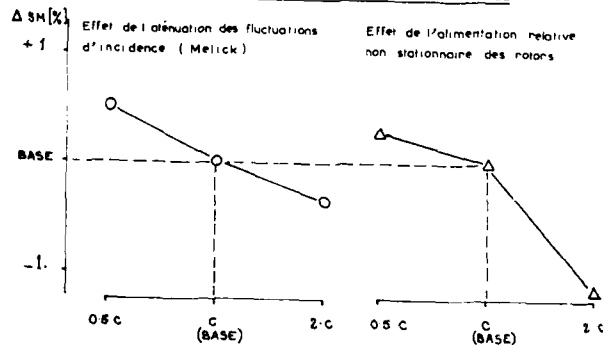


Fig 15 INFLUENCE THEORIQUE DES CORDES SUR LA SENSIBILITE A LA DISTORSION D'UN COMPRESSEUR BP 3 ETAGES AVEC RDE U/Un = 0.85

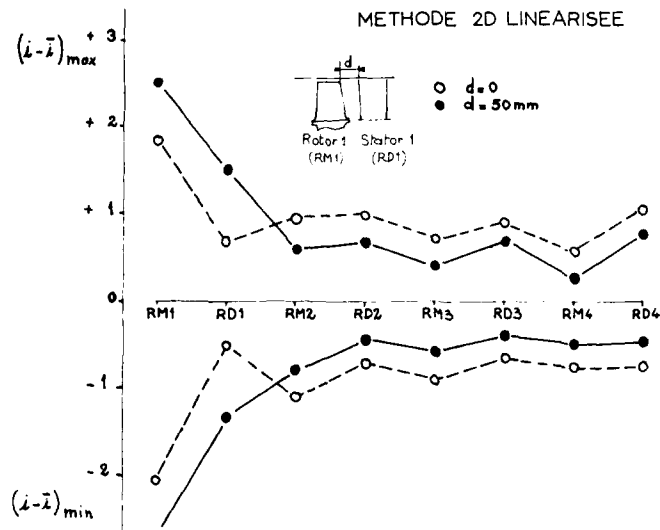


Figure 16: PERTURBATIONS D'INCIDENCE DANS UN COMPRESSEUR A 4 ETAGES
SOU MIS A UNE DISTORSION - EFFET DE DISTANCE RM1 - RD1

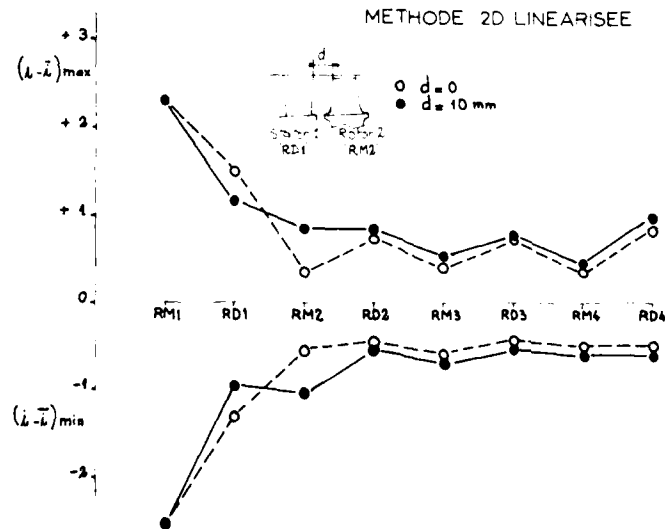


Figure 17: PERTURBATIONS D'INCIDENCE DANS UN COMPRESSEUR A 4 ETAGES
SOU MIS A UNE DISTORSION - EFFET DE DISTANCE RD1 - RM2

NEW TRENDS IN INTAKE/ENGINE COMPATIBILITY ASSESSMENT

F. Aulehla and D. M. Schmitz
 Messerschmitt-Bölkow-Blohm GmbH
 Helicopter and Military Aircraft Group
 P.O. Box 801160
 8000 München 80
 Federal Republic of Germany

SUMMARY

The measurement of dynamic pressure distortion requires noticeable effort in instrumentation and data processing. Considerable reductions in cost can be achieved by simpler methods. Examples of which will be given. In addition, the relevance of dynamic distortion on intake/engine compatibility has been overestimated as will be demonstrated by the experience gained from Tornado where swirl emerged as the decisive compatibility parameter. Also, during the Airbus A300 APU intake development, swirl turned out to be an important criterion. In conclusion, it is argued whether, in many cases, dynamic distortion measurements can be avoided in favour of swirl measurements in combination with simplified methods for dynamic distortion predictions based on steady state measurements and, in some methods, on statistical models.

LIST OF SYMBOLS AND ABBREVIATIONS

| | | | |
|---------------------------|--|------------------|---|
| AIP | Aerodynamic interface plane | RMS | Root mean square value |
| APD | Amplitude probability density | WAT | Corrected engine mass flow |
| APU | Auxiliary power unit | V_o/V_c | Free stream velocity / velocity in compressor entry plane |
| A_o/A_c | Mass flow ratio | α | Incidence |
| DC60 | Rolls Royce pressure distortion coefficient, ($P_{tAIP} - P_{t60^\circ\text{min}}$) / q_{AIP} | β | Yaw angle |
| IGV | Inlet guide vanes | γ, δ | Front/rear auxiliary door angle |
| M | Free stream Mach number | ϵ | First/second ramp angle |
| n | Number of Kulites in AIP | λ | Subsonic diffuser loss coefficient |
| P_t | Total pressure | η | Intake pressure recovery |
| $P_{t60^\circ\text{min}}$ | Minimum of mean total pressures in a 60° sector in AIP | σ | Standard deviation |
| PSD | Power spectral density | τ | Circumferential flow angle |
| q | Dynamic pressure | $\bar{\tau}$ | Mean value of τ at constant radius (bulk swirl) |

1. INTRODUCTION

It appears trivial to request that the compatibility of the intake and the engine, especially of high performance combat aircraft, must be ensured under all ground and flight conditions. Although this has been well known, serious draw-backs occurred in the past in many aircraft projects because decisive incompatibilities were not detected during development testing but only in prototype flying. Expensive post-developments became then necessary.

In this context incompatibility means that the quality of the intake flow is not sufficient relative to the tolerance of the engine. This usually results in a degradation of the performance and in a reduction of the stall margin. Flame-out may also occur and, in severe cases, the structural integrity of the compressor or the inlet may be lost.

Compatibility problems were encountered in the early versions of the F-111, the F-14, the MIG 25, the Tornado and the Airbus A300 APU to name just a few examples. It should be noted that in most cases these problems had occurred although the specifications of the engine manufacturers had been met according to the intake wind tunnel test results. It may be questioned, therefore, whether past wind tunnel tests were not fully representative or whether the compatibility parameters specified by the engine manufacturers were not sufficiently descriptive of the intake flow quality required by their engines.

As was done in previous publications (Ref.12,18,19) this paper tries to stress again, especially for engines without inlet guide vanes, the importance of a more recent compatibility parameter, that is intake swirl. However, the main purpose of the present paper is to review simpler methods of obtaining time variant total pressure peak distortion values as alternatives to the standard fully dynamic measurement. This implies accepting slightly larger uncertainties and, therefore, increased safety margins. Depending on the degree of simplification considerable cost savings will then be achieved.

2. TOTAL PRESSURE DISTORTION SYNTHESIS METHODS

To avoid the time-consuming and expensive measurement of dynamic pressure distortion, a number of different synthesis methods have been developed (Borg, Motyka, Melick, et al.). All these methods replace the measurement, storage, and processing of steady-state and time dependent pressures of each probe for calculating the required distortion coefficient from measured total pressure patterns by the measurement of steady-state pressures and the RMS-values of the dynamic component for each probe.

2.1 General Description of Distortion Synthesis Methods

The patterns required to calculate the distortion coefficient are generated by a random number process: the fluctuating pressure components are assumed to have an amplitude probability density (APD) which is normally distributed. A normally distributed random number is generated for each of the dynamic probes. This random number is converted to an equivalent instantaneous dynamic pressure component using the curve of cumulative amplitude probability density APD. The random dynamic components and the steady-state components for each probe are superimposed, thus generating a random total pressure pattern for which the required distortion coefficient is calculated. This process is repeated several hundred or thousand times for each test point. The maximum distortion coefficient of these patterns is retained as the relevant peak value of time variant distortion. The main difference in the methods mentioned above is the process of filtering the dynamic pressure components.

2.1.1 Distortion Synthesis Method by Motyka

The method described by Motyka (Ref.1) requires the measurement of the RMS values of the fluctuating pressure components as a function of their frequency. In addition, the power spectral density PSD for each probe has to be measured. The random pressures generated from the cumulative APD are scaled to the PSD of the test data by a digital filter before the distortion coefficients are calculated.

2.1.2 Distortion Synthesis Method by Melick

Melick assumes a random distribution of vortices to be the reason for dynamic distortion. These vortices are convected downstream at the local flow velocity. Their strength is related to the measured RMS values, the size of the vortices is described by the power spectral density. A comparison of unfiltered and filtered RMS data provides the PSD. With the given PSD, the random pressures can be filtered to the specific conditions (Ref. 2,3).

2.1.3 Distortion Synthesis Method by Borg

The Borg method (Ref.4) assumes an equally distributed PSD (white noise). However, the pressure fluctuations can be filtered by a low pass filter describing the sensitivity of a specific engine before being converted to RMS values. This method has been applied by MBB in 1982. It was extensively tested by comparison with experimental data. Good agreement was achieved, as will be shown in this paper. After these successful tests, it was introduced to project work where it is still applied regularly to obtain Rolls Royce and General Electric distortion parameters.

2.1.4 Other Distortion Synthesis Methods

The synthesis method described by Stevens, Spong, and Oliphant (Ref.5) is very similar to the Borg method. Sedlock's prediction method (Ref.6) is also based on random pressures. It includes two digital filters to shape the random number PSD to that of the measured PSD. A 'map averaging' approach is made to improve the prediction of instantaneous total pressure patterns. A more detailed survey of the different synthesis methods is given in Ref.6 and 17.

2.2 Tests with Reduced Dynamic Instrumentation

The use of these distortion synthesis methods allows a significant reduction in computer hard- and software for data storage and processing during and after intake tests. An additional simplification of test equipment can be reached by reducing the number of dynamic pressure transducers in the aerodynamic interface plane AIP. However, the total pressure patterns for which the required distortion coefficients are calculated have to be generated on the basis of the complete rake arrangement of 40 (or 36) dynamic transducers, i.e. an assumption has to be made on the distribution of the RMS values for the deleted transducers. The reason is that for the assumption of non-correlated normally distributed

pressure fluctuations for each transducer an increase in the number of assumed transducer locations will smooth the synthesized patterns (for n approaching infinity the distortion coefficient will approach the steady-state distortion level), while a reduction will increase the roughness of the pattern, thus increasing the distortion coefficient. The rake geometry, however, has to remain the same as for fully dynamic measurements as an increase in the number of rake arms (for a constant total number of transducers) will increase steady-state and time-variant DC60.

A comparison has been made to assess the influence of a reduced dynamic instrumentation on the synthesized DC60, compared with a complete dynamic instrumentation (Ref.10). For this comparison, the Borg synthesis method was applied. The intake data were measured on a 1/7 scale intake model (TKF-18) with twin single wedge intakes with variable cowl in an under-fuselage position. Tests were made in the DFVLR Braunschweig low speed tunnel at incidences between 0 and 45° and yaw angles between -15° and +15°. The AIP instrumentation consisted of a rake with 84 steady-state total pressure probes on 7 rings and 36 dynamic transducers on 3 rings. Before being integrated to RMS values, the dynamic signals were filtered to a cut-off frequency of 1244 Hz, equivalent to 178 Hz for full scale. The instantaneous distortion parameter DC60 was calculated from 2000 synthesized patterns. Fig.1 and 2 compare the synthesized DC60, based on a reduced number of dynamic transducers, to the equivalent DC60 synthesized from the complete instrumentation of 36 transducers on 3 rings (Ref.10). They show that there is nearly no deterioration for 12 transducers, and even a synthesis based on 6 measured RMS values yields acceptable results. However, if only 4 transducers are used, the difference increases significantly. In Fig.3 (Ref.14), the mean value and the standard deviation of the difference between the synthesized DC60 for reduced instrumentation and for the complete instrumentation with 36 transducers are plotted vs. the number of transducers. For 12 transducers, for example, the standard deviation in DC60 is $\pm 0,013$ which is well within the limits of measurement accuracy.

2.3 Extreme Value Analysis

The extreme value analysis proposed by Jacocks and Kneile (Ref.7) is an addition to any distortion synthesis method. Its aim is to reduce the observation time, i.e. the number of patterns to be synthesized. It assumes the distortion factors to be random variables and predicts the maximum which can be reached with an increased number of samples by an asymptotic function.

2.4 Simplified Methods for Dynamic Distortion Assessment

At MBB, a simple method for estimating peak time-variant DC60 was developed by Habig. In contrast to the synthesis methods described above, this method is based on the average turbulence of the dynamic signals in the AIP. The peak value of DC60 is approached as

$$DC60_{max} = DC60_{steady\ state} + 1,5 \text{ RMS}_{mean}$$

with RMS_{mean} being the mean absolute value of the RMS-values of all transducers, normalized by q_{AIP} . A preliminary comparison, based on an intake model with 8 Kulites in the AIP, showed good agreement between the Borg and Habig methods (Ref.8).

A further simplification of dynamic distortion assessment is the deletion of all high response transducers in the AIP. The influence of the dynamic component of the pressure fluctuation is accounted for by steady-state data. For example, the subsonic diffuser loss coefficient λ , defined as $\lambda = (P_{t1} - P_{tAIP}) / q_{AIP}$

with: P_{t1} avg. total pressure at subsonic diffuser entry

P_{tAIP} avg. total pressure in AIP

q_{AIP} dynamic pressure in AIP

could be one of the factors increasing with turbulence, and, hence, with dynamic distortion. Based on test data from different aircraft configurations, Hercock (Ref.15) made the approach

$$DC60_{max} = DC60_{steady\ state} + f(\lambda)$$

with: $f(\lambda) = 0,723 \cdot \lambda$ for $\lambda \leq 0,455$

and $f(\lambda) = 0,329 = \text{const.}$ for $\lambda > 0,455$

In a similar way, Malefakis (Ref.16) correlated DC60 and λ , proposing the equation

$$DC60_{max} = 0,5122 + 0,1739 \cdot \ln(\lambda).$$

Another empirical method proposed in (Ref.9) is

$$DC60_{max} = DC60_{steady\ state} + 0,5 \cdot \lambda.$$

The Hercock method was derived purely from subsonic data; the $\lambda/2$ method was applied also to supersonic test data after shock pressure losses had been subtracted.

The different methods, their complexity and the required instrumentation are described in Table 1.

underpredicting the measured values, i.e. for test points where a severe intake flow separation will occur (Fig.6, Ref.10). Any other combination of cowl position and angle of attack (for example, normal position with 30° angle of attack or cowl rotated 30° down with 45° angle of attack) provides very good agreement, see Fig.5. The reason for these discrepancies is the assumption of uncorrelated random pressures in the synthesis method which is correct for normal flow conditions, but not for severe separations. The analysis of the discrepancies between synthesis and measurement shows that the difference does not increase with the absolute value of DC60. For very low distortion, this may result in relatively high percentage values for an intake test condition where the intake distortion is far below the engine limits. However, at higher distortion values, which are closer to the engine limits, the absolute error is still the same order of magnitude, resulting in a low percentage of error.

The Habig method shows a very similar trend as the Borg synthesis method; however, the trend towards underprediction for the test conditions with intake flow separation and, hence, with correlated signals, is less significant (Fig.7, Ref.14). The Hercock method shows a similar scatter band with a trend towards overpredictions, especially at the higher distortion values (Fig.8, Ref.14).

Compared with the Borg synthesis, the $\lambda/2$ method shows an increased scatter band. However, the accuracy of the prediction is slightly less sensitive to flow separation (Fig.9, Ref.14). Fig.10,11 and 12 (Ref.9) compare the $\lambda/2$ method with experimental data. In contrast to Fig.4 and 5, a wider variation in cowl position and incidence is covered here. It is evident that even for this simple method without any direct information about the dynamics of the flow the trend of DC60 versus mass flow is clearly duplicated. The absolute values are also in excellent agreement except for two test conditions where strong separation occurs. These are: $M = 0$ with the cowl at 0° (Fig.10) and $v/v_{\infty} > 0$ at $\alpha = 45^\circ$, cowl at 0° (Fig.11). However, for these off-design conditions the error is within acceptable limits.

2.5.2 Tests with Tornado 1/6,5 Intake Model

The high response instrumentation of the Tornado 1/6,5 model (MC19) consisted of 36 transducers on 3 rings. 280 test points were investigated, and the results of the different prediction methods were compared with the measured dynamic distortion DC60. The Mach number range was from $M = 0$ to $M = 1,3$; the angle of attack varied from -3° to $+35^\circ$, and the angle of sideslip from -10° to $+10^\circ$. The configuration represented the early intake standard without fences. In Fig.13-16 (Ref.14) the results of the Borg, Habig, and $\lambda/2$ methods and the measured DC60 are plotted vs. engine mass flow for $M = 0,2$; $M = 0,4$; $M = 0,9$ and $M = 1,2$ at different angles of attack. This comparison shows that at low and moderate angles of attack the results of the different prediction methods (Borg, Habig, $\lambda/2$) and the dynamic measurement agree quite well. However, at high incidence, the measured DC60 exceeds the results of the Borg and Habig methods significantly. These two methods yield very similar values over the whole range of Mach numbers, incidence, and engine mass flow. At high incidence (i.e. flow separation at the cowl lip), the $\lambda/2$ method provides better agreement with test data than the more complicated Borg and Habig methods. The general trends of the prediction methods are shown in Fig.17-19 (Ref.14) for all 280 test points. The Borg and Habig methods provide good agreement at lower distortion values with a trend towards underprediction with increasing distortion, corresponding to increasing incidence. The reliability of the simple $\lambda/2$ method is less dependent on flow separation and, hence, on incidence. The scatter band is slightly wider than those for the two other methods; however, there is nearly no trend towards underprediction (nearly symmetrical error distribution).

2.5.3 Tests with Tornado 1/9 Intake Model

An isolated Tornado inlet model was tested at $M = 1,91$ by NGTE (Ref.13). These tests provided reliable distortion data for the high supersonic flight regime. The RMS values were not available at MBB, therefore only a comparison with the $\lambda/2$ method could be made. The subsonic diffuser loss coefficient λ was calculated from measured intake pressure recoveries and from computed shock losses (Ref.9).

The comparison between the $\lambda/2$ method and the measurement is shown in Fig.20-22 (Ref.9). They comprise twelve different test conditions (three different incidences, two different ramp angles δ_2 and configurations with/without the cowl fence) over the whole mass flow range $((A_0/A_c)/\eta - WAT)$.

Excellent agreement in the trend and fairly good agreement in the absolute level were obtained. The greatest deviation occurs for $\alpha = +5^\circ$, $\delta_2 = 12^\circ$ (Fig.22). For these high effective wedge angles ($\alpha + \delta_1, \delta_2$) the inviscid computation of the shock system and thus of λ is not very accurate, which probably explains this deviation.

3. INTAKE SWIRL

A rather comprehensive discussion on the generation of intake swirl and its effects on intake/engine compatibility was given in Ref.12 and 18. Some of the main issues will be repeated in the following.

3.1 Generation of Different Types of Swirl

The centrifugal forces acting on a viscous flow in a bent duct produce the well

known cross-flow (secondary flow) which is called here "twin swirl". Similarly, if the flow separates at or near the leading edge of an intake, i.e. ahead of a bend, this low energy air near the duct wall is forced to move inwards while the high energy air is displaced outwards in the bend. If the separation zone does lie in the plane of symmetry of the bend, a solid body type cross flow is generated which is called "bulk swirl". In every curved intake twin swirl, therefore, must be present; under extreme conditions bulk swirl is superimposed, Fig.23 (Ref.12).

Bulk swirl can be suppressed effectively by simple flow straightening devices e.g. by a fence, while twin swirl is very stable and is only little affected by simple flow straighteners. For the Tornado series aircraft a fence was fitted in each intake. This solution proved to be as simple as effective so that Tornado now is not limited in incidence and Mach number from compatibility point of view.

3.2 Relevance of Swirl on Compatibility

In the early Tornado prototypes (without cowl fence) a twin swirl was found which was nearly constant up to moderate incidences in subsonic flight. Exceeding this incidence level a sudden onset of bulk swirl occurred combined with an increase of the existing twin swirl. This was caused by flow separation at the cowl lip. At high supersonic Mach numbers the analogue phenomenon occurred at large second ramp angles δ_2 (separation due to too high diffuser angle), Fig.24 (Ref.12). However, the sense of rotation was opposite to that in subsonic flight at high incidences.

Naturally, both intakes had the same flow patterns, which were symmetric to the aircraft symmetry plane. That is, the sense of rotation of the swirl in both intakes was in opposite direction. Therefore, at any time the swirl was co-rotating relative to the engine in one intake, while it was counter-rotating in the other. As a consequence, in the critical subsonic flight conditions only the left hand engine surged, while in high supersonic flight the right hand engine was affected. Although pressure distortion and swirl in both intakes increased simultaneously, (Fig.25, Ref.12), only the engine with counter-rotating swirl surged.

Since the usual pressure distortion coefficients do not take into account any swirl, it is clear that these pressure distortion coefficients alone cannot be the decisive factor for the RB199 and other engines without inlet guide vanes which have a certain flow straightening effect. The other, probably more important factor must be swirl, including its magnitude and sense of rotation. Swirl may not only trigger surge but can also cause blade vibrations, due to the periodic loading of a compressor blade during one revolution.

According to Lecht and Weyer, circumferential non-uniformities in total pressure as well as in pre-swirl flow (twin swirl) "... do not only affect the compressor stall margin but result in severe unsteady aerodynamic load of the rotor blades thus initiating or aggravating airfoil vibrations and flutter Pre-swirl distortions tend to create more intense blade force fluctuations than even very strong total pressure distortions" (Ref.19). These investigations on a research compressor were confirmed not only by the fan vibration of the unmodified Tornado near the maximum flight Mach number but also by a high cycle fatigue problem on the APU TSCP 700-5 of the early versions of the Airbus A300: "To the same extent as the number of aircraft increased, a growing number of cracks or blade separations was experienced in the low pressure compressor, especially in the first stage. In a number of failures, blade dovetail and/or disk single platform separations occurred (Fig.26). The inspection of the blade dovetails revealed that the cracks had been induced by fretting" (Ref.18). Swirl measurements in the unmodified APU intake revealed a twin swirl without any bulk swirl. This caused blade oscillations and, in combination with the same material for both, blade and disk (Ti-6Al-4V), blade dovetail fretting. By simple modifications of the intake the maximum swirl angles were reduced by nearly 50% (Fig.27, Ref.18). These modifications were:

- a modified position of the baffle plates (parallel to each other)
- a fairing between the two baffle plates attached to the rear plenum chamber wall (Fig.28, Ref.18).

In addition, the blade dovetails were copper/nickel coated to avoid surface contact between the two titanium parts. Thus the problem was successfully tackled from both ends, i.e. the aerodynamic disturbances were reduced and the structural tolerance of the engine towards flow non-uniformities was increased.

3.3 Prediction of Swirl Patterns from Wall Streamlines

The visualization of the streamlines at the intake wall by the so called oil dot technique is a very simple and cheap method, which was applied by MBB in many model and full scale tests, the latter also in flight. The oil traces were copied simply by pressing a sheet of paper onto the wall. For the quantitative assessment of the flow angle this method proved to be superior to the evaluation of photographed streamlines; this method is particularly useful for cylindrical surfaces. Fig.29 (Ref.12) compares the cross-flow angles from the wall stream lines in the Tornado full scale intake with a swirl pattern in a 1/6,5 scale model at static conditions. It can be seen that the extrapolation of the measured swirl pattern towards the wall agrees well with the oil flow values, which suggests that the Reynolds number effect is negligible here.

All combat aircraft with an S-shaped duct investigated by MBB confirm that the swirl pattern in front of the engine consists of twin swirl and - if separation occurs ahead of the bend - also of bulk swirl (see para. 3.1). There are a few exceptions, e.g.

if a disturbance is generated by a fence or a similar device immediately upstream of the measuring plane.

Whether above rule holds also for other intakes can be easily verified during a test by the wall streamlines. A circumferential swirl distribution as shown in Fig.23 must then be found. Assuming a linear distribution of the circumferential mean value versus radius (solid body type) for bulk swirl and a sinusoidal distribution for twin swirl, the swirl pattern in the complete duct cross-section can be reconstructed from the wall streamlines as follows:
The maximum/minimum swirl angles are directly obtained from the wall streamlines. The two components bulk and twin can then be computed by the following equations:

$$\tau_{\max} = \tau_{\text{bulk}} + \tau_{\text{twin}}$$

$$\tau_{\min} = \tau_{\text{bulk}} - \tau_{\text{twin}}$$

With the above assumptions for the radial distribution the cross-flow angles in the whole cross-section are defined. An example is shown in Fig.30 (Ref.11).

Even if there are no swirl measurements at all, i.e. neither at the wall nor in the inner of the duct, a qualitative swirl pattern for the entire cross-section can be predicted from the isobar pattern if there is a distinct high and low total pressure region (no concentric isobars). The maximum swirl angle is at the duct wall. Its circumferential position coincides with the low pressure region. The minimum swirl angle (be it positive or negative) lies diametrically opposite at 180°. The "sense" of rotation of the bulk component is defined by the direction from the high to the low pressure region along the larger circumference, Fig.24. The symmetry line of the twin component lies at 90°/270°. Above findings are purely empirical and are based on numerous test data from different configurations.

4. TEMPERATURE DISTORTION

Ingestion of hot gas causes in principle the same problems as total pressure losses: apart from the thrust loss equivalent to the mean temperature rise, there are additional thrust losses due to the non-uniformity of the temperature distribution. In severe cases engine surge and flame-out will occur. Hot gas ingestion may be encountered during V/STOL operation, thrust reversing, formation flying and armament firing. Gas ingestion during armament firing can be so severe that the engine must be temporarily deloaded, which means that the engine produces less thrust for a short while. However, during V/STOL operation the maximum thrust is required and, therefore, hot gas reingestion has to be avoided. Comprehensive investigations in this respect were conducted in the sixties by many industry and research groups. The conditions during V/STOL are better reproducible than during armament firing. Although no exact limits for surge onset are known, temperature limits can be defined below which surge does not occur. Above such limits surge may or may not happen. An example is shown in Fig.31 (Ref.20).

These results were obtained from NASA Ames who tested in 1966 the MBB V/STOL configuration No.5 using a half scale model with six YJ-85 GE 5 engines, the nozzle throat of which were increased by about 15%. As shown in Fig.31 the limits can be expressed by the mean or maximum overtemperature. Engine No.1 had twice the tolerance than engine No.2 for the mean and maximum overtemperature. This can be due to the different location on the aircraft, different engine modification or measuring error. The main conclusion from this diagramme, however, is not affected.

5. CONCLUDING REMARKS

5.1 Intake Swirl

A pure twin swirl (i.e. without any bulk component) of larger magnitude can produce serious structural damage via forced blade vibration. A pure bulk swirl cannot exist in curved inlet ducts. Due to the boundary layer a twin swirl component is always present. If separation occurs in an S-shaped duct there is always a combination of bulk and twin swirl. It is expected that any combination of bulk and twin swirl will trigger surge provided that the local counter-rotating swirl is of sufficiently large magnitude and extends over a reasonable sector of the compressor face.

For engines without IGV dynamic distortion is not the only relevant parameter as the Tornado experience has shown. The same pressure distortion in the left/right hand intake produced engine surges only in combination with counter-rotating swirl (relative to the fan rotation). Intake fences have proven to be a simple and powerful means to reduce swirl. This was demonstrated very clearly on Tornado which now is not limited in incidence and maximum Mach number from compatibility point of view.

5.2 Simplified Distortion Assessment Methods

The Borg synthesis method was applied to nearly 400 test points from two completely different intake configurations. The synthesized pressure distortion coefficient DC60 agrees very well with the measured values except for test points where strong separation occurs. The Borg method then yields too optimistic values. Even if the number of dynamic pressure transducers is reduced from 36 down to 6 or 8 only small errors are introduced.

The Habig method in general agrees well with the Borg method. However, the trend towards underprediction in cases with strong separation is less pronounced. The methods by Hercock and Malefakis over- and underpredict, respectively, the measured data in general with a fairly large scatter band. The simple $\lambda/2$ method gives surprisingly good agreement with the measured data for test conditions with attached flow. Especially for cases with separation this method proves to be superior to all other methods investigated.

5.3 Recommendations

For preliminary design it is recommended to delete the fully dynamic pressure distortion measurement (by 36 or 40 transducers) in favour of swirl assessment plus measurements of a reduced number of RMS values (Borg and Habig methods). It is even worth-while considering to abandon dynamic pressure measurements completely and apply the $\lambda/2$ method instead. Considerable cost savings will then be achieved. The degree of simplification for the different methods is shown in Table 1. Certain safety margins in DC60 to cope with the deviations shown in this paper will then have to be added. The complete deletion of the dynamic pressure measurement cannot be yet recommended for the final design phase. The same holds for other test objectives like hammer shock or surge interaction tests.

6. ACKNOWLEDGEMENT

The authors acknowledge the permission given by NAMMA, NGTE and MBB to publish this paper. The work of Herr M. Schneider from MBB who did most of the computations for the simplified methods comparison is also gratefully acknowledged. The views expressed by the authors are entirely their own and not necessarily those of MBB.

7. REFERENCES

- 1 David L. Motycka
Determination of Maximum Expected Instantaneous Distortion Patterns from Statistical Properties of Inlet Pressure Data
AIAA-76-705, Palo Alto, California, 1976
- 2 H. C. Melick, Jr., A. H. Ybarra, and D. P. Bencze
Estimating Maximum Instantaneous Distortion from Inlet Total Pressure RMS and PSD Measurements
AIAA-75-1213, Anaheim, California, 1975
- 3 H. C. Melick, Jr., A. H. Ybarra, and D. P. Bencze
Estimating Maximum Instantaneous Distortion from Inlet Total Pressure RMS Measurements
AIAA-78-970, Las Vegas, Nev., 1978
- 4 R. Borg
A Synthesis Method for Estimating Maximum Instantaneous Inlet Distortion Based on Measured Inlet Steady State and RMS Pressures
AGARD CP-301, Toulouse, France, 1981
- 5 C. H. Stevens, E. D. Spang, and R. C. Oliphant
Evaluation of a Statistical Method for Determining Peak Inlet Flow Distortion Using F-15 and F-18 Data
AIAA-80-1109, Hartford, Connecticut, 1980
- 6 D. Sedlock
Improved Statistical Analysis Method for the Prediction of Maximum Inlet Distortion
AIAA-84-1274, Cincinnati, Ohio, 1984
- 7 J. L. Jacocks, and K. R. Kneile
Statistical Prediction of Maximum Time-Variant Inlet Distortion Levels
AEDC-TR-74-121, Arnold Engineering Development Center, 1975
- 8 J. Malefakis
Analyse der Einlaufmessungen mit Modell CC12 bei BA-Warton - Meßphase 5
MBB/TN/JF-90/367, 09.04.1986 (restricted)
- 9 F. Aulehla
Die Korrelation der dynamischen Druckungleichförmigkeit in Triebwerkeinläufen mit rein stationär gemessenen Werten
MBB/TN/S/0040, 10.11.1982 (restricted)

- 10 D. M. Schmitz, J. Kruse, and S. Weichert
Grundsatzuntersuchungen an Einlaufkonzepten für zukünftige Kampfflugzeuge
(Phase III)
MBB/FE124/S/R/1539, 1982 (restricted)
- 11 J. Joerg, and D. M. Schmitz
Kompatibilität von Einlauf und Triebwerk bei Kampfflugzeugen
MBB/LKE124/S/R/1557, 1984 (restricted)
- 12 F. Aulehla
Intake Swirl - a Major Disturbance Parameter in Engine/Intake Compatibility
MBB/FE124/S/PUB/74, 1984, also ICAS-82-4.8.1, Seattle, Aug.1982
- 13 J. E. Flitcroft
An Evaluation of the Tornado Intake Cowl Fence at $M = 1,9$
NGTE Memorandum No. 80036, Dec.1980 (restricted)
- 14 M. Schneider
Vergleich verschiedener Methoden zur einfacheren Bestimmung der Druckungleich-
förmigkeit in Umfangsrichtung
MBB/TN/S/149, Aug.1986 (restricted)
- 15 R. G. Hercock
Personal Communication
- 16 J. Malefakis
Personal Communication
- 17 E. M. Sanders
An Evaluation of Statistical Methods for the Prediction of Maximum Time-Variant
Inlet Total Pressure Distortion
AIAA-80-1110, Hartford, Connecticut, 1980
- 18 K. W. Lotter, and J. Joerg
The Effect of Intake Flow Disturbances on APU Compressor Blade High Cycle
Fatigue in the Airbus A300
ICAS-82-4.6.2, Seattle, Aug.1982
- 19 M. Lecht, and H. B. Weyer
Unsteady Rotor Blade Loading in an Axial Compressor with Steady-State Inlet
Distortions
AGARD CP-248-30, Cleveland, Oct.1978
- 20 F. Aulehla, and G. K. Kissel
Experience with High Performance
V/STOL Fighter Projects at MBB
AIAA-81-2614, Palo Alto, California, Dec.1981

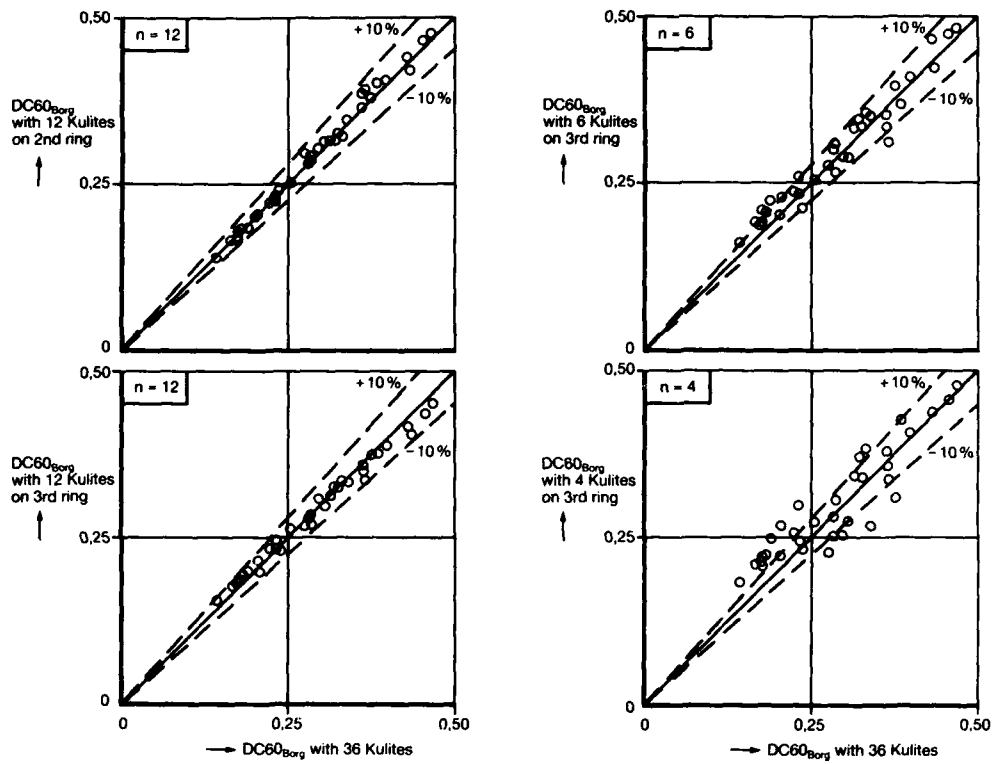


Fig. 1, 2 Effect of reduced number of pressure transducers on synthesized DC60

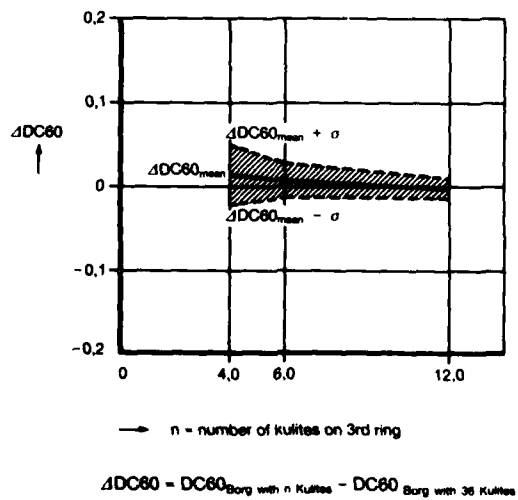


Fig. 3 Mean and standard values of deviation in DC60 due to reduced number of transducers

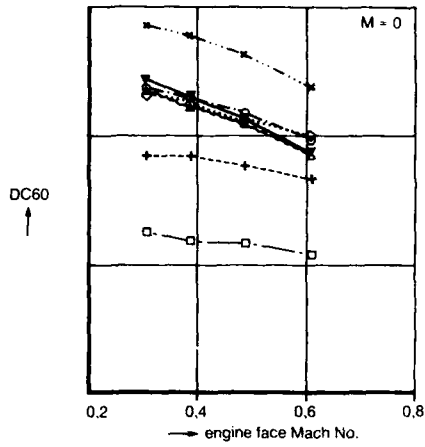


Fig. 4 Comparison of different prediction methods from TKF 1:7 intake model (cowl position = 30°)

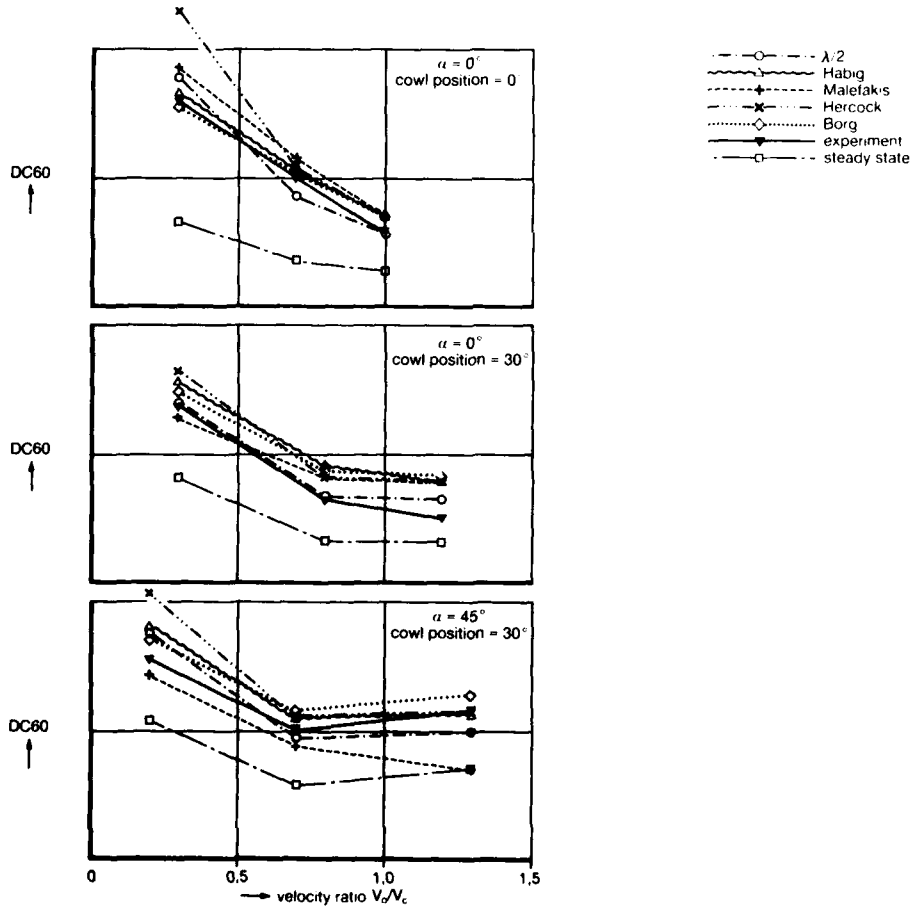


Fig. 5 Comparison of different prediction methods from TKF 1:7 low speed tests at different cowl positions and angles of attack

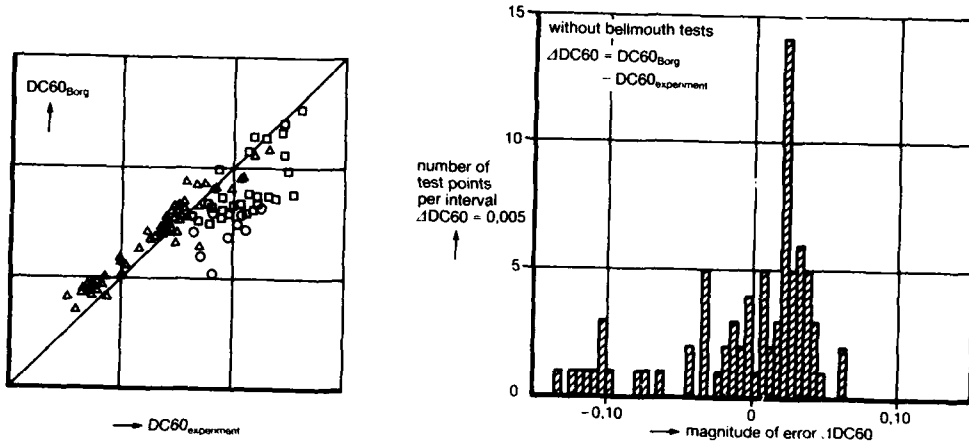


Fig. 6 Error of Borg method, from TKF 1:7 low speed tests

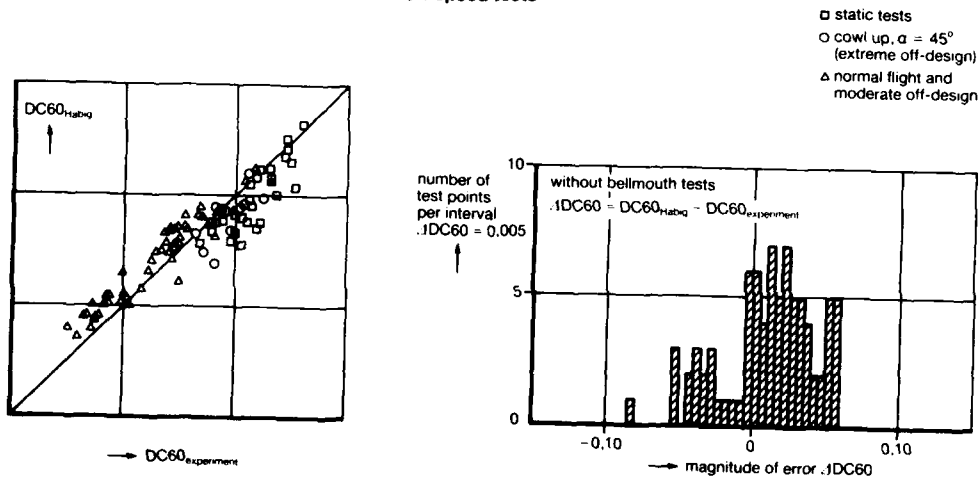


Fig. 7 Error of Habig method, from TKF 1:7 low speed tests

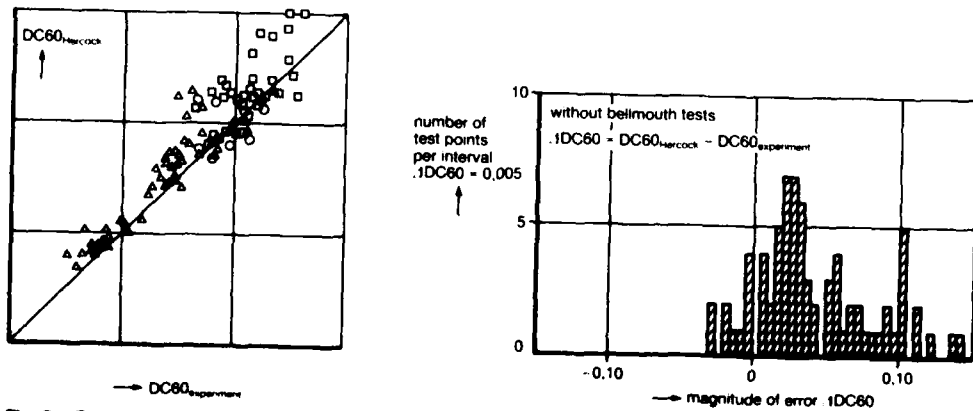


Fig. 8 Error of Hercock method, from TKF 1:7 low speed tests

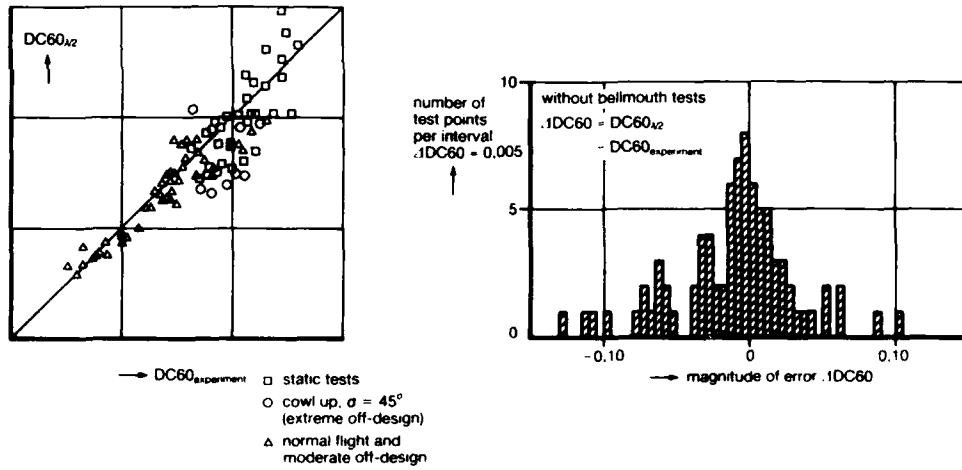


Fig. 9 Error of $\lambda/2$ method, from TKF 1:7 low speed tests

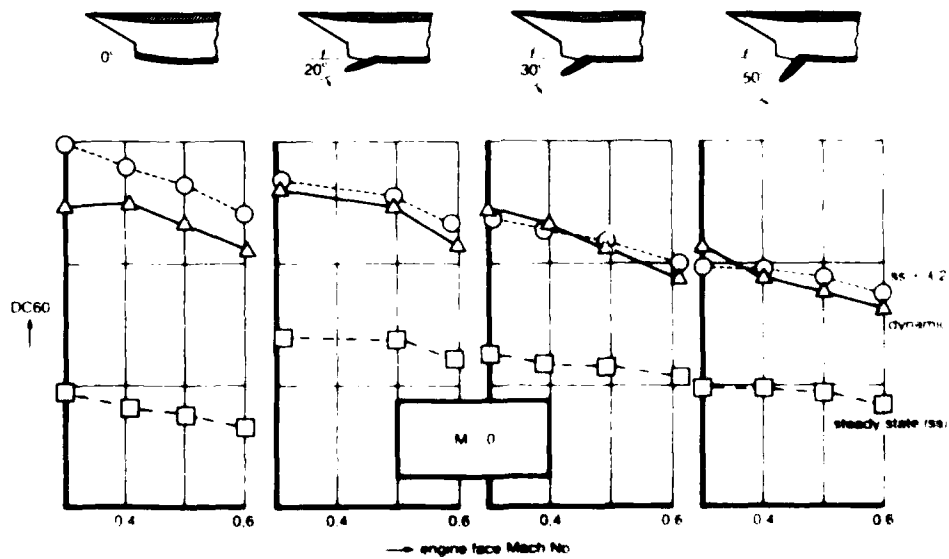


Fig. 10 Comparison of measured $DC60$ with $\lambda/2$ prediction method, from TKF 1:7 intake model, static tests, Ref. 9

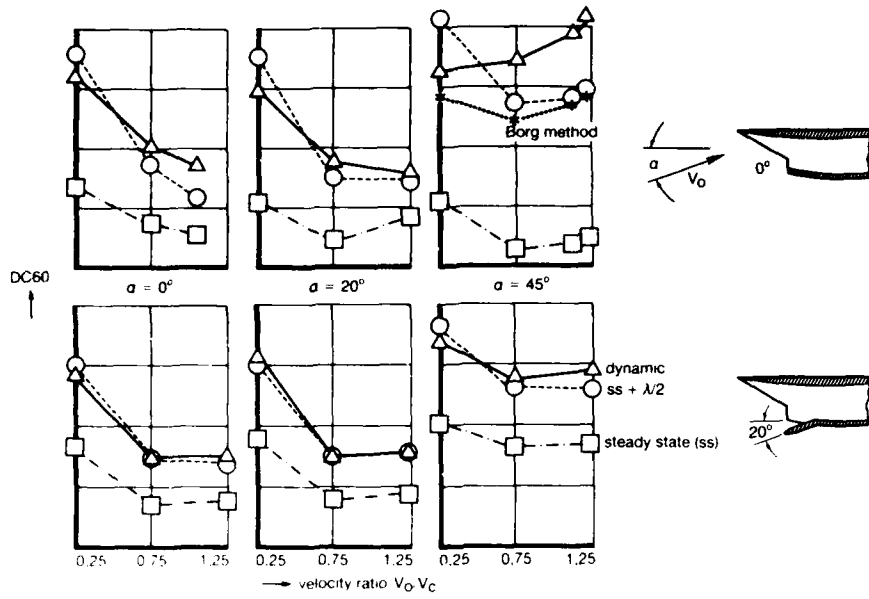


Fig. 11 Comparison of measured DC60 with $\lambda/2$ prediction method, from TKF 1:7 low speed tests, Ref. 9

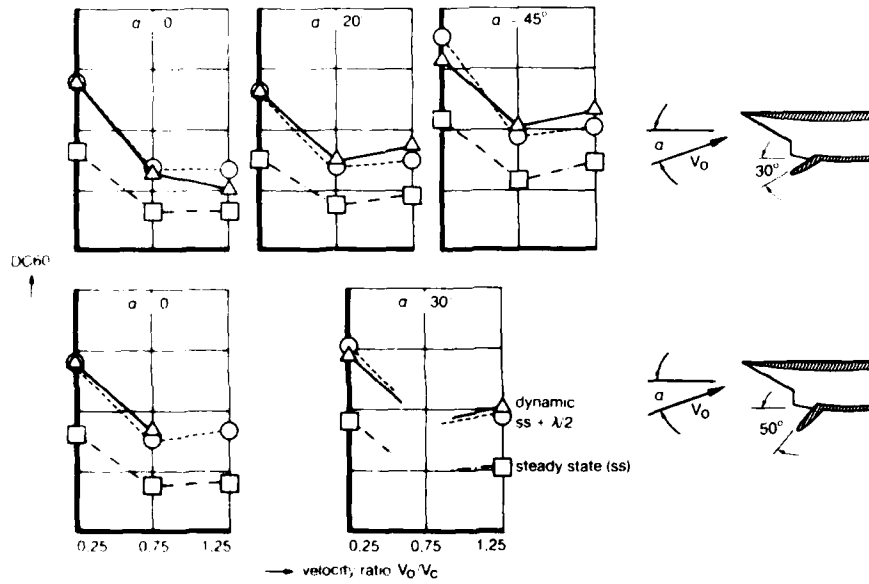


Fig. 12 Comparison of measured DC60 with $\lambda/2$ prediction method, from TKF 1:7 low speed tests, Ref. 9

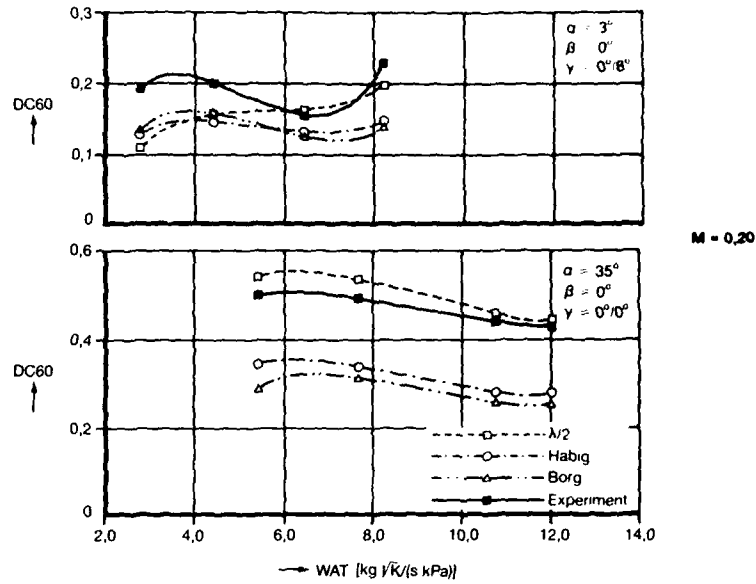


Fig.13 Comparison of simplified distortion assessment methods with experiment, from Tornado 1:6,5 intake model

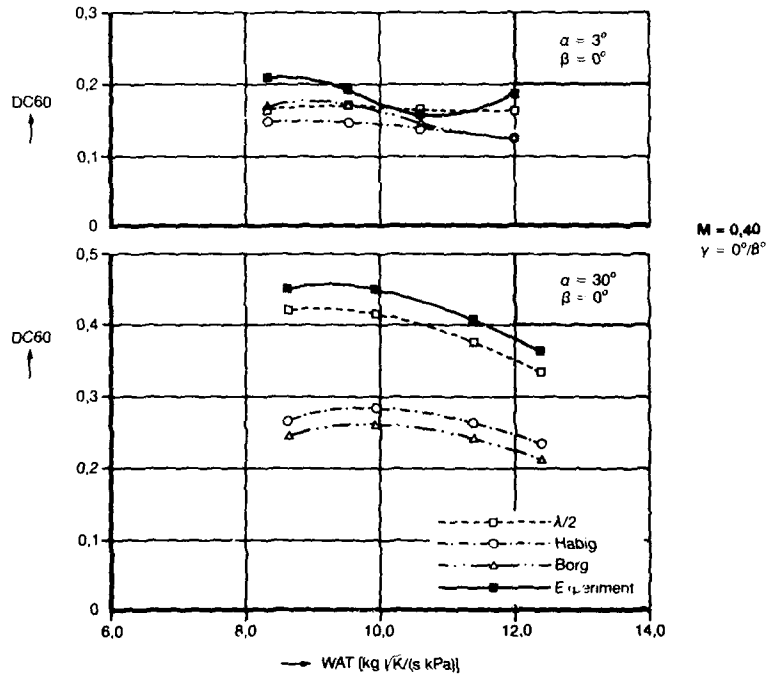


Fig.14 Comparison of simplified distortion assessment methods with experiment, from Tornado 1:6,5 intake model

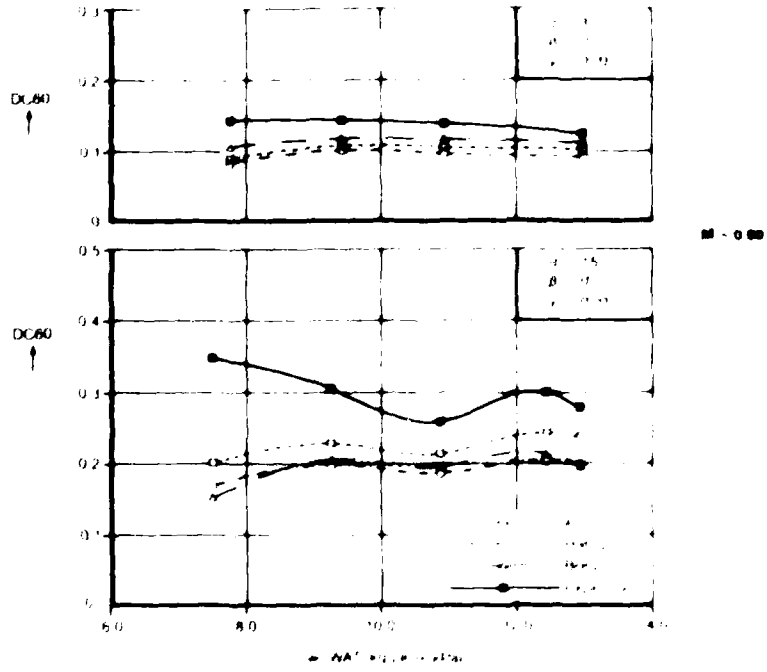


Fig. 15 Comparison of simplified distortion assessment methods with experiment from Tornado 1:6.5 intake model

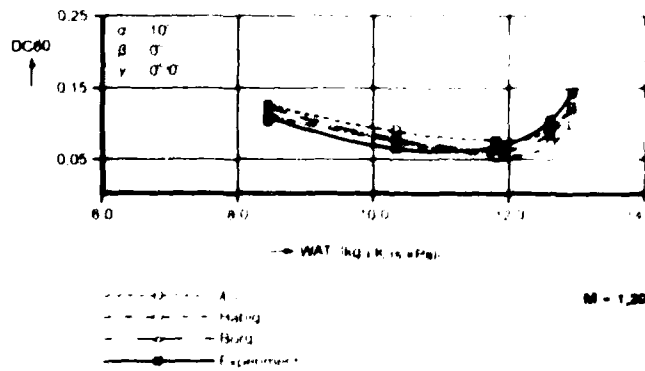


Fig. 16 Comparison of simplified distortion assessment methods with experiment from Tornado 1:6.5 intake model

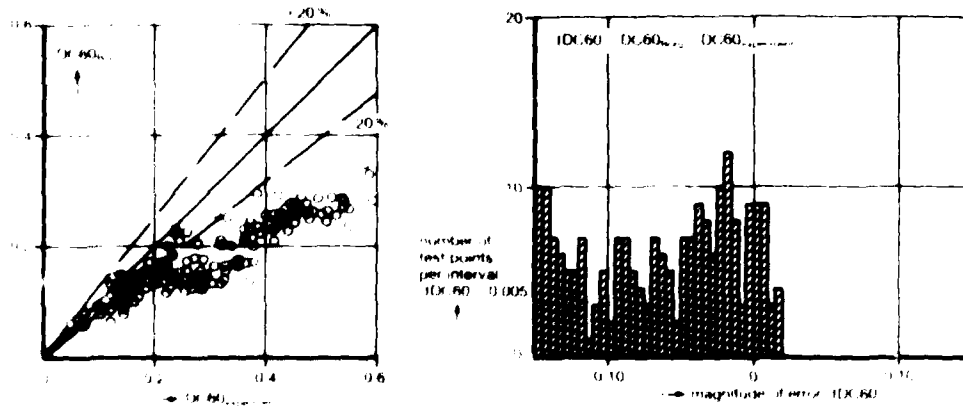


Fig 17 Error of Borg synthesis method, from Tornado 1:0.5 intake model

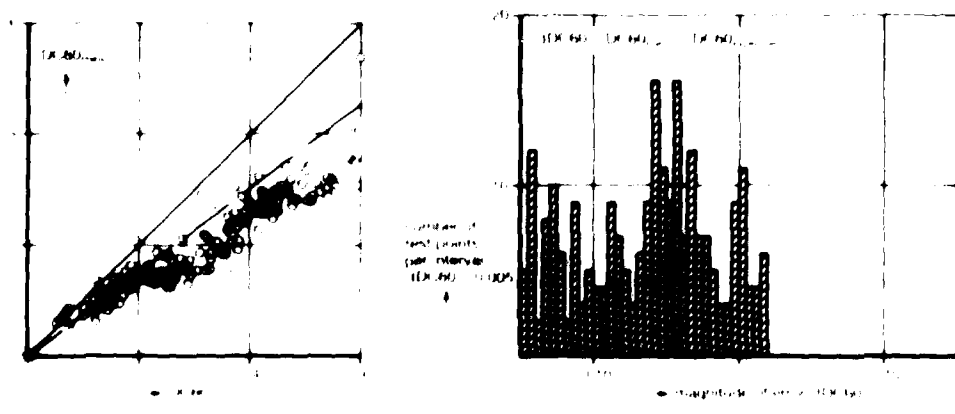


Fig 18 Error of Hebig method, from Tornado 1:0.5 intake model

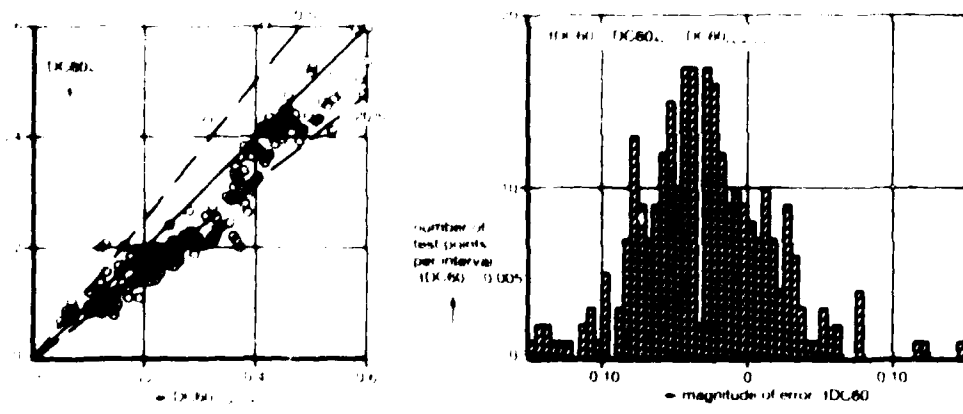


Fig 19 Error of A 2 method, from Tornado 1:0.5 intake model

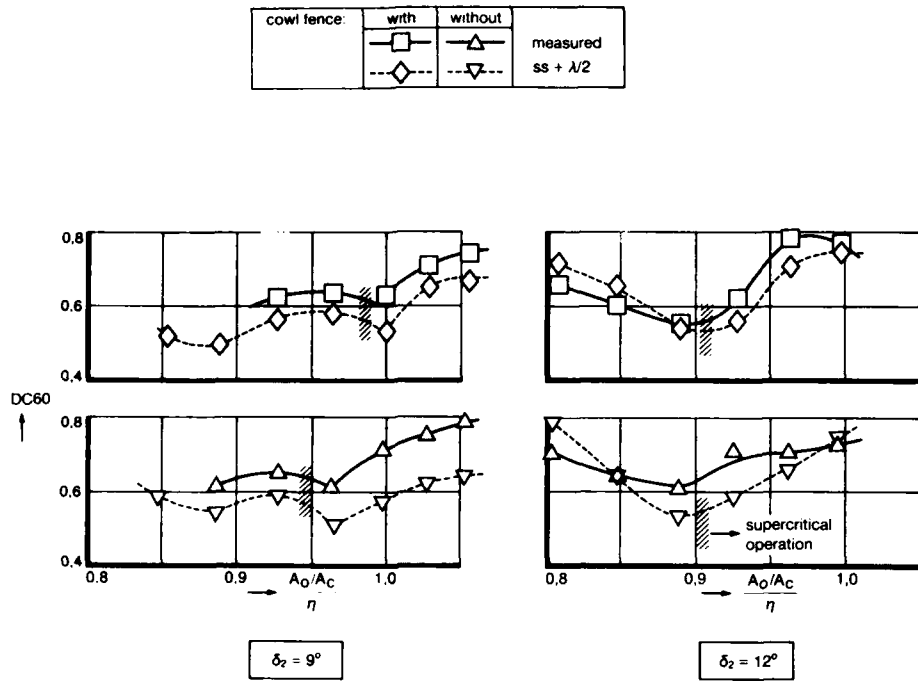


Fig. 20 Comparison of measured dynamic DC60 with $\lambda/2$ prediction method, from Tornado NGTE 1:9 isolated intake model, $M = 1.91$; $\alpha = -2^\circ$; Ref. 9, 13

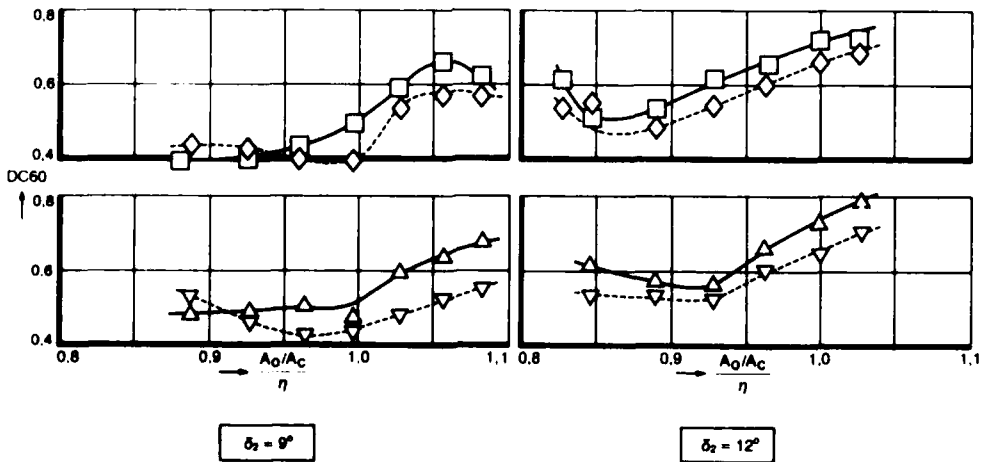


Fig. 21 Comparison of measured dynamic DC60 with $\lambda/2$ prediction method, from Tornado NGTE 1:9 isolated intake model, $M = 1.91$; $\alpha = +2^\circ$; Ref. 9, 13

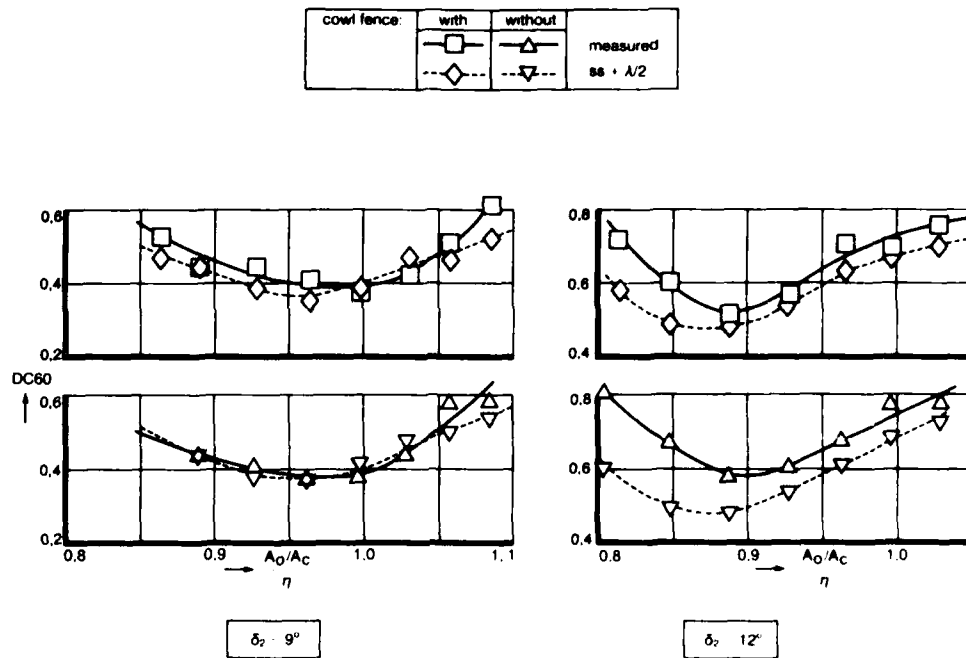


Fig. 22 Comparison of measured dynamic DC60 with $\lambda/2$ prediction method, from Tornado NGTE 1:9 isolated intake model, $M = 1.91$; $\alpha = +5^\circ$, Ref. 9, 13

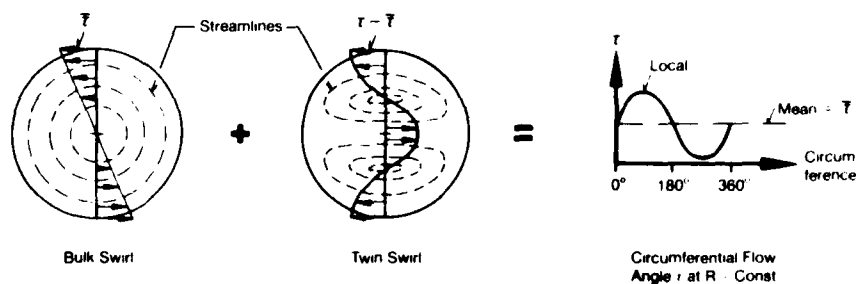


Fig. 23 Superimposing of Bulk and Twin Swirls

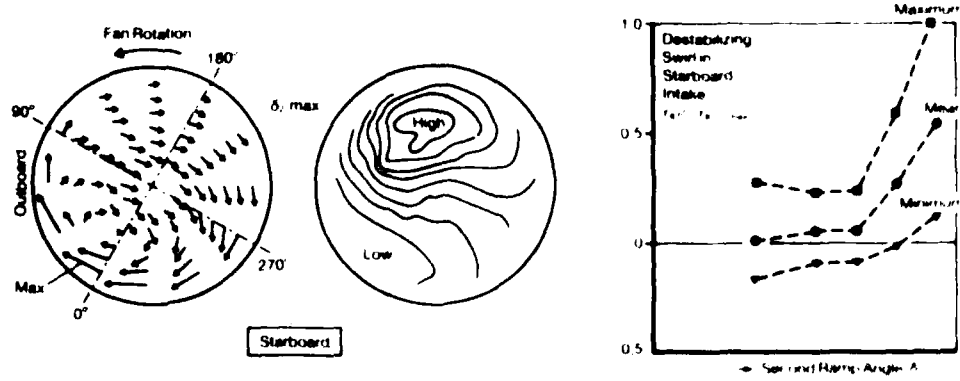


Fig. 24 Swirl of Basic Tornado Inlet at High Ramp Angles. $M_{\infty} = 1.8$, $\alpha = 3^\circ$
 Combat Engine Mass Flow, AICS Controlled

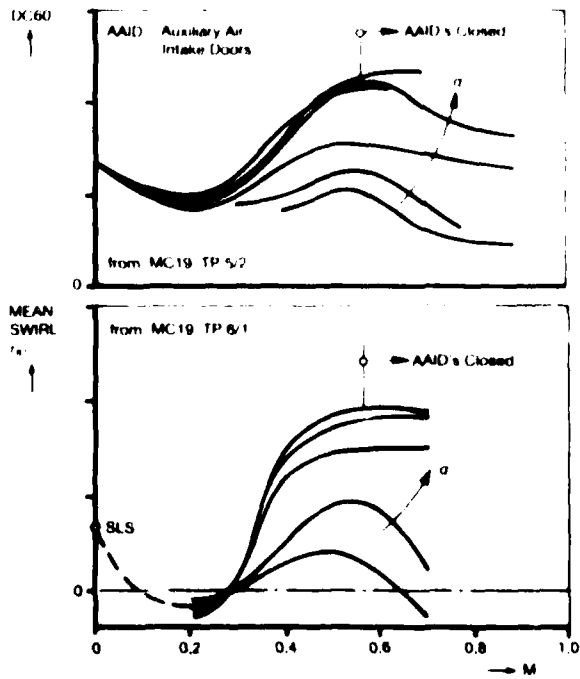


Fig. 25 Comparison of Instantaneous Total Pressure Distortion with Mean Swirl Angles.
 Basic Intake, Sea Level, $R = 0.87 R_{max}$

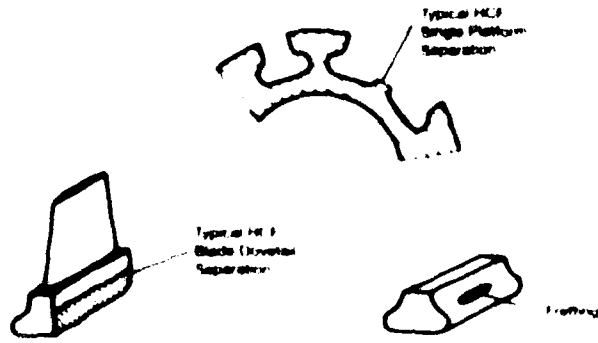


Fig. 26 Blade Root Fracture and Typical High Cycle Fatigue Failure

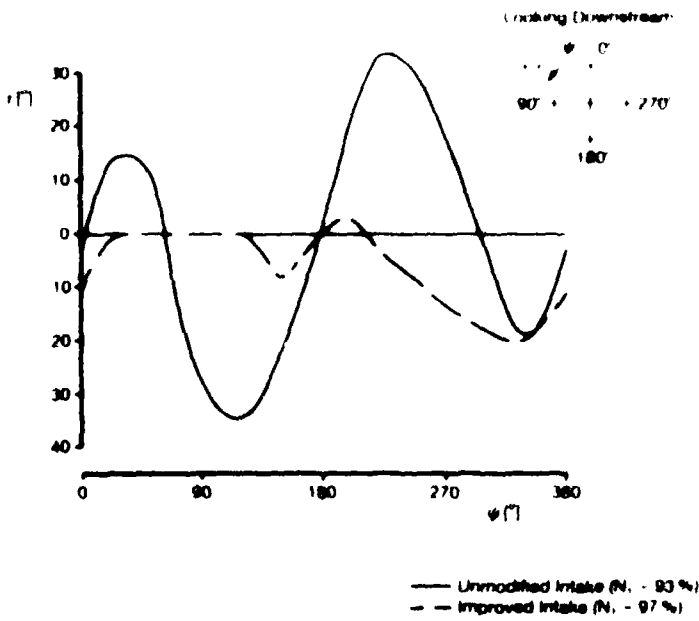


Fig. 27 Intake Dual Wall Flow Visualization Results (APU Ground Operation)

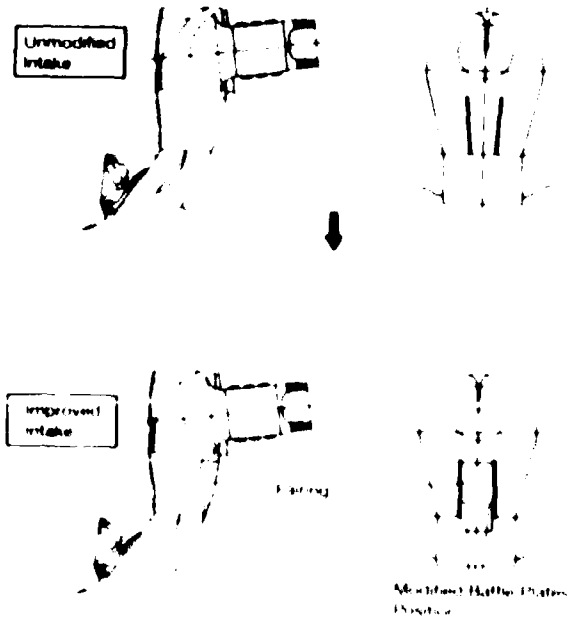


Fig. 28 A300 APU Intake Modification

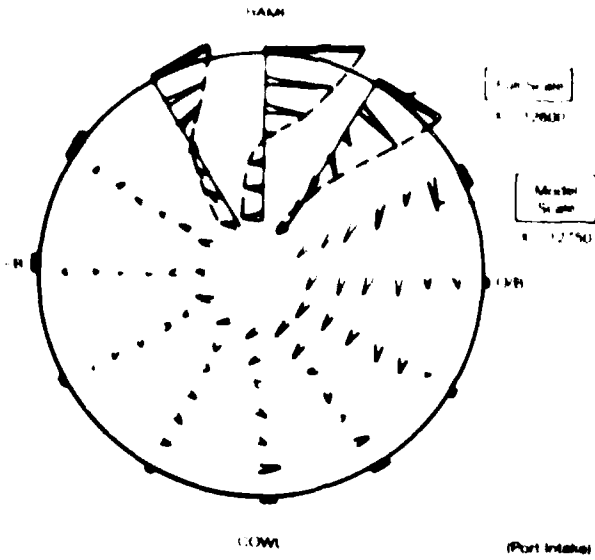


Fig. 29 Model/Full Scale Comparison of Intake Swirl at $M=0$

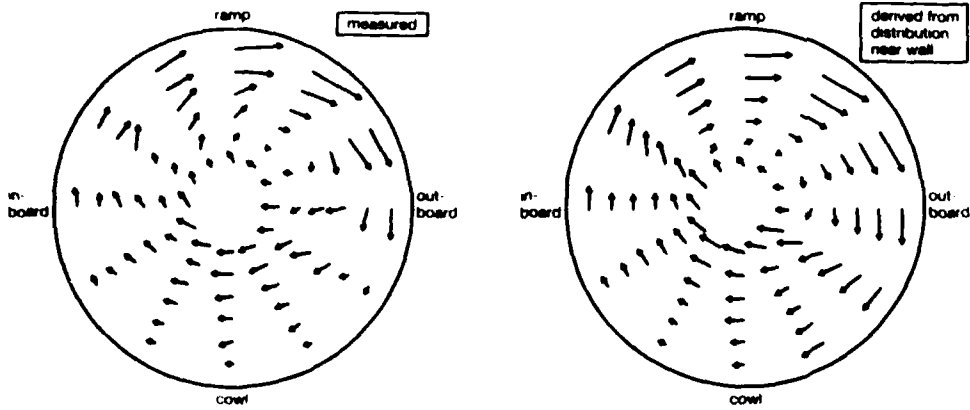


Fig. 30 Comparison of measured swirl angles with computed values derived from measured near wall distribution

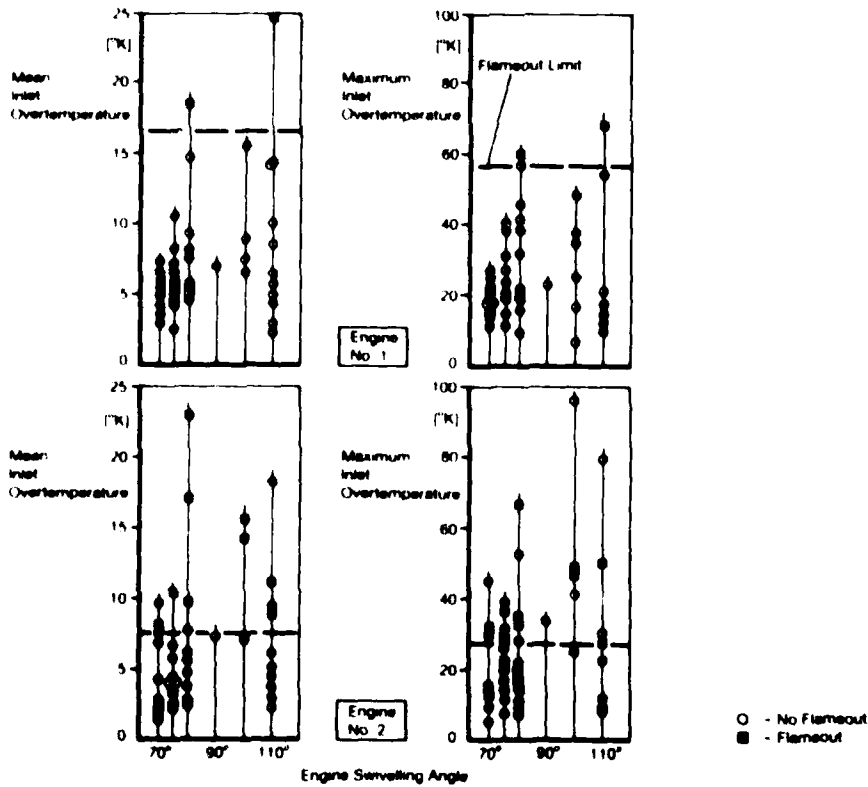


Fig. 31 Effect of Inlet Overtemperature on Engine Flameout

DISCUSSION

J. Hourmouzidiis, Gc

Mr Williams told us in the first lecture this morning that inlet swirl is not a problem any more since you can use fences. Could you comment on that please?

Author's Reply

There can be no doubt that intake swirl is a decisive compatibility parameter for engines without inlet guide vanes. Paramount examples for this are the flight test results from the unmodified inlets of Tornado and the Airbus APU and also the work by Lecht and Weyer on a research compressor. These examples have been only briefly mentioned in our paper and are described in more detail in the referenced literature.

Although we were very successful in suppressing counter-rotating bulk swirl on Tornado for all flight conditions by the embodiment of intake fences, I would not dare to say that this excellent result can be directly transferred to any new combat aircraft inlet. In any case, numerous wind tunnel and flight tests will be necessary to achieve the same or a similarly good result as on Tornado.

Since one cannot assume to completely eliminate bulk swirl on a new inlet configuration for all ground and flight conditions, the remaining tolerable bulk swirl needs to be specified by the engine manufacturer. The same holds for twin swirl which can only partially be suppressed by simple flow straightening devices.

For future aircraft and particularly for aircraft which attain high angles of attack we would prefer fuselage or wing shrouded inlets to avoid the generation of large swirl angles right from the beginning of a new aircraft development.

D.D. Williams, UK

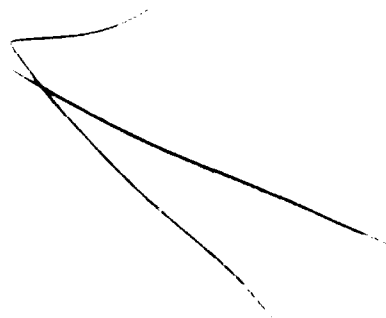
In my paper you will find some results from general research on an S-shaped duct which are useful. We found we can control swirl and eliminate it with fences there as well. The fences also reduce the total-pressure distortion (they mix the flow and reduce the circumferential distortion). They are cost-effective devices. I agree, though, that it is better to have an intake without swirl. Straight intakes.

Author's Reply

The more important question probably is whether future engines should have inlet guide vanes or not from the compatibility point of view. As stated in my Seattle paper (Ref 12 in Paper 68A-3) we prefer fences instead of inlet guide vanes for weight reasons. Would you like to comment?

D.D. Williams, UK

Whatever it takes to get a good propulsion system. One pays large penalties for inlet guide vanes - they weigh a lot, reduce flow per frontal area, have a bird strike problem etc, so where there is an alternative, simple, lightweight fence it is a more attractive solution, as in fact we have shown on Tornado



EFFECT OF STEADY STATE INLET TEMPERATURE DISTORTION ON THE ENGINE COMPRESSOR FLOW

by

W. Koschel
 Institute for Jet Propulsion and Turbomachinery
 Technical University of Aachen
 Templergraben 55, D-5100 Aachen, West-Germany

H. Künkler and H. Tönskötter
 Industrieanlagen-Betriebsgesellschaft m.b.H. (IABG),
 Einsteinstraße, D-8012 Ottobrunn, West-Germany

SUMMARY

A prediction model for the effects of a steady state temperature distortion on the overall performance of a multistage engine compressor is presented. In contrast to the well-known parallel compressor model, this method takes into account the circumferential interaction of the distorted and undistorted compressor flow. An extensive experimental program has been carried out on a single-spool jet engine with steady-state inlet temperature and pressure distortion tests. The experimental set-up is briefly described. Detailed results of the flow measurements obtained at the compressor inlet and exit and at the compressor interstage positions are presented and discussed. The experimental results support the validity of the prediction model developed within this project.

NOMENCLATURE

| | | | |
|-----------|-------------------------------------|--------|----------------------------|
| A | Area | ψ | Flow function |
| a | Velocity of sound | | |
| c | Absolute velocity | | |
| M | Mach number | | |
| \dot{m} | Air mass flow | z | Toll (undistorted section) |
| N | Rotor speed | cor | Corrected |
| n | Polytropic exponent | CR | Compressor inlet |
| OP | Operating point | z | Exit (distorted section) |
| p | Pressure | W | Exhaust nozzle |
| p_0 | Dynamic pressure ($\rho_0 V_0^2$) | z | Without distortion |
| T | Temperature | z | Isentropic |
| V_0 | Circumferential velocity | z | Stage |
| w | Relative velocity | * | Total |
| β_1 | Relative flow angle at rotor inlet | EN | Turbine nozzle |
| γ | Specific heat ratio | 0 | Ambient condition |
| η | Efficiency | z | Compressor inlet |
| π | Total pressure ratio | z | Compressor exit |

Subscripts

1. INTRODUCTION

Aircraft jet engines encounter inlet flow distortions under some operating flight conditions. The resulting degradation in engine performance depends mainly on the extent to which the compressor operation is affected by the distortion. Typical flight situations where inlet compressor distortion often occurs with swirl currents, are

- aircraft operation at high angles of attack or yaw producing partial flow separation in the intake,
- shock-wave/boundary-layer interaction at supersonic flight speeds,
- strong crosswinds or fuselage interference affecting the intake air flow.

Inlet temperature distortion often in combination with pressure distortion is experienced in hot gas ingestion after airborne missile launch or by gas recirculation during thrust reverse operation.

One of the major effects of the distorted inlet flow is the loss of the surge margin of the compressor which limits the maneuverability of the aircraft. Therefore a lot of experimental and theoretical work has been dedicated in the past to establish relationships between the loss in the surge pressure ratio and the extent of pressure and temperature distortion. Detailed experimental investigations have been carried out at the NASA Lewis Research Center on single-spool engines and on turbofan engines [1], [2], [3], [4] to get a better physical understanding of the pressure and temperature distortion effects on the compressor performance. A so-called "parallel compressor model" has been used to predict the overall compressor surge degradation [5]. This model is based on the assumption that the compressor may be segmented into two or more subcompressors each operating independently from one another and having the same performance characteristics as the undistorted compressor. No crossflow between the subcompressors is admitted. A so-called parallel compressor index has been derived from this simple model and used to correlate with the experimental data [6]. A fairly good agreement between the experiment and the prediction was achieved as well for pressure distortion as for temperature distortion with an extent of more than 30%. Korn [7] refined the simple parallel compressor theory by introducing a

AD-P005 464

dynamic stall delay which improved the accuracy of the prediction of the surge point pressure loss for single stage compressors.

The insufficient agreement between the test data and the predictions using the parallel compressor model, which is obtained for multistage compressors at steady-state inlet condition, is due to the fact that this model is only based on the overall performance and does not account for the identification of the stalling stage and for the circumferential interaction of the distorted and undistorted sections.

By combining the parallel compressor concept with a steady-state calculation, a more accurate prediction of the performance of multistage axial compressors at steady-state inlet distortion has been achieved [8].

This analytical approach including circumferential interaction has been successfully applied to distorted cases with a smaller circumferential extent of distortion [9]. The multiple segment parallel compressor model, which is presented in [10] and [11], for circumferential cross flow inlet flow angle variation, circumferential angle variation and provides an individual blade row by blade row description, and design methods. In prediction methods include circumferential interaction for the stalling stage and the pressure performance at distorted inlet conditions [12], [13], [14], and [15]. However, this approach, so far as known, is limited to the case of single-stage compressors.

The theoretical approach and the detailed experimental results, which are presented and discussed in this paper, may contribute to a better understanding of the flow phenomena implied by a steady-state pressure and temperature distribution in a multistage compressor and by the circumferential interaction of the stalling stage and the undistorted stage at distorted inlet conditions.

1. SCOPE AND DEFINITION OF TERMINOLOGY

For the general case of radial temperature and density distributions in a multistage compressor inlet and inlet conditions of distortion, the inlet conditions are defined as the levels at which the temperature, density, and velocity are constant. The inlet conditions are defined as the inlet conditions.

It seems to be reasonable to distinguish the flow conditions in the inlet of the compressor into the distorted and undistorted regions. The distorted region is defined as the region where the flow conditions are distorted and the undistorted region is defined as the region where the flow conditions are not distorted. The distorted region is defined as the region where the flow conditions are distorted and the undistorted region is defined as the region where the flow conditions are not distorted.

In this paper the effects of steady-state inlet distortion on the performance of a multistage axial compressor inlet of a multistage axial compressor are investigated. The effects of inlet distortion on the performance of a multistage axial compressor are investigated.

The theoretical approach is based on the following assumptions:

- a) Separation of the inlet of the compressor into distorted and undistorted regions.
- b) The flow conditions in the distorted region are defined as the inlet conditions.
- c) The flow conditions in the undistorted region are defined as the inlet conditions.
- d) The flow conditions in the distorted region are defined as the inlet conditions.
- e) The flow conditions in the undistorted region are defined as the inlet conditions.
- f) The flow conditions in the distorted region are defined as the inlet conditions.
- g) The flow conditions in the undistorted region are defined as the inlet conditions.
- h) The flow conditions in the distorted region are defined as the inlet conditions.
- i) The flow conditions in the undistorted region are defined as the inlet conditions.
- j) The flow conditions in the distorted region are defined as the inlet conditions.
- k) The flow conditions in the undistorted region are defined as the inlet conditions.
- l) The flow conditions in the distorted region are defined as the inlet conditions.
- m) The flow conditions in the undistorted region are defined as the inlet conditions.
- n) The flow conditions in the distorted region are defined as the inlet conditions.
- o) The flow conditions in the undistorted region are defined as the inlet conditions.
- p) The flow conditions in the distorted region are defined as the inlet conditions.
- q) The flow conditions in the undistorted region are defined as the inlet conditions.
- r) The flow conditions in the distorted region are defined as the inlet conditions.
- s) The flow conditions in the undistorted region are defined as the inlet conditions.
- t) The flow conditions in the distorted region are defined as the inlet conditions.
- u) The flow conditions in the undistorted region are defined as the inlet conditions.
- v) The flow conditions in the distorted region are defined as the inlet conditions.
- w) The flow conditions in the undistorted region are defined as the inlet conditions.
- x) The flow conditions in the distorted region are defined as the inlet conditions.
- y) The flow conditions in the undistorted region are defined as the inlet conditions.
- z) The flow conditions in the distorted region are defined as the inlet conditions.

The terms of the inlet conditions are defined as the inlet conditions.

2. DEFINITION OF FLOW CONDITIONS

Flow fields in the inlet of a compressor are usually defined as distorted and undistorted regions. The distorted region is defined as the region where the flow conditions are distorted and the undistorted region is defined as the region where the flow conditions are not distorted. The distorted region is defined as the region where the flow conditions are distorted and the undistorted region is defined as the region where the flow conditions are not distorted.

A qualitative analysis was made for the effects of inlet distortion on the performance of a multistage axial compressor inlet of a multistage axial compressor. The effects of inlet distortion on the performance of a multistage axial compressor are investigated.

3. FLOW FIELD AT COMPRESSOR INLET AND EXIT

When using the so-called "parallel" compressor model the compressor characteristics of the original distorted compressor with the operating point P_0 is valid as shown schematically in Fig. 1. The operating points P_1 and P_2 refer to the inlet and the

According to Eq. (4) the pressure loss in the hot sector of the combustor is lower than in the cold one. Therefore we get by Eq. (5)

$$P_{t3h} \leq P_{t3c} \quad (8)$$

Now the area ratios A_{t3h}/A_1 of the hot and cold sectors have to be examined. They compare the turbine nozzle area used by one sector flow with the corresponding compressor face area. For critical nozzle flow we obtain

$$(\dot{m}/\sqrt{T_3}/P_{t3}A_{t3})_h = (\dot{m}/\sqrt{T_3}/P_{t3}A_{t3})_c$$

At the considered rotor speeds the sector air flow can be assumed to be proportional to $A_1 P_{t1}/T_{t1}$. Hence and from equations (1), (7) and (8) we get

$$\frac{(A_{t3}/A_1)_h}{(A_{t3}/A_1)_c} \leq \sqrt{\frac{T_{t1c}}{T_{t1h}}} \quad (9)$$

Therefore it can be concluded that the hot sector is strongly narrowing in the combustor and in the rear compressor part especially after having expanded within the first stages. Pressure has to drop from cold to hot sector. Static pressure p_{3h} at turbine inlet (as well as total pressure p_{t3h}) has to be significantly lower than the corresponding values of the cold sector:

$$P_{3h} < P_{3c} \quad (10)$$

In contrary to the assumption of Eq. (3) the static pressures at compressor exit will also differ a little:

$$P_{2h} \leq P_{2c} \quad (11)$$

When replacing the preliminary assumption of Eq. (3) by Eq. (11) the results of the equations (4) to (6) will be intensified.

1.2. DISTORTION INFLUENCE IN AXIAL DIRECTION

Fig. 1 shows the cross section of the compressor blading. It is assumed that the hot sector arrests hot air, due to the static pressure drop from the cold sector. The hot sector expands in front of the compressor face and within the first stages. The expansion will partly be reversed in the rear compressor (Eq. 11). The hot sector will be shifted circumferentially about 180 deg. after the last stage of the compressor. In spite of the expansion of the hot sector a significant pressure drop shall be assumed at first for the following considerations: the total pressure in the cold sector are equal to those of the undistorted compressor.

Fig. 2 shows the variation of the static pressure ratio over the compressor stages. This leads to the total pressure drop in the hot sector. The pressure ratio in the hot sector is compared to the cold sector. The pressure ratio in the rear part. This results from the expansion of the hot sector. The pressure ratio is higher than that of the cold sector. The pressure ratio is lower in the rear part. The pressure ratio is lower in the rear part. The pressure ratio is lower in the rear part.

The compressor face pressure of the hot sector is lower than that of the cold sector. The pressure ratio is lower in the rear part. The pressure ratio is lower in the rear part. The pressure ratio is lower in the rear part.

The pressure ratio is lower in the rear part. The pressure ratio is lower in the rear part. The pressure ratio is lower in the rear part. The pressure ratio is lower in the rear part. The pressure ratio is lower in the rear part.

The pressure ratio is lower in the rear part. The pressure ratio is lower in the rear part. The pressure ratio is lower in the rear part. The pressure ratio is lower in the rear part. The pressure ratio is lower in the rear part.

The pressure ratio is lower in the rear part. The pressure ratio is lower in the rear part. The pressure ratio is lower in the rear part. The pressure ratio is lower in the rear part. The pressure ratio is lower in the rear part.

The pressure ratio is lower in the rear part. The pressure ratio is lower in the rear part. The pressure ratio is lower in the rear part. The pressure ratio is lower in the rear part. The pressure ratio is lower in the rear part.

The pressure ratio is lower in the rear part. The pressure ratio is lower in the rear part. The pressure ratio is lower in the rear part. The pressure ratio is lower in the rear part. The pressure ratio is lower in the rear part.

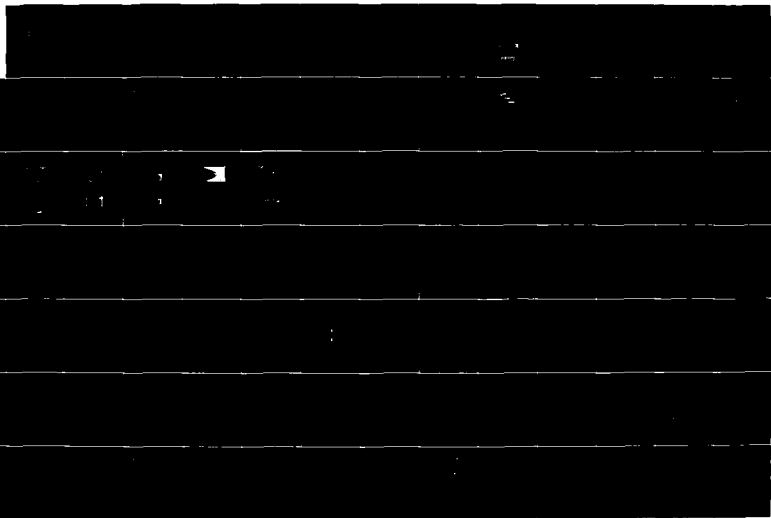
AD-A182 635

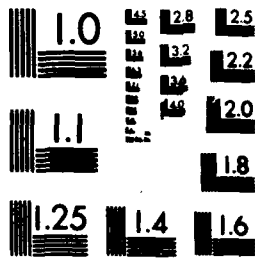
ENGINE RESPONSE TO DISTORTED INFLOW CONDITIONS:
CONFERENCE PROCEEDINGS OF (U) ADVISORY GROUP FOR
AEROSPACE RESEARCH AND DEVELOPMENT NEWELL... MAR 87
AGARD-CP-400 F/G 20/4

2/4

UNCLASSIFIED

NL





MICROCOPY RESOLUTION TEST CHART
NATIONAL BUREAU OF STANDARDS-1963-A

can be more than 25 % at high temperature distortion and is caused by the circumferential pressure gradient. The expansion of the hot sector corresponds to a narrowing of the cold sector. As a result the compressor section of the cold sector has a new effective flow path, which is different to the geometry of the present compressor. From this it is to be concluded that the behavior is quite different to that of the totally undistorted compressor. Even for the undistorted sector the correlation of corrected rotor speed, pressure ratio and corrected air flow of the original compressor map is invalid.

At high rotor speeds the air flow through the compressor is determined by the capacity of the first stages. The so called "undisturbed" sector will get a narrowed flowpath in the front part of the compressor if there is a temperature distortion. The throttling of the first stages will be increased and the airflow ingested will be shifted to lower values. Therefore it is expected that the operating point of the cold sector is shifted to the left side of the corresponding constant speed line of the original compressor map, contrary to the simplified assumption of the "parallel compressor model" as depicted in Fig. 1. The same statements can be made for the operating points of the hot sector: The corrected constant speed lines are shifted to higher corrected airflows.

Fig. 6 shows the slopes of stage pressure ratios and total pressures versus compressor axial position considering the deviations of the superimposed flowpath. The slopes of the cold sector now differ from those of the undistorted compressor. The relative parameters on the right side illustrate this tendency very distinctively.

The stage pressure ratio of the cold sector exceeds somewhat the level of the undistorted operation within the front stages. Due to the narrowing of flow path they are stronger throttled in this section. Downstream of the mid stages the "cold" values are below the undistorted as the whole compression ratio decreases a little if the compressor inlet flow is distorted. In the hot sector the stage pressure ratios follow the slope shown in Fig. 4.

In Fig. 7 the static pressure is plotted versus the compressor axial position. In the front part static pressures exceed the values of undistorted operation even in the cold sector. As the first stages are stronger throttled by the superimposed narrowing of the flow path the Mach number level at the compressor face is lower even in this sector. In the rear compressor part the static pressure corresponds to the total pressure slope of the cold sector. The lower Mach numbers of the inlet flow cause a change of incidence even in the primarily undisturbed sector (Fig. 7 bottom) and lead to the small increase of stage pressure ratio shown in Fig. 6.

All considerations are based on the assumption that a mixing of the distorted and the undistorted flow through the compressor is negligible. This assumption seems to be justified due to the following reasons and if minor effects are neglected.

- Only within the axial gaps between the blade rows the flow is not ducted circumferentially. These unducted distances sum up to 10 to 15 % only of the total compressor length.
- within the rotor blading the hot and the cold stream lines mainly follow each other on the same tracks. Between the cold and the hot flow particles of different velocity kinetic energy is exchanged. A mass exchange can be neglected.

Therefore it is to be expected that even at the compressor exit the hot sector will have a significant core that almost consists totally of "distorted" hot material.

3.5 PARTIAL FLOW SEPARATION AND COMPRESSOR STALL

From the above considerations it can be derived that - contrary to the "parallel-compressor model" - the surge lines cannot be treated separately for the distorted and for the undistorted sector.

In Fig. 8 the flow conditions at the first stage rotor are shown schematically. Due to the circumferential gradient of static pressure an asymmetric flow field is obtained already at the rotor inlet:

Caused by an increased deflection of the rotor flow within the transition zone on the left side of the distorted sector the throttling of the front stages is reduced in this area. The induced larger flow velocity decreases the strong incidence of the rotor that results from the superimposed circumferential component of the absolute velocity.

In the transition zone from the distorted to the undistorted sector - in Fig. 8 at the right boundary of the hot sector - there will be a lower total pressure rise in the front stages due to a minor deflection (lower α_{c1}). Therefore the front stages are stronger throttled in this area. In combination with the narrowed flow path this leads to lower local inlet Mach-numbers M_{1c} and p_1/p_{1o} is increased with p_{1c} being constant. As the influences of the reduced absolute velocity and of its circumferential component induced by the pressure gradient will nearly compensate each other, therefore the rotor incidence remains low in this transition zone. But a strong incidence of the following stator will occur. As Fig. 8 shows this is very distinct on the hot side of the transition zone (dotted velocity triangles).

Therefore it is to be expected, that even at high rotor speeds flow separation within the hot sector will not occur in the rear stages. As Fig. 8 shows the flow separates in one of the front stages and there locally on the right side of the distorted sector. Downstream of the separation now the superimposed narrowing of the flow path is intensified caused by the larger pressure gradient (Fig. 3). Due to this the local flow separation will normally not propagate into the rear part of the hot sector.

On the other hand in the case of such flow separation, the cold sector expands strongly within the whole rear half of the compressor. In combination with the described higher throttling of the front stages and with the airflow through the cold sector being diminished this may - depending on the aerodynamic design of the compressor - lead to a compressor stall induced by a flow separation in the rear stages of the primarily undistorted sector.

4. EXPERIMENTAL INVESTIGATIONS

The experimental investigations were carried out on the turbojet engine ATAR F at the test bed of the Institute for Jet Propulsion and Turbomachinery, Technical University of Aachen [15].

The single-spool ATAR engine incorporates a 7-stage axial compressor, an annular combustion chamber and a single-stage turbine. For the investigations the exhaust nozzle position could be varied independently from the engine control. The hub/tip ratio at compressor inlet is 0.55. Some characteristic engine data at takeoff power (ISA/SLS) are:

| | |
|------------------------|------------------------|
| Rotor speed | 8300 min ⁻¹ |
| Overall pressure ratio | 4.2 |
| Air mass flow | 52 kg/s |

Aerodynamic design of the compressor stages:

| | |
|---------------|---------------------------------------|
| Front stages: | solid body |
| Mid stages: | constant reaction versus blade height |
| Rear stage: | free-vortex design |

4.1 SET-UP FOR GENERATION OF DEFINED TEMPERATURE AND PRESSURE DISTORTION

For the simulation of defined circumferential distortions a special inlet duct was installed in front of the engine (Fig. 9). This duct is divided into quadrants by four separation walls. The walls are fixed at the same circumferential position as the four struts at compressor inlet. Hence, the extent of the distortion is exactly defined up to the inlet guide vanes of the compressor (Fig. 10). The steady-state total temperature distortion was produced by the injection of hot air into the inlet air flow. Therefore, pressurized air from the central air distribution system of the institute was heated up in a three-flow combustion chamber operated by natural gas (Fig. 9). Passing a distributor with electropneumatic valves the hot air was injected into one sector of the inlet duct through cascades. The temperature distribution in the distorted sector at compressor inlet was satisfactorily. Electromagnetic bleed valves were synchronized with the distributor valves, so that a continuous operation of the gas combustion chamber was possible.

By computer control it was possible to establish a certain level of temperature distortion at harmonized total pressures in the distorted and the undistorted sector. For generating a steady-state total pressure distortion a screen was installed in one sector of the inlet duct.

4.2 MEASURING TECHNIQUE AND DATA REDUCTION

A survey of the measuring planes is given in Fig. 10. The compressor inlet (plane E) was equipped with 24 rakes. Each rake had a thickness of 1.6 mm and incorporated 4 measuring points at different radii. According to the type of distortion investigated the inlet plane was equipped predominantly with temperature or pressure rakes. Static pressures were measured by pressure taps in the compressor outer casing.

Interstage measurements were carried out in two diametrical sectors with combined p_0/T_0 -probes and wall pressure taps. The probes were installed in front of each rotor. The measuring points were positioned at 60 % blade height in the center of the flow-path at the exit of two guide vanes. To reduce the interaction of the probes with the vanes the probes had only a thickness of 1.5 mm, so that the blockage of the flow area between two vanes was less than 2 %. Due to the fact that the circumferential position of the distortion changes by approximately 120 degrees in the direction of rotation when passing the compressor, the interstage probes were positioned in such a manner that they were continually in the center of the distorted respectively undistorted sector.

At compressor exit the p_0/T_0 -probes and wall pressure taps were positioned about 50 mm downstream of the guide vanes of the last compressor stage between the 10 struts (plane 2 in Fig. 10) of the compressor exit casing. Due to the very large spacing (36 degrees) of the struts compared to the blades and vanes, it can be assumed that the static pressure gradients which existed within the boundary zones of the distorted sector at the outlet of the guide vanes of the last compressor stage are substantially attenuated at the measuring plane 2.

To get additional information on the circumferential total pressure and total temperature distribution at the inlet of the combustion chamber (plane EB) 14 total pressure and 14 total temperature probes were installed about 100 mm downstream of plane 2 near the fuel nozzles.

Due to the great number of measured values (more than 200, including 144 pressures and 63 temperatures) and to realize short engine running time because of the high fuel cost, data acquisition was carried out by a computer.

The measured values with distortion were related to the values without distortion measured at the same point - without any change of probe position - and were corrected according to the actual environmental conditions. Due to this procedure even small changes of the

aero-thermodynamic data could be measured and data scattering because of different characteristics of the probes (e.g. thermocouples) was eliminated. As an example Fig. 11 shows the absolute values and the changes of total pressures and total temperatures with and without distortion versus circumferential angle at combustion chamber inlet.

5. EXPERIMENTAL RESULTS OF THE PRESSURE DISTORTION INVESTIGATIONS

The effect of distortion on compressor behaviour was investigated at three different corrected speeds ($N_{cor} = N/\sqrt{T_1/288K}$) and two different exhaust nozzle positions (A_N). Several tests with two screens (48 % and 55 % area blockage) were carried out. Some of the results of the investigations with the 55 %-screen at high corrected speed and minimum exhaust nozzle area (A_N closed) are presented herein. For all other operating points qualitatively similar results were obtained.

5.1 DISTORTION AT COMPRESSOR INLET

The levels of pressure distortion ($\Delta p_t = p_{tmax} - p_{tmin}$ and $\Delta \bar{p}_{t,60} = \bar{p}_t - \bar{p}_{tmin,60}$) are summarized in Tab. 1 for the test points. The DC₆₀-factor ($=\Delta \bar{p}_{t,60}/\bar{q}$) was about 0.62 and only less influenced by the operating point of the engine. Fig. 12 shows the total pressure and static pressure distributions at compressor inlet (plane E) for the selected operating point. The total pressures are average values of the four radially distributed measuring points of each rake and were related to the values without distortion ($p_{tE}/p_{tE,0}$). The static wall pressures were also related to the corresponding values without distortion. Due to the separation walls in the inlet duct the circumferential extent of the distortion at compressor inlet was still 90 degrees and quite homogeneous within the distorted sector. This was especially advantageous for the evaluation of interactions in the boundary zones between the distorted and undistorted flow.

TAB. 1: Distortion indices at compressor inlet

| N_{cor} [min ⁻¹] | A_N | $\frac{\Delta p_t}{\bar{p}_t}$ | $\frac{\Delta \bar{p}_{t,60}}{\bar{p}_t}$ | $\frac{\Delta \bar{p}_{t,60}}{\bar{q}}$ |
|-----------------------------------|--------|--------------------------------|---|---|
| 6000 | closed | 0,051 | 0,038 | 0,65 |
| | open | 0,055 | 0,039 | 0,65 |
| 7500 | closed | 0,108 | 0,081 | 0,61 |
| | open | 0,115 | 0,084 | 0,61 |
| 8000 | closed | 0,140 | 0,105 | 0,62 |
| | open | 0,145 | 0,109 | 0,62 |

Assuming that the total pressure loss does not really change between plane E and plane 1 - in the area of struts and inlet guide vanes - the correlation of total pressure distribution (Fig. 12) and static pressure distribution (Fig. 13) gives information on the local changes of Mach number and corrected air mass flow at compressor inlet. In the distorted sector the corrected air flow is reduced whereas in the undistorted sector the air flow is - except for the transition zones - almost unchanged. The small differences in static pressure level at plane E and plane 1 are a result of some air mass flow exchange through the axial gap between the struts and inlet guide vanes (Fig. 10).

Comparing the static pressure distribution at the inlet of the first and third stage ($p_{tE}/p_{tE,0}$) in Fig. 13, the interactions between the sectors become evident. These interactions are primarily a result of the circumferential pressure gradients within the axial gaps.

5.2 BEHAVIOUR OF THE COMPRESSOR WITHIN THE DISTORTED AND UNDISTORTED SECTOR

Fig. 14 shows the total pressure changes from compressor inlet to exit for the distorted and undistorted sector. The total pressures are local values measured in the center of the two sectors. It is demonstrated that the level of pressure distortion is substantially reduced when passing the compressor. Throttling of the compressor in the undistorted sector is slightly decreased. The continuous increase in total pressure in the distorted sector shows that none of the seven stages has reached its surge line. The static pressures in Fig. 15 correspond to the total pressures and are harmonized in both sectors at compressor exit.

5.3 DISTORTION AT COMPRESSOR EXIT AND EFFECT ON ENGINE BEHAVIOUR

The distortion at compressor exit (inlet of the combustion chamber) is demonstrated in Fig. 16. Due to the static pressure gradient the circumferential extent of the distorted sector was reduced to 75 degrees and the offset of the distorted flow when passing the compressor was about 120 degrees in the direction of rotation, almost independent from the level of rotor speed. Furthermore, the pressure distortion at compressor inlet has changed into a temperature distortion at compressor exit.

The asymmetry of the curves in Fig. 16 indicate that the circumferential pressure gradients at the boundaries of the distorted sector influence the flow angle at rotor inlet. Therefore, blade incidence is increased at the right boundary and decreased at the left where now the total pressure minimum can be observed. Fig. 17 shows the attenuation of pressure distortion and the generation of temperature distortion at compressor exit ($\Delta T_{t,60} = T_{t,max,60} - T_t$) for different engine operating points.

A pressure distortion at compressor inlet results in a combined pressure and temperature distortion for the downstream engine components. Nevertheless it should be mentioned that the compressor exit distortion of a single compressor engine is not necessarily the same as the distortion at the inlet of the high pressure compressor of a twin compressor engine, because a downstream compressor causes a different throttling compared with a downstream combustion chamber and turbine.

Fig. 18 shows the compressor map of the undistorted compressor and the operating points of the distorted and undistorted sector at corrected speeds of 7500 and 8000 min^{-1} and at two exhaust nozzle positions (open and closed). Although the operating points of the distorted sector (closed nozzle) have reached the surge line of the undistorted compressor and according to the "parallel compressor model" surge could have been induced, no surge was observed during steady state operation nor at accelerations. This demonstrates that the characteristic of the undistorted compressor cannot be used to predict surge by the position of the operating point of the distorted sector relative to the surge line of the undistorted compressor. The surge line of the distorted sector has moved towards higher pressure ratios mainly due to the constriction of the sector from 90 to 75 degrees.

6. EXPERIMENTAL RESULTS OF THE TEMPERATURE DISTORTION INVESTIGATIONS

The investigations were carried out at the same engine operating points as the pressure distortion tests. The results which are presented below were obtained at $N_{COR} = 8000 \text{ min}^{-1}$ and closed exhaust nozzle. These are similar to those results obtained at lower rotor speeds and at an open position of the exhaust nozzle. Three different temperature distortion levels were adjusted (see Fig. 19).

6.1 TEMPERATURE DISTORTION AT COMPRESSOR INLET

Fig. 19 shows the total temperature distribution versus circumferential angle at compressor inlet (plane E) and exit (plane EB). The temperature increase at the boundaries of the distorted sector is induced by the separation walls in the inlet duct. These walls provided an almost exact limitation of the circumferential extent of the distortion. The radial uniformity within the distorted sector was also satisfactory.

6.2 DISTORTION AT COMPRESSOR EXIT

The lower part of Fig. 19 shows the total temperature distribution at compressor exit (inlet of combustion chamber). The extent of the distorted sector is still 90 degrees and attenuation of distortion level was only about 30%. In parallel the pressure distortion shown in Fig. 20 and 21 was induced. The level of pressure distortion at compressor exit is about $DC_{60} = 0.15$ to 0.4.

6.3 BEHAVIOUR OF THE COMPRESSOR WITHIN THE DISTORTED AND UNDISTORTED SECTOR

In Fig. 22 the total pressure changes in the center of the distorted and undistorted sector are presented. The static pressure curves in Fig. 23 indicate that the circumferential extent of the distorted sector increases in the first three stages and decreases in the following four stages. The extension of the distorted sector results in a rapid increase in stage pressure ratios (Fig. 24). Therefore, and due to the shape of the stage characteristic line the operating points of the fourth and sixth stage are located on the left side of the characteristic line more or less near the flow separation point.

The slope of the total pressure curve for $\Delta T = 90 \text{ K}$ in Fig. 22 indicates an increased local flow separation at the right boundary of the distorted sector. The impact of the flow separation is attenuated by the constriction of the distorted sector downstream of the third stage. The situation is similar to the local flow separation in the front stages at low rotor speeds (rotating stall) but without rotation of the separated flow cells.

Ten bleed air taps are introduced in the compressor outer casing above the guide vanes of the fifth stage. These taps are connected by a collecting duct and their circumferential position corresponds to the position of the transition zone from the distorted to the undistorted sector. Therefore, the reason for the kink in the static pressure curves of the distorted sector at plane E 6 in Fig. 23 may be an exchange of air mass flow through the collecting duct.

The interactions between the distorted and undistorted flow have already been discussed in section 3.4. Fig. 25 shows the static pressure distribution at compressor inlet (plane 1). At constant total pressure these curves give an information on the circumferential distribution of the corrected air mass flow.

A similar asymmetry as for the static pressure curves at compressor inlet can be observed for the static pressure curves at the inlet of the third stage (plane E 3) in Fig. 26. The extension of the distorted sector from 90 to 110 degrees is also demonstrated in this figure. The significant pressure peak at $\Delta T = 90 \text{ K}$ on the right side of the distorted sector causes together with the total pressure decrease according to Fig. 5 and 8 (minor flow deflection) a significant reduction in flow velocity. The resulting

guide vane incidence is increased in the area of negative circumferential pressure gradients on the right side of the pressure peak. The pressure distribution at $\Delta T = 90$ K indicates that a local flow separation has already been induced. This also gives an explanation for the increased throttling within the first quadrant at compressor inlet in Fig. 25.

It can be seen that the flow separation tendency within the right boundary zone of the hot sector, that has already been discussed in section 3.4 (Fig. 8), is transferred from the distorted sector to the originally undistorted sector when the air flow is passing the front compressor stages. Furthermore, for local flow separations the level of maximum circumferential pressure gradients often is more critical than the level of an average distortion index.

6.4 EFFECT ON ENGINE BEHAVIOUR

Fig. 27 shows the operating points of the distorted and undistorted sector in the map of the completely undistorted compressor. The increased impact on the flow in the undistorted sector at high compressor throttling (nozzle closed) becomes evident. The correlation of corrected rotor speed and corrected air mass flow of the completely undistorted compressor is no longer relevant. The level of corrected air mass flow in the distorted sector is significantly higher than that of the undistorted compressor at the same corrected speed ($N_{cor,h}$).

7. CONCLUSIONS

A procedure for a qualitative analysis of the impact of steady-state circumferential pressure and temperature distortion on the flow characteristics within a multistage compressor and of the interactions between the distorted and undistorted compressor flow is described.

This qualitative analysis was carried out in advance of the experimental investigations and of the publication of relevant experimental results (p_t - and T_t -distortion) in the literature. The theoretical analysis revealed the deficiency of the parallel compressor model for a multistage engine compressor and significantly reduced the amount of experimental investigation.

The theoretical analysis model was verified by the experimental results discussed in this paper. Due to a high accuracy measuring technique and the procedure of data reduction even pressure and temperature changes of about 0.1 % could be identified. Although a high level of pressure and temperature distortion with strong gradients at the boundaries of the distorted sector was selected for the tests, no compressor surge could be observed. It has been demonstrated that the characteristic of the undistorted compressor cannot be used to predict compressor surge in the case of circumferential pressure and temperature distortion.

REFERENCES

- [1] Calogeras, J.E., Mehalic, C.M. and P.L.Burstadt: Experimental Investigation of the Effect of Screen-Induced Total-Pressure Distortion on Turbojet Stall Margin. NASA TM X-2239, 1971
- [2] Mehalic, C.M. and R.A.Lottig: Steady-State Inlet Temperature Distortion Effects on the Stall Limits of the J 85-GE-13 Turbojet Engine. NASA TM X-2990, February 1974
- [3] De Bogdan, C.E., Moss, J.E. and N.M.Braithwaite: Internal Flow Characteristics of a Multistage Compressor with Inlet Pressure Distortion. NASA TM X-3446, February 1977
- [4] Braithwaite, W.M.: Experimental Evaluation of a TF 30-P-3 Turbofan Engine in an Altitude Facility: Effect of Steady-State Temperature Distortion. NASA TM X-2921, 1973
- [5] Braithwaite, W.M., Graber, E.J., Jr. and C.M.Mehalic: Inlet Temperature and Pressure Distortion on Turbojet Performance. Paper 73-1316, AIAA, November 1973
- [6] Graber, E.J.Jr. and W.M.Braithwaite: Summary of Recent Investigations of Inlet Flow Distortion Effects on Engine Stability. AIAA-Paper No. 74-236, January 1974
- [7] Korn, J.A.: Estimated Effect of Circumferential Distortion on Axial Compressors Using Parallel Compressor Theory and Dynamic Stall Delay. AIAA-Paper No. 74-233, January 1974
- [8] Milner, E.J. and L.M.Wenzel: Performance of a J85-13 Compressor with Clean and Distorted Inlet Flow. NASA TM X-3304, December 1975
- [9] Willoh, R., Graber, E.J., Teren, F. and R.E.Coltrin: Engine Systems Technology. Aeronautical Propulsion NASA SP-381, 1975
- [10] Mazzawy, R.S. and G.A.Banks: Circumferential Distortion Modeling of the TF 30-P-3 Compression System. NASA CR-135124, January 1977
- [11] Baghdadi, S. and J.E.Lueke: Compressor Stability Analysis. ASME Paper 81-WA/FE-18, 1981
- [12] Min, Z.H. and J.Hu: Propagation of Steady Circumferential Distortion through an Axial Compressor Rotor. ASME-Paper 85-IGT-81, 1985
- [13] Billet, G., Laval, P. and P.Chevalier: Numerical Simulation of the Response of an Axial Compressor to a Nonhomogeneous Flow. La Recherche Aerospatiale, No. 4, 1985
- [14] Künkler, H.: Zur Auswirkung stationärer Gesamtdruck- und Gesamttemperatur-Distortion im Einlauf eines TL-Triebwerks auf das Strömungsverhalten innerhalb eines vielstufigen Verdichters. Mitteilung Nr. 75-03 Institut für Strahltriebwerke, RWTH Aachen, 1975
- [15] Tönskötter, H.: Experimentelle Untersuchung des Verhaltens eines vielstufigen Verdichters im Turbostrahltriebwerk bei stationärer Temperatur- und Druckdistortion. Mitteilung Nr. 77-06 Institut für Strahltriebwerke, RWTH Aachen, 1977

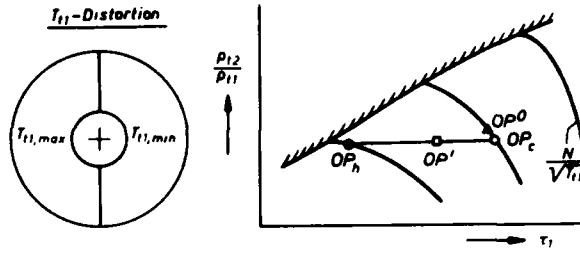


Fig. 1: Parallel compressor model, temperature distortion

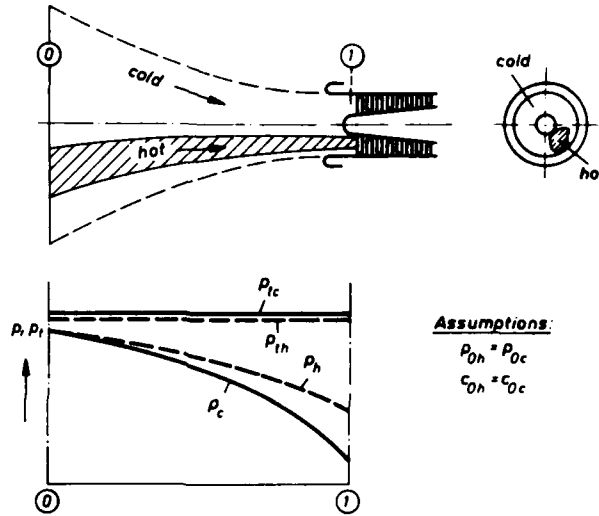


Fig. 2: Flow field and pressure distribution in front of the compressor

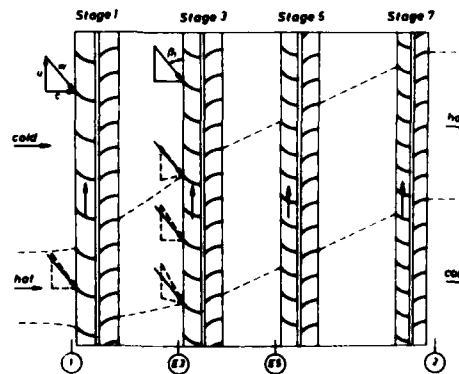


Fig. 3: Compressor blading with distorted and undistorted sectors

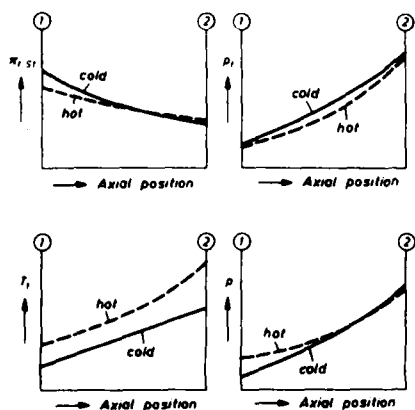


Fig. 4: Pressures and temperatures along the compressor axis

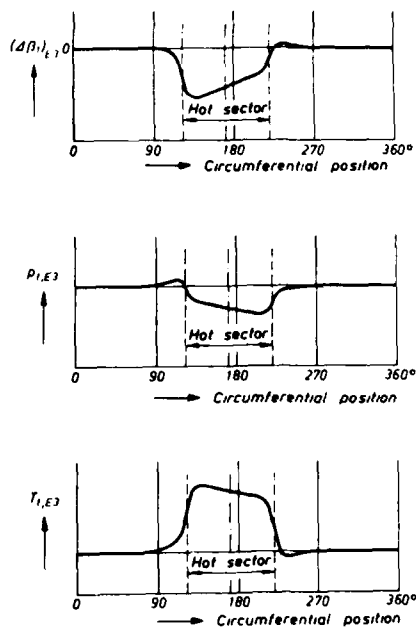


Fig. 5: Flow incidence, total pressure and total temperature distribution at the inlet of stage 3

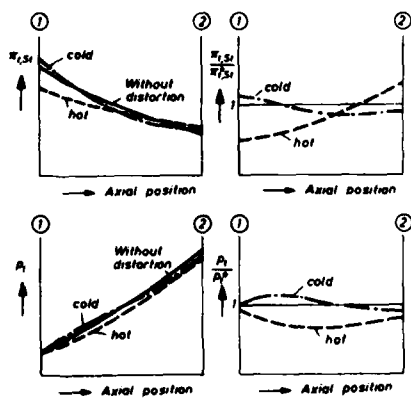


Fig. 6: Axial distribution of stage pressure ratios and total pressures compared to undistorted operation

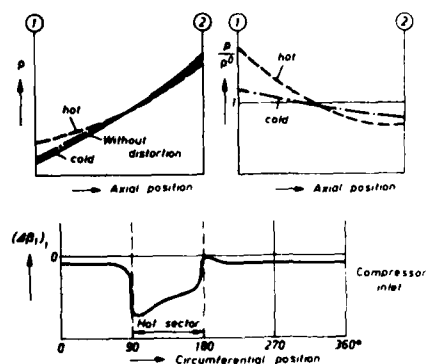


Fig. 7: Axial distribution of pressures and circumferential flow incidence compared to undistorted operation

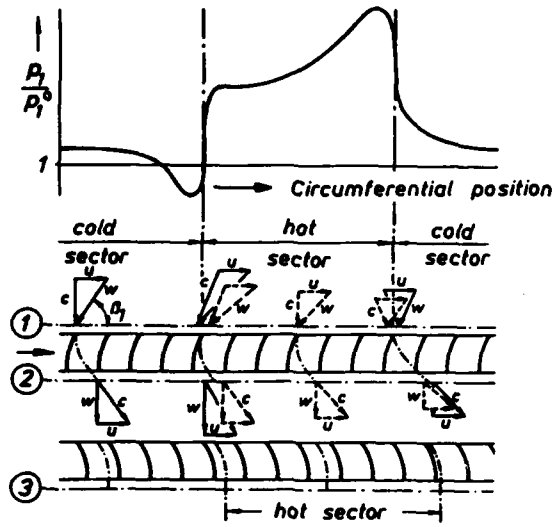


Fig. 8: Flow condition at first stage

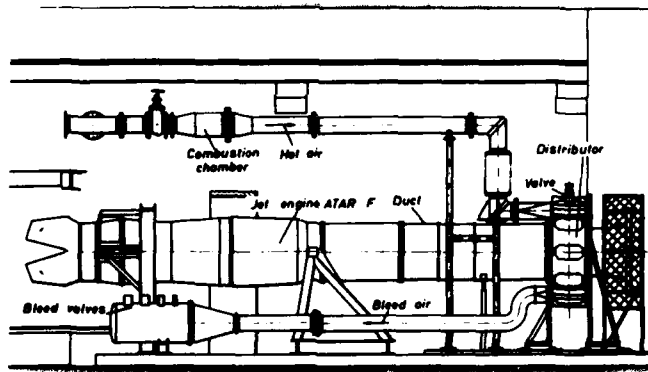


Fig. 9: Experimental set-up

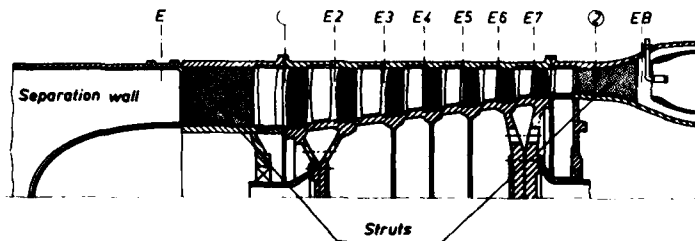


Fig. 10: Measuring planes in the 7-stage axial compressor

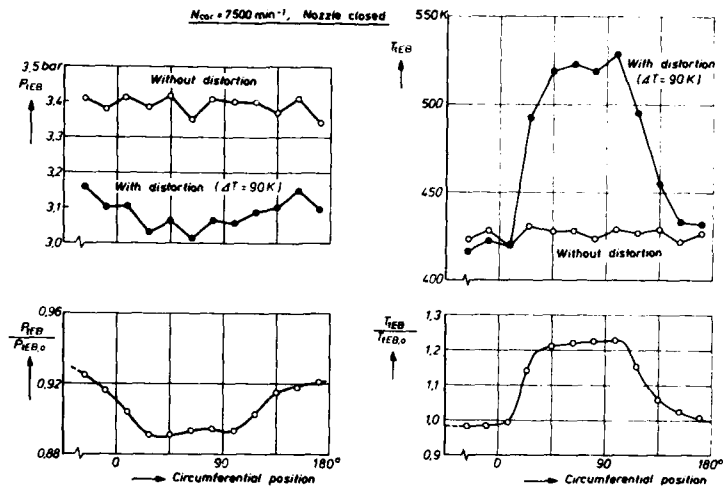


Fig. 11: Circumferential distribution of pressures and temperatures at the compressor exit (combustor inlet)

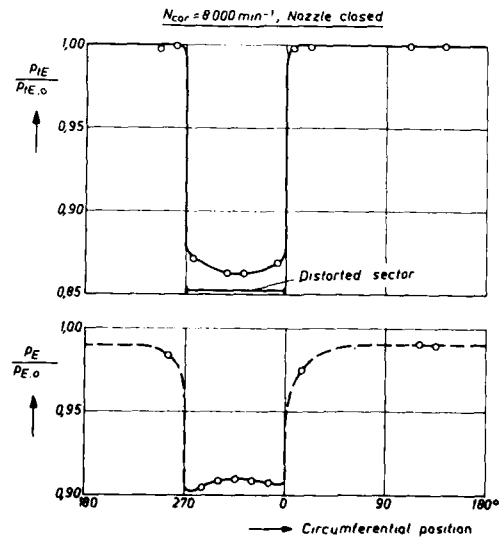


Fig. 12: Circumferential distribution of total and static pressures at compressor inlet, pressure distortion

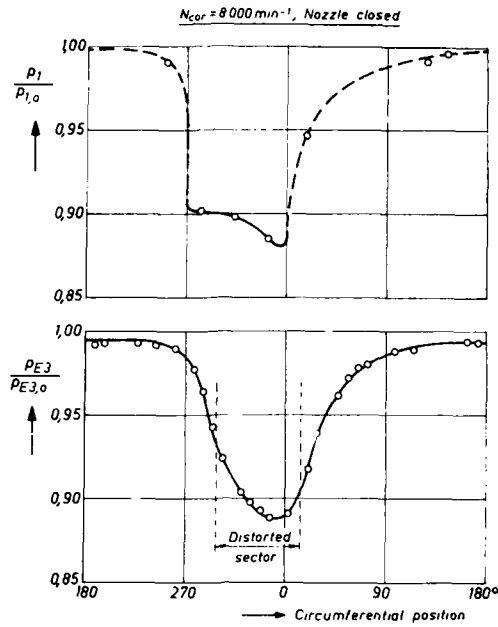


Fig. 13: Circumferential distribution of wall pressures at the inlet of stage 1 and stage 3, pressure distortion

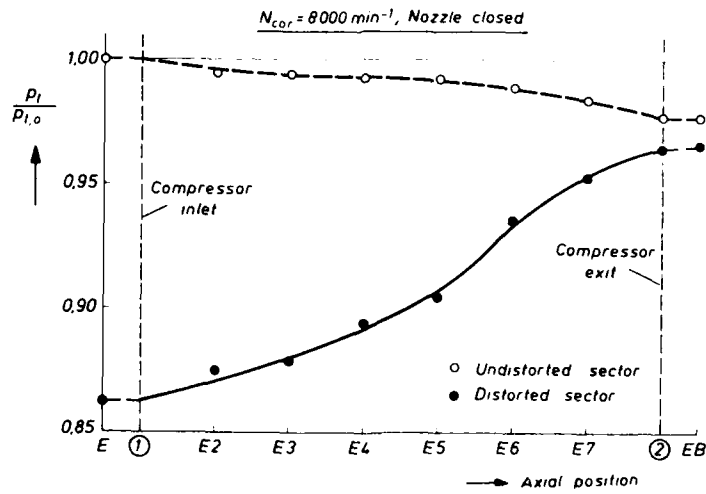


Fig. 14: Development of the total pressure along the compressor axis, pressure distortion

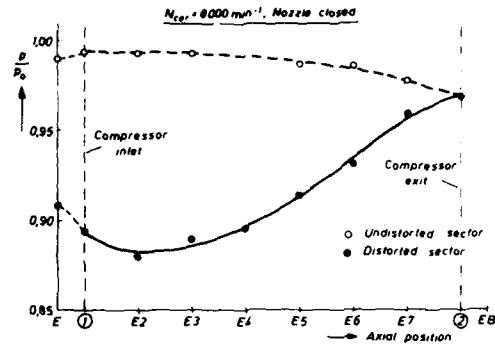


Fig. 15: Distribution of wall pressures along the compressor axis, pressure distortion

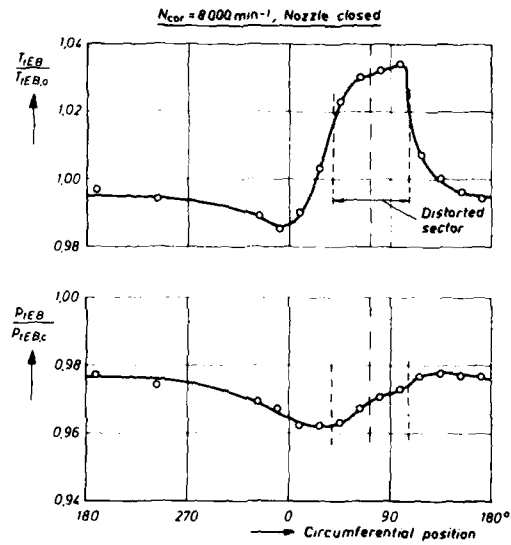


Fig. 16: Circumferential distributions of total temperature and total pressure at compressor exit, pressure distortion

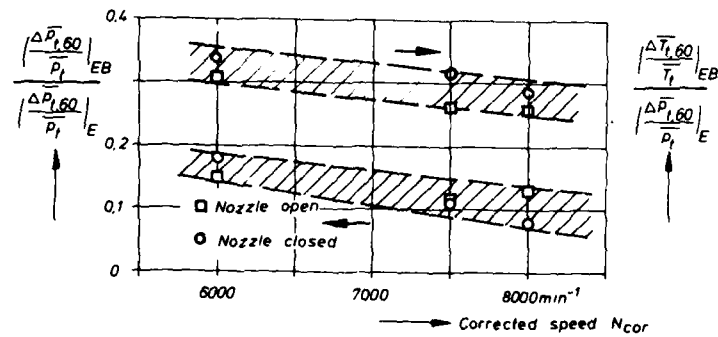


Fig. 17: Relative distortion indices at the compressor exit, pressure distortion

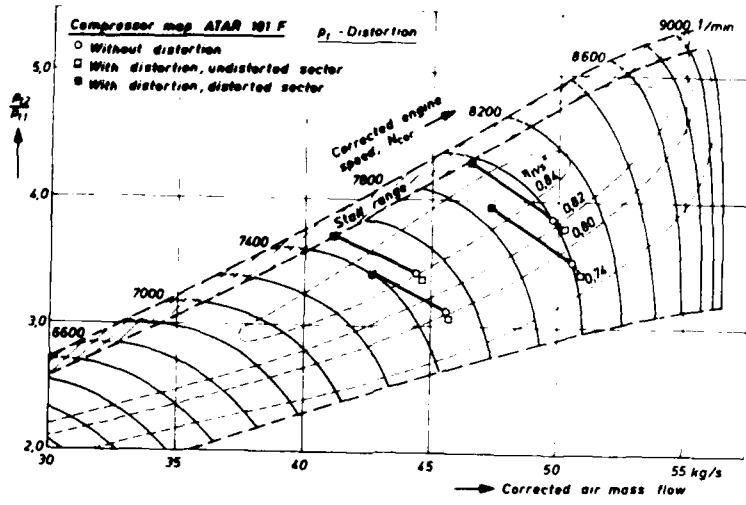


Fig. 10. Compressor map ATAR 101 F with and without distortion.

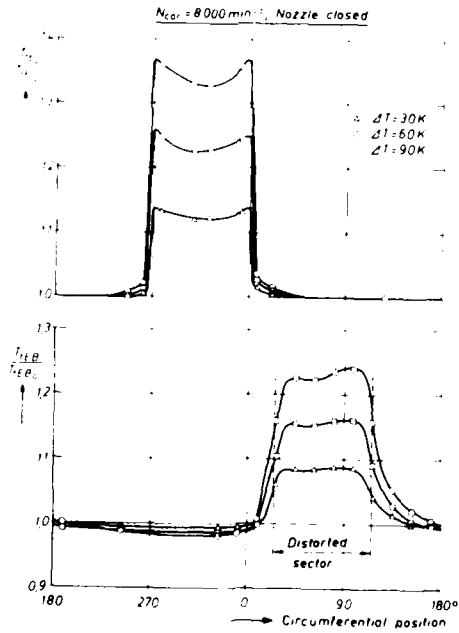


Fig. 11. Circumferential distribution of total temperature at the compressor inlet and outlet for different temperature differences.

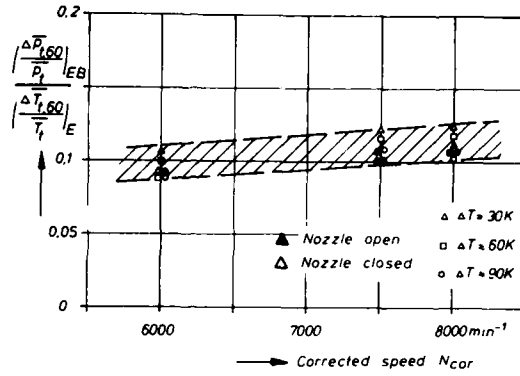


Fig. 20: Pressure distortion index at the compressor exit related to the temperature distortion index at the compressor inlet. temperature distortion

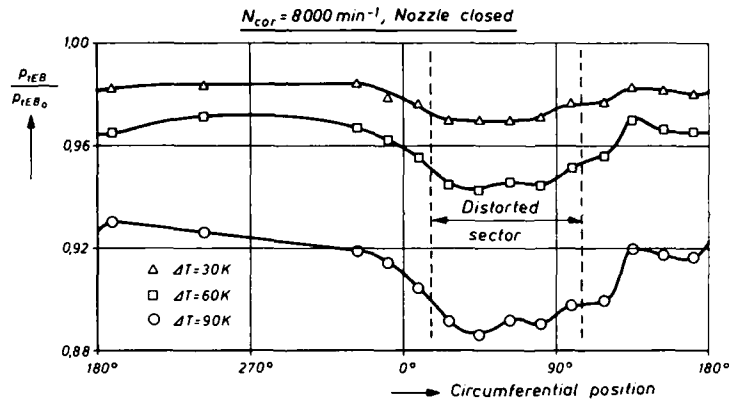


Fig. 21: Circumferential distribution of total pressure at compressor exit, temperature distortion

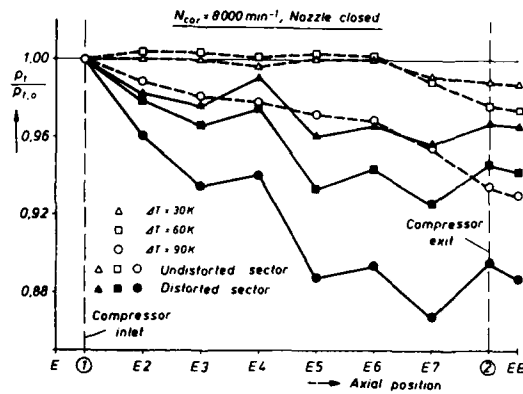


Fig. 22: Distribution of pressure along the compressor axis. temperature distortion

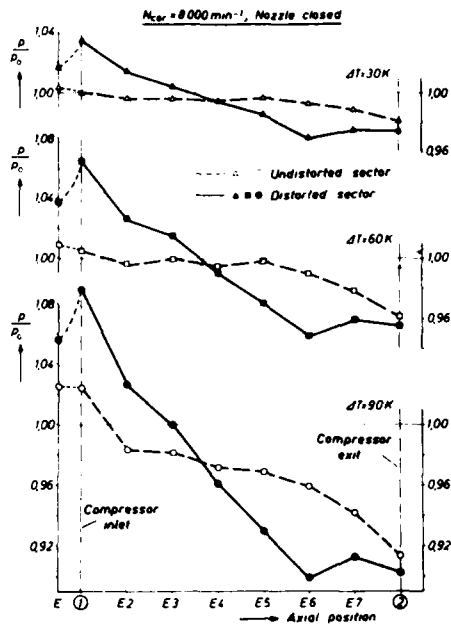


Fig. 23: Distribution of static pressures along the compressor axis, temperature distortion

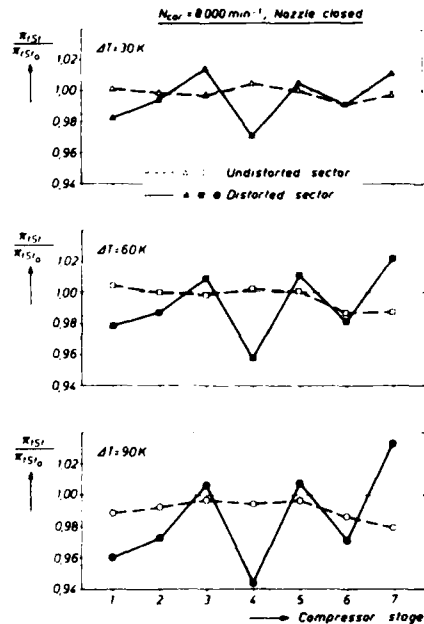


Fig. 24: Development of stage pressure ratios, temperature distortion

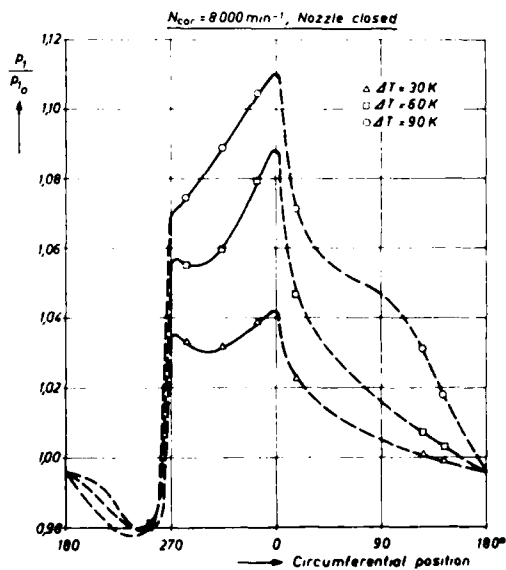


Fig. 25: Circumferential distribution of wall pressures at the compressor inlet, temperature distortion

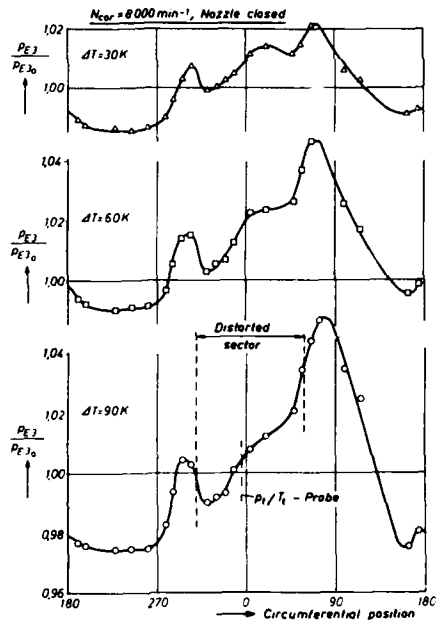


Fig. 26: Circumferential distribution of wall pressures at the inlet of stage 3, temperature distortion

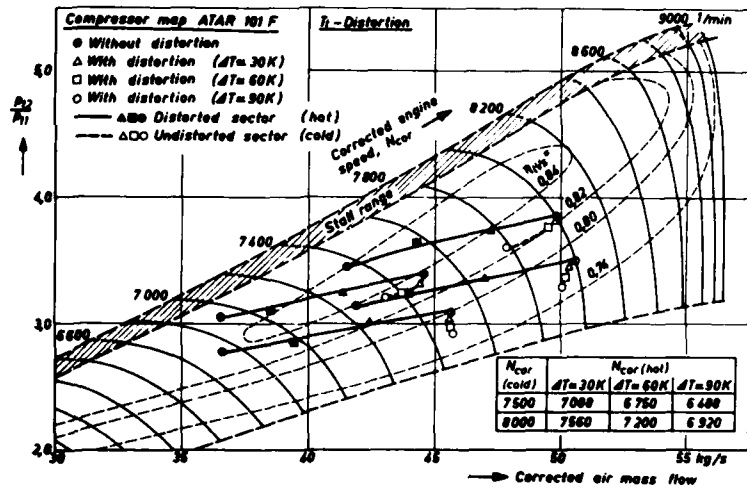


Fig. 27: Compressor map with distorted operating points, temperature distortion



Viscous Analyses for Flow Through Subsonic and Supersonic Intakes

Louis A. Povinelli and Charles E. Towne
National Aeronautics and Space Administration
Lewis Research Center
Cleveland, Ohio 44135 U.S.A.

SUMMARY

A parabolized Navier-Stokes code was used to analyze a number of diffusers typical of a modern inlet design. The effect of curvature of the diffuser centerline and transitioning cross sections was evaluated to determine the primary cause of the flow distortion in the duct. Results are presented for S-shaped intakes with circular and transitioning cross sections. Special emphasis is placed on verification of the analysis to accurately predict distorted flow fields resulting from pressure-driven secondary flows. The effect of vortex generators on reducing the distortion of intakes is presented. Comparisons of the experimental and analytical total pressure contours at the exit of the intake exhibit good agreement. In the case of supersonic inlets, computations of the inlet flow field reveal that large secondary flow regions may be generated just inside of the intake. These strong flows may lead to separated flow regions and cause pronounced distortions upstream of the compressor.

INTRODUCTION

The importance of computational fluid dynamics as an analysis tool for external flow about aircraft and aerospace configurations has been illustrated in the literature on numerous occasions. Less clearly demonstrated, however, has been the applicability of computational methods for internal flows in propulsion systems. Clearly, a need exists for analyzing the components of engine systems. In particular, the effect of intake design on air flow quality at the compressor face constitutes the initial step required in the overall flow analysis. High performance aircraft frequently employ complex intake ducting which, in turn, leads to highly three-dimensional flows. The complexity of the intake may include changes in curvature, cross-sectional area and out-of-plane bends. These geometric changes lead to cross-stream pressure gradients which drive secondary flows along the walls, and possibly result in strong vortex flow or separations. There exists a critical need, therefore, to properly model and calculate the flow in a variety of intake shapes in order to ensure reasonable flow quality to the engine over a wide flight range.

Numerous approaches have been used for the analysis of the flow for intake ducts. Inviscid computations coupled with a boundary layer analysis appear inadequate to describe the flow since the boundary layer thickness can grow to be a major portion of the duct height. Euler solvers can yield the velocity field but will not account for the viscous pressure losses. Fully elliptic Navier-Stokes solutions can provide an accurate flow field, but require hours of computer time. In addition, the grid size that can be efficiently analyzed is limited by computer storage for the full Navier-Stokes solutions. Computation time becomes important in the preliminary design process where a large number of intake configurations and operating conditions are analyzed. Parabolized Navier-Stokes solvers (PNS), however, offer a considerable reduction in computer time by making a single pass through the duct. Coupling of the elliptic pressure field with a fast PNS solver offers many desirable features. The PNS solvers are more economical than the full Navier-Stokes equations and less expensive to operate on present-generation computers. Most importantly, the PNS codes have been shown to yield accurate predictions within their domain of applicability.

This paper presents a review of the viscous analyses used by the NASA Lewis Research Center for application to aircraft intakes and the ducting upstream of the compressor. The computer methods discussed are based on the PNS equations. Analytical and experimental secondary flow and distortion patterns are reviewed for subsonic as well as high speed intakes.

APPROACH

The approach used in this paper is to review a number of computational studies for which selected aerodynamic parameters have also been measured, and to arrive at conclusions regarding our predictive capability for intakes. Three separate flow cases will be reviewed in sequence. A brief description of each study will be presented, including, as appropriate, the intake geometries, starting conditions, analysis method, grid size, experimental measurements and computational results of pressure and velocity. Each of the three cases will be examined as to the adequacy of the computational scheme to predict reasonable values. On the basis of the comparison, an evaluation or assessment of the predictive capability of the PNS solvers will be presented. In addition, potential difficulties associated with the PNS codes will be identified. Specific examples will also be discussed regarding the needs for additional code verification.

The three cases chosen for review involved an examination of:

- (1) Pressures and velocities for intakes with centerline curvature and cross-sectional shape transitioning (Ref. 1).
- (2) Secondary flows and total pressure coefficients for an S-duct with and without vortex generators (Ref. 2).
- (3) Mach number and secondary velocities in a Mach 5 inlet, including spillage effects (Refs. 3 and 4).

The paper now proceeds to the Results section in which the three flow cases will be discussed in sequential fashion.

RESULTS

Centerline Curvature and Cross Section Transitioning (Ref. 1)

Summary of Analysis Method. Subsonic intakes at Lewis are typically studied using a three-dimensional PNS computer code (Refs. 5 to 7). This analysis is compressible and fully viscous. The flow is computed by a single sweep spatial marching procedure which solves an approximate form of the Navier-Stokes equations. It is assumed that the flow is primarily in the direction of the duct centerline, with transverse secondary flow. This allows two basic assumptions to be made. The first is that second derivatives in the primary flow direction are negligible. The second is that the pressure in the primary, or streamwise, momentum equation can be represented during a marching step by the sum of a known three-dimensional pressure field and a one-dimensional correction for viscous blockage. A two-dimensional pressure correction Poisson equation is also solved after each step to ensure that the computed velocity and pressure fields are consistent. The known three-dimensional pressure field can be obtained from any available source. Normally a potential flow solution is used. When these assumptions are applied to the Navier-Stokes equations, a set of equations can be derived that can be solved by forward marching in the primary flow direction. The equations are solved in a body-fitted nonorthogonal coordinate system using an implicit finite-difference technique. The analysis has been verified by comparing computed results with benchmark experimental data for a variety of duct configurations and flow conditions (Refs. 6 to 10).

Duct Configurations and Inlet Conditions. Examples of the types of geometries studied with this analysis are shown in Fig. 1. These configurations were used to investigate the effects of centerline curvature and cross section transitioning on the distortion in modern complex intake ducts (Ref. 1). The first, called the baseline configuration, represents a typical modern intake design. The cross section is represented by a superellipse, and transitions from nearly rectangular at the inlet to circular at the exit. The exit-to-entrance area ratio is 1.31. The other two configurations are derived from the first, and were used to isolate the effects of cross section transitioning and centerline curvature on the flow. The second configuration has the same distribution of cross section shape, but with a straight centerline. The third configuration has the same centerline shape and area distribution as the baseline configuration, but with a circular cross section.

Conditions used at the inlet were a total pressure of 800 psf and a Mach number of 0.5. This corresponds to flight at about 28 000 ft altitude. An initial turbulent boundary layer thickness equal to 4.8 percent of the duct half width was used for the baseline and straight centerline configurations. For the circular cross section configuration a thickness of 5.6 percent was used to give the same inlet blockage.

Computed Results. The effect of centerline curvature on flow distortion was determined by analyzing the circular cross section configuration of Fig. 1(c). In Fig. 2 the computed secondary flow field is shown at six stations through the duct. At the first station the cross flow velocities are small. The effect of the first bend can be seen at station b. The core flow moves toward the left side of the duct, responding to centrifugal effects. The low energy boundary layer flow moves away from the pressure side of the duct, on the left, toward the suction side of the duct, on the right. A vortex motion thus begins to develop but is quickly dissipated, as shown by the results at station c, when the cross flow pressure gradients reverse in the second bend. At station c the secondary flow in the boundary layer has reversed direction, flowing toward the low pressure region now on the left side of the duct. By station d a pair of counter rotating vortices has formed. These persist into the third bend and continue to move the low energy flow toward the left side of the duct. By station e the cross flow pressure gradients have again reversed direction, causing the formation of an additional pair of counter rotating vortices in the left half of the duct. These two pairs of vortices interact, driving the low energy flow away from the wall.

In Fig. 3 the distortion resulting from these secondary flows is shown in the form of constant total pressure contours at the six stations. The total pressure values are referenced to the inlet total pressure. The thickened boundary layer on the right side of the duct at station c is a result of the vortex pattern shown at station b in Fig. 2. As previously described, these vortices dissipate and a new pair is set up in the second bend. These persist into the third bend, where another pair develops. The two pairs of vortices interact, driving the low energy flow away from the wall, as shown by the bulges in the total pressure contours at stations e and f.

The computed secondary flow field for the baseline configuration of Fig. 1(a) is presented in Fig. 4. Even though this duct has the additional geometric complication of a transitioning cross section, the physics of the flow are essentially the same as in the circular cross section configuration just discussed. The same types of vortices are present, and they result in the same type of distortion pattern, as shown by the total pressure contours in Fig. 5. This indicates that for this intake duct the effect of the curved centerline on the flow is much more important than the effect of the changing cross-sectional shape.

To further confirm this, a straight centerline configuration, shown in Fig. 1(b), was analyzed. This duct has the same distribution of cross-sectional shape as the baseline configuration. As shown by the computed total pressure contours in Fig. 6, the transitioning cross section by itself does not cause any significant distortion of the flow.

It is noted that a small separation bubble was predicted along the right side of the duct between the first and second bends for both the circular cross section and baseline configurations. This is caused by the local adverse streamwise pressure gradient in this region. The marching analysis proceeds through this region using the "FLARE" approximation (Ref. 11). In the PNS analysis, this approximation is implemented by resetting the streamwise velocity to a small positive value if it falls below that value during a marching step. This stabilizes the analysis and allows it to march through small regions of separated flow. The flow details within the recirculation region are not modeled accurately, but if the separation bubble is small its effect on the rest of the flow is usually well modeled.

Vortex Generators in a Diffusing S-Duct (Ref. 2)

Summary of Analysis Method. In efforts to save weight and thereby fuel, it is common to design modern intake ducts to be as short as possible. The designer must therefore be concerned with the possibility of flow separation due to a strong adverse pressure gradient. To alleviate this problem, vortex generators are often used as a flow control device. Most vortex generators in use today are simply small wing sections mounted on the inside of a duct or on the wing of an airplane. Figure 7 shows a typical vortex generator. The vortex generators are inclined at an angle to the oncoming flow to generate the shed vortex. Also, the vortex generator is sized so that the tip lies just outside the edge of the boundary layer. This allows for the best interaction between the shed vortex and the boundary layer. The vortex generators are usually placed in groups of two or more upstream of the problem flow area. The vortex generator will cause a mixing of the high momentum core flow with the low momentum flow in the boundary layer, resulting in a net increase of momentum near the surface. This can delay or even eliminate the separation region.

In order to provide an analytical capability for these flows, the PNS analysis discussed in the previous section has been modified to include a model for vortex generators within a duct flow field (Ref. 12). The transverse momentum equations in the analysis are solved using a stream function - vorticity formulation. The vortex generator model takes advantage of this. The shed vortex is modeled by introducing a source term into the vorticity transport equation that is a function of the vortex generator characteristics. The effect of the drag of the vortex generator is also included in the model. The drag on the wing section is a combination of profile drag, which is due to viscous and pressure effects, and induced drag, which is due to the shed vortex. In this model the profile drag of the vortex generator is neglected in comparison to the induced drag because in the cases studied here the generators were small. The induced drag is then proportional to the vortex strength and the crossflow velocity at a point. This term is included in the governing equations as a negative source term in the primary momentum equation.

Duct Configuration and Inlet Conditions. Figure 8 shows a circular cross sectioned $30^\circ - 30^\circ$ S-bend diffuser that was tested experimentally both with and without vortex generators (Refs. 13 and 14). For the cases with vortex generators, three pairs were placed well upstream of the separation point. The axial location is indicated in Fig. 8. They were set at incidence angles of $\pm 16^\circ$ to form three pairs of counter rotating vortices. They were placed along the inside of the bend at azimuthal locations of -38.0° , 0.0° , and $+38.0^\circ$, as measured from the inside of the bend. The flow in this duct was turbulent with a Mach number of 0.6 and a Reynolds number based on the duct diameter of 1 760 400. The initial conditions were measured at 1.65 duct diameters upstream of the first bend to remove the influence of the bend on the static pressure. The initial boundary layer thickness was 0.1 times the initial duct radius and the area ratio was 1.51.

Computational and Experimental Results. Figure 9(a) shows the computed total pressure coefficient contours at six stations in the duct for the case without vortex generators. The inlet values were used as the reference conditions in computing the total pressure coefficient.

Figure 9(b) shows the experimental results. The maximum and minimum values at each streamwise station are shown on the figure. Comparing the computed and experimental results indicates that the analysis is able to adequately predict the total pressure distortions for the duct. A separated flow region exists in both the experimental and computed results along the lower surface near the inflection point between the two bends. Although the computed results in the separated region will not be correct because of the "FLARE" approximation, the global effect of the separated region

is well modeled. The comparison also shows that at $\theta = 30^\circ$, the fourth contour plot, the experimental results indicate a larger separated region. In the experiment the streamwise separated region was found to be between $\theta = 22^\circ$ and $\theta = 44^\circ$, while in the computation the separated region was between $\theta = 30^\circ$ and $\theta = 54^\circ$. Figures 10 and 11 show comparisons between the computed and experimental secondary velocity profiles at the inflection plane and at the bend exit. The agreement between the two results is very good. At the inflection point the vortex due to the curvature of the centerline is evident in both plots. Also at the inside of the first bend the separated region can be seen in the experimental results, by the region with no data. In the computed results the onset of separation is also evident where there is minimal secondary flow. At the bend exit both results in Fig. 11 show that the separated region is gone by the large amount of flow being swept toward the outside of the second bend. These results differ from those of a nondiffusing circular cross section S-bend, where the vortex due to the centerline curvature is strengthened in the second bend.

Figures 12(a) and (b) show the computed and experimental total pressure coefficients in the S-bend for the case with vortex generators. Again the maximum and minimum values are shown at each streamwise station. At the $\theta = 15^\circ$ point the effect of the vortex generators is evident in the contours. The computed results compare qualitatively well with the experimental results. In both sets of contours the distortion caused by the generators is pushed toward the outside of the first bend, opposed to the pressure driven secondary flow. The total pressure values in these contours are higher than in those of Figs. 9(a) and (b) near the inside wall. This indicates that the vortex generators successfully mixed the high energy flow with the low energy flow to suppress the separation. Although the contours in Figs. 12(a) and (b) still show a very distorted flow, the difference between the maximum and the minimum values is much less here than in the duct without vortex generators. Figures 13 and 14 show the secondary flow development at the inflection plane and at the duct exit. In the experimental results at the inflection plane, the vortices due to the pressure driven secondary flow have washed out the vortices from the vortex generators except near the inside of the first bend. The contour plot indicates that in this region there may still be some interaction between the vortex generator vortices and the ones induced by the pressure difference. The computed results at the inflection point show that all of the vortices have been washed out by the pressure driven secondary flow. This is why the distorted region in the experimental results moves more toward the outside of the bend than in the computed results. At the exit of the bend both the experimental and computed results indicate less secondary flow toward the outside of the second bend than without the vortex generators. Also near the walls they indicate more flow back toward the inside of the second bend. The experimental results show a higher level of flow toward the outside of the bend in the core flow than do the computed results.

High Speed Inlet (Refs. 3 and 4)

Analysis Method. A three-dimensional supersonic viscous marching analysis was used in this study. The code solves the PNS equations for supersonic flow by a linearized block implicit scheme (Ref. 15). The code has been extensively verified at Lewis, with particular emphasis on the calculation of the glancing shock/boundary layer interaction (Ref. 16). The work has demonstrated the numerical capability to realistically model the complex three-dimensional phenomena occurring in this interaction. The work in Ref. 16 also established the importance of grid resolution in modeling this interaction.

Intake Configuration. A schematic drawing of the mixed compression intake is shown in Fig. 15. This inlet was originally designed using the method of characteristics with the surfaces corrected for boundary layer displacement effects. It is rectangular in cross section and has a pre-compression ramp and three compression ramps external to the cowl. Operation at angle of attack generates a shock wave at the leading edge of the pre-compression plate. The pre-compression and ramp shocks were designed to fall outside the cowl lip at the design Mach number of 5.0. The shock generated at the cowl lip is cancelled at the ramp shoulder and the cowl is contoured to provide further internal compression. A swept sideplate runs from the leading edge of the pre-compression plate to the leading edge of the cowl to minimize the drag generated by compressed flow spilling over the sides.

Two-Dimensional Computed Results. The PNS code was initially run two-dimensionally at a free stream Mach number of 5.0, angle of attack of 9.0° , and a Reynolds number of 2.5×10^6 . Fig. 16 shows the computed Mach number profiles at various positions. Proper cancellation of the cowl shock at the shoulder is observed in spite of the extremely large displacement correction. The figure also shows the extremely thick boundary layer that forms on the ramp surface; i.e., about 1/3 of the flow into the inlet is boundary layer. Near the inlet throat, the two boundary layers are merged. Predictions of static pressure rise and total pressure loss through the compression system agree well with method of characteristic results corrected for boundary layer effects.

Three-Dimensional Computed Results. The Mach 5.0 inlet described in a previous section was analyzed three-dimensionally using the PNS analysis program. The free stream conditions for the three-dimensional case were the same as those in the two-dimensional inlet case. The computations were performed on an 80 by 60 cross-sectional grid, which corresponds to the levels of grid resolution required for accurate modeling of glancing shock boundary layer interactions (Ref. 16). The inviscid Mach

number aft of the pre-compression shock is on the order of 4.0, which is very close to our established data base.

The results from the three-dimensional calculation are presented in Figs. 17 to 20. At the top of each figure is a schematic of the inlet, with the location of the cross-sectional plane given by a vertical line and a prescribed distance from the inlet leading edge. The bottom of the figure shows the flowfield in a cross section of the inlet; the ramp surface is at the bottom, the cowl surface at the top, and sideplates are on both sides. Because of flow symmetry, only half of the inlet was calculated. The left side of the figure shows Mach number contours, while the right side shows secondary velocity within the cross-sectional plane. The figures proceed from a location just downstream from the inlet leading edge to a location inside the cowl near the throat. On the solid surface of the ramp, cowl and sideplate, one will note the development and growth of the boundary layer by a concentration of Mach contours near these surfaces. Shock waves are noted by a concentration of Mach contours away from the solid surfaces. They can also be detected by an abrupt change in the secondary velocity vectors. In this calculation, the compression shocks and the Mach contours are parallel to the ramp and cowl surfaces.

Entering the region of the compression ramps, Fig. 17 shows the flowfield just downstream of the first ramp. The shock generated by this ramp is evident in the Mach contours; near the center of the flowfield this shock is flat while near the sideplate the shock forms a characteristic λ as it interacts with the boundary layer of the sideplate. In the secondary velocity vectors, one sees a cross flow being induced along the sideplate and feeding forward of the inviscid shock location. Near the cowl lip, the flow field appears as Fig. 18. The secondary velocity vectors also show extremely strong flow along the sideplate, while the Mach number contours show the sideplate boundary layer to be highly distorted. The boundary layer has been thickened in the vicinity of the shock waves and thinned in the corner formed by the ramp and sideplate. The secondary velocity vectors show flow being drawn along the ramp surface into this corner. The boundary layer along the ramp surface is quite thick and corresponds to the thickness predicted in the two-dimensional calculations. The strong secondary flows induced by the multiple shock interactions persist even though the shock waves have left the flow domain over the cowl. The flowfield from the inlet leading edge to the cowl lip has been shaped by the thick boundary layer that grows on the ramp and sideplate and the multiple shock interactions that occur on the sideplate due to the compression ramps. The flow is highly three-dimensional at the cowl lip with low energy boundary layer flow being swept up along the sideplate. As the flow enters the cowl, Fig. 19 shows that a shock wave is generated by the cowl lip. This shock, indicated by the horizontal lines in the Mach contours, moves down through the flow field as shown in Fig. 20. The strong secondary flow moving up the sideplate encounters the internal cowl surface and the secondary velocity vectors indicate that this flow turns through the corner formed by the cowl and sideplate. Figure 20 shows that two things happen as the secondary flow turns this corner; first, the secondary flow rolls up into a vortex, and second, the low energy flow is concentrated in the corner. The internal surface of the cowl has been shaped to further compress the flow. As the low energy flow in the corner is subjected to the adverse pressure gradient created by this turning, a large separation occurs. The last calculated cross section is shown in Fig. 20. The shock from the cowl is about to hit the ramp surface, while the large separation region exists in the corner. The secondary flow has rolled into a vortex near the sideplate, while along the ramp, flow continues into the corner.

Even though the FLARE approximation was employed, the magnitude of the separation was so severe that the analysis did not march further. The existence of a large separation in the corner of the inlet would probably trigger an inlet unstart at these conditions. Even if the inlet remained started, the existence of the vortex near the sideplate and the distortion of the sideplate boundary layer as shown in Fig. 20 would pose major problems for the propulsion system.

Experimental Observations. A subscale model of the Mach 5 inlet was tested at Lewis. Figure 21 shows oil flow results which indicate that the flow near the ramp surface is drawn in towards the sideplates. This figure shows velocity vectors on the surface of the ramp from the third ramp to the cowl. In the lower left corner of the figure the computed velocity vectors near the ramp surface are shown. The velocity vectors also indicate that flow is drawn in toward the sideplate because of the glancing sidewall boundary layer interactions. This is the first qualitative verification of the results of the Mach 5.0 inlet study.

Additional confirmation of the strong secondary flow patterns computed for the inlet may be found in Ref. 17. In Ref. 17, a two-dimensional mixed compression Mach 3.05 intake was experimentally tested. Total pressure measurements were obtained at a number of stations within the inlet. Figure 22 shows total pressure contours downstream of the normal shock which clearly indicate vortex-like flow. These measured flow contours yield further qualitative confirmation of the PNS computed results described above.

Sideplate Spillage Computations Further development of the PNS solver (Ref. 4) has yielded the capability of analyzing the flow spilled over the intake side plates. Initial results obtained are shown in Figs. 23 and 24. The static pressure distribution both upstream and downstream of the cowl are shown.

CONCLUSIONS

Computer results of the flow distortion and total pressure variation in complex intakes were reviewed. The analyses were performed using parabolized Navier-Stokes marching analyses. The first set of results were for intakes with centerline curvature and cross-sectional transitioning. It was concluded that the distortions and losses in the S-shaped duct were primarily related to the centerline curvature, whereas the transitioning cross section had little effect on flow quality and pressure loss. The second set of results reviewed were for a diffusing S-duct with subsonic entrance flow. Numerical analysis of the flow was performed both with and without vortex generators located near the entrance of the diffuser. The generators were found to be computationally effective in suppressing the flow separation that occurred previously. Although flow distortion was not eliminated, the difference between the maximum and minimum total pressure at the compressor face was significantly reduced. The computed results compared favorably with the experimental data. Further analytical refinements are needed to improve the vortex generator model in the analysis.

The final set of results presented were for a Mach 5.0 intake. Both a two-dimensional and a three-dimensional version of a supersonic PNS code were run. The two-dimensional version verified the original method of characteristics design, while the three-dimensional version revealed entirely new information relative to the nature of the flow. High amounts of distortion, strong secondary flows and flow separation were computed in the supersonic intake. These phenomena are caused by thick boundary layers which develop on the inlet surfaces and their interaction with the shock waves of the compression system. The results from these calculations indicate that the sideplates require redesigning. In addition, provisions for bleeding the sideplate and the corner may be required to improve flow quality. In that case, a compromise would be necessary between recovery, distortion, spillage drag and bleed drag. Limited experimental data provided some verification of the occurrence of secondary flows in the intake.

REFERENCES

1. Towne, C.E., and Schum, E.F., "Application of Computational Fluid Dynamics to Complex Inlet Ducts," AIAA Paper 85-1213, July 1985.
2. Kunik, W.G., "Application of a Computational Model for Vortex Generators in Subsonic Internal Flows," AIAA Paper 86-1458, June 1986.
3. Benson, T.J., "Three-Dimensional Viscous Calculation of Flow in a Mach 5.0 Hypersonic Inlet," AIAA Paper 86-1461, June 1986.
4. Kim, Y.N., Buggeln, R.C., and McDonald, H., "Numerical Analysis of Some Supersonic Viscous Flows Related to Inlet and Nozzle Systems," AIAA Paper 86-1597, June 1986.
5. Briley, W.R., and McDonald, H., "Analysis and Computation of Viscous Subsonic Primary and Secondary Flows," AIAA Paper 79-1453, July 1979.
6. Levy, R., McDonald, H., Briley, W.R., and Kreskovsky, J.P., "A Three-Dimensional Turbulent Compressible Subsonic Duct Flow Analysis for Use with Constructed Coordinate Systems," AIAA Paper 80-1398, July 1980.
7. Levy, R., Briley, W.R., and McDonald, H., "Viscous Primary/Secondary Flow Analysis for Use with Nonorthogonal Coordinate Systems," AIAA Paper 83-0556, Jan. 1983.
8. Towne, C.E., "Computation of Viscous Flow in Curved Ducts and Comparison With Experimental Data," AIAA Paper 84-0531, Jan. 1984.
9. Anderson, B.H., "Three-Dimensional Viscous Design Methodology for Advanced Technology Aircraft Supersonic Inlet Systems," AIAA Paper 84-0194, Jan. 1984.
10. Vakili, A., Wu, J.M., Hingst, W.R., and Towne, C.E., "Comparison of Experimental and Computational Compressible Flow in an S-Duct," AIAA Paper 84-0033, Jan. 1984.
11. Reyhner, T.A., and Flugge-Lotz, I., "The Interaction of a Shock Wave with a Lamina Boundary Layer," *Int. J. Non-Linear Mechanics*, vol. 3, no. 2, June 1968, pp. 173-199.
12. Levy, R., "Vortex Generator Modeling," NASA CR- Report in Preparation, 1986.
13. Vakili, A.D., Wu, J.M., Liver, P., and Bhat, M.K., "Experimental Investigation of Secondary Flow in a Diffusing S-Duct," NASA CR- Report in Preparation, 1986.
14. Vakili, A.D., Wu, J.M., Liver, P., and Bhat, M.K., "Flow Control in a Diffusing S-Duct," AIAA Paper 85-0524, Mar. 1985.
15. Buggeln, R.C., McDonald, H., Levy, R., and Kreskovsky, J.P., "Development of a Three-Dimensional Supersonic Inlet Flow Analysis," NASA CR-3218, 1980.

16. Anderson, B.H., and Benson, T.J., "Numerical Solution to the Glancing Sidewall Oblique Shock Wave/Turbulent Boundary Layer Interaction in Three Dimensions," AIAA Paper 83-0136, Jan. 1983.
17. Fisher, S.A., "Three-Dimensional Flow Effects in a Two-Dimensional Air Intake with Mixed Supersonic Compression," Seventh International Symposium on Air-Breathing Engines, AIAA, 1985, pp. 118-124.

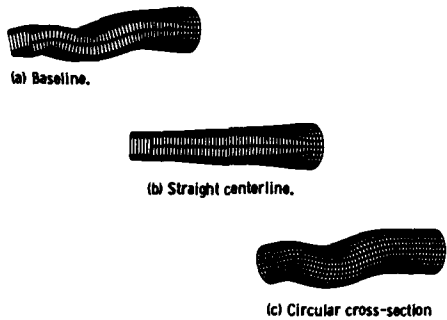


Figure 1. - Inlet configurations.

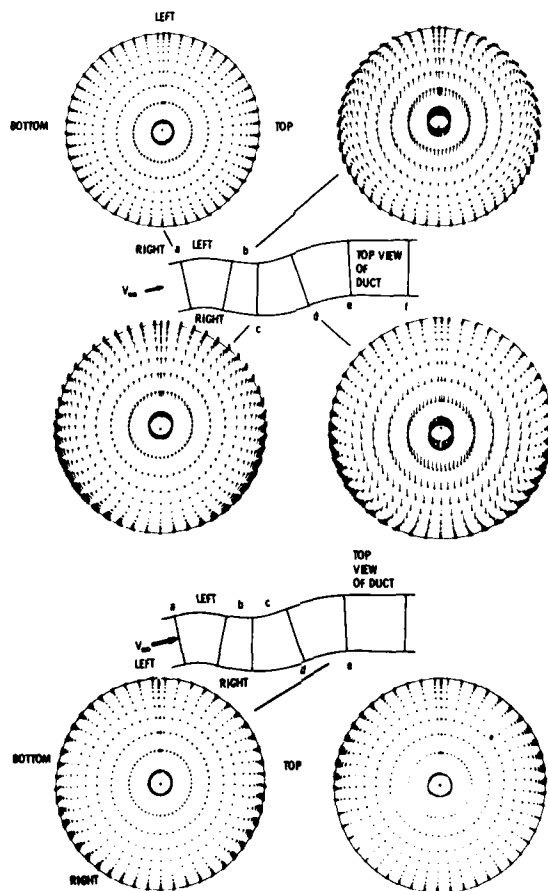


Figure 2. - Computed cross stream velocities in circular cross-section configuration, $M = 0.5$, $\delta = 0.004$, $90 \times 90 \times 105$ mesh.

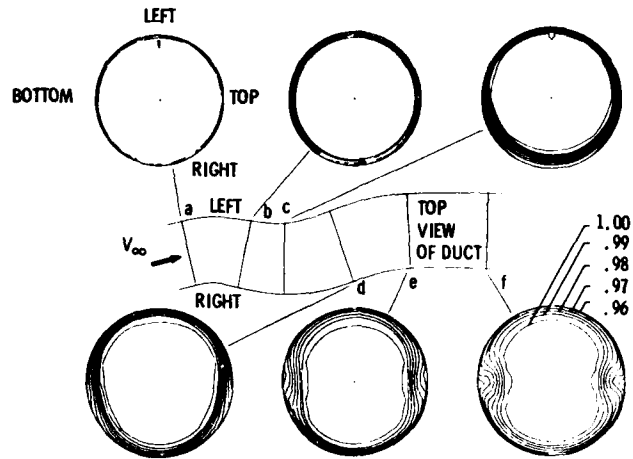


Figure 3. - Computed total pressure contours in circular cross-section configuration, $M = 0.5$, $\delta = 0.056$, $50 \times 50 \times 105$ mesh.

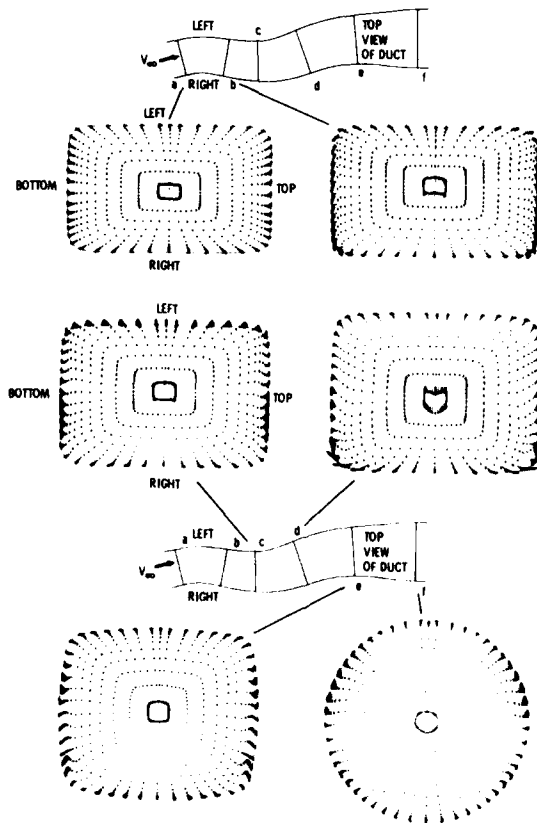


Figure 4. - Computed cross stream velocities in baseline configuration, $M = 0.5$, $\delta = 0.048$, $50 \times 50 \times 105$ mesh.

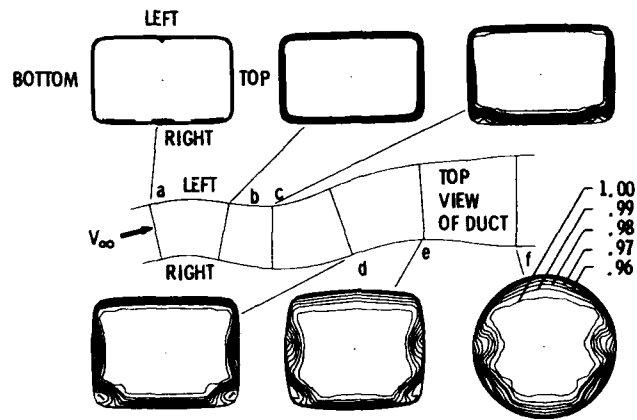


Figure 5. - Computed total pressure contours in baseline configuration, $M = 0.5$, $\delta = 0.048$, $50 \times 50 \times 105$ mesh.

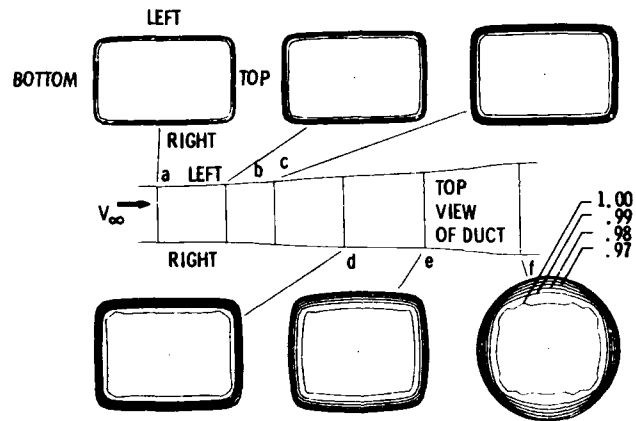


Figure 6. - Computed total pressure contours in straight centerline configuration, $M = 0.5$, $\delta = 0.048$, $50 \times 50 \times 105$ mesh.

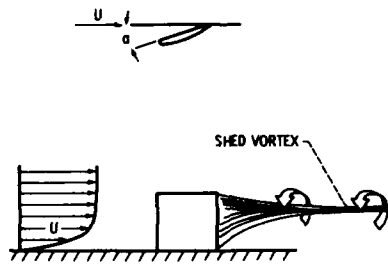


Figure 7. - A typical vortex generator.

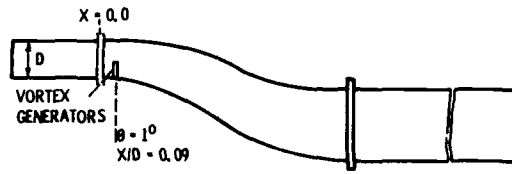
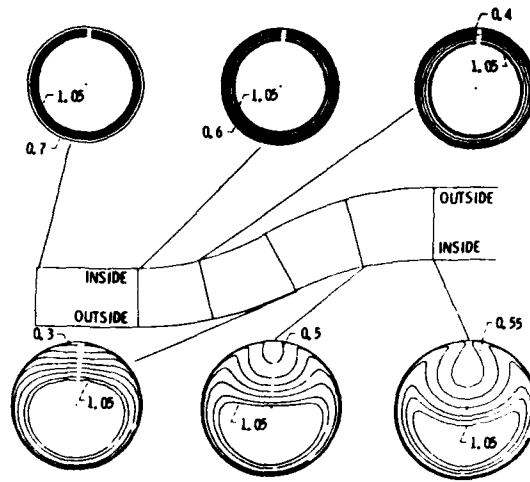
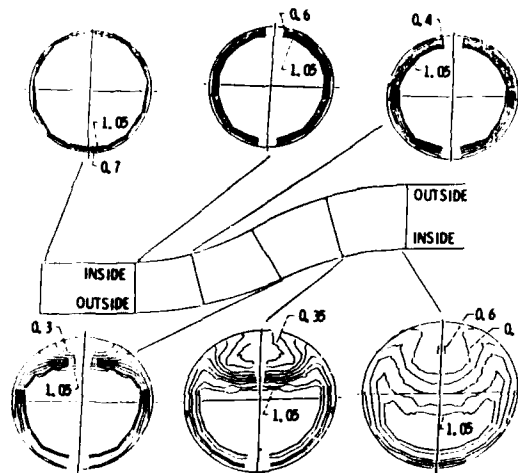


Figure 8. - Schematic of diffusing S-duct showing the axial location of the vortex generators.



(a) Computed results.



(b) Experimental results.

Figure 9. - Total pressure coefficient contours for S-duct without v.g.'s.

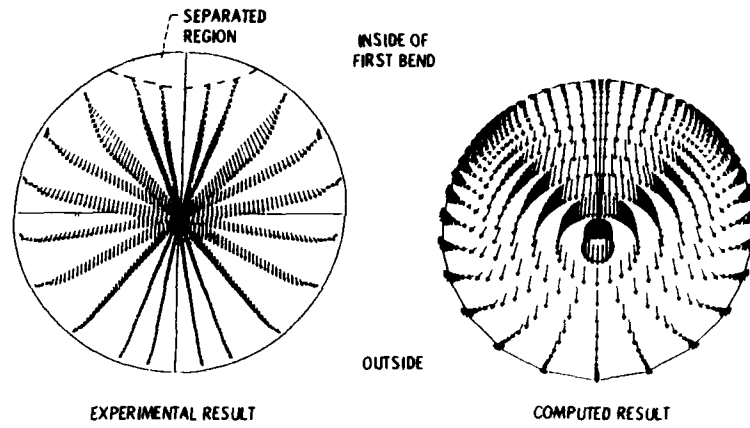


Figure 10. - Comparison of secondary flow at the inflection plane for S-duct without v.g.'s.

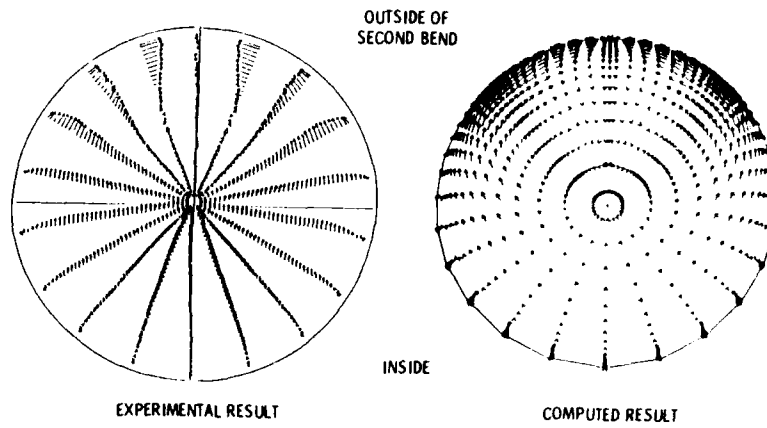
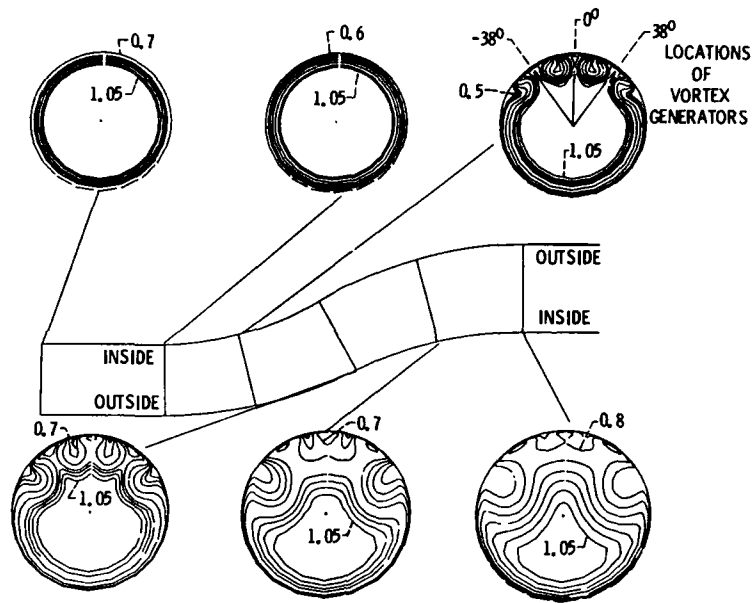
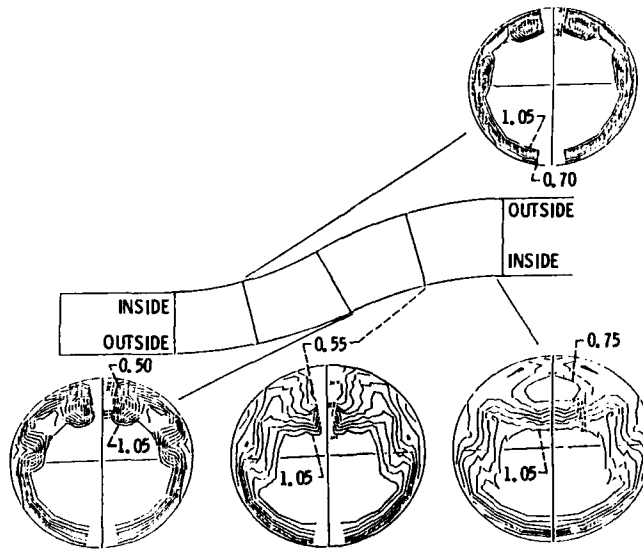


Figure 11. - Comparison of secondary flow at the exit plane for S-duct without v.g.'s.



(a) Computed results.



(b) Experimental results.

Figure 12. - Total pressure coefficient contours for S-duct with v.g.'s.

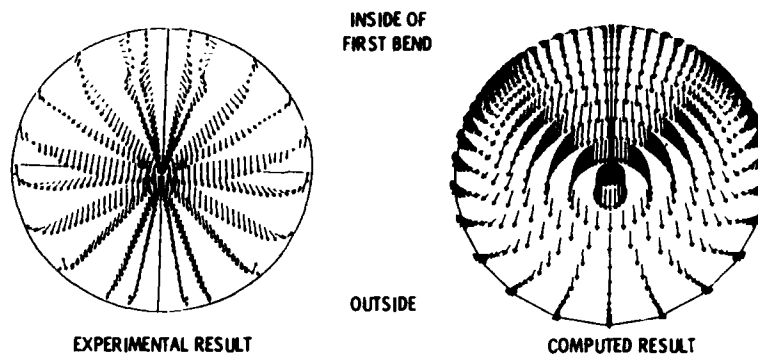


Figure 13. - Comparison of secondary flow at the inflection plane for S-duct with v.g.'s.

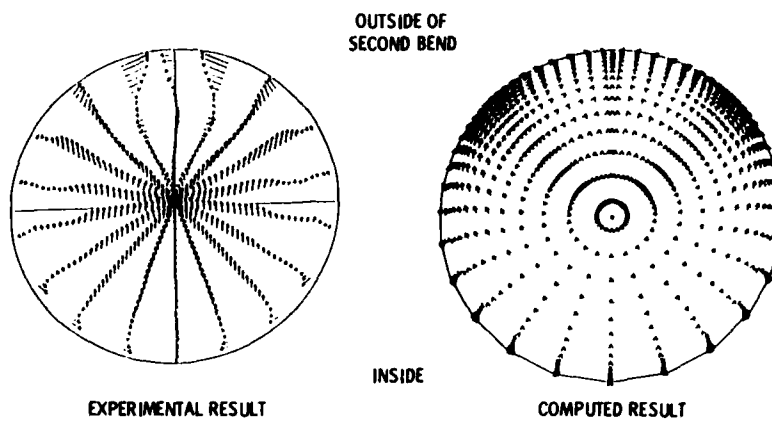


Figure 14. - Comparison of secondary flow at the exit plane for S-duct with v.g.'s.

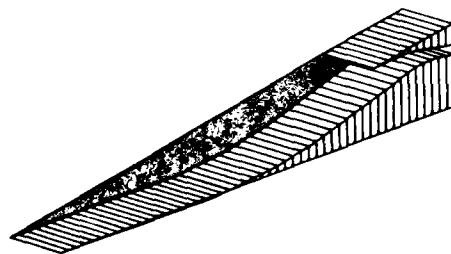


Figure 15. - Mach 5.0 Hypersonic Inlet Geometry.

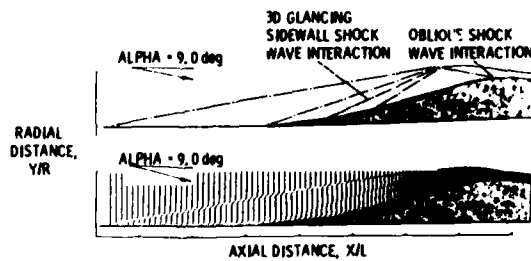
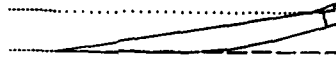


Figure 16. - Shock structure and 2D Mach number profiles.



STATION 549
 $X/HC = 0.6655E 01$

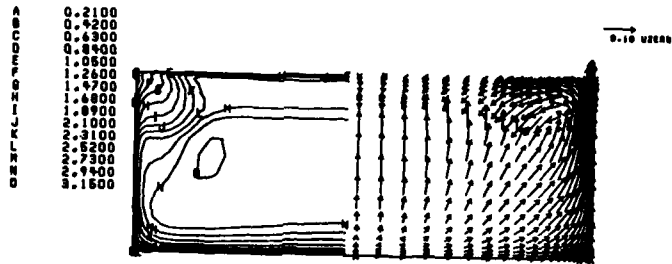
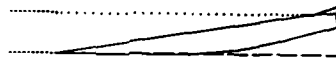


Figure 19. - Mach number contours and secondary velocity vectors aft of cowl lip.



STATION 629
 $X/HC = 0.6887E 01$

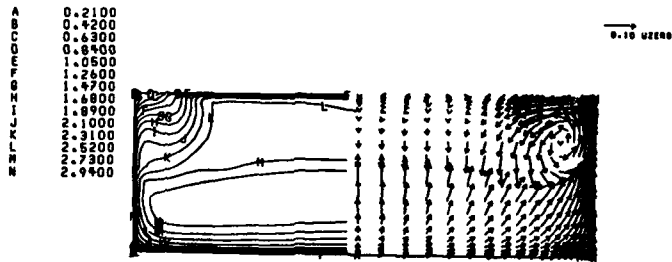


Figure 20. - Mach number contours and secondary velocity vectors at corner separation.

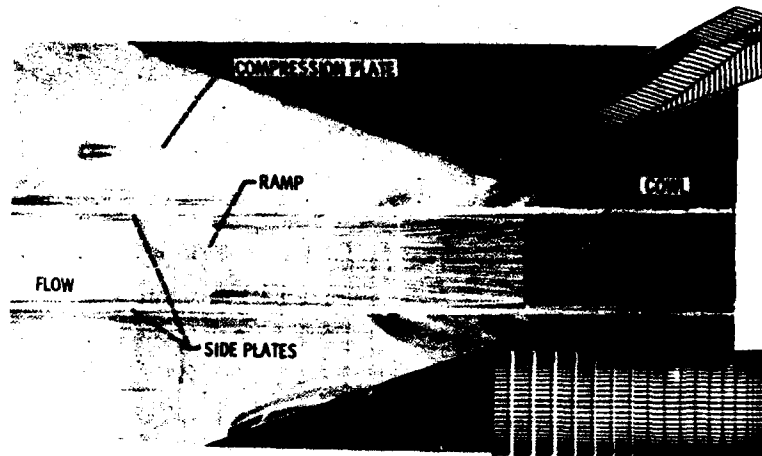


Figure 21. - Surface oil flow and calculated velocity vectors for Inlet ramp surface.

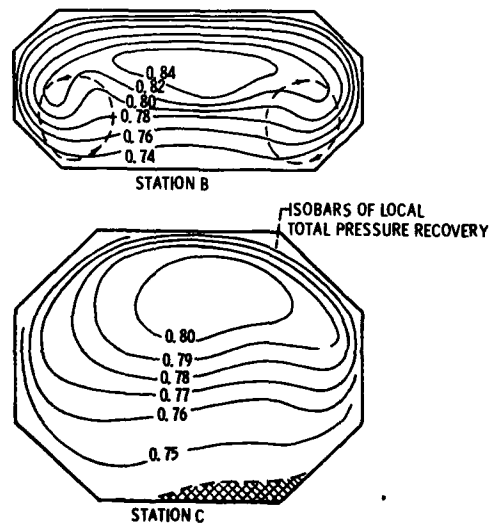


Figure 22. - Flow Distributions in Subsonic Diffuser.

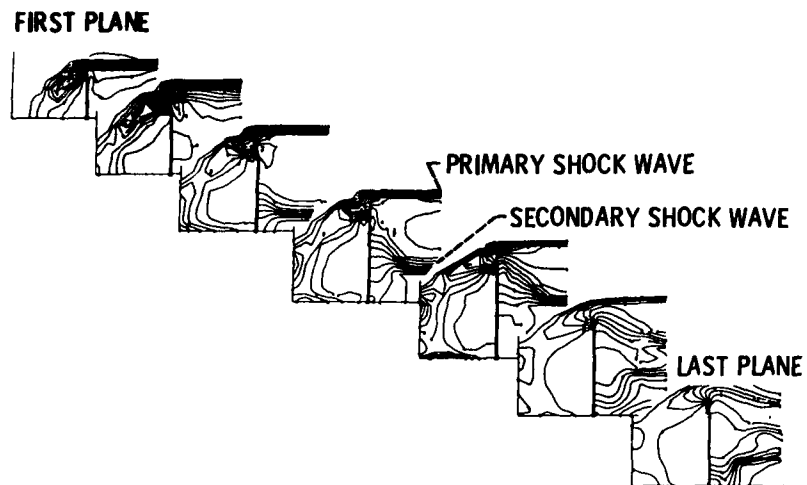


Figure 23. - Static pressure distribution upstream of the cowl entrance in planes normal to the 'Streamwise' direction. Planes from left to right proceed downstream.

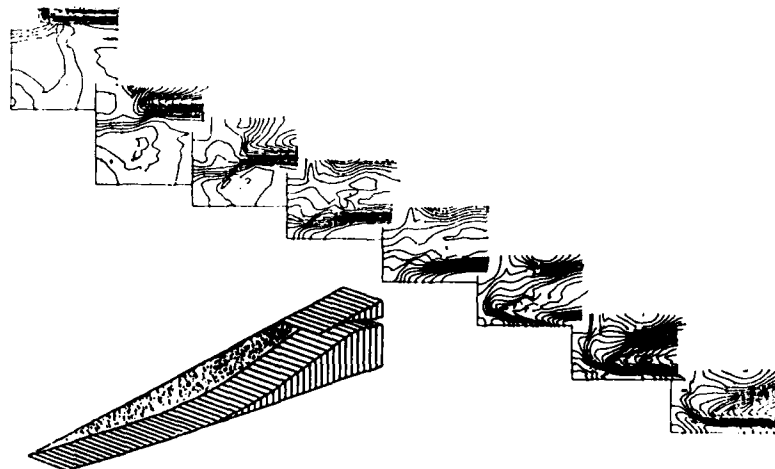


Figure 24. - Static pressure distribution downstream of the cowl entrance.

DISCUSSION

J.Fabri, Fr

Pourriez vous présenter ce papier à nouveau dans la partie "B" de cette réunion de spécialistes où de nombreux chercheurs en "ondes de choc" seront présents?

Author's Reply

I would be pleased to repeat the portion of the paper dealing with the supersonic inlet and shock structure in the second panel (Part B) of the Specialists' Conference. In addition, I will also present some results obtained for a Mach 7.4 inlet configuration.

G.Winterfeld, Ge

You showed in this S-shaped duct, which has the offset, that you had separation on the first part of the inner curvature. Would you think that this separation is caused only by the secondary flows? Could you please comment on the contribution of the side-wall boundary layer?

Author's Reply

I believe the separation is caused by the geometry, not by the secondary flows. The secondary flows interact with that separated region to give some resulting pressure distortion downstream, but it is primarily the geometric design that creates the problem, as you suggested.

A similar S-duct was tested experimentally, which had no diffusion. In that duct, the secondary flow pattern was similar to the one in the present paper, and no separation was detected.

G.Winterfeld, Ge

Have you tried to predict this separation with a normal boundary layer code?

Author's Reply

For this particular problem of the diffusing S-duct we have not tried to use a boundary layer approach. It could be used, although the PNS analysis used here does not employ as many approximations in the governing equations, and therefore should give a better prediction of the boundary layer behaviour. I do not believe that a boundary layer analysis would give a good prediction of the extent of the separated region.

D.D.Williams, UK

I would be interested to know whether you can speculate on the ability of the approach to model an S-bend subsonic diffuser with offset and a heavy one-sided separation at inlet — as this appears to be the source of bulk swirl affecting engine stability — discussed this morning.

Author's Reply

If the separation is "big", the parabolised analysis would not be able to march through the region. As far as starting the calculation with a separated initial profile, the analysis would not be able to handle that either. The type of problem would need a full Navier-Stokes analysis and the solution would need to be started upstream of the separated region.

A possibility exists, however, that if one were to model around the separated region of the inlet, ie treat the separation as a zone of zero flow, then the PNS analysis with proper inlet conditions might be able to compute the flow field. Offset bends, of themselves, do not present computational difficulties.

J.Hourmouziadis, Ge

The parabolised model used in your investigation cannot be applied to cases with reverse flow. How did you cope with this problem in the high supersonic intake example in the vicinity of the shock/boundary layer interaction of the side wall?

Author's Reply

The PNS model used to calculate the high-speed inlet incorporates a FLARE model in the vicinity of flow separation. This model was originally developed by Reyhner and Flugg-Lotz, in 1968 Int Jour of Non-Linear Mechanics. The model assumes that the recirculation is small compared to the dimensions of the inlet. Within the recirculation, the negative, streamwise convective velocity is overwritten by a small positive value and the solution is marched as usual. The solution may continue to produce negative streamwise velocities, which require the FLARE approximation to be used at the next marching station. When compared with experimental results, we have found the FLARE model to accurately reproduce the displacement effects of separation on the external flow, but it does not properly model the details of the recirculation region itself, particularly the upstream influence. For small separation regions within the inlet, this model is accurate; for details within a large separated region, it is inadequate.

Ph.Ramette, Fr

For a supersonic intake at a free-stream Mach number of 5.0, what is the average Mach number at the entrance of the engine? Have you done similar calculations at higher Mach number, and what is the evolution of the Mach number at the entrance of the engine (which is then a scramjet)?

Author's Reply

For the Mach 5.0 inlet, the Mach number at the end of the calculation was in the order of 1.3. The calculation procedure will only handle the supersonic/hypersonic part of the inlet system. In the actual inlet, the flow just downstream of the throat would encounter a normal shock and then pass on through the diffuser to the ramjet burner. The Mach number at the entrance to the burner would probably be on the order of 0.6.

The PNS code which has been used to calculate the Mach 5.0 inlet is now being modified and tested for higher Mach numbers. At Mach numbers greater than 5.0, the real gas effects associated with heating the flow become quite important. Models to account for real gas chemistry are being incorporated in the PNS inlet code. The code has been used to calculate flow in a Mach 7.4 inlet and these results will soon be presented at the AIAA Reno conference.

Ph.Ramette, Fr

Have you made comparisons between your Navier-Stokes calculations and other models like LES (Large Eddy Simulation)?

Do you think that LES models, which are used mainly for the combustor, could be used for inlet flow calculation?

Author's Reply

No comparison has been made between results of the Lewis PNS calculations and Large Eddy Simulation (LES) calculations. The verification of the codes has concentrated on comparison with experimental data obtained from benchmark experiments. A thorough description of the verification process and the associated experiments was given by Anderson at the AIAA 22nd Aerospace Sciences Meeting as NASA TM 83558. LES work at NASA Lewis chiefly concerns the combustor problem. Because of the long run times associated with LES calculations, this method would probably not be suitable for full inlet calculations. The resolution of the multiple phenomena present in the inlet (shock waves, boundary layers, shock/boundary layer interaction, boundary separation, recirculation, reattachment, three-dimensional effects) demands large, high-speed calculations. The optimum solution to this resolution problem has been the use of PNS codes, given the current computing speed and size.

R.LeBoeuf, Fr

What is the lowest Mach number you could handle with your code?

Do you have any special treatment for the points located very near to the wall (that is, to say in a subsonic zone)?

Author's Reply

In regard to the near-wall treatment, the supersonic PNS code does have special logic for solution of the flow equations in the subsonic part of the boundary layer. This region is assumed to be small in a supersonic inlet, so within the calculations, a boundary layer type model is employed. The pressure is imposed from the edge of the subsonic part of the boundary layer, and the flow is assumed to be parallel to the nearest wall. In regard to the lowest Mach number calculated, the supersonic PNS code has been run in a nozzle mode where the calculation begins near the throat of the nozzle. A free-stream Mach number of 1.05 worked the best for this case; smaller free-stream Mach numbers sometimes encountered small wavelets from the wall boundary which produced embedded subsonic packets and the solution would become unstable.

The main part of the flow field must remain supersonic, without embedded subsonic regions, for code stability.

H.Kordulla, Ge

Comment: Having 100 points in the "wall-normal" direction should result in more than 1 point within sublayer ($t^+ < 5-10$)?

Question: Could you comment further on the method used? (I understand that the NS equations are used in steady-state form in a space-marching manner. Do you experience any problems with the choice of the size in the marching step? How do you treat the gradient term in the marching direction in super- and hypersonic flow?)

Author's Reply

For detailed inlet calculations, one must resolve boundary layers on both top and bottom surfaces and resolve the shock waves which move from one surface to another. It has been our experience, when comparing computational results with experiment, that at least 25 points are required in each boundary layer to properly resolve the turbulent boundary layer profile, with at least one point at $y^+ = 10$. The remaining 50 mesh points are used to resolve the shock wave.

The PNS method used for the hypersonic flow calculation solves the complete Navier-Stokes equation in steady state, neglecting only the streamwise viscous terms. The flow variables are linearised in the marching (streamwise) direction and a Douglas-Gunn ADI scheme is used to march the solution in a single pass from free stream through the inlet. The

pressure is evaluated in terms of the density, which is a solution variable: therefore the pressure gradient term is treated exactly like a linearised density gradient and becomes part of the solution. We have not encountered any limitation on the minimum step size, except that the smaller the step size, the larger and more expensive the calculation. There are practical limits on the maximum step size so that one does not violate regions of influence in supersonic flows.



AD-P005 466

7-1

CALCULATIONS OF INLET DISTORTION INDUCED COMPRESSOR FLOWFIELD
INSTABILITY

by

T.P.Hynes
Whittle Laboratory
Cambridge University
Madingley Road
Cambridge CB3 0EL, UK

and

R.Chue, E.M.Greitzer and C.S.Tan
Dept of Aeronautics and Astronautics
M.I.T.
Cambridge, Mass 02139, USA

SUMMARY

Calculations are presented predicting the onset of flow instability for a multistage low speed axial compressor operating in circumferentially distorted inlet flow. The most important feature of the model used is that it attempts to properly account for the fluid dynamic interaction between the spoiled and unspoiled sectors of the compressor. The calculations show that there is an approximate stability criterion, the annulus averaged slope of the compressor pressure rise characteristic equal to zero, that is valid whenever the dynamics of the compressor distorted flowfield can be considered independent of the compressor environment. This approximate criterion is used to investigate the relationship between the present model and the "parallel compressor" model. Further calculations are performed to investigate cases of interest when the dynamics of the compressor flowfield are coupled to the environment. Resonant cases and cases when the distortion is unsteady are studied. In particular, it is shown that rotating distortions which propagate in the rotor direction can have a greater effect on stability margin than stationary or counter-rotational ones. Finally, it is shown that the general predictions of the model are insensitive to the details of the unsteady bladerow dynamics.

1. INTRODUCTION

The adverse effects on gas turbine engine operation due to inlet distortion are well known and need no detailed introduction. Because of its consequences, the distortion problem has received considerable attention, and substantial experimental and theoretical work has been done on the topic.

The most important aspect of the problem is the assessment of the effect on stability that a given inlet distortion produces. In a previous paper [1] a method was presented for computing this loss in stability, by examining the conditions under which small disturbances, which propagate round the annulus, will grow. The analysis, which appears to be the first to treat this problem from the point of view of a rigorous fluid dynamic instability calculation, showed trends in compressor behaviour that were in good agreement with existing experimental observations.

The crucial feature of the method is the ability to properly account for the fluid dynamic interaction between the spoiled and unspoiled sectors of the compressor. As will be discussed below, it is this, rather than any "critical residence time" (in the distorted region) that is the key issue in determining the stability of the distorted flow. To model this interaction small perturbations are taken about a (time) mean flow that is circumferentially strongly non-uniform. The "background" flow is thus a nonlinear disturbance (distortion), and the calculation of this flow is therefore an important part of the overall computational procedure [1].

In [1] the emphasis was in describing the method and presenting some initial computations to show the type of results that could be obtained. The scope of that paper was such that there was only brief discussion of the structure of the disturbances, the question of the existence of a simple overall criterion for instability, the relation between the computational results and previous attempts to deal with this problem (such as the "parallel compressor" method), and the basic physical mechanisms that are associated with the observed behaviour. This paper covers these aspects as well as discussing two other facets of the problem. The first is the behaviour of a compressor subjected to a rotating inlet distortion, such as might be imposed by a low pressure compressor feeding a rotating stall into a high pressure compressor. The second is the examination of the impact of some of the different loss models that have been proposed for this problem on the conclusions of the method.

2. BRIEF DESCRIPTION OF THE MODEL

This topic was described in detail in [1] so that only a brief description will be presented here. The most important element is how the compressor performance is calculated. We assume that the compressor is low speed, with IGV's, and of sufficiently high hub-to-tip ratio that a two-dimensional treatment is valid. The pressure rise across any bladerow is taken to be made up of that achieved in steady uniform flow at the current entry conditions plus that necessary to balance the acceleration of the fluid within the bladerow [2]. When the contributions from each bladerow are added, this implies a performance for the compressor as a whole of, for each value of θ ,

$$\frac{P_2 - P_{t1}}{\rho U^2} = \psi(\phi) - \lambda \frac{\partial \phi}{\partial \theta} - \frac{\mu r}{U} \frac{\partial \phi}{\partial t} \quad (1)$$

where λ and μ are determined by the inertia of the fluid in the rotors and in all bladerows respectively. ϕ is the local value of axial flow coefficient ($= C_x/U$) and ψ is the clean flow inlet total to exit static pressure rise characteristic. ψ is assumed to be a smooth continuous function of flow coefficient and is the performance that would be obtained if the flow through the compressor were steady and axisymmetric. Parts of this performance curve cannot be realised unless some means of stabilising the compressor flow, such as a second compressor close up behind the first, is employed. Unless otherwise specified, the particular form used for ψ in the calculations presented is that shown in Figure 1. This is taken from [3] and is taken from a low speed three stage compressor. The problem of assessing the effect of inlet distortion on the stability of the flow through the compressor is inherently a nonlinear one. We maintain that it is the nonlinearity of the compressor performance, ψ , as a function of flow coefficient that is by far the most important one in the problem. It is treated fully nonlinearly in our calculations.

Before a solution of Eq. (1) can be attempted some way of relating the pressure terms to ϕ must be specified. This involves a calculation of the flowfields upstream and downstream of the compressor and is in itself a nonlinear problem. We regard this nonlinearity as being of lesser importance. The equations used to specify the upstream and downstream flowfield are taken to be those describing linear perturbations about a uniform flow. This way of treating the flowfield has been adopted by many authors, eg [4], [5], to study inlet distortion. Further discussion of this approach and some justification for it can be found in [1].

The compression system studied is shown in Figure 2 as a compressor pumping to a downstream plenum (situated at least a couple of radii downstream) which exhausts through an ideal throttle. Density changes in the plenum are related to pressure changes through an isentropic relationship and the inertia of the fluid in the throttle is neglected. This again is a conventional approach to modelling plenum flows. It was used extensively in, for example, [6] and [7] where it is shown that the non-dimensional parameters which characterize the compressor and system dynamic behaviour are

$$\eta = \frac{L_{TOT}}{r} = \frac{\text{effective compressor length}}{\text{mean radius}}$$

and

$$B = \frac{U}{2a} \sqrt{\frac{V_{\text{plenum}}}{A L_{TOT}}}$$

To complete the formulation of the problem some way of specifying the inlet distortion must be added. Because the flow through the compressor is nonlinear and often unsteady it will influence that through any practical distortion generator. This is a complication of detail rather than of principle that we do not wish to address here. We will assume that the total pressure P_t is specified as a function of θ (and sometimes also t) at a plane upstream of the asymmetric static pressure field ahead of the compressor.

3. STABILITY ASSESSMENT

Once the inlet distortion is specified a solution to Eq (1) can be found. Under the assumptions discussed in the previous section, Eq (1) and those for the various flowfields, become a coupled set of ordinary, nonlinear differential equations. If the distortion is steady, then a steady solution is demanded. Another case discussed later is that of a rotating distortion and in this case a solution which rotates at the prescribed frequency is sought. There are various ways of accomplishing this solution, we found that a Fourier Collocation method [8], which exploits the circumferential periodicity of the flow, to be a particularly suitable method. The important points are that a solution can be obtained and that it can be obtained whether or not such a flow would be stable in practice. For the case of steady distortion Eq (1) reduces to, for this "background" flow,

$$\frac{P_2 - P_{t1}}{\rho U^2} = \psi(\phi) - \lambda \frac{d\phi}{d\theta} \quad (2)$$

The linear treatment of the upstream and downstream flowfields means (a) that P_{11} is purely a function of θ and equal to the specified distorted value and (b) that p_2 is circumferentially uniform taking a value determined by the throttle setting.

The stability issue is decided by a separate calculation. To the "background" flow is added a small, unsteady general perturbation. If any such perturbation grows with time then the flow through the compressor is adjudged unstable. It is only if all possible solutions decay away with time that stability is assured. If perturbation quantities are denoted by $\delta(\)$, then Eq (1) implies

$$\frac{\delta p_2 - \delta P_{11}}{\rho U^2} = \frac{d\psi}{d\phi} \delta\phi - \lambda \frac{\partial \delta\phi}{\partial \theta} - \frac{i\mu}{U} \frac{\partial \delta\phi}{\partial t} \quad (3)$$

In general $d\psi/d\phi$ is a strong function of θ and the separate solutions of this equation differ radically from the comparable ones (proportional to $\exp(i\omega t)$) obtained in stability analyses of clean (undistorted) flow. This small perturbation approach is a standard technique in stability theory and represents in effect an eigenmode and eigenvalue problem. In physical terms, the unsteady perturbations to the flow may be viewed as small stall cells (NOT fully developed) when they propagate around the annulus and as small system transients when they are predominantly one dimensional in character.

4. COMMENTS ON A GENERAL STABILITY CRITERION FOR DISTORTED FLOW

In [1] it was suggested that the point of instability, for a compressor in a steady, circumferentially distorted flow, would occur when the area averaged value of the compressor characteristic slope was zero,

$$\frac{1}{2\pi} \int_0^{2\pi} \frac{d\psi}{d\phi} d\theta = 0 \quad (4)$$

where the integrand is evaluated using the solution for the background steady distorted flow, as given by Eq (2). This statement was based upon the results of applying the perturbation stability analysis to a wide variety of different distortion/compression system combinations. Quantities that were varied included; the compressor characteristic; the shape, extent and amplitude of the distortion; the system dynamics parameters B and η ; and the bladerow inertia parameters λ and μ . In all, over 250 cases were studied and in about 90% Eq (4) was found to hold at the instability onset operating point with surprising accuracy.

An heuristic argument for the validity of Eq (4) can be based upon a simplified treatment of Eq (3). If for the moment the pressure terms on the left hand side of the equation are omitted, Eq (3) becomes

$$\frac{i\mu}{U} \frac{\partial \delta\phi}{\partial t} + \lambda \frac{\partial \delta\phi}{\partial \theta} - \frac{d\psi}{d\phi} \delta\phi = 0 \quad (5)$$

Eq (5) has as general solution the sum of terms of the form

$$\delta\phi = f(\theta) e^{i\omega t}$$

where

$$\frac{df}{d\theta} + \frac{1}{\lambda} \left[i\mu \frac{\omega}{U} - \frac{d\psi}{d\phi} \right] f = 0$$

The solution for $f(\theta)$ is given by

$$f(\theta) = \exp \left[\frac{1}{\lambda} \int_0^\theta \frac{d\psi}{d\phi} d\theta' - \frac{i\mu \omega}{\lambda U} \theta \right]$$

Since f must be periodic as a function of θ , the argument of the exponential must take the value $2\pi iN$ for some integer N . This condition determines the eigenvalue ω , and means that

$$\frac{\omega}{U} = \frac{N\lambda}{\mu} - \frac{i}{\mu} \int_0^{2\pi} \frac{d\psi}{d\phi} d\theta \quad (6)$$

When the imaginary part of ω is less than zero the solutions to equation (5) will grow in time and the system is unstable. At the neutral stability operating point ω must be purely real, implying Eq (4). At this point solutions to Eq (5) can then be written

$$\delta\phi = \exp \left[\frac{1}{\lambda} \int_0^\theta \frac{d\theta}{d\phi} d\theta' + iN \left(\theta - \frac{\lambda U t}{\mu r} \right) \right] \quad (7)$$

This form is that of a wave travelling around the annulus with amplitude growing exponentially in regions where $d\psi/d\phi$ is positive and decaying in regions where $d\psi/d\phi$ is negative. In this way a balance is achieved between the stable and unstable sectors of the annulus. It should be stressed that $d\psi/d\phi$ is a strong function of θ , as shown in Figure (3). This represents a background flow calculated for a 120° sector "square wave" distortion at the neutral stability point (as calculated using the full perturbation analysis). It is also worth noting that the axial velocity variation is in quadrature with the imposed total pressure distortion.

Returning to Eq (3) one can examine what affect the inclusion of the pressure terms would have on the above heuristic argument. If solutions to Eq (3) do not have a strong $n = 0$ component then the unsteady pressures associated with them will decay away exponentially upstream and downstream of the compressor. They simply balance local fluid accelerations and so tend to be in quadrature with the axial velocity perturbations, $\delta\phi$. It is not hard to see nor difficult to prove that their inclusion does little to alter the heuristic solution (7) other than to modify the speed at which the wave travels around the annulus. Their inclusion certainly does not contribute to growth or decay of a perturbation over a cycle, leaving our argument for Eq (4) as a stability criterion intact.

The above provides a plausibility argument for the use of the integrated mean slope (IMS) equal to zero as a stability criterion, but it is to be noted that it is the large body of more rigorous computations which underpins our belief in its generality. In addition a number of similarities between the calculated perturbations and the heuristic solutions are evident. The regions of the annulus where the calculated perturbation amplitude grows and where it decays correlates well with the sign of $d\psi/d\phi$. All travelling wave type of disturbances appeared to become unstable together (as is the case in Eq (6) where no preference for N is apparent). Finally those 10% of cases where $IMS = 0$ was found not to apply were precisely those cases where the validity of the heuristic argument might be questioned. These cases form the substance of the next section.

5. "RESONANCE" (FREQUENCY COINCIDENCE)

The results of one of the sets of calculations for which the IMS criterion appeared not to be valid is shown in Figure 4. This shows the throttle setting at instability as a function of B for a "square wave" 120° sector distortion. There is a ten percent drop in the value of throttle setting at instability, corresponding to roughly a five per cent increase in mass flow, when compared with the IMS prediction. In order to understand this effect it is necessary to examine in more detail the structure of the unsteady perturbations at the onset of instability. The general form for a perturbation, or mode, is

$$\delta\phi = \sum_k a_k e^{ik\theta + i\omega t} \quad (8)$$

with the value of ω being determined from the stability analysis. Figure 5 gives the Fourier components of the axial velocity perturbation for the modes which have as their strongest component a single lobed and a two lobed propagating axial velocity disturbance. The nomenclature to be followed is to call the former, the first mode, and the other the second mode. The mode which has its zeroth Fourier component largest is similarly referred to as the zeroth order mode. One can (loosely) view the zeroth order mode as a surge type disturbance and the other modes as different order propagating stall type disturbances.

Several points can be seen from the harmonic analysis. First the coupling between different components is strongest for the near neighbours. This is due to the fact that the imposed distortion has as its strongest component the first harmonic. Distortions of practical interest in the present context, ie those which have a significant effect on the stall point, will also tend to have this same first harmonic dominance. There is an extra consideration, however, for the zero harmonic in that it represents variations in the annulus averaged mass flow through the compressor. These variations persist throughout the rest of the system and as a result their amplitude is strongly affected by the system properties. One might expect that if, in addition, the mass flow variations were at a frequency close to the natural frequency of the system that amplification of the zero harmonic component would take place.

The frequency of the first mode (a rotating stall-like disturbance) and that of the zeroth mode (a surge-like disturbance) are shown in Figure 6 as a function of the system B parameter. A change in B is a change in the system (ie plenum volume, overall compressor length) parameters. The computations show that the velocity of the propagating type of modal disturbances essentially scales with rotor speed and that it is not much affected. The frequency of the surge-like type of disturbance on the other hand is a strong function of B . At $B =$

0.34, for this particular system, the two frequencies coincide. In the neighbourhood of frequency coincidence the coupling between the zeroth and first Fourier components becomes stronger. This can be seen in Figure 7 which shows a plot of the zeroth and first harmonic components of the most unstable mode (the first mode, propagating type).

The most important point, from an applications point of view, is that this strengthening of the coupling between the zero and first harmonics is accompanied by a shift of the instability onset point to a higher flow than predicted by using the IMS criterion. In Figure 8 the throttle setting at instability onset point is shown as a function of the ratio of surge to rotating stall frequencies. Also shown in this figure is a similar effect to that produced by varying B obtained by keeping B constant and varying the other parameter which determines the system natural frequency, η .

6. APPLICATIONS OF THE INTEGRATED MEAN SLOPE CRITERION AND CONNECTION WITH PARALLEL COMPRESSOR THEORY

The $IMS = 0$ criterion is, when valid, a very useful result, since one can then compute the instability point in a simple manner. To explore the importance of parameters such as λ we will, in this section, deal with a simple case. It will be assumed that the compressor characteristic takes a particularly convenient form - that of a parabola

$$\psi = \psi_m - a^2 (\phi - \phi_m)^2$$

The stability criterion $IMS = 0$ reduces to

$$0 = \int \frac{d\psi}{d\phi} d\theta = \int -2a^2 (\phi - \phi_m) d\theta$$

that is

$$\bar{\phi} = \phi_m \quad (9)$$

Further, the inlet distortion will be of "square wave" type, as shown in Figure 9. The equation that determines the distribution of ϕ around the annulus Eq (1) becomes

$$\lambda \frac{d\phi}{d\theta} = \psi_m - R_L - a^2 (\phi - \phi_m)^2 \quad (10)$$

where R_L is the pressure rise in the θ^- (distorted) sector of the annulus, while in the rest of the annulus

$$\lambda \frac{d\phi}{d\theta} = \psi_m - R_L + \frac{\Delta P_t}{\rho U^2} - a^2 (\phi - \phi_m)^2 \quad (11)$$

At neutral stability, when equation (9) holds, ϕ must have the form shown in Figure 9. Examination of the sign of $d\phi/d\theta$ in the distorted sector implies from equation (10) that $R_L > \psi_m$.

It is a simple matter to solve equations (10) and (11) to obtain ϕ as a function of θ and to integrate the forms found to obtain $\bar{\phi}$. One obtains

$$\phi = \phi_m - \frac{(R_L - \psi_m)^2}{a} \tan \left[\frac{a(R_L - \psi_m)^2}{\lambda} \left(\theta - \frac{\theta^-}{2} \right) \right] \quad \theta < \theta^-$$

and

$$\phi = \phi_m - \frac{\left(\psi_m + \frac{\Delta P_t}{\rho U^2} - R_L \right)^2}{a} \tanh \left[\frac{a \left(\psi_m + \frac{\Delta P_t}{\rho U^2} - R_L \right)^2}{\lambda} (\pi - \theta + \theta^-) \right] \quad \theta > \theta^- \quad (12)$$

The pressure rise, R_L , at neutral stability is determined by the $IMS = 0$ conditions that $\phi = \phi_m$.

It can be seen from equation (12) that if ϕ is to remain finite in the distorted sector then $\frac{a(R_L - \psi_m)^{1/2}}{\lambda} \frac{\theta}{2}$ must not exceed $\pi/2$. When this condition is added to that obtained already, that $R_L > \psi_m$, we obtain,

$$\psi_m < R_L < \psi_m + \frac{\pi^2 \lambda^2}{a^2 \theta^2}$$

It is immediately obvious that as $\lambda \rightarrow 0$, $R_L \rightarrow \psi_m$ or "Instability onset is when the pressure rise in the θ sector reaches the clean flow instability onset point": the criterion applied in early versions of the parallel compressor model.

Examination of equation (12) indicates that λ only occurs in the combination λ/a . Thus, when characteristics have high curvature near their peak pressure rise, λ becomes less important and the predictions of this model approach those of the parallel compressor model. The loss of stability margin, defined in terms of pressure rise at constant speed, is shown in Figure 10 for an example case. It appears that the two compressors in parallel estimate is always pessimistic.

The corresponding axial velocity profiles at the neutral stability case are shown for a 180° square wave in Figure 11. The $IMS = 0$ criterion implies that comparable amounts of the annulus must be at negative $d\psi/d\phi$ ($\phi > \phi_m$) and a stable condition as are at positive $d\psi/d\phi$ ($\phi < \phi_m$) and an unstable condition. The most interesting aspect of Figure 11 is the manner in which the value λ/a dominates the way this balance is achieved. The (locally) least stable part of the annulus is not in phase with the spoiled sector, and indeed, as $\lambda/a \rightarrow 0$ is wholly in the unspoiled sector. The $\lambda/a \rightarrow 0$ limit results, of course, in the whole of the compressor annulus operating on the undistorted characteristic. Figure 12 emphasizes the differences in high (stable) flow cases and the neutral stability case.

7. ROTATING INLET DISTORTIONS

There has recently been interest in distortions that are not stationary but propagate (rotate) at some fraction of rotor speed. A practical situation in which this occurs is a high pressure compressor in a two (or three) spool engine subjected to the distortion created by a rotating stall in the low pressure compressor. Rotating distortions can be regarded as one out of the general class of dynamic distortions, with which the present analysis is capable of dealing.

The detailed experimental evidence is somewhat sparse, but one of the striking results that has been seen with rotating distortions is the strong decrease in stability if the rotation speed becomes close to the stall cell propagation speed. This was observed in [9] where an analogy with resonant behaviour of a simple system was drawn. The experimental results of [9] are shown in Figure 13 where the increase in the value of stall flow coefficient when the propagation speed of the distortion is close to the natural stall propagation speed can be clearly seen.

To examine this, calculations have been carried out with inlet distortions rotating at various fractions of rotor speed, f , from $f = -.6$ (against rotor rotation) to $f = .6$ (with rotor rotation). The background flow upstream and downstream of the compressor is taken to be steady in a frame that rotates at the distortion frequency. The equation expressing the compressor pressure rise, Eq (1), is then

$$\frac{P_2 - P_{11}}{\rho U^2} = \psi(\phi) - (\lambda - \mu f) \frac{d\phi}{d\theta} \quad (13)$$

At first sight this equation appears identical to Eq (2), the corresponding equation for steady distortion. There are, however, two crucial differences. Because the flow ahead of the compressor is unsteady P_{11} is no longer simply the upstream distorted value. It is strongly affected by, and must emerge from, a calculation of, the compressor entry flowfield. Secondly, the flow downstream of the compressor is unsteady and p_2 must reflect this fact.

The solutions for the background flow as given by Eq (13) are shown in Figure (14) for a square wave distortion of extent 120° for the range of distortion rotation rates studied. When $f = -.6$ the coefficient of $d\phi/d\theta$ in Eq (13) is more than double the steady ($f = 0$) value. This effective increase of the rotor inertia parameter, λ , is mirrored in the form obtained for ϕ , which shows relatively small variations about its mean value. When $f = .6$, this coefficient has opposite sign to the steady value. At least as far as the right hand side

of Eq (13) is concerned, this is equivalent to changing the sign of $d\phi/d\theta$. The form of the ϕ curve is thus almost a mirror image of the steady ($f = 0$) value.

Too much attention should not be focused on the sign of $\lambda - \mu f$, since the pressure terms in Eq (13) are also important, but it does imply that somewhere between $f = 0$ and $f = .6$ (for this compressor) the axial velocity profile must undergo a radical transition. The nature of this transition is seen in Figure 15 which shows the velocity profiles for $f = 0.1, 0.2,$ and 0.3 . The last one is very close to the stall cell speed. At this condition the velocity profile has a large amplitude and does not look unlike a stall cell. What appears to be occurring is that one is "forcing" the system at frequencies that are getting nearer and nearer to its resonant frequency, ie the frequency of stall cell propagation. Thus the response is expected to be larger although, again, it should be emphasized that the system we are dealing with is strongly nonlinear and one cannot push simple analogies too far.

The speed of the distortion has a marked effect on the overall distorted flow compressor characteristic as well as on the stall point, and this is shown in Figure 15. As the propagation speed is increased from zero there is a drop in the compressor performance (due to the increase in axial velocity non-uniformity) and a shift in the stall point. In particular for $f = 0.3$ there is only a small regime in which the flow is stable.

In common with the case of steady distortion, it appears from Figure 14 that the least stable parts of the annulus are to be found outside the spoiled sector. It seems that any attempt to investigate what determines the stall point must model the fluid dynamic coupling of the spoiled and unspoiled sectors. It is difficult to see, for example, how one might do this with an approach based simply on total pressure patterns and any type of "critical residence time".

8. EFFECT OF LOSS MODELLING ON STABILITY PREDICTION

In analysing the distortion problem there have been a number of attempts to model the unsteady blade response. All of these, at least for multistage compressor models are quite rudimentary when compared to the actual situation, and it is therefore worthwhile to investigate the overall impact of the choice of model on the predictions of the analysis.

In the preceding sections we assumed that the effect of the unsteadiness could be modelled by an inertia-like term and that the losses were traced out in a quasi-steady manner. In this section we will assume that bladerow exit flow angles follow changes in bladerow inlet flow angles in a quasi-steady manner, but the instantaneous loss across a bladerow lags incidence changes. It can be shown that, under these assumptions, all internal flow angles will be a function only of ϕ , the local flow coefficient. The particular lag law to be used is

$$\tau_L^r \frac{dL}{dt} = L_{ss} - L \quad (14)$$

where L is a loss coefficient and L_{ss} is the steady state value of the loss coefficient at the instantaneous flow condition. The time constant, τ_L , has been shown to have a value approximately equivalent to the time necessary for a particle to convect through a bladerow [10]

$$\tau_L \approx \frac{b_a U}{C_{x,r}} \approx 0.1 - 0.3$$

If the distortion is steady, the equation replacing Eq (2) which describes the steady background flow becomes

$$\frac{P_2 - P_{11}}{\rho U^2} = \psi_{ID} - L_s - L_R - \lambda \frac{d\phi}{d\theta} \quad (15)$$

where ψ_{ID} is an "ideal" pressure rise characteristic, being that obtained for the current internal flow angles but assuming zero loss. ψ_{ID} together with the stator loss, L_s , are purely functions of ϕ . The term L_R is the sum of the losses through the rotors and is given by

$$\tau_L \frac{dL_R}{d\theta} = L_{Rm} - L_R \quad (16)$$

assuming similar rotors for each stage (as is the case for the compressor used throughout this paper). For small values of the left hand side (recall $\tau_L \approx 0.1 - 0.3$) it can be shown that to first order in τ_L

$$L_R = L_{Rm} - \tau_L \frac{dL_{Rm}}{d\phi} \frac{d\phi}{d\theta}$$

When this term is substituted into (15) that equation takes a form exactly equivalent to Eq (2),

$$\frac{P^2 - P_{11}}{\rho U^2} = \psi(\phi) - \lambda_{eff} \frac{d\phi}{d\theta} \quad (17)$$

where ψ_{ID} , L_s and L_R have been regrouped for form ψ while

$$\lambda_{eff} = \lambda - \tau_L \frac{dL_{ss}}{d\phi} \quad (18)$$

Strictly speaking λ_{eff} is a function of θ , but given the approximate nature of the analysis an annulus average value will suffice.

As an example of this, Figure 16, shows the axial velocity profiles at neutral stability for a 180° degree square wave distortion. The three curves shown are calculated using (a) the simple inertia unsteadiness model (as used in the preceding sections of this paper), (b) the full unsteady loss model and (c) the inertia model with a suitably increased value of λ , at least as far as the steady axial velocity profile is concerned.

Given the similarity between axial velocity profiles it is hardly surprising that the calculated stability onset point for the unsteady loss model and the effective λ model are indistinguishable. There is, however, a marked difference in which modes are predicted to be the least stable. This occurs because the inclusion of an unsteady loss model means that, near stall, the instantaneous slope of the compressor characteristic will be less positive than with quasi-steady losses. This can be seen qualitatively by reference to equation (14), which for small disturbances, becomes for rotors

$$\frac{\tau_L r}{U} \left\{ \frac{\partial \delta L}{\partial t} + \frac{U}{r} \frac{\partial \delta L}{\partial \theta} \right\} = \delta L_{ss} - \delta L$$

For the n 'th harmonic and for a time dependence of the form $e^{i\omega t}$ this reduces to

$$\delta L = \frac{\delta L_{ss}}{1 + i\tau_L \left(\frac{\omega r}{U} + n \right)}$$

which decreases rapidly with increasing n . This effect would not have been predicted just by increasing the effective λ .

A quantitative illustration of this is Figure 17, where the separation of the different modes can be seen. As alluded to, the first mode, becomes unstable first followed by the second mode etc.

The condition at which the first mode becomes unstable is not much different than that computed with the quasi-steady loss model so that inclusion of unsteady losses does not have a major effect on predicted stall point. What the computation does emphasise, however, is that it is the first mode that one should focus on since this is the most unstable.

SUMMARY AND CONCLUSIONS

1. A fluid dynamic stability analysis has been used to examine several phenomena associated with inlet distortion in multistage axial compressors.
2. The structure of the disturbance eigenmodes has been shown to have a distribution that is rich in harmonics. The simple inertia lag model does not distinguish a most unstable disturbance except near resonance conditions.
3. The regimes of validity of the approximate distorted flow instability criterion

$$\int_0^{2\pi} \frac{d\psi}{d\phi} d\theta = 0$$

have been examined. It is shown that this is valid except in the neighbourhood where surge (system) type frequencies and compressor (stall cell) type propagating frequencies coincide. Further the use of this criterion allows one to show clearly that the basic parallel compressor stability criterion is recovered as a limiting case of the present analysis.

4. It is found that a rotating disturbance, whose propagation speed is close to that of the natural eigensolutions of the system can cause rotating stall at a considerably higher flow rate than for a disturbance that rotates with speed far from the natural value. This is shown to be in agreement with experimental results. In general counter rotating disturbances have less of an adverse effect than do co-rotating disturbances.
5. In the neighbourhood where the system (surge type) frequencies and the compressor (propagating type frequencies) coincide there is also a decrease in stability compared to regimes in which these frequencies are quite different.
6. The inclusion of pitch average models of unsteady losses in a computation of steady-state distorted flow has an effect very similar to that of an increase in the inertial unsteady terms, and thus appears not to introduce any new fluid mechanic effects.
7. The unsteady loss calculation, however, does separate the stability points of the different modes, with the result that the first (propagating) mode is the most unstable, and hence most important to consider.

ACKNOWLEDGEMENT

T.P. Hynes and E.M. Greitzer wish to gratefully acknowledge the AGARD travel grant that made this work possible. T.P. Hynes would like to thank Mr D.D. Williams for all his help and guidance. This work was also supported by a research grant from the NASA Lewis Research Centre, Number NSG 3208 which the authors gratefully acknowledge. This work has been carried out with the support of the Procurement Executive, Ministry of Defence.

REFERENCES

- [1] Hyners T.P. and Greitzer E.M. 'A Method for Assessing Effects of Inlet Flow Distortion on Compressor Stability' from 'Stability, Stall and Surge in Compressors and Pumps' ASME Winter Meeting, New Orleans, 1984 and Journal of Engineering for Power 1986 (to appear).
- [2] Moore F.K., 'A Theory of Rotating Stall of Multistage Compressors, Parts I-III' ASME J. Eng. Gas Turbines and Power, Vol. 106, 1984 pp 313-336.
- [3] Koff F.K., 'Stalled Flow Characteristics for Axial Compressors', Master's thesis, MIT 1983.
- [4] Dunham J. "Non-Axisymmetric Flows in Axial Compressors". Mechanical Engineering Science Monograph No 5, 1963.
- [5] Mokelke H. "The Prediction of Steady, Circumferential Pressure and Temperature Distortions in Multistage Axial Flow Compressors". ASME Journal of Engineering for Power, Vol 102, April 1980.
- [6] Greitzer E.M. 'Surge and Rotating Stall in Axial Flow Compressors' ASME Journal of Engineering for Power, Vol 98, April 1976, pp 190-217.
- [7] Greitzer E.M. "Axial Compressor Stall Phenomena" ASME J. of Fluids Engineering, Vol 102, 1980.
- [8] Peyret R., Taylor-T.D. Computational Methods for Fluid Flow, Springer-Verlag 1983.
- [9] Ludwig G.R., Nenni J.P., and Arendt R.H. 'Investigation of Rotating Stall in Axial Flow Compressors and the Development of a Prototype Stall Control System' Technical Report USAF-APL-TR-73-45, 1973.
- [10] Massawy R.S. 'Multiple Segment Parallel Compressor Model for Circumferential Flow Distortion', ASME J. Eng. Power, Vol 99, April 1977, pp 228-246.

NOMENCLATURE

| | |
|------------------|--|
| a | Speed of sound |
| a_n | Fourier coefficients of axial velocity perturbation at compressor face |
| A | Flow-through area |
| b_x | Axial chord |
| B | non-dimensional system parameter; $B = \frac{U_1 \sqrt{V_{\text{plenum}}}}{2a_1 A L_{\text{TOT}}}$ |
| C_x | Axial velocity |
| f | distortion frequency (fraction of rotor rotation rate) |
| L_{TOT} | Overall effective length of compressor ducting |
| n | Harmonic number |
| p | Static pressure |
| P_t | Total pressure |
| r | Mean radius |

| | |
|------------|---|
| R_L | Pressure rise in distorted sector |
| T | Non-dimensional throttle setting |
| U | Wheel speed |
| $\delta()$ | Perturbation quantity |
| η | Non-dimensional effective length = L_{TOT}/r |
| λ | Inertia parameter (rotors) = $\frac{\sum b_x}{r \cos^2(\text{stagger})}$ |
| μ | Inertia parameter (all bladerows) = $\frac{\sum b_x}{r \cos^2(\text{stagger})}$ |
| τ_L | Unsteady loss lag parameter |
| ϕ | Axial velocity coefficient; $\phi = Cx/U$ |
| ψ | Non-dimensional compressor pressure rise in axisymmetric flow |
| | $\psi = \frac{P_2 - P_{t1}}{\rho U^2}$ |
| ω | Radian frequency of perturbation |

Subscripts

| | |
|----|--------------------------|
| 0 | Inlet to compressor duct |
| 1 | Compressor inlet |
| 2 | Compressor exit |
| 3 | Plenum inlet |
| 4 | Throttle outlet |
| R | Rotor |
| S | Stator |
| SS | Steady state |

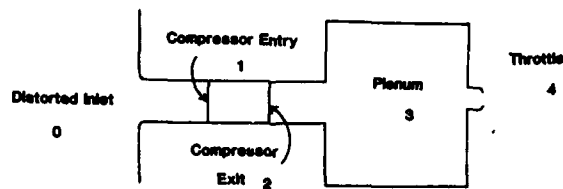
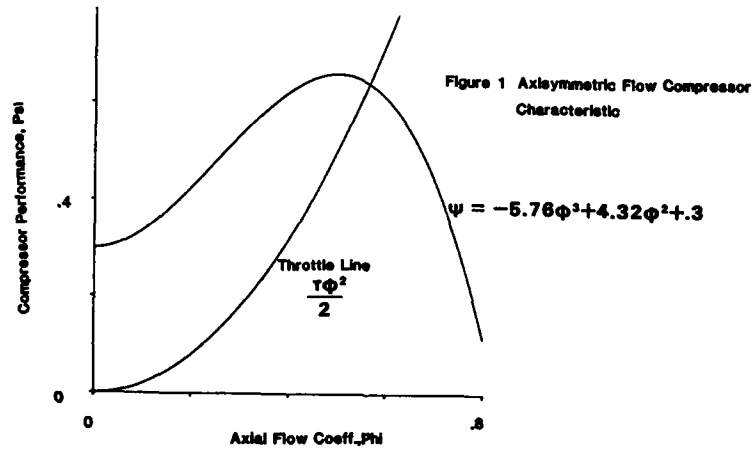


Figure 2 Simple Compression System

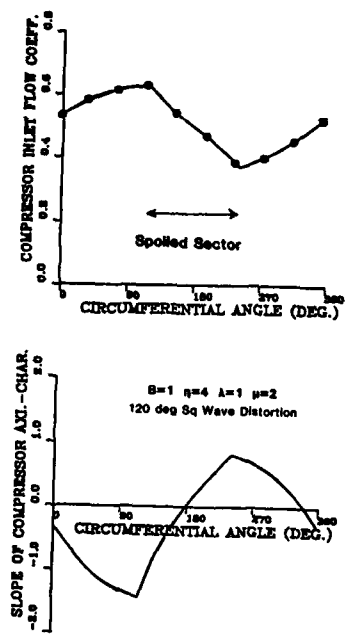


Figure 3 Typical Axial Velocity Profile at Instability Onset

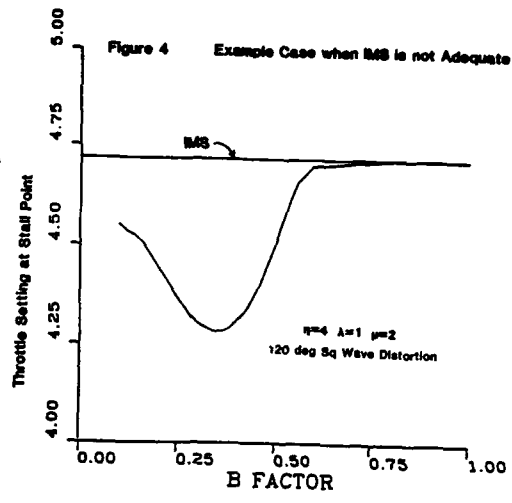


Figure 4 Example Case when RMS is not Adequate

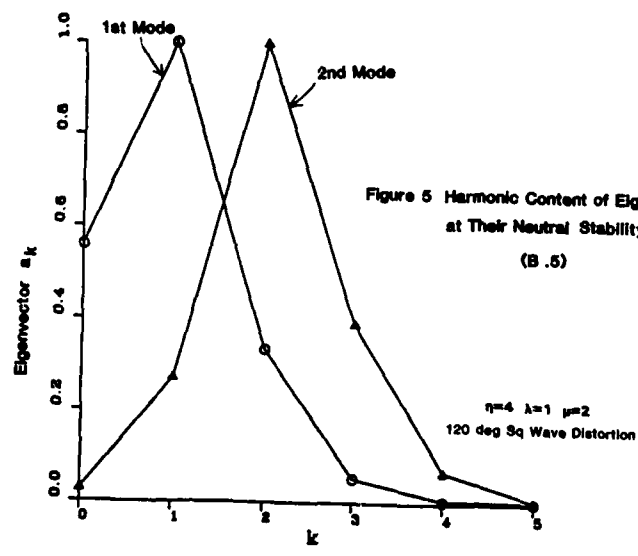
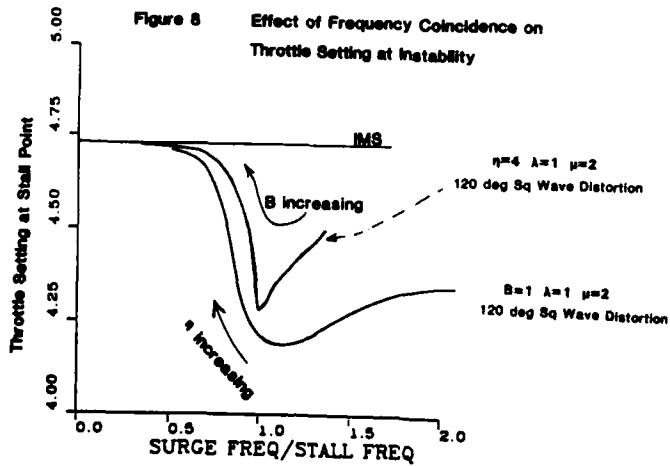
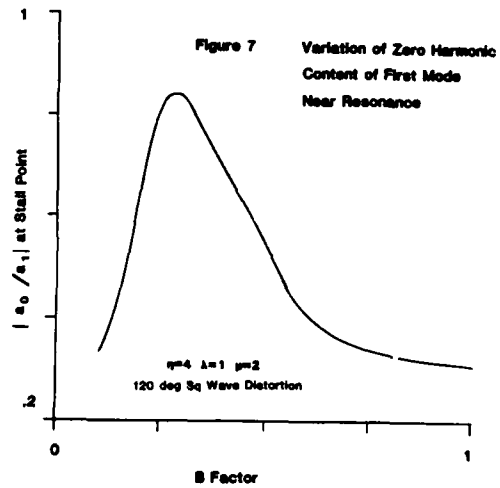
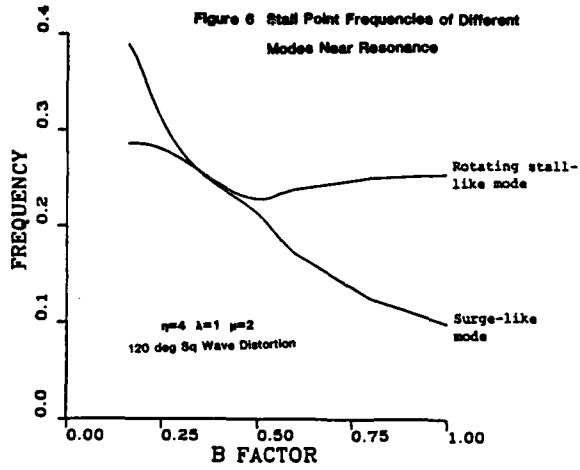


Figure 5 Harmonic Content of Eigenvectors at Their Neutral Stability Point (B .5)



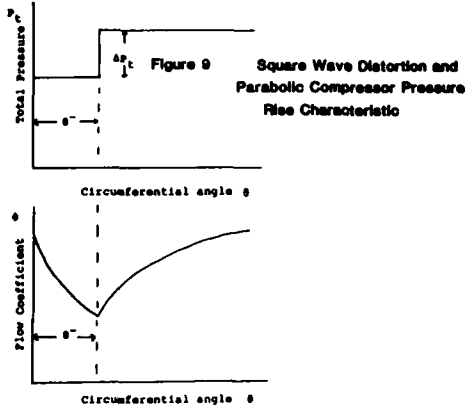
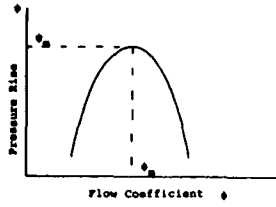


Figure 9 Square Wave Distortion and Parabolic Compressor Pressure Rise Characteristic

Figure 11 Effect of λ/a on Φ at Instability Using IMS

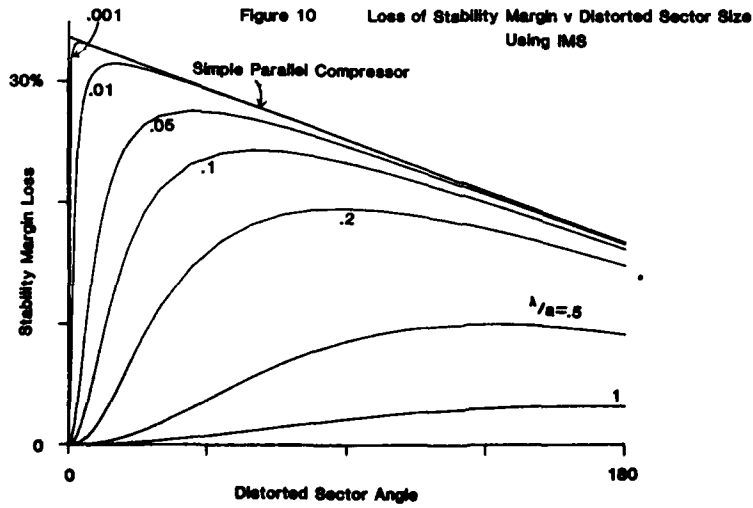
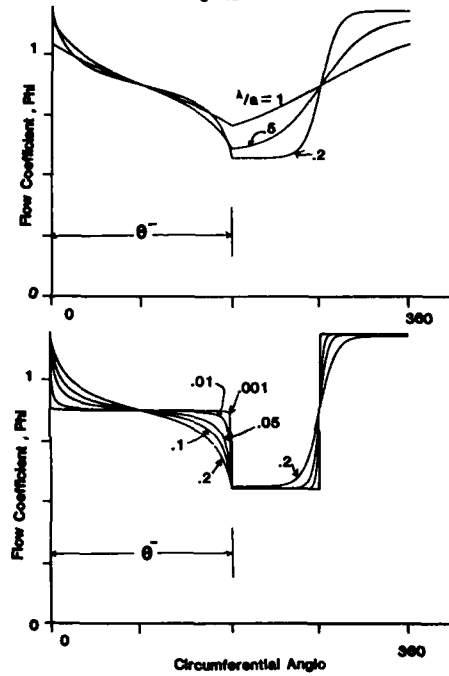


Figure 10 Loss of Stability Margin v Distorted Sector Size Using IMS

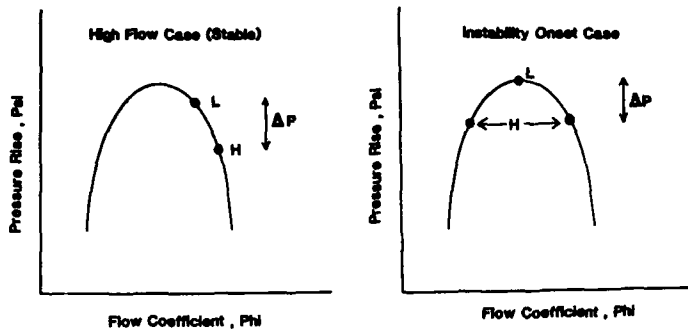


Figure 12 Low λ/a Limit of Present Model

Figure 13 Experimentally Determined Effect of Distortion Rotation Rate on Stall Point. From Reference 5.

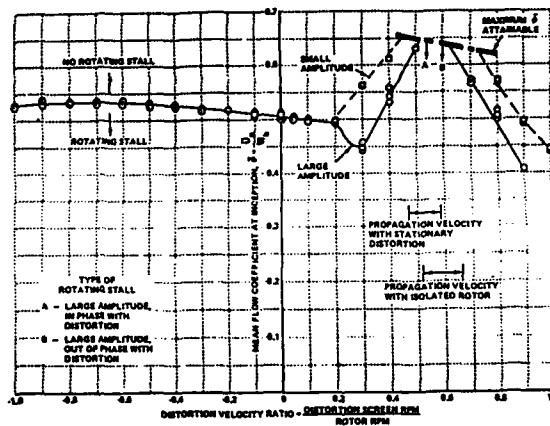
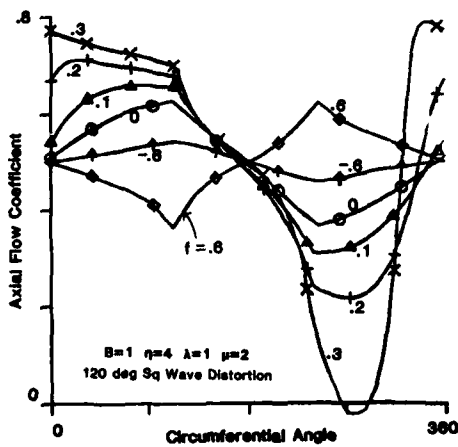


Figure 14 Axial Velocity Profiles for Rotating Distortions at Mean Phi .5



N.B. Frame Rotates with Distortion

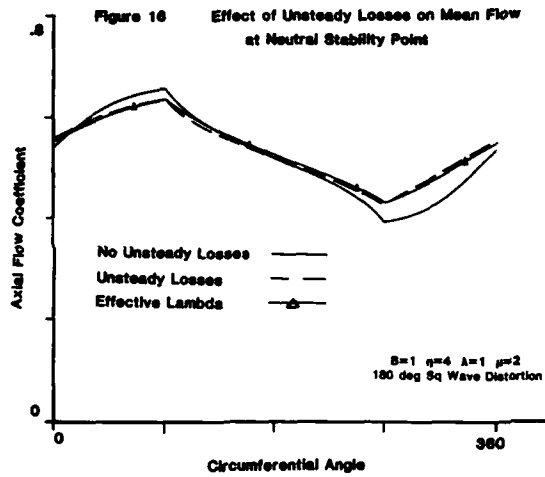
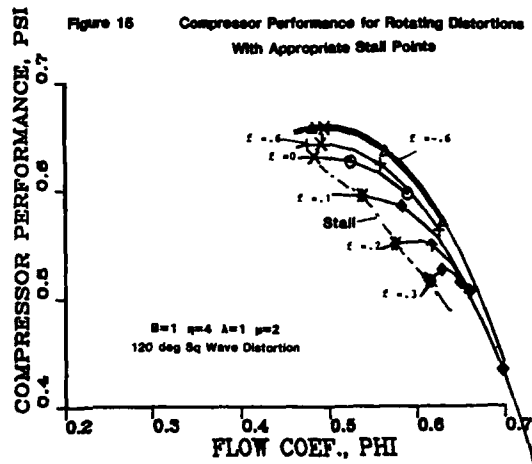
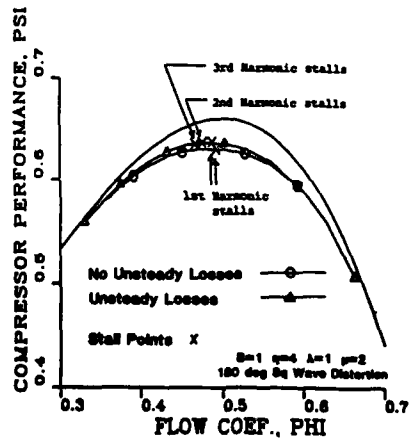


Figure 17 Effect of Unsteady Loss Model on Stall Point for Different Modes



DISCUSSION

Ph. Ramette, Fr

For a low-pressure compressor in a full engine, what is the downstream plenum volume which is used for the non-dimensional parameter B?

Author's Reply

I do not know the answer to that. We are developing this model for higher-order compression systems. We are putting in a single compressor followed by a second compressor and modelling the flow in the second compressor. I do not think that the simple compression system can model a multi-compressor system. Our model cannot shed any light on the volume that should be taken.

J. Fabri, Fr

A few years ago Ed Greitzer demonstrated in several ASME papers that there is no valid two-dimensional solution for three-dimensional flows. It is a pleasure to see that he is working again in two-dimensional flows.

Author's Reply

For the high hub-tip-ratio compressors modelled here I think that the two-dimensional theory is a good approximation for long wavelength circumferential distortions. The model does not address radial or mixed distortions and is not applicable to a fan.

R. Van Den Braembussche, Be

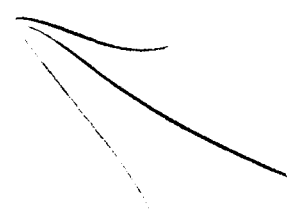
In your paper you compare surge frequency and rotating stall frequency. How do you define rotating stall frequency? Is it the rotational speed of the stall cells or is it the frequency in a fixed reference point?

What are the types of compressor where both frequencies are the same?

Author's Reply

The model provides an eigenvalue analysis so there is a solution for every value of n , a circumferential harmonic. The solutions for non-zero n propagate around the annulus. The solution for $n = 0$ is primarily a one-dimensional oscillation. By surge frequency we mean the natural frequency that emerges as a solution of the eigenvalue problem for the $n = 0$ mode. The rotating stall frequency is the frequency that emerges for the $n = 1$ mode.

When it comes to assigning a stall frequency to a compressor we would claim that the surge frequency is a strong function of the system in which the compressor operates and of the B parameter. The rotating stall frequency tends to be a property of the compressor, described by unsteadiness within the compressor itself.



ETUDE NUMERIQUE DE LA TRANSMISSION D'UNE DISTORSION DANS UN COMPRESSEUR AXIAL

par Germain BILLET, Philippe CHEVALIER et Pierre LAVAL

Office National d'Etudes et de Recherches Aéronautiques
29, avenue de la Division Leclerc
92320 - CHATILLON SOUS BAGNEUXRESUME

Une modélisation mathématique représentant le fonctionnement des grilles fixes ou mobiles d'un compresseur axial est couplée à une simulation numérique de l'écoulement tridimensionnel hors grilles. Le code de calcul développé permet d'étudier les écoulements tridimensionnels compressibles non uniformes dans les turbomachines. Le fluide est supposé parfait dans les espaces hors-grilles, les effets visqueux étant pris en compte dans les grilles. Les résultats numériques sont comparés aux données expérimentales obtenues sur un compresseur monoétage basse pression soumis à une distorsion stationnaire de pression d'arrêt, de forte amplitude, dans la section d'entrée. Les comparaisons montrent que cette approche numérique est capable de prédire la réponse globale du compresseur. Ce travail s'inscrit dans un projet visant à prévoir la réponse d'un compresseur à un écoulement d'entrée non uniforme périodique dans le temps ou complètement instationnaire.

NUMERICAL STUDY OF THE PROPAGATION OF AN INLET FLOW DISTORTION
THROUGH AN AXIAL COMPRESSORABSTRACT

A model representing the response of fixed or rotating axial compressor blade rows is coupled to a 3-D numerical simulation of the flow outside the blade rows. The code can be used to study nonuniform compressible 3-D flows through turbomachines. The fluid is assumed to be inviscid in the space outside the rows, while the viscous effects are taken into account inside. Numerical results are compared with experimental data in the case of a low speed single stage compressor with an inlet steady total pressure distortion. These comparisons show that the numerical approach is able to predict the global response of the compressor. This work is part of a larger project aimed at predicting the response of a compressor to a nonuniform inlet flow that is periodic in time, or fully unsteady.

Travail effectué sous contrat DRET.

1. INTRODUCTION

L'ONERA développe depuis plusieurs années des codes de calcul dans le but de déterminer la réponse des compresseurs à des hétérogénéités azimutales d'alimentation. En particulier, les méthodes linéarisées, qui ont l'avantage d'être rapides, apportent de précieux renseignements lorsque l'hétérogénéité n'est pas trop importante [1]. Par contre en présence de fortes hétérogénéités engendrant des phénomènes non linéaires, il est nécessaire de faire appel à une approche numérique qui permet d'analyser ce problème complexe du compresseur soumis à de fortes distorsions azimutales d'alimentation, ou fonctionnant près de la limite du décrochage, à forte contrepression et à faible débit, dans une zone où de faibles perturbations peuvent être considérablement amplifiées. Les approches du problème dans le domaine non linéaire ont surtout fait appel à des modélisations bidimensionnelles [2 à 5]. Or Greitzer et Strand [6] ont montré que la superposition d'une giration importante et d'hétérogénéités de pression d'arrêt induit des effets tridimensionnels que ne peuvent appréhender les approches bidimensionnelles. Dans ces conditions, il est apparu nécessaire de développer un modèle numérique plus complet qui soit capable de capter les effets radiaux en plus des phénomènes azimutaux. Dans ce but, cet article est particulièrement consacré à l'étude numérique d'un écoulement hétérogène tridimensionnel compressible et instationnaire dans un compresseur monoétage à veine cylindrique dont l'alimentation est soumise à une distorsion stationnaire et dont la charge est comparable à celles rencontrées sur les compresseurs industriels.

L'approche numérique est basée sur une méthode aux différences finies à pas fractionnaires purement instationnaire qui a été développée pour l'étude d'un écoulement hétérogène non visqueux dans un canal annulaire simulant la partie du moteur située en amont du compresseur [7]. Dans le présent travail nous avons repris cette approche pour résoudre les équations d'Euler dans les zones hors-grilles. La résolution a été effectuée, dans les grilles fixes ou mobiles, en couplant les équations globales, modélisant le fonctionnement d'une roue, aux équations d'Euler utilisées dans les espaces hors grilles. Cette modélisation instationnaire, à base essentiellement phénoménologique, associe trois relations intégrales (conservation de la masse, de la quantité de mouvement et de l'énergie) et deux équations de retard concernant respectivement le coefficient de perte de charge et l'écart flux-profil (à une constante angulaire près) en sortie d'aubages. Une dernière relation sur l'évolution radiale des lignes de courant à la traversée des grilles permet de fermer le système d'équations qui relie les diverses grandeurs aérodynamiques définies respectivement en amont et en aval de chaque grille.

Les comparaisons entre les valeurs expérimentales et les résultats obtenus par le programme de calcul sont présentées dans plusieurs sections transversales, en particulier en aval et en amont de la roue mobile où des relevés expérimentaux détaillés sont fournis.

2. NOTATIONS

r, θ, z : coordonnées cylindriques dans le domaine physique,

R, Θ, Z : coordonnées transformées dans le domaine de calcul,

t : temps,

V : vitesse absolue,

v : vitesse relative,

V_r, V_θ, V_z : composantes de la vitesse absolue,

v_r, v_θ, v_z : composantes de la vitesse relative,

ω : vitesse angulaire du rotor (peut dépendre du temps),

γ : rapport des chaleurs spécifiques,

c : célérité du son locale,

M : nombre de Mach local,

ϕ : angle de déflexion radiale,

β : angle relatif de déflexion azimutale,

ϕ_i : angle de déflexion radiale d'entrée,

β_i : angle de déflexion azimutale d'entrée,

ρ : masse volumique,

p : pression statique,

P : pression d'arrêt,

P_i : pression d'arrêt d'entrée,

T : température absolue,

T_i : température d'arrêt d'entrée,

s : entropie spécifique,

\dot{q} : taux de chaleur volumique,

$\mathcal{P}_{ext}(\sigma)$: puissance des forces extérieures dans le repère relatif,

σ_{ij} : tenseur des contraintes visqueuses,

χ : coefficient de pertes,

δ : angle de calage,

r : rayon,

\bar{r} : hauteur du canal,

r^* : fonction linéaire des pentes des carters interne et externe,

l_z : corde axiale des aubes,

l : pas des canaux interaubes,

h : hauteur du tube de courant Ω ,

n : normale unitaire extérieure,

N : nombre d'aubes de la grille.

Indice inférieur

1 : entrée de la grille,

2 : sortie de la grille,

i : moyeu,

e : carter externe,

SS : état stationnaire.

3. PRINCIPE DE LA METHODE

Le domaine de calcul est composé d'un canal annulaire à section évolutive limité par les carters interne et externe de la machine et par un plan d'entrée et un plan de sortie qui se situent respectivement en amont de la première grille et en aval de la dernière grille.

Afin d'avoir un domaine de calcul à mailles orthogonales, une transformation des coordonnées spatiales qui préserve le caractère conservatif des équations d'Euler est appliquée :

$$r \rightarrow R = \frac{r - r_1(z)}{r_e(z) - r_1(z)} \quad (1)$$

Le champ physique est alors transformé en un domaine parallélépipédique.

(a) Equations résolues dans le domaine hors-grilles

L'écoulement étant supposé non-visqueux dans ce domaine, nous considérons le système des équations d'Euler exprimé dans le nouveau système de coordonnées $Z = z, \Theta = \theta, R, C$:

$$\frac{\partial U}{\partial t} + \frac{\partial F}{\partial Z}(U) + \frac{\partial G}{\partial \Theta}(U, Z, \Theta, R) + \frac{\partial H}{\partial R}(U, Z, R) = 0 \quad (2)$$

avec

$$U = r \tilde{r} \begin{bmatrix} \rho \\ \rho V_z \\ \rho(V_r \sin \theta + V_\theta \cos \theta) \\ \rho(V_r \cos \theta - V_\theta \sin \theta) \\ E \end{bmatrix}$$

où E représente l'énergie totale par unité de volume qui, dans le cas considéré d'un gaz parfait régulier ($\gamma = Cte$), a pour expression :

$$E = \frac{p}{\gamma - 1} + \frac{1}{2} \rho V^2$$

Les expressions des composantes des vecteurs F, G et H sont données dans [7].

b) Modélisation des grilles

Le calcul du "véritable" écoulement tridimensionnel dans la totalité des canaux interaubes d'un

étage n'est actuellement pas envisageable avec les calculateurs disponibles, les durées d'exploitation étant prohibitives. Il faudra attendre l'arrivée d'une nouvelle génération d'ordinateurs pour réaliser ces calculs.

De ce fait, notre choix s'est porté sur une modélisation de l'écoulement dans les grilles qui évite l'utilisation d'un maillage axial à l'intérieur des aubages. Il est donc possible, dans ce cas, d'étudier les phénomènes physiques dans un compresseur complet avec un nombre de mailles raisonnable. Mais en contrepartie les modèles utilisés n'approchent que de manière globale les phénomènes physiques et doivent souvent faire appel à des valeurs expérimentales (en particulier sur le coefficient de perte χ et l'angle de sortie en axes relatifs β_2) pour combler le manque d'information à l'intérieur des grilles.

Le modèle de roues, similaire à un "semi-actuator disk" s'obtient par simplification des équations de Navier-Stokes complètes écrites sous forme conservative dans le domaine transformé. Ces équations sont tout d'abord intégrées dans un tube de courant (Ω) qui a une épaisseur finie (cette hypothèse généralise le modèle présenté dans [8] où l'épaisseur de Ω était supposée infiniment petite). Chaque domaine (Ω) est limité par les profils de deux aubages adjacents dans la direction azimutale, par les sections d'entrée et de sortie du canal interaubes dans la direction axiale et par deux surfaces de courant dans la direction radiale (Fig. 1). Si $\partial\Omega$ représente la frontière qui entoure (Ω), les trois équations peuvent s'écrire dans le repère relatif, après quelques calculs [9] :

$$\left. \begin{aligned} (a) \quad & \int_{\Omega} \frac{\partial p}{\partial t} d\Omega + \int_{\partial\Omega} \rho \mathbf{v} \cdot \mathbf{n} d\Omega = 0, \\ (b) \quad & \int_{\Omega} \frac{\partial}{\partial t} \left(\rho \frac{v^2}{2} - \rho \frac{\omega^2 r^2}{2} \right) d\Omega + \int_{\partial\Omega} \left(p + \rho \frac{v^2}{2} - \rho \frac{\omega^2 r^2}{2} \right) \mathbf{v} \mathbf{n} d\Omega - \int_{\Omega} p \operatorname{div} \mathbf{v} d\Omega \\ & + \int_{\Omega} \rho r (v_{\theta} + \omega r) \frac{d\omega}{dt} d\Omega = \mathcal{P}, \\ (c) \quad & \frac{1}{\gamma-1} \int_{\Omega} \frac{\partial p}{\partial t} d\Omega + \int_{\Omega} p \operatorname{div} \mathbf{v} d\Omega + \frac{1}{\gamma-1} \int_{\partial\Omega} p \mathbf{v} \cdot \mathbf{n} d\Omega = -\mathcal{P}, \end{aligned} \right\} (3)$$

avec :

$$\mathcal{P} = - \int_{\partial\Omega} \mathcal{P}_{ext} (\mathbf{c} \cdot \mathbf{n}) d\Omega + \int_{\Omega} \dot{q} d\Omega + \omega \int_{\Omega} \sigma_{\theta} d\Omega - \int_{\Omega} \rho T \frac{ds}{dt} d\Omega.$$

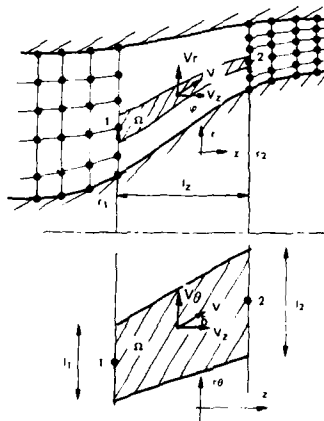


Fig. 1. MODELISATION DES GRILLES DANS LE PLAN PHYSIQUE

Il est évident que les relations (3) ne peuvent être utilisées sous cette forme et que quelques hypothèses simplificatrices sont nécessaires. Nous supposons donc que les variables aérodynamiques :

- varient linéairement le long de chaque tube de courant (Ω) ;
- sont constantes dans les sections d'entrée et de sortie du domaine (Ω) c'est-à-dire que la longueur d'onde de la perturbation circonférentielle est grande par rapport au pas du canal.

Nous admettons que dans chaque tube de courant (Ω) :

- l'écoulement est tangent au squelette du profil de l'aube : $v_\theta = v_z \operatorname{tg} \delta$;
- l'évolution radiale des lignes de courant à la traversée des roues est connue et ne dépend pas du temps. Elle est donnée par un calcul d'écoulement méridien à l'instant initial t_0 :

$$v_r = v_z r^{**} \quad \text{à } t = t_0 \quad (4)$$

avec

$$r^{**} = r^{**}(r) .$$

Si nous supposons de plus que l'évolution est adiabatique, que les effets visqueux dans les sections d'entrée et de sortie sont négligeables et que l'épaisseur de déplacement des couches limites sur les profils reste toujours faible vis-à-vis du pas du canal le terme \mathcal{P} se réduit à :

$$\mathcal{P} = - \int_a^b \rho T \frac{ds}{dt} d\Omega .$$

Écrit sous cette forme, ce terme de perte instationnaire est difficile à calculer. L'analogie avec le terme de perte stationnaire d'un écoulement incompressible traversant une roue fixe [3] suggère d'exprimer \mathcal{P} , sous forme discrète, par la relation :

$$\mathcal{P} = - \frac{1}{2} \rho_1 v_1^2 \left(\frac{v_{z1} S_1 + v_{z2} S_2}{2} \right) \chi ,$$

où $S_1 = h_1 l_1$ et $S_2 = h_2 l_2$ définissent respectivement l'aire des sections d'entrée et de sortie du tube de courant (Ω).

χ est déterminé, comme dans [2 à 5], par le modèle de transfert suivant :

$$\tau \frac{\partial \chi}{\partial t} + \chi = \chi_{ss} \quad (5)$$

où τ représente une constante de temps liée à la convection des perturbations dans la couche limite et χ_{ss} est une fonction de β_1 obtenue expérimentalement.

Les équations instationnaires (3) peuvent être alors écrites sous une forme discrète qui relie les grandeurs d'entrée (masse volumique, énergie cinétique spécifique axiale et pression statique) au point du maillage 1 aux grandeurs de sortie au point du maillage 2 du modèle de roue (fig. 1) :

$$\left. \begin{aligned} (a) \quad & \frac{V_\Omega}{2} \frac{\partial}{\partial t} (\rho_1 + \rho_2) + \rho_2 v_{z2} S_2 - \rho_1 v_{z1} S_1 = 0, \\ (b) \quad & \frac{V_\Omega}{4} (\operatorname{tg}^2 \delta + 1 + \frac{(r_1^{**} + r_2^{**})^2}{4}) \frac{\partial}{\partial t} (\rho_1 v_{z1}^2 + \rho_2 v_{z2}^2) - \frac{V_\Omega}{4} \frac{\partial}{\partial t} (\rho_1 \omega^2 r_1^2 + \rho_2 \omega^2 r_2^2) \\ & + \left[(\rho_2 - \rho_1) + \left(\rho_2 \frac{v_{z2}^2}{2} - \rho_1 \frac{v_{z1}^2}{2} \right) - \left(\rho_2 \frac{\omega^2 r_2^2}{2} - \rho_1 \frac{\omega^2 r_1^2}{2} \right) \right] \left(\frac{v_{z1} S_1 + v_{z2} S_2}{2} \right) + \frac{1}{4} (v_{z2} S_2 - v_{z1} S_1) \\ & (\rho_1 v_{z1}^2 - \rho_1 \omega^2 r_1^2 + \rho_2 v_{z2}^2 - \rho_2 \omega^2 r_2^2) + \frac{V_\Omega}{2} [\operatorname{tg} \delta (\rho_1 r_1 v_{z1} + \rho_2 r_2 v_{z2}) + \omega (\rho_1 r_1^2 + \rho_2 r_2^2)] \frac{d\omega}{dt} = \mathcal{P}, \\ (c) \quad & \frac{V_\Omega}{2(\gamma-1)} \frac{\partial}{\partial t} (\rho_1 + \rho_2) + \left(\frac{\rho_1 + \rho_2}{2} \right) (v_{z2} S_2 - v_{z1} S_1) + \frac{1}{\gamma-1} (\rho_2 v_{z2} S_2 - \rho_1 v_{z1} S_1) = -\mathcal{P}, \end{aligned} \right\} (6)$$

où $\mathcal{P} = \frac{N}{2\pi} \mathcal{P}$ et $V_\Omega = \frac{l}{3} \left[l_1 \left(h_2 + \frac{h_1}{2} \right) + l_2 \left(h_1 + \frac{h_2}{2} \right) \right]$ représente le volume approché du tube de courant (Ω).

A partir de ces relations, il est intéressant de remarquer que la variation de la vitesse de rotation (équation 6b) est prise en compte et permet d'étudier le comportement du compresseur lors de phases d'accélération ou de décélération.

Les noeuds 1 et 2 appartiennent aussi au domaine hors-grilles, et nous pouvons y appliquer les équations définies dans ce domaine.

La vitesse axiale de l'écoulement est supposée subsonique dans les plans d'entrée et de sortie des grilles. Dans ce cas, en nous basant sur la théorie des caractéristiques, nous pouvons intégrer quatre équations à l'entrée et une seule en sortie. Pour le point d'entrée 1, compte tenu de la relation (4), une des équations dégénère et le système s'exprime, dans le repère relatif, comme suit :

$$\left. \begin{aligned} (a) \quad & v_{r1} = v_{z1} r_1^{**} \\ (b) \quad & \frac{\partial p_1}{\partial t} + \rho_1 c_1 \frac{\partial v_{z1}}{\partial t} + A_1 = 0 \\ & \text{(le long de la caractéristique } C^+), \\ (c) \quad & \frac{\partial \rho_1}{\partial t} + B_1 = 0, \\ (d) \quad & \frac{\partial v_{\theta 1}}{\partial t} + C_1 = 0, \end{aligned} \right\} (7)$$

où

$$\begin{aligned}
A_1 &= (v_{z_1} + c_1) \frac{\partial p_1}{\partial Z} + \rho_1 c_1 (v_{z_1} + c_1) \frac{\partial v_{z_1}}{\partial Z} + \frac{\rho_1 c_1^2}{r_1} \frac{\partial v_{\theta_1}}{\partial \Theta} + \left(\frac{v_{\theta_1}}{r_1} - t \frac{d\omega}{dt} \right) \frac{\partial p_1}{\partial \Theta} \\
&+ \rho_1 c_1 \left(\frac{v_{\theta_1}}{r_1} - t \frac{d\omega}{dt} \right) \frac{\partial v_{\theta_1}}{\partial \Theta} + \rho_1 c_1 (v_{z_1} + c_1) (r_1^{**} - r_1^*) \frac{\partial v_{z_1}}{\partial R} \\
&+ \frac{1}{r_1} \left[v_{z_1} (r_1^{**} - r_1^*) - c_1 r_1^* \right] \frac{\partial p_1}{\partial R} + \frac{c_1^2 \rho_1 v_{z_1}}{r_1} \frac{\partial r_1^{**}}{\partial R} + \frac{c_1^2 \rho_1 v_{z_1} r_1^{**}}{r_1}, \\
B_1 &= \frac{\partial}{\partial Z} (\rho_1 v_{z_1}) + \left(\frac{v_{\theta_1}}{r_1} - t \frac{d\omega}{dt} \right) \frac{\partial \rho_1}{\partial \Theta} + \frac{\rho_1}{r_1} \frac{\partial v_{\theta_1}}{\partial \Theta} + \frac{r_1^{**} - r_1^*}{r_1} \frac{\partial}{\partial R} (\rho_1 v_{z_1}) + \frac{\rho_1 v_{z_1}}{r_1} \frac{\partial r_1^{**}}{\partial R} + \rho_1 v_{z_1} r_1^{**}, \\
C_1 &= v_{z_1} \frac{\partial v_{\theta_1}}{\partial Z} + \left(\frac{v_{\theta_1}}{r_1} - t \frac{d\omega}{dt} \right) \frac{\partial v_{\theta_1}}{\partial \Theta} + \frac{1}{\rho_1 r_1} \frac{\partial p_1}{\partial \Theta} + \frac{v_{z_1} (r_1^{**} - r_1^*)}{r_1} \frac{\partial v_{z_1}}{\partial R} + \omega v_{z_1} r_1^{**} + \frac{v_{\theta_1} v_{z_1} r_1^{**}}{r_1} + r_1 \frac{d\omega}{dt}.
\end{aligned}$$

Pour le point de sortie 2, la relation (4) et l'équation le long de la caractéristique C- donnent le système suivant :

$$\begin{aligned}
(a) \quad & v_{r_2} = v_{z_2} r_2^{**} \\
(b) \quad & \frac{\partial p_2}{\partial t} - \rho_2 c_2 \frac{\partial v_{z_2}}{\partial t} + A_2 = 0
\end{aligned} \quad \left. \vphantom{\begin{aligned} (a) \\ (b) \end{aligned}} \right\} (8)$$

(le long de la caractéristique C-).

$$\begin{aligned}
\omega \quad A_2 &= (v_{z_2} - c_2) \frac{\partial p_2}{\partial Z} - \rho_2 c_2 (v_{z_2} - c_2) \frac{\partial v_{z_2}}{\partial Z} + \frac{\rho_2 c_2^2}{r_2} \frac{\partial v_{\theta_2}}{\partial \Theta} + \left(\frac{v_{\theta_2}}{r_2} - t \frac{d\omega}{dt} \right) \frac{\partial p_2}{\partial \Theta} - \rho_2 c_2 \left(\frac{v_{\theta_2}}{r_2} - t \frac{d\omega}{dt} \right) \frac{\partial v_{z_2}}{\partial \Theta} \\
&- \rho_2 c_2 (v_{z_2} - c_2) (r_2^{**} - r_2^*) \frac{\partial v_{z_2}}{\partial R} + \frac{1}{r_2} \left[v_{z_2} (r_2^{**} - r_2^*) + c_2 r_2^* \right] \frac{\partial p_2}{\partial R} \\
&+ \frac{c_2^2 \rho_2 v_{z_2}}{r_2} \frac{\partial r_2^{**}}{\partial R} + \frac{c_2^2 \rho_2 v_{z_2} r_2^{**}}{r_2}.
\end{aligned}$$

Une dernière équation est nécessaire pour fermer le système. Elle utilise un modèle de transfert sur l'angle de sortie instationnaire β_2 .

Cette équation peut s'exprimer ainsi :

$$r' \frac{\partial \beta_2}{\partial t} + \beta_2 = \beta_{2m}, \quad (9)$$

où β_{2m} , comme χ_{2m} , est une fonction de β_1 obtenue à partir des résultats expérimentaux. r' est une constante qui peut varier en fonction de β_2 .

Ce modèle simple a déjà été utilisé dans d'autres travaux (cf. [2] par exemple). Il apparaît souhaitable de pouvoir disposer d'un modèle plus physique. Dans ce but, une étude expérimentale a été menée à l'ONERA [11] et l'introduction du nouveau modèle, dans le code de calcul, est en cours.

La relation qui relie β_2 aux composantes de la vitesse relative s'écrit :

$$\beta_2 = \text{Arctg} \frac{v_{\theta_2}}{v_{z_2}}.$$

Le couplage des équations (6a), (6b), (6c), (7b), (7c), (7d), (8b) et (9) aboutit au système de huit équations suivant :

$$\frac{\partial \mathcal{U}}{\partial t} + \mathcal{A} \frac{\partial \mathcal{U}}{\partial Z} + \mathcal{B} \frac{\partial \mathcal{U}}{\partial \Theta} + \mathcal{C} \frac{\partial \mathcal{U}}{\partial R} + \mathcal{D} = 0, \quad (10)$$

avec :

$$\mathcal{U} = [\rho_1, v_{z_1}, v_{\theta_1}, \rho_1, \rho_2, v_{z_2}, v_{\theta_2}, p_2].$$

Les éléments des matrices \mathcal{A} , \mathcal{B} et \mathcal{C} et les composantes de \mathcal{D} dépendent des composantes de \mathcal{U} et de la géométrie de la veine [9]. Après résolution de ce système, les composantes radiales de la vitesse aux points 1 et 2 sont obtenues par les relations (7a) et (8a). Le coefficient de perte instationnaire donné par (5) apparaît dans le terme non homogène \mathcal{D} .

4. APPROCHE NUMERIQUE

Le problème est résolu numériquement par une méthode à pas fractionnaires, dite de désintégration, explicite, du second ordre. C'est une extension à l'espace tridimensionnel de la méthode à pas fractionnaires développée dans [10] et appliquée aux calculs d'écoulements transsoniques bidimensionnels. Cette méthode consiste à décomposer l'opérateur spatial tridimensionnel en opérateurs unidimensionnels auxquels est associé le schéma de MacCormack [12].

Le domaine de calcul concernant le compresseur étudié ci-dessous est divisé en trois régions.

La région 1 comprend les zones hors-grilles situées en amont de la roue mobile et en aval du redresseur.

La région 2 inclut les zones hors-grilles situées juste devant la roue mobile, entre les deux grilles et juste après le redresseur.

La région 3 se situe au niveau des plans d'entrée et de sortie de chaque grille.

Les pas d'espace de ces trois régions sont respectivement $\Delta z; \Delta \theta, \Delta R$ (région 1), $\frac{\Delta z}{2}, \Delta \theta, \Delta R$ (régions 2 et 3).

Soit U_{ijk}^n l'approximation de $U(t^n, z_i, \theta_j, R_k)$ au temps $t^n = n \Delta t$ ($n \in \mathbb{N}, \Delta t > 0$) et aux points $z_i = i \Delta z, \theta_j = j \Delta \theta$ et $R_k = k \Delta R$.

Le schéma à chaque double pas entier s'exprime dans la région 1 de la manière suivante :

$$U_{ijk}^{n+2} = \mathcal{L}_z \left(\frac{\Delta t}{3} \right) \mathcal{L}_\theta \left(\frac{\Delta t}{3} \right) \mathcal{L}_R \left(\frac{\Delta t}{3} \right) \mathcal{L}_R \left(\frac{\Delta t}{3} \right) \mathcal{L}_\theta \left(\frac{\Delta t}{3} \right) \mathcal{L}_z \left(\frac{\Delta t}{3} \right) U_{ijk}^n, \quad (11)$$

où $\mathcal{L}_z \left(\frac{\Delta t}{3} \right), \mathcal{L}_\theta \left(\frac{\Delta t}{3} \right)$ et $\mathcal{L}_R \left(\frac{\Delta t}{3} \right)$ définissent les opérateurs aux différences finies unidimensionnels dans les directions respectives z, θ et R . Le produit commutatif des opérateurs dans (11) est indispensable pour obtenir une précision du second ordre [10].

Bien que les différents schémas à pas fractionnaires (tel que $U_{ijk}^{n+(1/3)} = \mathcal{L}_z \left(\frac{\Delta t}{3} \right) U_{ijk}^n$) discrétisent des systèmes unidimensionnels pseudo-instationnaires, il a été démontré que le schéma à pas entier (11) est consistant avec les équations instationnaires, c'est-à-dire qu'il discrétise le système écrit sous forme conservative (2) avec une précision du second ordre [10].

En tenant compte que dans la région 2 le pas d'espace dans la direction axiale est $\Delta z/2$, le schéma à pas entier dans cette région s'obtient directement à partir du schéma (11) en remplaçant chaque opérateur $\mathcal{L}_z \left(\Delta t/3 \right)$ par un produit de deux opérateurs unidimensionnels :

$$\mathcal{L}_z \left(\frac{\Delta t}{3} \right) \equiv \mathcal{L}'_z \left(\frac{\Delta t}{6} \right) \mathcal{L}''_z \left(\frac{\Delta t}{6} \right).$$

Pour construire le schéma à pas entier qui discrétise le système (10) (région 3), nous décomposons la matrice \mathcal{B} qui apparaît dans (10) en une matrice triangulaire supérieure \mathcal{B}^+ et une matrice triangulaire inférieure \mathcal{B}^- . Cette décomposition supplémentaire permet d'obtenir analytiquement une condition de stabilité approchée pour ce schéma.

Le schéma à pas entier utilisé dans la région 3 est défini comme suit :

$$Q_{ijk}^{n+2} = H'^2 \left(\frac{5 \Delta t}{6} \right) \mathcal{L}_\theta \left(\frac{\Delta t}{3} \right) H'^1 \left(\frac{5 \Delta t}{6} \right) Q_{ijk}^n, \quad (12)$$

$$\text{avec : } H'^2 \left(\frac{5 \Delta t}{6} \right) = \mathcal{L}'_z \left(\frac{\Delta t}{6} \right) \mathcal{L}''_z \left(\frac{\Delta t}{6} \right) \mathcal{L}'_z \left(\frac{\Delta t}{6} \right) \mathcal{L}''_z \left(\frac{\Delta t}{6} \right) \mathcal{L}'_R \left(\frac{\Delta t}{6} \right),$$

$$H'^1 \left(\frac{5 \Delta t}{6} \right) = \mathcal{L}'_R \left(\frac{\Delta t}{6} \right) \mathcal{L}''_z \left(\frac{\Delta t}{6} \right) \mathcal{L}'_z \left(\frac{\Delta t}{6} \right) \mathcal{L}''_z \left(\frac{\Delta t}{6} \right) \mathcal{L}'_z \left(\frac{\Delta t}{6} \right).$$

Ce schéma discrétise le système (10) et par conséquent les schémas associés à chaque opérateur $\mathcal{L}'_z \left(\Delta t/6 \right), \mathcal{L}''_z \left(\Delta t/6 \right)$ et $\mathcal{L}'_R \left(\Delta t/6 \right)$ discrétisent des systèmes unidimensionnels sous forme non conservative.

Le schéma $U_{ijk}^{n+(1/6)} = \mathcal{L}'_z \left(\frac{\Delta t}{6} \right) U_{ijk}^n$, par exemple, s'écrit [13] :

$$\tilde{Q}_{i+1,j,k}^{n+(1/6)} = Q_{i+1,j,k}^n - \frac{\Delta t}{\Delta z} \mathcal{A}_{ijk}^n (Q_{i+1,j,k}^n - Q_{i,j,k}^n),$$

$$\tilde{Q}_{ijk}^{n+(1/6)} = Q_{ijk}^n - \frac{\Delta t}{\Delta z} \mathcal{A}_{ijk}^n (Q_{ijk}^n - Q_{i-1,j,k}^n),$$

pour les prédicteurs et :

$$Q_{ijk}^{n+(1/6)} = \frac{1}{2} \left[Q_{ijk}^n + \tilde{Q}_{ijk}^{n+(1/6)} - \frac{\Delta t}{\Delta z} \mathcal{A}_{i+(1/2),j,k}^n (\tilde{Q}_{i+1,j,k}^{n+(1/6)} - \tilde{Q}_{ijk}^{n+(1/6)}) \right],$$

pour le correcteur, où : $\mathcal{A}_{ijk}^n = \mathcal{A}(\mathcal{Q}_{ijk}^n)$ et $\tilde{\mathcal{A}}_{i+(1/2),j,k}^{n+(1/6)} = \mathcal{A} \left[\frac{1}{2} (\mathcal{Q}_{i+1,j,k}^{n+(1/6)} + \mathcal{Q}_{ijk}^{n+(1/6)}) \right]$.

Les schémas à pas fractionnaires :

$$\mathcal{Q}_{ijk}^{n+(1/2)} = \mathcal{L}_0 \left(\frac{\Delta t}{6} \right) \mathcal{Q}_{ijk}^{n+(1/3)} \quad \text{et} \quad \mathcal{Q}_{ijk}^{n+(2/3)} = \mathcal{L}_0 \left(\frac{\Delta t}{6} \right) \mathcal{Q}_{ijk}^{n+(1/2)}$$

discrétisent respectivement les systèmes pseudo-instationnaires :

$$\frac{1}{6} \frac{\partial \mathcal{Q}}{\partial t} + \mathcal{D}_1 \frac{\partial \mathcal{Q}}{\partial \Theta} = o(\Delta t^2, \Delta \Theta^2) \quad \text{et} \quad \frac{1}{6} \frac{\partial \mathcal{Q}}{\partial t} + \mathcal{D}_2 \frac{\partial \mathcal{Q}}{\partial \Theta} = o(\Delta t^2, \Delta \Theta^2).$$

Le schéma à pas fractionnaires : $\mathcal{Q}_{ijk}^{n+(7/6)} = \mathcal{L}_0 \left(\frac{\Delta t}{3} \right) \mathcal{Q}_{ijk}^{n+(5/6)}$

discrétise la partie non homogène du système (10) (de la même manière qu'une méthode de désintégration discrétise la partie non homogène d'un système parabolique [14]) et est donné par :

$$\mathcal{Q}_{ijk}^{n+(7/6)} = \mathcal{Q}_{ijk}^{n+(5/6)} - 2 \Delta t \mathcal{D} \left(\mathcal{Q}_{ijk}^n - \Delta t \left(\frac{\partial \mathcal{Q}}{\partial t} \right)_{ijk}^n \right).$$

Le schéma à pas entier (12) est consistant avec les véritables équations c'est-à-dire qu'il discrétise le système (10) avec une précision du second ordre.

La condition linéaire de stabilité des schémas à pas entiers utilisés dans chacune des zones est obtenue analytiquement en considérant la norme L_2 de ces schémas. Ils sont stables si la norme de chaque opérateur fractionnaire est bornée par l'unité. Les schémas à pas entiers appliqués dans les zones hors-grilles doivent satisfaire la condition suivante (liée au critère de Courant Friedrichs Lewy) :

$$\Delta t_{HG} \leq \text{Min} \left[\frac{\Delta Z}{\Lambda_Z}, \frac{\Delta \Theta}{\Lambda_\Theta}, \frac{\Delta R}{\Lambda_R} \right], \quad (13)$$

avec :

$$\Lambda_Z = \text{Max}_i |\lambda^{(i)}| = |V_Z| + c, \quad \Lambda_\Theta = \text{Max}_i |\mu^{(i)}| = \frac{1}{r} (|V_\Theta| + c),$$

$$\Lambda_R = \text{Max}_i |\delta^{(i)}| = (|V_r - V_z r^0| + c \sqrt{1+r^0}) / \tilde{r}, \quad i = 1, \dots, 5.$$

$\lambda^{(i)}$, $\mu^{(i)}$ et $\delta^{(i)}$ sont respectivement les valeurs propres des matrices jacobiniennes des vecteurs F, G, H (système 2) par rapport à U.

Cette condition est nettement moins restrictive que celle à laquelle doivent satisfaire les schémas "tridimensionnels" explicites (schémas obtenus par discrétisation directe de l'opérateur spatial tridimensionnel).

L'étude de la condition de stabilité associée aux schémas (12) est plus compliquée. Cependant avec les hypothèses suivantes :

$$v_{z1} = v_{z2}, \quad c_1 = c_2, \quad \frac{d\omega}{dt} = 0 \quad \text{et} \quad \chi_{\ell}^{**} - \chi_{\ell}^* \approx 0 \quad (\ell = 1, 2)$$

(cette dernière condition revient à supposer que les pentes radiales des lignes de courant et des lignes du maillage, à l'entrée et à la sortie des roues, ont des valeurs peu différentes), il est possible de déterminer les valeurs propres des matrices \mathcal{A} , \mathcal{B}_1 , \mathcal{B}_2 et \mathcal{C} qui s'écrivent respectivement :

$$a_{mm} = \begin{pmatrix} 0 \\ a_{22} \\ v_{x_1} \\ v_{x_1} + c_1 \\ 0 \\ v_{x_1} - c_1 \\ 0 \\ 0 \\ 0 \end{pmatrix}, \quad b_{mm}^1 = b_{mm}^2 = \begin{pmatrix} \frac{v_{\theta_1}}{2r_1} \\ \frac{(tg^2 \beta_2 + 1 + r_2^{*2}) v_{\theta_1}}{2r_1 k} \\ \frac{v_{\theta_1}}{2r_1} \\ \frac{(1 + r_1^{*2}) v_{\theta_1} + c_1 tg \beta_1}{2r_1 k} \\ 0 \\ \frac{(1 + r_1^{*2}) v_{\theta_2}}{2r_2 k} \\ \frac{(1 + r_1^{*2}) c_2 tg \beta_2}{2r_2 k} \\ \frac{(tg^2 \beta_2 + 1 + r_2^{*2}) v_{\theta_2}}{2r_2 k} \end{pmatrix}.$$

$$\text{avec : } a_{22} = \frac{v_{x_1} (3 tg^2 \beta_2 - tg^2 \beta_1 + 3 r_2^{*2} + r_1^{*2} + 4) + \frac{\omega^2}{2 v_{x_1}} (r_1^2 - r_2^2)}{k}$$

$$\text{et } c_{mm} = 0 \quad (m=1 \text{ à } 7), \quad c_{88} = c_1 \left[-\frac{r_1^*}{r_1} + \frac{tg^2 \beta_2 + 1 + r_2^{*2}}{k} \left(\frac{r_1^*}{r_1} + \frac{r_2^*}{r_2} \right) \right],$$

$$\text{avec } k = tg^2 \beta_2 + 2 + r_1^{*2} + r_2^{*2}.$$

L'application des schémas à pas entiers dans la zone des grilles est assujettie à une condition similaire à (13) ; le pas de temps unique pour les trois zones doit vérifier la condition [9] :

$$\Delta t \leq \overline{\Delta t} = \text{Min} \left[\Delta t_{HC}, \frac{\Delta Z}{|a_{22}|}, \frac{r \Delta \Theta}{|b_{44}^1|}, \frac{\Delta R}{|c_{88}|} \right]. \quad (13')$$

Le traitement des conditions aux limites, qui a déjà été exposé en détails dans la référence [7] est ici brièvement résumé :

- la condition aux limites la plus simple se situe dans la direction azimutale où une condition de périodicité est utilisée dans les plans $\Theta = 0$ et $\Theta = 2\pi$;
- une condition de glissement $V_x/V_z = \tan \gamma$ est appliquée sur les carters interne ($R = 0$) et externe ($R = 1$) à chaque pas entier. Les opérateurs \mathcal{L}_z^+ , \mathcal{L}_z^- , \mathcal{L}_R^+ et \mathcal{L}_R^- y sont appliqués comme dans tout autre plan $R = C^*$. Par contre, suivant la direction radiale, un schéma décentré [15] remplace le schéma classique de Mac Cormack ;
- Dans le plan d'entrée ($Z = 0$), les quatre grandeurs suivantes : P_c , T_c , γ_c et β_c sont imposées dans les cas traités où V_z a une valeur subsonique. La cinquième inconnue est calculée par intégration de l'équation de compatibilité le long de la ligne caractéristique C^- :

$$\frac{\partial Q}{\partial t} + A^1 \frac{\partial Q}{\partial Z} + A^2 \frac{\partial Q}{\partial R} + A^3 \frac{\partial Q}{\partial \Theta} + A^4 \frac{\partial V_z}{\partial Z} + A^5 = 0, \quad (14)$$

où $Q = \text{Log } p$. Les coefficients A^1 à A^5 sont fonction des conditions d'entrée P_c , T_c , γ_c et β_c .

L'équation (14) est discrétisée au moyen d'un schéma à pas entier du second ordre, semblable à (11), dans lequel les schémas à pas fractionnaires s'appliquent à des équations sous forme non conservative.

Dans le plan de sortie, la pression statique est donnée et quatre équations sont intégrées dans les cas traités où V_z a une valeur subsonique : l'équation de compatibilité le long de la caractéristique C^+ et trois équations provenant du système de base (2). Ces équations sont discrétisées au moyen d'un schéma à pas entier similaire à (11).

Un terme de viscosité artificielle [16] est utilisé afin d'atténuer les oscillations numériques parasites qui peuvent se développer et nuisent à la convergence du calcul. L'ajustement des paramètres intervenant dans ce terme permet de conserver une précision du second ordre. L'introduction d'une viscosité artificielle conduisant à une condition de stabilité un peu plus restrictive que la condition (13'), les calculs ont été réalisés avec un pas de temps égal $0.7 \Delta \overline{t}$, où $\Delta \overline{t}$ est défini par l'équation (13').

RESULTATS

Les calculs ont été réalisés sur un ordinateur CRAY-1S en mode vectoriel. Le maillage comprend approximativement 78000 noeuds (78 dans la direction axiale, 91 dans la direction azimutale et 11 dans la direction radiale) (fig. 2). La convergence vers la solution stationnaire nécessite environ 1000 pas en temps, ce qui correspond à 1 heure de calcul et à un temps physique de 20 ms. Tous les résultats présentés ont été obtenus à convergence (état stationnaire).

Le code de calcul LABICHE permet d'étudier différentes distorsions d'entrée : une distorsion de température d'arrêt et (ou) une distorsion de pression d'arrêt peuvent être couplées à une distorsion radiale et (ou) à une distorsion azimutale de la direction de l'écoulement. Ici, seule une distorsion d'entrée de la pression d'arrêt est considérée (les autres variables étant supposées rester constantes dans le plan d'entrée).

Le code a été appliqué à un banc expérimental comportant un compresseur monoétage basse pression à veine non évolutive de rapport de moyeu égal à 0.668.

Les principales caractéristiques au point nominal sont les suivantes :

| | |
|------------------------------------|---------------------------------|
| Accroissement moyen de la pression | $\frac{\Delta P_1}{P_1} = 0.62$ |
| débit | 6,96 kg/s |
| puissance absorbée | 18,73 Kw |
| vitesse de rotation | 3500 tr/an. |

Bien que la vitesse de rotation soit faible, ce compresseur a l'avantage d'avoir une charge semblable à celles des compresseurs industriels. L'étude a été réalisée en un point de la caractéristique où le dévannage est maximum, c'est-à-dire pour la valeur du débit la plus élevée possible.

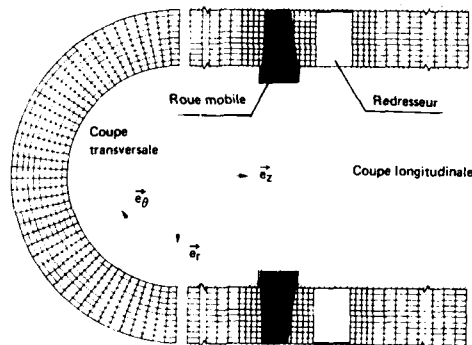


Fig. 2. MAILLAGE DU DOMAINE HORS-GRILLES

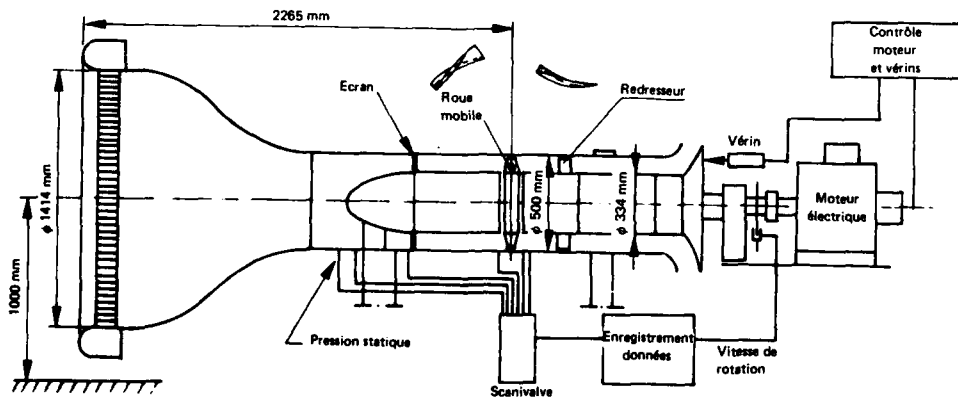


Fig. 3. DESCRIPTION DU MONTAGE EXPERIMENTAL

La figure 3 présente l'organisation générale du banc expérimental ainsi que la forme des subages.

Un écran à porosité variable, fixé à un diamètre en amont de la roue mobile, crée une distorsion de pression d'arrêt qui se propage ensuite le long de la veine. Cette perturbation induit une distribution quasi-sinusoidale de la pression d'arrêt à chaque rayon $r = \text{cte}$ dans le plan d'entrée de la veine et les incidences suivantes sur les subages de la roue mobile :

| r/re | incidence en présence de l'écran |
|--------|----------------------------------|
| 0.96 | -3° à $+2^\circ$ |
| 0.92 | $-3,8^\circ$ à $+2,7^\circ$ |
| 0.84 | $-4,4^\circ$ à $+2,6^\circ$ |
| 0.76 | $-5,2^\circ$ à $+4,2^\circ$ |
| 0.70 | $-5,4^\circ$ à $+2,6^\circ$ |

Une procédure spéciale est utilisée pour introduire les conditions à la limite dans le plan amont : les valeurs obtenues par un calcul d'écoulement méridien sont progressivement modifiées au cours du temps jusqu'à ce qu'elles atteignent les valeurs imposées de l'écoulement hétérogène. Les résultats présentés correspondent aux conditions aux limites suivantes :

- à l'entrée de la veine :

$$P_i(r, \theta) = P_{im}(r) + \sum_{n=1}^5 a_n(r) \cos n\theta + b_n(r) \sin n\theta$$

$$T_1 = 288^\circ \text{K}$$

$$\alpha_1 = 0^\circ$$

$$\beta_1 = 0^\circ$$

Les évolutions radiales de $P_{im}(r)$, $a_n(r)$ et $b_n(r)$ ($n=1, \dots, 5$) sont obtenues à partir des données expérimentales. Les figures (4b) et (4c) décrivent les évolutions radiales de P_{im} et de a_1 . La distribution de pression d'arrêt à l'entrée est présentée sur la figure 4a.

$P_{i0} = 101325 \text{ Pa}$ et $\rho V^2/2 = 2430 \text{ Pa}$ définissent respectivement la pression d'arrêt et la pression dynamique à l'entrée de la veine en écoulement homogène (sans écran).

L'amplitude de la distorsion est importante puisqu'elle atteint 50 % de la valeur de la pression dynamique moyenne à l'entrée (voir figure 4c).

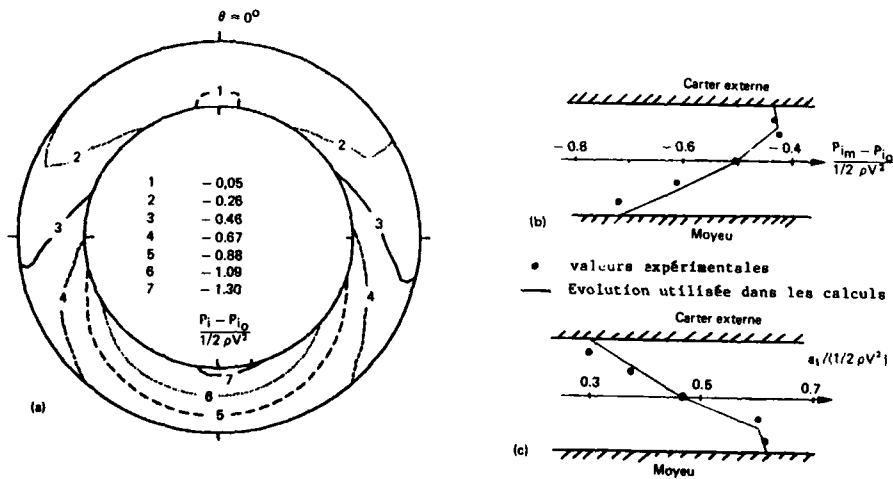


Fig. 4. DISTRIBUTION DE LA PRESSION D'ARRÊT A L'ENTRÉE

a) Coupe transversale $P_i(r, \theta) = P_{im}(r) + \sum_{n=1}^5 a_n(r) \cos n\theta + b_n(r) \sin n\theta$

b) Evolution radiale de $P_{im}(r)$

c) Evolution radiale de $a_1(r)$

- En sortie de veine :

la pression statique imposée dans le cône est donnée par la fonction suivante :

$$p_s = P_{i0} [1,0017(1-R) + 1,0012R + 2 \times 10^{-4} \cos \theta]$$

où R est donné par (1).

Elle permet de retrouver avec une bonne précision les valeurs expérimentales fournies dans ce plan de sondage.

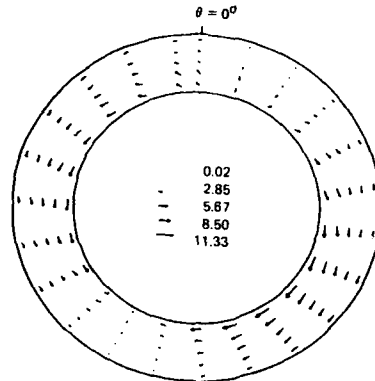


Fig. 5. PROJECTION DU VECTEUR VITESSE ABSOLUE DANS LE PLAN D'ENTREE DE LA ROUE MOBILE (en m/s)

La figure 5 montre la projection de la vitesse absolue, dans le plan d'entrée de la roue mobile obtenue par le calcul. Deux régions distinctes sont observées. Dans chacune de ces régions l'écoulement a tendance à plonger des zones de fortes pressions vers les zones de faibles pressions. De plus, à cause de l'existence de gradients radiaux l'écoulement s'infléchit vers le carter externe dans les zones de fortes pressions tandis que dans les zones de faibles pressions l'écoulement s'incurve vers le moyeu. Ces phénomènes montrent que l'écoulement est effectivement tridimensionnel quand une distorsion semblable à celle imposée dans le calcul est engendrée à l'entrée de la veine même lorsque, dans le cas étudié ici, le compresseur a des parois cylindriques.

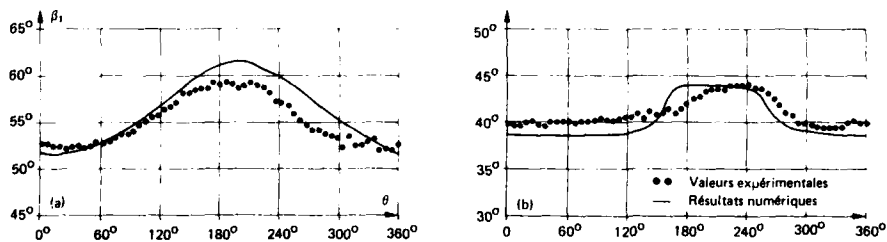


Fig. 6. REPARTITION DES ANGLES RELATIFS AZIMUTAUX β_1 et β_2 AU RAYON MOYEN

a) devant la roue mobile b) derrière la roue mobile

Les répartitions, au rayon moyen, des angles relatifs azimutaux β_1 et β_2 de l'écoulement respectivement à l'entrée et à la sortie de la roue mobile sont tracées sur les figures 6a et 6b. La valeur du débit obtenue numériquement est légèrement plus faible que la valeur du débit déterminée expérimentalement (3 I). Par conséquent, les valeurs numériques de β_1 (liées directement dans notre cas au débit) sont un peu plus élevées dans certaines régions (2,5° maximum) mais les deux évolutions sont comparables et ont tendance à calquer leur allure quasi-sinusoidale sur celle de la pression d'arrêt à cet endroit. Pour l'angle β_2 , les valeurs stationnaires expérimentales β_{2s} sont introduites dans le calcul et la distribution de l'angle β_2 est obtenue par l'intermédiaire de l'équation de transfert (9) où $\tau' = 0.5$.

Au rayon considéré, l'évolution de l'angle β_2 n'a pas un aspect sinusoidal et montre bien que les effets non-linéaires sont importants dans cette région à la traversée de la roue mobile.

L'accord entre les valeurs expérimentales et numériques est convenable sur une grande partie de l'azimut mais il est aussi évident que le modèle (9) est perfectible en particulier aux moments du décollement progressif (100° → 240°) et du recollement rapide de la couche limite le long du profil (240° → 300°).

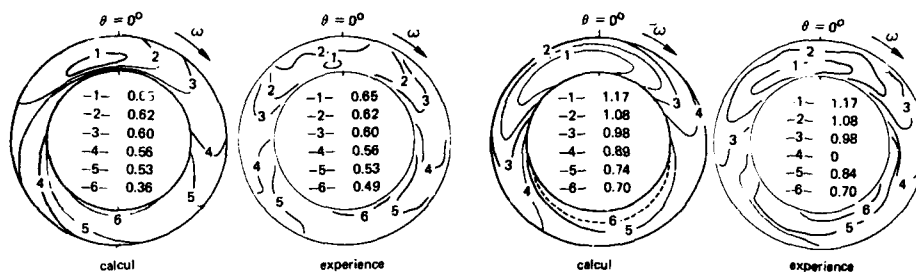


Fig. 7. COEFFICIENT DE DEBIT EN AVAL DE LA ROUE MOBILE $V_2/\omega\theta$

Fig. 8. REPARTITION DE LA PRESSION TOTALE EN AVAL DE LA ROUE MOBILE

La figure 7 présente les lignes iso-coefficient de débit obtenues expérimentalement et numériquement à l'aval de la roue mobile. Les niveaux sont bien représentés dans cette section excepté dans la partie où la pression d'arrêt est la plus faible et où un écart entre le débit numérique et le débit expérimental apparaît. La forme des isolignes obtenues par le calcul et par l'expérience est similaire. En particulier, dans la partie gauche de l'anneau l'étirement des lignes 4 et 5 est aussi visible dans le calcul ; dans la partie droite, la remontée de ces mêmes lignes vers le carter externe est bien représentée. Dans la zone de forte pression d'arrêt, les isolignes se referment autour d'un noyau (ligne 1) décalé de 10° (par rapport à $\theta = 0^\circ$) dans la direction opposée à celle de la vitesse de rotation. Ce phénomène est aussi perceptible sur la figure 8 où les isolignes de la pression d'arrêt sont tracées dans le même plan. Ce déplacement de la valeur maximale de la pression d'arrêt (P_0) est dû à un fort gradient négatif de l'incidence dans la direction de la vitesse de rotation qui produit une réduction du travail dans la roue mobile et par conséquent déplace le maximum de P_0 dans la direction opposée. Comme sur la figure précédente, la répartition de P_0 obtenue par le code de calcul est proche des données expérimentales dans la majeure partie du plan de sondage. Un écart entre les valeurs numériques et expérimentales apparaît dans la zone où la P_0 est la plus basse, c'est-à-dire là où le décollement progressif de la couche limite sur le profil n'est pas correctement représenté par le modèle utilisé (figure 6b). Tous ces résultats montrent que ce code est capable de prévoir la réponse globale d'un compresseur à une distorsion, mais des améliorations doivent être apportées en particulier sur les modèles de transfert (équations 5 et 9) afin de mieux appréhender certains détails de l'écoulement.

CONCLUSION

Le code de calcul LABICHE est validé par les résultats présentés et leur comparaison avec l'expérience. Son application s'est élargie à des compresseurs industriels [17] mais sans possibilités de comparaisons jusqu'à présent. L'utilisation de ce code devrait permettre de mieux appréhender les phénomènes complexes engendrés lors de phases transitoires dans les compresseurs et en particulier d'améliorer leur marge au pompage pour des configurations de vol peu étudiées jusqu'à maintenant.

Les modèles utilisés, pour représenter les pertes et l'écart flux-profil, ont leur propre limitation car ils ne sont pas bien adaptés lorsque de forts décollements de la couche limite apparaissent. Un nouveau modèle concernant l'écart flux-profil a été élaboré à l'ONERA et est en cours d'introduction dans le code LABICHE.

REFERENCES

- [1] - FABRI J. - Growth of a perturbation in an axial flow compressor. ASME Paper n° 78-GT-30.
- [2] - NAGANO S. and TAKATA H. - Non-linear analysis of rotating stall. Institute of Space and Aeronautic Science, University of Tokyo. Report n° 449, (1970)
- [3] - ADAMCZYK J.J. and CARTA F.O. - Unsteady fluid dynamic response of an axial flow compressor stage with distorted inflow. Project SQUID. Technical Report UARL-2-PU, (1973).
- [4] - PANDOLFI M. and COLASURDO G. - A contribution to the prediction of distorted flow in axial compressors. Recent developments in theoretical and experimental fluid mechanics. Springer-Verlag, (1979), p. 284-292.
- [5] - COLPIN J. - Propagation of inlet flow distortions through an axial compressor stage. ASME Paper n° 78-GT-109.
- [6] - GREITZER E. M. and STRAND T. - Asymmetric swirling flows in turbomachine annuli. ASME Paper n° 78-GT-109.
- [7] - BRY P., LAVAL P. and BILLET G. - Distorted flow field in compressor inlet channels. 27th Annual International Turbine Conference (ASME). London (1982) ASME Paper 82-GT-125.

- [8] - BILLET G., LAVAL P. and CHEVALIER P. - Response of an axial compressor to distorted inlet flow. Conference on computational methods in turbomachinery. University of Birmingham, TP ONERA 1984-13.
- [9] - BILLET G. et LAVAL P. - Méthode de calcul de l'écoulement tridimensionnel instationnaire dans une turbomachine axiale alimentée sous conditions hétérogènes. Rapport technique ONERA non publié (1981).
- [10] - LAVAL P. - Schémas explicites de désintégration du second ordre pour la résolution des problèmes hyperboliques non linéaires : théorie et application aux écoulements transsoniques. NT ONERA 1981-10. English translation ESA-TT-768.
- [11] - HUARD J. - Détermination expérimentale des lois de transfert de perturbations à la traversée d'un compresseur axial. PEP 68th specialists' meeting on engine response to distorted inflow conditions. Munich 8-9 sept. 1986.
- [12] - MACCORMACK R.W. - The effect of viscosity in hypervelocity impact cratering. AIAA Paper n° 69-364.
- [13] - LAVAL P. - Nouveaux schémas de désintégration pour la résolution des problèmes hyperboliques et paraboliques non linéaires : applications aux équations d'Euler et de Navier-Stokes. La Recherche Aéronautique n° 1983-4, French and English editions.
- [14] - LAVAL P. - Théorie et méthodes numériques de résolution des équations aux dérivées partielles. NT ONERA n° 1979-2. English translation ESA-TT-606.
- [15] - KUTLER P., REINHARDT W.A. and WARMING R.F. - Numerical computation of multishocked three-dimensional supersonic flow field with real gas effects. AIAA Paper n° 72-702.
- [16] - LAVAL P. - Calcul de l'écoulement instationnaire transsonique autour d'un profil oscillant par une méthode à pas fractionnaires. XII Biennial Fluid Dynamics, Pologne. Septembre 1975. Archives of Mechanics, Warszawa, (1976).
- [17] - BILLET G., CHEVALIER P. et LAVAL P. - Simulation numérique du comportement d'un compresseur axial alimenté par un flux hétérogène. La Recherche Aéronautique n° 1985-4 p.229-242.

DISCUSSION

Ph.Ramette, Fr

Ceci n'est pas une question, mais plutôt un commentaire:

- (a) Votre conférence montre clairement l'importance des gradients radiaux qui conduisent à un écoulement fortement tridimensionnel.
- (b) Les moyens informatiques nécessaires pour traiter ce type de calcul deviennent très importants, surtout en capacité mémoire, et risquent de limiter l'extension de ce type de méthode. Vous avez en effet indiqué un maillage de 78,000 points, et pour le film que vous avez présenté, une heure de calcul sur CRAY-1S avec 1,500 iterations.

Author's Reply

Je ne pense pas que les risques de limitation dans l'extension de ce type de méthode soient grands, car on doit compter dans les années à venir, sans être trop optimiste, sur des progrès encore très spectaculaires (en capacité mémoire et en rapidité) des ordinateurs.

H.B.Weyer, Ne

I wonder whether it is possible that the stator has no effect on the distortion pattern, particularly if the stator load is not equal to zero. Please comment.

Author's Reply

For this compressor it is normal because this compressor has a constant channel. This is also observed in the experiment.

CALCUL DU COMPORTEMENT D'UNE GRILLE D'AUBES EN REGIME
DE DECROCHAGE DYNAMIQUE*

P. GILLANT - P. SAGNES - JP. OLLIER

Société BERTIN et CIE

Allée Gabriel Voisin - 78373 PLAISIR CEDEX - France

RESUME

La méthode de calcul décrite dans ce document permet la représentation pour un coût relativement faible de l'écoulement subsonique instationnaire à travers une grille d'aubes bidimensionnelle de compresseur. Cette modélisation utilise la méthode des singularités ; celles-ci sont disposées sur les profils et sur les filets tourbillonnaires formant un sillage en aval des aubes. Dans les cas où l'on tient compte d'une variation de hauteur de veine, de la compressibilité du fluide ou encore lorsque l'on considère une roue mobile (avec variation du rayon de la nappe) des singularités discrètes sont ajoutées dans le canal interaube.

Des lois de transfert de grille établies lorsqu'aucun décollement de la couche limite n'intervient sont présentées.

Une extension au régime de décrochage dynamique est introduite. Les résultats déjà obtenus montrent qu'au voisinage du point de décollement, un calcul capable de décrire convenablement à la fois la ligne de déplacement et l'écoulement local est nécessaire.

LISTE DES NOTATIONS

Z : affixe complexe
 β : angle relatif à la direction axiale
V : vitesse complexe de l'écoulement
 ψ : potentiel de l'écoulement
F : poussée induite sur le profil
 \bar{Q} : débit de sources lié au profil
 λ : densité de circulation d'un tourbillon lié au profil ou libre
 γ : densité de circulation d'un tourbillon situé sur les lanières du sillage
N : nombre de segments sur le profil
p : pas de la grille
c : corde de l'aube génératrice
h : hauteur de veine
r : rayon
 m, θ : coordonnées cylindriques
x, y : coordonnées cartésiennes
 ΔS : longueur d'un segment
 ω : vitesse de rotation
 Γ_0 : circulation totale
 Γ : circulation autour du profil
X : coefficient de pertes
 $fr = \frac{\omega c}{2\pi |V_\infty|}$: fréquence réduite

* travaux financés par la Direction des Recherches et Etudes Techniques (Direction Générale de l'Armement).

INDICES

k : numéro du segment du profil
 m : numéro du tourbillon libre
 TL : indice d'affixe d'un tourbillon libre
 NT : indice du temps t
 n : indice de maille dans le canal interaube
 f : caractérise la source résiduelle
 ej : numéro d'un segment sur le sillage extradados
 ij : numéro d'un segment sur le sillage intrados
 1 : valeur en amont de la grille
 2 : valeur en aval de la grille
 k_{dac} : caractérise le point de décollement
 ∞ : valeur infinie moyenne

1. - INTRODUCTION

Les défauts d'alimentation à l'entrée des turboréacteurs aéronautiques provoqués par des causes extérieures ou par des configurations de vols particulières, induisent des inégalités circonférentielles et radiales de l'écoulement en amont du compresseur.

Les travaux de modélisation des phénomènes mis en jeu comportent deux types d'approches : d'une part, l'élaboration de codes de calculs étudiant la propagation de ces hétérogénéités dans le champ du compresseur, d'autre part, la recherche de méthodes de détermination théorique des lois de transfert (au sens généralisé du terme) de grilles d'aubes de turbomachines, ces lois intervenant comme conditions limites dans les calculs de propagation.

Ces phénomènes instationnaires se traduisent au niveau des roues du compresseur par des variations locales de l'incidence de l'écoulement relatif et des sollicitations dynamiques. Le point de fonctionnement de chaque étage peut également varier et pénétrer dans la zone de pompage provoquant ainsi la dégradation des performances et des risques mécaniques importants.

La démarche qui a conduit à mettre en oeuvre les deux approches décrites précédemment vise une formulation peu complexe des phénomènes physiques mais doit permettre d'établir des outils numériques suffisamment souples d'emploi pour être utilisés dès le stade de l'avant-projet.

La suite de cet article détaille les calculs permettant la représentation de l'écoulement dans une grille d'aubes, tout d'abord dans le cas du fluide parfait, incompressible. La prise en compte des effets dus à la compressibilité et des effets visqueux est ensuite présentée. Enfin après l'établissement de lois de transfert bidimensionnelles correspondant à de tels écoulements, les problèmes que posent l'étude et la représentation du décollement de la couche limite sur l'extrados des profils d'aubes sont exposés.

2. - DETERMINATION DES LOIS DE TRANSFERT DE GRILLE D'AUBES BIDIMENSIONNELLE EN ECOULEMENT VISQUEUX NON DECOLLE

La méthode de calcul utilisée est la méthode des singularités ; elle a l'avantage de réduire d'un degré la dimension des équations puisqu'il s'agit d'une méthode intégrale et est par conséquent moins coûteuse en temps calcul. De plus, bien qu'elle ne soit rigoureusement applicable qu'en écoulement incompressible, une extension au domaine compressible sans choc par adjonction de puits ou de sources judicieusement placés dans le champ de l'écoulement est possible. De telles méthodes permettent également de représenter l'écoulement en repère relatif.

2.1. - Écoulement en fluide parfait

Hypothèses de calcul

L'ensemble des équations à résoudre est constitué des équations d'Euler, de conservation de la masse et des conditions aux limites.

L'écoulement est supposé bidimensionnel, irrotationnel, et dans un premier temps incompressible ; le fluide est considéré de plus comme parfait ; il s'écoule à travers une grille d'aubes infinie. Cet écoulement admet une périodicité spatiale, c'est-à-dire que l'écoulement se reproduit identiquement pour une distance égale au pas de la grille d'aubes.

Le schéma de la grille d'aubes étudiée et les notations utilisées sont rassemblés figure 1.

Le principe du calcul est le suivant : le profil d'une aube est discrétisé en segments auxquels sont associés des répartitions linéiques uniformes de sources G_k et de tourbillons d'intensités λ_k . La donnée d'une vitesse infinie moyenne et la connaissance des intensités des singularités déterminent entièrement l'écoulement.

Remarque : pour des questions de commodité et d'efficacité d'écriture, l'ensemble des calculs est effectué en notations complexes.

Vitesse induite en un point Z

Le profil de l'aube génératrice de la grille est découpé en N segments comme le montre la figure 2.

A chacun des N segments sont associés une source et un tourbillon lié. La résolution numérique de l'écoulement implique des résolutions de systèmes linéaires de rang élevé. Ces calculs sont rapides si la diagonale du système est dominante. Cette condition est réalisée en choisissant une répartition de sources variables et une répartition de tourbillons constants, soit $\lambda_k = \lambda = cte$

En ajoutant les vitesses induites en Z par tous les segments de tous les profils, il vient :

$$V(Z) = - \sum_{k=1}^N \frac{G_k - \lambda}{2\pi} e^{-\lambda \beta_k} \ln \frac{\operatorname{sh} \frac{\pi}{p} (Z - Z_{k+1})}{\operatorname{sh} \frac{\pi}{p} (Z - Z_k)}$$

où G_k est l'intensité de la source répartie uniformément sur le segment $[Z_k, Z_{k+1}]$

En écoulement instationnaire, le principe de conservation de la circulation globale et la condition de Kutta-Joukowski conduisent à l'émission d'un tourbillon libre d'intensité λ_m et d'affixe Z_{TLM} à un instant t considéré. La vitesse induite en Z par l'ensemble des tourbillons d'intensité λ_m s'écrit

$$v(Z) = \sum_{k=-\infty}^{+\infty} -\frac{i\lambda_m}{2\pi} \frac{1}{Z - Z_{TLM} - ikp} = -\frac{i}{2p} \lambda_m \coth \frac{\pi}{p} (Z - Z_{TLM})$$

En ce point, la vitesse globale sera obtenue en sommant les deux expressions précédentes soit

$$v(Z) = -\sum_{k=1}^N \frac{\sigma_k - i\lambda}{2\pi} e^{-i\beta_k} \ln \frac{\operatorname{sh} \frac{\pi}{p} (Z - Z_{k+1})}{\operatorname{sh} \frac{\pi}{p} (Z - Z_k)} - \frac{i}{2p} \sum \lambda_m \coth \frac{\pi}{p} (Z - Z_{TLM}) + v_\infty$$

Calcul des singularités en fluide parfait

Les inconnues du problème sont :

- N sources ou puits σ_k répartis linéairement sur les segments du profil
- λ intensité du tourbillon lié
- $\lambda_{t+\Delta t}$ intensité du tourbillon émis au bord de fuite.

Celles-ci sont déterminées à partir du système formé par :

- (I) $\left\{ \begin{array}{l} - N \text{ conditions de glissement sur le profil} \\ - \text{ la condition de Kutta-Joukowski} \\ - \text{ la conservation de la circulation totale.} \end{array} \right.$

En fait, la condition de Kutta-Joukowski se traduit par une égalité des pressions au bord de fuite extrados et intrados : si de plus φ représente le potentiel de l'écoulement, nous avons, en écrivant l'équation de Bernouilli aux deux points de contrôle des segments 1 et N ,

$$\frac{\partial}{\partial t} (\varphi_1 - \varphi_N) + \frac{1}{2} (v_1^2 - v_N^2) = 0$$

soit

$$\frac{\partial \Gamma}{\partial t} = \frac{1}{2} (v_N^2 - v_1^2)$$

si $\Delta V = |v_1| - |v_N|$ le système (I) se transforme en

- N conditions de tangence
- expression de ΔV en fonction des singularités

$$(II) \left\{ \begin{array}{l} (1) - \frac{\partial \Gamma}{\partial t} = \frac{1}{2} (v_N^2 - v_1^2) \\ (2) - \Gamma_{Nt+\Delta t} = \Gamma_{Nt} + \lambda_{t+\Delta t} \end{array} \right.$$

la résolution du système (II) donne ΔV et $\lambda_{t+\Delta t}$ et la résolution du système formé par les autres équations permet de déterminer la valeur des singularités.

Remarquons que si V_1 représente la vitesse de l'écoulement à l'infini amont et si Γ_0 représente la circulation totale initiale, nous aurons

$$V_1 = V_\infty + \frac{\Gamma_0}{2p}$$

Cela signifie que, connaissant la relation biunivoque liant V_∞ et Γ_0 déterminée en écoulement quasi-stationnaire, la donnée de V_1 permet de connaître la vitesse infinie moyenne V_∞ (en quasi-stationnaire nous avons $\Delta V = 0$) à chaque instant.

Convection des tourbillons libres

Les tourbillons libres émis aux instants précédents se déplacent sous l'influence du champ global des vitesses induit par l'ensemble des singularités. Nous remarquons que s'ils sont suffisamment éloignés du profil, il est possible de coalescer les tourbillons de même signe car leur influence sur le profil devient pratiquement indépendante de leur position. Cela permet de réduire le nombre de tourbillons libres et donc le temps du calcul de l'écoulement à chaque pas de temps.

2.2. - Extension aux écoulements à travers une grille mobile à hauteur de veine variable et aux écoulements compressibles subsoniques (application de la méthode de VAN DEN BRAEMBUSSCHE)

Les hypothèses que l'on fait dans de telles configurations sont les suivantes :

- l'écoulement est supposé irrotationnel en dehors de la zone de couche limite et de courant axisymétrique, invariante au cours du temps, la force et la densité de tube de courant sont fournies par un calcul préalable et sont représentées sur la figure 3.
- la vitesse de rotation de la grille est supposée constante dans le temps.
- l'introduction de l'équation d'état des gaz parfaits permet de tenir compte des effets de compressibilité du fluide ; l'écoulement est supposé adiabatique et sans onde de choc.

Dans le cas où les écoulements sont étudiez sur des aubes de courbure cylindriques, on applique une transformation conforme de façon à définir une périodicité p spatiale de l'écoulement à partir du pas angulaire $\Delta\theta$ de la grille. Cette transformation est de la forme :

$$dx = \frac{r_1}{r} dm \quad \text{et} \quad dy = -r_1 d\theta$$

où r_1 représente un rayon de référence.

Dans la grille d'aubes plane ainsi obtenue, on peut calculer un champ de vitesse v_1 par la méthode des singularités.

L'application de cette méthode, à l'aide de théories de courbes, permet de connaître de la distribution dans le champ d'écoulement :

- de la divergence de la vitesse, fournie par l'équation de continuité
- de la composante normale du rotationnel de vitesse.

L'équation de continuité s'écrit :

$$v = \frac{\partial v_x}{\partial x} - \frac{\partial v_y}{\partial y} = -v_\theta \frac{1}{r} \frac{dr}{dx} - \frac{r^2}{r^2} \frac{1}{p} \frac{D\rho}{Dt} \quad (2)$$

L'équation du rotationnel :

$$\lambda = \frac{\partial v_y}{\partial x} - \frac{\partial v_x}{\partial y} = 2 \omega \frac{r}{r_1} \frac{dr}{dx} \quad (4)$$

Les équations (3) et (4) impliquent que le rotationnel ainsi que la divergence de l'écoulement sont imposés en tout point du champ. Une répartition surfacique de sources ou puits d'intensités σ et de tourbillons d'intensités λ permet de décrire une telle distribution.

La vitesse induite par ces singularités, placées dans le canal inter-aube, s'écrit de la façon suivante :

$$v_z = -\frac{1}{2p} \int_{-\infty}^{+\infty} dx \int_0^{LP} \lambda_j \coth \frac{\pi}{p} (z-z_j) dy + \sum_{n=1}^{NC} \iint_{S_n} \frac{\sigma}{2p} \coth \frac{\pi}{p} (z-z_0) dx_0 dy_0$$

Le champ d'écoulement est en effet discrétisé en NC mailles trapézoïdales dans lesquelles sont définis des points de contrôle ZC_n permettant de localiser et calculer des sources ponctuelles. Une telle maille est représentée figure 4. La répartition surfacique de sources sur la maille n est remplacée par une source ponctuelle d'intensité équivalente

$$\sigma_n = \iint_{S_n} \left(v_x \frac{1}{h} \frac{dh}{dx} + \frac{1}{r_1^2} \frac{1}{\rho} \frac{Dr\rho}{Dt} \right) dx dy$$

$$\text{soit } \sigma_n \approx \Delta y_n \left[v_{x_n} L_n \frac{h_{n+1}}{h_n} + (x_{n-1} - x_n) \frac{r_{n+1}^2 + r_n^2}{r_1^2} \frac{1}{\rho} \frac{Dr\rho}{Dt} \right]$$

$$\text{soit } v_z = -\frac{L\omega}{r_1} \left(r^2 - \frac{r_1^2 + r_2^2}{2} \right) + \sum_{n=1}^{NC} \frac{\sigma_n}{2p} \coth \left(\frac{\pi}{p} z - ZC_n \right)$$

On expose le calcul d'écoulement compressible est montré sur les figures 5 et 6. La figure 5 présente le canal inter-aube avec la position des 44 sources retenues pour tenir compte de la divergence de la vitesse d'écoulement dont correspond à Mach 0,6 et à une incidence de 2°. Les sources sont tracées sur la figure 6.

Une étude de sensibilité sur la finesse de discrétisation du maillage (c'est-à-dire sur le nombre et la position des sources du canal) reste nécessaire pour déterminer la taille optimale des mailles conduisant à une bonne modélisation de l'écoulement.

3.1. Prise en compte des effets visqueux

Les effets visqueux sont concentrés le long des profils des aubes en une couche limite. Le calcul de cette couche limite a été effectué à l'aide du code de calcul mis au point au CERN par Messieurs CHUSTIL et HOUDYLOT ; il permet de développer une couche limite laminaire et turbulente à la fois sur l'extrados et l'intrados des aubes.

Le calcul est effectué par une méthode intégrale basée sur l'utilisation de solutions semblables ; il est applicable à des nombre de Mach modérés inférieurs à 2, en paroi adiabatique.

Cette couche limite est prolongée après le bord de fuite par un sillage sur lequel sont concentrés des tourbillons dans à l'extrados et à l'intrados. En régime permanent, les intensités de ces tourbillons sont égales et de signes opposés (conservation de la circulation totale).

Couplage, écoulement potentiel, couche limite en régime permanent

En régime permanent, les inconnues du problème sont les N singularités σ_k réparties sur le profil, les intensités du tourbillon λ et des tourbillons $\pm \delta$ émis aux bords de fuite extrados et intrados. Une dernière inconnue σ_f est rajoutée lors de la résolution de ce calcul. Son intensité est telle que la somme des sources est nulle ce qui garantit rigoureusement la conservation du débit ; elle est répartie uniformément sur l'ensemble du sillage tourbillonnaire. Le choix de ce positionnement résulte de l'influence de cette source sur le profil de vitesse sur l'aubage, car dans ce cas, aucune déformation locale des vitesses sur le profil n'a été observée.

L'écoulement est entièrement déterminé dès que sont connues :

- les valeurs des singularités
- la forme du sillage
- l'épaisseur de déplacement de la couche limite.

Calcul des singularités en écoulement permanent

La condition de Kutta-Joukowski est remplacée par deux égalités ; elles traduisent que les intensités des tourbillons émis aux bords de fuite intrados et extrados sont égales aux rotationnels locaux de la couche limite en ces points c'est-à-dire aux vitesses locales de l'écoulement potentiel.

Les N conditions de tangence sont exprimées sur le profil engrainé ; celles-ci ainsi que l'équation caractérisant l'émission du rotationnel au bord de fuite sont rassemblées en une équation matricielle de rang $N + 1$:

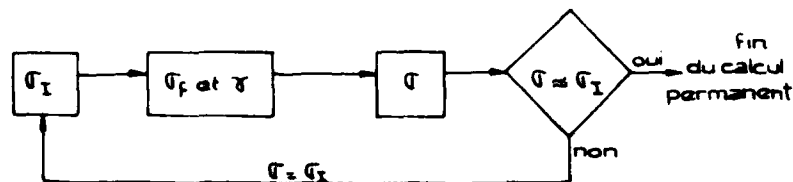
$$A \cdot \sigma = SM + AF \cdot \sigma_f + BF \cdot \sigma_f + S \delta$$

La matrice A est indépendante des grandeurs aérodynamiques de l'écoulement et ne contient que des termes liés aux coordonnées géométriques du profil. Ce système est donc résolu de manière implicite ce qui présente l'avantage de n'inverser qu'une seule fois la matrice A . La solution du vecteur σ est obtenue par convergence du système suivant :

$$\sigma = \sigma^I$$

$$\sigma = A^{-1} \cdot SM + A^{-1} \cdot AF \cdot \sigma^I + A^{-1} \cdot BF \cdot \sigma_f + A^{-1} \cdot S \delta$$

σ_f et δ sont ici supposées connues. Leur calcul est effectué au préalable par résolution du système formé par les équations de l'émission du rotationnel de couche limite au bord de fuite extrados et de conservation du débit global d'où le schéma suivant :



Principe de résolution du problème en écoulement permanent

Après un calcul effectué en fluide parfait (on prend $\Delta V = 0$) un calcul de couche limite donne les épaisseurs de déplacement en tout point du profil.

La couche limite étant figée, la forme du sillage tourbillonnaire est obtenue par itérations successives consécutivement au calcul des singularités, donc du champ de vitesses.

La solution finale est obtenue quand :

- l'allure de la couche limite est figée,
- les sillages tourbillonnaires sont confondus avec des lignes de courant.

L'organigramme présenté sur la figure 7 montre le principe de résolution de l'écoulement permanent.

Couplage écoulement potentiel, couche limite en instationnaire

Le calcul instationnaire diffère du précédent en ce sens que les tourbillons répartis sur chaque filet tourbillonnaire ne sont plus d'intensités égales.

Les lanières tourbillonnaires sont donc découpées en NSE ou NSI segments d'intensité σ_j ou σ_{Lj} qui sont convectés au cours du temps. Si ΔS_{e_j} est la longueur du $j^{\text{ème}}$ segment le théorème de Kelvin permet d'écrire que la circulation $\sigma_{e_j} \Delta S_{e_j}$ se conserve lors de sa convection.

La figure 8 détaille la forme du sillage situé derrière le bord de fuite de l'aube.

Par ailleurs si les intensités des tourbillons émis au bord de fuite à l'extrados et à l'intrados sont égales à σ_{e_1} et σ_{L_1} , le principe de conservation de la circulation permet d'écrire :

$$\Gamma_{NT} = \Gamma_{NT+1} + \Delta S_{L_1} \sigma_{L_1} + \Delta S_{e_1} \sigma_{e_1}$$

On notera enfin que le sillage a été prolongé relativement loin au-delà du profil ; il est tronqué à une distance choisie arbitrairement et un tourbillon libre résiduel est émis à cet endroit ; celui-ci est suffisamment loin pour que son influence sur le calcul de vitesse au voisinage du profil ne dépende plus guère de sa position. Son intensité résulte d'une coalescence des intensités tourbillonnaires des derniers segments du sillage que l'on doit convecter.

Principe de résolution

Le calcul de l'écoulement dans le canal interaube, de la déformation de la couche limite et du sillage, s'effectue de la façon suivante au temps $t + \Delta t$:

- convection du sillage, détermination de $\sigma_{e_j}, \sigma_{L_j}$ ($j \neq 1$) par application du théorème de Kelvin et de l'intensité du tourbillon situé au bout du sillage,
- calcul des singularités σ_f, σ_f et σ_{L_1} , la nouvelle forme du sillage étant donnée,
- calcul de σ_{e_1} à partir de σ_{L_1}
- calcul du champ de vitesse induit par les nouvelles singularités ; ces vitesses sont évaluées sur les points de contrôle du profil engraisé
- ce nouveau champ de vitesses évalué, on réalise un calcul de couche limite.

2.4. - Formulation des lois de transfert (en régime non décollé)

Remarque : les distorsions choisies sont des pulsations sinusoïdales de débit.

L'écoulement étant plan, ces lois de transfert de grilles sont constituées :

- d'une loi de transfert tangentiel correspondant à la projection tangentielle de l'équation du mouvement,
- d'une loi de transfert axial correspondant à la projection de l'équation du mouvement sur une ligne de courant ou à l'évolution isentropique de l'écoulement.

Les formulations présentées sont établies à partir d'une approche monodimensionnelle fournissant des bilans entrée/sortie moyens (intégration du moment cinétique et du débit sur le pas de la grille). Les coefficients intervenant dans chacune des deux formulations peuvent à leur tour être explicités, pour des grilles données, en fonction des paramètres de l'écoulement et de la distorsion.

La première loi de transfert est couramment établie à partir de l'angle d'entrée β_1 et de l'angle de sortie β_2 ; la modélisation classique au premier ordre utilisée est de la forme :

$$\beta_2 = \bar{\beta}_2 - A_2 (\beta_1 - \bar{\beta}_1) - B_2 \frac{\partial \beta_1}{\partial t} \quad (5)$$

Compte tenu de l'allure de la caractéristique permanente déviation/incidence (figure 9) et de la plage d'incidence balayée, une loi au premier ordre s'est avérée suffisante.

La figure 10 présente l'influence de la fréquence réduite de la distorsion sur les cycles déviation/incidence. On notera que l'évolution de l'ensemble des cycles instationnaires est tout à fait similaire à celle obtenue avec des hypothèses de fluide parfait.

La figure 9 montre l'évolution de $\bar{\beta}_2$, angle de sortie moyen du cycle, en fonction de l'incidence moyenne, de l'amplitude, de la fréquence réduite et du nombre de Mach. L'angle de sortie moyen, $\bar{\beta}_2$ varie, pour la fréquence réduite considérée (0.37) suivant l'incidence moyenne du cycle. Le point moyen du cycle n'est pas en général sur la caractéristique quasi-stationnaire et l'écart semble s'accroître de manière importante vers les grandes incidences.

Les variations de A_2 , B_2 sont précisées sur les figures :

- 11 en fonction de la fréquence réduite
- 12 en fonction de l'incidence moyenne de la distorsion
- 13 en fonction de l'amplitude (pour 2 valeurs du taux de turbulence α 0.01 et 0.05)
- 14 en fonction du nombre de Mach moyen.

Il est à noter que lorsque l'on fait varier le taux de turbulence, les résultats deviennent constants à partir d'un taux de turbulence de 5 %. Le point de transition est en effet pratiquement remonté au bord d'attaque et les effets dus à son déplacement disparaissent.

Les variables β_1 , β_2 sont des grandeurs classiques couramment utilisées pour représenter les caractéristiques permanentes d'une grille d'aubes de compresseur axial. Néanmoins, ces angles n'interviennent pas directement, en tant que variable aérodynamique de base, dans les équations instationnaires de mécanique des fluides.

Cette notion de déviation peut être abordée par le biais du moment cinétique dont le comportement est décrit dans la projection tangentielle de l'équation du mouvement.

Le bilan de moment cinétique appliqué sur une nappe de courant cylindrique s'écrit :

$$\int_0^L \frac{1}{V_2} \frac{\partial V \theta}{\partial t} dz + V \theta_2 = V \theta_1 + \frac{F \theta}{\rho P V_2}$$

Compte tenu de la forme de la distorsion étudiée (pulsation sinusoïdale de débit), cette équation peut être modélisée au premier ordre sous la forme :

$$V \theta_2 + A \frac{dV \theta_2}{dt} + B V_{z1} + C V \theta_1 + D \frac{dV \theta_1}{dt} = 0$$

$F \theta$ est ici supposée fonction linéaire de V_{z1} et $V \theta_1$.

Ce type de formulation paraît plus physique dans la mesure où les coefficients qui y interviennent pourront être identifiés à des expressions intégrales des paramètres aérodynamiques dans le champ d'écoulement, ce qui facilite leur formulation en fonction des paramètres de l'écoulement et de la distorsion.

La deuxième loi de transfert fournit la variation au cours du temps du coefficient de perte χ dont la formulation a été proposée par TAKATA et NAGANO :

$$\chi = \frac{2}{V_1^2} \left[H_1 + \frac{1}{2} V_1^2 - H_2 - \frac{1}{2} V_2^2 - L \frac{\partial V_2}{\partial t} \right]$$

Pour rester cohérent avec la formulation de la loi de déviation, la loi de perte est présentée sous la forme :

$$A \frac{d\chi}{dt} + (\chi - \bar{\chi}) + B (\beta_1 - \bar{\beta}_1) = 0$$

La figure 15 montre l'influence de la fréquence réduite sur les cycles pertes/incidence. Au cours de ces cycles la valeur du coefficient de pertes χ peut être négative ; ce fait n'est cependant pas en contradiction avec les lois de la mécanique des fluides, car il s'agit de comparaisons entre des valeurs entrée/sortie évaluées au même instant et ne tenant donc pas compte du temps de convection des particules fluides. Ce coefficient de pertes offre l'avantage d'être accessible expérimentalement en faisant des bilans entrée/sortie de pressions totales instantanées.

5. - EXTENSION AU DÉCOLLEMENT DYNAMIQUE

Il s'agit, dans ce chapitre, de considérer les cas d'écoulement à grandes incidences provoquant le décollement prématuré de la couche limite, en général sur l'extrados des profils d'aubes. Une poche de recirculation prend naissance au point de décollement et est d'autant plus importante que le point de décollement s'éloigne du bord de fuite.

Le principe de résolution de l'écoulement est tout à fait identique à celui décrit précédemment ; seuls quelques points délicats demandent à être approfondis, l'objectif étant de n'introduire aucun élément expérimental dans le calcul.

5.1. - Conditions de l'écoulement

Le principe de modélisation adopté repose essentiellement sur l'hypothèse que les zones fortement cisailées où la viscosité joue un rôle prépondérant, restent extrêmement minces.

Le champ d'écoulement peut donc être décrit en deux zones potentielles à pression totale constante.

A l'intérieur de la poche de recirculation, la vitesse du fluide est faible et conduit pratiquement à l'obtention de la poche à pression statique uniforme (correspondance avec la pression d'eau morte).

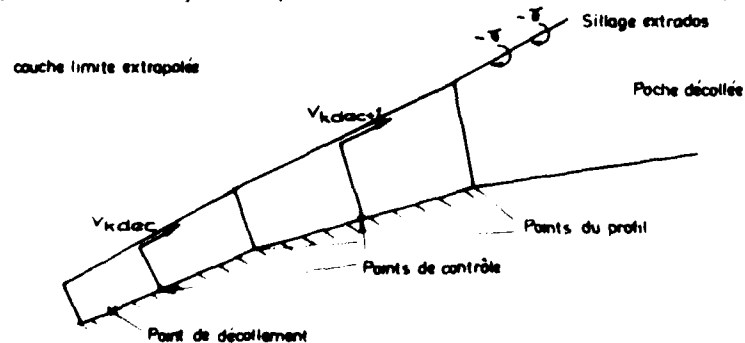
Les deux zones étant ainsi définies, les N conditions de tangence s'écrivent :

- tangence de l'écoulement au profil engraisé de l'épaisseur de couche limite, en dehors de la poche décollée,
- tangence de l'écoulement au profil réel de l'aube, à l'intérieur de la poche.

Quelle que soit la position du point de décollement, le système matriciel constitué des N équations de tangence et de l'expression du rotationnel de l'écoulement au bord de fuite intrados reste constamment de rang $N + 1$. Par conséquent le principe de résolution adopté en écoulement non décollé peut être conservé, et la matrice d'influence A n'est inversée qu'une seule fois au cours de cycles instationnaires.

3.2. - Traitement au voisinage du point de décollement

Le point de décollement est l'endroit le plus sensible du point de vue numérique. En effet, trois conditions sont imposées dans le voisinage de ce point : deux conditions de tangence (à l'intérieur et à l'extérieur de la poche) et une condition d'émission du rotationnel de la couche limite. La modélisation adoptée met en oeuvre un calcul particulier de l'épaisseur de déplacement à proximité du point de décollement, qui est un point singulier dans un calcul direct de couche limite. Ce calcul n'a pas pour ambition de résoudre les équations de couche limite, en particulier après le décollement turbulent : il consiste à extrapoler l'épaisseur de déplacement sur le segment suivant le segment du point de décollement selon le schéma ci-après.



Une critique que l'on peut faire est que ce schéma ne résoud évidemment pas l'écoulement au voisinage du point de décollement. L'objectif des travaux présentés étant de qualifier l'approche globale, cette technique doit être considérée comme une première approximation du problème, qui sera traité ultérieurement de manière plus approfondie.

3.3. - Résultats en écoulement permanent

Le code numérique a été appliqué sur une grille d'aubes à profil NACA 65M définie par les paramètres suivants :

- angle 23.5°
- corde 96.25 mm
- pas 72.95 mm
- nombre de segments $N = 40$.

Déviation

La forme de la courbe de déviation (figure 16) s'incurve de manière classique quand l'incidence augmente ; on remarque que pour ce type de grille les effets visqueux en régime décollé ont une influence progressive.

Distribution de pression

Celle-ci est montrée figure 17 pour une incidence de 30° ; le point de décollement extrados se situe à environ 70 % de corde du bord d'attaque ; à proximité de celui-ci, la pression varie de manière significative pour se raccorder au niveau de pression qui s'applique au bord de fuite intrados.

Des comparaisons théorie/expérience ont été effectuées sur un profil isolé LC 90 D (pour des raisons de disponibilité des résultats) à des incidences où l'on peut observer un décollement. Les calculs ont été comparés aux résultats expérimentaux obtenus par l'ONERA ; la coïncidence est excellente jusqu'au point de décollement. A ce niveau, le calcul détermine dans la poche un palier de pression se décalant vers les valeurs obtenues au voisinage du bord de fuite intrados, pour respecter la condition de Kutta-Joukowski. Les relevés expérimentaux montrent que c'est plutôt la pression intrados qui s'adapte à celle de la poche décollée (figure 18).

Coefficient de perte

En régime décollé, il apparaît que la valeur du coefficient de perte dépend énormément de la position du point de décollement ; celui-ci d'après les hypothèses énoncées au paragraphe précédent ne peut se déplacer que sur les points du maillage définissant le profil de l'aube. Il s'ensuit que pour les incidences provoquant un décollement de la couche limite, la valeur du coefficient suit une évolution par paliers et non forcément continue.

3.4. - Déformation du sillage en écoulement instationnaire

L'écoulement amont correspond dans le cas étudié à une pulsation sinusoïdale de débit dont les caractéristiques sont :

$$\begin{aligned} V_y &= 27.8 && (\text{m/s}) \\ V_x &= 29.5 - 2 \cos \omega t && (\text{m/s}) \\ \text{avec } \omega &= 1289 && (\text{rd/s}) \end{aligned}$$

La fréquence réduite associée à ce cas vaut 0.48. Ces valeurs ont été choisies de telle manière que le point de décollement se situe à l'instant initial à environ 2/3 de la corde et qu'il puisse se déplacer à la fois vers le bord d'attaque et vers le bord de fuite extrados.

La déformation du sillage est représentée sur la figure 19. Si T représente la période du cycle étudié, les sillages tracés correspondent aux temps $t = 0$ et $t = 2T$.

Les ondulations observées sont dues à la différence des densités tourbillonnaires sur chacun des segments situés le long du sillage.

3.5. - Critique du modèle en régime décollé et perspectives de développement

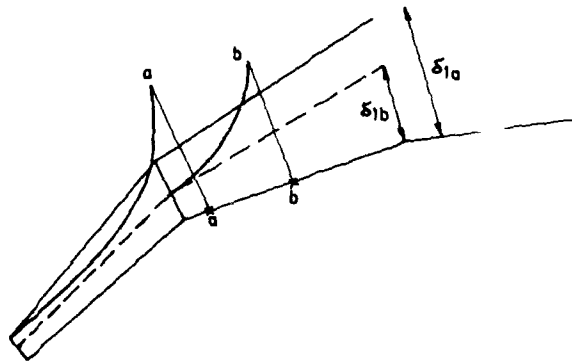
Les planches présentées précédemment montrent que la résolution de l'écoulement au voisinage du point de décollement est relativement grossière.

La vitesse calculée sur les segments situés après ce point, diminue très rapidement et le gradient de pression défavorable correspondant empêche, pratiquement la remontée du point de décollement vers le bord de fuite, lors d'un cycle instationnaire.

Au cours de la convergence du calcul en écoulement permanent, ce phénomène ne se produit pas. En effet, le premier calcul de couche limite effectué après la résolution en fluide parfait, permet d'obtenir un point de décollement situé plus près du bord de fuite qu'il n'est en réalité ; au fur et à mesure des itérations, ce dernier se déplace vers le bord d'attaque jusqu'à sa position finale.

Il est clair que la zone de recompression au niveau du point de décollement est à l'origine du problème rencontré. Il en résulte que la pression statique (constante dans la poche) est vraisemblablement mal calculée. On notera que l'hypothèse d'une pression totale constante (qui résulte de la manière de poser le problème) dans la poche, est discutable.

On notera enfin que la manière d'extrapoler l'épaisseur de déplacement de la couche limite reste peu précise étant donné le nombre limité de points situés sur le profil (environ 45). La méthode de calcul de la couche limite étant directe, il se peut que l'épaisseur de déplacement à l'un des points de contrôle situés en amont du point de décollement soit relativement grande (présence de la singularité de Goldstein) ; les grandeurs extrapolées peuvent alors être très variables suivant la discrétisation adoptée.



Les points de décollement a et b sont relativement peu éloignés, les épaisseurs δ_a et δ_b sont cependant très différentes.

Une façon de résoudre le problème de manière satisfaisante serait de ne pas calculer l'écoulement dans la poche (suppression des conditions de tangence) et d'évaluer la pression de celle-ci à partir d'un calcul de couche limite inverse. Il apparaît clairement, à la lumière des connaissances acquises par ailleurs, qu'on obtiendrait ainsi une bonne évaluation de l'évolution de l'épaisseur de déplacement au début du décollement, ce qui déterminerait correctement à la fois, le point de décollement, et la pente initiale du sillage tourbillonnaire.

L'inconvénient majeur concernera l'obligation de considérer, en fonction du mouvement du point de décollement, le système permettant la résolution des singularités, de rang variable et non plus constamment égal à $N + 1$.

4. - CONCLUSION

Les travaux décrits dans cet exposé ont abouti à la modélisation de divers écoulements bidimensionnels à travers une grille d'aubes de compresseur. Des extensions de la méthode de base ont permis de prendre en compte divers effets tels que :

- compressibilité dans le domaine subsonique,
- calcul sur nappe de courant à rayon et épaisseur variables,
- variation de la vitesse d'entraînement dans le cas d'une roue mobile,
- effets visqueux par couplage, avec des calculs de couche limite instationnaire.

Les résultats obtenus en écoulement permanent et instationnaire non décollé sont satisfaisants, mais ils ne peuvent être validés quantitativement, car peu de résultats expérimentaux sont actuellement disponibles dans le domaine des grilles d'aubes.

Dans le cas du décrochage dynamique, les études menées jusqu'à présent ont permis de mettre en évidence l'importance de la résolution de l'écoulement au voisinage du point de décollement.

Les travaux futurs sont orientés vers l'intégration au modèle d'un calcul de couche limite en mode inverse, permettant d'initialiser correctement l'allure du sillage tourbillonnaire extrados.

A court terme, ce code sera utilisé par les motoristes dans le cadre des procédures d'évaluation de la sensibilité de compresseurs axiaux multi-étages aux distorsions d'entrée d'air, et de définition de machines plus tolérantes. Des applications plus générales sont envisagées pour l'étude du comportement dynamique de turbomachines (pompes, ventilateurs, compresseurs centrifuges, turbines ...) couplées à des circuits particuliers, et soumises à des conditions limites fluctuantes.

REFERENCES

- 1 Numerical solution of subsonic flow
I.C. HESS
Numerical methods in fluid dynamics - Von Karman Institute
- 2 Méthode pratique de prévision des couches limites turbulentes bi et tridimensionnelles
R. MICHEL, G. QUEMARD, J. COUSTEIX
Note technique ONERA "La recherche aérospatiale" - Janvier 72
- 3 Programme de calcul des couches limites instationnaires et turbulentes par une méthode intégrale
R. HOUDEVILLE, J. COUSTEIX
Rapport technique ONERA OA 31/2259 AYD - Août 1979
- 4 Couches limites tridimensionnelles ou instationnaires
J. COUSTEIX
Conférence AAAF 18ème colloque d'aérodynamique appliquée, Poitiers 11/81
- 5 Calcul des écoulements à forte interaction visqueuse au moyen de méthodes de couplage
J.C. LE BALLEUR
T.P. ONERA 1980-121 - Octobre 1980
- 6 Investigation of separation models for the prediction of Cl_{max}
B. MASKEW, A. DVORAK
33rd Annual National Forum of the A.H.S. - Mai 1977
- 7 A solution to the 2D separated wake modeling problem and its use to predict Cl_{max} of arbitrary airfoils sections
M.L. HENDERSON
A.I.A.A. 16th Aerospace Science Meeting - Janvier 1978
- 8 Theoretical prediction of dynamic stall on oscillating airfoils
R. RAO, B. MASKEW
34th Annual National Forum of the A.H.S. - Mai 1978
- 9 A vortex sheet method for calculating separated two dimensional flow
M. RIBAUT
A.I.A.A. Journal - Vol 21 n° 8 - août 1983
- 10 Analysis of stalled airfoils by simultaneous perturbations to viscous and inviscid equations
B.R. GILMER, D.R. BRISTOW
A.I.A.A. Journal - vol 20 - Septembre 1982
- 11 The phenomenon of dynamic stall
W.J. Mc CROSKEY
VKI Lecture serie - Mars 1981
- 12 Calculation of compressible subsonic flow in cascades with varying blade height
R.A. VAN DEN BRAENBUSSCHE
Journal of Engineering for Power - Octobre 1973

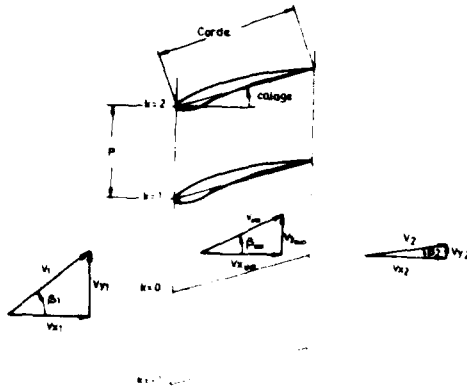


Fig 1 - Schema d'une grille d'aubes bidimensionnelle

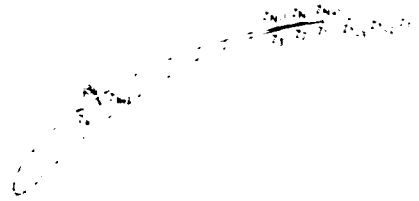


Fig 2 - Discretisation du profil de l'aube

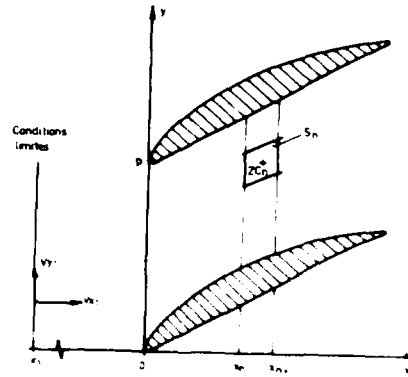


Fig 4 - Surface de contrôle pour le calcul de la divergence locale



Fig 5 - Maillage du canal interaube

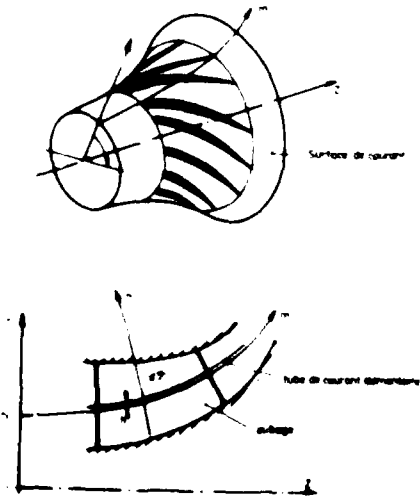


Fig 3 - Schema de la veine d'écoulement

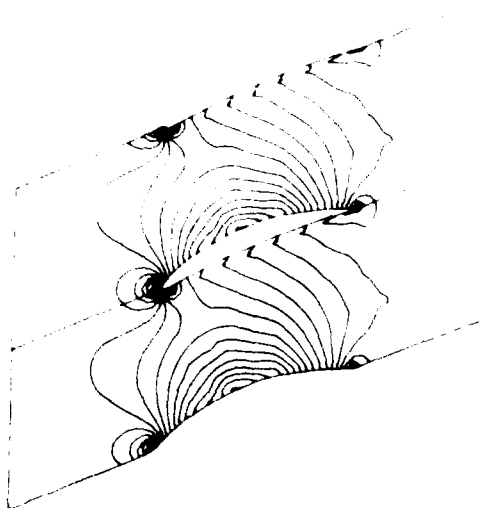


Fig 6 - Écoulement compressible - Mach amont 0,6
Lignes isomach

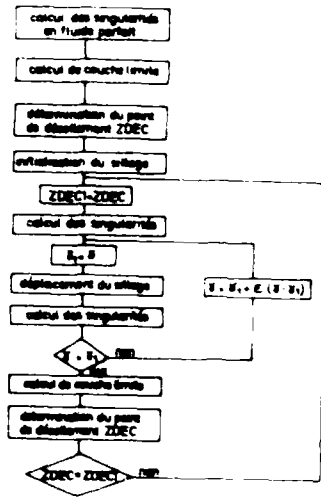


Fig 7 - Organigramme du programme d'écoulement permanent

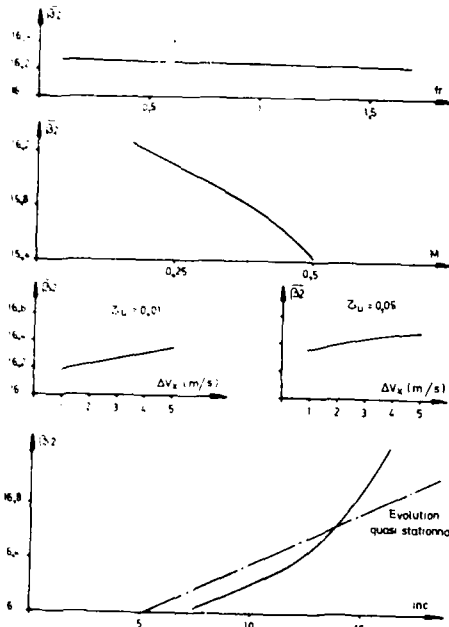


Fig 9 - Evolution de β_2 dans la loi de déviation

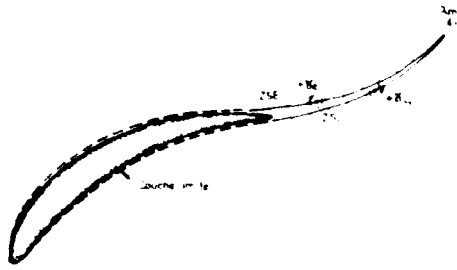


Fig 8 - Principe de discrétisation du profil et du sillage

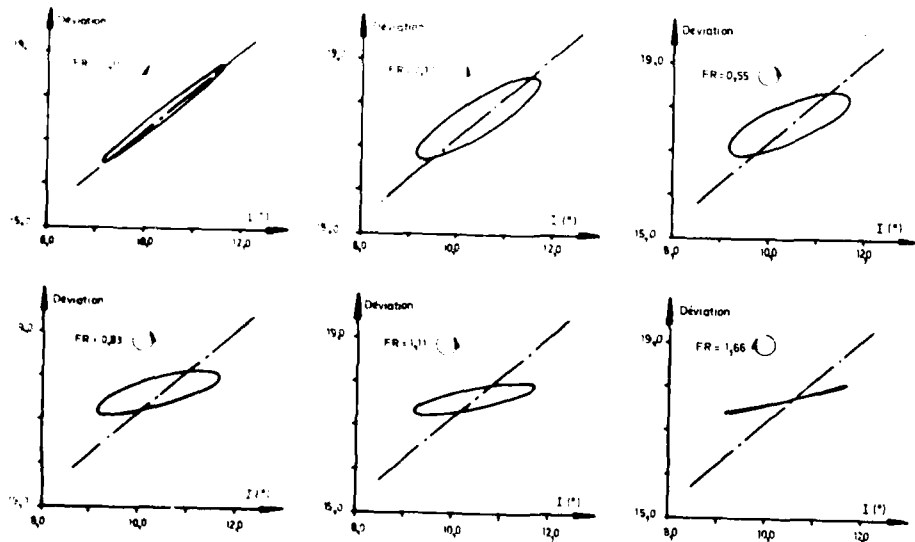


Fig 10 - Influence de la fréquence FR sur les cycles déviation incidence

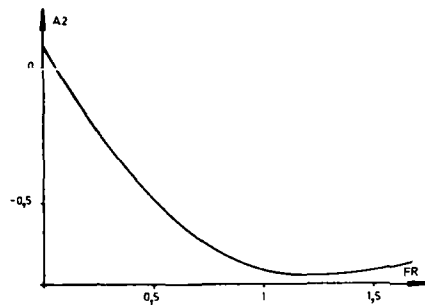
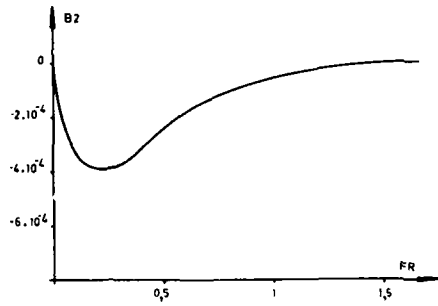


Fig 11 - Etude en fréquence de la loi de déviation

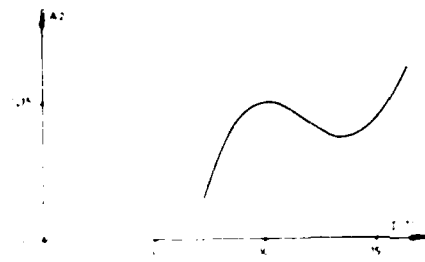
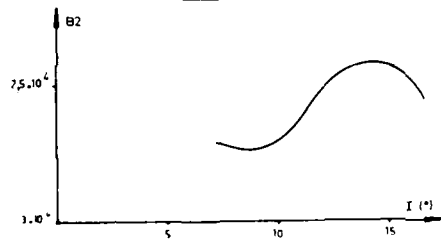


Fig 12 - Etude en incidence de la loi de déviation

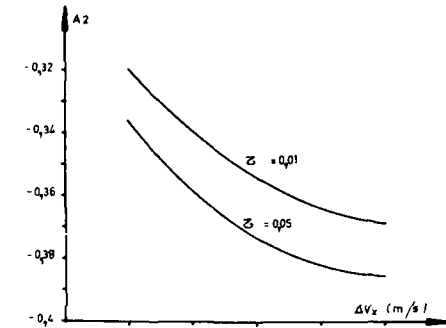
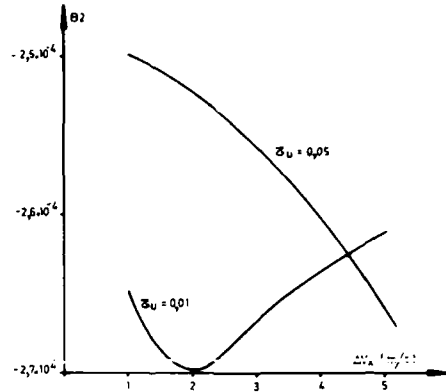


Fig 13 - Etude en amplitude de la loi de déviation

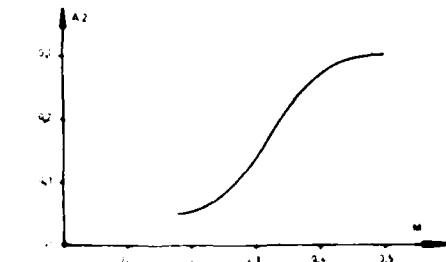
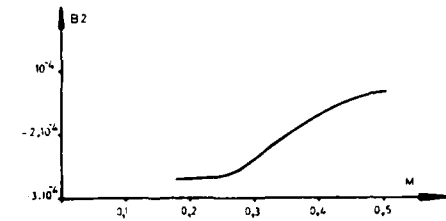


Fig 14 - Etude en Mach de la loi de déviation

Fig 15. influence de la fréquence FR sur les cycles porte incidente

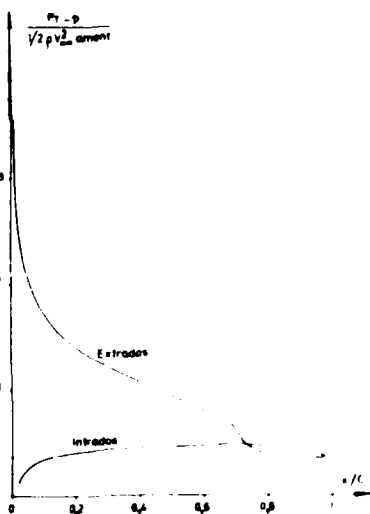
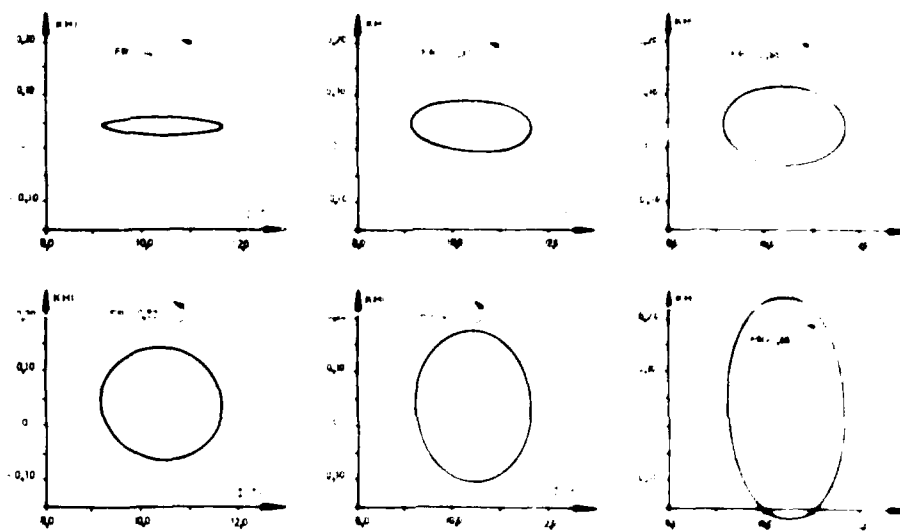


Fig 17. Profil de pression statique sur l'aubage

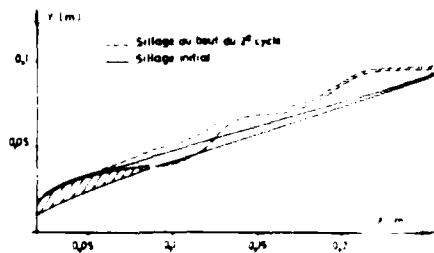


Fig 19. Déformation du silage au cours du temps

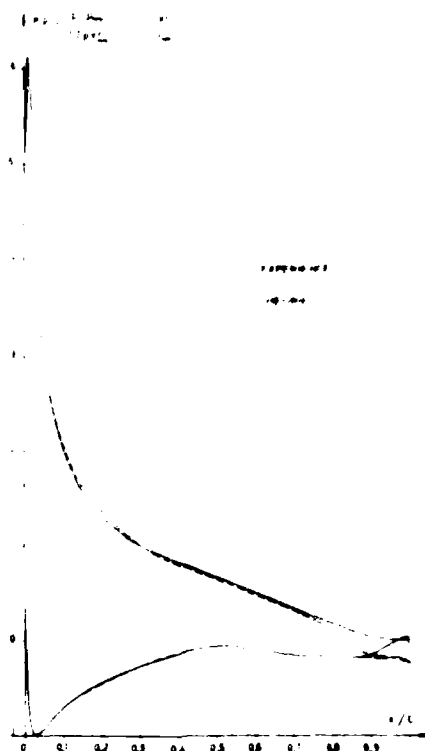


Fig 18. Comparaison théorie expérience de la pression sur un profil réel LC 900

M.P. Plesner, U.S.

1. What was the Reynolds Number in your calculations?
2. How did you compute the transition point?
3. Did you find an influence of frequency on transition and therefore on the boundary layer behaviour, especially on separation?
4. Do you have experimental unsteady boundary layer measurements available for comparison?

Author's Reply

Reynolds Number range between 1.5×10^5 and 4×10^5

Transition Point: The potential flow model is iteratively coupled with an unsteady boundary layer model (laminar/turbulent) adopted from that developed by ONERA-CERF (COSIEX-MODEL VII) in which the transition point is determined through the following calculation (called MR 141 - improved GILMAN) starting from a critical point is determined by application of critical Reynolds Number criteria depending on the form parameter. Then the position of the transition point is calculated through a transition Reynolds Number criteria including turbulence effects and transition parameter. This latter Gomanville criteria describes quite well the onset of turbulent spots in the laminar boundary layer but does not take into account the convection of these spots during a time step. Therefore the transition may occur before the transition point so the convection velocity of the spots is set to half of the local potential velocity and the actual transition point is the nearest position from the instantaneous stagnation point.

Influence of Frequency: Through a parametric study we analysed the influence of various factors (frequency, inlet relative angle, amplitude of incidence variation, Mach number, level of turbulence). Unfortunately we only measured global performance of the typical cascade under consideration (inlet relative angle and loss coefficient).

The comparison between quasi-steady and unsteady boundary layer coupling was made for only one configuration (reduced frequency 0.22). The transition points were found to have a larger range of displacement in the case of a full unsteady calculation both on suction and pressure sides. On the other hand, the form factor of the turbulent boundary layer had a very different behaviour between the two calculations likely to lead to large differences in dynamic stall regime. Further on going studies will give more precise information on this point but we already believe that the unsteady boundary layer modelisation is necessary.

4. **Unsteady Boundary Layer Measurements:** The unsteady boundary layer model developed by ONERA-CERF has been qualified with experiments in which a flat plate was subjected to sinusoidally oscillating flow. In our case the stagnation point is not fixed and we had to introduce some modifications to treat the movement of this point. Some improvements were also necessary to deal with the initial part of the laminar boundary layer.

Specific measurements are conducted at MR 119 with an annular cascade subjected to a rotating distortion but no boundary layer measurements are possible on the test bench. Analysis of the unsteady wakes will nevertheless provide useful information to qualify the boundary layer and separation modelisation.

J. Minamoto, Jc

Do you have an unsteady boundary layer method available?

Author's Reply

Oui le method numerique utilise est une methode effectivement instationnaire.

P.J. Benetto, F.

Pourquoi faites-vous l'hypothese que la pression totale est constante dans la poche de decollement? N'est ce pas plutôt la pression statique?

Author's Reply

L'hypothese d'une pression totale constante dans la poche de decollement est consideree comme decrivant d'un potentiel dans la poche decollee. Le champ de vitesse que nous avons nous pu calculer est assez tres faible et la pression statique regnant dans la poche est quasiment constante ce qui est verifie experimentalement.

IMPROVEMENT OF THE PARALLEL COMPRESSOR MODEL BY CONSIDERATION OF UNSTEADY
BLADE AERODYNAMICS

M. Lecht

DFVLR, Institut für Antriebstechnik
Linderhöhe, D 5000 Köln 90, Germany

SUMMARY

To predict compressor performance with circumferential total inlet distortion the parallel compressor model has been applied. In comparison with the experiment, however, this model will give too pessimistic results for the predicted stall line shift considering sector angles of distortion up to 120 degree. Detailed experimental evaluation of a compressor stage leads to unsteady performance effects obviously being responsible for this discrepancy. In order to improve the original model, the performance characteristic of the compressor was extended to account for a short time overload capability analogous to an airfoil in an unsteady flow. The governing factor of this modification will be the time-to-stall versus the time for a blade channel to pass the distorted sector. The model improvement has been demonstrated for a DFVLR and a NASA single stage transonic compressor subjected to a screen induced total pressure distortion.

LIST OF SYMBOLS

| | | | |
|-------|--|------------|--------------------------------------|
| A | flow channel area | α | angle of attack |
| a | velocity of sound | β | rotor relative flow angle |
| c | absolute flow velocity | ζ | screen pressure coefficient |
| C_L | lift coefficient | ρ | relative mass flow density |
| D_H | hub diameter | r | circumferential coordinate |
| D_T | tip diameter | π | total pressure ratio |
| F_L | lift force | ρ | density |
| k_p | cascade influence parameter (flat plate) | τ | time constant |
| L_a | Laval number | | |
| l | blade chord length | Subscripts | |
| m | mass flow | eff. | effective |
| n | design speed | F | screen free sector |
| p^A | pressure | i | instantaneous |
| R | gas constant | red | reduced to standard inlet conditions |
| T | temperature | s | steady state |
| t | time | S | screen sector |
| U_b | blade tip velocity | t | total condition |
| w | relative flow velocity | 1 to 4 | flow channel positions |
| z | number of blades | * | critical condition ($M = 1$) |

INTRODUCTION

Following an evermore range and challenge of flight missions for the propulsion system to account for inlet distortion and its effect on stable engine operation has become a major problem. Distortion at a compressor inlet plane itself may be of a very complex nature in reality, such as total pressure, total temperature and swirl angle nonuniformity - steady state as well as unsteady.

Within the range of this paper the steady state circumferential total pressure distortion is focussed. Its experimental and theoretical treatment from a research point of view might therefore be only a glimpse into one section of problems concerning inlet distortion.

By selecting a spanwise circumferential sector of a steady state total pressure defect in front of a compressor a real distortion pattern has already been idealized (Fig. 1) in order to keep main parameters limited. Such a type of distortion can easily be simulated by wire mesh screens of different porosities and various sector angles and even for this it is very important to understand and model the effects on compressor behaviour.

From the experimental investigation it is known that circumferential distortion will decrease the range of stable operation of a compressor by shifting its stall-line characteristic to a higher mass flow. A tool to predict this change in compressor performance is the known parallel compressor model. Since it is based on a steady state compressor characteristic only it cannot account for unsteady effects seen by the rotor blades passing a distorted region. Some new ideas on the unsteady response of compressor rotor blading combined with experimental results and a new way of modifying the original model are given in the following.

EXPERIMENT AND SIMPLE PARALLEL COMPRESSOR MODEL

In order to understand what the modelling of a theory is for, the impact of a circumferential distortion on compressor performance may be outlined first. In Fig. 2 the main design data of the DFVLR single stage transonic test compressor and the flow channel with the screen spoiler arrangement one blade height in front of the rotor is shown. Two spoiled sector angles and different screen porosities had been investigated and the evaluation of performance measurements without and with distortion is given in Fig. 3. From this the main detrimental effect on engine stall margin loss i.e. the shift of the limits of stable operation to a higher reduced mass flow is revealed. To predict this effect the idea of two compressors operating in parallel i.e. the parallel compressor

model had been established, shown in Fig. 4. Considering two separate compressors operating on the same speed line characteristic, the one at the inlet condition aft of the spoiled section (S), the other at a screen free inlet condition (F), two different operating points will be obtained (upper right diagram), if a common static outlet pressure from a common plenum is prescribed. Putting those two separate compressors together along the circumference a square wave pattern of total pressure and total temperature like in the upper left diagram will be expected symbolizing that no cross flow and interaction throughout the two sections is assumed. From these distributions an average has to be taken to give an overall operating point. In this theory the compressor as a whole is expected to reach its limit of operation, if the compressor correlated with the distorted section (S) has reached the stall limit at the common speed line characteristic.

From this a simple one-dimensional computer code had been built up, using the following data as an input:

the screen loss coefficient (ζ_s) as a function of screen inlet Laval number (La), the compressor pressure ratio (π_c) and isentropic efficiency (η_s) as a function of reduced mass flow, and the considered undistorted (A_u) and distorted (A_d) flow channel areas (lower part of Fig. 4)

Due to the spoiler installation near to the rotor inlet a direct coupling of the screen and the compressor stage had been preferred.

From the minimum reduced mass flow of the compressor the relative mass flow density θ_{3S} at the distorted inlet plane 3 will then be

$$\theta_{3S} = \left(\frac{\rho c}{\rho^* a^*} \right)_{3S} = \frac{m_{3S} red}{A_3 \frac{\rho^*}{\rho_1} a^* \frac{P_{t2}}{R T_{t0}}} \quad (1)$$

(* marked quantities are the critical values at $La = 1$)

Matching plane 1 to 3 by the continuity equation

$$\theta_{1S} = \theta_{3S} \left(\frac{P_{t3}}{P_{t1S}} \right)_S \quad \text{with} \quad T_{t1S} = T_{t3S} \quad (2)$$

will be made iteratively by using the total pressure loss coefficient of the screen

$$\left(\frac{P_{t3}}{P_{t1S}} \right)_S = 1 - \zeta_s \left[1 - \left(\frac{P_{t1}}{P_{t1S}} \right)_S \right] \quad (3)$$

The assessment of ζ_s as a function of Laval number and screen porosity is given in detail in Ref. 1.

In order to get the compressor exit data the continuity equation in its general form is then used for either section (distorted and undistorted)

$$\theta_4 = \theta_3 \frac{A_3}{A_4} \frac{\sqrt{T_{t4}/T_{t3}}}{P_{t4}/P_{t3}} \quad (4)$$

In this the pressure ratio as well as the temperature ratio are given for an selected operating point out of the performance characteristic. With θ_4 the Laval number La_4 and the pressure ratio P_4/P_{t4} (static/total) are determined.

The exit static pressure then becomes

$$P_4 = \frac{P_0}{P_{t4}} \frac{P_{t4}}{P_{t3}} \frac{P_{t3}}{P_{t1}} P_{t1} \quad (5)$$

Having done this procedure for the minimum mass flow value of the distorted sector first, the undistorted sector will then be calculated this way by stepwise increasing its mass flow to reach an equal exit static pressure. Thus the corresponding operating point of the screen free compressor section can be found. The results of both the undistorted and distorted section have been averaged at the inlet and outlet plane to give a common operating point as follows:

$$\begin{aligned} m &= m_S + m_F \\ \bar{P}_{t3} &= P_{t3S} A_S/A + P_{t3F} (1 - A_S/A) \\ \bar{P}_{t4} &= P_{t4S} A_S/A + P_{t4F} (1 - A_S/A) \\ \bar{T}_{t4} &= T_{t4S} A_S/A + T_{t4F} (1 - A_S/A) \\ \bar{m}_{red} &= m / (\bar{P}_{t3} / P_{t0}) \\ \bar{\pi}_t &= \bar{P}_{t4} / \bar{P}_{t3} \end{aligned} \quad (6)$$

In this way the parallel compressor model was applied to the test compressor stage. In Fig. 5 the calculated values for the limits of stable operation out of this model (open symbols) are shown in comparison with the experimental results (solid symbols). Compared with reality the model prediction is too pessimistic in its tendency especially for smaller sector angles of distortion.

The main reason for these pessimistic results may be suspected in the assumption of the model inherent criterion on the limits of stable operation i.e. not to exceed the steady state speed line stall limit within the distorted region.

Relative to a steady state circumferential distorted flow region the rotor blade will see an incoming unsteady flow. As it is known for an airfoil in unsteady flow a short time lift overshoot combined with a time lag in stalling can be expected during a sudden increase of angle of attack. Therefore the steady state performance characteristic might not be the suitable criterion for predicting the limits of operation within this model.

A BASIS FOR A MODIFIED PARALLEL COMPRESSOR MODEL

Detailed compressor flow field measurements had been evaluated to reveal an unsteady characteristic of the rotor blade passing the low total pressure region (Ref. 11). The compressor inlet plane had been divided into 30 circumferential sectors each considering as the inlet condition of a separate compressor. For each sector a circumferential correlation between inlet and outlet plane along 20 radial spine positions had been established following the absolute flow path throughout the compressor to find the corresponding outlet condition.

Radially averaged values then had been taken to give a separate operating point representing each sector along the circumference. The results of this multiple sector evaluation is shown in Fig. 6, where these operating points are plotted into a performance map. Following these plots (upper left diagram) in the direction of blade rotation a hysteresis loop is given representing one revolution of the compressor blading. From this it can be seen, that indeed the steady state stall limit will be exceeded entering the distorted sector (solid symbols). After this a break down may be observed followed by a release having left this sector to begin a new loop. This seems to be a typical behaviour to be found similar on an airfoil under oscillatory angle of attack. This may be an explanation, why the original parallel compressor model with a steady state stall limit criterion must give those pessimistic results. Therefore an unsteady characteristic of the rotor blading should be taken into account. Two typical effects are known from a single airfoil subjected to an instantaneous angle of attack, one is the response to a step wise change of angle of attack in a stall free regime prescribed by the lift transfer function

$$\frac{F_L(t)}{F_L(t-\infty)} = 1 - e^{-t/\tau} \quad (1)$$

where a time constant τ is given from the ratio of blade chord length and flow velocity (Fig. 7a).

The other is a possible short time lift overshoot ΔC_{Lmax} as a response to a ramp increase of the angle of attack exceeding the steady state stall angle known as Prandtl effect (Fig. 7b)

$$\Delta C_{Lmax} = 217 \frac{l}{w} \frac{d\alpha}{dt} \quad (2)$$

Using this characteristic behaviour to determine the unsteady stall limits of an airfoil when exceeding its steady state stall angle instantaneously, Melick and Simpkin (Ref. 8) developed a hypothesis of an "effective angle of attack". This hypothesis has been successfully applied by the present author to predict the response of an axial compressor stage to inlet flow distortion.

In order to understand the procedure it is necessary to give a brief outline of Melick and Simpkin's hypothesis first.

They substituted the airfoil by its transfer function (eq. 1) and considered the "effective angle of attack" α_{eff} as a systems output to a ramp input of the instantaneous angle of attack α_1 . Then α_{eff} can be found as a function of α_1 yet to be determined "time-to-stall" constant by using the Laplace transformation technique

$$\text{input} \quad \alpha_1(t) = \alpha_0 + \frac{d\alpha}{dt} t \quad (9)$$

$$\text{output} \quad \alpha_{eff}(t) = \alpha_0 + \frac{d\alpha}{dt} \tau \left(\frac{t}{\tau} - 1 + e^{-t/\tau} \right) \quad (10)$$

This "effective angle of attack" α_{eff} lags the instantaneous angle of attack α_1 (Fig. 8).

Melick and Simpkin now made the hypothesis, that unsteady stall might occur, if this "effective angle of attack" will have reached the steady state stall angle. Next they defined the time up to which unsteady stall will be delayed as the governing time constant τ of a single airfoil in this special situation.

For this the overshoot of the angle of attack will then be given from eq. 9 and 10

$$\Delta \alpha_{max} = \alpha_1(\tau) - \alpha_{eff}(\tau) = \frac{d\alpha}{dt} \tau \left(1 - \frac{1}{e} \right) \quad (11)$$

Since for a single airfoil the corresponding lift overshoot can be taken from

$$\Delta C_{l,max} = 2\pi \Delta \alpha_{max} \quad (12)$$

a value of the time constant will be found by combining this with eq. 8 and 11 to give

$$T_{airfoil} = 55 \frac{l}{w} \quad (13)$$

where l is the blade chord length and w flow velocity. Following this theory of Melick and Singh their hypothesis of an "effective angle of attack" was taken as a useful basis to modify the parallel compressor model in order to account for unsteady aerodynamic effects. To do so the rotor relative flow angle, which is coupled with the mass flow condition at the rotor inlet has been considered as an angle of attack analogue. If within the distorted sector of the model the reduced mass flow is decreased, the instantaneous relative flow angle β is increased in a step function and according to the foregoing hypothesis an "effective relative flow angle" β_{eff} is to follow up to the steady state limit β_{max} . As outlined in the lower diagram of Fig. 9, the "effective relative flow angle" β_{eff} is considered to follow in a transfer function similar to eq. 13, so that a criterion $\beta_{eff} = \beta_{max}$ stipulate relative flow angle overshoot corresponding to a mass flow undershoot within this area may be established

$$\frac{\beta_{eff}(t) - \beta_{max}}{\beta_{max} - \beta_{min}} = 1 - e^{-t/T} \quad \text{with } \beta_{min}(t) = \beta_{max} - \beta_{max} \quad (14)$$

In this the ratio of time Δt for a rotor blade to pass the distorted sector is a time constant T will be the dominant parameter. The time constant is expected to be in the range of that value given in eq. 13.

In order to implement this new criterion of unsteady stall limits the parallel compressor model requires operating for the distorted sector with a lower reduced mass flow than given from the steady state performance characteristics. Therefore this characteristic has to be extrapolated beyond its steady state stall limit. Remembering the hysteresis of operating points being found by the multiple use for evaluation (see Fig. 8) a suitable compromise for the extrapolation of the pressure ratio should be to keep the maximum pressure ratio constant for the respective speed, the section being fixed in diameter.

For the aerodynamic influence within this range a linear extrapolation has been chosen as indicated in the above diagram of Fig. 9. This might be justified by the fact that for additional cases within the distorted region the mass flow is decreased, the stall angle of attack is to begin already before leaving the distorted sector with a decreasing velocity within the undistorted region. Therefore in reality, these areas are expected to show as well a severe hysteresis.

With these approximations the extended parallel compressor model works in a quasi-steady state manner, but to a certain extend beyond the steady state stall limit. In accordance with the above given criterion, during the time constant T of the model the function was deduced from a single cycle, which terminates at stall. This approximation, as an side effect was made, a certain influence of airfoil geometry on stall angle of attack might be expected as well. The simplest way to approximate this is to substitute eq. 13 by

$$\Delta C_{l,max} = 2\pi \Delta \alpha_{max} K_0 \quad (15)$$

where K_0 is the correction factor for a flat plate, as side with respect to stagger angle and pitch to chord ratio given by Weising (Ref. 4). The time constant T eq. 13 then changes to

$$T_{corrected} = 55 \frac{l}{K_0 w} \quad (16)$$

For the DFVLR compressor rotor the order of magnitude of the time constants which might be applied to the model are shown in Fig. 10 along the relative blade height. It might be questionable, which value could be representative for a transonic compressor rotor. Moreover no transition flow aspects have been considered deriving the time constant. Therefore only a comparison of experimental results and model prediction can give an answer.

COMPARISON OF EXPERIMENT AND EXTENDED PARALLEL COMPRESSOR MODEL

The unsteady modification of the parallel compressor model just described had been applied for the DFVLR test compressor as well as for a NASA single stage compressor. For the first a comparison between experiment and model prediction for a 60 and 120 degree sector angle of distortion is given in Fig. 11, showing plots of the predicted stall limit of the steady state (open symbols) as well as of the unsteady (closed symbols) version of the parallel compressor model. The results in Fig. 11a have been obtained by using the time constant derived for the single airfoil, those in Fig. 11b by correcting for a cascade influence. For either cases the mid span value of the time constant has been chosen to represent the overall behaviour. Matching the time constant for a cascade influence the results fit best with respect to a stall-limit prediction. A discrepancy

Fig. 1
Simulation of total pressure
inlet distortion

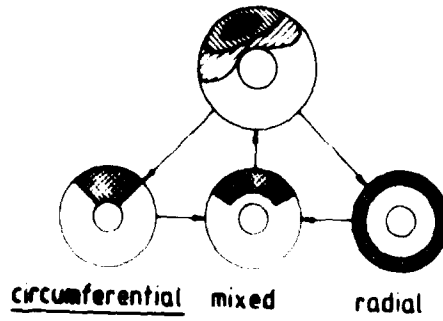


Fig. 2
DVVR transonic compressor
stage test arrangement

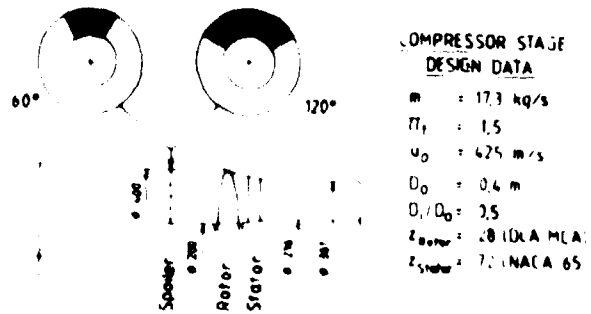
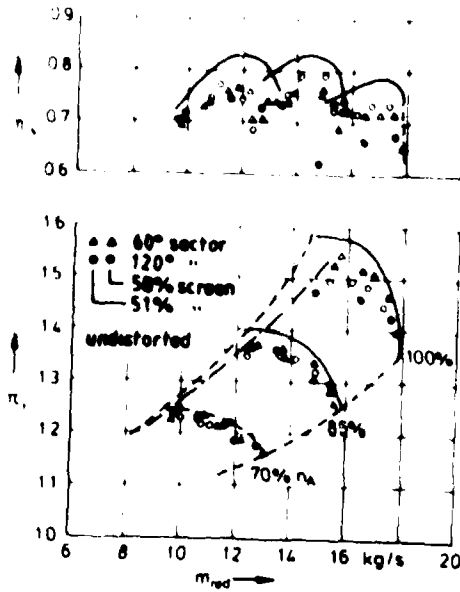


Fig. 3
Effect of distortion on compressor
performance



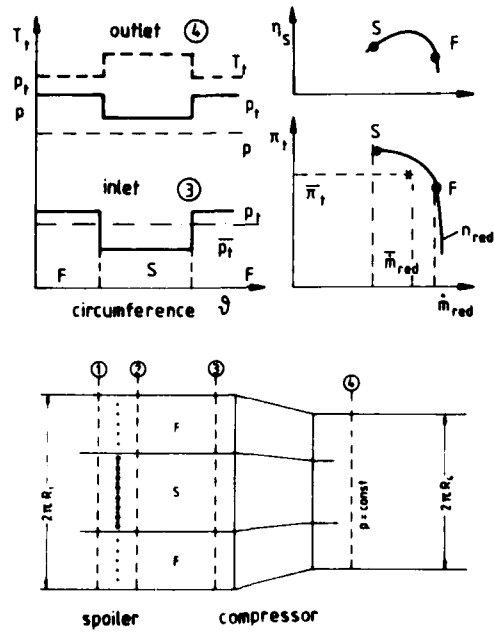


Fig. 4
Schematic outline of the parallel compressor idea

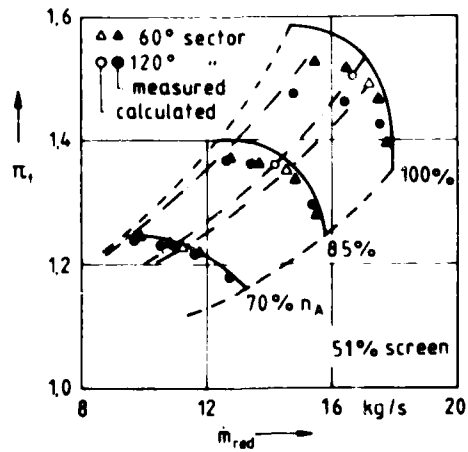


Fig. 5
Result of the parallel compressor model stall line prediction (open symbols) compared with the experiment for the DFVLR compressor stage

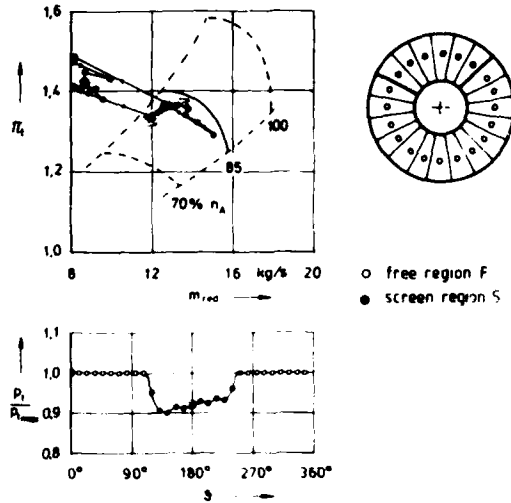


Fig. 6
Result of a multiple sector evaluation of flow field measurements
(Each sector represents a separate compressor within the performance map)

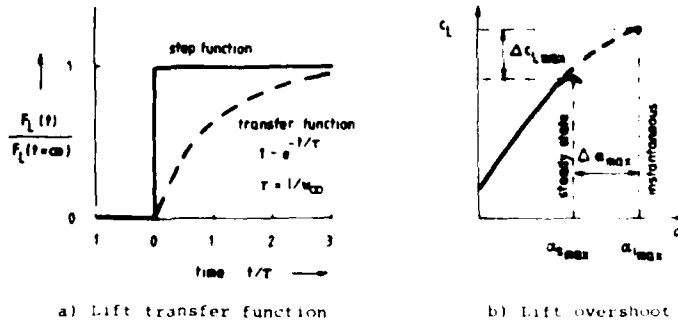


Fig. 7
Typical characteristics of an airfoil in unsteady flow

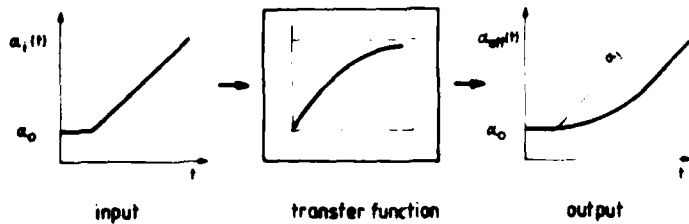


Fig. 8
Response of an airfoil representing transfer system to a ramp input signal

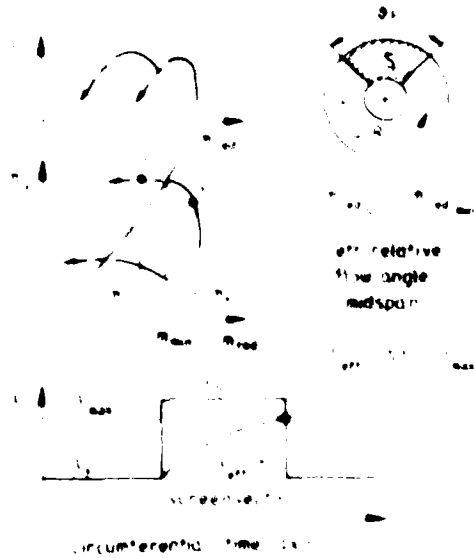


Fig. 9
 Schematic of the basic compressor rotor blade. The
 hypothesis of a "frozen" flow field is used in the
 analysis of the flow within the blade.

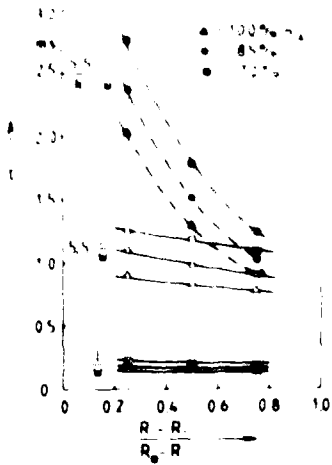


Fig. 10
 Spanwise magnitude of time constants for the DFVLR
 compressor rotor blading

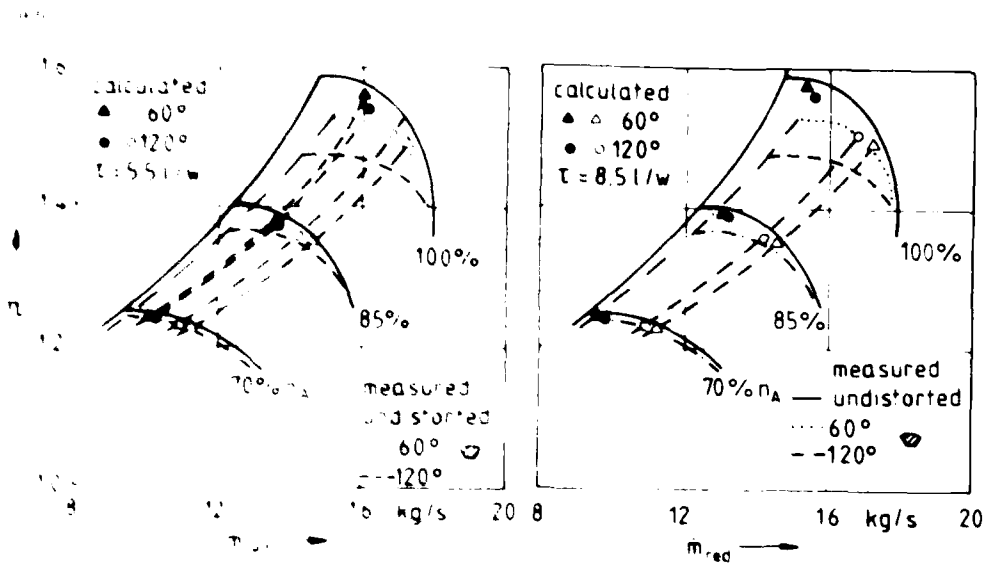


Fig. 11. Comparison of calculated and measured performance of a compressor stage (a) with a time constant $\tau = 5.51/w$ and (b) with a cascade corrected time constant $\tau = 8.51/w$.

1. The test results show that the compressor stage is highly sensitive to inlet flow distortion. The performance of the stage is significantly degraded when the inlet flow is distorted. The test results also show that the compressor stage is highly sensitive to inlet flow distortion. The performance of the stage is significantly degraded when the inlet flow is distorted.

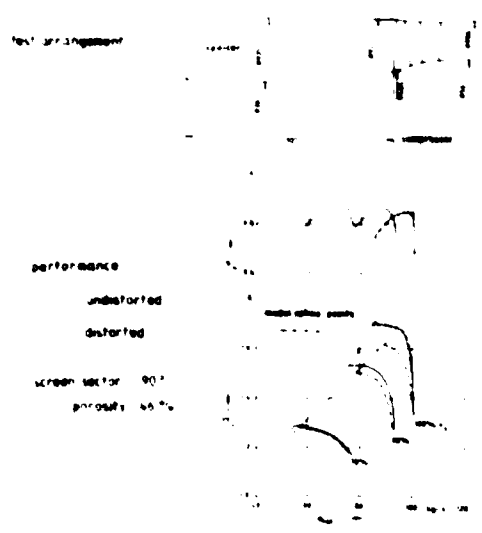


Fig. 12. Test arrangement and performance of a NASA transonic compressor stage with distorted inlet flow (from Ref. 5).

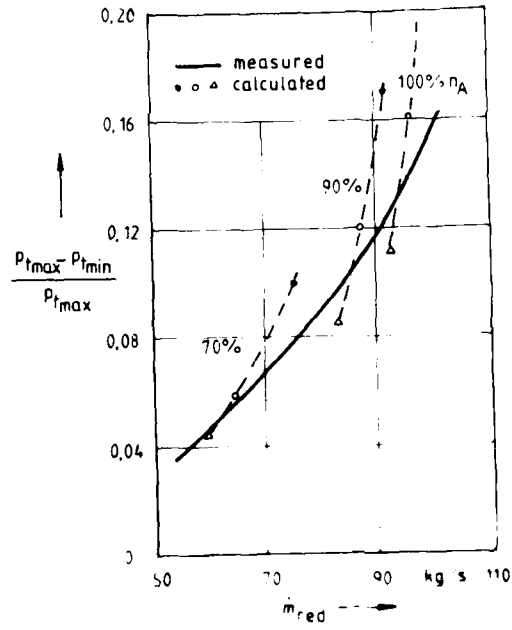


Fig. 11
Comparison of measured and calculated values of
NASA nondimensional static pressure loss coefficient
(1) 70% efficiency; (2) 90% efficiency; (3) 100% efficiency.

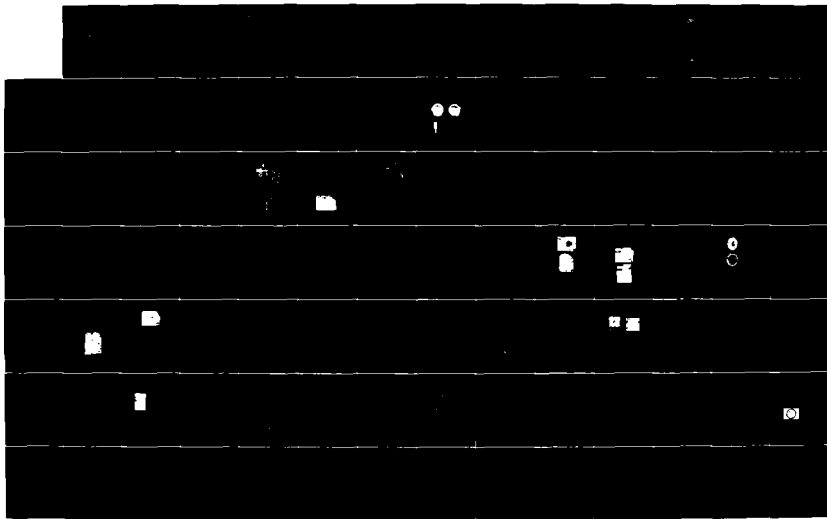
AD-A182 635

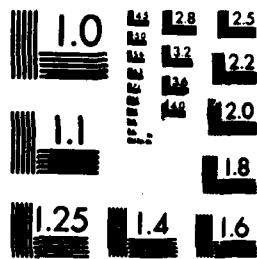
ENGINE RESPONSE TO DISTORTED INFLOW CONDITIONS:
CONFERENCE PROCEEDINGS OF (U) ADVISORY GROUP FOR
AEROSPACE RESEARCH AND DEVELOPMENT NEUILLY, MAR 87
AGARD-CP-400 F/G 20/4

3/87

UNCLASSIFIED

NL





MICROCOPY RESOLUTION TEST CHART
NATIONAL BUREAU OF STANDARDS 1963-A

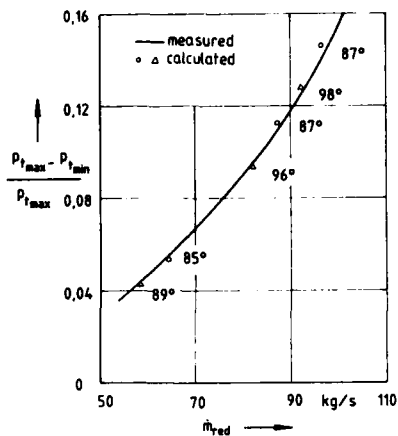


Fig. 15
 Effect of screen decoupling on the prediction of distortion level
 (Numbers denote subsequent sector angles of distortion at the compressor inlet)

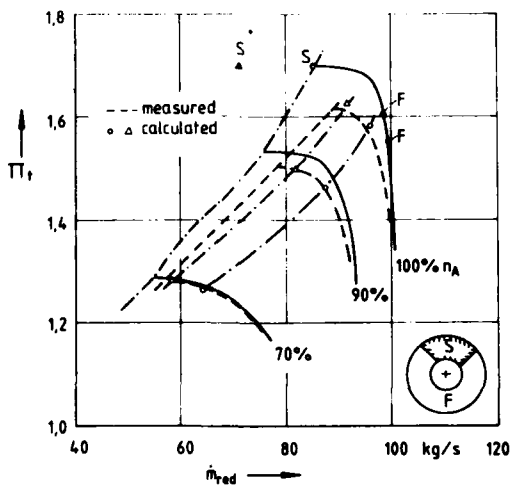


Fig. 16
 Parallel compressor model performance prediction for the NASA compressor stage in a screen-decoupling mode
 (Circles = steady, triangles = unsteady, S and F on the undistorted 100% speed line are operating points of the parallel compressors)

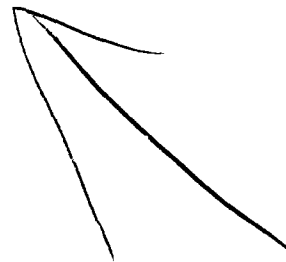
DISCUSSION

Ph. Ramette, Fr

1. In Figure 11b, at nominal speed, the measurement show a large difference between a 60° and a 120° screen, which is not the case for the calculated stall points which are close together. Can you comment on this?
2. In Figure 16, how do you extrapolate the screen unsteady stall point S outside the stable operating zone of the compressor? Should the operating nominal speed line not go down at reduced mass flow from the stall point?

Author's Reply

1. The model cannot in all cases reproduce the level of pressure ratio experienced in the experiment. This may be due to the fact that, firstly, the blade operating point does not follow the steady-state speed line. Instead, the hysteresis loop can be found on a somewhat lower pressure level as illustrated by Figure 6. Additionally, from experiments with a 120° distortion it can be supposed that the hysteresis loop of the blade operating point could be wider. Secondly, the model is one-dimensional and assumes only an idealised square-wave distribution of the pressure-time history over the distorted sector.
2. The extrapolation of the steady-state operating line with respect to an unsteady overshoot of the stability limit has been made as a suitable compromise, which I have found out of the multiple sector evaluation (Fig.6). Of course, it can be discussed whether holding a constant quasi-steady-state maximum pressure ratio is an adequate extrapolation to represent the average of an unsteady effect. I really do not have sufficient experimental validation to use any other type of extrapolation. In this part of the model extension I mainly looked for a suitable prediction of the limits of the stability line. Therefore I assumed that this approach might be a fitting compromise.



AD-P005 468

TURBOFAN ENGINE POST-INSTABILITY BEHAVIOR
- COMPUTER SIMULATIONS, TEST VALIDATION, AND APPLICATION OF SIMULATIONS -

by

William G. Steenken
Manager, Engine Operability
Aircraft Engine Business Group
General Electric Company
Evendale, Ohio 45215
U.S.A.

SUMMARY

This paper presents a method that can be used to predict the post-stability operation of a turbofan engine and is based upon extending the capabilities of engine transient cycle decks. Typical predictions are presented and compared with results obtained from the testing of a modern augmented turbofan engine. The potential manners in which this new digital-computer-simulation tool may be utilized are also discussed.

SYMBOLS

- H - Compressor hysteresis
- M - Mach number
- PS3 - Compressor discharge static pressure
- W_c - Corrected flow
- WF - Mainburner fuel flow
- rpm - Revolutions per minute
- η_B - Combustor efficiency

1.0 INTRODUCTION

It is becoming generally accepted that hot starts, hung starts and nonrecoverable stalls (also known as stagnation stalls), which may occur in turbofan engines, are all characterized by the presence of a compressor instability - rotating stall. However, the aerothermodynamic path taken during instability by the high-pressure compression system, the system of prime importance, can be quite complex. This end state can be reached in basically two ways. In one way, it can be caused by a destabilizing event at high compressor speeds that induces surge. This surge can then degenerate into rotating stall as compressor speed decreases. In the other way, if an instability is induced at low speeds, such as in the start or idle regions, then rotating stall may be induced directly.

If hot starts, hung starts, and/or nonrecoverable stalls, all which have the potential for jeopardizing the integrity of an engine, are to be prevented or controlled, then a tool is required that will provide the requisite understanding of the post-stability processes involved.

Based upon our studies (References 1 and 2), this necessary tool is a time-dependent digital computer simulation of the engine such as an "expanded" engine transient cycle deck. Although these simulations can differ in the details associated with solving the governing equations (e.g. implicit or explicit technique), the aerophysics that must be represented are common to all. To that end, volume dynamics, in-stall and reverse-flow compressor characteristics, stall-development and stall-recovery time constants, rich-side combustor-heat-addition characteristics, and rich-side flammability limits have been added to the standard low-frequency engine-transient-cycle deck to provide the needed capability.

While this paper presents results obtained using an implicit solution technique (Reference 1), the methods used to represent the components and the engine have proved equally valid when using explicit solution techniques as in the case of a high-bypass-ratio non-augmented, separated flow turbofan engine with a single-stage fan (Reference 2). Further, both of these techniques have been used with equal validity to represent a high-speed, high-pressure-ratio compressor in a rig-test configuration and a high-speed compressor in a variable cycle configuration. This multiplicity of successes has provided the confidence required for using this type of simulation tool as an aid for interpreting test data, validating the geometrical design of new engine configurations, predicting the stall recovery characteristics of engine configurations, and developing stall-recovery control strategies.

2.0 MODEL FORMULATION

The manner in which the post-stability simulation was constructed is described in the following subsections. Substantial consideration was given to breaking the engine into its component parts so that the important and necessary aerophysical features could be represented.

As background, it should be noted that the mixed-flow augmented-turbofan engine that was used for this study consisted of a three-stage fan with variable inlet guide vanes, a nine-stage compressor with variable inlet guide vanes and variable stators in stages 1 through 3, an annular combustor, a single-stage high-pressure turbine, a two-stage low-pressure turbine, a mixer for mixing the fan bypass and core streams, augmentor spray bars whose ports were controlled to provide afterburner modulation over the whole augmentor fuel-flow range, and a variable convergent-divergent nozzle. A schematic of the engine components and volumes is given in Figure 1. The fan and compressor variable geometry was controlled as a function of corrected speed, and the nozzle area was controlled by a fan-duct Mach-number signal in order that the fan operating line would be maintained at the desired pressure ratio. This engine had a bypass ratio of approximately one.

The starting point for the development of the computer simulation begins with the usual steady-state and transient cycle decks. In our deck development system, the transient cycle deck uses the steady-state cycle deck as its beginning point to which the rigid body rotor dynamics (moments of inertia) are added as well as are models of the engine control, variable geometry actuators, and control sensors with their attendant response (amplitude and time) functions. Also included are heat soak and parasitic flow representations. Computer models constructed in this manner are adequate for normal accel and decel type studies because the characteristic times associated with them are at least two orders of magnitude slower than the associated acoustic propagation times. In order to give the models the necessary 25-30 Hz frequency response and the post-stability capability that is desired, the additions described in the following paragraphs were made to the transient cycle deck.

2.1 Compression Component Representations

The three-stage fan was represented in a single block by hub and tip maps that included in-stall and reverse flow representations in addition to the normal unstalled flow characteristics. The compressor was represented as a single block by a pitch-line characteristic that had in-stall, reverse flow, and unstalled representations included in a manner similar to the fan representation. Figure 2 provides an illustration of the unstalled and in-stall compressor characteristics used at two speeds. Time constants characteristic of the time it takes for a stall cell to develop (three-to-four rotor revolutions) and for a stall cell to disappear (11-to-12 rotor revolutions) were also included (see Reference 3).

In retrospect and if funds and schedule had permitted, we believe that the fidelity of the amplitudes of some of the fluctuations during the occurrence of the surge instabilities could have been improved by breaking the compressor into three blocks - variable geometry stages 1-3 in the first block, stages 4 and 5 with the fifth stage bled at the exit of the second block, and stages 6-9 in the third block. This would have made the acoustic reflection plane less hard.

2.2 Combustor

There are three key combustor characteristics that must be represented: (1) the ideal temperature rise, (2) the combustor efficiency, and (3) the flammability limits. Of special import are the rich-side fuel-air-ratio portions of the ideal-temperature-rise and the flammability-limit characteristics.

The schematic representation of these characteristics is shown in Figure 3. In the case of the ideal-temperature-rise characteristic, the decrease of temperature rise with increasing fuel-air ratio for fuel-air ratios greater than stoichiometric is represented. This feature simulates the effect that excess fuel has on quenching the flame. The flammability limits are handled in a similar manner for the rich-side fuel-air ratios. As can be seen, the flammability limits are represented as a function of the fuel-air ratio and a combustor loading parameter that is proportional to the "flame thickness" and reaction time.

The combustor efficiency consists of a base curve and a relation for modifying this curve for use at conditions other than for which the base curve was derived. The base efficiency curve is represented as a function of fuel-air ratio and falls off monotonically on either side of the maximum. For conditions other than the base conditions, the combustor efficiency is modified according to the following relation:

$$\eta_B = \eta_{Base} \left(\frac{P}{P_{Base}} \right)^M \left(\frac{T}{T_{Base}} \right)^N$$

During surge or rotating stall, the combustor efficiency was further modified to account for the severity of surge and the extent of the rotating-stall cell.

In addition to these characteristics, the burner total-pressure loss was represented in a manner that accounts for the pressure drop across the liner and the loss associated with "Rayleigh Line" heat addition.

2.3 Turbines

Standard turbine characteristics were used for both the high-pressure and the low-pressure turbines. Because of the pressure ratios involved, the turbines operate choked, thus relieving the need for reverse flow characteristics. However, it was found necessary to modify the turbine efficiencies with empirically formulated scalar modifiers during surge and rotating stall as was done for the combustor efficiency so that engine decel rates and turbine blade temperatures matched those measured during the engine test.

2.4 Volume Dynamics

In addition to including key compression component and combustor off-design performance characteristics, the representation of the volumes within the engine takes on critical importance if the desired frequency response is to be achieved - in our case 25-30 Hz.

The motion of the air within these volumes is completely described by the equations of change (conservation of mass, momentum, and energy) and a thermodynamic relationship (see References 1 and 4). Figure 4 gives a schematic representation of the manner in which the volumes in the engine are chosen. Unless otherwise indicated, all volumes are represented by quasi one-dimensional volumes whose dimensions are chosen to represent the physical engine flow areas and lengths. Long volumes with no natural breaks are broken into volumes consistent with the frequency response desired. The area distribution is continuous. The only two-dimensional volumes are the one located ahead of the fan and the other located downstream of the fan but ahead of the splitter. These two-dimensional volumes are chosen to allow for radial redistribution of the flow downstream of the fan in the case of a compressor surge and to allow for radial redistribution of the flow upstream of the fan in the cases of core-induced fan-hub surge and throttling-induced fan-tip surge as well as bypass-ratio variation effects associated with normal instability-free operation.

2.5 Control

It was noticed during mainburner fuel stepping to instability on the engine that the fuel flow was being cut back as a result of the T4B (turbine blade temperature) limiter. This limiter used a signal from a pyrometer, and during fuel stepping was reacting to flashes (temperature spikes) caused by the burning of excess fuel in the turbine rather than the temperature of the blades. The computer simulation did not provide this fuel cut-back since the logic calculated only an average gas path temperature with which T4B was correlated.

The problem was solved by empirically correlating the temperature spikes with the rate of change of fuel-air ratio at the plane of the fuel nozzles. When the rate increases beyond the empirically determined value, a temperature spike is expected. This approach worked well since temperature spikes were simulated at times comparable to those measured in the test data.

3.0 PRETEST PREDICTIONS AND VALIDATION

Prior to accomplishing pretest predictions for post-stability events, this new computer model was demonstrated to reproduce the normal accel and decel characteristics of the engine. Following these validation cases, the model was configured to allow for stability-limit-line degradation and a fuel-step instability-inducement technique in manners consistent with actual engine operation.

A method for degrading the stability limit line (also known in the past as the stall line or surge line) was necessary since it had been demonstrated on an earlier engine with a nearly identical core engine that this core engine had excellent surge recovery characteristics. In fact, in order to significantly lower the stability limit line, the engine had to be significantly malconfigured from its normal operational configuration (i.e., compressor variable geometry opened five degrees as measured at the inlet guide vanes and combustor operation with continuous ignition), and/or subjected to large magnitude inlet total-pressure distortions that were maintained for a significant period after the initial surge by an airjet distortion generator. Incorporation of capability to lower the stability limit line as an approximation to the effect of distortion on the compressor and adding the ability to switch to a false PS3 signal allowed simulating the manner in which the engine was operated and responded.

In order to initiate compressor instability, a mainburner fuel-step technique was used whereby upon the initiation of a speed demand, the fuel flow was required to go to an accel schedule in terms of WF/PS3 (the ratio of mainburner fuel flow to combustor burner static pressure) that was a function of compressor corrected speed. At the same time the accel schedule was demanded, a false PS3 was introduced to the control to create an artificially high fuel flow which created a step-like rise in combustor burner pressure.

Two typical cases have been chosen to illustrate the capabilities of the model and for comparison with test data. The first case illustrates a simulation of recoverable surge and the second case illustrates simulation of a nonrecoverable surge. These cases are presented in the following paragraphs.

3.1 RECOVERABLE SURGE

This recoverable surge was initiated by a mainburner fuel step and was conducted at inlet conditions consistent with $M = 1.05$ and 52KFT altitude. During the test, the stability limit line was lowered by installation of an inlet distortion screen. This was simulated during the computer simulation by artificially lowering the compressor stability limit line. After initiation of the instability, continuous ignition was used with a rate of five sparks per second. Instability was induced by creating a speed demand of 600 rpm and switching to a false PS3 of 100 psi for three seconds. Similar values were used for the computer simulation.

The results of the simulation and the comparable test data are shown in Figures 5a thru d. Both sets of results are plotted on the same scale for Figures 5a, b, and c where the fuel flow - PS3 ratio, compressor discharge static pressure, and compressor speed are plotted, respectively. Figure 5d provides the compressor trajectory in terms of pressure ratio and corrected flow as obtained from the computer simulation.

The sequence of events is described by the letters "a thru e" on each part of Figure 5. At "a," a surge is initiated by a mainburner fuel step. Coupled fan and compressor surges accompanied by compressor blowout and relight sequences (region "b") occur with a frequency of approximately 4-5 Hz. Finally, the combustor blows out due to rich side quenching (region "c"). During these two periods, the compressor speed is decreasing. At "d," the fuel step is terminated and the engine returns to normal fuel scheduling whereupon the combustor relights causing the compressor to surge at a frequency of approximately 13-14 Hz (region "e"). Compressor speed begins to increase, the surging stops, and the engine recovers and accelerates to normal operation at the selected power setting.

3.2 NONRECOVERABLE STALL

This nonrecoverable stall was initiated at the same inlet conditions as was the previously discussed recoverable surge. All other parameters were also the same except the fuel step was held for a four-second step duration. The comparison of the model simulation and test results are shown in Figures 6a, b, and c for the fuel flow - PS3 ratio, compressor discharge pressure, and compressor speed, respectively. The pressure ratio - corrected flow trajectory as computed by the model simulation is shown in Figure 6d.

This mainburner-fuel-step-induced surge behaves in a manner very similar to the recoverable surge up to the point the false PS3 is removed (point "d") and the engine returns to the normal fuel control schedule. However, the compressor speed is lower than was the case for the recoverable surge due to the longer duration fuel step. In this case, the compressor incurs an instability (point "e") and degenerates to the rotating stall state (point "f").

3.3 VALIDATION

Examination of the previous two sets of figures show that the engine transient computer model with post-stability capability correctly predicts the rotating stall state as well as the measured parameters in trend, mean levels, frequencies, and to a lesser degree, predicts the amplitude and waveform shape of the surge perturbations. It is anticipated that the previously discussed more detailed compressor representation would improve this latter situation. In addition, it was noted as a result of installing flame detectors in the combustor and at the exit of the low pressure turbine, that during surging, significant burning was not taking place in the combustor, but rather that significant burning in the turbines was occurring. A model for this type of burning was not developed. However, it is anticipated that development of a "burning-in-the-turbine" model would lead also to lower compressor discharge pressure perturbations.

The model was used to estimate the critical speed (References 3 and 5) of this engine, the critical speed being the speed at which the instability behavior of the compressor transitions from surge to rotating stall. In reality, the critical speed is a critical speed range for a given engine depending on factors other than just the

combustor volume-compressor volume relationship such as stability limit line degradation due to clearances, thermal transients, and/or variable stator position. Analysis of the test data presented in Paragraphs 3.1 and 3.2 show that the critical speed for this type of transient occurs at a corrected speed of approximately 10,400 rpm. The model simulations showed that relights at corrected speeds of 10,530 rpm and 10,250 rpm resulted in surge and rotating stall, respectively. Hence, the critical speed as predicted by the model is expected to lie between these two speeds which is then commensurate with the test results.

The results of the simulations presented here as well as many others, including some conducted at other inlet conditions, leads us to the conclusion that computer simulations constructed as described in the beginning of this paper provide adequate fidelity to represent the major features of the aerophysics associated with the post-stability characteristics of an augmented turbofan engine.

4.0 APPLICATION OF RESULTS

Validated models such as the one described in this paper are useful for conducting the trade studies necessary to design an engine with good recoverability characteristics and for developing recovery control strategies. The first step in conducting trade studies is to assure that the combustor-volume to compressor-volume ratio is sufficiently large to cause the critical speed range to occur at low engine speeds, preferably sub-idle. It is the author's contention that this is a fundamentally necessary condition that must be met if an engine is to have good recoverability characteristics. In and of itself however, a low critical speed range will not guarantee good recoverability characteristics. Other factors known to affect the recoverability characteristics of an engine are the level of the stability limit line, the level of compressor hysteresis, and control of the decel schedule and of combustor blow-out and relight as both affect the compressor operating line.

4.1 STABILITY LIMIT LINE

Experimental and analytical studies have shown that a high stability limit line promotes recovery most probably because the potential energy stored in the combustor provides the source of energy necessary to back flow the compressor and drop the operating line sufficiently so that normal flow can properly be re-established.

As a corollary, it is important that the compressor sensitivity to thermal transients or to inlet distortion not be too great because a significantly reduced stability limit line would give rise to an elevated critical speed range.

4.2 COMPRESSOR HYSTERESIS

This effect of compressor hysteresis is illustrated by a modelling study that was conducted on the compression-combustor system of a nonaugmented turbofan engine that had a relatively high critical speed. For our purposes here, compressor hysteresis is related to the relationship between the in-stall corrected flow obtained by throttling to stall and the in-stall corrected flow at which the compressor recovers back to its unstalled flow characteristic and could be defined by the relationship

$$H = 1 - \left(\frac{W_c \text{ In-stall}}{W_c \text{ Recovery}} \right) \quad (2)$$

In this parametric study, the compressor was tested at constant speed until compressor instability was induced. Four milliseconds after instability initiation, the throttle was opened to a lower throttle (higher flow). This was successively done until the throttle line upon which the compressor recovered was determined. Figure 7 illustrates that for a compressor with a stability limit point at "S₁" and an in-stall recovery point of "R," the compressor would recover if the throttle was dropped to throttle line "1" or lower. If the stability limit point was maintained at "S₁" and the hysteresis, H, is reduced by reducing the in-stall recovery point to "R₁," then the compressor would recover on a much higher throttle line ("2"). Thus, the reduction in hysteresis significantly reduced the amount of unthrottling required to recover the compressor. This study illustrated the strong effect of compressor hysteresis on the recoverability characteristics of a compressor.

4.3 OPERATING LINE CONTROL

An understanding of the effect of operating line can be gained by examining the pressure ratio-corrected flow map for a compressor (Figure 8). This map shows the unstalled constant-corrected-speed lines, the compressor stability limit line, and the

in-stall constant-corrected-speed lines together with the rotating stall recovery line. The nominal operating line is superposed for reference. In order to gain an appreciation for this representation, let us suppose the compressor is being throttled on the 97.5 percent corrected speed line towards the stability limit line. After the stability limit line is reached, assume speed remains constant and that the compressor ends up on the 97.5 percent corrected speed in-stall characteristic. The compressor would have to be unthrottled to a flow approximately equivalent to the flow on the unstalled 92.5 percent corrected speed line before the compressor would recover and return to the 97.5 percent corrected speed unstalled characteristic.

Now let us add three operating lines to the compressor map as in Figure 9 - the maximum accel schedule operating line, the decel schedule operating line, and the combustor blow-out throttle line. Assume for the purposes of this discussion that the compressor-combustor volume relationship is such as to allow the occurrence of stable rotating stalls at all speeds. If instability occurred at part power (< 97.5 percent corrected speed) and the main fuel control went to the accel schedule, then engine operation on the accel schedule would prevent recovery from rotating stall until the compressor corrected speed was in excess of 97.5 percent. If an instability occurred and the engine control went to the decel schedule, then recovery from rotating stall could be attained for corrected speeds down to approximately 88 percent. If the combustor should blow out, then the compressor would be unthrottled in a manner that would allow recovery from rotating stall down to speeds less than 80 percent corrected speed. Notice that if the blow-out throttle line should cross and remain above the recovery line at some speed less than 80 percent, as is suggested by the slopes of the stall recovery line and the blow-out throttle line, then rotating stall would not clear until speed drops sufficiently such that the strength of the rotating stall cell is reduced and begins to lose coherency. At this point, viscous forces will begin to cause it to dissipate. Following its dissipation, the compressor could then be re-accelerated without instability.

Hence, if control recovery logics can be designed that take into account the various operating lines and associated speed ranges, then the desired control of the operating line can be obtained. Obviously, upon the occurrence of instability, it is desirable to keep the control from going to the accel schedule. Depending on speed range and spool-down rates, rotating stall can be prevented or cleared by going to the decel schedule or the blow-out throttle line. Fuel and/or bleed-air dynamic effects have been demonstrated to have utility for clearing a compressor of rotating stall and to alleviate the need for unthrottling as much as steady-state unthrottling studies would indicate (Reference 6). Dynamic effects on recovery are also illustrated by the example discussed in Paragraph 4.2.

5.0 CONCLUSIONS

Studies have been accomplished which show that an engine transient cycle deck with extended capabilities will naturally predict the post-stability behavior of turbofan engines, be the instability surge or rotating stall or the transition from surge to rotating stall as speed decreases. In order that an engine transient cycle deck have this capability, it is necessary that the compressor component representations have in-stall and reverse flow characteristics and the associated stall-development and stall-recovery time constants, the combustor have rich-side heat addition and flammability characteristics, and the flow volumes of the engine be represented by one- or two-dimensional volumes as appropriate and both with reverse flow capability. In our studies, we have chosen to use the complete set of the equations of change together with a thermodynamic relationship to provide proper representation of the flow dynamics.

Models such as these have the capability for determining if the critical speed range of an engine system lies within an acceptable portion of the corrected speed spectrum, for determining the post-stability dynamics of an engine system (an aid for interpreting the source of measured frequencies), and for developing appropriate stall-recovery control strategies in relation to the speed range at which the inception of instability takes place.

REFERENCES

1. Hoony, W.M., Bitter, S.J., and Steenken, W.G., "Turbofan Engine Nonrecoverable Stall Computer-Simulation Development and Validation," AIAA Paper Number 85-1432, July 1985.
2. Leamy, K.R., Chung, K., Collins, T.P., and Lorenzo, C.P., "A Turbine Engine Aerodynamic Model for In-Install Transient Simulation," AIAA Paper Number 85-1429, July 1985.
3. Steenken, W.G. and Mani, R., "Aerodynamic Instabilities in Axial Flow Compressors," AIAA Professional Study Series - Air Breathing Propulsion, June 1984.
4. Steenken, W.G., "Modelling Compression Component Stability Characteristics - Effects of Inlet Distortion and Fan Bypass Duct Disturbances," AGARD Conference on Engine Handling, AGARD-C7-324, February 1983.

5. Greitzer, E.M., "Surge and Rotating Stall in Axial Flow Compressors, Part II: Experimental Results and Comparison with Theory," ASME Paper Number 75-GT-10, March 1975.
6. Hopf, W.R. and Steenken, W.G., "Stall Recovery Control Strategy Methodology and Results," AIAA Paper Number 85-1433, July 1985.

ACKNOWLEDGEMENT

A significant portion of the material used in this paper was generated under contract to the Air Force Aero Propulsion Laboratory, Air Force Systems Command, United States Air Force. Their support throughout the investigative program is deeply appreciated.

The author gratefully acknowledges the help of Dr. Wishaa Hosny in preparing this paper. His timely discussions of the material and review efforts are greatly appreciated.

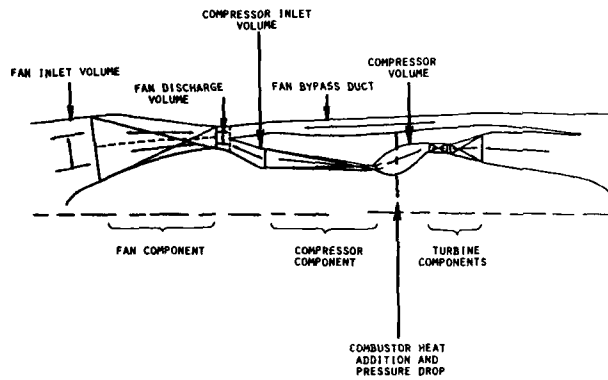


Figure 1. Schematic of Engine Components and Volumes.

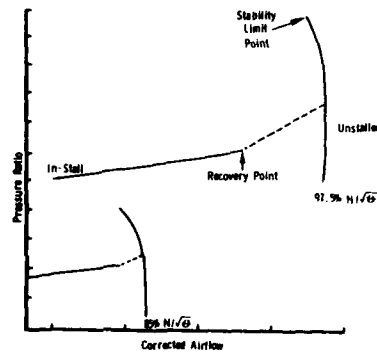


Figure 2. Relationship of In-Install and Unstalled Compressor Characteristics.

Combustion Efficiency Effect

Main Burner Flammability Limits

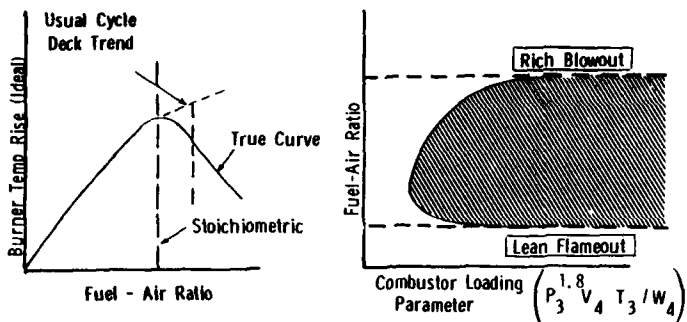


Figure 3. Key Combustor Characteristics.

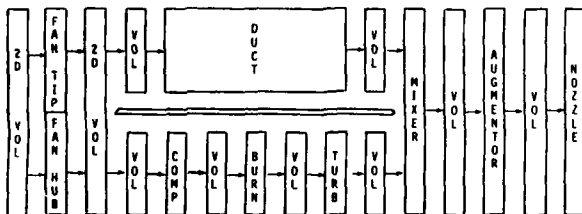
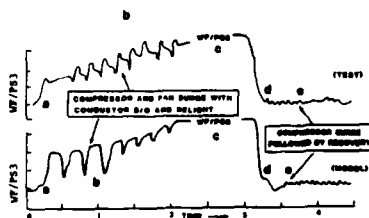
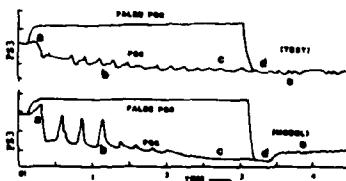


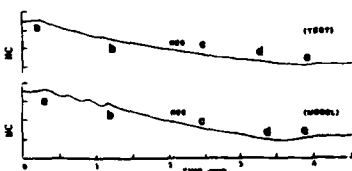
Figure 4. Model Volume Selection.



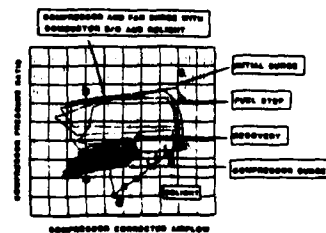
(a) Combustor Fuel Flow.



(b) Compressor Discharge Pressure Response.

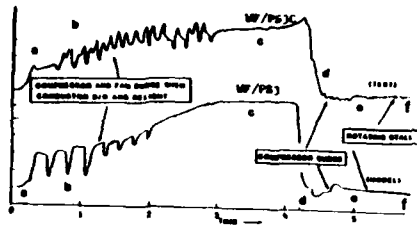


(c) Compressor Speed Response.

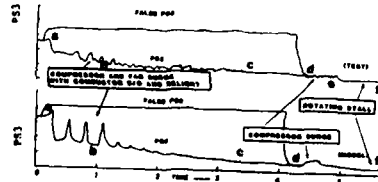


(d) Compressor Operating Point Migration.

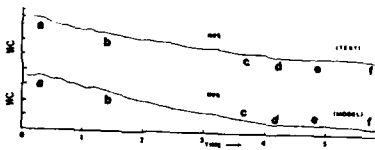
Figure 5. Recoverable Surge.



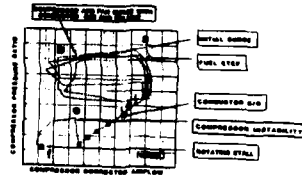
(a) Combustor Fuel Flow



(b) Compressor Discharge Pressure Response.



(c) Compressor Speed Response.



(d) Compressor Operating Point Migration.

Figure 6. Nonrecoverable Surge.

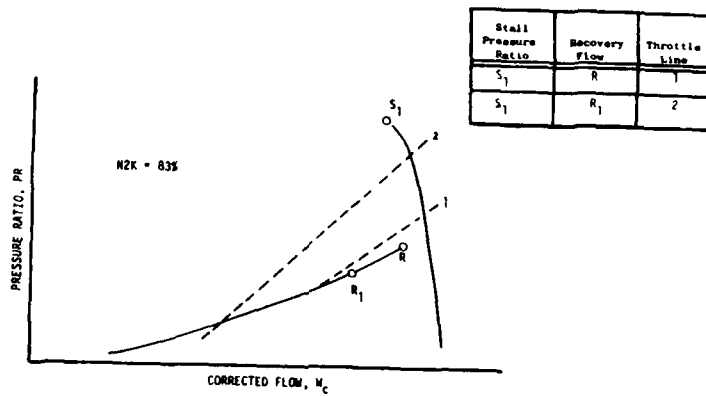


Figure 7. Stall-Pressure-Ratio and Recovery-Flow Effects.

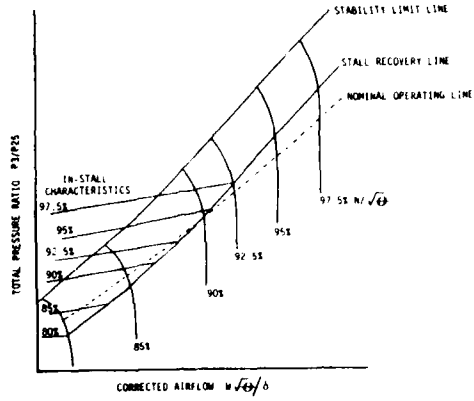


Figure 8. Compressor Recovery Line.

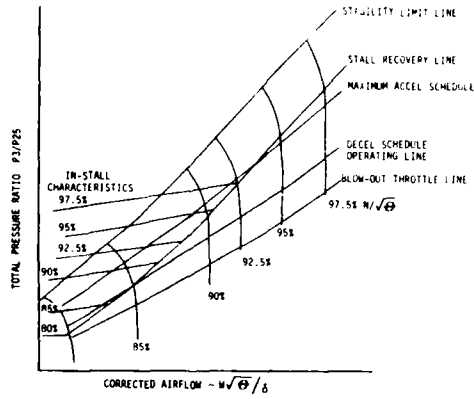


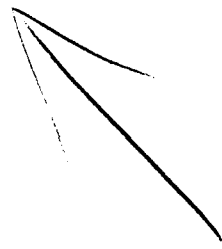
Figure 9. Compressor Operation with Respect to Recovery Line.

DISCUSSION**D.W. Stephenson, US**

1. Please explain the need for the volumes included in your engine performance modelling. Is this because there is a time element required for the flow leaving one component to reach that same level in the next component during transients?
2. Are your in-stall compressor characteristics obtained from engine or rig testing?

Author's Reply

1. The volumes were included to assure that the convective and acoustic velocity propagation paths simulated the actual propagation paths in the engine. This is necessary if system frequencies are to be replicated. Thus, the volumes were chosen in a manner to represent the lengths of ducting within the engine so that the acoustic reflection planes would be simulated. The entrance and exit flow areas to the volume with the above-chosen length were selected in a manner so the calculated volume was representative of the engine internal volumes. In this way, the resonance (eg Helmholtz type) associated with the volumes of the engine will also be simulated.
2. To date, we have obtained in-stall compressor characteristics during rig testing of compressors. Automatic control systems, which use the output of vane-mounted thermocouples as input, allow conducting the required testing without thermally distressing the compressor blades or vanes.



TRANSMISSION OF INLET DISTORTION THROUGH A FAN

by

J E Flitcroft
J Dunham
W A Abbott

Royal Aircraft Establishment, Pyestock
Farnborough, Hants, GU14 0LS, UK

SUMMARY

The effect of inlet swirl on the propagation of total pressure distortion through a 3-stage fan without inlet guide vanes has been investigated on a compressor rig. The tests gave the unexpected finding that the presence of a swirl counter to the rotation of the fan generally reduced the level of steady state distortion transmitted to the core compressor. Dynamic pressure measurements made at the exit from the fan, however, revealed that the swirl also caused a sudden early breakdown of the flow in a sector of the hub region, resulting in high time-variant distortion levels in the core flow. This observation is compatible with the destabilising effect of a swirl counter to fan rotation on engines. A theoretical analysis confirmed that a swirl, concentrated at the fan tip at entry, could drive some of the hub blade rows strongly towards stall.

NOMENCLATURE

PT = Total pressure (kPa)

TT = Total temperature (°K)

θ = Angular circumferential extent (degrees)

$$DC(\theta) = \frac{\text{Annulus or face mean total pressure} - \text{Lowest mean total pressure in a } \theta^\circ \text{ sector}}{\text{Dynamic head}}$$

$$PC(\theta) = \frac{\text{Annulus or face mean total pressure} - \text{Lowest mean total pressure in a } \theta^\circ \text{ sector}}{\text{Annulus or face mean total pressure}}$$

$$TC(\theta) = \frac{\text{Highest mean total temperature in a } \theta \text{ sector} - \text{Annulus mean total temperature}}{\text{Annulus mean total temperature}}$$

$$\text{Pressure distortion transfer ratio} = \frac{PC(\theta) \text{ fan exit}}{PC(\theta) \text{ fan inlet}}$$

$$\text{Temperature creation ratio} = \frac{TC(\theta) \text{ fan exit}}{PC(\theta) \text{ fan inlet}}$$

$$\text{Normalised PTIN} = \frac{\left[\frac{PT(\text{arm average})}{PT(\text{annulus mean})} - 1 \right] \text{ fan inlet}}{\left[1 - \frac{PT(\text{minimum arm average})}{PT(\text{annulus mean})} \right] \text{ fan inlet}}$$

$$\text{Normalised PTDEL} = \frac{\left[\frac{PT(\text{arm average})}{PT(\text{annulus mean})} - 1 \right] \text{ fan exit}}{\left[1 - \frac{PT(\text{minimum arm average})}{PT(\text{annulus mean})} \right] \text{ fan inlet}}$$

$$\text{Normalised TTDEL} = \frac{\left[\frac{TT(\text{arm average})}{TT(\text{annulus mean})} - 1 \right] \text{ fan exit}}{\left[1 - \frac{PT(\text{minimum arm average})}{PT(\text{annulus mean})} \right] \text{ fan inlet}}$$

TU = Maximum RMS pressure fluctuation observed at an operating point (Radial average).

TU_{Max} = Maximum RMS pressure fluctuation observed (Radial average).

INTRODUCTION

During the development of the Tornado powerplant it became apparent that a swirl in the inlet flow, counter to the rotation of the engine ("contraswirl"), had a significant destabilising influence, substantially reducing the level of total pressure distortion that could be tolerated. The adverse effect of a circumferential variation in total pressure on engine stability is, of course, well established^{1,2}. Although the solution adopted on the aircraft was to incorporate aerodynamic fences in the curved intake, in locations which inhibited the secondary flow behaviour responsible for the swirl³, the situation had highlighted a lack of knowledge of the manner in which swirl affected engine stability. Since curved inlet ducts are frequently required for practical installations, a better understanding of the effect of swirl was clearly needed to enable its significance to be assessed fully for future powerplant designs.

A variety of explanations for the adverse effect of contraswirl were considered. One was the creation of a significant mismatch between the spools. However an examination of measurements on an engine showed that, although contraswirl caused a small reduction in the speed of the fan relative to the core, the operating point remained on a similar working line to that followed without swirl. Since the operating lines of the core compressors are established by choking of the HP turbine nozzle guide vanes, and are therefore insensitive to the fan exit conditions, there was no evidence for the mismatched spool hypothesis. Given that the surges had been observed to initiate in the core compressors rather than the fan it was clearly not just a consequence of the fact that contraswirl increased the incidence of the first blade row to the point where stall occurred; since the first blade row in this case was a rotor in practice only a small increase in incidence occurred. The only feasible explanation for the effect of contraswirl was therefore that it resulted in higher levels of flow distortion entering the core engine.

To test the above hypothesis, and provide data for the evaluation of prediction methods, measurements of the transmission of inlet total pressure distortion were made on a representative military fan. The results are presented in this paper. Although the stabilising influence of the core engine, due to the coupling between closely spaced spools, would not be represented in this experiment, it was anticipated that the correct trends would be obtained⁴. A theoretical analysis of the effect of swirl on the fan aerodynamics was also undertaken, to provide a qualitative means of assessing the changes likely to be taking place within the turbomachinery to produce the observed behaviour.

RIG DESCRIPTION

The general arrangement of the test rig is shown in Figure 1. Air is drawn in by the fan through an inlet silencer and calibrated air meter. A non-uniform inlet pressure distribution, representing an off-design aircraft intake flow pattern, was produced by inserting a gauze screen in the distortion generator. For tests without swirl the gauze was supported by a honeycomb mesh, Figure 2a. For investigations with swirl the honeycomb support was replaced by a series of radial vanes, which were twisted along their length to create a rotation which varied from 0° at the hub to a maximum at the tip, Figure 2b. The gauze blockage could be rotated through 350°.

The fan module comprised a 3 stage low-hub/tip ratio research machine without inlet guide vanes, representative of current military engine technology. The fan discharged into a split-flow collector box which incorporated two concentric dump diffusers. Both core and by-pass streams passed through airmeters prior to discharge through a common throttle valve. The fan by-pass ratio was pre-set using a bias gauze.

During the investigation it was discovered that the bend downstream of the dump diffusers produced a circumferential variation of the flow properties at the fan exit measurement plane. A subsequent comparison, using the measurements made with a single rake arm and rotating the blockage, showed that results obtained with a fixed gauze blockage could be corrected by considering the bias induced by the bend to be superimposed on the measured exit circumferential variation.

INSTRUMENTATION

Two types of inlet flow survey instrumentation were used; a symmetrical 8-arm array of rakes with 5 probes per arm, each probe incorporating a miniature pressure transducer and thus able to measure both time-averaged and time-variant total pressure, or a single arm containing five 5-hole conical yawmeter probes. The inlet rakes were removed when taking the definitive exit flow measurements with swirl. Fan delivery pressures were measured using 8 rakes, each containing 5 steady-state total pressure probes in both core and by-pass flow annuli. The centre probe in the by-pass and the second and fourth probe in the core on each arm contained a miniature pressure transducer for time-variant pressure measurement (Figure 3). The time-variant pressure signals were recorded on magnetic tape. The system was limited to 40 channels so when the delivery conditions were being recorded only 16 inlet probes could be monitored. Fan exit temperature was measured using a single rake with 4 thermocouples in each annulus.

TEST CONDITIONS

For the first phase of testing a range of throttle settings was examined at 80, 85 and 90% design speed with both clean and non-uniform inlet flow conditions. The swirl vanes and gauze were tested both separately and in combination. In the second phase of

the investigation the distortion generator was rotated in 30° increments to provide a full flow-survey at entry using the single yaw meter rake and at exit from the single temperature rake.

A structural loading limit on the inlet silencer system precluded surging of the fan during these tests.

DISCUSSION OF THE STEADY-STATE RESULTS Fan inlet flow conditions

The gauze used to generate the circumferential pressure variation gave a once-per-revolution pattern. A contour plot is shown in Figure 4. There was no net swirl associated with the gauze alone. At the measurement plane the maximum deviations from axial flow, measured at the sides of the low pressure region, were less than ±2°.

The swirl vanes in isolation gave a rotation counter to the fan which varied from 3° at 32% radius to 12° at 92% radius. In combination with the gauze, swirls of almost double the above levels were observed in the low pressure region, (Figure 5).

Fan overall operating characteristics

The overall performance of the fan with a clean inlet, and with the gauze and swirl vanes both separately and in combination, is summarised in Figure 6. The gauze and swirl combination produced a marked reduction in both flow and pressure ratio, a contrast to the limited change from the clean inlet performance observed with the gauze alone. The reduction in pressure ratio and flow with swirl alone as the fan was throttled was unexpected. Simple theory would indicate that a rotation in the flow in the opposite sense to the fan would normally result in the movement of the operating line to the right⁴.

Distortion transmission without swirl

The steady-state distortion transmission behaviour of the fan measured with the gauze alone is illustrated in Figure 7. Normalised curves showing the circumferential variation of inlet total pressure, exit total pressure and exit temperature for core and by-pass regions are presented. For calculation purposes the inlet flow was divided into concentric circular stream tubes with the measured core/by-pass flow split. The greater attenuation of pressure distortion achieved in the by-pass region is clearly apparent, a finding consistent with the much steeper operating characteristic of that region of the fan (Figure 8). Both the core and by-pass flows exhibited peak temperatures in the region where, at inlet, the rotor was sweeping into a rising total pressure field, a feature seen by other workers^{6,7}. A local increase in blade incidence occurs in the region, due to the tendency of the fan to induce a static pressure distortion ahead of the rotor, in sympathy with the total pressure variation⁸.

The effect on the distortion transfer characteristics of fan speed and operating point are illustrated in Figure 9. Although the parameter used to characterise the transfer is based on a 60° sector angle, similar levels were obtained for a range of angles up to 135°. The results show little variation with fan speed. The initial increase in attenuation in the core as the fan is throttled, followed by a subsequent rise, was also observed in Reference 5. The consistently high levels of attenuation achieved in the by-pass region render it the more attractive location for engine control instrumentation for monitoring the fan working point, since such instrumentation needs to be relatively insensitive to the orientation of any inlet flow distortion.

The effect of swirl on distortion transfer

Figure 10 shows the equivalent inlet and exit flow measurements for the gauze and swirl combination at an equivalent operating condition to that illustrated for the gauze alone in Figure 7. Whilst the basic features are similar, it will be noted that the levels of attenuation achieved are greater. As Figure 11 shows this was also the case at the other operating conditions examined. On the above evidence it therefore appeared that a swirl counter to the rotation of the fan did not result in higher levels of circumferential distortion entering the core engine.

Since a strong radial variation in total pressure could also affect the surge margin of the core compressor, a comparison was made of the mean total pressures on each ring of probes. The magnitude of the local circumferential variation on each ring was also examined. Typical comparisons are shown in Figure 12. There was no indication that the tests with swirl produced a more severe hub-low pattern, which would be the most likely to cause a loss of core compressor stability. Furthermore, with swirl, the level of circumferential distortion was lower in the hub region than without swirl. The radial variation was also less. There was therefore no evidence that a swirl counter to the fan rotation caused a more adverse radial distortion.

From the tests where the blockage had been rotated to provide exit temperature surveys it was found that the levels of total temperature distortion in the fan core delivery region were also lower with contra-swirl in combination with the gauze (Figure 13). Although when compared on the basis of pressure ratio the level with swirl does rise to equal the value measured with the gauze alone, it should be noted that the condition does relate to a higher operating point because of the adverse effect swirl had on overall fan performance.

Comparison with predictions

In the absence of a fully 3-D model the predictions of the steady-state distortion transfer were made using a linearised two-dimensional method, which models the upstream and downstream ducting and the fan as a series of control-volumes⁴. The mean flow properties in the fan control-volumes were calculated using a blade-row stacking model. The core and by-pass regions of the fan were treated as two separate machines, the location of the dividing streamline being determined using a streamline curvature calculation program. Only the mean value of circumferential swirl could be specified at the upstream boundary.

Examples of the measured and predicted exit profiles for the core region are presented in Figure 14 for cases both with and without swirl. Although there was generally good agreement in the basic shapes, the measured increase in attenuation observed with the swirl present in combination with the gauze was not correctly reproduced. A small decrease was usually indicated. In the by-pass region the predictions differed substantially from experiment because the calculated levels of attenuation were comparable with those for the core. The reason for this was apparently due to the predicted by-pass compressor characteristic having a lower slope than the measured one. A simple calculation using the slope of the measured characteristic gave levels of attenuation comparable with those observed in the experiment.

DISCUSSION OF THE DYNAMIC MEASUREMENTS

A comparison of the maximum values of Root Mean Square (RMS) pressure fluctuation measured in the core annulus at exit from the fan gave the first indication of a mechanism by which the presence of contraswirl could make conditions worse for the core turbomachinery. At all three speeds examined during the initial phase of testing a dramatic increase in turbulence was noted with the gauze and swirl combination as the fan was throttled to the highest operating point (Figure 15). In an engine this would result in a large rise in the level of time-variant distortion entering the core compressor, and would more than offset the slight reduction in steady-state distortion obtained with contraswirl. At lower operating points the much smaller increment in turbulence with contraswirl would only result in comparable peak instantaneous levels.

From the second phase of testing, where the blockage was rotated, it was evident that the peak turbulence occurred in the same region as the peak temperature and not the lowest steady-state pressure. A circumferential shift between the instantaneous peak and steady-state distortion patterns would therefore be indicated. As mentioned previously the location of the peak temperature corresponds to the region where at entry the local crossflow induced by the static pressure distortion, produced in sympathy with the total pressure variation by the rotor, leads to increased blade incidence. On the other side of the trough, where the induced swirl perturbation would be co-rotational, the levels of turbulence were similar to those obtained at lower operating points.

A comparison of the circumferential variation of steady-state total pressure in the core as the operating point was raised revealed that a marked local deterioration in fan performance had occurred in the region of high turbulence. As Figure 16 shows, at the highest operating point the left hand edge of the low pressure region was no longer clearly defined. A comparison of the respective inlet pressure and turbulence measurements showed no substantial difference, confirming that the observed behaviour was due to a local breakdown of flow within the fan. An examination of the associated transducer signals from the by-pass region confirmed that the effect was concentrated at the hub. Spectral analysis of the turbulence revealed a dominant sub-rotor speed frequency, in the manner of a rotating stall, which was not present at the other operating conditions.

Supporting evidence for the explanation that a local breakdown of flow in the hub region of the fan can occur without initiating surge directly, only to trigger it subsequently in the core turbomachinery, is provided by the findings of Miatt and Schaffler⁹. In that case, with a uniform inlet flow, surges of the HP compressor were induced by closing the nozzle to well below the normal operating area. The cause was found to be a rotating stall in the fan hub. The presence of a circumferential variation in inlet total pressure could be regarded as imposing a cyclic variation on such behaviour.

The absence of any inter-blade-row instrumentation on the fan meant that no evidence was available to indicate at what point within the fan the flow breakdown was occurring. Some guidance was however provided by a theoretical analysis of the effect of a circumferential swirl on the flow within the fan, using an axisymmetric streamline curvature computer program¹⁰.

THEORETICAL ANALYSIS OF FAN INTERNAL AERODYNAMICS

The streamline curvature program required a specification of air outlet angle (or deviation) and pressure loss coefficient at the outlet from each blade row as a function of radius. Since this information was not available for the full range of conditions likely to arise in the presence of swirl, a representative specification, which matched the fan performance at a working line pressure ratio at 90% speed without swirl, was used for all calculations. Although the findings must therefore be regarded as providing a qualitative, rather than quantitative, guide to the effect of swirl on the internal flow behaviour, the correct trends were expected to be present.

Figure 17 shows the overall performance characteristics obtained. For comparison the measured characteristics are also presented. It is immediately obvious that with fixed loss coefficients the marked turnover of the measured characteristics is not obtained; since the measured pressure rise is lower, either the loss or deviation (or both) must be greater.

A possible justification for higher loss and/or deviation can be seen from the following table, showing the effect of inlet contraswirl on the local incidence angles at three radial stations, representative of hub, mean and tip conditions.

EFFECT OF SWIRL ON LOCAL INCIDENCE ANGLES

| % N _D | BLADE ROW | HUB | MEAN | TIP |
|---------------------|--------------|------|------|------|
| 85 | rotor 1 | -0.4 | +0.2 | +0.2 |
| | stator 1 | +2.5 | +0.7 | -3.3 |
| | rotor 2 | +4.1 | 0 | -0.5 |
| | stator 2 | +3.2 | -0.9 | -1.8 |
| | rotor 3 | +2.1 | -0.3 | -0.3 |
| | stator 3 | +0.8 | -0.7 | -0.6 |
| 90 | rotor 1 | -0.5 | +0.2 | +0.2 |
| | stator 1 | +2.9 | +1.3 | -2.9 |
| | rotor 2 | +4.9 | +0.4 | -0.5 |
| | stator 2 | +4.4 | -0.2 | -1.3 |
| | rotor 3 | +3.5 | +0.2 | 0 |
| | stator 3 | +2.3 | +0.2 | +0.3 |

At each speed the pressure ratio was taken on the relevant working line. It is interesting to note that although the inlet swirl used in the calculation was zero at the hub, and increased linearly to a maximum of 10° at the tip, it is the hub incidences which increase. This is because the axial velocity distribution has to adjust itself in order to maintain radial equilibrium.

The effect of these higher incidences is to increase significantly the loading parameter \dot{P}/D (static pressure rise/inlet dynamic head) at the stator hub of stages 1 and 2 to values at which stall might well occur. The local axial velocity profile is also expected to deteriorate, as shown in Figure 18. It is relevant to note that if the calculations were repeated with the increased loss and deviation apparently indicated by the test results, the changes in incidence and axial velocity profile with swirl would have been greater.

The theoretical analysis in combination with the experimental results, provide a convincing explanation of how a contraswirl, concentrated at the fan tip at inlet, can result in a substantial deterioration of the quality of the flow entering the core compressors and in turn account for the increased sensitivity of the engine to inlet distortion.

CONCLUSIONS

Time-averaged measurements of the transmission of distortion through a split-flow military fan showed that, at fan exit in the by-pass region, the level of distortion was only about 20% of the value at inlet. Substantially less attenuation was achieved in core, with about 60% of the inlet value being measured. The effect of a swirl counter to the fan rotation was, surprisingly, favourable, increasing attenuation in the core so that the level of distortion at exit was now only about 45% of the inlet value.

Calculations of the steady-state distortion transmission behaviour, in the core predicted the circumferential variation well, but gave an incorrect indication of the effect of swirl.

The picture changed markedly when the dynamic content of the exit pressure distortion was taken into account. On the normal working line of the fan the addition of contraswirl resulted in turbulence more than three times the level observed with distortion alone. The large implied increase in the time-variant total pressure distortion in the flow entering the core compressors could well account for the observed reduction in stability margin of engines when subjected to distortion in combination with contraswirl. Calculations using an axisymmetric flow program showed that for this fan there was a strong tendency for inlet swirl to increase the incidences of blading in the hub, supporting the experimental evidence that the high turbulence was due to a local region of hub stall.

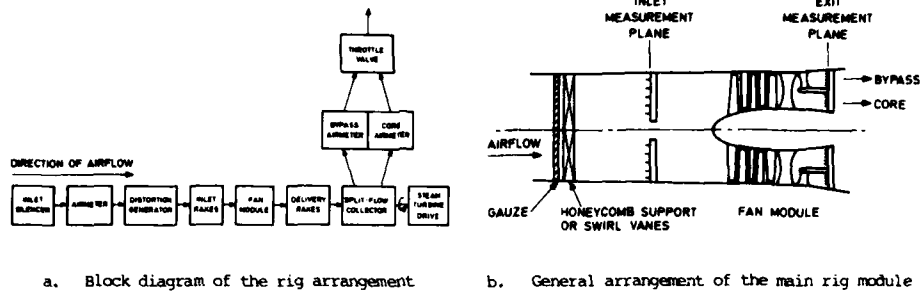
Dynamic instrumentation in the fan exit is clearly desirable in rig or engine tests where potential fan-core interactions are being examined.

ACKNOWLEDGEMENTS

The authors would like to acknowledge the assistance of Dr Hynes of the Whittle Laboratory, Cambridge who provided the theoretical calculations of distortion transfer for comparison with the experimental results, Mr McKenzie and Mrs Beaven of RAE Pyestock who helped with the testing and the analysis of the dynamic measurements respectively, and to colleagues at Rolls-Royce for helpful discussion of the aerodynamic analysis.

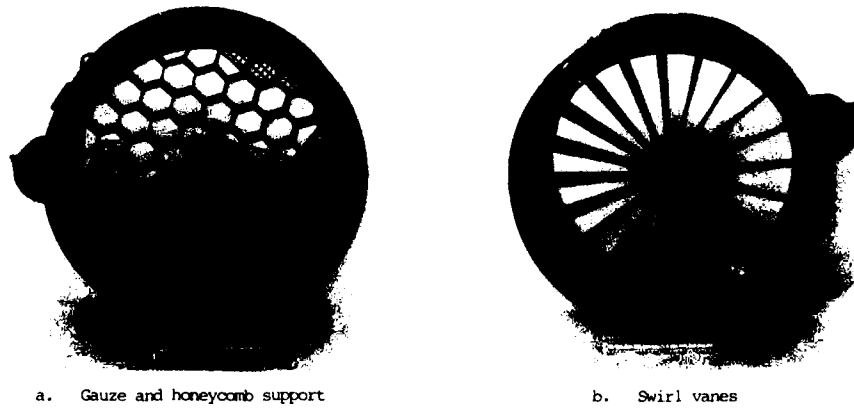
REFERENCES

1. Hercock R G Aerodynamic response
Williams D D AGARD LS72. Nov 1974
2. Bowditch D N A survey of inlet/engine distortion compatibility
Coltrin R E NASA TM 83421. June 1983
3. Stocks C P The design and development of the Tornado engine air intake.
Bissinger N C AGARD CP301. May 1981
4. Ham C J Some applications of Actuator and Semi-Actuator disk theory to
Williams D D the problems of intake/engine compatibility.
IGTC-50. Tokyo 1983
5. Hercock R G Effect of intake flow distortion on engine stability.
AGARD CP234. October 1982
6. Mazzaway R S Multiple segment parallel compressor model for circumferential
flow distortion.
ASME Journal of Engineering for Power. April 1977
7. Evans D G Some comparisons of the flow characteristics of a turbo-
de Bogdan C E fan compressor system with and without inlet pressure distortion.
Soeder R H NASA TMX-71574. July 1974
Pleban E J
8. Flourde G A Attenuation of circumferential inlet distortion in multistage
Stenning A M axial compressors.
Journal of Aircraft Volume 5 No 3. May-June 1968
9. Schaffler A Experimental evaluation of heavy fan-high-pressure compressor
Miatt D C interaction in a three shaft engine Parts 1 and 2.
Papers 85-GT-173 and 85-GT-222 ASME 30th International Gas Turbine
Conference, Texas - March 1985
10. D H Frost A streamline curvature through-flow computer program for analysing
the flow through axial-flow turbomachines.
ARC R&M 3687 - 1972



a. Block diagram of the rig arrangement b. General arrangement of the main rig module

FIG 1 DETAILS OF THE RIG LAYOUT

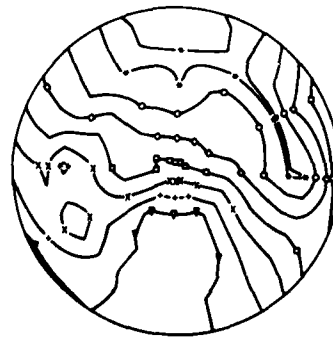


a. Gauze and honeycomb support b. Swirl vanes

FIG 2 DISTORTION GENERATOR CONFIGURATIONS



FIG 3 FAN DELIVERY TOTAL PRESSURE RAKE ARM



KEY

| | |
|---|-------|
| ▲ | 0.920 |
| ▼ | 0.940 |
| • | 0.960 |
| x | 0.980 |
| ○ | 1.000 |
| ◊ | 1.020 |
| ◌ | 1.040 |
| ◐ | 1.060 |

FIG 4 INLET TOTAL PRESSURE DISTRIBUTION WITH GAUZE

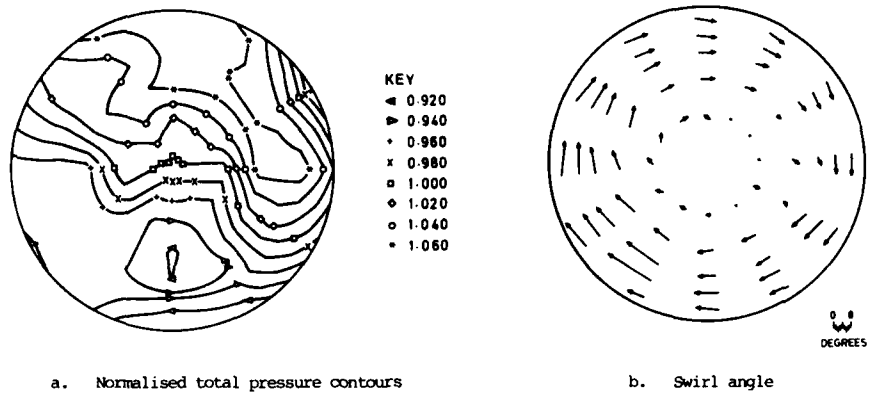


FIG 5 INLET FLOW WITH GAUZE AND SWIRL

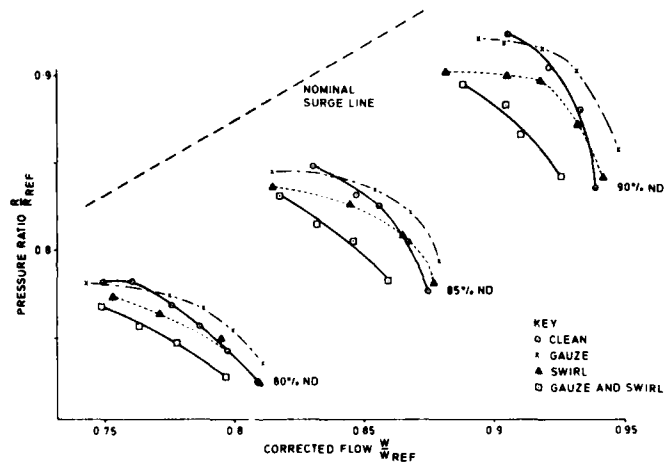


FIG 6 OVERALL FAN CHARACTERISTICS

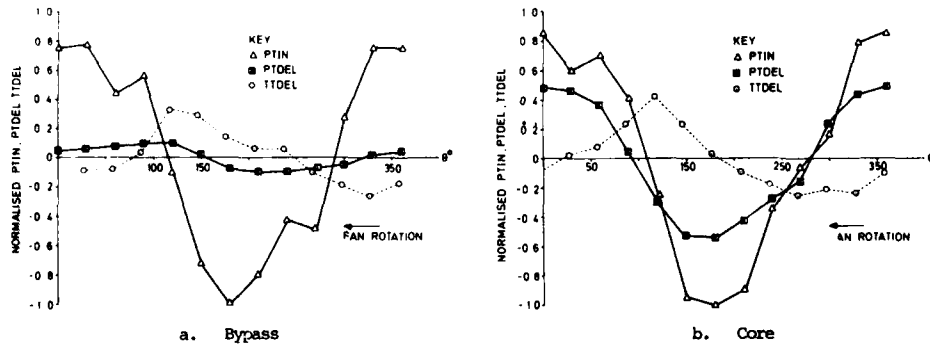


FIG 7 GAUZE ALONE, 90% SPEED

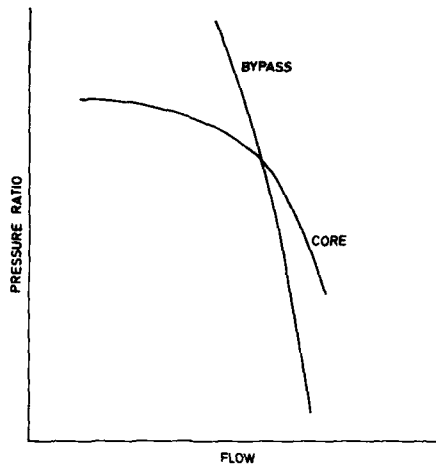


FIG 8 EXAMPLE SPLIT-FLOW CHARACTERISTIC

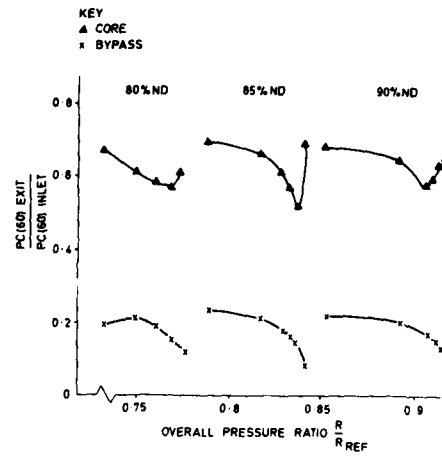


FIG 9 PRESSURE DISTORTION TRANSFER BEHAVIOUR WITH GAUZE

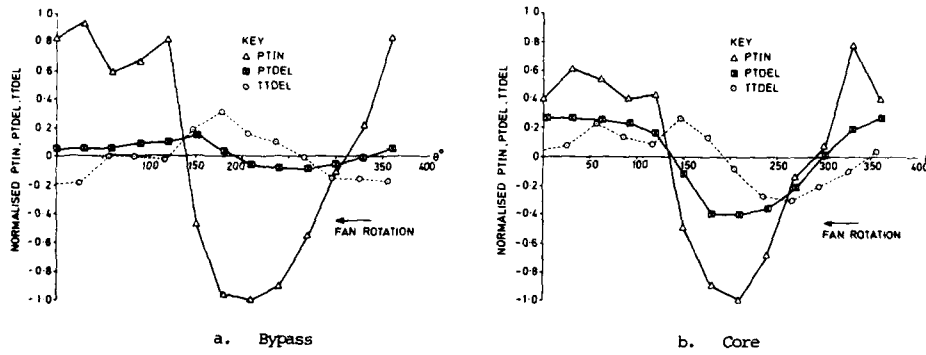


FIG 10 GAUZE AND SWIRL, 90% SPEED

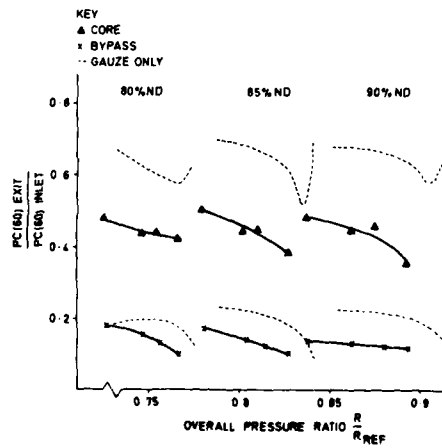


FIG 11 PRESSURE DISTORTION TRANSFER BEHAVIOUR WITH GAUZE AND SWIRL

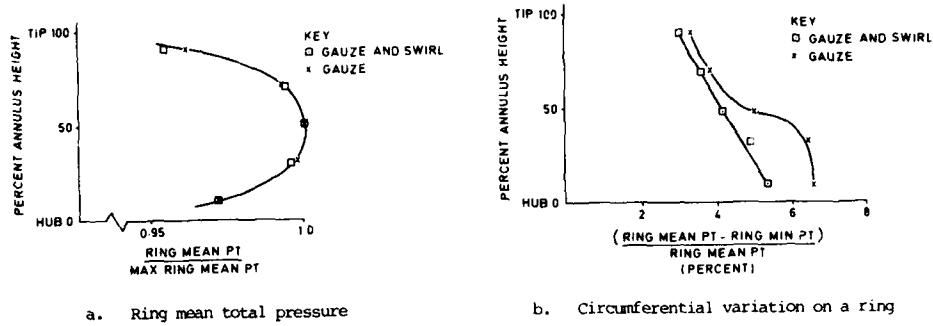


FIG 12 COMPARISON OF RADIAL PROFILES IN THE CORE ANNULUS

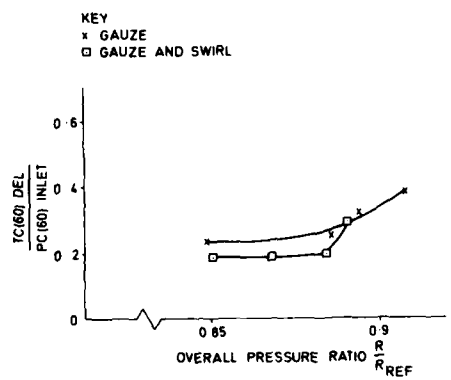


FIG 13 CORE TEMPERATURE DISTORTION COMPARISON FOR 90% SPEED

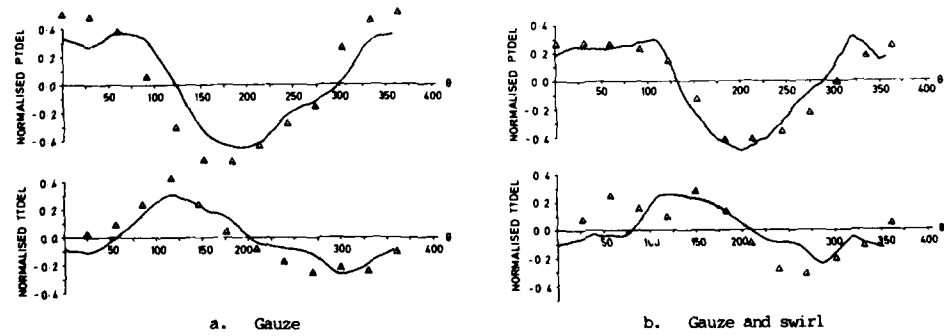


FIG 14 COMPARISON WITH PREDICTIONS

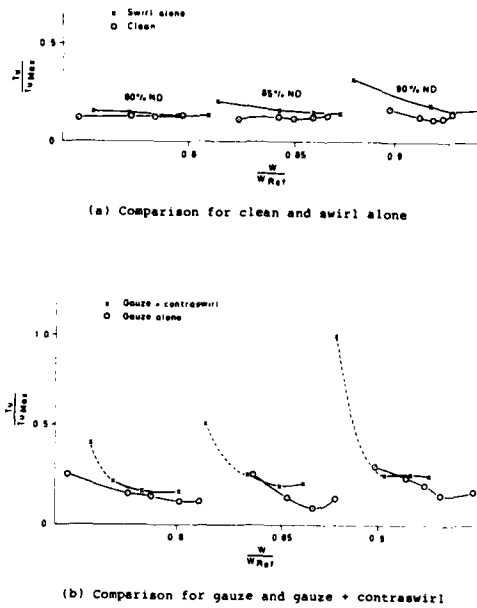


FIGURE 15 THE VARIATION OF CORE EXIT TURBULENCE WITH SPEED AND OPERATING POINT

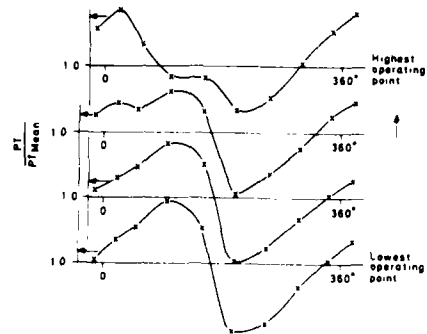


FIGURE 16 VARIATION OF CORE EXIT PRESSURE WITH OPERATING POINT (GAUZE + CONTRASWIRL)

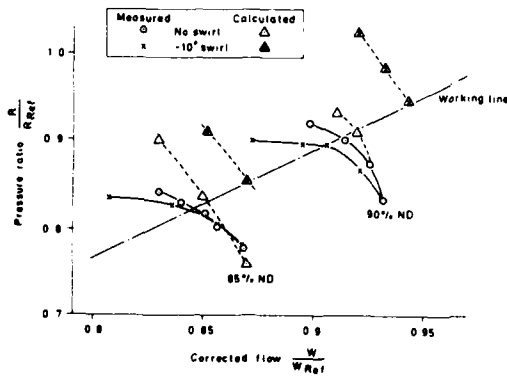


FIGURE 17 PREDICTED COMPRESSOR CHARACTERISTICS

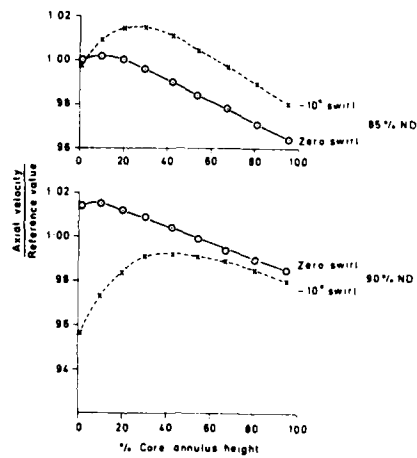


FIGURE 18 OUTLET AXIAL VELOCITY PROFILE (CALCULATED)

**EXPERIMENTAL INVESTIGATION ON SMALL TURBOPROP BEHAVIOUR
UNDER COMPRESSOR ROTATING STALL FOR DIFFERENT INLET FLOW CONDITIONS**

by

S.Colantuoni and G.Liotti
ALFA ROMEO AVIO
Direzione R & D
80038 Pomigliano d'Arco
Napoli, Italy

SUMMARY

This paper deals with an experimental investigation on compressor rotating stall and acoustic noise in a small turboprop. The intent of the study, undertaken in Alfa Romeo Avio using the engine test bed, during the initial phase of the AR 318 turboprop development program, was to clarify the noisy and unstable behaviour of some engines at part-speeds.

The overall performances of the centrifugal compressor, the time-dependent wall static pressure measurements, to visualize impeller rotating stall regions on the compressor map, and the acoustic noise signals, detected at the engine air-intake inlet, are presented.

Finally, the engine performances in stalled compressor conditions are analyzed and main results discussed.

NOMENCLATURE

| | | |
|----------|-------------------------------------|-------|
| e | Neper's number | |
| EGT | Exhaust gas temperature | deg K |
| ETAB | Combustion efficiency | |
| FAR | Fuel-air-ratio | |
| LHV | Lower heating value of the fuel | J. Kg |
| N | Rotor speed | RPM |
| ND | Corrected design rotor speed | RPM |
| PR | Compressor T-T pressure ratio | |
| P0 | Compressor inlet pressure | kPa |
| P2 | Compressor exit total pressure | kPa |
| TET | Turbine entry temperature | deg K |
| T0 | Compressor inlet temperature | deg K |
| T2 | Compressor exit total temperature | deg K |
| WF | Fuel flow | g/s |
| δ | Pressure factor = $P0/101$ kPa | |
| θ | Temperature factor = $T0/258$ deg K | |
| W | Air flow rate | Kg/s |

1. INTRODUCTION

1.1 Problem statement

The AR 318 is a single-shaft turboprop of the 450 kw engine class. In fig. 1 the engine cross-section is shown.

The main elements are a S-shape air intake, a single stage centrifugal compressor, a reverse flow annular combustor and a two stage uncooled axial turbine.

The reduction gearbox is driven by a forward extension of the compressor shaft and provides a maximum propeller speed of 2000 RPM.

The centrifugal compressor had an impeller of 290 mm exit diameter, 13 entire/13 splitter blades, a 25 vanes radial diffuser, a 90° bend and an axial straightener diffuser.

The compressor was designed for design point pressure ratio PR of 6.8 : 1 and 2.85 Kg/s of mass flow, at the speed ND = 38100 RPM with an isentropic efficiency of 78% T-T. At design speed a transonic flowfield is present at the inlet of the impeller as well as of the diffuser.

The configuration was tested on the rig (see fig. 2) and the results satisfied the target, as shown by the compressor map in fig. 3, in terms of pressure ratio, mass flow and efficiency.

Furthermore, the surge margin was adequate for the engine requirements in the complete range, from the Ground-Idle (72.5% ND) to the Cruise condition (105% ND). A more accurate analysis of the overall performance shows that the impeller/diffuser matching is realized as follows:

- A) the maximum efficiency of 79% is at 95% ND;
- B) the peak efficiency line in the working range of the engine (70% ND to 105% ND) is near the surge line, and therefore is not possible to operate here;
- C) at part-speeds (around 70% ND) the impeller is clearly in deep stall and so the overall efficiency level is degraded.

Such good compressor performances were not available always on the engine hardware, i.e. sensitive variations of mass flow and efficiency were measured on some builds. Furthermore, hysteresis' phenomenon at transient conditions were experienced.

Another relevant observation done during the dynamometer engine test is about the noise, whose variation was clearly audible in tone and intensity level along the operating line, from Ground-Idle (GI) to Take-off (TO) and viceversa.

It is important to point out that, the main differences between rig and engine were:

- A) the compressor casing configuration (see fig. 2 vs. fig. 1);
- B) the geometry of the plenum chamber at the compressor exit of the rig, compared to the annular combustion chamber of the engine;
- C) the impeller axial tip clearance, whose variation with speed is greater on the engine.

The last is a penalty for the compressor and the engine performances. Nevertheless, on first prototype engines, in order to avoid a rub between casing and impeller at 105% ND, it was necessary to increase the compressor build clearance from the rig value of 0.89 mm to the engine value of 1.37 mm.

1.2 Objective of the investigation

Looking at the experimental data available and briefly presented, an experimental program was carried out on the engine, having the following targets:

- I) to get for the engine compressor configuration more accurate information on the aerodynamic phenomenon of the impeller rotating stall;
- II) to verify the existence of a connection between engine noise and rotating stall.

So, it was decided to carry out an engine test, in order to get:

- 1) the engine compressor performance map;
- 2) the time-dependent wall static pressure measurements, detected on the compressor casing at the impeller throat;
- 3) the noise signals, detected near the inlet of the engine air-intake.

2. COMPRESSOR EXPERIMENTAL INVESTIGATION ON THE ENGINE TEST BED

2.1 Test facility, Engine instrumentation and Data acquisition system

The engine has been tested on the ALFA ROMEO AV10 dynamometer test bed shown in fig. 4. It is an hydraulic dynamometer FROUDE FO 271, fit for taking up a power of 1000 kw, with a maximum speed of 3000 RPM.

In order to evaluate the engine performances, during the test recording of torque, speed, fuel flow, ambient temperature and pressure have been done. Turbine Exit Gas Temperature (EGT) has been measured by 30 thermocouples assembled in 10 rakes circumferentially equispaced.

The standard engine compressor instrumentation is given by the air intake static pressure taps, to compute massflow rate at the compressor inlet, using a calibration curve, plus 4 thermocouples for total temperature, and 4 probes for total pressure at the compressor exit plane, to evaluate pressure ratio and efficiency.

In order to detect impeller rotating stall, two Kistler piezoelectric transducer have been placed on the compressor casing (in the Top position 'T' and Bottom 'B', 180° a part), in the inducer zone of the impeller, just after the throat of the entire blade channel (see fig. 5). The pressure signals from the transducer have been amplified and stored on a magnetic tape recorder.

A microphone B & K has been placed in the proximity of the engine air-intake and the noise signal has been stored on the magnetic tape for the successive elaboration.

2.2 Test procedure

Each engine operating condition was stabilized for the necessary time and then monitored. Any power level was set by acting on the dynamometer load, so that the engine speed remains firm when the fuel flow was increasing. In this way the operating point on the compressor map moves from choke towards the surge line.

The data acquisition has been done firstly at the engine condition of minimum loading, from GI at 72.5% design speed (ND=38100 RPM), to TO speed (100% ND), every 2.5% interval. Then, the compressor speed-line 70%, 80%, 87.5%, 90%, 92%, 95%, 98% and 100% ND have been explored, from the condition of minimum loading (condition at choking) to the one at maximum fuel allowable (maximum EGT of 950 deg K).

3. TEST RESULTS

3.1 Overall engine performances

The engine components chosen for this build are to a great extent derived from other prototypes, which have already carried out heavy tests. The overall engine performances are not very representative of this engine class.

Engine performances were established by means of a test analysis computer code, which calculates those parameters not directly measured, like Turbine Entry Temperature and reduces to the reference standard conditions all the performances parameters.

During the test the maximum power reached was 400 kW, at 51.3 g/s of fuel flow, with a TET of 1240 deg K.

3.2 Overall compressor performances

The engine compressor map is presented in fig. 6.

It is possible to see in fig. 7 the difference between rig and engine results. From the analysis of these results we observe the following:

- at 100% ND the engine compressor reaches the mass flow and the pressure ratio required at design condition;
- at off-design conditions, the reduction of mass flow at choke for every speed-line is substantial. This is mainly due to the difference of the impeller tip clearance between rig and engine (1.37 mm of the engine respect to 0.89 mm of the rig);
- the speed-line at 87.5% ND of the engine compressor map has a double characteristic as shown by fig. 7. In fact during the data acquisition of the test point T/P 411 ($\dot{W}/\dot{S} = 1.90$ Kg/s, $PR = 4.71$), the compressor jumps abruptly into rotating stall condition, and the engine reaches the new equilibrium point T/P 412 ($\dot{W}/\dot{S} = 1.70$ Kg/s, $PR = 4.29$);
- the jump of the compressor into rotating stall region corresponds to a strong engine noise.

The increase of the impeller tip clearance, reduces the massflow at the diffuser choked condition at each speed and shifts the engine compressor map on the left. Together with a decrease of the efficiency due to greater clearance, an extension of the impeller stall region on the compressor map at part-speeds is also present. The region influenced by rotating stall, moves from 75% ND on the rig to 89% ND in the engine configuration.

This is due to the higher level of incidence at the impeller inlet, because of the lower massflow through the compressor that is imposed by the diffuser.

The hysteresis was observed only on the engine configuration, where a compressor double characteristic was detected. Such phenomenon is typical of a compressor jumping in a rotating stall rather than in surge condition.

For the clarity of the following discussion, we define the double compressor characteristic at 87.5% ND with an "unstalled" and a "stalled part" (fig. 7 bis).

3.3 Analysis of dynamic pressure transducer signals

Along the line of engine minimum loading from 80% ND to 90% ND (see fig. 7 bis) the signals of pressure transducers have been recorded and later analyzed. In fig. 8 we present the time-dependent wall pressure measurements for each Test-Point.

The upper trace is from the transducer (T) and the lower trace from (B), placed respectively, at the top and the bottom of the compressor casing.

They show the blade passage loading or the static pressure between the blade. In fact between

the blade there is a constant pressure rise indicating no stalled region and there is a sudden change in pressure as the blade passes under the transducer. Stalled regions between the blades appear as regions of constant static pressure.

We observe in fig. 8 the progressive passage from a blade-to-blade inducer flowfield completely deteriorated (fully stalled conditions below 80% ND), to a periodic structure of the flowfield, characterized by a stalled and unstalled group of blade passages, much more clearly detected at 87.5% ND(T/P 704) in fig. 8-D.

Let's note, here, that in the upper trace there are several blade passages which are fully loaded and, at the same time, the lower trace shows a group of blade passages completely stalled. The region of stall propagates around the impeller and so is rotating. We can see a 180° phase between the transducer signals. This is an indication of a single cell pattern.

The flowfield is completely axisymmetric and out of rotating stall region at 90% ND (see fig. 8-E).

The results of the frequency spectral analysis of these transient pressure signals are shown in fig. 9. Looking at the figures, in the range of frequencies from 0 to 10 kHz we can observe:

- at T/P705 (fig. 9-E): only the impeller full blade passage frequency, equal to 13 times the rotor frequency E is present;
- at T/P 704 (fig. 9-D): we distinguish the fundamental frequency of rotating stall I - 425 Hz, equal to 0.76 E, and its harmonics: second order II - 850 Hz, and third order III - 1275 Hz;
- besides, we note the components 12E and 14E, that may be due to oscillation of the engine speed during the time of detection of the signals;
- it is interesting to observe finally that the ratio I/E between the fundamental frequency of the rotating stall I and the engine rotor frequency E, is almost constant with the rotor speed, and it is around the value of 0.75 (see from fig. 9-A to 9-D).

3.4 Engine noise signals

The noise signals have been processed using a FFT frequency analyzer. The results of the spectral analysis are shown in fig. 10. We observe the following:

- for the test points from 80% to 87.5% ND a pure tone is always present, having an average value of 0.75 E. There are also the multiplies of 2nd and 3rd order (see from fig. 10-A to fig. 10-D);
 - these pure tones are absent from 90% up to 100% ND;
 - let's note also the presence of the pure tone of frequency 4E, that is of less intensity compared to the previous one in the region of 80% to 87.5% ND, but it is predominant at 90% ND (there, it corresponds to 2300 Hz) (see fig. 10-E).
- The intensity of this pure tone of 4E reduces as the rotor speed is greater than 90% ND.

4. COMPARATIVE ANALYSIS OF THE EXPERIMENTAL RESULTS

4.1 Compressor impeller rotating stall and engine noise

The experimental data of this investigation may be presented using a Campbell diagram. As shown in fig. 11, the results of the engine test are plotted in the following way:

- thin lines correspond to engine order frequency 1E, 2E, 3E, etc., where E is the Engine rotor frequency (N/60);
- thick lines correspond to compressor impeller rotating stall frequencies, the fundamental one, I = 0.75 E, and its multiplies II and III;
- symbols correspond to the pure tone frequencies of the engine noise, as obtained by the spectra shown in fig. 10. Their size is proportional to the component amplitude.

So, we can observe the correspondence between the fundamental rotating stall line I, and the noise frequencies components that are in the range below 500 Hz. More interesting is the fact that pure tones are just in correspondence to I and II rotating stall frequencies at 87.5% ND.

Moreover there is a pure tone noise, having a frequency of 2300 Hz in correspondence to 4E engine order line, at 90% ND.

So, we conclude that the low frequency noise, below 500 Hz, is connected to the aerodynamic phenomenon of rotating stall (first fundamental frequency involved). At 87.5% ND, well into rotating stall region, the change in tone and noise level, is due to the pure tones corresponding to I and II frequency.

The drastic change in tone, observed between 87.5% and 90% ND, is due to the fact that the compressor gets out from the rotating stall, so that the correlated tones disappear, but some acoustic phenomenon, not anymore connected to rotating stall, is responsible for the pure tone at the frequency of 4E, at 90% ND.

4.2 Compressor casing resonant frequency and engine noise

In order to verify if the mechanical vibration of the compressor casing is responsible for the production of noise at 90% ND, the experimental investigation of the resonant frequencies of the structure has been done, using a technique that investigates the vibration response to an impulse.

The transducer output has been processed by NICOLET FFT analyzer and the results are shown in fig. 12-A. There are the resonant frequency values of 830, 930, 1450, 2280, 2430, 3130, 3250 and 4380 Hz in the range from 0 to 5000 Hz.

This information has been used in the Campbell diagram of fig. 12-B, where in addition, symbols are representative of pure tone noise components, determined from the spectral analysis results of fig. 10. We note that the pure tone noise locations in the frequency range 2200-2300 Hz are in correspondence to the intersection between 4E line and resonant frequencies at 90% ND.

Moreover, the pure tone noise observed at 87.5% ND is close to the frequency of 830 Hz. So, we make the hypothesis that the mechanical vibration of the casing is the responsible for the pure tone noise at 90% ND, and at the same time, we cannot exclude an interaction between the aerodynamic phenomenon of rotating stall and the mechanical vibration of the compressor casing in resonant condition at 87.5% ND, since the resonant frequency 830 Hz is near to the double fundamental frequency of rotating stall II, 850 Hz.

4.3 Engine performances under compressor rotating stall

The loss in engine performances due to rotating stall, was evaluated doing the comparison of the overall engine performances at the test points of the compressor double characteristic detected at 87.5% ND.

In fig. 13-A the compressor pressure ratio vs. corrected fuel flow is shown, along both the "unstalled" and "stalled" part of that speed-line. Let's remember that at the same fuel flow, the maximum compressor pressure ratio measured goes from the "unstalled" T/P 411, PR=4.71, to the "stalled" T/P 412, PR = 4.29.

It is noted that at 36 g/s of fuel flow there are two stabilized conditions. In effect the condition at the greater pressure ratio may be considered as an unstable equilibrium point. In fact, due to any cause, like a small speed variation, suddenly the engine stabilizes to a new equilibrium condition with the compressor in rotating stall. The two stable operating regimes, that exist along the speed-line, are separated by an unstable region.

Reducing the fuel flow, we observe that the stalled condition remains, with a consequent loss of engine performance. To be remembered, is the unsuccessful attempt to return to the "unstalled" speed-line without increasing engine speed, even with the minimum dynamometer load ($W_f=20$ g/s).

The comparison in the following figures shows clearly the engine sensitivity in changing compressor characteristic. In fig. 13-B, 13-C and 13-D are plotted respectively the turbine exhaust and entry temperature and the shaft power against the pressure ratio, so that it is possible to visualize the performance parameters variation along the double characteristic.

From the analysis of these test results, the following items can be stated:

- the compressor map shows a net difference of flow capacity between the tests in and out compressor rotating stall condition (about 10% lower at 87.5% ND with $W_f = 36$ g/s), as previously shown;
- there is a significant drop in the compressor efficiency (at $W_f = 36$ g/s, from 74.1% to 69.3%);
- the maximum power drop, at the same EGT, is 60 kW due to stalled condition (fig. 13-E);
- in the diagram of fig. 13-F we note that at TET constant the exhaust gas temperature EGT is higher, meaning a different behaviour of the engine hot section in the stall condition;
- as indicated in fig. 13-H, the maximum TET is about 80 deg K higher at the stalled condition;
- finally, at constant fuel flow, the engine power drop due to stalled condition is about 25 kW (fig. 13-I).

The overall engine performance loss is not only due to the lower compressor massflow, pressure ratio and efficiency, but also to the other components rematching.

With the same fuel flow, the turbine flow capacity seems to be 1.5% lower and the turbine efficiency is one percent lower.

The combustion chamber exit temperature profiles in the stalled condition does not suffer substantial change, as approximately can be deduced from the circumferential and radial exhaust temperature profiles, measured by means of 30 thermocouples.

The influence of the rotating stall on the combustion chamber efficiency has been evaluated in two ways. The first method calculates the combustion efficiency ETAB iteratively, using the following relation:

combustion temperature increase = $f(T_2, LHV, FAR)$

where: T_2 is compressor exit temperature,
 LHV is lower heating value of the fuel,
 FAR is the fuel-air-ratio, obtained as $FAR = W_f \div ETAB/W$

This temperature increment is compared to the note value coming from the power.

In the second method, the loss of the combustion efficiency is evaluated by means of the combustor loading function THETA:

$$THETA = (P_2^{1.75} \cdot e^{-(T_2/300)} \cdot 10^{0.5})/W$$

where: P_2 is the compressor exit pressure (lb/in²),
 T_2 is the compressor exit temperature (deg K),
 W is the air massflow (lbm/s).

THETA is a single function of the combustion chamber efficiency ETAB for constant fuel-air-ratio.

In both cases, a loss of combustion efficiency has been estimated in about 2%, doing the comparison at the same fuel flow.

Using our engine simulation computer code, the 13% power loss, from "unstalled" to "stalled" engine condition, at 87.5% ND, has been shared to 8%, due to overall compressor deterioration, and 5% due to components rematching. In fact 3.5% drop is due to combustion efficiency, 3.5% drop to the turbine efficiency and 1.7% is the positive contribution of the turbine rematching, due to the reduced flow capacity.

CONCLUDING REMARKS

The experimental investigation described in this paper revealed that the tested prototype engine had the compressor map different from the one obtained by the rig, specially at part-speeds, where lower massflow, pressure ratio and efficiency had been measured. Moreover, a double characteristic at 87.5% ND was found.

This difference was caused mainly by the stronger variation with rotor speed of the compressor impeller axial tip clearance, in the tested engine build considerable higher than the rig value.

Based on the results obtained, a clear relation between the compressor impeller rotating stall and a noisy behaviour of the engine at part speeds was found.

An attempt has been made to relate the noise frequency components having no aerodynamic origin, observed at 87.5% as well as 90% ND, with the mechanical vibrations of the compressor casing. Some correlations have been found with resonant frequencies of this structure.

The compressor impeller rotating stall influences the engine performance at part-speed (87.5% ND), in fact this phenomenon causes a penalty of 13% in power, from the "unstalled" condition to the stalled one at the same fuel flow.

Finally, the engine simulation code is applied to this test case, using the experimental compressor speed-line data at 87.5% ND. The results show that the effect of drop in engine power is not only due to the compressor performance deterioration, caused by the impeller rotating stall, but also to its negative influence on the engine components "downstream", i.e. affecting the combustion efficiency and the turbine efficiency.

ACKNOWLEDGEMENT

The authors are grateful to the ALFA ROMEO AVIO DIRES for the permission to publish this paper. They also wish to thank their colleagues of DIRES/SPER and in particular Mr. V. BUONANNO, without their contribution this paper would not have been possible. Many thanks to Miss P. MALATO for the kind collaboration to prepare final printing of the paper.

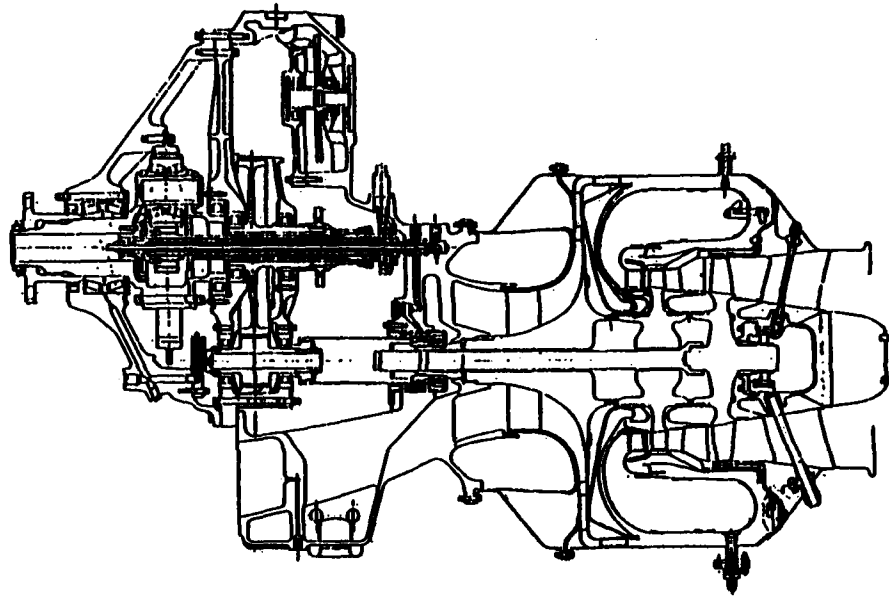


Fig. 1 - AR 318 turbopropengine cross-section

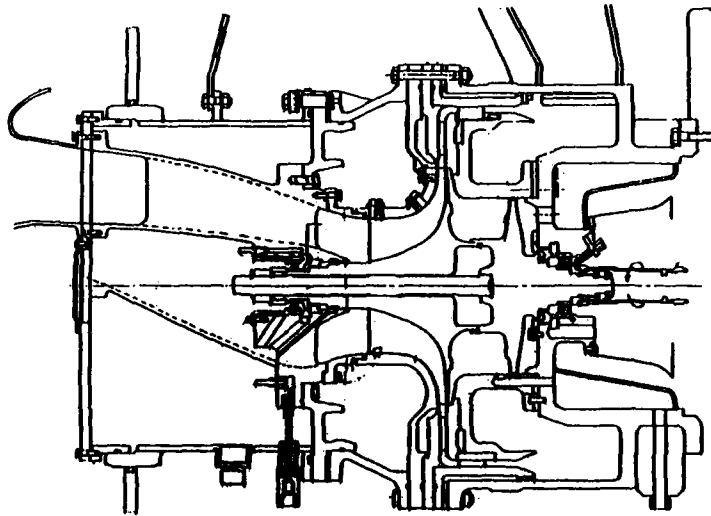


Fig. 2 - Compressor rig cross-section

AR318 COMPRESSOR

CONFIGURATION BUILD CLEARANCE
KIT 0.03 mm

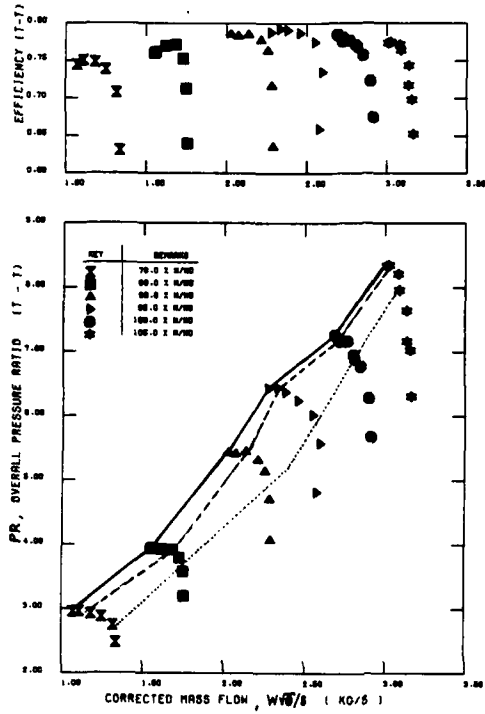
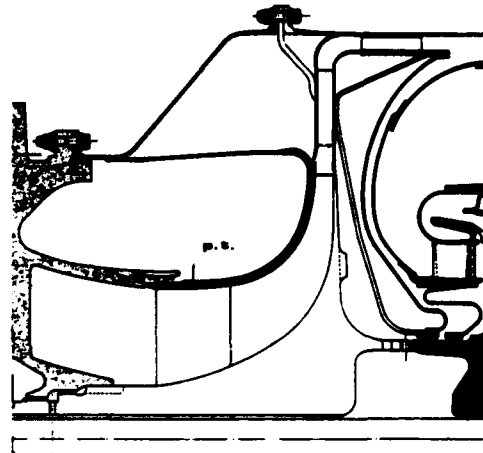


Fig. 3 - Rig compressor map

Fig. 4 - Engine dynamometer test bed



Fig. 5 - Engine compressor cross-section



AR318 COMPRESSOR

CONFIGURATION BUILD CLEARANCE
 ENTIRE 1.39 MM

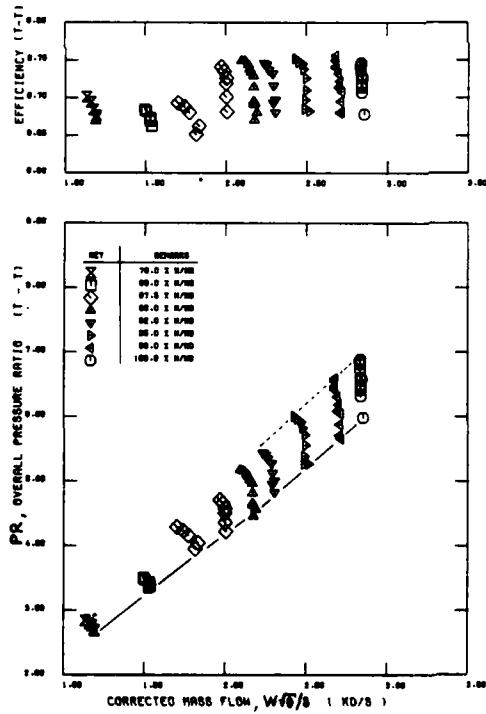


Fig. 6 - Engine compressor map

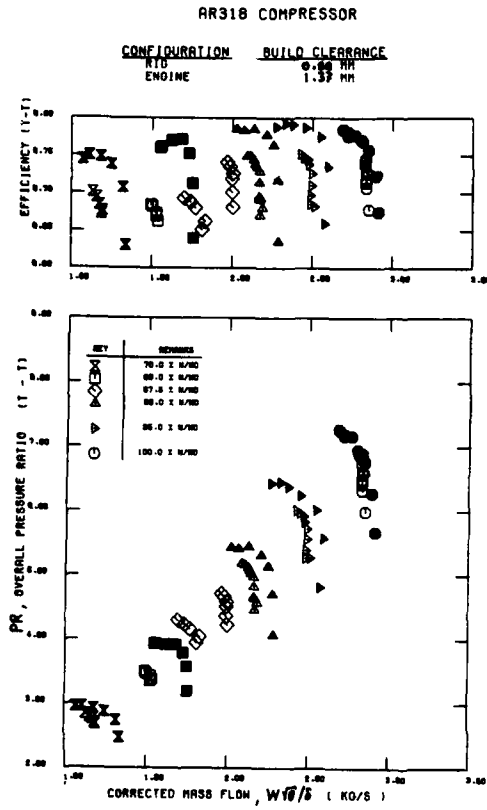


Fig. 7 - Comparison between engine and rig compressor performances

Fig. 7 bis - Engine compressor performances at part-speeds

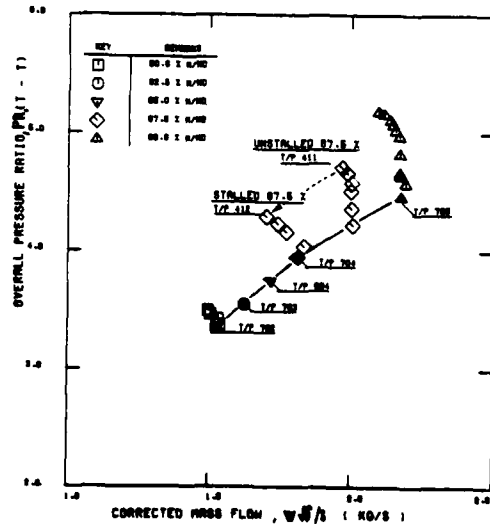


Fig. 8 - Time dependent wall static pressure traces from transducers at part-speeds

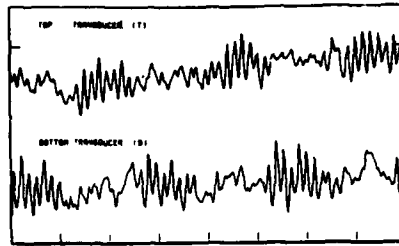


Fig. 8-A
T/P 702, 80% ND

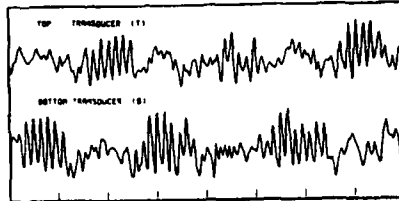


Fig. 8-B
T/P 703, 82.5% ND

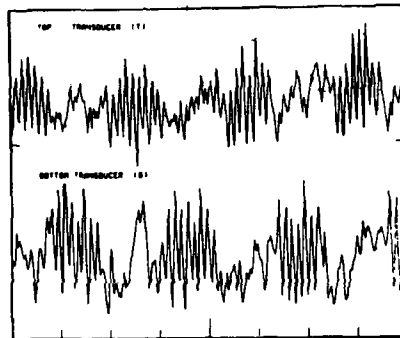


Fig. 8-C
T/P 804, 85% ND

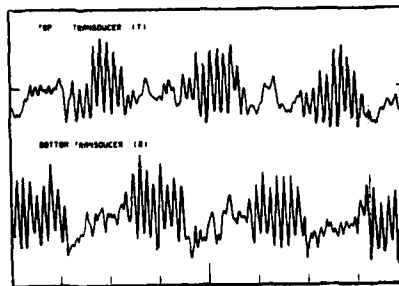


Fig. 8-D
T/P 704, 87.5% ND

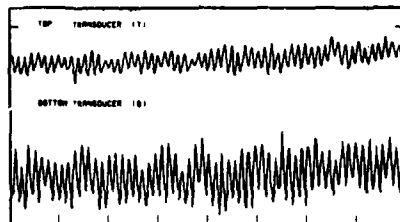


Fig. 8-E
T/P 705, 90% ND

0 2 4 6 8
time, millisecc

Fig. 9 - Frequency spectra of the dynamic pressure transducer signals at part-speeds

| KEY | REMARKS |
|-----|-------------------------------|
| ◆ | SHOULDER FREQUENCY |
| ▲ | IMPELLER BLADE FREQUENCY 1/4E |
| ○ | ROTATING STALL FREQUENCY I |
| □ | ROTATING STALL FREQUENCY II |
| ▽ | ROTATING STALL FREQUENCY III |

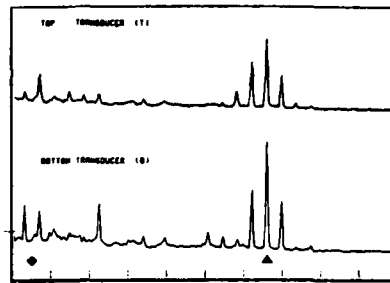


Fig. 9-A
T/P 702, 80% ND

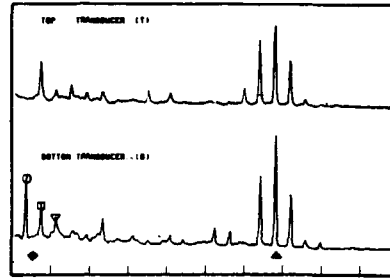


Fig. 9-B
T/P 703, 82.5% ND

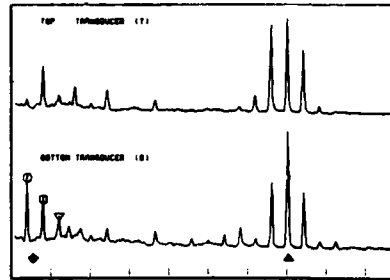


Fig. 9-C
T/P 804, 85% ND

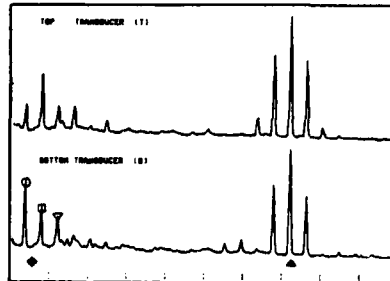


Fig. 9-D
T/P 704, 87.5% ND

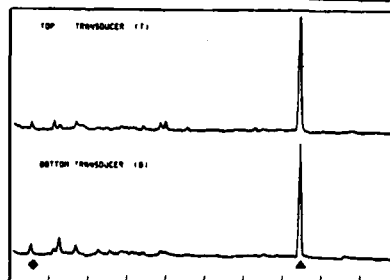


Fig. 9-E
T/P 705, 90% ND

0 5 10
frequency, kHz

Fig. 10 - Engine noise frequency spectra at part-speeds

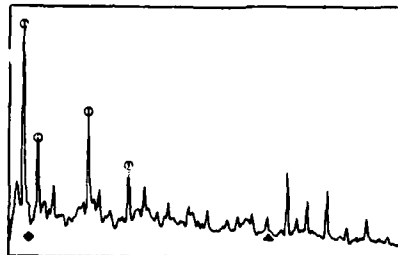


Fig. 10-A
T/P 702, 80% ND

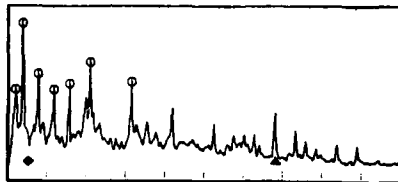


Fig. 10-B
T/P 703, 82.5% ND

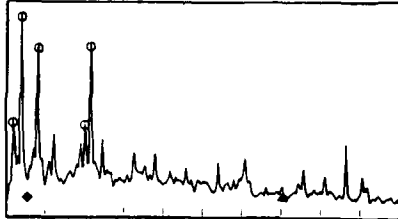


Fig. 10-C
T/P 804, 85% ND

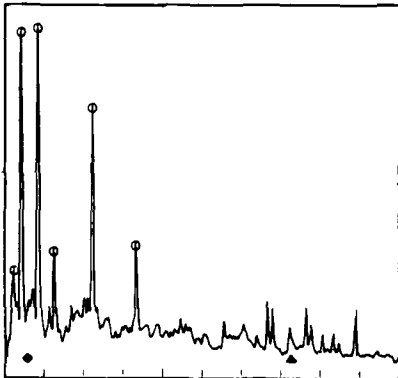


Fig. 10-D
T/P 704, 87.5% ND

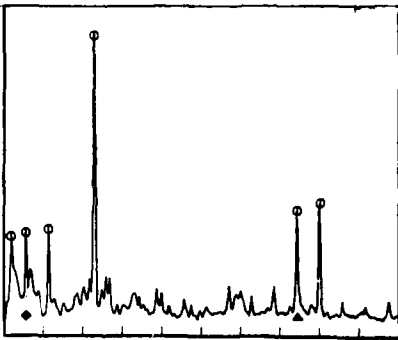


Fig. 10-E
T/P 705, 90% ND

| KEY | REMARKS |
|-----|-------------------------------|
| ◆ | ENGINE ORDER FREQUENCY |
| ▲ | IMPELLER BLADE FREQUENCY 1344 |
| ○ | WIRE PURE TONE FREQUENCY |

0 5 10
frequency, kHz

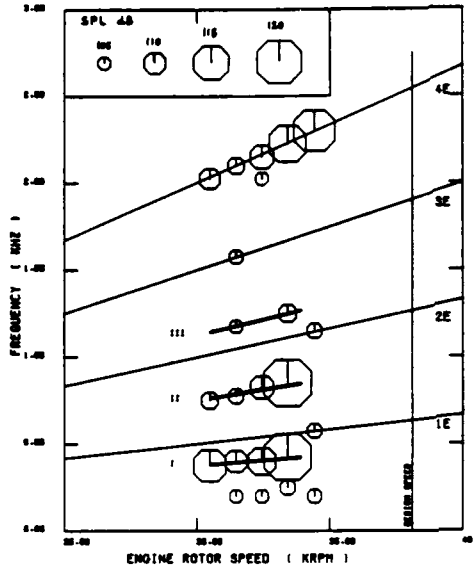


Fig. 11 - Compressor impeller rotating stall frequencies and engine noise pure tones at part-speeds

Fig. 12-A - Compressor casing impulsive test results

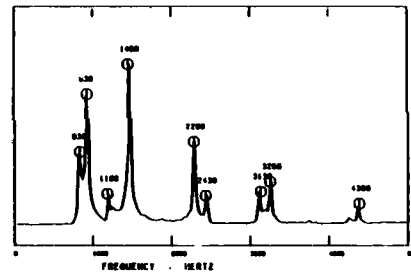


Fig. 12-B - Compressor casing Campbell diagram and engine noise pure tones at part-speeds

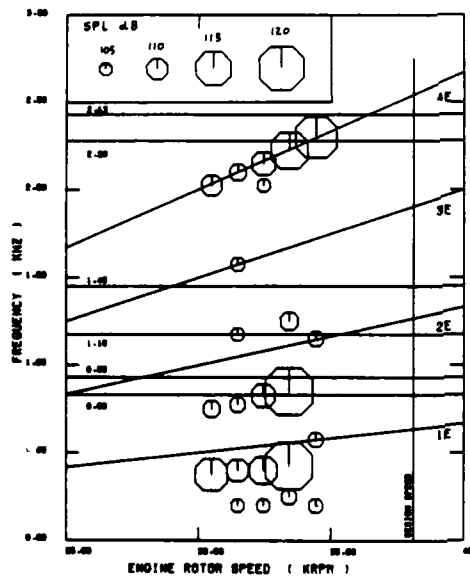
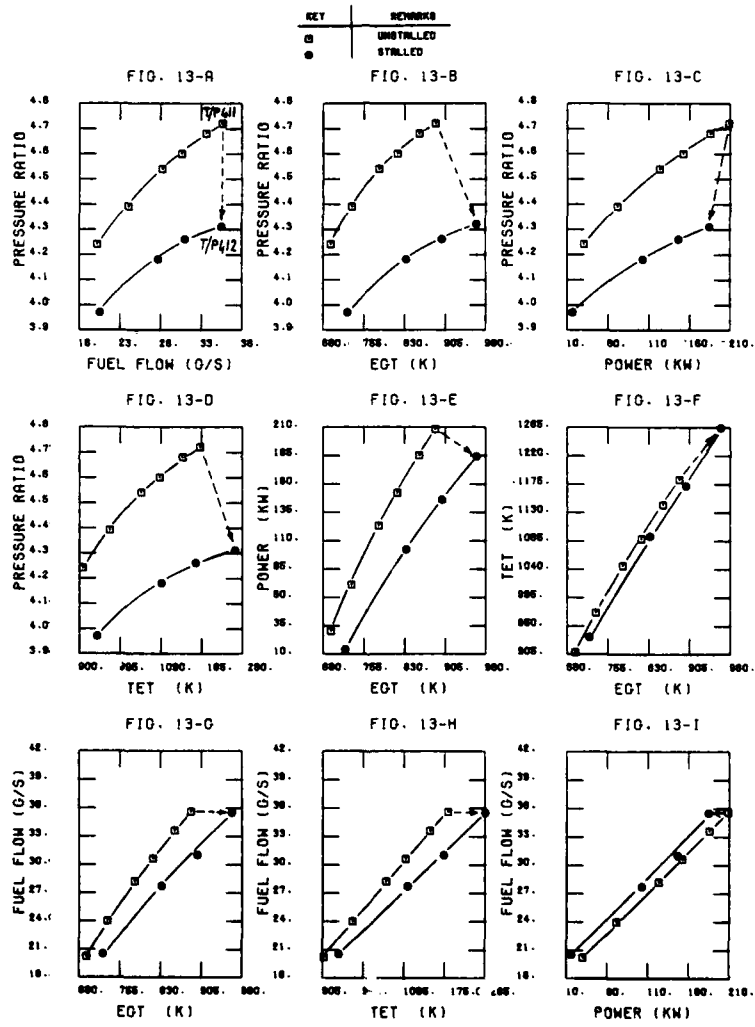


Fig. 13 - Overall engine performance comparison between "unstalled" and "stalled" conditions at 57.5% ND compressor speed line



DISCUSSION

P.Griffiths, US

How was the engine put into stall to take the "in-stall" steady-state data?

Author's Reply

After the data acquisition of Test Point 411 (see Fig.7 bis) — that was observed to be an *unstable equilibrium condition* for the engine — a little variation of the engine speed caused the compressor to jump into a rotating stall condition. So the engine was simply stabilised at the new equilibrium point (T/P 412), reducing the dynamometer load, in order to provide the same corrected speed. The fuel flow remained constant.

P.Griffiths, US

Could the stall be cleared to get back to the unstalled characteristic without shutting the engine down?

Author's Reply

It was not necessary to shut down the engine.

Since it was impossible to get out of rotating stall by reducing the dynamometer load, the only way to reach the compressor unstalled condition was to increase the engine speed.

Unidentified speaker

Je voulais savoir si sur ce moteur le problème de bruit est un problème important. Par exemple: la Figure 10, qui montre des spectres de bruit. Ce sont des spectres obtenus sur un moteur réel?

Author's Reply

No. This problem we found only on this engine which was an earlier version of the AR 318 engine. In particular, we found the problem because the compressor map was much different from the one found from rig results. We do not now have this problem on the engine.

Unidentified speaker

Oui, d'accord, parce-que les "peaks" sur ce moteur sont très importants. Habituellement en basse fréquence on voit surtout du bruit largement en général sur ce type de moteur, à cause de la combustion, à cause de l'écoulement interne, et pas des raies — les raies on les voit surtout au "fundamental blade passage frequency".

Author's Reply

The microphone to detect the engine noise signal was very near the air intake — 20 to 30 cm from the air intake, so I think that explains the level of noise that was measured.



AD-P005 471

SUMMARY OF INVESTIGATIONS OF ENGINE RESPONSE TO DISTORTED INLET CONDITIONS

Thomas J. Biesiadny, Willis M. Braithwaite, Ronald H. Soeder,
and Mahmood Abdelwahab
National Aeronautics and Space Administration
Lewis Research Center
Cleveland, Ohio 44135 U.S.A.

SUMMARY

A survey is presented of experimental and analytical experience of the NASA Lewis Research Center in engine response to inlet temperature and pressure distortions. There has been a continuing NASA effort over the past decade and a half to improve the understanding of the effects of inlet distortion on engine performance, particularly on the compression system performance. Results of experimental investigations and analytical modeling work at NASA are reviewed together with a description of the hardware and the techniques employed. Distortion devices successfully simulated inlet distortion, and knowledge was gained on compression system response to different types of distortion. A list of NASA research references is included.

INTRODUCTION

A persistent problem in the development of airbreathing propulsion systems for new aircraft, be they turbojet, turbofan or turboshaft engines, is the detrimental effect of nonuniform inlet flow on engine stability. When rotary-wing aircraft are operating near the ground (i.e., in ground effect), engine exhaust can be contained by the rotor downwash and recirculated to the engine inlet (Fig. 1, Ref. 1). With vertical/short takeoff and land (V/STOL) aircraft the jet stream impinges on the ground, flows outward from the impingement points, and eventually reaches the engine inlet. This leads to hot gas ingestion. Other potential sources of inlet flow distortion are gun- or rocket-exhaust gas ingestion, wakes from other aircraft, aircraft maneuvers, interaction of airframe and inlet, and off-design operation of the inlet.

The effect of this inlet distortion, be it a pressure or temperature distortion or a combination of the two, is that the power available is reduced along with the engine-compression-system surge margin (i.e., the difference between the operating line and surge line). The confident prediction of ingestion levels, or inlet distortion patterns, for any arbitrary aircraft/engine design and their effect on compression system performance requires a comprehensive set of design data not easily obtained. Ground-level engine tests and flight tests are required to measure the magnitude and the effects of inlet distortion on the engine in question.

A continuing experimental and analytical program has been in progress at the Lewis Research Center for more than a decade to further the understanding of inlet distortion and its effects on engine stability, particularly that of the compression system. This work includes investigations using turbojet, turbofan, and turboshaft engines subjected to distortions of inlet pressure, temperature, and a combination of pressure and temperature. As byproducts of these investigations, devices to generate steady-state and time-variant pressure and temperature distortions were developed.

The effects of inlet flow distortions as defined by total pressure variations were extensively investigated by NASA's predecessor, the National Advisory Committee for Aeronautics (NACA), in the 1950's. Relatively simple analytical models and indices were developed to predict the effects of pressure distortion on engine stability. However, in the 1960's, higher speed aircraft encountered stability problems not predicted by these models. It was determined that these problems were the result of time-varying inlet total pressure distributions. At that time it was deemed desirable to also investigate the effect of nonuniform inlet temperature on engine stability. Although temperature distortion caused several known aircraft incidents, it had not been examined except for a few investigations in the 1950's (Refs. 2 to 4).

In the mid-1960's NASA returned to the investigation of engine stability and inlet flow distortion. Prime interest was in time-variant pressure distortion and both steady-state and time-variant temperature distortions. The results of these investigations were incorporated into analytical models and thus provided a base for a better understanding of the phenomenon.

Steady-state and time-variant devices to create inlet temperature and pressure distortions, and combined temperature and pressure distortion were required to simulate the inlet flow distortion occurring in the field. NASA Lewis developed the devices which are described in this report. Highlights of results of the NASA work with these distortion devices over the past decade and a half are also presented.

Because of the large number of programs involving inlet distortion and its effects on engine performance, and the large amount of data generated in these programs, some limit to the information presented is required. This report reviews NASA investigations into the engine response to distorted inlet conditions and covers, briefly, the results of experimental investigations, some analytical modeling work, and hardware and techniques used to simulate inlet pressure and temperature distortions.

The presentation of experimental results is divided into three sections:

- (1) Steady-state and time-variant temperature distortion
- (2) Steady-state and time-variant inlet pressure distortion
- (3) Steady-state combined inlet pressure and temperature distortion

Analytical modeling work and comparisons with experimental work are also presented. The devices used to create these distortions included screens, both stationary and rotatable, and a pressure jet system capable of injecting air counter to the inlet flow, thus canceling inlet air momentum, to create both dynamic and steady-state pressure distortions. Temperature distortions were created by using hydrogen-fueled temperature distortion generators of two different designs; the larger for experimental work involving turbojet and turbofan engines, and the smaller for turboshaft engine investigations.

TEMPERATURE DISTORTION

Temperature Distortion Generators

Gaseous hydrogen burners were used to develop inlet temperature distortion. Because of the larger flows required, the inlet temperature distortion tests involving turbojet and turbofan engines required a different temperature distortion generator design than that used for the turboshaft engine tests. In addition the power output shaft in the center of the turboshaft engine inlet ducting and bellmouth imposed different design requirements on the generator for that installation.

The gaseous hydrogen burner (Figs. 2 and 3) used for tests with the turbojet and turbofan engines was installed upstream of the inlet bellmouth (Ref. 5). Hydrogen was used because it is cleaner burning--generating water vapor rather than pollutants--and requires a lower fuel-to-air ratio for a given temperature rise than other fuels that were considered. Therefore, its effects on engine performance parameters are of much less concern. Also, the low flammability limits of hydrogen permitted low levels of temperature rise. In addition, flame propagation is faster than other fuels considered. This was borne out in early investigations, which showed that temperature rise rates of 10 000 K/sec could be generated (Fig. 4 and Ref. 6) and that the distortion pattern remained nearly constant as flow approached the engine inlet (Fig. 5 and Ref. 7). In Fig. 4 the indicated, or measured, temperatures were corrected for time lag, Mach number/pressure recovery, and radiation by using the procedures and equations found in Ref. 8. For the larger burners used with the turbofan and turbojet installations, the distance from the burner to the engine inlet was three to six duct diameters, while in the case of the generator for the turboshaft engine this distance was two duct diameters. A later version of the burner used for turbojet and turbofan testing (Fig. 6) has the capability of being remotely rotated $+30^\circ$ from the center position (Ref. 9). Each of the four quadrants, or circumferential extents, is individually controlled so that many combinations are possible. In addition, each gutter, or radial extent, in a quadrant is controllable. An added feature is that one quadrant is designed so that a 30° sector can be inserted if an extent smaller than 90° is desired. Rotating the burner distortion pattern past the engine instrumentation permits mapping of the distortion and its effect through the compressor by using minimal instrumentation.

There are additional features of the burners shown in Figs. 2, 3, and 6 which are worthy of note. Each quadrant of the burner has five swirl-can pilot burners. Also in each quadrant is an ignition source for the hydrogen, five annular flameholder gutters, one radial gutter, and tubes to supply the hydrogen to the proper location for ignition. The control system is capable of fast response for temperature transients by way of a high-speed valve. For the time-variant temperature distortions, the desired hydrogen pressure is established in a trapped volume upstream of the flow control valve and a high-speed valve for the specified quadrants (Fig. 7). The swirl-can pilot burners at those quadrants are lit, and the engine-inlet temperature distortion pattern is set prior to each transient. At each engine condition, circumferential extents of the fan inlet can be exposed to a range of peak temperature magnitudes and/or temperature rise rates. The rate and magnitude are functions of the pressure and quantity of trapped hydrogen, respectively. The pressure of the trapped hydrogen can be changed and the process repeated until a compressor stall limit is reached. For steady-state distortions the valves for the quadrants of interest are opened slowly until the desired temperature level is reached at the engine inlet.

The temperature distortion generator for turboshaft engine application can create both steady-state and time-variant temperature distortion at the engine inlet by using gaseous hydrogen. It is an adaptation of a device described in Ref. 10. The burner (Fig. 8) consists of eight individually controlled sectors, with three swirl-cup combustors (Fig. 9) per sector. These swirl cups for the turboshaft engine distortion generator are the same size as the swirl-can pilot burners used for the turbojet and turbofan engine temperature distortion generator. Many sector combinations, or temperature distortion patterns, were possible. The hydrogen distribution system from the fuel supply point to the swirl-cup combustors and its operation are described in detail in Ref. 11.

In a typical operation to find the response of the turboshaft engine to inlet temperature distortion, the swirl cups in those sectors where the temperature distortion was being imposed were lit (there were no pilots) while the engine was at idle. The hydrogen flow was adjusted, and the engine power was increased to the desired operating level. Once conditions were stabilized, the hydrogen flow was either increased to a fixed level to produce the desired steady-state distortion or, if a transient distortion

was desired, pulsed at increasingly greater pressures until stall occurred. Each pulse produced a unique combination of temperature rise and temperature rise rate at the engine inlet.

Temperature Distortion Results

The results of the temperature distortion investigations are categorized in terms of the effects of sensor location, distortion extent, distortion magnitude, and Reynolds number index (i.e., altitude operation) changes.

Inlet temperature distortion can have a significant effect on engine stability, especially when it causes the engine control to operate at an incorrect equivalent rotor speed (i.e., the equivalent speed under standard sea-level-static inlet conditions). When the inlet temperature sensor detects either the cold or hot part of the distorted flow, the control adjusts variable geometry accordingly and changes the compressor stall margin differently than if the sensor detects the warm average inlet temperature. Therefore the location of the sensor is critical to engine stability and to the analysis of temperature distortions.

As the extent of the distortion increased to a certain level, the engines tested were less tolerant of circumferential distortion at a fixed operating condition. Moreover, the results from an investigation involving steady-state temperature distortion and a turbojet engine revealed that between 90 and 180° extent there was no significant change in compression system response (Ref. 12). This was also true for time-variant distortion testing with a turboshaft engine, even though it had an integral inlet particle separator (Fig. 10 and Ref. 13). Figure 10 shows a leveling off of temperature rise with increasing extent as 180° is reached.

In general, diametrically opposed circumferential distortion sectors such as those shown in Fig. 11(a) have less effect on the compression system than single distorted sectors such as that shown in Fig. 11(b) (Ref. 12). While this was noted for a turbojet engine, it is also in agreement with results of temperature distortion experiments for the turboshaft engine with inlet particle separator (Fig. 12 and Ref. 13). The engine compression system was more tolerant not only of a balanced distortion such as 180° opposed distortion cells but also of such patterns as a four-per-revolution distortion uniformly spaced.

In addition to tests to determine the effect of circumferential distortion extent, the magnitude of the distortion and its effect on compressor performance were investigated. It was determined in Refs. 5 and 14 that, for the turbofan engine tested, the time-variant circumferential temperature distortion required to produce stall was independent of the rise rate (Fig. 13) and was a function of the equivalent steady-state distortion in the critical stage in the compressor. Thus the temperature distortion at the compressor face was greater than steady-state for increasing rise rates because of the time required for the flow (distortion) to reach the critical stage. In Fig. 13 it should be noted that below approximately 1000 K/sec the burner design did not permit high enough temperature rises for determining whether stall would occur at those conditions. However, since the steady-state threshold for stall was shown to be the same as that for the available time-variant data, it is assumed that the critical temperature rise is the same for the temperature rise rates between steady state and 1000 K/sec.

Attempts were made to measure the magnitude of the steady-state distortion required to surge the turboshaft engine. None of these attempts were successful because the distortion levels that could be imposed were limited by an engine-inlet hardware temperature limit. Another consideration was the engine-inlet particle separator. A simplified analysis of the compressor operating point of the turboshaft engine during these steady-state distortion tests indicated that the particle separator desensitized the engine to the extent of circumferential temperature distortion possibly by mixing the heated and unheated inlet air to produce a more uniform temperature profile at the compressor face.

Figure 14 shows a plot of the uniform-inlet-flow compressor map generated experimentally. It should be noted that the map was constructed by using inferred compressor inlet conditions because space limitations made it impossible for truly representative temperatures and pressures to be measured at that station. Plotted on the compressor map is a steady-state data point where a 180° circumferential temperature distortion was created at the particle separator inlet (solid triangle). The engine did not surge for these conditions up to the steady-state temperature limit for the engine inlet hardware. If it is assumed that the compressor inlet will see the 180° circumferential distortion imposed at the separator inlet, experience shows that the average compressor operating point will be on the normal operating line, as shown by the solid triangular symbol. This represents the compressor speed equated to standard sea-level-static conditions by using the average engine inlet temperature. From parallel-compressor-theory assumptions (Refs. 15 and 16), the two sectors of the compressor operate at the same pressure ratio but at different equivalent speeds, as indicated by the solid diamond symbol for the hot sector and the solid cone symbol for the cold sector. As shown, the hot-sector operating point is considerably to the left of the surge line, and the compressor should have surged. Since no surge occurred, it may be assumed that the compressor inlet did not see the pure 180° distortion pattern but probably saw a more homogeneous temperature leaving the particle separator.

Finally, with inlet temperature distortion present, it was also found that the Reynolds number index (RNI) affected the stall margin. As an example, for the turbojet,

even with a moderate distortion, the stall margin decreased as the RNI decreased from 0.65 to 0.30 (Fig. 15 and Ref. 12). However, this was not as pronounced as for the turbofan engine (Ref. 17).

PRESSURE DISTORTION

Pressure Distortion Generators

Steady-state pressure distortions were generated by two methods. The first, and older, method involved screens of different densities. The second method of generating steady-state and, in addition, time-variant distortions of the inlet total pressure used a NASA-developed air jet device (Refs. 18 and 19). The device and its position relative to the engine inlet, approximately one duct diameter upstream, are shown in Fig. 16. This device produces total pressure distortion patterns by the cancellation of inlet airflow momentum. This is accomplished by injection of secondary air into the inlet duct in the direction opposite to the primary flow. The device contains 54 individual jets divided into six 60° sectors of nine jets each. A remotely controlled, hydraulically driven valve governs the flow to each sector independently. The degree of pressure distortion is controlled by the amount of this flow.

Pressure Distortion Results

Discussion of the pressure distortion results includes highlights of the effects of both steady-state and time-variant distortions. These highlights include the effects of the distortion generator on inlet conditions, the effects of a total pressure distortion as it travels through the engine compression system, the effects of a distortion rotating with or opposed to engine rotation, the effects of the frequency of the distortion pattern, and the relation between steady-state and time-variant distortions.

The total pressure distortion did not change significantly when traveling from the source that produced it to the engine face (Fig. 17). The static pressure distortion, however, increased exponentially from the source to the leading edge of the compressor first-stage rotor blades (Fig. 18 and Refs. 20 and 21). The behavior of the static pressure distortion is the key to satisfying the inlet flow condition for the analytical model, as is explained in the section MODELING. For a single distortion zone in a constant-area duct, this static-pressure-distortion axial distribution can be represented by the following equation (Refs. 22 and 23):

$$\frac{DPS}{(DPS)IGV} = e^{-x/R}$$

where

DPS maximum - minimum static pressure at a location x
 (DPS)IGV maximum - minimum static pressure at mean radius of IGV
 IGV inlet guide vane assembly
 x distance upstream of IGV
 R mean radius of IGV

The rate at which the total pressure distortion is attenuated within the compressor increased with increasing rotor speed (Fig. 19 and Ref. 24). A total pressure distortion was generated by the two unequal pressure ratios created by the pressure distortion and was maximum at the exit. Since the compressor flow exits into a plenum (combustor), the static pressure is uniform. Also the exit Mach number is low, and therefore the total pressure distortion is small.

An inlet total pressure distortion rotating about the engine axis increased stall margin when the distortion pattern rotated in the opposite direction to the compressor rotation but decreased the stall margin when the distortion rotated in the same direction as the compressor rotation (see Fig. 20 and Ref. 25). The increase and decrease in stall margin are relative to the steady-state condition, where there is no rotation of the distortion. The decrease of stall margin is also a function of the rotational velocity of the distortion as a fraction of the rotor speed.

Other time-variant inlet total pressure distortions investigated were full-face-sinusoidal total pressure variations and 180° circumferential distortions, where (1) only the distorted sector, or the sector with its pressure below the average pressure, varied, and (2) both the distorted and undistorted sectors varied sinusoidally but 180° out of phase. As would be expected, the effect on the compressor was greater when both the distorted and undistorted sectors were active.

Discrete inlet pressure variations covering a variety of circumferential extents, amplitudes, and durations (or frequencies) for a given rotor speed were also investigated (Ref. 26). An example of this work is presented in Fig. 21, a plot of relative inlet total pressure amplitude as a function of pressure pulse duration, which shows the conditions that induced compressor stall for extents from 60 to 360°. Depending on the extent of the pressure distortion, this threshold was from a pulse duration of 5 to 14 msec, or a frequency of approximately 100 to 35 Hz, respectively. These data

indicate that stall is most likely to occur over a particular low frequency range, and the probability of it occurring above this range is low. A possible explanation for this behavior is that there is a finite time interval required for a rotor blade to stall in response to a total pressure distortion. During shorter durations, or higher frequencies, the distortion is too brief for a rotor blade to respond. The results showed that stall tolerance is a function of not only the instantaneous distortion level, but also the rate of change of the inlet pressure and the dwell-time of the fan-compressor rotor blading in an engine-inlet distortion.

It is possible to relate time-variant pressure distortions to steady-state distortions (Fig. 22) by using instantaneous distortion theory as presented in Ref. 27. Pressure distortions were observed with proper frequency filtering, or elimination of extraneous frequencies above and below the range of interest, or the critical frequency range. However, the effects of a given distortion pattern are a function of the particular geometry of an engine, such as combustor volume dynamics and compressor discharge conditions, and the results presented should only be used to show trends.

Overall it was found that a convenient descriptor for total pressure distortions was (max - min)/average. This can be related to individual and average compressor pressure ratios and their position on compressor maps.

COMBINED PRESSURE AND TEMPERATURE DISTORTION

Combined Pressure and Temperature Generators

To avoid undue complexity in analyzing the results, the study of combined temperature and pressure distortion was limited to a steady-state investigation of various combinations of 180° circumferential temperature and pressure patterns. The effect of combined pressure and temperature distortion on compressor stability limits was determined by slowly increasing the temperature in a 180° sector with a 180° extent distortion screen in place until stall was reached. Since the screen could be indexed independently of the temperature distortion generator, the effects of the relative positions of the pressure and temperature distortions could be investigated. A different approach was followed for the experimental investigation reported in Ref. 12. Stall data were obtained once an inlet distortion was established by reducing the exhaust nozzle area while maintaining constant equivalent engine speed.

Combined Pressure and Temperature Results

It was discovered that, when pressure and temperature patterns were fully overlapped, the distortion created in the compression system resulted in the greatest loss of stall margin (Refs. 21 and 28). If the combined pressure and temperature distortion were properly oriented, one distortion could counteract the other and actually increase stall margin. This occurred when there was no overlap of the distortions. Varying the amount of overlap resulted in a proportional loss in stall margin. Again, there was a minimum extent of combined distortion that reduced the stall margin.

By using the techniques involved in creating combined pressure and temperature distortion patterns, it was found that an operating envelope for an engine could be developed that defined the distortion sensitivity limits. For example, Soeder (Ref. 21) found that a distortion sensitivity map relating pressure and temperature distortion could be developed relatively easily by using a rotatable screen of approximately 50 percent density and a temperature distortion generator to cover both the full overlap and no overlap conditions for the pressure and temperature distortions (Fig. 23).

MODELING

An understanding of the effects of inlet flow distortions--pressure, temperature, and combined pressure and temperature--on stall margin can be obtained from a simplified model such as the one described in Refs. 15 and 16. These references also present a listing of some of the more common distortion indices and how they relate to the model. This theory predicted to a fair degree the pressure ratios and limiting distortions which cause compressor stall, but it did not consistently predict the equivalent air flow rates. However, the distorted and undistorted airflow rates were measured approximately 1 m in front of the engine inlet. Because static pressure distortion increases exponentially with distance along the inlet duct wall (Refs. 20 and 21), this discrepancy was reduced when the flows at the leading edge of the compressor first-stage blades were considered. Under NASA sponsorship this simplified model was further refined to yield a more reliable prediction for a low-bypass-ratio turbofan engine (Refs. 22 and 23).

NASA was also involved in other modeling efforts. These included the following: another low-bypass-ratio turbofan engine model (Ref. 29); a turbojet engine dynamic distortion model which provided a multipath analysis of circumferential temperature, pressure, and combined distortions (Refs. 30 and 31); and a high-bypass-ratio multispool engine compression system dynamic model (Ref. 32). However, to simplify this report only a representative sample (Refs. 22 and 23) of the modeling effort is presented. The steady-state model was more closely related to the experimental programs being conducted at NASA in addition to being a more well developed code before NASA's participation. Another consideration is that the models presented in Refs. 30 to 32 were dynamic models and as such were directed less toward inlet distortion and more toward stagnation stall, a subject beyond the scope of this report. Finally, the research emphasis at NASA has

shifted from inlet distortion, and therefore the dynamic models (Refs. 29 to 32) were not exercised extensively with experimental data.

An adaptation of the simplified model of Refs. 15 and 16, based on multiple flow paths (or parallel compressors) through the compression system, was developed by Mazzawy (Refs. 22 and 23) and extended under contract to achieve greater fidelity, especially with temperature distortion. Also, the model of the engine used for the experiment utilized compressor maps refined by using experimental data. Flows were permitted circumferentially across flow boundaries. Also, the temperature distortion was assumed to follow a particle through the compressor, whereas the pressure distortion was regarded as acoustic (Refs. 22 and 23) and exhibited less swirl in passing through the compressor. Comparison of the predictions obtained with this model and experimental data are presented in Ref. 28. This refined parallel compressor model was useful in obtaining an understanding of the stability phenomenon because it helped to relate pressure, temperature, and combined pressure and temperature distortions. A general list of the assumptions used in applying the refined parallel compressor theory are summarized as follows:

(1) The compressor is divided into subcompressor elements, with each element, or parallel compressor, operating as an identity defined by the undistorted compressor map.

(2) Swirl of the flow passing through the compressor is accounted for by the theory. The swirl associated with a pressure distortion is not identical to the swirl associated with a temperature distortion. Pressure passes through the compressor as an acoustic wave (i.e., little swirl), while temperature has the properties of a gas particle and follows the gas flow path (i.e., the temperature distortion has more swirl than the pressure distortion). This modifies the edges of the distortions, or blurs the distinction between distorted and undistorted regions.

(3) The exit static pressure is the same for all elements.

(4) For pressure distortion the elements operate at uniform equivalent rotor speed but at different pressure ratios dependent on the distortion, which results in unequal temperature ratios (i.e., pressure distortion is attenuated, and a temperature distortion is created).

(5) For temperature distortion, the elements operate at a constant pressure ratio, and therefore the temperature distortion is not modified except by inefficiency in the compressor.

(6) Individual element performance is adjusted to account for two-dimensional and unsteady flow effects, including engine-induced inlet flow redistribution, circumferential crossflows, and unsteady flow due to rotor movement through a distorted flow field.

In the work done by Braithwaite and Soeder (Ref. 28), it was reported that there was good agreement in duplicating analytically (Refs. 22 and 23) the experimental results by using the temperature and pressure profiles measured at the engine inlet. The flow angles measured at the engine inlet were satisfactorily duplicated analytically (Fig. 24). The internal response of the compression system, with regard to pressure and temperature profiles through the compressor (Fig. 25), swirl angles (Fig. 26), attenuation of the distortion (Fig. 27), and the values of limiting pressure and temperature distortions required to stall as determined analytically, was also found to be in good agreement with experimental results (Fig. 28).

The amount of pressure distortion required to stall the compression system is shown in Fig. 28 as a function of various levels of temperature distortion. Two regions are shown in the figure; one in which the high temperature is aligned with the low pressure region ($-\Delta T$), and one in which the high temperature and low pressure are opposed to each other (ΔT). For $-\Delta T$, or pure temperature distortion, it is shown that, as the temperature distortion decreases, larger total pressure distortions are required to stall the compression system until a pure pressure distortion is obtained. If the temperature distortion is then located in the opposite side of the inlet, increasing levels of pressure distortion are required for increasing temperature distortions. A second limit line is observed for the opposed distortions. For a pure temperature distortion, the distortion required to stall the engine is the same on either side of the engine. There is a stall region to the right of this point.

The refined parallel compressor model worked well when airflow was determined at the leading edge of the compressor first-stage blades, where high static pressure gradients exist. The experimental validation that static pressure distortion increases exponentially as the inlet flow approaches the compressor face (Refs. 20 and 21), previously mentioned in this section, was instrumental in explaining lack of agreement in equivalent inlet airflow rate between experimental data and the analytical model.

CONCLUDING REMARKS

A review of NASA Lewis experimental and analytical experience in engine response to inlet temperature and pressure distortions has been presented. Highlights of this work are the following:

1. Devices to generate inlet temperature and pressure distortion patterns have been developed and used successfully in conjunction with turbojet, turbofan, and turboshaft engines.

2. Inlet temperature distortion has a significant effect on engine stability.

3. The engines tested were less tolerant of circumferential temperature distortion at a fixed operating condition as the extent of the distortion increased.

4. Diametrically opposed temperature distortion sectors had less effect on the compression system than single distorted sectors.

5. A critical temperature distortion level, independent of temperature rise rate, had to be reached before stall occurred.

6. With inlet temperature distortion present, stall margin decreased as the Reynolds number index decreased.

7. The location of the engine-inlet temperature sensor can have a significant effect on response to inlet temperature distortion.

8. The total pressure and temperature distortions did not change significantly when traveling from the source that produced them to the engine inlet, but the static pressure distortion increased exponentially from the source to the engine inlet.

9. The compressor dissipated the total and static pressure distortions by the time the flow reached the compressor exit. However, a total temperature distortion was generated at the compressor exit.

10. A time-variant distortion pattern rotating in the opposite direction as the compressor rotation increased the stall margin, while a distortion rotating in the same direction decreased the stall margin relative to the steady-state condition. The decrease of stall margin is also a function of the rotational velocity of the distortion as a fraction of the rotor speed.

11. In general, stall could be achieved more easily at longer pulse durations which correspond to lower frequencies, but became more difficult as the duration decreased (i.e., higher frequencies) until a duration was reached where stall could not be achieved.

12. Combined pressure and temperature distortion patterns were used to generate a distortion sensitivity map which could be used as a guide to surge-free engine operation.

13. There was good agreement between experimental data and analytical models which were developed for the engines investigated. More work is required in this area before generalized models are available.

REFERENCES

1. Sheridan, P.F.; and Wiesner, W.: Aerodynamics of Helicopter Flight Near the Ground. AHS Paper 77-33-04, 1977.
2. Wallner, L.E.; Useller, J. W.; and Saari, M. J.: A Study of Temperature Transients at the Inlet of a Turbojet Engine. NACA RM-E57C22, 1957.
3. Gabriel, D.; Wallner, L.; Lubick, R.; and Vasu, G.: Some Effects of Inlet Pressure and Temperature Transients on Turbojet Engines. Aeronaut. Eng. Rev., vol. 16, no. 9, Sept. 1957, pp. 54-59, 68.
4. Childs, J.H.; et al.: Stall and Flame-Out Resulting from Firing of Armament. NACA RM-E55E25, 1955.
5. Braithwaite, W.M.: Experimental Evaluation of a TF30-P-3 Turbofan Engine in an Altitude Facility: Effect of Steady-State Temperature Distortion. NASA TM X-2921, 1973.
6. Rudey, R.A.; and Antl, R.J.: The Effect of Inlet Temperature Distortion on the Performance of a Turbofan Engine Compressor System. AIAA Paper 70-625, June 1970.
7. Soeder, R.H.; and Bobula, G.A.: Effect of Steady-State Temperature Distortion and Combined Distortion on Inlet Flow to a Turbofan Engine. NASA TM-79237, 1979.
8. Glawe, G.E.; Simmons, F.S.; and Stickney, T.M.: Radiation and Recovery Corrections and Time Constants of Several Chromel-Alumel Thermocouple Probe in High-Temperature, High-Velocity Gas Streams. NACA TN-3766, 1956.
9. Abdelwahab, Mahmood: Effects of Fan Inlet Temperature Disturbances on the Stability of a Turbofan Engine. NASA TM-82699, 1981.

10. Pawlik, E.V.; and Jones, R.E.: Experimental Evaluation of Swirl-Can Elements for Propane-Fuel Combustor. NASA Memo 5-15-59E, 1959.
11. Klann, G.A.; Barth, R.L.; and Biesiadny, T.J.: Temperature Distortion Generator for Turbohaft Engine Testing. Advances in Aerospace Propulsion, SAE SP-594, SAE, 1984, pp. 89-99.
12. Mehalic, C.M.; and Lottig, R.A.: Steady-State Inlet Temperature Distortion Effects on the Stall Limits of a J85-GE-13 Turbojet Engine. NASA TM X-2990, 1974.
13. Biesiadny, T.J.; Klann, G.A.; and Little, J.K.: Response of a Small-Turbohaft-Engine Compression System to Inlet Temperature Distortion. NASA TM-83765, 1984.
14. Abdelwahab, Mahmood: Effects of Temperature Transients at Fan Inlet of a Turbofan Engine. NASA TP-1031, 1977.
15. Graber, E.J.; and Braithwaite, W.M.: Summary of Recent Investigations of Inlet Flow Distortion Effects on Engine Stability. AIAA Paper 74-236, Jan. 1974.
16. Braithwaite, W.M.; Graber, E.J, Jr.; and Mehalic, C.M.: The Effect of Inlet Temperature and Pressure Distortion on Turbojet Performance. AIAA Paper 73-1316, Nov. 1973.
17. Soeder, R.H.; Mehalic, C.M.; and Stancik, K.: Effect of Steady-State Temperature Distortion on Inlet Flow to a High-Bypass-Ratio Turbofan Engine. NASA TM-86896, 1985.
18. Meyer, C.L.; McAulay, J.E.; and Biesiadny, T.J.: Technique for Inducing Controlled Steady-State and Dynamic Inlet Pressure Disturbances for Jet Engine Tests. NASA TM X-1946, 1970.
19. Baumbick, R.J.: Device for Producing Dynamic Distortion Patterns at Inlets of Air-Breathing Engines. NASA TM X-2026, 1970.
20. Soeder, R.H.; and Bobula, G.A.: Effect of Steady-State Pressure Distortion on Flow Characteristics Entering a Turbofan Engine. NASA TM-79134, 1979.
21. Soeder, R.H.; and Mehalic, C.M.: Effect of Combined Pressure and Temperature Distortion Orientation on High-Bypass-Ratio Turbofan Engine Stability. NASA TM-83771, 1984.
22. Mazzawy, R.S.; and Banks, G.A.: Modeling and Analysis of the TF30-P-3 Compressor System with Inlet Pressure Distortion. (PWA-5302, Pratt and Whitney Aircraft; NASA Contract NAS3-18535.) NASA CR-134996, 1976.
23. Mazzawy, R.S.; and Banks, G.A.: Circumferential Distortion Modeling of the TF30-P-3 Compression System. (PWA-5448, Pratt and Whitney Aircraft; NASA Contract NAS3-18535.) NASA CR-135124, 1977.
24. deBogdan, C.E.; et al.: Effect of a 180°-Extent Inlet Pressure Distortion on the Internal Flow Conditions of a TF30-P-3 Engine. NASA TM X-3267, 1975.
25. McAulay, J.E.: Effect of Dynamic Variations in Engine-Inlet Pressure on the Compressor System of a Twin-Spool Turbofan Engine. NASA TM X-2081, 1970.
26. Wenzel, L.M.: Experimental Investigation of the Effects of Pulse Pressure Distortions Imposed on the Inlet of a Turbofan Engine. NASA TM X-1928, 1969.
27. Melick, H.C.; and Simkin, W.E.: A Unified Theory of Inlet/Engine Compatibility. AIAA Paper 72-1115, Nov. 1972.
28. Braithwaite, W.M.; and Soeder, R.H.: Combined Pressure and Temperature Distortion Effects on Internal Flow of a Turbofan Engine. AIAA Paper 79-1309, June 1979.
29. Mazzawy, R.S.; Fulkerson, D.A.; Haddad, D.E.; and Clark, T.A.: F100(3) Parallel Compressor Computer Code and User's Manual Final Report. (PWA-5549-8, Pratt and Whitney Aircraft; NASA Contract NAS3-20610.) NASA CR-135388, 1978.
30. Tesch, W.A.; and Steenken, W.G.: Blade Row Dynamic Digital Compressor Program, Volume I, J85 Clean Inlet Flow and Parallel Compressor Models. (R75-ABG406, General Electric; NASA Contract NAS3-18526.) NASA CR-134978, 1976.
31. Tesch, W.A.; and Steenken, W.G.: Blade Row Dynamic Digital Compressor Program, Volume II, J85 Circumferential Distortion Redistribution Model, Effect of Stator Characteristics, and Stage Characteristics Sensitivity Study. (R76-ABG484-VOL-2, General Electric; NASA Contract NAS3-18526.) NASA CR-134953, 1978.
32. Hosny, W.M.; and Steenken, W.G.: TF34 Engine Compression System Computer Study. (R78-ABG612, General Electric; NASA Contract NAS3-20599.) NASA CR-159889, 1979.

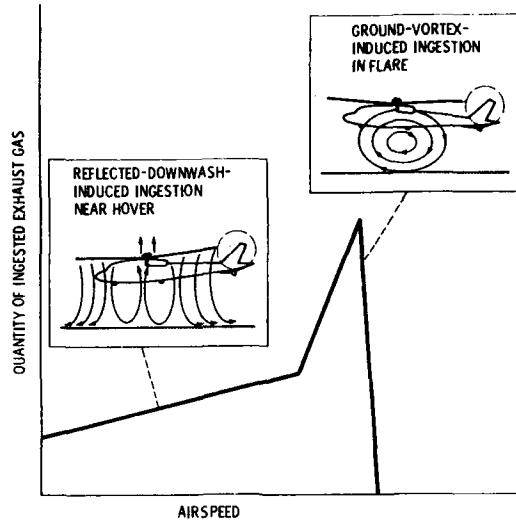


Figure 1. - Patterns of exhaust ingestions near ground (from ref. 1).

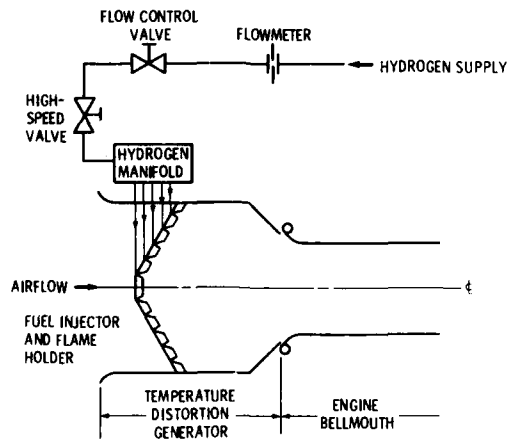
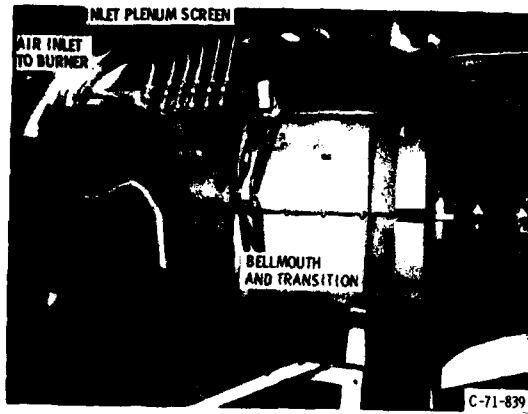
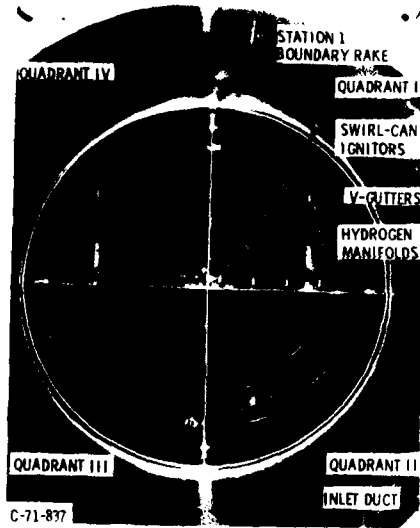


Figure 2. - Hydrogen-fueled temperature distortion generator.



(a) External view.



(b) Internal view looking forward.

Figure 3. - Gaseous hydrogen burner installed in altitude chamber

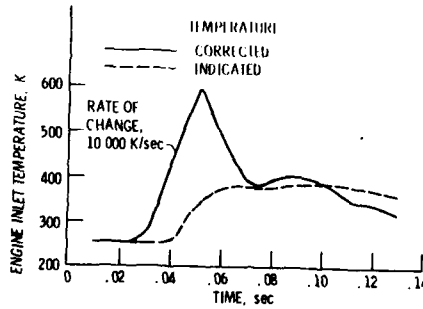


Figure 4. - Typical engine inlet temperature transients.

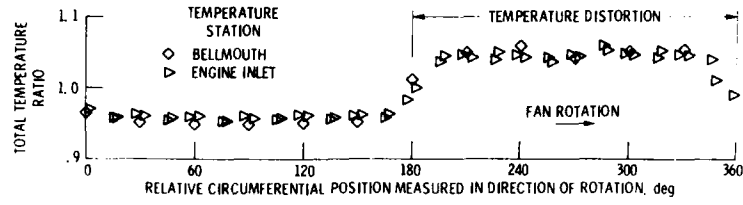
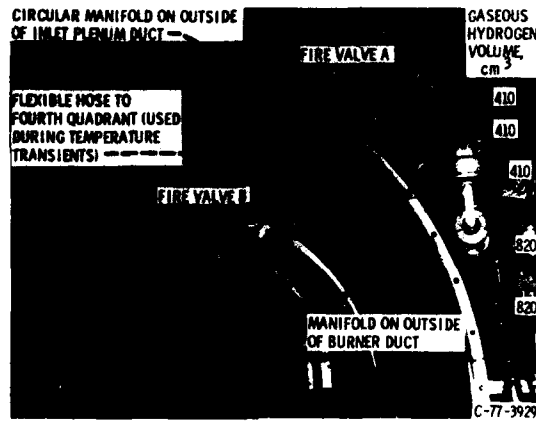
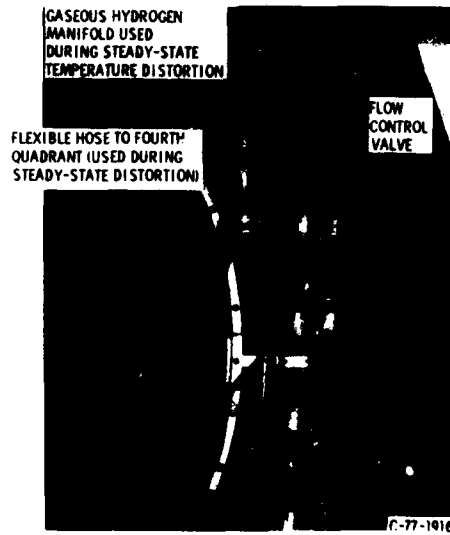


Figure 5. - Circumferential variation of total temperature profiles.



(a) For producing temperature transients.



(b) For producing steady-state distortion.

Figure 6. - Gaseous-hydrogen-fueled burner (quadrant IV) installation.

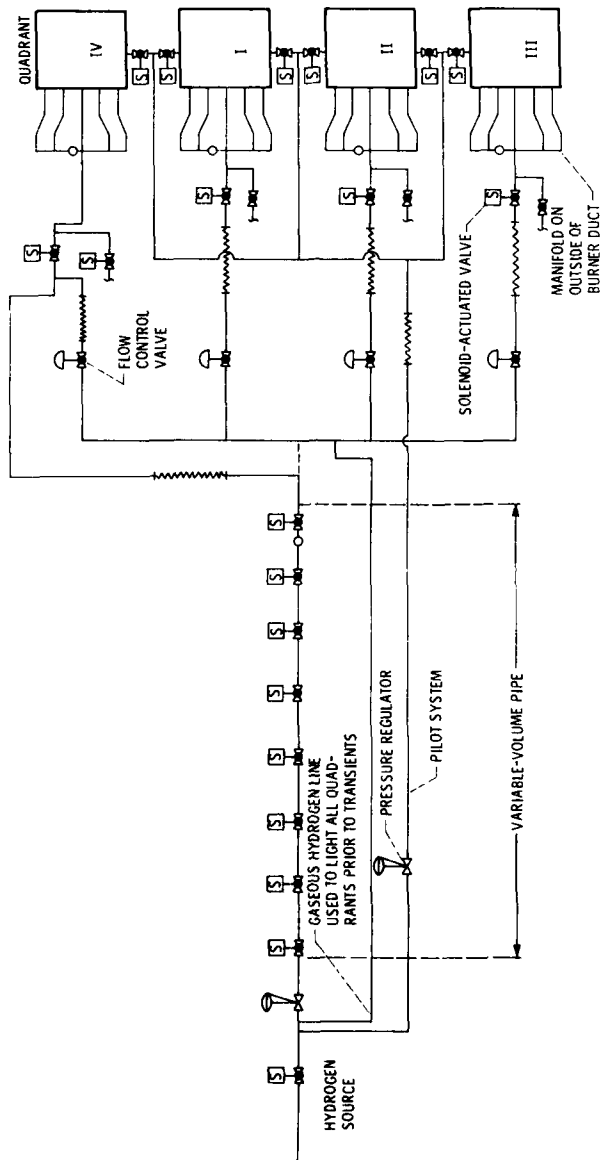
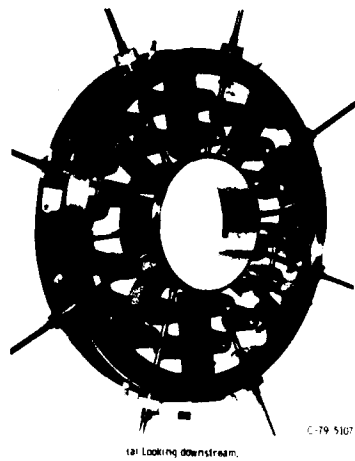
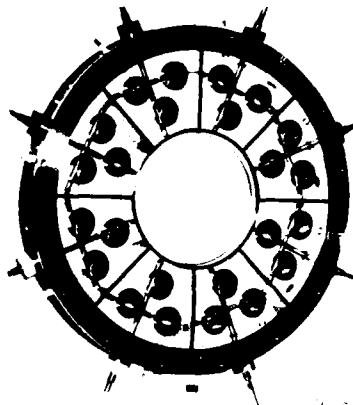


Figure 7. - Gaseous-hydrogen-fueled burner schematic.



(a) Looking downstream.



(b) Looking upstream.

Figure 8. - Temperature distortion generator for turboshaft engine testing.

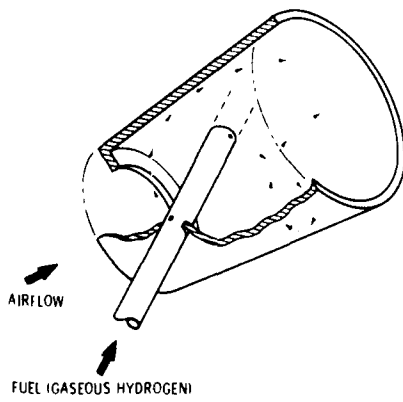


Figure 9. - Operation of typical swirl-cup combustor.

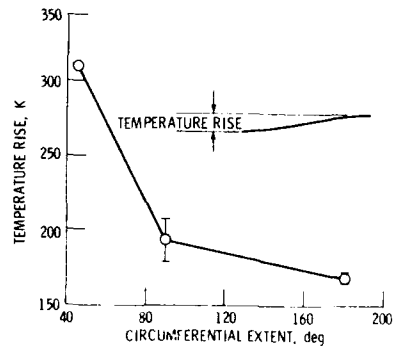
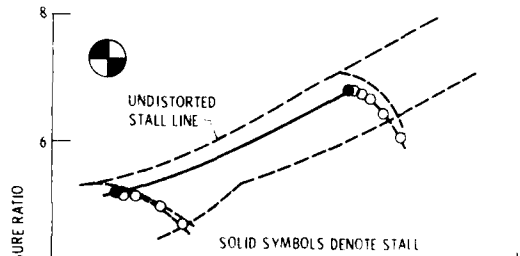
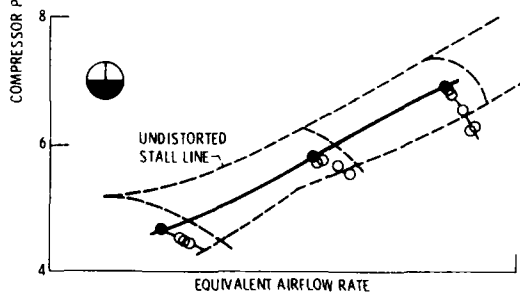


Figure 10. - Inlet temperature rise before onset of surge as a function of circumferential extent.



(a) Compressor performance with 90° extent, two-per-revolution distortion.



(b) Compressor performance with 180° extent circumferential distortion.

Figure 11. - Comparison of single distorted zone and diametrically opposed distorted zones.

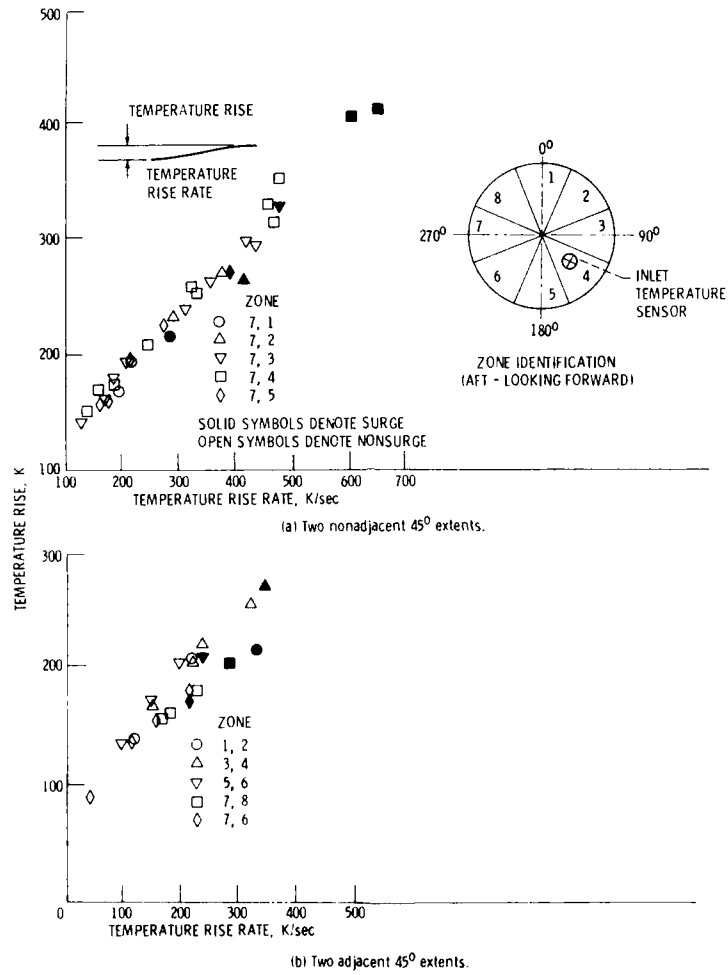


Figure 12. - Comparison of adjacent and nonadjacent distorted zones for a turboshaft engine.

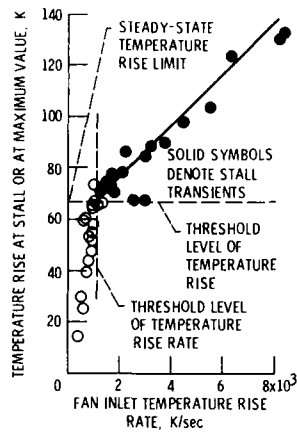


Figure 13. - Fan inlet temperature rise as a function of temperature rise rate.

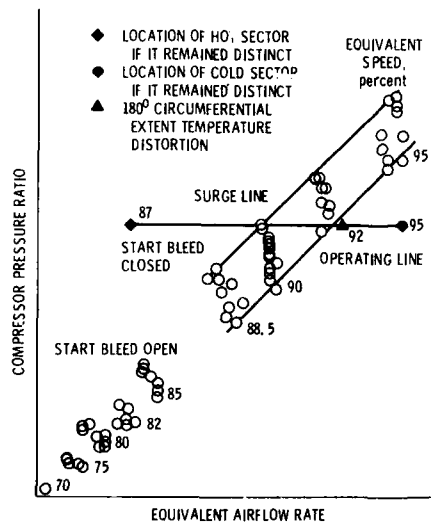


Figure 14. - Typical compressor performance map, showing effects of mixed and unmixed distorted areas.

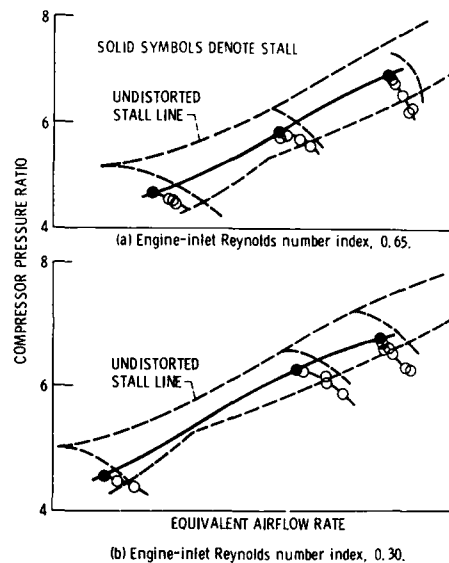
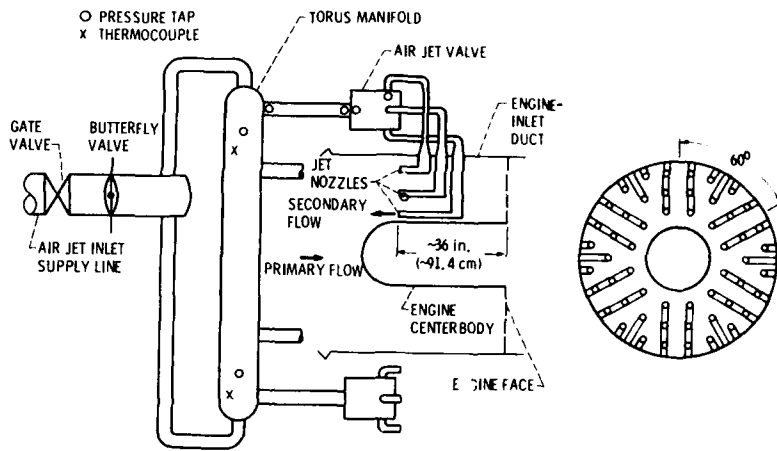
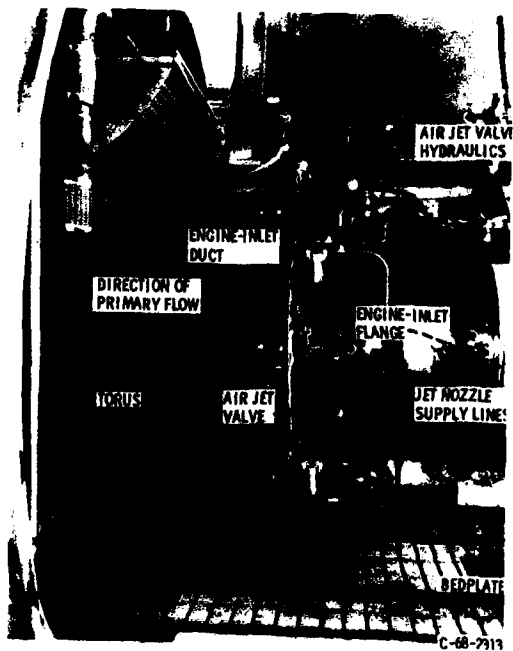


Figure 15. - Compressor performance with 180° extent circumferential distortion.



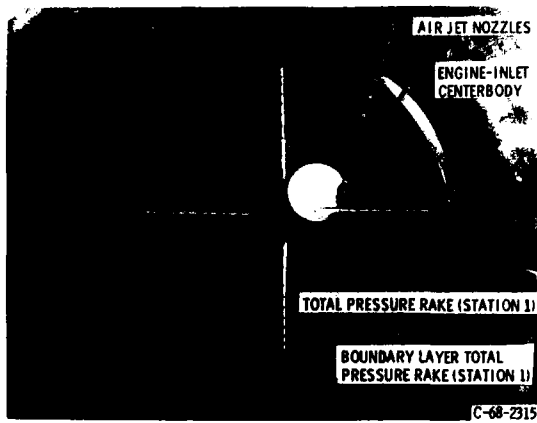
(a) Overall schematic.

(b) Frontal schematic of jets in engine-inlet duct.



(c) Air jet system and engine-inlet duct.

Figure 16. - Air jet system.



(d) Air jets installed in engine-inlet duct (view looking downstream).

Figure 16. - Concluded.

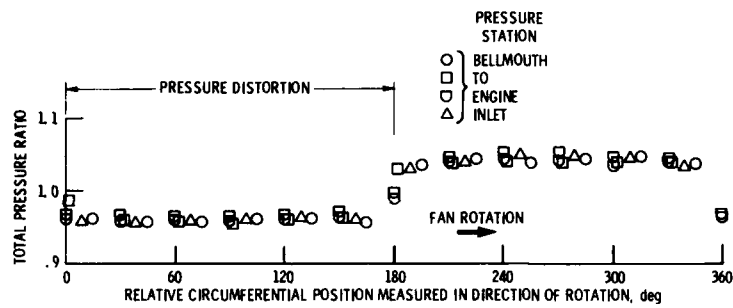


Figure 17. - Circumferential variation of total pressure profiles.

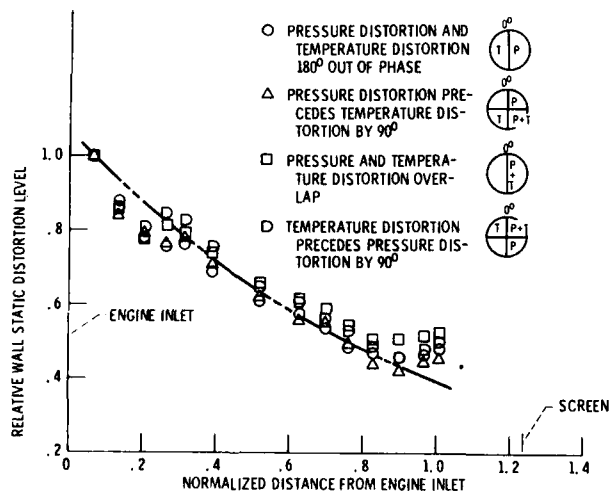


Figure 18. - Effect of total pressure and total temperature distortion orientation on static pressure distortion along inlet-duct wall.

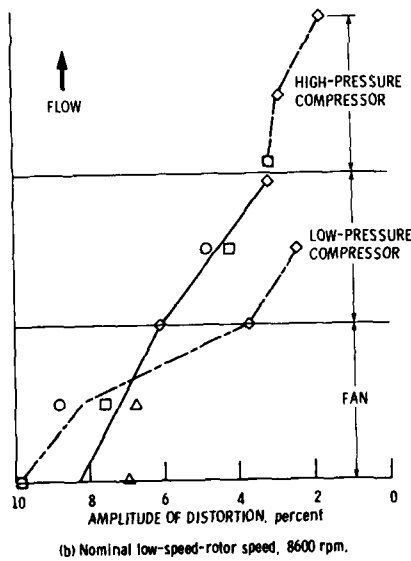
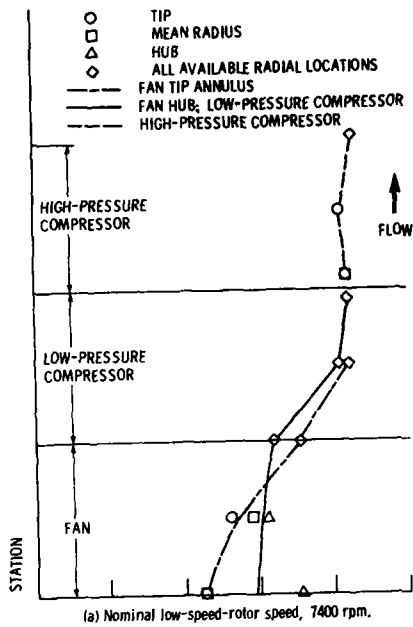


Figure 19. - Total pressure distortion - axial variation in amplitude.

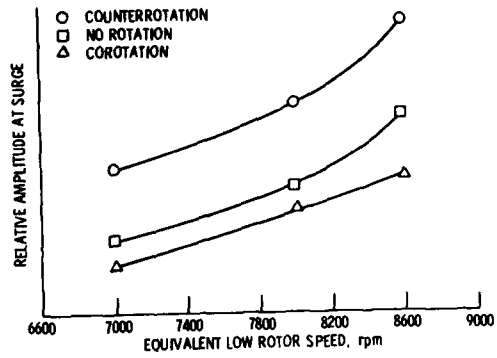


Figure 20. - Effect on stability of turbofan engine of rotating 180° square wave total pressure distortion at 20 Hz.

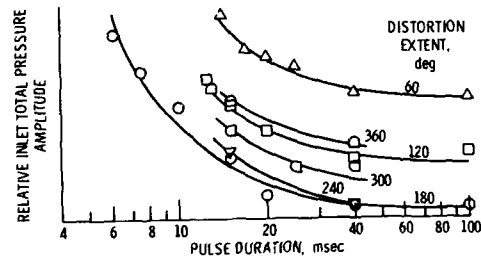


Figure 21. - Stall boundary as function of pulse amplitude, pulse duration, and distortion extent.

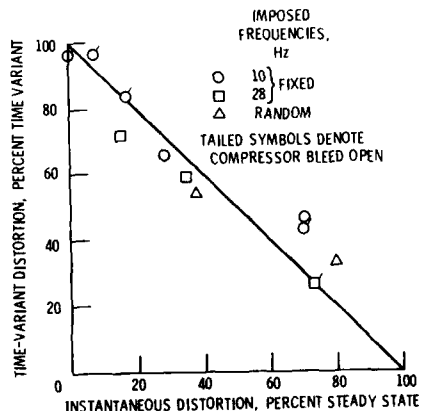


Figure 22. - Relation between steady-state and time-variant components of inlet flow distortion.

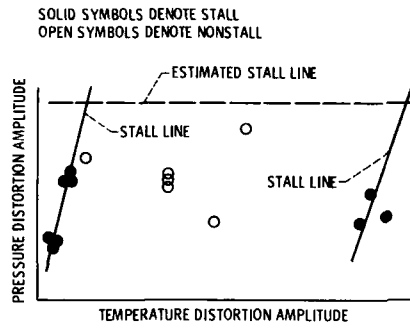


Figure 23. - Distortion sensitivity at engine inlet.

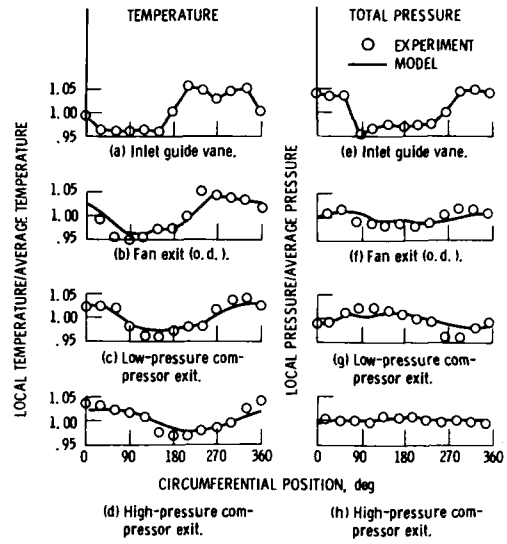


Figure 25. - Comparison of measured and predicted internal compressor profiles for combined pressure and temperature distortions.

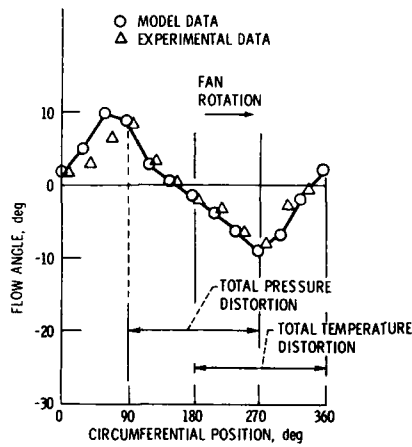


Figure 24. - Comparison of model and experimental approach angles for a complex flow distortion.

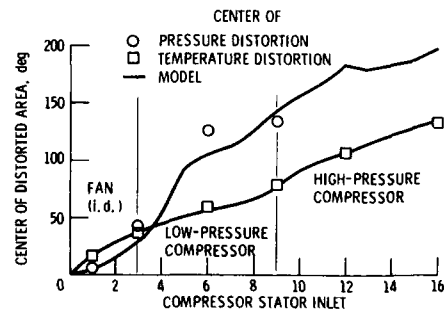


Figure 26. - Predicted swirl of total pressure and temperature distorted flow passing through compressor system.

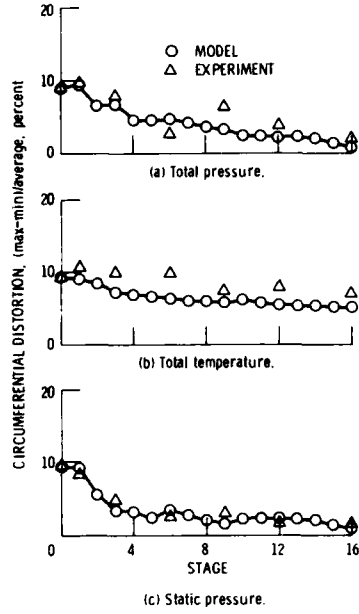


Figure 27 - Attenuation of distortion by compression system for combined pressure and temperature inlet distortion.

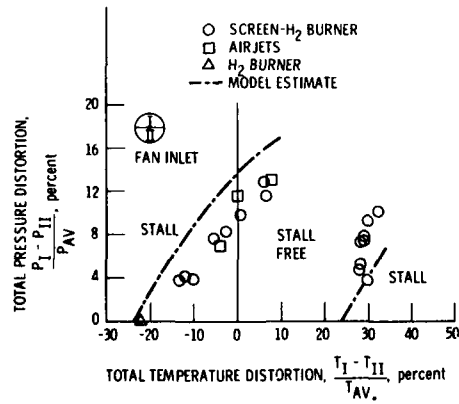


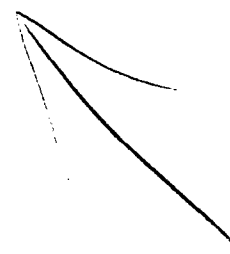
Figure 28. - Effect of relative position on limiting distortion for combined pressure and temperature distortions.

DISCUSSION**H.I.H.Saravanamuttoo, Ca**

Have you found any influence of engine size on susceptibility to inlet temperature distortion? In particular, are small turboshafts more sensitive to this problem?

Author's Reply

NASA had only subjected one turboshaft engine to inlet temperature distortion. However, a number of different turbofan engines, both low- and high-bypass-ratio, have been subjected to inlet temperature distortion and the trends, particularly with regard to temperature rise to cause stall, are similar.



UNSTEADY INLET DISTORTION CHARACTERISTICS WITH THE B-1B

by

C. J. MacMiller
 W. R. Haagenson
 ROCKWELL INTERNATIONAL
 NORTH AMERICAN AIRCRAFT OPERATIONS
 P.O. Box 92098
 Los Angeles, CA 90009
 USA

SUMMARY

An extensive wind tunnel and flight test program has been conducted to verify inlet performance and distortion characteristics on the B-1B aircraft. During the course of these investigations, several unsteady, total-pressure disturbances at various discrete frequencies were encountered:

- 1) Inlet duct resonance at low power settings;
- 2) ECS precooler duct resonance;
- 3) Nose gear wake ingestion.

This resulted in the need to quantify these effects and assess the impact on engine stability characteristics. As a result, engine control features were modified, and aircraft configuration changes were implemented. Results and findings of these investigations are summarized.

SYMBOLS

| | | | |
|----------|--|------------|--|
| α | angle of attack | IDTH | total distortion index, high-pressure (compressor) component, combined spatial and planar distortion index |
| AIP | aerodynamic interface plane | INT | intermediate power setting |
| B | superposition factor | K | 1,000 |
| β | sideslip angle | KIAS | knots indicated airspeed |
| c | speed of sound | L | length |
| d | diameter | LG | landing gear |
| ψ | yaw angle | M | mach number |
| ECS | environmental control system | ΔP | pressure differential |
| f | frequency | P3G | planar pressure pulse generator |
| FAVG | engine face average total pressure (PTI) | PK-PK | peak to peak |
| FOD | foreign object damage | PLF | power for level flight |
| IUC | inlet distortion, circumferential | PSD | power spectral density |
| IDH | inlet distortion index, high-pressure (compressor) component | PTI | engine face average total pressure (FAVG) |
| IDL | inlet distortion index, low-pressure (fan) component | PTO | freestream total pressure |
| IDP | index of planar distortion | RAVG | ring average total pressure |
| IDPH | index of planar distortion, high-pressure (compressor) component | RCS | radar cross section |
| IDPL | index of planar distortion, low-pressure (fan) component | RMIN | ring minimum total pressure |
| IDR | inlet distortion, radial | RMS | root mean square |
| IGV | engine inlet guide vanes | S | Strouhal number |
| IDTL | total distortion index, low-pressure (fan) component, combined spatial and planar distortion index | T | temperature |
| | | Wk | engine corrected airflow |
| | | X | organ pipe end correction (sometimes set to 1.4d) |
| | | θ | sweep angle of ramp leading edge |
| | | Y_N | nacelle station, inches |

INTRODUCTION

Stability characteristics of current high-performance turbofan engines are adversely affected by pressure fluctuations at the compressor face. One class of random pressure variations, frequently referred to as inlet-induced turbulence, is normally present in the flow. Engine stalls may result if sufficient energy/flow angularities exist at frequencies to which the compression system may respond. Dynamic distortion factors are used to correlate these types of pressure variations with losses in engine surge margin. Critical events can be difficult to define and usually require stochastic techniques. Correlations between the resulting spatial distortion characteristics and loss in surge margin have been the subject of considerable resources during recent decades (References 1 and 2).

Another class of pressure fluctuations can be destabilizing and is attributed to the occurrence of one-dimensional, unsteady-pressure oscillations at the compressor face. Inlet buzz during supersonic operation at low inlet mass flow ratios is one classic example of a large-amplitude, planar wave coupled with spatial distortion. These transients are generally characterized by discrete frequency components and thus classified deterministic. Although higher frequency components are present, events are readily identified.

Reported sources of planar pressure oscillations include both internally and externally generated disturbances. Internally-generated disturbances include flow separation/reattachment, turbulence, buzz, unstart/restart cycles, interaction with adjacent engines and inlets, response to control system inputs and secondary air inlet designs. Examples of externally generated disturbances include armament firing, atmospheric gusts, wakes of previous aircraft, external explosions and ingestion of wakes emanating from forward protuberances - landing gear, external stores and pylons, aerodynamic surfaces, and weapon bay doors and spoilers. Methods for dealing with the simultaneous effects of planar and spatial total-pressure fluctuations are not well understood.

An extensive wind tunnel program was conducted to develop the B-1B propulsion system, and a flight test program to verify operational suitability is well underway. During the course of the investigations, numerous instances were encountered where discrete frequency components were evident in total pressures at the engine inlet. This resulted in the need to quantify the effects and assess impact on engine stability characteristics. As a result, engine control features were modified, and aircraft configuration changes were implemented. Results and findings of these investigations, including wind tunnel and flight test comparisons, are summarized.

B-1B PROPULSION SYSTEM

The B-1, Figure 1, is a long-range strategic aircraft operated by a crew of four. Distinctive features relative to the propulsion system are variable sweep wings, nose gear protuberances forward of the inlets, external stores, structural mode control vanes and weapon bay doors and spoilers. The variable wing changes the wing sweep angle from 15 to 67.5 degrees. The aft sweep position (67.5 degrees) is used at high speeds and during low altitude penetration. The structural mode control vanes are located on the lower sides of the forward fuselage and vary to control structural bending mode oscillations and to provide a smoother ride quality.

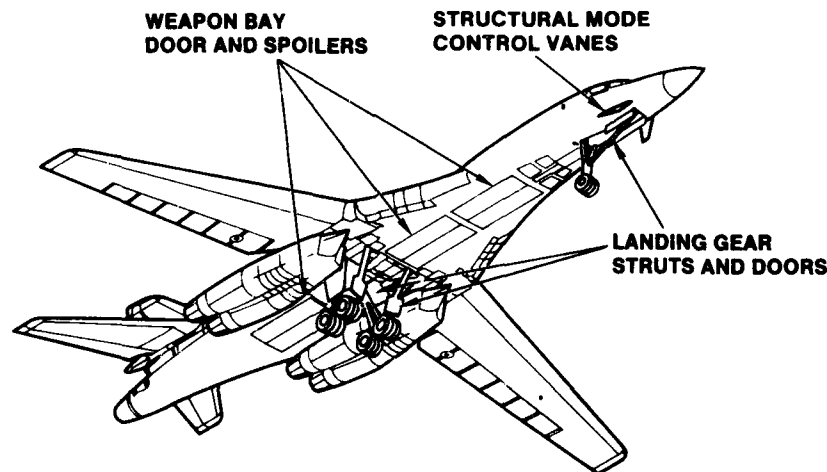


Figure 1. B-1B Air Vehicle

The B-1 propulsion system consists of two nacelles mounted under the fixed portion of the wing. Each nacelle contains two General Electric afterburning turbofan engines, and separate, independent inlets and

diffusers. Inlets are two-dimensional, with vertical compression ramps, and are located aft of the wing glove leading edge, outboard of the aircraft centerline. Forebody/wing boundary layer air is removed by a gutter located between the nacelle and wing. The off-centerline location required a complete flow field investigation because of wing flow outwash that varied with angle of attack, particularly at the aft wing sweep position. Nacelles are toed-in 1/2 degree to align with local flow at nominal angles of attack.

The B-1B inlet nacelle is a modification of the B-1A nacelle and not a complete redesign. A drawing of the B-1B inlet, illustrating some of its unique features, is shown in Figure 2. External nacelle mold lines were unchanged from the B-1A so as to not impact structural attachments and/or landing gear and nacelle clearances. Internal mold lines were modified with gradual bends and vanes to improve RCS characteristics. The region in the center of the nacelle, which housed the variable ramps and actuators of the B-1A, provided the space for the bends and vanes. Leading edges of cowls and vanes were canted 15 degrees to further enhance RCS characteristics. The center ramp was cut back 41 degrees to reduce planar pulse amplitudes and to reduce RCS. A three-position, movable cowl lip is employed to improve takeoff and low-speed performance and distortion. ECS scoops, internal to the inlet, precool engine bleed air above mach 0.5. This air exhausts between engine nozzles at the rear of the nacelle. At speeds below mach 0.5, precooler air is provided through separate inlets located outside the nacelle, above the wing, operating in conjunction with a blower. Flapper valves are used to prevent blower air from entering the main inlets.

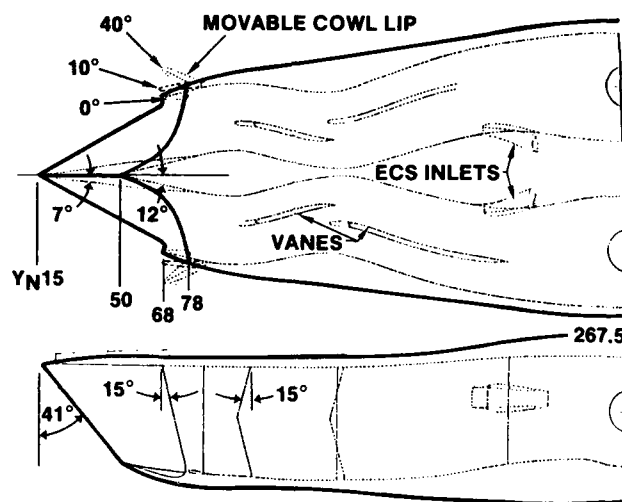


Figure 2. B-1B Inlet Nacelle

AERODYNAMIC INTERFACE PLANE INSTRUMENTATION

The inlet/engine aerodynamic interface plane (AIP) is the instrumentation station used to define total-pressure recovery and distortion interfaces between the inlet and the engine. In the B-1 program, the interface was defined at the leading edge of the engine inlet guide vanes (IGV). All airflow passing through this plane enters the engine. This instrumentation station was used throughout the inlet development and verification wind tunnel program, during engine qualification tests, and is being used in the ongoing flight test program.

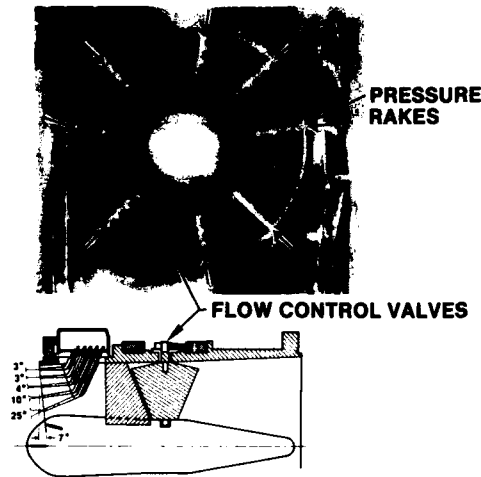
Eight rakes, each with five probes located at the centroid of equal annular areas, were used to measure pressures. Small differences in angular location were necessary among models due to the evolving nature and availability of particular IGV locations. All probes in the resulting 40-probe matrix were designed to measure both the steady-state and high-response components of total pressure. Leading edges of probes were chamfered to minimize sensitivity to flow direction. Distortion components, both radial and circumferential, were computed for each of five rings from eight total-pressure measurements on each ring.

A photograph of the AIP instrumentation used during 0.2-scale wind tunnel testing is shown in Figure 3. To maintain required frequency response, miniature high-response transducers were physically located at the AIP. Signals were high-pass filtered (A.C. coupled) to maintain accuracy over a wide range of pressure levels. These same dual-purpose probes provided a sensed location for the low-response (steady state) pressure measurements with larger, more accurate transducers. These transducers were located remotely in an environmentally-controlled area. A flow-control valve was located as close as possible to the AIP. During most tunnel operating conditions, airflow through this valve was choked, providing a reflection plane to simulate inlet acoustic properties.

Flight test AIP instrumentation is also shown in Figure 3. High-response transducers were installed integrally with selected IGV's. With appropriate signal conditioning, measurements of steady-state and

high-response outputs were recorded separately from the same transducer. An inflight calibration system was used to automatically provide a zero and a one-point pressure calibration throughout the flight at one-minute intervals. Generally, experience has shown good agreement between wind tunnel and flight test results (Reference 3). The relatively small differences in AIP instrumentation matrices and signal conditioning systems between wind tunnel and flight test produced only second-order effects on measured inlet distortion characteristics.

WIND TUNNEL



FLIGHT TEST

INSTRUMENTED IGV'S



Figure 3. Aerodynamic Interface Plane Instrumentation

DISTORTION ASSESSMENT PROCEDURES

Distortion methodology is defined as the set of procedures used to specify numerical values of spatial and planar total-pressure components at the selected measurement plane. Distortion descriptors are calculated from the spatial and time-dependent distribution of total pressures at the aerodynamic interface plane and are based on measurements from the 40 total-pressure probes defined in the previous section. They are used to define inlet spatial distortion characteristics with a time duration of sufficient length to affect engine stability. Additionally, they are used to describe amplitudes and frequency variations in the spatially-averaged pressure time histories, sometimes referred to as planar distortion. Variations occurring at discrete frequencies are "book-kept" as planar distortion and may also contribute to engine instabilities. Accurate measurement of these frequency components depends on the simulated engine face acting as an acoustic reflection plane.

Spatial distortion factors were generated in accordance with the procedures defined in Reference 1. With the 8 x 5 instrumentation array, circumferential and radial distortion components for each of the five rings are computed according to the following relationships:

CIRCUMFERENTIAL

$$IDC = \frac{RAVG-RMIN}{FAVG}$$

RADIAL

$$IDR = \frac{FAVG-RAVG}{FAVG}$$

Ring components can be combined in various ways to define overall engine face descriptors. Radial distortion components located in the outer diameters are frequently referred to as "tip radials", radial components located in the inner diameter are referred to as "hub radials". Distortion components are computed from high-response total-pressure signals filtered to the critical engine frequency and digitally sampled at rates sufficiently high to retain wave form. Resulting envelopes, encompassing all combinations of circumferential and radial distortion components, are used to describe distortion characteristics for a particular operating condition and/or inlet geometry and are illustrated in Figure 4. By imposing estimated engine limits on this same grid, a particular distortion pattern can be identified that consumes more stall margin than any other point and can be used to characterize spatial distortion for that particular data point. Estimated engine limits for a particular operating condition can also be used to normalize measured distortion levels and thus provide convenient indices, IDL and IDH, whose values are unity when measured distortion equals engine distortion allocations. These procedures can be applied separately to both the fan and compressor to gain insight on the controlling engine module.

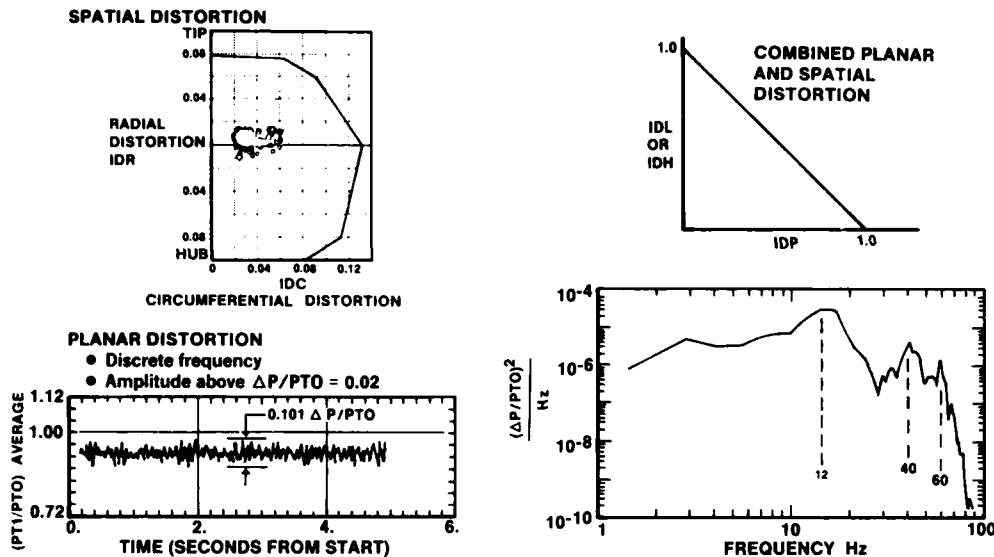


Figure 4. Distortion Assessment Procedures

Planar distortion components on the B-1B were measured during wind tunnel tests by routing all 40 high-response AIP signals to a summing circuit and outputting the numerical average. Power spectral densities (PSD) of the resulting analog signal were used to identify the presence of discrete frequency components and the magnitude of the energy contained within each frequency band. Initial estimates on sensitivity to planar distortion were based on extrapolations from F101 fan/P3G testing completed in 1973 (Reference 4). A PSD of a signal containing multifrequency planar distortion components is illustrated in Figure 4. An index of planar distortion (IDP) is generated by normalizing measured energy to estimated limits. When more than one discrete frequency component exists, individual contributions are summed linearly to obtain the total index.

Above assessments of planar distortion are based on two assumptions. One, that planar distortion is transferred without diminishment by the fan; and two, the fan and compressor planar distortion sensitivities are similar. Data supporting these assumptions are sparse, but it is logical to expect that at high levels of IDP, at some frequencies, fan or compressor instabilities can result even in the absence of spatial distortion. When planar distortion is imposed on spatial distortion, it follows that allowable spatial distortion is therefore decreased. Again, data supporting this premise are essentially nonexistent.

Screening procedures used on B-1B wind tunnel and flight test data assume that spatial and planar distortion indexes add linearly ($B = 1.0$) to provide a combined measure of inlet distortion.

$$\begin{array}{l} \text{FAN} \\ \text{IDTL} = \text{IDL} + B (\text{IDPL}) \end{array}$$

$$\begin{array}{l} \text{COMPRESSOR} \\ \text{IDTH} = \text{IDH} + B (\text{IDPH}) \end{array}$$

In subsequent sections, these indexes are used as an initial step in assessing B-1B inlet/engine compatibility. They provide useful tools to screen a large number of data points to identify potential areas of concern and to quantify incremental differences among a host of configuration and operating variables. Distortion characteristics that survive initial screening procedures are subject to more detailed analysis. These may include transient runs with engine dynamic simulations, stability stack-ups more tailored to the particular configuration and operating procedures, and statistical assessment procedures to put potential problems in perspective and suggest design alternatives.

INTERNALLY-GENERATED DISTURBANCES

Two sources of inlet-generated disturbances encountered during the development of the B-1B propulsion system are discussed. In one case, local flow separation occurred along the external inlet ramp surface and resulted in duct resonance during low-power engine operation at leeward sideslip. In another case, an ECS scoop, located within the inlet to precool engine bleed air, resonated under "no flow" conditions, and resulting disturbances were recorded with high-response, total-pressure instrumentation located at the aerodynamic interface plane. Both instances were characterized by a coupling between discrete frequency

components and spatial distortion components normally present in the flow. Although engine response to this coupling is not well understood, a need to evaluate inlet-to-engine compatibility in the presence of combined planar and spatial distortion was clearly identified.

INLET DUCT RESONANCE

Low-airflow planar distortion is caused by local flow separation and reattachment along the ramp surface forward of the cowl during leeward sideslip as shown in Figure 5. Separation and reattachment cycles occur at the 11 Hertz closed-end organ pipe frequency of the inlet duct measured to the acoustic interface of the engine. Circular flow patterns shown on the sketch were evident from oil-dot flow patterns measured in wind tunnel tests.

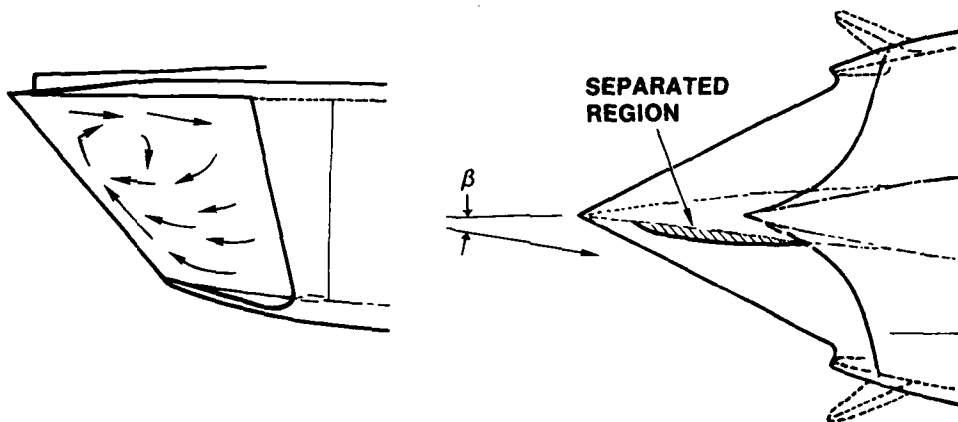


Figure 5. Local Flow Separation on Inlet Ramp During Off-Design Operation at Low-Airflow

Local ramp separation at low airflows and leeward sideslip is due to a highly adverse pressure gradient forward of the cowl lip station interacting with boundary layer along the forward ramp surface. As leeward sideslip increases, the flow expands around the ramp leading edge, then decelerates rapidly to the inlet station. Local ramp pressures decrease near the leading edge which allow boundary layer thickness to increase prior to entering the high-pressure-gradient region. The process is similar, although at much lower amplitudes, to buzz at supersonic speeds caused by shock wave and boundary layer interactions. Horizontal ramp inlets experience this phenomena at low or negative angles of attack; vertical ramp inlets at leeward sideslip.

Representative distortion characteristics recorded during wind tunnel tests at mach 0.85 with the outboard inlet are shown in Figure 6. The model was positioned at nine-degrees angle of attack and five degrees sideslip. Flow field measurements identified that local outwash, generated by the fuselage and wing combination, increases proportionately with angle of attack. Angle of attack and sideslip thus act in concert to orient the outboard ramp leeward and produce the distortion characteristics shown as a function of engine corrected airflow.

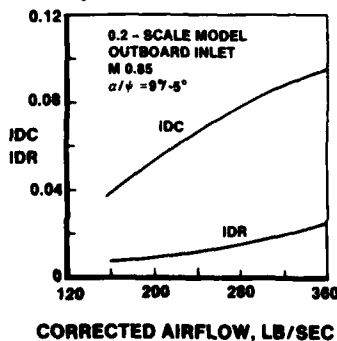


Figure 6. Spatial Distortion Characteristics

Circumferential distortion is the predominant spatial component, although both components increase almost proportionately with corrected airflow. Flight test results generally confirm wind tunnel results. Time histories of the average of the 40 individual AIP signals indicate that in addition to these spatial distortion components, the flow, at this off-design condition, is experiencing a one-dimensional oscillation about a mean, and peak-to-peak amplitudes of this combined signal can be used as a figure of merit. One example at low corrected airflow is shown in Figure 7. Power spectral densities identify the presence of discrete frequency components with a fundamental frequency of 60 Hertz (0.2-scale). This frequency corresponds well with organ pipe theory, $f = c/[4(L + X)]$, where the characteristic dimension is controlled by the distance between the average cowl leading edge and the AIP. The presence of odd-numbered harmonics is consistent with closed-end organ pipe theory.

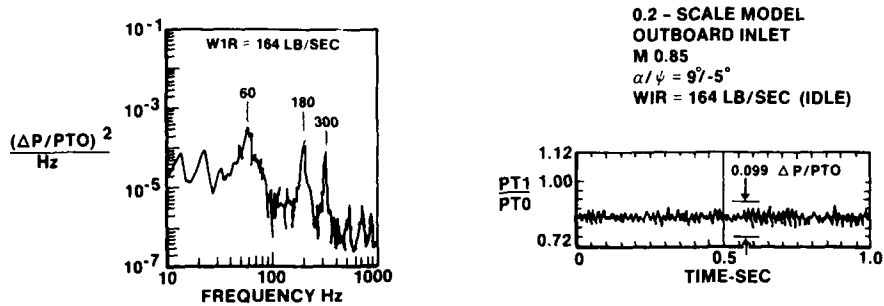


Figure 7. Planar Distortion Characteristics

Magnitudes of these planar waves are strong functions of several independent parameters - geometry, corrected airflow, attitude and mach number. The ramp serves as a separation plane to maintain inlet-to-inlet independence. However, tests were conducted to measure the effectiveness of increasing the sweep angle of the ramp leading edge in an attempt to eliminate, or at least minimize, the source of the flow separation. This proved to be an effective technique to reduce the magnitude of the planar wave. Variations of peak-to-peak amplitudes for two leading edge sweep angles are shown as a function of corrected flow in Figure 8. During off-design operation at mach 0.85, at airflows corresponding to operation at IDLE power, increasing the sweep angle from zero to 41 degrees reduced the amplitude of the planar wave by almost 50 percent. No evidence of disturbances at the AIP in the adjacent inlet was detected. Subsequent testing at other mach numbers and maneuver conditions verified that inlet-to-inlet independence could be maintained with the cut-back ramp.

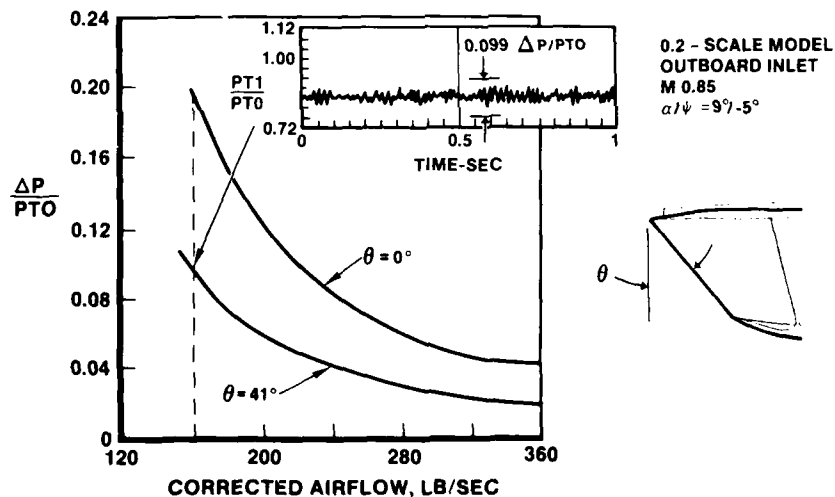


Figure 8. Effect of Ramp Leading Edge Sweep on Planar Wave Amplitude

Tests showed that the magnitude of the planar wave was sensitive to mach number, airflow and attitude as illustrated for the outboard inlet in Figure 9. At normal cruise attitudes, where the degree of outwash is small, planar amplitudes remain below two percent throughout the mach range. As local outwash is increased, by operation at combinations of angles of attack and sideslip, sensitivities to mach number increase markedly, and at sonic conditions, amplitudes can approach 12 to 15 percent of freestream total pressure. At high subsonic mach numbers, amplitudes of these planar waves can be reduced by almost 50 percent by increasing flight idle airflows to rates corresponding to 90 percent core corrected speed. This feature is sometimes referred to as "idle-speed lockup".

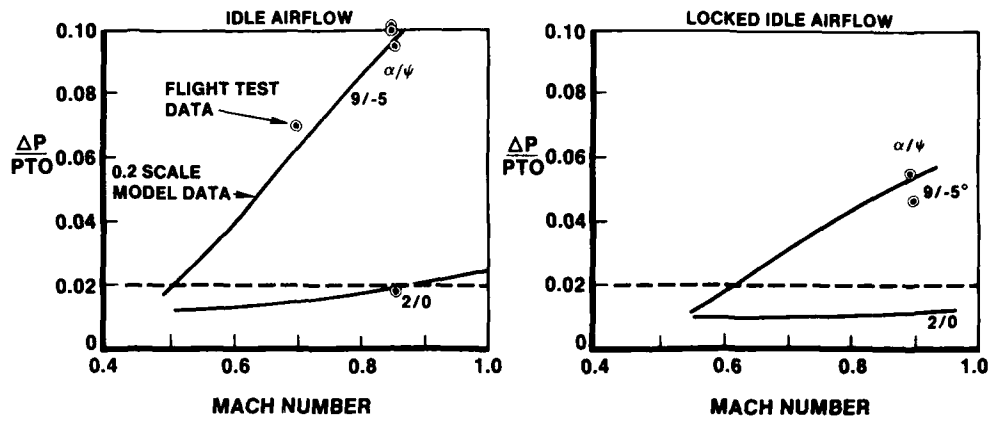


Figure 9. Planar Wave Amplitude Characteristics With Outboard Inlet

Good agreement in both magnitude and frequency of planar distortion were obtained between wind tunnel and flight test results. One example is shown in Figure 10, comparing time histories of comparable signals during leeward operation at mach 0.85 and airflows corresponding to IDLE power. Peak-to-peak amplitudes of ten percent were measured directly with both the airplane and the 0.2-scale wind tunnel model. And frequencies scaled directly with Strouhal number, $S = fL/\sqrt{T}$, resulting in a full-scale frequency of 12 Hertz, well within the frequency range to which engines respond.

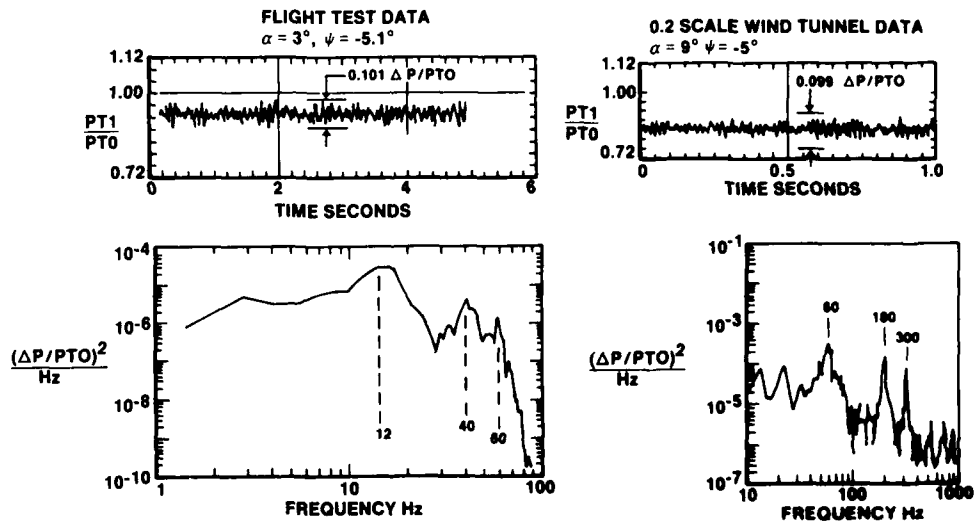


Figure 10. Wind Tunnel/Flight Test Comparison of Planar Distortion, Mach 0.85, Outboard Inlet, WIR = 164 lb/sec

Ramp separation and the associated planar distortion component are thus shown to be fundamentally a low-airflow phenomenon. Fortunately, spatial distortion components are directly proportional to airflow and are typically less than four percent at idle airflow. At first glance, one would expect this to be compensatory; however, engine tolerance to spatial distortion can be strong functions of engine corrected airflow and compression system rotational speeds. In fact, the need to accelerate the engine during periods of thermal mismatches between the engine case and rotor, as, for example, during a throttle body, can be one of the more difficult hurdles for inlet/engine stability assessments. Complexities of assessing the impact of adding a planar distortion component make it that much harder.

Using a simplifying assumption that superposition factors defining the relationship between planar and spatial distortion components are unity, assessments were conducted over a range of airflows, mach numbers, and angles of attack and sideslip using data recorded during wind tunnel tests with the 0.2-scale inlet verification model. Because engine sensitivity is also a function of altitude, conditions were evaluated at altitude extremes for each mach number, and for both fan and compressor engine modules.

Typical results are illustrated in Figure 11 during operation at mach 0.85. Maneuver conditions are identified where engine stability margin allocations to the inlet are fully utilized. In an adverse combination of events, where throttle transients are performed on deteriorated engines with worst case engine control tolerances, occasional engine stalls would be anticipated during operation outside the maneuver envelopes shown. In most cases, stability limits for the compressor are reached before margin runs out on the fan. Limiting maneuver conditions at negative yaw (positive sideslip) represent limitations of the No. 1 inlet (left-hand, outboard). Mirror images of these limitations, shown at positive yaw (negative sideslip) represent operation of the No. 4 inlet (right-hand, outboard). Occasional instabilities would be predicted for both outboard inlets during operation at angles of attack above the intersection of these lines.

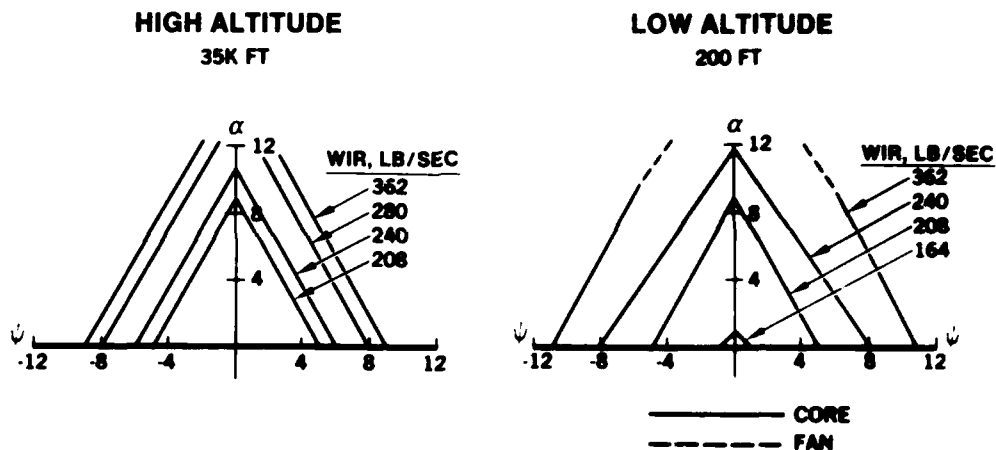


Figure 11. Stability Assessment During Mach 0.85 Maneuvers

Historically, one objective of good inlet/engine design is to maintain stall-free engine operation under fleet conditions throughout the anticipated flight and maneuver envelopes. To achieve this objective with the B-1B/F101, the foregoing methodology and analyses indicate that within portions of the flight envelope, engine corrected airflow should be maintained above 210 lb/sec. Consequently, an idle speed lock-up feature was incorporated and is implemented by a manual switch located in the crew station. When activated, one switch controls all four engines and limits core operation to 90 percent corrected speed. Thrust modulation with this setting is adequate to meet all aircraft requirements in all atmospheres. Temporary handbook instructions currently require activation of this mode of operation above 425 KIAS or mach 0.9, whichever is less. Ongoing flight test evaluations of this system will help to determine the need, and if need be, suggest potential means of automating implementation.

AUXILIARY AIR INLET

Auxiliary air inlets can be another source of internally generated disturbances. A scoop is installed on the ramp side of each B-1B inlet to precool ECS bleed air. During ground and low speed operation, when inlet pressure is lower than ambient, a hydraulically-driven blower supplies outside air to the heat exchanger. A flapper door, installed in the common duct connecting these sources of cooling air, is closed to prevent reverse flow during blower operation. Air is exhausted aft through exits located between engine nozzles to reduce base drag. At mach 0.5, pressure in the inlet duct is sufficiently above ambient pressure to service the heat exchanger. The blower is shut off and the flapper door opens allowing air to flow through the scoop inlet.

The design and relative location of the ECS precooler inlet assembly is shown in Figure 12. The scoop is located just above the duct centerline and extends four inches into the inlet. The scoop had to be redesigned to accommodate the redesign of the basic B-1B inlet. Advantage was taken of this opportunity to reshape the scoop cowl lip and external mold line to minimize external flow separation under "no flow" conditions. The scoop thus acts as a resonator (closed organ pipe) with the controlling volume located between the leading edge and the flapper valve. Since the flapper door is self-positioned by air loads, resonance can lead to structural damage, particularly during operation close to the transition point when the pressure differential across the door is small. Because of the low duct pressure, engine FOD can result, and during the initial B-1B flight test program, several instances were attributed to structural failure within this system.

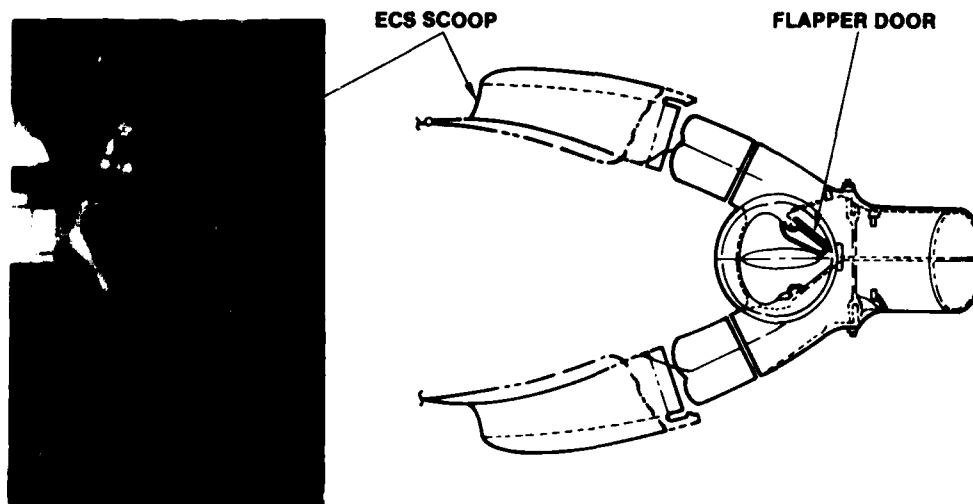


Figure 12. ECS Precooler Assembly

High-response pressure transducers located just upstream of the flapper door in the aircraft identified duct resonance at frequencies corresponding to a closed-end organ pipe. During static operation on the ground at maximum engine airflow, power spectral densities, Figure 13, identified a fundamental frequency at 77 Hertz as well as the presence of several harmonics. RMS amplitudes were approximately 2.4 psi. Similar results were obtained with the 0.2-scale inlet model. Although amplitudes were smaller, discrete components were measured at scaled frequencies, and a program was initiated to eliminate and/or reduce the magnitude of these oscillations.

M = 0 LIP 40°
WIR = MAXIMUM

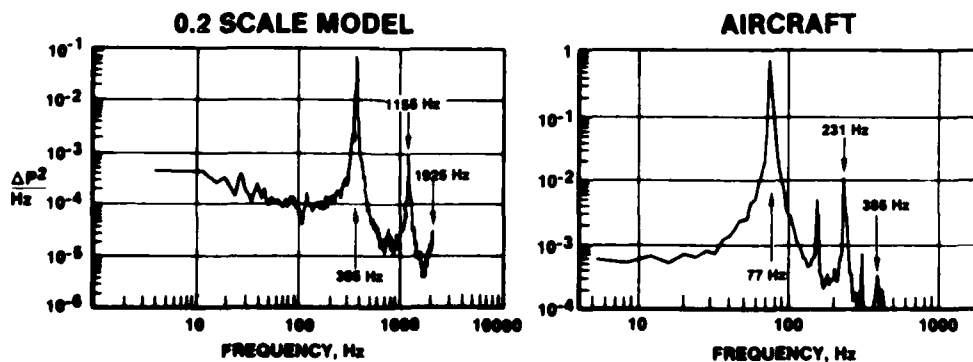


Figure 13. Resonance Characteristics in ECS Scoop Inlet

Two areas of concern were addressed. One was to explore potential configuration changes to eliminate the disturbance, and the other was to ensure that changes had no adverse impact on engine stability. Wind tunnel results showed that disturbances propagated both upstream and downstream in the duct as shown in Figure 14. Spatial measurements at the aerodynamic interface plane showed that a majority of the probes registered discrete frequency components, and could thus induce planar distortion components. Probes located on the same side as the ECS scoop contained more energy at discrete frequencies. While frequencies were generally beyond the engine 62.5 Hertz cut-off frequency corresponding to "one per rev" (300 Hertz at 0.2 scale), configuration changes could alter downstream frequency components, impact spatial distortion characteristics, and affect engine stability.

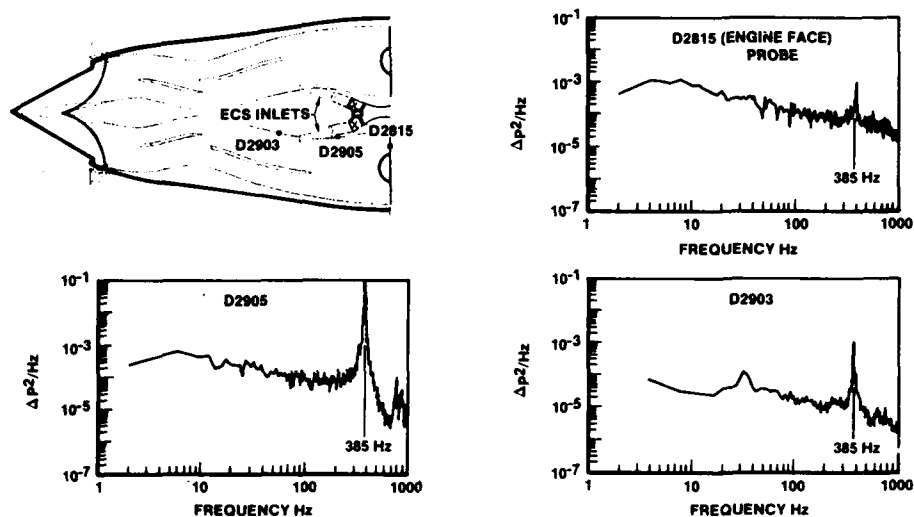


Figure 14. Acoustic Resonance Propagation From ECS Scoop Inlet

Tests were conducted in a Rockwell static facility with the 0.2-scale inlet model. Several concepts were investigated to reduce or eliminate duct resonance. One concept consisted of changing the valve design to "leak" reverse flow back through the scoop. By restricting the leakage flow rate, penalties on heat exchanger performance could be minimized. Another concept consisted of a bypass arrangement designed to provide continuous airflow through the scoop to reduce acoustic amplitudes. Yet another concept consisted of designing a resonator chamber upstream of the valve to attenuate specific frequencies.

Test results with the reverse-flow concept are shown in Figure 15. Power spectral densities generated from a high-response, static-pressure transducer located close to the valve are shown for three valve positions. Although discrete-frequency components are evident for all valve settings, total energy under the curve - a measure of peak-to-peak amplitude - decreases rapidly with increased flow area. With an area equivalent to 2.0 square inches full scale, total energy is reduced by approximately two orders of magnitude. Similar results were obtained with the bypass and resonator configurations. As a result of this experience, subsequently confirmed with full-scale tests, the B-1B production redesign incorporates a snubber and a leakage area of two square inches. No problems have been encountered upon incorporation of these changes.

EXTERNALLY-GENERATED DISTURBANCES

Several sources of externally generated disturbances were also encountered during the development of the B-1B. Generally, these disturbances can be traced to wakes and vortices shed from external surfaces. It is not unusual for these disturbances to contain discrete-frequency components. For example, structural mode control (SMC) vanes are located on the lower forward fuselage. Sinusoidal deflections of these vanes are designed to attenuate relative structural motion between the crew station and the aircraft center of gravity and thus provide good ride qualities. Under certain maneuver conditions, vortices generated by these surfaces can be ingested by the inlet. During the B-1A program, a considerable effort, including full-scale inlet/engine tests, was conducted to verify airframe/engine compatibility during operation of this system, and results are well documented in Reference 5.

Nose gear wake ingestion is another source of externally generated disturbances. Flight test investigations with the B-1 configurations have shown that nose gear wakes do contain discrete frequency components, identifying another need to assess engine stability characteristics with combined planar and spatial distortion components. Based on assessments derived from extensive wind tunnel tests and limited engine response characteristics, a movable cowl lip was incorporated in the B-1 inlet design. Cowl lip

angle is held in one of three positions, 40, 10 or 0 degrees, and is scheduled as a function of gear position and mach number as shown in Figure 16. Good performance and acceptable distortion characteristics during takeoff and low-speed operation result, and drag is minimized during high-speed flight.

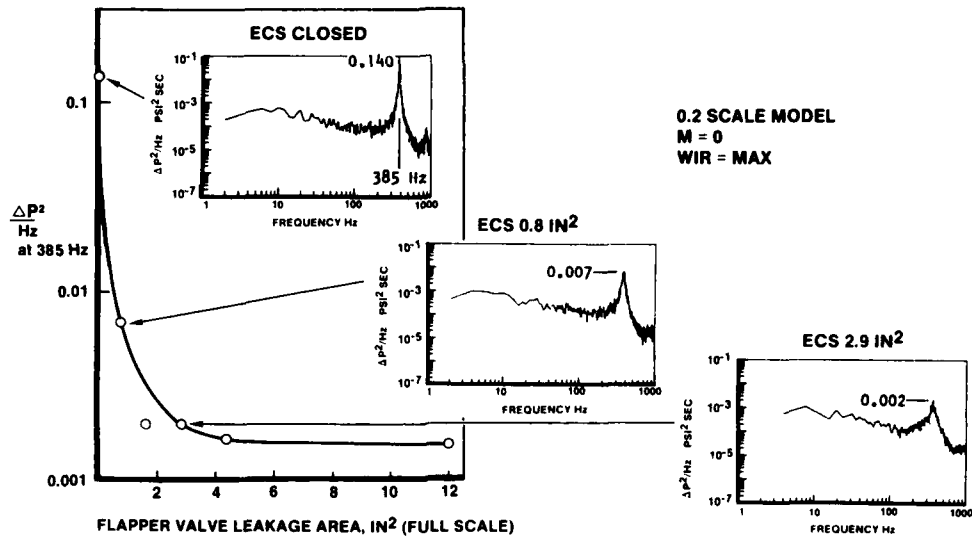


Figure 15. Effect of Reverse Flow on Acoustic Amplitude in ECS Scoop

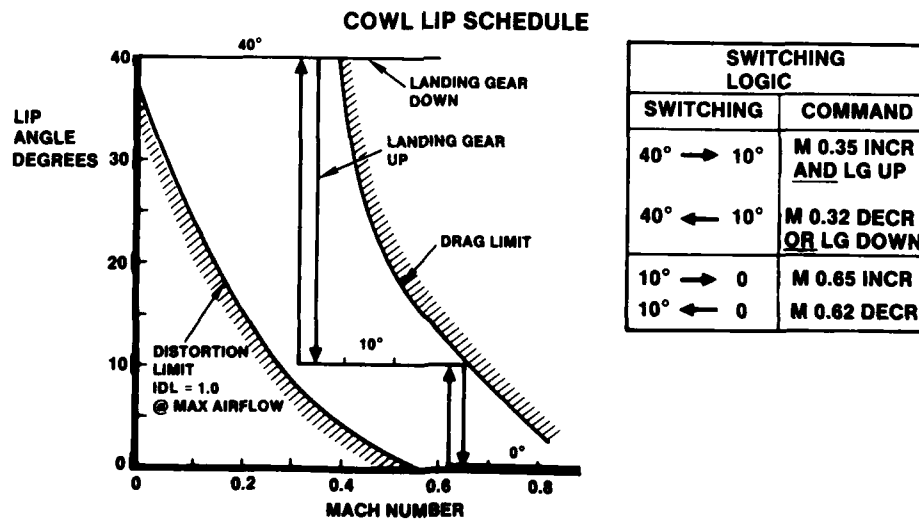


Figure 16. Cowl Lip Schedule

Limits that define regions of acceptable lip operation are also shown. The distortion limit was derived from wind tunnel data and defines regions where combined spatial and planar distortion levels remain within engine allocations. The limit shown for drag is somewhat arbitrary. Drag increases with increasing lip angle and/or mach number and eventually becomes excessive. Operation at mach numbers and lip angle combinations greater than this limit are avoided to minimize impact on specific fuel consumption during important mission conditions.

Switching among the 40-, 10-, and 0-degree cowl lip settings is based on flight mach number and landing gear position. The 40-degree lip setting is used for takeoff and all flight conditions where the landing gear is down and the nose gear wake could enter the inlet. The 10-degree lip position is used above mach 0.35 after the landing gear is raised. This position maintains inlet distortion levels within engine allocations for flight maneuvers up to mach 0.65. The fully closed, 0-degree position is used for high-speed operation above mach 0.65 where drag is critical. The cowl lip reopens as flight speed is reduced and/or the landing gear is lowered. An increment of 0.03 in mach number is used to separate opening and closing signals to provide a positive control input in both directions.

Circumferential distortion characteristics derived from high-response AIP signals during wind tunnel tests are shown in Figure 17 as a function of mach number and cowl lip angle at maximum engine corrected airflow. Both parameters have a profound impact on spatial distortion levels, and this is attributed to local flow separation on the cutback cowl lip. Large expansion turning angles between the stagnation streamline and local cowl mold line occur in this region at high inlet mass flow ratios. Levels are aggravated by sideslip in the direction making the inlet windward; i.e., nose left sideslip for inlets 2 and 4, and nose right sideslip for inlets 1 and 3. Spatial distortion levels measured during flight tests agree well with wind tunnel results as shown for selected configurations and mach numbers.

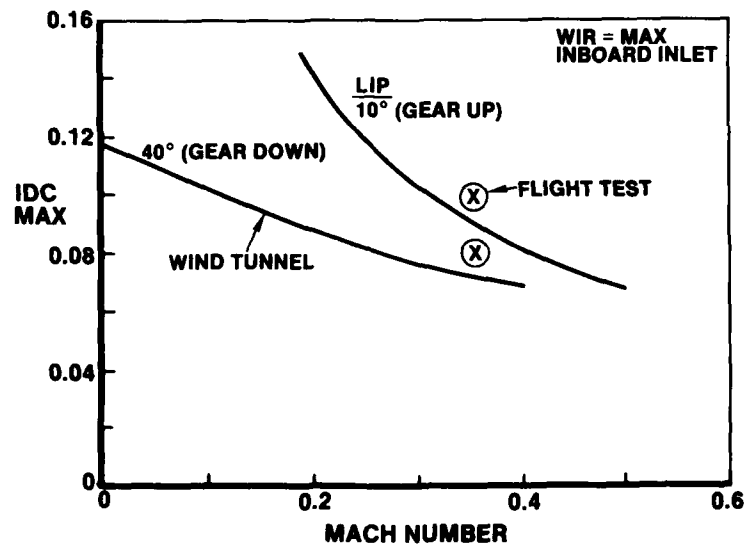


Figure 17. Effect of Cowl Lip Position on Spatial Distortion

With the gear extended, planar distortion components were also evident in the flow. Variations in peak-to-peak amplitudes of the average engine face total pressure are shown in Figure 18 as a function of freestream mach number. The amplitude is independent of lip position and is essentially eliminated by retracting the gear. Peak-to-peak amplitudes of approximately five percent were measured in the wind tunnel at mach 0.35. Amplitudes recorded during flight tests at comparable conditions approached seven percent. Differences are attributed to atmospheric uncertainties during flight test and to problems encountered in accurately simulating complex landing gear structure in small scale models. Discrete frequency components were evident in power spectral densities generated with these signals at all airflows. With flight test data, the fundamental frequency was 18 Hertz at mach 0.4, increasing to 28 Hertz at mach 0.6.

Sideslip transients with the gear extended were conducted during flight at mach 0.4 at an altitude of 10,000 feet. Resulting spatial and planar distortion characteristics are shown in Figure 19 for both inlets in the left-hand nacelle. As sideslip is increased to positive angles, evidence of nose gear wake ingestion is indicated initially in the inboard inlets as expected. Planar components maximized at a sideslip angle of approximately six degrees and then diminished at higher sideslip angles as the wake moved outboard of the nacelle. The impact of higher planar components in the outboard inlet is partially offset by lower spatial components.

Differences in flight test distortion characteristics between extended and retracted gear positions during operation at 5,000 feet, mach 0.35, are shown in Figure 20. With the gear up, the cowl lip is at 10 degrees, and with the gear down, the cowl lip is at 40 degrees. Angle of attack varies between 5.5 and 7 degrees, and engine airflow is maximum at 356 lb/sec. Extending the gear introduces a planar component with a peak-to-peak amplitude of 0.069. Circumferential distortion never exceeds eight percent, and the low-pressure defect appears in the upper cowl-side portion of the engine face. On the other hand, retracting the gear eliminates the planar component, and decreasing the cowl lip angle to 10 degrees increases circumferential distortion to approximately 11 percent. More radial distortion is evident, and the low pressure defect is located in the lower cowl-side quadrant. Operating the cowl lip at 40 degrees when the gear is down thus results in additional margin to accommodate potential ingestion of planar components.

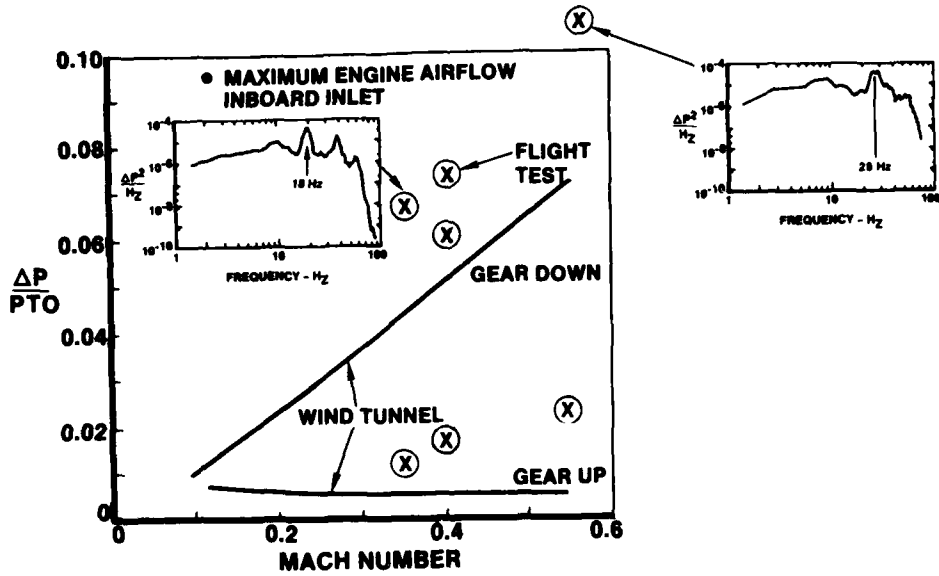


Figure 18. Effect of Gear Wake Ingestion on Planar Distortion

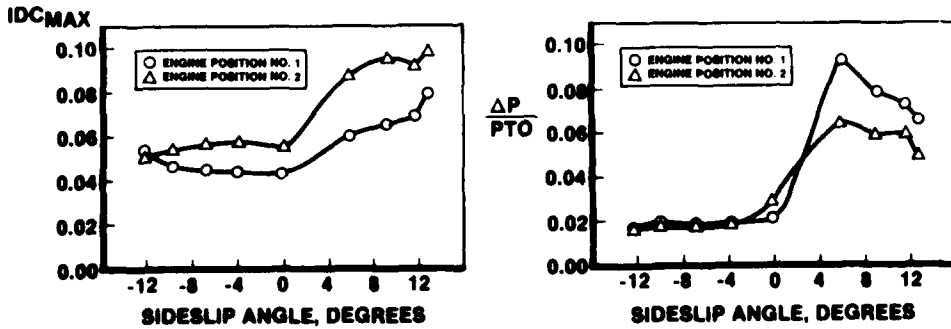
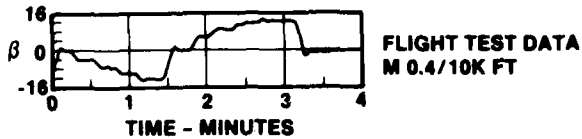


Figure 19. Nose Gear Wake Ingestion During Sideslip Operation

Wind tunnel and flight test distortion characteristics are compared in Figure 21. Test conditions were at mach 0.4, landing gear extended, with the aircraft (model) at 9 to 10 degrees sideslip and nominal angle of attack. Engine airflow was maximum at approximately 360 lb/sec. Differences in several distortion parameters are summarized in the table and are believed to be representative of the differences one should expect when comparing dynamic output of dynamic events.

| Source | IDC | IDR | ΔP/PTO | f |
|-------------|-------|-------|--------|-------------|
| Flight test | 0.095 | 0.031 | 0.068 | 18 |
| Wind tunnel | 0.086 | 0.047 | 0.060 | 20 (scaled) |

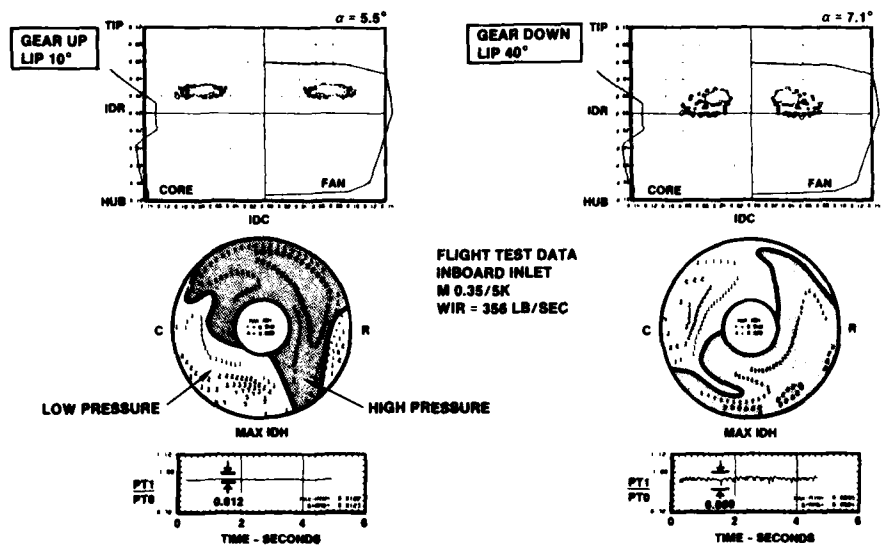


Figure 20. Effect of Gear Position on Inboard Inlet Distortion

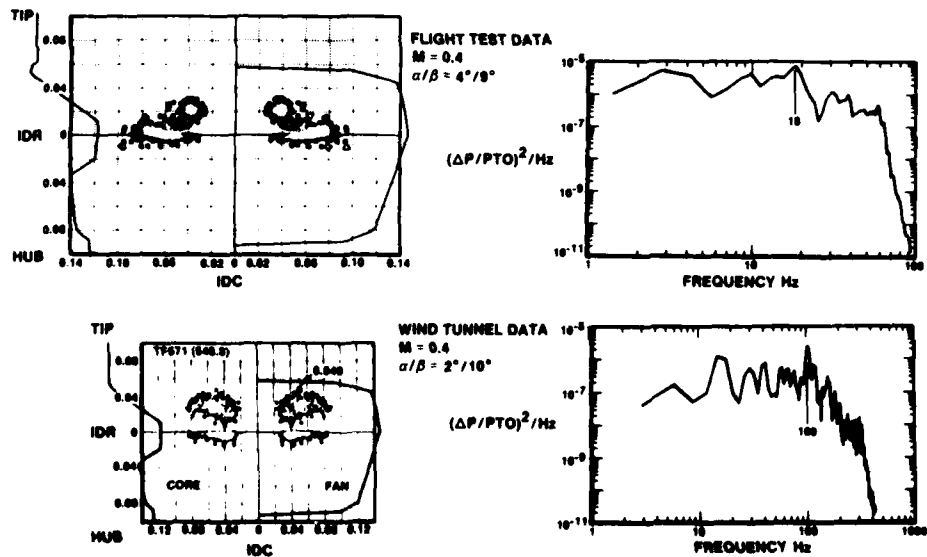


Figure 21. Wind Tunnel/Flight Test Comparison of Nose Gear Wake Effects

CONCLUDING REMARKS

Engine response to combinations of planar and spatial total-pressure distortion components is not well understood. Yet their consequences can be substantial, both in terms of engine stability and structural fatigue criteria. The most obvious solution is, of course, to eliminate the source of the disturbances. If this is not consistent with sound engineering practices, trades must be conducted to find cost-effective solutions.

Several sources of unsteady, one-dimensional pressure oscillations have been characterized with the B-18 program. Trends are summarized in Figure 22 and indicate that aircraft generated peak-to-peak amplitudes generally decrease as frequency increases. This is contrasted to estimated engine trends where one might expect more tolerance to amplitude at higher frequencies.

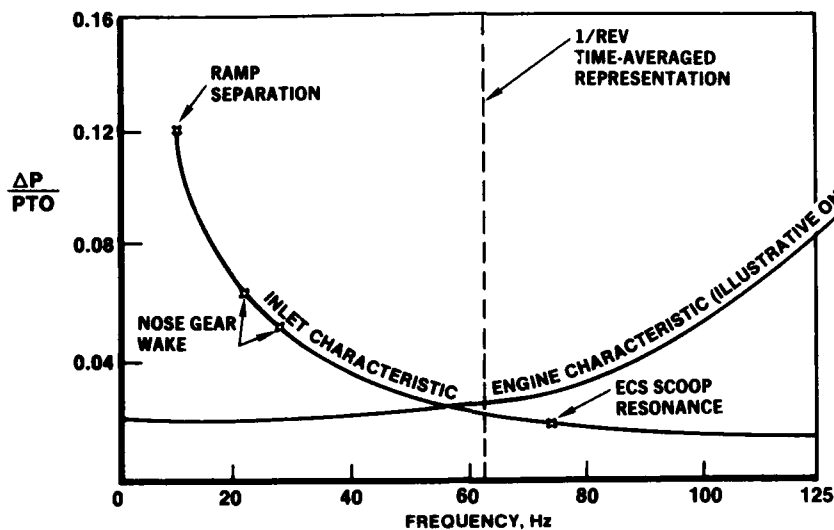


Figure 22. B-1B Planar Distortion Summary

Frequencies of planar components are generally configuration dependent. In cases where the source is duct resonance, good correlations exist between acoustic theory and test results. If wind tunnel models contain an acoustic reflection plane close to the simulated engine face, frequencies can be scaled accurately at constant Strouhal number, fL/\sqrt{T} . In the B-1B inlet development wind tunnel program, flow control vanes, located just aft of the aerodynamic interface plane, were operated choked over most conditions and provided this function.

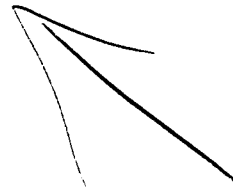
In cases where the source is attributed to the ingestion of wakes or vortices shed by forward protuberances, frequencies are difficult to predict. Accurate simulation of the protuberance in the wind tunnel model is necessary to obtain reasonable correlations with flight test results. Peak-to-peak amplitudes measured with the flight test aircraft were generally higher than magnitudes measured with the 0.2-scale model. Amplitudes can be strong functions of freestream mach number.

Several design features were incorporated in the B-1B propulsion system as a result of planar distortion considerations. The inlet ramp was cut back to reduce flow separation along the lower ramp surface and significantly reduced planar amplitudes. An idle speed lockup control was incorporated to limit flight idle operation to airflows corresponding to 90 percent corrected core speeds. This function is currently controlled with a cockpit switch and is implemented during operation at high speeds and freestream dynamic pressures. Planar distortion components contributed to the decision to incorporate a three-position cowl lip design. This control assures that the inlet lip is in the most open position when the landing gear is extended. The flapper door separating the ECS precooler scoop located in the inlet from the ground blower circuit was redesigned to reduce discrete frequency components and relax structural fatigue criteria.

Many of these features are being evaluated in the ongoing flight test program, and no compatibility problems have been encountered. But the fact remains that flight test programs do not provide much insight on losses in stall pressure ratio, and the real measure of success in a compatibility program occurs only after thousands of hours of operation have been accumulated by the fleet. To really understand engine response to these disturbances, a well-constructed program to explore sensitivities to planar components operating in conjunction with various combinations of radial and circumferential spatial distortion components is needed. Frequency content of most of these disturbances falls well within the range of computational fluid dynamics technology. Combining this analytical approach with a systematic test program to measure effects on current turbofan engines sounds like a logical next step. Benefits on future aircraft designs and operational procedures could be substantial.

REFERENCES

1. SAE ARP 1420, "Gas Turbine Engine Inlet Flow Distortion Guidelines", March 1978
2. SAE AIR 1419, "Inlet Total-Pressure-Distortion Considerations for Gas Turbine Engines", May 1983
3. R. H. Johnson, NASA-CR-144864, "Comparison of Inlet Distortion from Flight and Wind Tunnel Tests", April 1978
4. Reynolds, G. G. and Steenken, W. G., AFAPL-TR-76-76, "Dynamic Digital Blade Row Compression Component Stability Model - Model Validation and Analysis of Planar Pressure Pulse Generator and Two-Stage Fan Test Data", August 1976
5. J. H. Mykes, et al, NASA-CR-144887, "Analyses and Test of the B-1 Aircraft Structural Mode Control System", January 1980



DETERMINATION EXPERIMENTALE DES LOIS DE TRANSFERT DE PERTURBATIONS
A LA TRAVERSEE D'UN COMPRESSEUR AXIAL*

par Jacques HUARD

Office National d'Etudes et de Recherches Aérospatiales
BP 72 - 92322 Châtillon Cedex (France)

RESUME

L'alimentation des moteurs peut présenter des hétérogénéités très importantes dans certaines configurations de vol des avions de combat modernes ou lors de vent latéral. Un des problèmes posés au motoriste concerne donc l'étude de la sensibilité du compresseur à la distorsion de l'écoulement incident.

Néanmoins, la prise en compte de tous les aspects du problème théorique ne peut guère s'envisager qu'à très longue échéance. La solution classique retenue à l'ONERA pour traiter ce problème, consiste à modéliser les grilles par des disques où les caractéristiques de l'écoulement subissent des discontinuités ; les grandeurs situées de part et d'autre de ce disque sont alors reliées par des "lois de transfert". Ces lois non accessibles actuellement par le calcul ne peuvent être déterminées que par l'intermédiaire d'une analyse expérimentale détaillée. A cet effet un banc d'essai a été défini pour étudier la propagation de la distorsion de l'écoulement à la traversée d'un étage de compresseur axial. En amont de la roue mobile on génère une perturbation sinusoïdale de pression d'arrêt d'amplitude 50 % de la pression dynamique. On étudie la transmission de celle-ci dans l'étage, et l'on propose des formules de corrélation expérimentales.

EXPERIMENTAL DETERMINATION OF THE TRANSFER FUNCTION OF AN AXIAL COMPRESSOR
TO DISTORTED INLET FLOW

ABSTRACT

Many aircraft flight configurations can create difficult operating conditions for the engines ; these problems are related to air inlet disturbances which often result in a substantial decrease in the compressor surge margin. It is now known that the performance and operational stability of axial compressors are sensitive to nonuniformities in the inlet section.

In these conditions, it appeared necessary to develop a more complete numerical model. The classical solution retained at the Office, consists in representing the rotating or fixed blade rows by a model similar to a semi-actuator disk. The aerothermodynamic values of the flow located upstream and downstream of the disk, are linked by transfer functions. The numerical analysis being not able to determine these laws. A experimental detailed analysis has been used. At this effect, an experimental test facility designed for basic research on the transmission of an inlet distortion through a single stage axial flow compressor has been realized. Upstream of the rotor a distortion of total pressure is obtained by means of a variable permeability screen. This perturbation induces a quasi sinusoidal distribution of total pressure. The level of this amplitude is about 50 pour cent of dynamic pressure. The transmission of perturbation, is studied in the stage and experimental correlations are proposed.

* Travail effectué sous contrat DRET

1 - INTRODUCTION

La détermination expérimentale de la loi de transfert d'une distorsion stationnaire à travers la roue mobile d'un compresseur axial nécessite les conditions essentielles suivantes :

- l'écoulement dans le compresseur en l'absence de distorsion doit être aussi uniforme que possible afin que les effets de la distorsion puissent être clairement mis en évidence ;
- la perturbation imposée à l'entrée du compresseur doit être très simple afin que sa déformation à travers la roue puisse être analysée sans ambiguïté.

Mais même si ces deux conditions sont réalisées, et nous montrerons ci-dessous que c'est possible, il reste à s'assurer que les points homologues amont et aval que l'on utilise pour l'étude de la transmission d'une perturbation correspondent bien à la même ligne de courant en écoulement relatif.

C'est la technique expérimentale permettant de satisfaire ces trois conditions que nous allons décrire et nous allons montrer qu'il est alors possible de déterminer des lois empiriques de transfert s'appliquant aux deux grandeurs :

- angle de sortie de l'écoulement en axes relatifs,
- pertes à la traversée de la roue mobile,

pour lesquelles il n'existe pas actuellement de théorie permettant de les évaluer.

Ce n'est qu'après avoir établi un certain nombre de lois de transfert du type de celui que nous proposons ci-dessous qu'il sera possible de connaître les formules à introduire dans les calculs d'écoulements non uniformes dans les compresseurs.

2 - COMPRESSEUR A ECOULEMENT UNIFORME

L'étude aérodynamique de l'écoulement dans un compresseur axial montre que seuls les compresseurs dits à circulation constante induisent un écoulement à vitesse axiale uniforme en amont comme à l'aval de la roue.

En effet, à ce type de compresseur, au fonctionnement au débit de calcul, l'accroissement d'enthalpie est indépendant du rayon et, aux effets de la variation radiale du rendement près, la pression d'arrêt est également constante ou sensiblement constante le long du rayon (fig. 1 : schéma du montage).

Dans ces conditions les lignes de courant en écoulement relatif sont inscrites sur des cylindres coaxiaux à la veine et un point aval homologue d'un point amont se trouve au même rayon que celui-ci, avec simplement un léger déplacement azimutal.

Ceci reste vrai en fluide réel, du moins dans toute la partie saine de l'écoulement, c'est-à-dire située en dehors des zones d'écoulements secondaires limitées au voisinage des carter externe et interne.

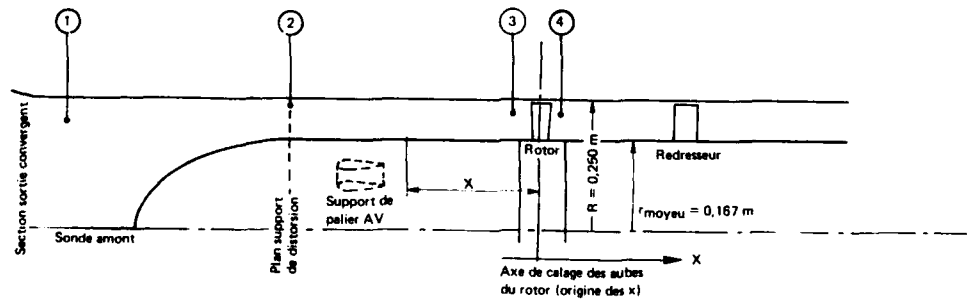


Fig. 1. IMPLANTATION DES PLANS DE SONDAGES

Afin de déterminer le point de mesure aval homologue d'un point amont on a utilisé un traceur chimique, mélange d'azote et de gaz carbonique injecté en amont de la roue mobile. Avec un analyseur de gaz classique il est possible de retrouver en aval de la roue mobile le point où la concentration en gaz carbonique est maximale : ce sera le point homologue du point d'injection.

La figure 2 représente le déplacement radial des lignes de courant : déplacées vers la périphérie aux grands débits ($\phi = 0,57$ et $\phi = 0,634$) ou vers le bas pour un débit proche du décrochage ($\phi = 0,40$) les lignes de courant restent sensiblement cylindriques dans un régime intermédiaire, ($\phi = 0,48$) sauf évidemment au voisinage des deux parois de la veine.

Evidemment en même temps que les lignes de courant se déplacent radialement, elles se déplacent aussi latéralement ce qui rend encore plus difficile de repérer les points homologues.

Ce déplacement latéral, nul en amont de la roue mobile en écoulement homogène se compose d'un déplacement $\Delta\theta_1$ correspondant à la traversée de la roue mobile pour lequel nous proposons la formule empirique :

$$\Delta\theta_1 = \frac{180}{\pi} \frac{C \cos \delta}{r} \left(\frac{1}{\varphi_1} - \operatorname{tg} \frac{\beta_1 + \varphi_1 \delta}{1 + \varphi_1} \right)$$

où C est la corde

r le rayon

δ l'angle moyen de calage

β_1 l'angle d'entrée de l'écoulement en axes relatifs

φ_1 le coefficient local de débit ($\varphi_1 = w_1/w_2 = \cotg \beta_1$)

et d'un déplacement aval $\Delta\theta_2$ directement proportionnel à la distance l du plan de mesure au plan de fuite de l'aube :

$$\Delta\theta_2 = \frac{180}{\pi} \frac{l}{r} \operatorname{tg} \alpha_2$$

La figure 3 montre que le déplacement global $\Delta\theta$ mesuré expérimentalement est bien représenté par la formule :

$$\Delta\theta = \Delta\theta_1 + \Delta\theta_2$$

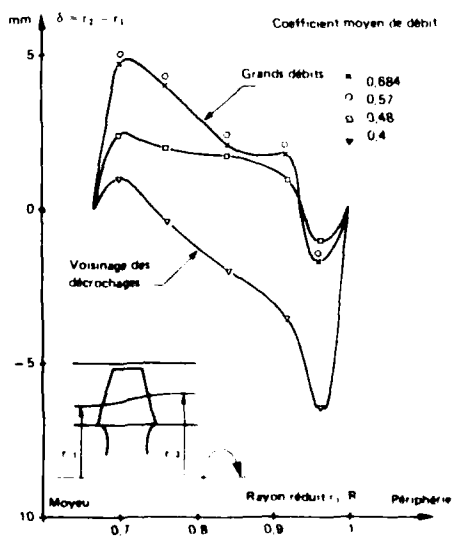


Fig. 2. DEPLACEMENT RADIAL DES LIGNES DE COURANT A LA TRAVERSE D'UNE ROUE MOBILE (Alimentation homogène)

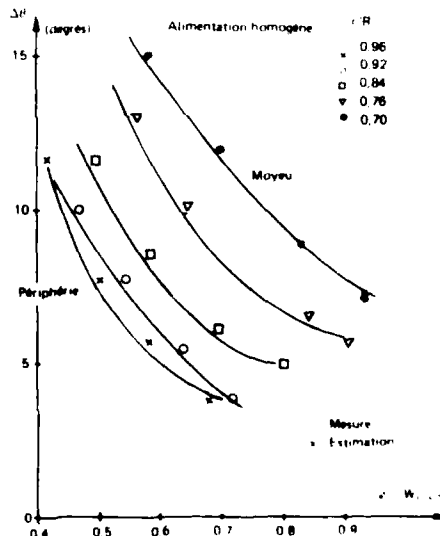


Fig. 1. DEPLACEMENT LATÉRAL DES LIGNES DE COURANT A LA TRAVERSE DE LA ROUE MOBILE (AXES RELATIFS)

1 - DISPOSITIF DE PERTURBATION DE L'ÉCOULEMENT AMONT

L'écoulement homogène non perturbé pouvant être considéré maintenant comme bien connu, nous pouvons étudier la perturbation qui donnera lieu à une distorsion de l'écoulement.

D'après les principes énoncés dans l'introduction cette perturbation doit être :

aussi simple que possible, c'est-à-dire proche d'une perturbation sinusoïdale à une période,

- telle que la perte de pression d'arrêt qu'elle induit soit indépendante du rayon,
- d'une intensité suffisante pour que la non-linéarité des phénomènes aérodynamiques puisse être mise en évidence (intensité choisie :

$$\Delta p = \frac{1}{4} \rho \bar{w}^2$$

où \bar{w} est la vitesse débitante moyenne).

Le perturbateur correspondant a été réalisé au moyen d'un grillage composé de barreaux et de fils circulaires dont l'écartement a été modifié jusqu'à ce qu'une perturbation quasi-sinusoidale soit obtenue (fig. 4). Cet écran a été placé dans le plan 2 (fig. 1).

Une analyse fine de l'écoulement à l'entrée de la roue mobile a montré que l'on peut écrire :

$$\frac{\Delta p}{\frac{1}{2} \rho \bar{w}^2} = \sum_{n=1}^5 (a_n \cos n\theta + b_n \sin n\theta)$$

où les coefficients a_n et b_n sont donnés sur le tableau I. Cette répartition azimutale a été représentée sur la figure 5. On y a également porté la fondamentale.

TABLEAU I

Décomposition de Fourier
de la perturbation limitée aux 5 premiers termes

| | |
|-----------------|-----------------|
| $a_1 = 0,3799$ | $b_1 = 0,0128$ |
| $a_2 = -0,0487$ | $b_2 = -0,0155$ |
| $a_3 = -0,0078$ | $b_3 = 0,0019$ |
| $a_4 = 0,0022$ | $b_4 = 0,0063$ |
| $a_5 = -0,0009$ | $b_5 = -0,0039$ |

L'origine des azimuts étant pur... Ces paramètres sont indépendants du débit du compresseur.

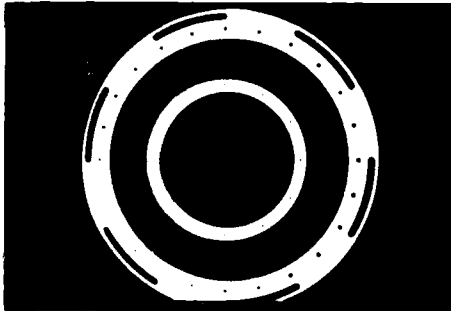


Fig. 4. ECRAN DE DISTORSION

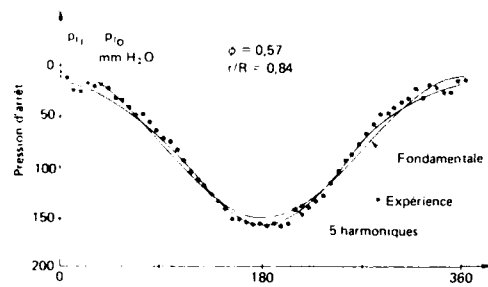


Fig. 5. REPARTITION AZIMUTALE DE LA PRESSION D'ARRÊT. MESURES EFFECTUEES ENTRE L'ECRAN DE DISTORSION ET LA ROUE MOBILE (plan 3)

4 - DESCRIPTION DE L'ÉCOULEMENT À L'ENTRÉE DE LA ROUE MOBILE

Du fait de la perturbation de l'écoulement amont il y a une réorganisation des vitesses et induction de gradients de pression statique.

La figure 6 représente les relevés effectués dans le plan 3 situé immédiatement en amont de la roue mobile ($X/R = -0,14$) (pression d'arrêt P_a , pression statique, angle absolu de la vitesse α) ainsi que l'angle β de la vitesse relative avec la direction axiale.

On remarque que l'angle de la vitesse relative avec la direction axiale, ou si on veut l'incidence de l'écoulement sur les profils, varie de 7 à 8° pendant un cycle (fig. 7).

Nous avons pu également représenter la variation de l'angle β , en fonction de θ par une série de Fourier tronquée :

$$\beta_1 = \bar{\beta}_1 + \sum_{n=1}^5 (a'_n \cos n\theta + b'_n \sin n\theta)$$

limitée à ses cinq premiers termes, et le tableau II donne la valeur des paramètres a'_n et b'_n .

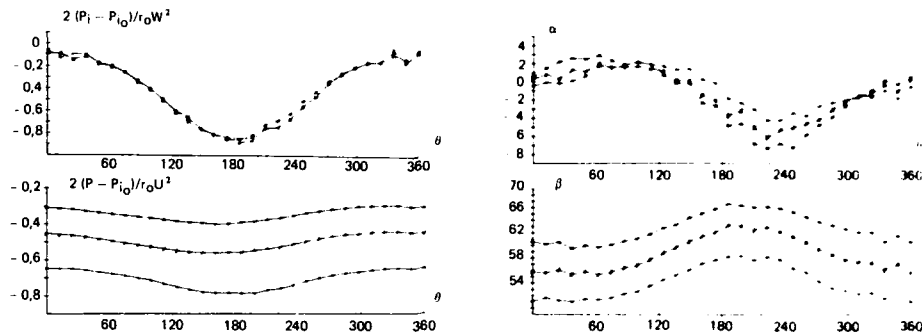


Fig. 6. REPARTITION AZIMUTALE DES CARACTERISTIQUES AERODYNAMIQUES DE L'ECOULEMENT EN AMONT DE LA ROUE MOBILE (plan 3)

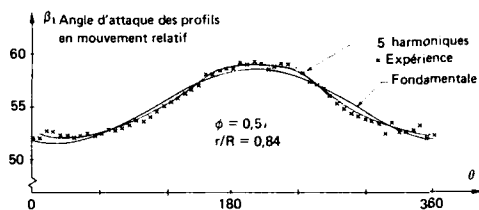


Fig. 7. ANALYSE HARMONIQUE DE L'EVOLUTION AZIMUTALE DE L'ANGLE D'ATTAQUE DES PROFILS EN MOUVEMENT RELATIF A MI-HAUTEUR DE VEINE

TABLEAU II

Décomposition de Fourier de l'angle d'attaque en axes relatifs

| | |
|------------------|-------------------|
| $a'_1 = -3,365$ | $b'_1 = -1,189$ |
| $a'_2 = 0,556$ | $b'_2 = 0,4858$ |
| $a'_3 = 0,1459$ | $b'_3 = 0,0030$ |
| $a'_4 = -0,0339$ | $b'_4 = -0,12135$ |
| $a'_5 = -0,0656$ | $b'_5 = 0,100$ |

On remarquera qu'ici encore la fondamentale l'emporte largement sur les harmoniques et on peut dire que même pour une perturbation de forte amplitude à l'amont de la roue les phénomènes restent linéaires.

5 - DESCRIPTION DE L'ECOULEMENT A LA SORTIE DE LA ROUE MOBILE

Il n'en est plus de même à la sortie de la roue mobile qui apparemment induit des non-linéarités. Comme nous l'avons vu ci-dessus il est possible de faire l'hypothèse que les lignes de courant sont concentrées sur un cylindre.

On voit cependant sur la figure 8 qu'aucun des paramètres de l'écoulement aval pression d'arrêt, pression statique, angle absolu ou angle relatif n'a une évolution sinusoidale à une période dans le plan aval.

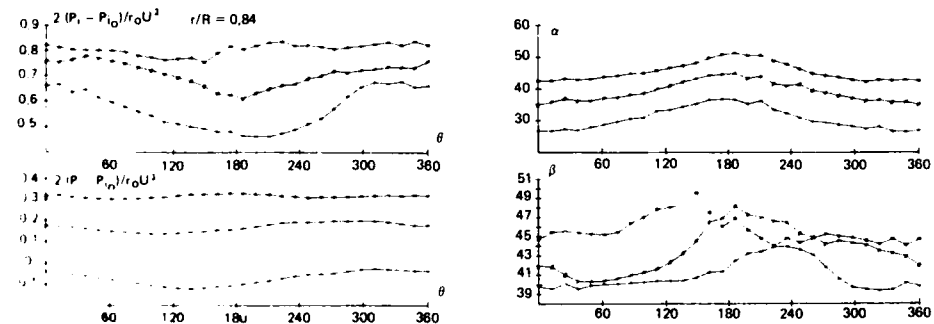


Fig. 8. REPARTITION AZIMUTALE DES CARACTERISTIQUES DE L'ECOULEMENT EN AVAL DE LA ROUE MOBILE (plan 4)

On voit sur la figure 9 que l'on peut encore représenter l'évolution azimutale de la pression au moyen d'un développement de Fourier à 5 harmoniques mais comme le montre le tableau III la fondamentale et la première harmonique sont prépondérantes. (La pression d'arrêt aval est adimensionnée par $\rho_0 U^2$)

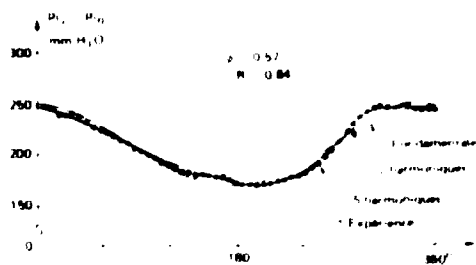


Fig. 9. ANALYSE HARMONIQUE DE L'EVOLUTION AZIMUTALE DE LA PRESSION D'ARRRET EN AVAL DU BROYEUR A MI HAUTEUR DE VEINE

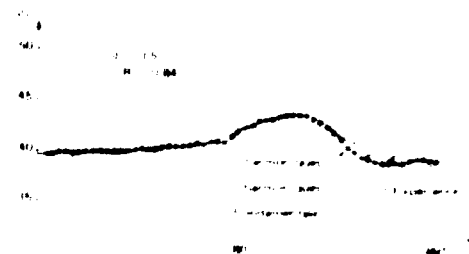


Fig. 10. ANALYSE HARMONIQUE DE L'EVOLUTION AZIMUTALE DE LA PRESSION D'ARRRET EN AVAL DU BROYEUR A MI HAUTEUR DE VEINE

TAB. 10

Tableau des coefficients de Fourier

| n | a_n | b_n |
|-----|--------|--------|
| 1 | 0.0000 | 0.0000 |
| 2 | 0.0000 | 0.0000 |
| 3 | 0.0000 | 0.0000 |
| 4 | 0.0000 | 0.0000 |
| 5 | 0.0000 | 0.0000 |

Il en est exactement de même pour les autres séries.

TAB. 11

| n | a_n | b_n |
|-----|--------|--------|
| 1 | 0.0000 | 0.0000 |
| 2 | 0.0000 | 0.0000 |
| 3 | 0.0000 | 0.0000 |
| 4 | 0.0000 | 0.0000 |
| 5 | 0.0000 | 0.0000 |

Les formules de Fourier sont les mêmes que dans le cas précédent.

6. RECHERCHE DES POINTS HOMOLOGUES AMONT ET AVAL EN PRESENCE D'UN BROYEUR

La détermination du déplacement relatif des lignes de courant est effectuée par le moyen du tracé d'isobares à partir de points homologues en amont et en aval du broyeur.

En ce qui concerne le déplacement de la ligne de courant, on a vu que les valeurs inévitables de dispersion près des broyeurs sont dues à la turbulence perturbée restant valables en présence d'un broyeur.

Sous ces conditions, les points homologues en amont et en aval du broyeur sont les points homologues correspondant



Fig. 11. DEPHASAGE ESTIME ET MESURE EN REMPLISSANT HETEROGENE A MI HAUTEUR DE VEINE

Il est possible de déduire les valeurs mesurées en aval de la roue mobile plan à $X/R = +0,19$ telles que l'on aurait eu dans le plan de fuite des aubes en déplaçant simplement les axes au moyen de la relation

$$\Delta\theta_2 = \frac{x}{R} \tan \alpha_2$$

MODELISATION DU FONCTIONNEMENT INSTATIONNAIRE DU ROTOR

En appliquant la méthode présentée dans les chapitres précédents il est possible d'obtenir, en reliant entre eux les points homologues amont et aval, les cycles représentatifs du fonctionnement instationnaire de la roue mobile.

1. Déflexion

Nous présentons pour le débit le plus dévancé de la caractéristique ($\theta = 0,57$) les cycles obtenus pour les cinq coupes analysées sur les figures 12 à 16.

Nous avons également porté sur chaque figure la réponse de la coupe considérée en écoulement homogène. Les cycles ont été tracés en n'appliquant aucun retard $\Delta\theta$ à l'établissement du phénomène. On peut remarquer, en étant vérifié lorsque les effets dynamiques sont importants (fig. 14 et 15), que les différentes branches du cycle sont décalées mais parallèles à la réponse stationnaire de la roue mobile.

Le point moyen de fonctionnement en écoulement hétérogène, représenté par une croix sur les figures, n'est pas situé sur la courbe correspondant à la réponse stationnaire du rotor. On observe d'un degré et demi environ d'après pour l'ensemble les coupes (sauf au moyen figure 16 où les écoulements se caractérisent indifféremment par une surdéflexion).

Nous nous tenté de modéliser la réponse de la roue mobile en tenant compte des enseignements tirés des chapitres précédents. En première approximation nous avons pu que l'on pouvait écrire

$$P_1 - \bar{P}_1 = a_1 \cos \theta + b_1 \sin \theta$$

$$P_2 - \bar{P}_2 = a_2 \cos 2\theta + b_2 \sin 2\theta + a_1 \cos \theta + b_1 \sin \theta$$

\bar{P} étant la réponse stationnaire de la roue mobile en écoulement homogène.

$$P_1 - \bar{P}_1 = g_1 (\beta_1 - \bar{\beta}_1)$$

$$P_2 - \bar{P}_2 = g_2 (\beta_2 - \bar{\beta}_2)$$

Les coefficients g_1 et g_2 sont des fonctions des coefficients a_i et b_i et de la fréquence ω . On peut les déterminer en comparant les cycles théoriques obtenus à partir de ces relations avec les cycles expérimentaux.

$$P_2 - \bar{P}_2 = g_1 (\beta_1 - \bar{\beta}_1) + g_2 \frac{d(\beta_1 - \bar{\beta}_1)}{dt} + g_3 (\beta_1 - \bar{\beta}_1)^2 + g_4 (\beta_1 - \bar{\beta}_1) \frac{d(\beta_1 - \bar{\beta}_1)}{dt} + g_5 \left[\frac{d(\beta_1 - \bar{\beta}_1)}{dt} \right]^2$$

$$g_1 = \frac{a_1 a_2 + b_1 b_2}{a_1^2 + b_1^2} \quad g_2 = \frac{a_1 b_2 - a_2 b_1}{a_1^2 + b_1^2} \quad g_3 = \frac{a_2^2 (a_1^2 - b_1^2) + 2b_1 a_1 b_2}{(a_1^2 + b_1^2)^2}$$

$$g_4 = \frac{4a_1 b_1 a_2 + 2b_1^2 (b_2^2 - a_2^2)}{(a_1^2 + b_1^2)^2} \quad g_5 = -g_2$$

Sur la figure 17 sont représentés sur les figures 12 à 16 les cycles ainsi modélisés. On peut constater que les courbes théoriques obtenues en effectuant une comparaison avec les cycles bruts expérimentaux ne s'accroît pas tant que les effets dynamiques sont modérés (fig. 12, 13 et 14) lorsque les effets deviennent grands pour les coupes centrales (figures 15 et 16) l'approximation employée n'est plus satisfaisante. Les écarts observés s'accroissent globalement.

Remarque : on aurait pu également essayer de généraliser les relations de type "relaxation" où intervient la dérivée de $\beta_2 - \bar{\beta}_2$

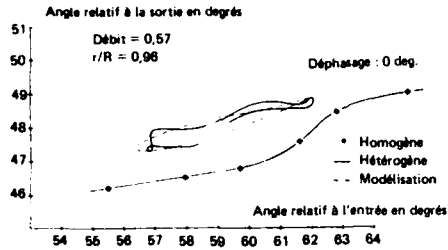


Fig. 12. CYCLE DES DEVIATIONS EN ECOULEMENT HETEROGENE

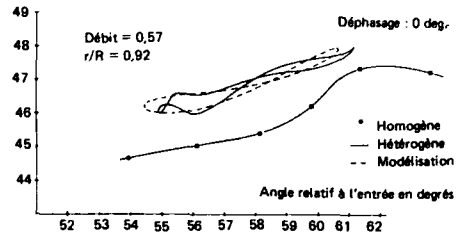


Fig. 13. CYCLE DES DEVIATIONS EN ECOULEMENT HETEROGENE

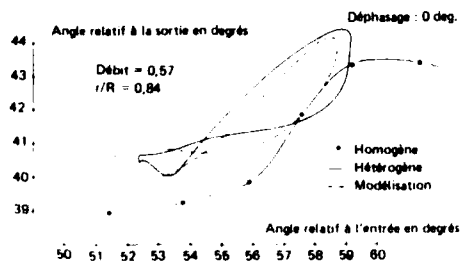


Fig. 14. CYCLE DES DEVIATIONS EN ECOULEMENT HETEROGENE

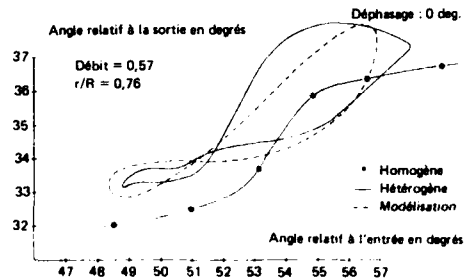


Fig. 15. CYCLE DES DEVIATIONS EN ECOULEMENT HETEROGENE

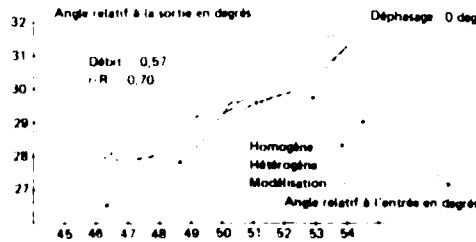


Fig. 16. CYCLE DES DEVIATIONS EN ECOULEMENT HETEROGENE

$$g_1' \frac{d(\beta_2 - \bar{\beta}_2)}{dt} + (\beta_2 - \bar{\beta}_2) = g_2' (\beta_1 - \bar{\beta}_1) + g_3' \frac{d(\beta_1 - \bar{\beta}_1)}{dt} + g_4' (\beta_1 - \bar{\beta}_1)^2 + g_5'$$

mais cette formulation nécessite l'introduction d'une constante qui ne permet plus de représenter correctement l'état stationnaire ($d/dt = 0$).

2.2 Pertes

L'équation de Bernoulli généralisée s'écrit en mouvement relatif si l'on considère le fluide parfait et incompressible, instationnaire dans un canal intersube V' :

$$\iiint_V \frac{\partial}{\partial t} \left(\frac{1}{2} \rho \vec{c}^2 \right) dV + \iint_S \left(p + \rho \frac{\vec{c}^2}{2} \right) \vec{c} \cdot \vec{n} dS = 0$$

Cette relation peut se mettre sous la forme suivante en explicitant les termes de flux :

$$\left(p_2 + \frac{1}{2} \rho C_2^2\right) W_2 A - \left(p_1 + \frac{1}{2} \rho C_1^2\right) W_1 A = - \iint_{\Omega} \frac{\partial}{\partial t} \left(\frac{1}{2} \rho C^2\right) dv$$

Les triangles de vitesse amont et aval fournissent l'expression des vitesses relatives :

$$C_1^2 = W_1^2 + (u_1 - v_1)^2$$

$$C_2^2 = (u_2 - v_2)^2 + W_2^2$$

on peut faire apparaître l'accroissement théorique de pression d'arrêt absolu :

$$(p_{i2} - p_{i1})_{th} = \rho (u_2 v_2 - u_1 v_1) - \frac{1}{AW} \iint_{\Omega} \frac{\partial}{\partial t} \left(\frac{1}{2} \rho C^2\right) dv$$

Les pertes étant obtenues par différence avec l'accroissement de pression expérimental.

Le bilan d'énergie exprimé par la relation ci-dessus montre qu'au terme "d'Euler" vient s'ajouter un terme dû à la contribution "instationnaire" de l'écoulement. Pour estimer cette contribution dans chaque canal interaube, la connaissance du champ de vitesse tridimensionnel est indispensable. En écoulement hétérogène un sondage stationnaire de part et d'autre de la roue mobile ne permet pas d'avoir accès aux pertes. Seule une instrumentation de type sonde à court temps de réponse (capteur Kulite) donne accès à la mesure de la perte de pression d'arrêt dans les sillages ou encore, la vélocimétrie laser qui donne le profil des vitesses dans les sillages permet de déterminer l'épaisseur de perte de quantité de mouvement qui est directement proportionnelle aux pertes. Toutefois, plus facile de mise en œuvre, les mesures stationnaires effectuées à l'aide d'une instrumentation classique peuvent donner déjà des indications intéressantes.

Nous avons tenté de modéliser cette contribution instationnaire due à la variation d'énergie cinétique relative dans le canal interaube de plusieurs façons :

- 1) en se donnant comme vitesse relative, celle d'entrée moyennée sur un pas de canal ;
- 2) en prenant en amont et en aval la vitesse relative moyennée comme précédemment, celle-ci variant linéairement le long d'un canal ;
- 3) en se donnant une répartition de vitesse relative qui évolue de la même manière que la géométrie des profils (modélisation type Adamczyk) ;
- 4) enfin un modèle où la vitesse relative varie d'une manière bilinéaire dans le canal interaube.

Les modèles 1, 2 et 4 donnent sensiblement la même importance aux effets instationnaires. Nous ne présenterons pas de résultats obtenus à l'aide du modèle 3 celui-ci exagérant les effets dus à l'hétérogénéité de l'écoulement.

Les effets instationnaires décrits par les différents modèles sont présentés pour la coupe centrale ($b/R = 0,84$) du débit maximum ($\beta = 0,57$) (fig. 17). L'évolution azimutale des pertes est présentée de quatre manières. Les pertes calculées par différence entre l'accroissement théorique de pression donné par le terme d'Euler et l'accroissement expérimental mesuré ; le terme instationnaire étant négligé. Ensuite on présente une estimation globale des pertes en modélisant le terme dû à l'hétérogénéité de trois façons différentes, on remarque que les trois modèles employés donnent sensiblement la même allure et le même niveau de pertes. Pour ce point de fonctionnement du compresseur le rotor est attaqué de part et d'autre de l'optimum avec une incidence variant de $-4,4$ à $+2,6$ degrés, les effets dynamiques sont importants et la contribution instationnaire peut représenter jusqu'à 100% des pertes évaluées par le théorème d'Euler.

L'évolution azimutale des pertes estimés à l'aide du modèle 1 tracée avec l'évolution azimutale de l'angle d'attaque des profils en mouvement relatif montre (fig. 18) qu'il faut appliquer un déphasage d'environ 60 degrés sur les pertes. Le cycle obtenu en traçant l'angle d'attaque en fonction des pertes en appliquant ce déphasage constant semble cohérent avec l'évolution des pertes stationnaires (fig. 19). Les pertes semblent plus importantes pour les incidences négatives (attaque des profils sur l'extrados $0 < \theta < 120^\circ$) tout ce passe comme si, en plus du décollement d'intrados, l'écoulement n'avait pas encore recollé l'extrados. Le cycle commence au point le plus haut, l'attaque sur l'extrados est maximale, les pertes sont maximales, l'angle d'attaque va augmenter jusqu'à atteindre sa valeur optimale environ 55 degrés, les pertes diminuent, elles sont minimales, le profil est alors recollé jusqu'à un angle d'entrée de 58 degrés où l'extrados commence à décoller. Dans la zone de $59 < \theta < 14^\circ$ les pertes restent sensiblement constantes, l'extrados ne recolle pas, les pertes vont même augmenter quand l'intrados va à son tour décoller. Les divers modèles employés pour quantifier les effets instationnaires montrent l'importance de ceux-ci. Toutefois les résultats présentés demandent confirmation. C'est pour cette raison que l'étape suivante de cette étude consiste en la mise en œuvre d'une instrumentation permettant l'accès aux écoulements interaube.

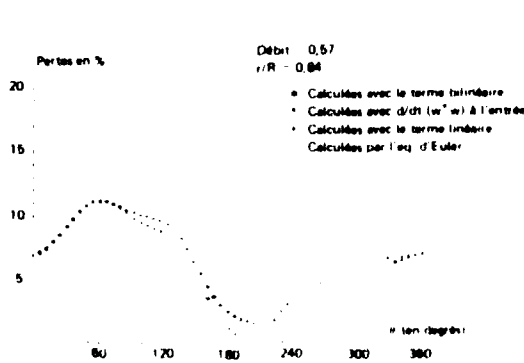


Fig. 17. EVALUATION DES EFFETS NON STATIONNAIRES

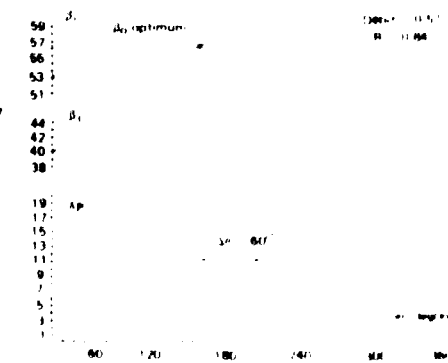


Fig. 18. EVOLUTION AZIMUTALE DE AP1A, AP1A, AP1B

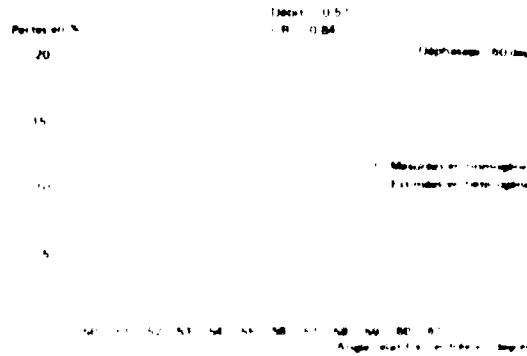


Fig. 19. ESTIMATION DES PERTES EN COURANT RETOURNANT

4. DESCRIPTION DE L'ÉCOULEMENT A LA SORTIE DE REDRESSEUR

La caractérisation de l'écoulement en aval du redresseur a été effectuée par sondage. Il a été constaté que pour chaque canal intercalaire le débit mesuré est équivalent à 1/3 du débit nominal par intégration de la quantité de mouvement et du débit massique pour chaque canal. On peut donc conclure que les pertes linéaires de chaque canal intercalaire sont faibles. Nous avons reporté ces pertes linéaires sur la figure 20 à une position azimutale correspondant au milieu de chaque canal intercalaire. Nous avons également reporté sur cette figure l'évolution azimutale correspondante de la pression d'arrêt obtenue en aval du rotor. Cette courbe montre que le redresseur ne fait que transmettre le signal d'entrée sans l'altérer. Les pertes linéaires sont relativement faibles. Quant à la déviation angulaire relative, elle est comprise entre 5 et 10 degrés d'incidence sur le rotor, qu'il doit aborder (tangente à la ligne moyenne au bord d'attaque). L'écoulement est ainsi caractérisé par un angle azimutal (Fig. 21). Il ne subsiste plus d'écoulement différentiel de pression statique, qui est donc constante azimutalement.

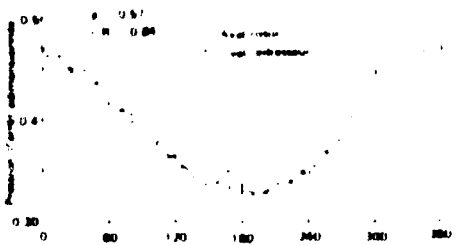


Fig. 20. EVOLUTION AZIMUTALE DE LA PRESSION D'ARRÊT

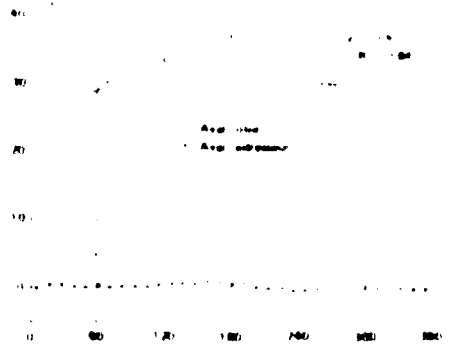


Fig. 21. EVOLUTION AZIMUTALE DE LA DIRECTION DE LA VITESSE ABSOLUE

9. CONCLUSION

L'analyse stationnaire à l'aide d'une instrumentation de type classique de la transmission d'une distorsion à la traversée d'un compresseur axial a été réalisée. Grâce à la technique du traceur chimique qui permet de relier sans ambiguïté un point amont du compresseur à son homologue aval, connaissant les grandeurs aérodynamiques pour chacun de ces points nous avons pu représenter sur des graphiques les cycles correspondant aux deux grandeurs essentielles pour lesquelles nous ne possédons pas de modèle théorique: l'angle de sortie en azimut relatif et la perte de pression d'arrêt.

Ayant pris soin d'utiliser pour ces essais une distorsion aussi proche que possible d'une sinusoïde à une période, nous avons pu mettre en évidence la non linéarité du processus de transfert et proposer, pour le compresseur étudié, des lois de transfert pour les deux paramètres à modéliser.

Il reste maintenant à vérifier que des relations de même type peuvent être obtenues sur d'autres compresseurs.

DISCUSSION

1. Waterford Co.

Is the response of the stator shown in your test data influenced by the large distance between the rotor and the stator which you showed in view of the test data?

Authors Reply:

Non. C'est un système de principe très simple, sans aucune rétroaction, qui permet de représenter l'un compresseur.



DEVELOPMENT OF INTAKE SWIRL GENERATORS FOR TURBOJET ENGINE TESTING

by

H. P. Genseler*, W. Meyer**, and F. Pottner***

- * Dipl.-Ing., RDA Helicopter and Military Aircraft Division, P.O. Box 501160, D-6000 München 60, Germany.
- ** Dipl.-Ing., Universität der Bundeswehr München, Werner Heisenberg Weg 19, D-8034 Neubiberg, Germany.
- *** Prof. Dr.-Ing., Universität der Bundeswehr München, Werner Heisenberg Weg 19, D-8034 Neubiberg, Germany.

ABSTRACT

The main objective of this investigation is to assess the influence of different types and magnitudes of swirl on the performance and combustibility of turbojet engines. The generation of intake swirl is typical for many types of combat aircraft engines. It is essentially of two basic types: the air swirl and bulk swirl. For swirl generators of the rotational type, the flow is selected in order to generate a desired swirl pattern in the intake swirl generator. In the case of air swirl, the swirl pattern is determined by these generators with good agreement with the desired pattern. In the case of bulk swirl, the desired swirl generator is not used. Instead, the flow is selected in order to generate a desired swirl pattern in the intake swirl generator. The results of the investigation are presented in the form of a series of graphs and tables.

| Symbol | Meaning | Units |
|------------|---------------|-------|
| α | Swirl angle | deg |
| β | Swirl angle | deg |
| γ | Swirl angle | deg |
| δ | Swirl angle | deg |
| ϵ | Swirl angle | deg |
| ζ | Swirl angle | deg |
| η | Swirl angle | deg |
| θ | Swirl angle | deg |
| ϕ | Swirl angle | deg |
| ψ | Swirl angle | deg |
| ω | Swirl angle | deg |
| ν | Swirl angle | deg |
| ξ | Swirl angle | deg |
| λ | Swirl angle | deg |
| μ | Swirl angle | deg |
| ρ | Swirl angle | deg |
| σ | Swirl angle | deg |
| τ | Swirl angle | deg |
| υ | Swirl angle | deg |
| ϕ | Swirl angle | deg |
| χ | Swirl angle | deg |
| ψ | Swirl angle | deg |
| ω | Swirl angle | deg |
| ν | Swirl angle | deg |
| ξ | Swirl angle | deg |
| λ | Swirl angle | deg |
| μ | Swirl angle | deg |
| ρ | Swirl angle | deg |
| σ | Swirl angle | deg |
| τ | Swirl angle | deg |
| υ | Swirl angle | deg |
| ϕ | Swirl angle | deg |
| χ | Swirl angle | deg |
| ψ | Swirl angle | deg |
| ω | Swirl angle | deg |
| ν | Swirl angle | deg |
| ξ | Swirl angle | deg |
| λ | Swirl angle | deg |
| μ | Swirl angle | deg |
| ρ | Swirl angle | deg |
| σ | Swirl angle | deg |
| τ | Swirl angle | deg |
| υ | Swirl angle | deg |
| ϕ | Swirl angle | deg |
| χ | Swirl angle | deg |
| ψ | Swirl angle | deg |
| ω | Swirl angle | deg |
| ν | Swirl angle | deg |
| ξ | Swirl angle | deg |
| λ | Swirl angle | deg |
| μ | Swirl angle | deg |
| ρ | Swirl angle | deg |
| σ | Swirl angle | deg |
| τ | Swirl angle | deg |
| υ | Swirl angle | deg |
| ϕ | Swirl angle | deg |
| χ | Swirl angle | deg |
| ψ | Swirl angle | deg |
| ω | Swirl angle | deg |
| ν | Swirl angle | deg |
| ξ | Swirl angle | deg |
| λ | Swirl angle | deg |
| μ | Swirl angle | deg |
| ρ | Swirl angle | deg |
| σ | Swirl angle | deg |
| τ | Swirl angle | deg |
| υ | Swirl angle | deg |
| ϕ | Swirl angle | deg |
| χ | Swirl angle | deg |
| ψ | Swirl angle | deg |
| ω | Swirl angle | deg |
| ν | Swirl angle | deg |
| ξ | Swirl angle | deg |
| λ | Swirl angle | deg |
| μ | Swirl angle | deg |
| ρ | Swirl angle | deg |
| σ | Swirl angle | deg |
| τ | Swirl angle | deg |
| υ | Swirl angle | deg |
| ϕ | Swirl angle | deg |
| χ | Swirl angle | deg |
| ψ | Swirl angle | deg |
| ω | Swirl angle | deg |
| ν | Swirl angle | deg |
| ξ | Swirl angle | deg |
| λ | Swirl angle | deg |
| μ | Swirl angle | deg |
| ρ | Swirl angle | deg |
| σ | Swirl angle | deg |
| τ | Swirl angle | deg |
| υ | Swirl angle | deg |
| ϕ | Swirl angle | deg |
| χ | Swirl angle | deg |
| ψ | Swirl angle | deg |
| ω | Swirl angle | deg |
| ν | Swirl angle | deg |
| ξ | Swirl angle | deg |
| λ | Swirl angle | deg |
| μ | Swirl angle | deg |
| ρ | Swirl angle | deg |
| σ | Swirl angle | deg |
| τ | Swirl angle | deg |
| υ | Swirl angle | deg |
| ϕ | Swirl angle | deg |
| χ | Swirl angle | deg |
| ψ | Swirl angle | deg |
| ω | Swirl angle | deg |
| ν | Swirl angle | deg |
| ξ | Swirl angle | deg |
| λ | Swirl angle | deg |
| μ | Swirl angle | deg |
| ρ | Swirl angle | deg |
| σ | Swirl angle | deg |
| τ | Swirl angle | deg |
| υ | Swirl angle | deg |
| ϕ | Swirl angle | deg |
| χ | Swirl angle | deg |
| ψ | Swirl angle | deg |
| ω | Swirl angle | deg |
| ν | Swirl angle | deg |
| ξ | Swirl angle | deg |
| λ | Swirl angle | deg |
| μ | Swirl angle | deg |
| ρ | Swirl angle | deg |
| σ | Swirl angle | deg |
| τ | Swirl angle | deg |
| υ | Swirl angle | deg |
| ϕ | Swirl angle | deg |
| χ | Swirl angle | deg |
| ψ | Swirl angle | deg |
| ω | Swirl angle | deg |
| ν | Swirl angle | deg |
| ξ | Swirl angle | deg |
| λ | Swirl angle | deg |
| μ | Swirl angle | deg |
| ρ | Swirl angle | deg |
| σ | Swirl angle | deg |
| τ | Swirl angle | deg |
| υ | Swirl angle | deg |
| ϕ | Swirl angle | deg |
| χ | Swirl angle | deg |
| ψ | Swirl angle | deg |
| ω | Swirl angle | deg |
| ν | Swirl angle | deg |
| ξ | Swirl angle | deg |
| λ | Swirl angle | deg |
| μ | Swirl angle | deg |
| ρ | Swirl angle | deg |
| σ | Swirl angle | deg |
| τ | Swirl angle | deg |
| υ | Swirl angle | deg |
| ϕ | Swirl angle | deg |
| χ | Swirl angle | deg |
| ψ | Swirl angle | deg |
| ω | Swirl angle | deg |
| ν | Swirl angle | deg |
| ξ | Swirl angle | deg |
| λ | Swirl angle | deg |
| μ | Swirl angle | deg |
| ρ | Swirl angle | deg |
| σ | Swirl angle | deg |
| τ | Swirl angle | deg |
| υ | Swirl angle | deg |
| ϕ | Swirl angle | deg |
| χ | Swirl angle | deg |
| ψ | Swirl angle | deg |
| ω | Swirl angle | deg |
| ν | Swirl angle | deg |
| ξ | Swirl angle | deg |
| λ | Swirl angle | deg |
| μ | Swirl angle | deg |
| ρ | Swirl angle | deg |
| σ | Swirl angle | deg |
| τ | Swirl angle | deg |
| υ | Swirl angle | deg |
| ϕ | Swirl angle | deg |
| χ | Swirl angle | deg |
| ψ | Swirl angle | deg |
| ω | Swirl angle | deg |
| ν | Swirl angle | deg |
| ξ | Swirl angle | deg |
| λ | Swirl angle | deg |
| μ | Swirl angle | deg |
| ρ | Swirl angle | deg |
| σ | Swirl angle | deg |
| τ | Swirl angle | deg |
| υ | Swirl angle | deg |
| ϕ | Swirl angle | deg |
| χ | Swirl angle | deg |
| ψ | Swirl angle | deg |
| ω | Swirl angle | deg |
| ν | Swirl angle | deg |
| ξ | Swirl angle | deg |
| λ | Swirl angle | deg |
| μ | Swirl angle | deg |
| ρ | Swirl angle | deg |
| σ | Swirl angle | deg |
| τ | Swirl angle | deg |
| υ | Swirl angle | deg |
| ϕ | Swirl angle | deg |
| χ | Swirl angle | deg |
| ψ | Swirl angle | deg |
| ω | Swirl angle | deg |
| ν | Swirl angle | deg |
| ξ | Swirl angle | deg |
| λ | Swirl angle | deg |
| μ | Swirl angle | deg |
| ρ | Swirl angle | deg |
| σ | Swirl angle | deg |
| τ | Swirl angle | deg |
| υ | Swirl angle | deg |
| ϕ | Swirl angle | deg |
| χ | Swirl angle | deg |
| ψ | Swirl angle | deg |
| ω | Swirl angle | deg |
| ν | Swirl angle | deg |
| ξ | Swirl angle | deg |
| λ | Swirl angle | deg |
| μ | Swirl angle | deg |
| ρ | Swirl angle | deg |
| σ | Swirl angle | deg |
| τ | Swirl angle | deg |
| υ | Swirl angle | deg |
| ϕ | Swirl angle | deg |
| χ | Swirl angle | deg |
| ψ | Swirl angle | deg |
| ω | Swirl angle | deg |
| ν | Swirl angle | deg |
| ξ | Swirl angle | deg |
| λ | Swirl angle | deg |
| μ | Swirl angle | deg |
| ρ | Swirl angle | deg |
| σ | Swirl angle | deg |
| τ | Swirl angle | deg |
| υ | Swirl angle | deg |
| ϕ | Swirl angle | deg |
| χ | Swirl angle | deg |
| ψ | Swirl angle | deg |
| ω | Swirl angle | deg |
| ν | Swirl angle | deg |
| ξ | Swirl angle | deg |
| λ | Swirl angle | deg |
| μ | Swirl angle | deg |
| ρ | Swirl angle | deg |
| σ | Swirl angle | deg |
| τ | Swirl angle | deg |
| υ | Swirl angle | deg |
| ϕ | Swirl angle | deg |
| χ | Swirl angle | deg |
| ψ | Swirl angle | deg |
| ω | Swirl angle | deg |
| ν | Swirl angle | deg |
| ξ | Swirl angle | deg |
| λ | Swirl angle | deg |
| μ | Swirl angle | deg |
| ρ | Swirl angle | deg |
| σ | Swirl angle | deg |
| τ | Swirl angle | deg |
| υ | Swirl angle | deg |
| ϕ | Swirl angle | deg |
| χ | Swirl angle | deg |
| ψ | Swirl angle | deg |
| ω | Swirl angle | deg |
| ν | Swirl angle | deg |
| ξ | Swirl angle | deg |
| λ | Swirl angle | deg |
| μ | Swirl angle | deg |
| ρ | Swirl angle | deg |
| σ | Swirl angle | deg |
| τ | Swirl angle | deg |
| υ | Swirl angle | deg |
| ϕ | Swirl angle | deg |
| χ | Swirl angle | deg |
| ψ | Swirl angle | deg |
| ω | Swirl angle | deg |
| ν | Swirl angle | deg |
| ξ | Swirl angle | deg |
| λ | Swirl angle | deg |
| μ | Swirl angle | deg |
| ρ | Swirl angle | deg |
| σ | Swirl angle | deg |
| τ | Swirl angle | deg |
| υ | Swirl angle | deg |
| ϕ | Swirl angle | deg |
| χ | Swirl angle | deg |
| ψ | Swirl angle | deg |
| ω | Swirl angle | deg |
| ν | Swirl angle | deg |
| ξ | Swirl angle | deg |
| λ | Swirl angle | deg |
| μ | Swirl angle | deg |
| ρ | Swirl angle | deg |
| σ | Swirl angle | deg |
| τ | Swirl angle | deg |
| υ | Swirl angle | deg |
| ϕ | Swirl angle | deg |
| χ | Swirl angle | deg |
| ψ | Swirl angle | deg |
| ω | Swirl angle | deg |
| ν | Swirl angle | deg |
| ξ | Swirl angle | deg |
| λ | Swirl angle | deg |
| μ | Swirl angle | deg |
| ρ | Swirl angle | deg |
| σ | Swirl angle | deg |
| τ | Swirl angle | deg |
| υ | Swirl angle | deg |
| ϕ | Swirl angle | deg |
| χ | Swirl angle | deg |
| ψ | Swirl angle | deg |
| ω | Swirl angle | deg |
| ν | Swirl angle | deg |
| ξ | Swirl angle | deg |
| λ | Swirl angle | deg |
| μ | Swirl angle | deg |
| ρ | Swirl angle | deg |
| σ | Swirl angle | deg |
| τ | Swirl angle | deg |
| υ | Swirl angle | deg |
| ϕ | Swirl angle | deg |
| χ | Swirl angle | deg |
| ψ | Swirl angle | deg |
| ω | Swirl angle | deg |
| ν | Swirl angle | deg |
| ξ | Swirl angle | deg |
| λ | Swirl angle | deg |
| μ | Swirl angle | deg |
| ρ | Swirl angle | deg |
| σ | Swirl angle | deg |
| τ | Swirl angle | deg |
| υ | Swirl angle | deg |
| ϕ | Swirl angle | deg |
| χ | Swirl angle | deg |
| ψ | Swirl angle | deg |
| ω | Swirl angle | deg |
| ν | Swirl angle | deg |
| ξ | Swirl angle | deg |
| λ | Swirl angle | deg |
| μ | Swirl angle | deg |
| ρ | Swirl angle | deg |
| σ | Swirl angle</ | |

1. INTRODUCTION

The design aim of advanced turbo jet engines and intakes is to achieve good installed performance for all power settings across the aircraft flight envelope. This requires high intake and engine performance and also sufficient intake/engine compatibility. Sufficient compatibility means that the intake flow quality is always better than that which the engine can tolerate (engine sensitivity). Intakes and engines have to be developed separately at first, before the compatibility of intake and engine can be measured directly. Only the specified compatibility parameters like pressure and temperature distortion, turbulence and swirl can be checked at the aerodynamic interface plane during the development wind tunnel model tests. The engine itself has to be developed behind a bellmouth intake. Special simulators or generators located between bellmouth intake and engine compressor face simulate typical intake flow patterns which yield the levels of the specified compatibility parameters up to the engine limits.

A comparison of the real and the simulated intake air flow pattern showed differences. These differences between the real and the simulated intake air flow pattern caused substantial time delays in many aircraft projects. For example, during the flight test phase of the aircraft F-111 additional model and full scale tests had to be performed. A reduction of the dynamic intake distortion was particularly addressed in order to solve these problems. Another example is the multi role combat aircraft TORNADO. Also, additional model and full scale tests were necessary. Flight operations at higher angles of incidence produced swirl in the air intake which caused the engine to surge. An intake fence was finally adopted and completely eliminated the problem. The intake fence reduced mainly the intake swirl. A reduction of the pressure distortion and the pressure turbulence was also measured.

Both examples and the experience from other past aircraft developments shows also that swirl intake flow simulators or generators shall be used during engine development as soon as possible. A big part of the time delays described above had to be used for the design and manufacture of intake flow pattern generators. The generator development began with distortion screens and later also with secondary air injection. These types of generator produced air intake flow patterns with different pressure and temperature distortion (steady state and instantaneous distortion) in front of the engine compressor. The TORNADO experience has shown again that a swirl generator is necessary in addition to the pressure and temperature distortion generator for future aircraft and engine projects. A swirl generator is not only necessary for the development of engines without inlet guide vanes (IGV) in front of the engine fan, like TORNADO engine RB199, it is also necessary for future engine projects with IGV's in front of the engine. The development of such swirl generators will be shown in this report.

2. SWIRL AND TYPES OF INTAKE SWIRL DISTORTION

Experiments and theoretical considerations have shown that all supersonic intakes of present combat aircraft produce essentially two types of swirl components of varying magnitude: bulk swirl and bulk swirl (see ref. 1). This is based on the similarity of these aircraft intakes and their flight envelopes. Such intakes normally require S-shaped diffusers because of the offset of the engine relative to the intake. The wall boundary layer creates the well known bulk swirl when the flow is turned through a simple bend. The same holds for a double bend (S-shaped duct, see paragraph 2.1). An additional type of swirl occurs at separation intakes placed at the entrance of the intake with subsequent turning of the flow passage (such a separation can happen e.g. at higher angles of incidence of separated intakes at subsonic flights or at low speed diffusers). Low streamlines of the separated flow at supersonic flights (see paragraph 2.2) depending on the geometry of the engine intake can disturb the intake engine compatibility problems such as, for example engine surge and fan flutter.

2.1 Bulk Swirl

The magnitude of the swirl of flow through a bend type has been well known for a long time. For a given energy stream lines towards the outer radii of the bend while the low energy stream lines are in fact for what we call swirl. For example, see theory of Betts and ref. 2. This phenomenon was investigated as well experimentally as the net result (ref. 1) and its effect on engines as regards performance degradation pointed out.

The intake walls and inlet guide vanes (see fig. 1 and ref. 1), which all had the same S-shaped intake diffuser, this bulk swirl could be identified. It proved to be the more stable component of the total swirl pattern measured at the engine face. That it was little affected by internal intake modifications like flow straighteners

2.2 Swirl at Separation

Bulk swirl is defined here as the arithmetical mean value of the flow angles for each radius R (see ref. 1). For the TORNADO aircraft, this type of swirl was found to be similar to the swirl type of rotation. Its generation can be explained in the same way as above if only one half of the "twins" is considered.

A region of low kinetic energy (low total pressure) located asymmetrically at one portion of the intake duct perimeter, e.g. either at the intake cowl or at the ramp (fig.1), is pushed towards the inner radius of the bend while the high energy air is moved outwards by centrifugal forces, as shown in fig.3.

Fig.3 also explains why the bulk swirl is contrarotational to the fan at subsonic speed and high angles of incidence in the left hand engine and at supersonic speed and low angles of incidence in the right hand engine respectively.

In contrast to the twin swirl, bulk swirl is rather sensitive, i.e. it changes considerable in magnitude and also in sign for varying external flow conditions (fig.3) which define the position and size of the region of low kinetic energy flow.

2.3 Combination of Twin and Bulk Swirl

Typical supersonic intake flow patterns as shown in fig.5, 6, 7 and 8 show a combination of twin and bulk swirl. Fig.4 illustrates the superimposing of these two basic intake swirl components.

2.4 TORNADO Intake Swirl (ref.1)

At subsonic speeds both the twin and the bulk swirl increase (fig.5): The extremes in deviation from the mean value, the local maximum and minimum values at the outermost measuring station $R = 0,87 \cdot R(\max)$, are a measure of the strength of the twin swirl, which is more than doubled towards the high incidence end. The swirl being contrarotational to the fan rotation of the left hand engine and obviously co-rotational to the right hand engine.

At subsonic speed, Mach = 0,7, fig.7 shows the influence of the engine mass flow. Reducing the engine mass flow at intermediate incidences produced swirl angles of similar magnitude, however, of opposite sign, fig.7 (shaded area).

At supersonic speeds an analogous dependence of swirl versus second ramp angle (α_2) of the intake shock system was found, fig.6. The swirl being now largely contra-rotational to the fan rotation of the right hand engine and obviously co-rotational to the left hand engine.

A comparison between model and full scale data was made under static conditions. As shown in fig.8, the flow angles at the duct wall of TORNADO prototype obtained by the oil flow technique agree quite well with the flow angles measured in a TORNADO wind tunnel model by a rotatable 8 arm rake having 24 five-hole probes. This agreement was also found in paragraph 4.1 and 4.2 (Moveable Swirl Generator). More details about the TORNADO model and full scale tests are described in ref.1.

3. SIMULATION OF INTAKE SWIRL

In the past only steady state and instantaneous (dynamic) pressure distortion were particularly attended during air intake and engine compatibility investigations. In 1977 tests with a twin swirl generator in front of a compressor were published by the DFVLR (ref.3). After that Rolls Royce performed RB199 engine rig tests with fixed bulk swirl generators (ref.4). Swirl angles of γ (bulk, max) = $\pm 5^\circ$ and $\pm 10^\circ$ were simulated. These swirl generators (DFVLR and Rolls Royce) simulated either twin or bulk swirl.

The simulation of typical supersonic aircraft intake flow patterns, as shown in fig.5, 6, 7 and 8 for example, is the objective of the present work. These flow patterns with some simplifications will be simulated by fixed and moveable swirl generators.

Fixed swirl generators simulate selected specific intake flow patterns at the static test rig. The advantages of a fixed swirl generator are their greater simplicity as compared with moveable ones and also the simulation of the swirl distribution with nearly no total pressure disturbances. The effects on the engine of the pressure and swirl distortion can be measured separately.

Moveable swirl generators simulate as well selected specific intake swirl patterns as time variant intake swirl patterns which correspond to the flow patterns measured for all ground and flight conditions. The main advantage of a moveable swirl generator, as described below, is the fact that the magnitude of the swirl can be continuously varied by the remote controlled variation of the wing incidence. This is important in an emergency situation, as for example, during a severe engine surge which requires immediate removal of the swirl disturbance.

4. MODEL INVESTIGATIONS

4.1 Model Simulation of Intake Swirl Distortion Model Wind Tunnel and Testing Technique

The model investigations were made in a low speed wind tunnel, installed in the engine test facility of the Jet Propulsion Institute at the Universität der Bundeswehr München. Fig.9 is a detailed sketch of its arrangement which consists of an orifice plate, a 90° bend, a 3° diffuser, a plenum chamber, a nozzle reducing the circular cross section to an internal diameter of 200 mm, the model swirl generator and the measuring section. In front of and in the plenum chamber screens and honeycombs are mounted in order to obtain uniform flow conditions over the whole cross section.

The air is supplied by a screw compressor with a pressure ratio of 2,8 and a constant mass flow rate of 3,7 kg/s. Part of this mass flow rate can be blown off through a regulating valve, so that the mass flow rate through the wind tunnel easily can be changed.

The device for measuring the flow patterns behind the model swirl generator consists of three 5-hole-probes with pyramidal probe heads (see fig.10). These probes are equally positioned in the circumferential direction of the measuring plane and can be traversed in radial direction. In addition wall static pressure holes are located midwise between the 5-hole-probes.

The fastening of the model swirl generator between nozzle and measuring section is constructed in such a way that it can easily be turned around the center-axis. In this way the whole flow field behind the swirl generator can be measured with the three 5-hole-probes. The distance between swirl generator and measuring plane can be varied by different lengths of pipes. In addition to these measurements tests were made by using the oil flow technique for getting informations about the flow conditions near the wall. This technique is based on the assumption that small droplets of high viscosity are moving slowly in the direction of the passing air flow. Thus a lot of small droplets of a suspension of oil and dye were applied at the duct wall in the plane to be measured. Then the model wind tunnel was set in operation and kept at the desired mass flow rate for about five minutes. After shutting-down the air supply a copy of the trails of the droplets was obtained by pressing a sheet of paper on the cylindrical duct wall. In this way it was possible to obtain the wall flow pictures at different distances behind the swirl generator.

Model Swirl Distortion Generators

The aim of this investigation was not primarily to simulate exactly the flow conditions measured in the Tornado intake (refer, Chapt.2), but to carry out basic investigations by generating two basic swirl types and also combinations thereof of different magnitudes. Therefore the following model swirl generators were designed:

FIXED SWIRL GENERATOR:

With this type of swirl generator the flow deflection is generated by guide vanes which are individually cambered with respect to the desired flow deflection. For this purpose the flow fields of the two basic swirl types are described in simple theoretical swirl models: According to its definition bulk swirl is similar to a solid type rotation. Thus the corresponding guide vane have to generate a flow deflection which is linearly increasing in radial direction to a maximum value τ B,MAX (see fig.11). The twin swirl is a counter rotating double swirl which is approximated by a swirl model as shown in fig.12a. The model for determination of the local flow deflection uses concentric semicircles and straight lines which define the direction of the cross flow. The flow deflection along the x-axis corresponds to a cosine-distribution with the maximum at τ T,MAX. The flow deflection along the semicircles and the straight parts follows also a cosine-distribution with the corresponding maximum at the point of intersection with the x-axis. In this way the flow deflection is defined in each point of the cross section. As examples for the resulting theoretical flow deflections, the distributions along the 45°, 135°, 225° and 315°-directions are shown in fig.12b.

Combinations of the two basic swirl types result from the superposition of these both swirl models specifying the values of τ B,MAX and τ T,MAX. Fixed model swirl generators were designed to simulate the following swirl configurations assuming zero deviation of the guide vanes as a rough approximation:

| Twin swirl | Bulk swirl |
|------------|------------|
| 20° | 0° |
| 15° | 5° |
| 10° | 10° |
| 5° | 15° |
| 0° | 20° |

Depending on the strength of the maximum deflection caused by bulk swirl and twin swirl, the combinations thereof have a different number of swirl centers. There exists only one swirl center if τ B,MAX > τ T,MAX, two centers if τ B,MAX < τ T,MAX and finally three centers if τ B,MAX = τ T,MAX (i.e. the maximum flow deflections of bulk swirl and twin swirl are equal).

As an example fixed model swirl generators for the swirl configurations τ B,MAX = 10°, τ T,MAX = 0° and τ B,MAX = 0°, τ T,MAX = 20° (i.e. pure twin swirl) are shown in fig.13 and fig.14.

MOVEABLE SWIRL GENERATOR:

A slender sharp-edged delta wing generates two symmetrical vortex sheets above its upper surface at specific angles of attack α (see fig.15). The vorticities are generated by flow separation at the sharp leading-edges of the wing.

Therefore a sharp-edged delta wing with trapezoidal cross section was used as a moveable swirl generator. Its geometry is shown in fig.16. The main data are the leading-edge sweep angle of 60° (i.e. an aspect ratio of 2,3), the maximum thickness ratio of 0,0 and the vertex angle of the bevelled leading-edges of about 8°.

The adjustment of the angle of attack is carried out by two moveable sticks. For aerodynamical purposes these sticks are covered by suitable shaped fairings (see fig.17).

This mechanism allows to change the angle of attack from 0° to 24° in steps of 1° .

4.2 Results of the Model Wind Tunnel Tests

As was explained before the main objective of the model investigations was to generate defined swirl patterns with the present subscale swirl generators and to investigate the influence of the distance between swirl generator and measuring plane on the stability of the generated flow field.

FIXED SWIRL GENERATORS

For the fixed swirl generators the following program of measurements using oil flow probes was conducted:

| fixed swirl generators for the following swirl combinations | distance between swirl generator and measuring plane | | |
|---|--|-------|-------|
| | 1,0 D | 2,0 D | 4,0 D |
| B, MAX = 20° T, MAX = 0° | X | | X |
| B, MAX = 15° T, MAX = 5° | X | X | X |
| B, MAX = 10° T, MAX = 10° | X | | X |
| B, MAX = 5° T, MAX = 15° | X | | X |
| B, MAX = 0° T, MAX = 20° | X | X | X |

Some of the results are presented in fig. 23a and b. The flow pattern for the combination B, MAX = 10° , T, MAX = 0° and the distance between swirl generator and measuring plane of 1,0 D is shown in fig. 23a. According to the design of this swirl generator there is a clockwise cross flow with one swirl center caused by the laminar flow swirl. For different distances between swirl generator and measuring plane very similar flow patterns were measured behind this swirl generator (see fig. 23b and c). This means that the generated swirl configuration and the magnitude of the flow deflection is tolerably stable. Regarding the locations of the swirl centers in fig. 23 the flow patterns it can be found that the swirl centers move clockwise around the center line with increasing distance of the measuring plane.

In fig. 23 the cross flow pattern of the pure twin swirl is shown. The center line double swirl can be recognized being symmetrical with respect to the x-axis. In fig. 23c the flow deflection curves along the x-axis resulting from the theoretical twin swirl model (see chart 1.11), the geometrical blade exit angles, and the measured values are shown. According to the desired teardrop-shaped flow deflection the theoretical swirl model the trailing edges of the guide vanes had to obtain a corresponding contour. However, it was not possible to realize this contour because of manufacturing problems. Thus guide vanes were built with linearly approximated contours at the trailing edges assuming zero deflection. A comparison of the measured values with the required distribution shows that the desired magnitudes could not be generated. However, the theoretical maximum and minimum flow deflection. Nevertheless the tendency of the distribution is comparable even though further research in this subject seems to be necessary. New considerations should take into account also the deviation between the geometrical blade exit angles and the real flow angles.

MOVEABLE SWIRL GENERATOR

In order to investigate the flow deflections behind the moveable swirl generator the oil flow technique as well as probe-probes were used. Wall flow pictures applying the oil flow technique were produced for several angles of attack, varying measuring plane distance and mass flow rate according to the following test program:

| α | distance generator-measuring plane | | mass flow rate (kg/s) | measurement technique | |
|----|------------------------------------|-------|-----------------------|-----------------------|-------------|
| | 1,0 D | 2,0 D | | oil flow | probe-probe |
| 0 | | X | 1,7 | X | |
| 6 | | X | 1,7 | X | |
| 12 | | X | 1,7 | X | |
| 15 | | X | 1,7 | X | X |
| 18 | X | X | 1,7 | X | |
| 18 | X | X | 1,49 | X | |
| 18 | X | X | 1,0 | X | |
| 21 | | X | 1,7 | X | |

Some of these results are shown in fig. 21 and fig. 24.

6. CONCLUSIONS

On the basis of a detailed investigation of the engine inlet flow pattern behind a typical supersonic intake of a military fighter aircraft it has been shown that also swirl distortions have to be considered as dominant influence parameters on engine performance and intake/engine compatibility. Two basic types, i.e. twin swirl and bulk swirl and also combinations thereof had to be considered. Model tests with fixed and moveable generators have proven their ability to reproduce those swirl distortions, and they showed good agreement with the target patterns. The engine performance investigations with full scale generators will be performed with a Larzac 04 low by-pass engine in the engine test facility using comprehensive instrumentation for flow field measurements in the inlet duct as well as engine performance measurements.

7. REFERENCES

- /1/ Aulehla, F.
Intake Swirl - a Major Disturbance Parameter in Engine/Intake Compatibility
ICAS/AIAA, -82-4.8.1, Seattle, August 1982
- /2/ Detra, R. W.
The Secondary Flow in Curved Pipes
Thesis, ETH Zürich 1953
- /3/ Lecht, M., and Weyer, H. B.
Unsteady Rotor Blade Loading in an Axial Compressor with Steady-State Inlet Distortion
AGARD CP 248-30, Cleveland, Oct. 1978
- /4/ Yates, B., and Eagles, C.
Engine 3/23B Gauze and Swirl Tests
Rolls Royce Ltd. Bristol, 1979 (Restricted)
- /5/ Stocks, C. P., and Bissinger, N. C.
The Design and Development of the Tornado Engine Air Intake
AGARD CP 301-10, Toulouse, May 1981
- /6/ Staudacher, W.
Auslegung eines Delta-Flügels
MBB-LKE 127, 1985
- /7/ Hummel, D., and Srinivasan, E. S.
Vortex Breakdown Effects on the Low-Speed Aerodynamics of Slender Delta Wings in Symmetrical Flow
J. Royal Aero.Soc., Vol. 77, 1967, pp. 11-14
- /8/ Hummel, D.
On the Vortex Breakdown over a Slender Wing
AGARD CP 247, 1978
- /9/ Pazar, W.
Entwurf einer Drallsimulationsanlage
UniBW-München, Institut für Strömungslehre
Diplomarbeit Nr. 86/87, 1987

ACKNOWLEDGEMENT

The work reported herein was performed in the framework of the research programme of the German Bundesministerium für Wissenschaft und Technologie (BMBW) München and Universität der Bundeswehr München in the framework of the research programmes of the German Bundesministerium für Wissenschaft und Technologie (BMBW) München. The results are gratefully acknowledged.

AD-A182 635

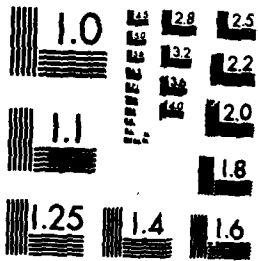
ENGINE RESPONSE TO DISTORTED INFLOW CONDITIONS:
CONFERENCE PROCEEDINGS OF... (U) ADVISORY GROUP FOR
AEROSPACE RESEARCH AND DEVELOPMENT NEUILLY... MAR 87
AGARD-CP-400 F/G 20/4

4/4

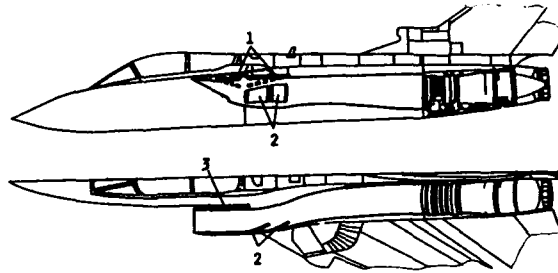
UNCLASSIFIED

NL





MICROCOPY RESOLUTION TEST CHART
NATIONAL BUREAU OF STANDARDS-1963-A



- 1 = variable ramps
- 2 = auxiliary air intake doors (AAID)
- 3 = boundary layer diverter

Figure 1. Tornado Inlet Geometry

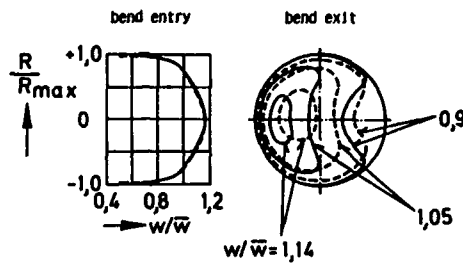


Figure 2. Comparison of Computed (Solid Lines) and Measured Twin Swirl (Dashed Lines) in a 21° Bent Pipe. Lines of Constant Axial Velocity Ratios; $\bar{w} = 41,6 \text{ m/s}$; Ref.2

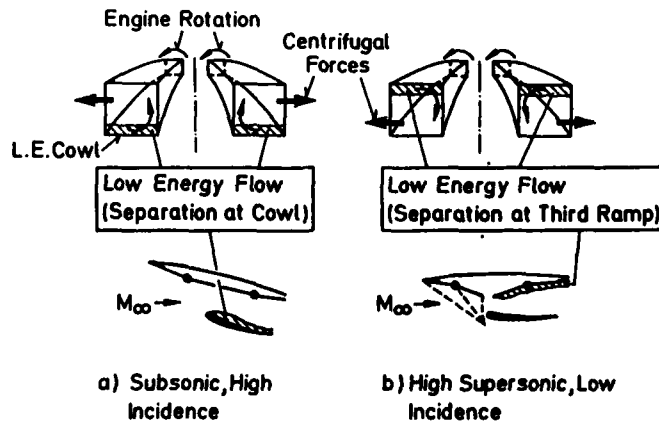


Figure 3. Generation of Intake Swirl, Ref.1

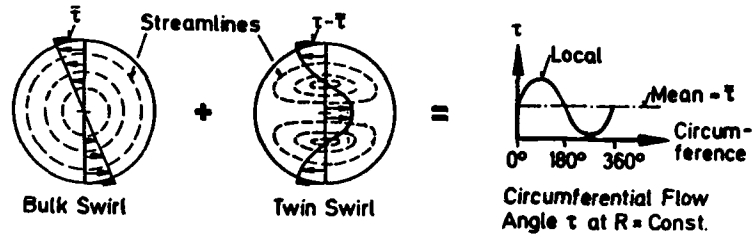


Figure 4. Superimposing of Bulk and Twin Swirls

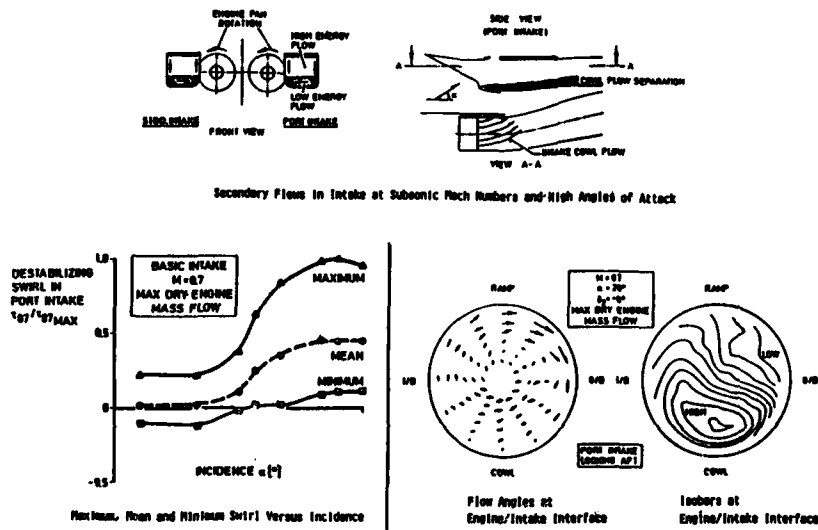


Figure 5. Tornado Inlet Swirl at High Angle of Attack (Subsonic Flight) , Ref.5

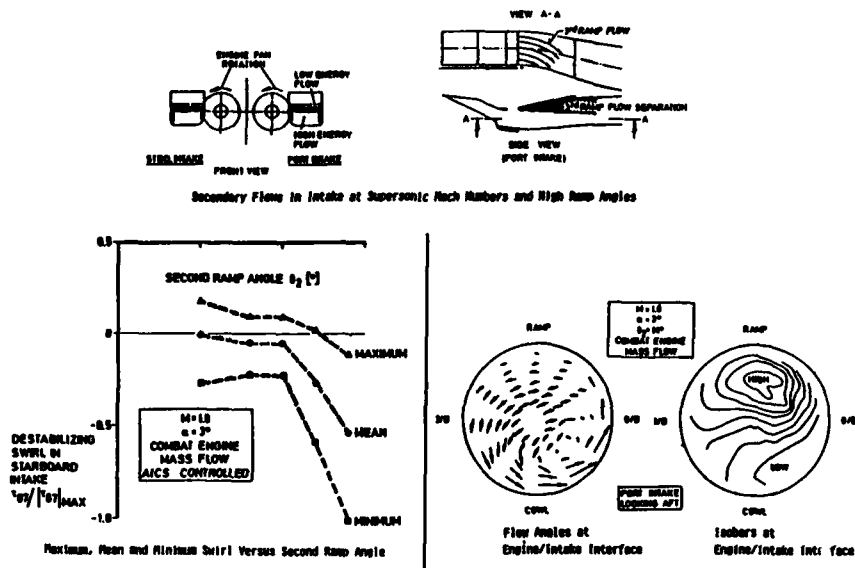


Figure 6. Tornado Inlet Swirl at High Ramp Angles (Supersonic Flight), Ref.5

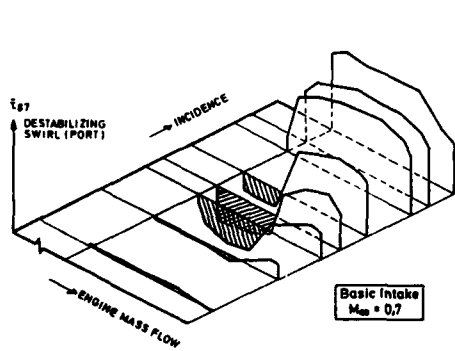


Figure 7. Effect of Incidence and Engine Mass Flow on Mean Swirl ($R = 0.87 \cdot R_{max}$), Ref.1

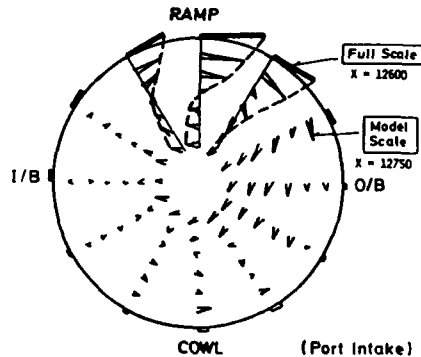


Figure 8. Model / Full Scale Comparison of Intake Swirl at $M_{\infty} = 0$

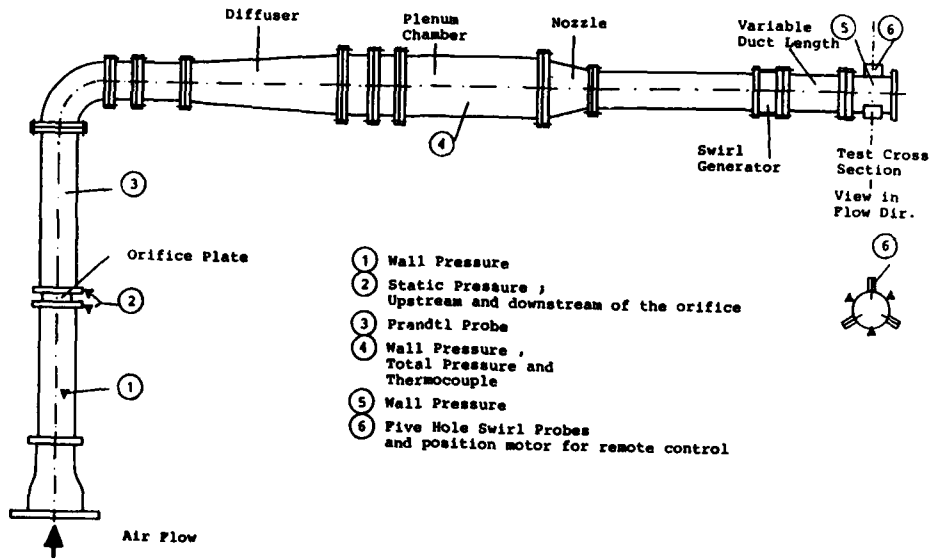


Figure 9. Arrangement and Instrumentation of the Low Speed Model Wind Tunnel

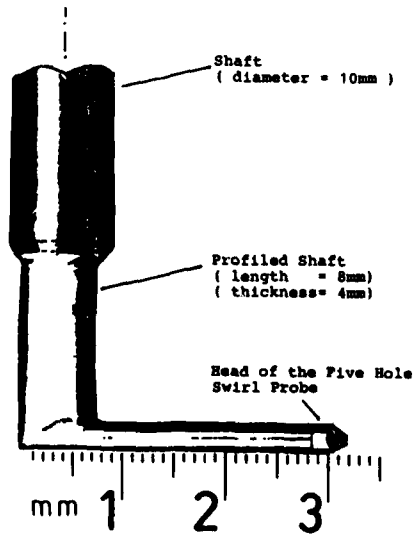


Figure 10. Five Hole Swirl Probe

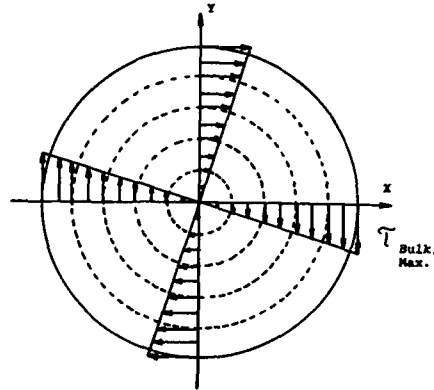


Figure 11. Theoretical Model for Bulk Swirl

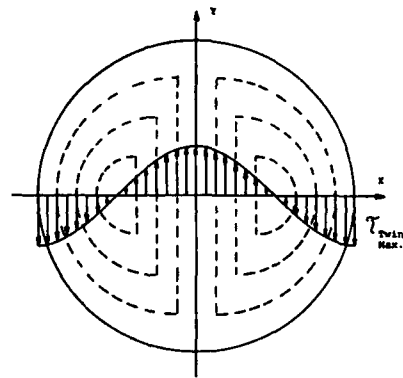


Figure 12a. Theoretical Model for Twin Swirl, Flow Deflection Along the x-Axis

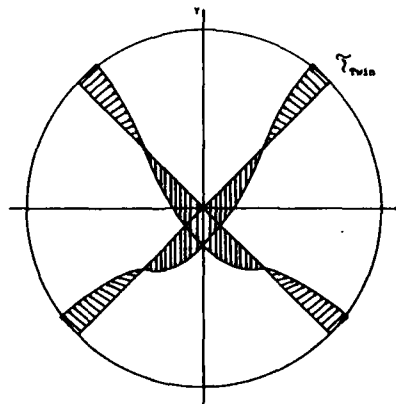


Figure 12b. Theoretical Model for Twin Swirl

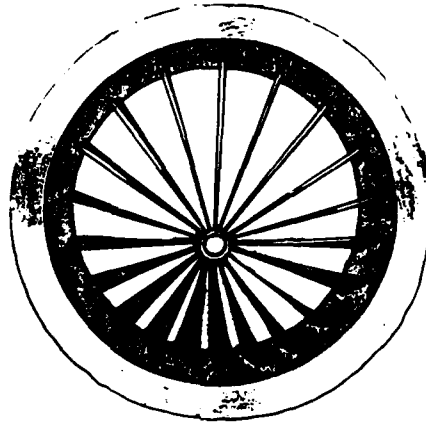


Figure 13. Model Fixed Swirl Generator for Simulation
of Swirl Combination
 $\tau_{B,max} = 15^\circ$ $\tau_{T,max} = 5^\circ$

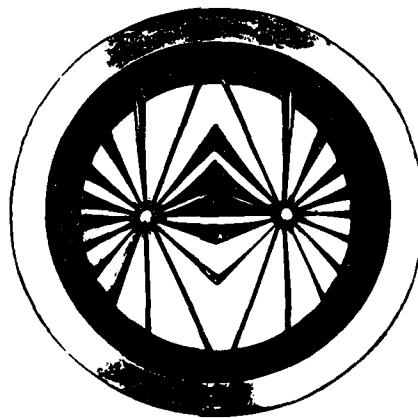


Figure 14. Model Fixed Swirl Generator, Twin Swirl
 $\tau_{T,max} = 20^\circ$

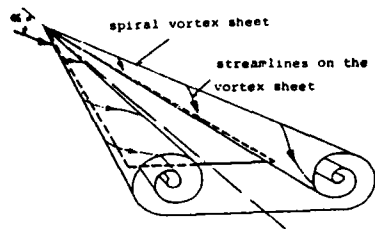


Figure 15. Vortex Formation Over a Sharp-Edged Slender Delta Wing (Ref.7)

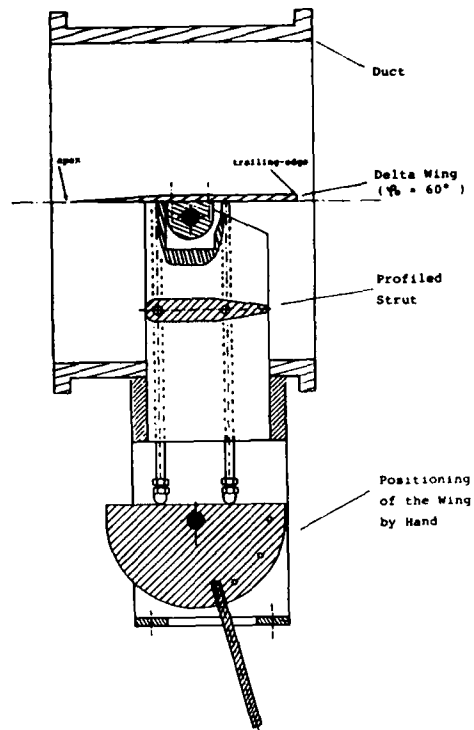


Figure 17. Fastening and Mechanism for Positioning of the Subscale Moveable Swirl Generator

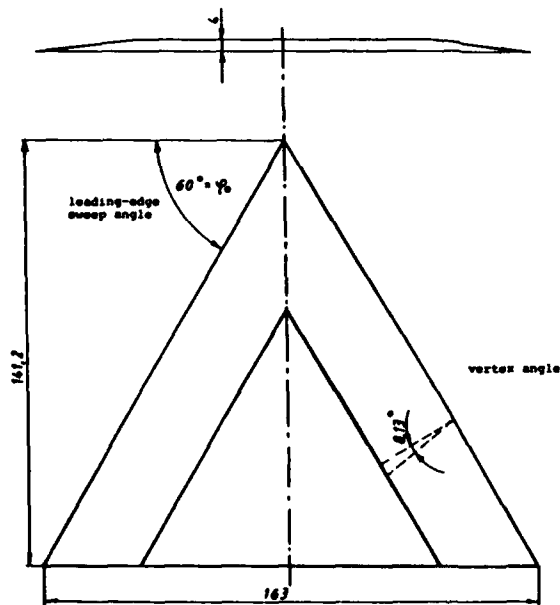
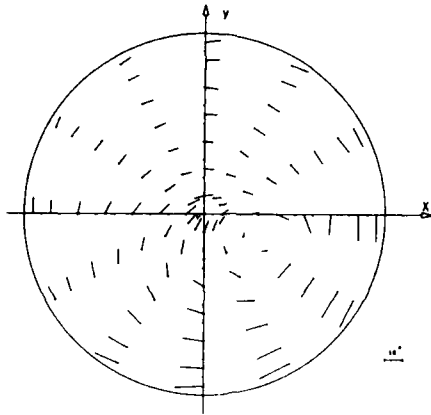
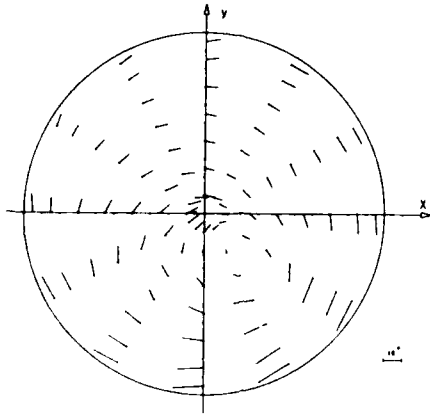


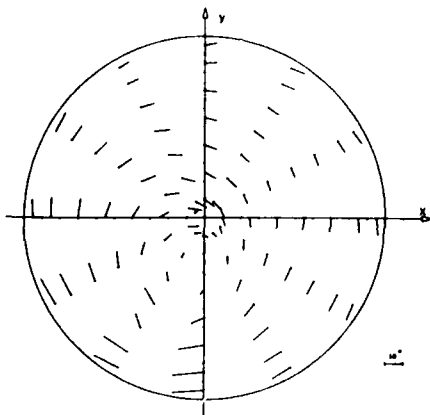
Figure 16. Geometry of the Model Delta Wing - Moveable Swirl Generator -



a) Distance Swirl Generator / Rake Plane
 $= 1,5 \cdot D = 300 \text{ mm}$



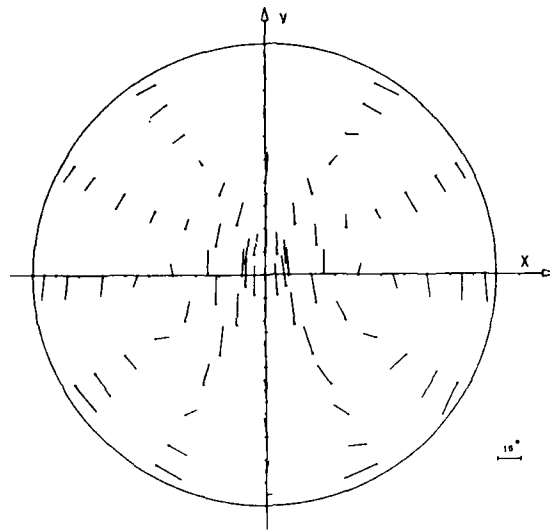
b) Distance Swirl Generator / Rake Plane
 $= 2,5 \cdot D = 500 \text{ mm}$



c) Distance Swirl Generator / Rake Plane
 $= 4,5 \cdot D = 900 \text{ mm}$

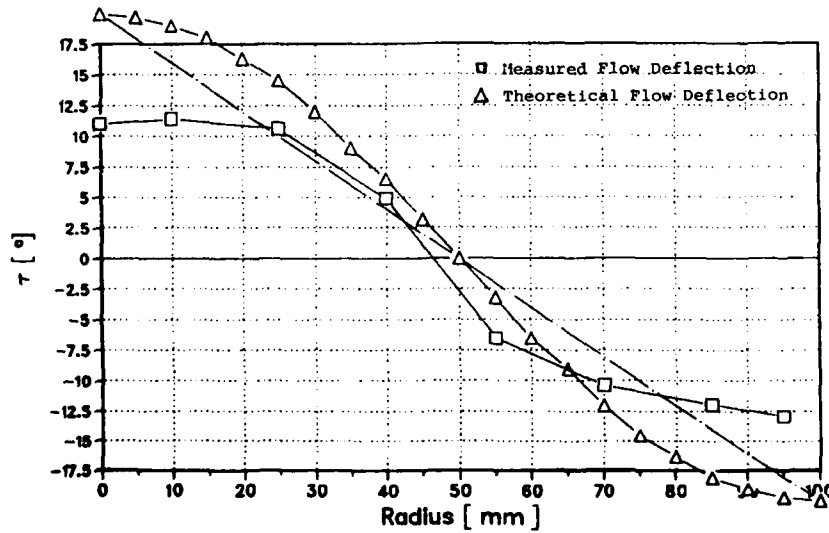
Figure 18. Cross Flow Pattern behind the Fixed Swirl Generator

$$\tau_{B,\max} = 15^\circ, \tau_{T,\max} = 5^\circ$$



Distance Swirl Generator / Rake Plane
 = $1,5 \cdot D = 300 \text{ mm}$

Figure 19. Cross Flow Pattern behind the Fixed Twin Swirl Generator
 $\tau_{T,max} = 20^\circ$



Distance Generator / Rake Plane
 = $1,5 \cdot D = 300 \text{ mm}$

Figure 20. Comparison of the Flow Deflections along the X-Axis ($\theta = 0^\circ$), $-\tau_{B,max} = 0^\circ$, $\tau_{T,max} = 20^\circ$

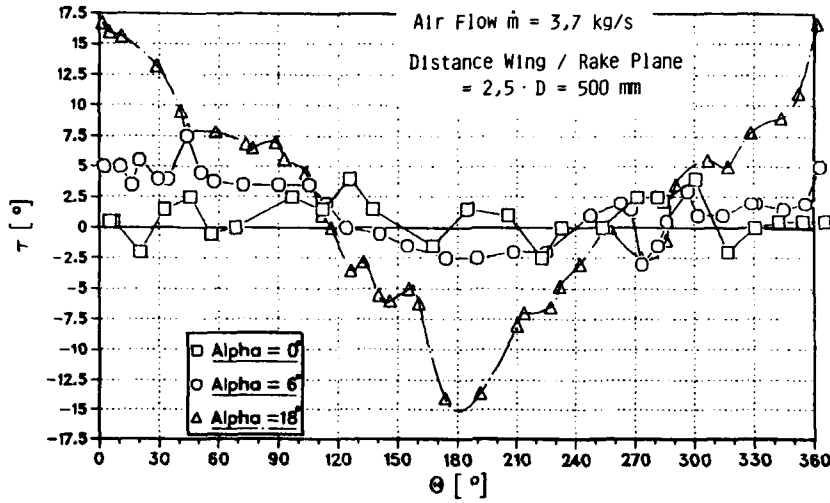


Figure 21. Wall Flow Picture behind the Moveable Swirl Generator, 60° Delta Wing, for Different Angles of Incidence (Alpha)

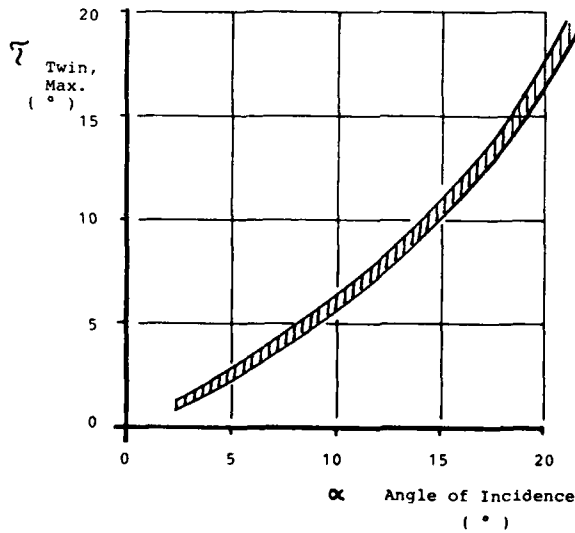


Figure 22. Maximum Flow Deflection behind the Moveable Swirl Generator as a Function of the Angle of Incidence

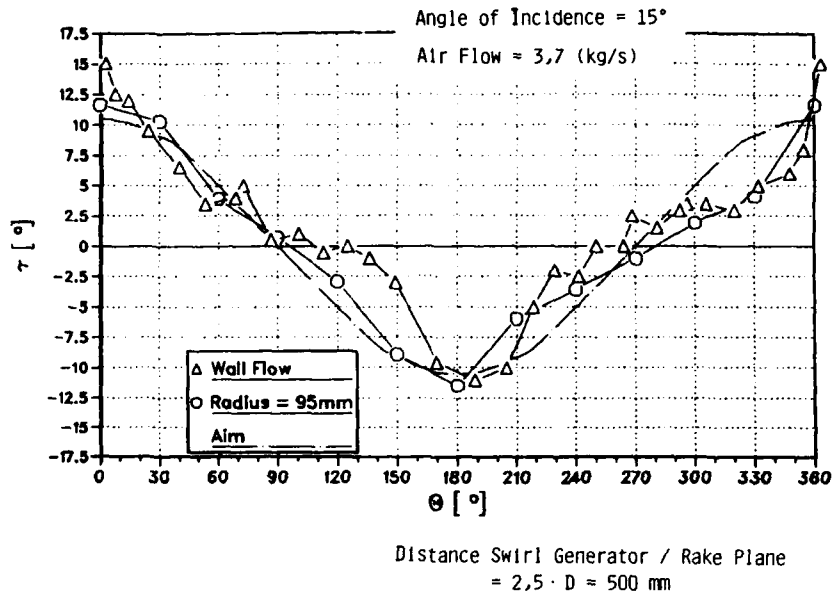


Figure 23. Comparison of the Measurement Techniques - Oil Flow Picture, Five Hole Swirl Probes

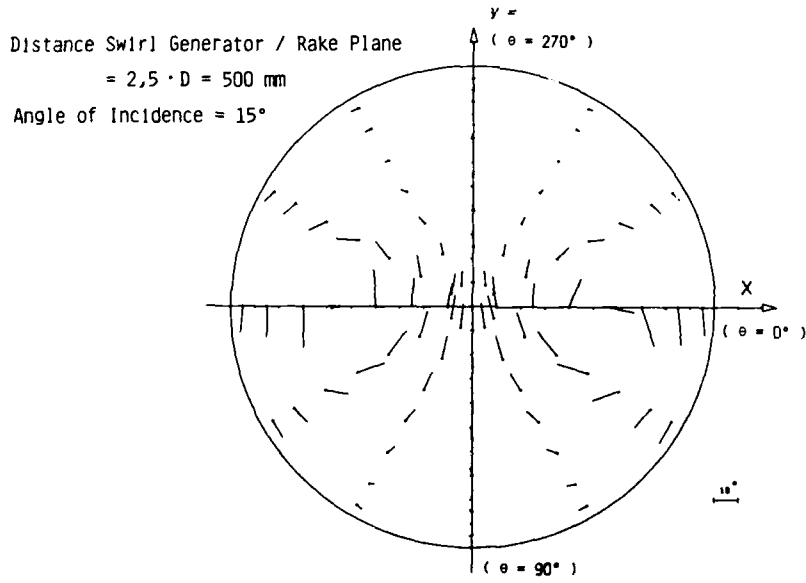


Figure 24. Cross Flow Pattern behind the Moveable Swirl Generator, Delta Wing 60°

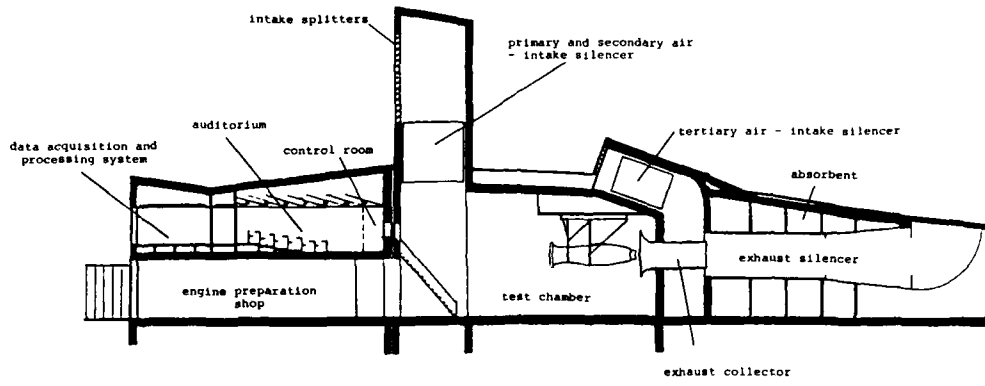


Figure 25. Side View of the Engine Test Facility

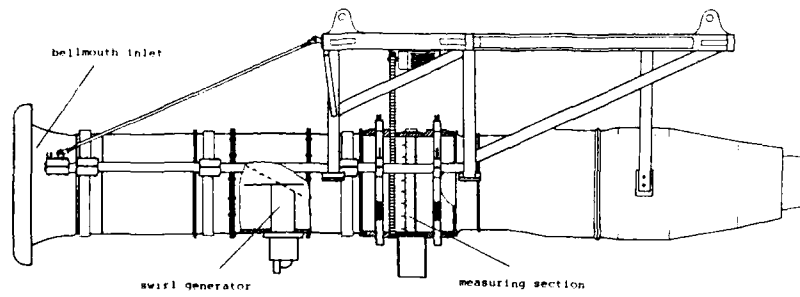


Figure 26. Test Arrangement of the Full Scale Investigations

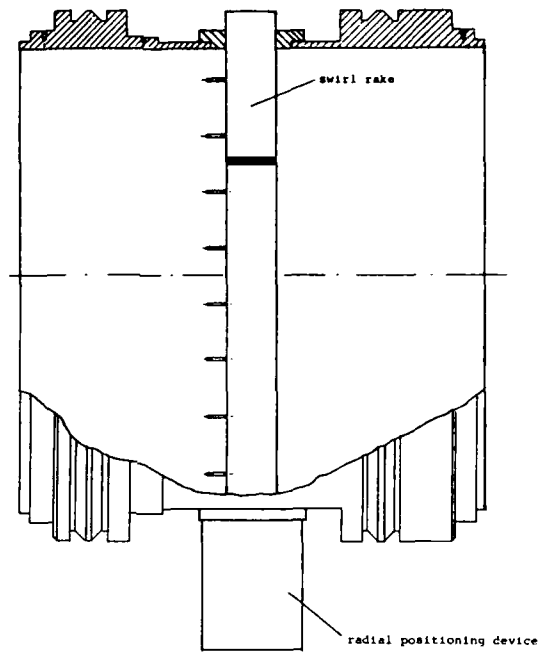


Figure 27. Device for Measuring the Flow Conditions
In Front of the Engine
(equipped with 8 five hole swirl probes)

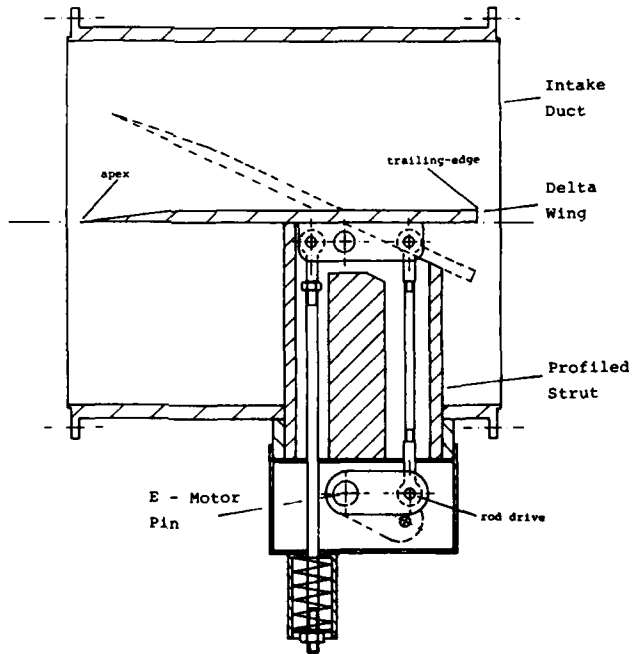


Figure 28. Moveable Swirl Generator for the Full Scale Investigations

DISCUSSION

Ph.Ramette, Fr

How do the distortions caused by a fixed twin-swirl generator and a moveable-swirl generator compare and which one do you think would give the best simulation of the actual distorted flow in the intake of an engine in the same flight case? I am thinking about distortion and turbulence.

Author's Reply

We could not find turbulence during our test but we have started only with model tests. The engine tests will be carried out in the immediate future.

Ph.Ramette, Fr

The first part of my question was: which kind of swirl generator would you prefer?

Author's Reply

We started with the moveable one, the delta wing.

M.Dupslaff, Ge

Could you say something about the pressure loss of the different kinds of swirl generators, especially the circumferential distribution of the loss?

Author's Reply

Would you like to have the distortion values? The DC(60) for the moveable-swirl generator is less than 0.1. About 0.05 or 0.06, I do not know exactly at the moment.

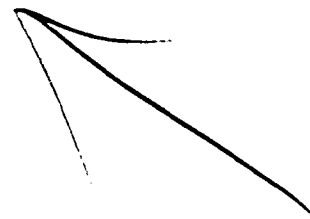
R.G.Hercock, UK

Do you propose to test the engine with total-pressure distortion as well as swirl? If so how are you to generate it?

Author's Reply

At first we will start with swirl generators only, as it was our clear intent to investigate the two disturbances separately.

That is, we simulate either swirl or pressure distortions measured for a typical case in the real inlet flow. In order to get the engine response (surge) either the simulated disturbances will be increased (proportionally) or the engine will be made more surge prone, eg by reducing the throat of the thrust nozzle. The simultaneous simulation of swirl and pressure distortion may then not be necessary, but could be accomplished as outlined in Reference 1.



15-22

| REPORT DOCUMENTATION PAGE | | | | | | | | | | | | | |
|-----------------------------------|---|----------------------|--|------------------------|---------------------|----------------------------|---------------------|-----------------------------|------------------|-----------------------------|------------------------|-----------------------------------|--------------------------|
| 1. Recipient's Reference | 2. Originator's Reference | 3. Further Reference | 4. Security Classification of Document | | | | | | | | | | |
| | AGARD-CP-400 | ISBN 92-835-0412-7 | UNCLASSIFIED | | | | | | | | | | |
| 5. Originator | Advisory Group for Aerospace Research and Development North Atlantic Treaty Organization 7 rue Ancelle, 92200 Neuilly sur Seine, France | | | | | | | | | | | | |
| 6. Title | ENGINE RESPONSE TO DISTORTED INFLOW CONDITIONS | | | | | | | | | | | | |
| 7. Presented at | the Propulsion and Energetics 68th (A) Specialists' Meeting held in Munich, Germany, 8-9 September 1986. | | | | | | | | | | | | |
| 8. Author(s)/Editor(s) | Various | | 9. Date March 1987 | | | | | | | | | | |
| 10. Author's/Editor's Address | Various | | 11. Pages 308 | | | | | | | | | | |
| 12. Distribution Statement | This document is distributed in accordance with AGARD policies and regulations, which are outlined on the Outside Back Covers of all AGARD publications. | | | | | | | | | | | | |
| 13. Keywords/Descriptors | <table border="0"> <tr> <td>Compressor performance</td> <td>Pressure distortion</td> </tr> <tr> <td>Computation of engine flow</td> <td>Response of engines</td> </tr> <tr> <td>Distorted inflow in engines</td> <td>Swirl in intakes</td> </tr> <tr> <td>Intake-engine compatibility</td> <td>Temperature distortion</td> </tr> <tr> <td>Performance prediction of engines</td> <td>Unsteady flow in engines</td> </tr> </table> | | | Compressor performance | Pressure distortion | Computation of engine flow | Response of engines | Distorted inflow in engines | Swirl in intakes | Intake-engine compatibility | Temperature distortion | Performance prediction of engines | Unsteady flow in engines |
| Compressor performance | Pressure distortion | | | | | | | | | | | | |
| Computation of engine flow | Response of engines | | | | | | | | | | | | |
| Distorted inflow in engines | Swirl in intakes | | | | | | | | | | | | |
| Intake-engine compatibility | Temperature distortion | | | | | | | | | | | | |
| Performance prediction of engines | Unsteady flow in engines | | | | | | | | | | | | |
| 14. Abstract | <p>The Conference Proceedings contain 16 papers presented at the Propulsion & Energetics Panel 68th (A) Specialists' Meeting on Engine Response to Distorted Inflow Conditions, which was held 8-9 September 1986 in Munich, Germany.</p> <p><i>meeting</i></p> <p>The Specialists' Meeting was opened with a review of current knowledge on the meeting subject arranged in the following sessions: Unsteady Flow and Validation of Empirical Distortion Parameters (3); Computation Technique for Engine/Compressor Performance Predictions of Distorted Inflow (5); Characterization of Distorted Inflow (4); and Experimental Investigations of Engine Instability and Response to Flow Distortion (3). The Technical Evaluation Report is included at the beginning of the Proceedings. Questions and answers of the discussions follow each paper.</p> <p><i>the proceedings on 16 papers.</i></p> <p>The meeting was intended to provide scientists and development engineers with a broad information on acceptable inflow distortion parameters to be applied to airframe-intake integration, computation technique for engine/compressor performance prediction of distorted inflow, distortion inflow detection, and experimental investigation of engine instability. The achievements were discussed in the Technical Evaluation Report.</p> <p><i>4</i></p> | | | | | | | | | | | | |

| | | | |
|--|---|--|---|
| <p>AGARD Conference Proceedings No. 400 Advisory Group for Aerospace Research and Development, NATO ENGINE RESPONSE TO DISTORTED INFLOW CONDITIONS Published March 1987 308 pages</p> <p>The Conference Proceedings contain 16 papers presented at the Propulsion & Energetics Panel 68th (A) Specialists' Meeting on Engine Response to Distorted Inflow Conditions, which was held 8-9 September 1986 in Munich, Germany.</p> <p>The Specialists' Meeting was opened with a review of current knowledge on the meeting subject and arranged P.T.O.</p> | <p>AGARD-CP-400</p> <p>Compressor performance Computation of engine flow Distorted inflow in engines Intake-engine compatibility Performance prediction of engines Pressure distortion Response of engines Swirl in intakes Temperature distortion Unsteady flow in engines</p> | <p>AGARD Conference Proceedings No. 400 Advisory Group for Aerospace Research and Development, NATO ENGINE RESPONSE TO DISTORTED INFLOW CONDITIONS Published March 1987 308 pages</p> <p>The Conference Proceedings contain 16 papers presented at the Propulsion & Energetics Panel 68th (A) Specialists' Meeting on Engine Response to Distorted Inflow Conditions, which was held 8-9 September 1986 in Munich, Germany.</p> <p>The Specialists' Meeting was opened with a review of current knowledge on the meeting subject and arranged P.T.O.</p> | <p>AGARD-CP-400</p> <p>Compressor performance Computation of engine flow Distorted inflow in engines Intake-engine compatibility Performance prediction of engines Pressure distortion Response of engines Swirl in intakes Temperature distortion Unsteady flow in engines</p> |
| <p>AGARD Conference Proceedings No. 400 Advisory Group for Aerospace Research and Development, NATO ENGINE RESPONSE TO DISTORTED INFLOW CONDITIONS Published March 1987 308 pages</p> <p>The Conference Proceedings contain 16 papers presented at the Propulsion & Energetics Panel 68th (A) Specialists' Meeting on Engine Response to Distorted Inflow Conditions, which was held 8-9 September 1986 in Munich, Germany.</p> <p>The Specialists' Meeting was opened with a review of current knowledge on the meeting subject and arranged P.T.O.</p> | <p>AGARD-CP-400</p> <p>Compressor performance Computation of engine flow Distorted inflow in engines Intake-engine compatibility Performance prediction of engines Pressure distortion Response of engines Swirl in intakes Temperature distortion Unsteady flow in engines</p> | <p>AGARD Conference Proceedings No. 400 Advisory Group for Aerospace Research and Development, NATO ENGINE RESPONSE TO DISTORTED INFLOW CONDITIONS Published March 1987 308 pages</p> <p>The Conference Proceedings contain 16 papers presented at the Propulsion & Energetics Panel 68th (A) Specialists' Meeting on Engine Response to Distorted Inflow Conditions, which was held 8-9 September 1986 in Munich, Germany.</p> <p>The Specialists' Meeting was opened with a review of current knowledge on the meeting subject and arranged P.T.O.</p> | <p>AGARD-CP-400</p> <p>Compressor performance Computation of engine flow Distorted inflow in engines Intake-engine compatibility Performance prediction of engines Pressure distortion Response of engines Swirl in intakes Temperature distortion Unsteady flow in engines</p> |

| | |
|--|--|
| <p>in the following sessions: Unsteady Flow and Validation of Empirical Distortion Parameters (3); Computation Technique for Engine/Compressor Performance Predictions of Distorted Inflow (5); Characterization of Distorted Inflow (4); and Experimental Investigations of Engine Instability and Response to Flow Distortion (3). The Technical Evaluation Report is included at the beginning of the Proceedings. Questions and answers of the discussions follow each paper.</p> <p>The meeting was intended to provide scientists and development engineers with a broad information on acceptable inflow distortion parameters to be applied to airframe-intake integration, computation technique for engine/compressor performance prediction of distorted inflow, distortion inflow detection, and experimental investigation of engine instability. The achievements were discussed in the Technical Evaluation Report.</p> <p>ISBN 92-835-0412-7</p> | <p>in the following sessions: Unsteady Flow and Validation of Empirical Distortion Parameters (3); Computation Technique for Engine/Compressor Performance Predictions of Distorted Inflow (5); Characterization of Distorted Inflow (4); and Experimental Investigations of Engine Instability and Response to Flow Distortion (3). The Technical Evaluation Report is included at the beginning of the Proceedings. Questions and answers of the discussions follow each paper.</p> <p>The meeting was intended to provide scientists and development engineers with a broad information on acceptable inflow distortion parameters to be applied to airframe-intake integration, computation technique for engine/compressor performance prediction of distorted inflow, distortion inflow detection, and experimental investigation of engine instability. The achievements were discussed in the Technical Evaluation Report.</p> <p>ISBN 92-835-0412-7</p> |
| <p>in the following sessions: Unsteady Flow and Validation of Empirical Distortion Parameters (3); Computation Technique for Engine/Compressor Performance Predictions of Distorted Inflow (5); Characterization of Distorted Inflow (4); and Experimental Investigations of Engine Instability and Response to Flow Distortion (3). The Technical Evaluation Report is included at the beginning of the Proceedings. Questions and answers of the discussions follow each paper.</p> <p>The meeting was intended to provide scientists and development engineers with a broad information on acceptable inflow distortion parameters to be applied to airframe-intake integration, computation technique for engine/compressor performance prediction of distorted inflow, distortion inflow detection, and experimental investigation of engine instability. The achievements were discussed in the Technical Evaluation Report.</p> <p>ISBN 92-835-0412-7</p> | <p>in the following sessions: Unsteady Flow and Validation of Empirical Distortion Parameters (3); Computation Technique for Engine/Compressor Performance Predictions of Distorted Inflow (5); Characterization of Distorted Inflow (4); and Experimental Investigations of Engine Instability and Response to Flow Distortion (3). The Technical Evaluation Report is included at the beginning of the Proceedings. Questions and answers of the discussions follow each paper.</p> <p>The meeting was intended to provide scientists and development engineers with a broad information on acceptable inflow distortion parameters to be applied to airframe-intake integration, computation technique for engine/compressor performance prediction of distorted inflow, distortion inflow detection, and experimental investigation of engine instability. The achievements were discussed in the Technical Evaluation Report.</p> <p>ISBN 92-835-0412-7</p> |

AGARD

NATO OTAN

7 rue Ancelle · 92200 NEUILLY-SUR-SEINE
FRANCE

Telephone (1)47.38.57.00 · Telex 610 176

**DISTRIBUTION OF UNCLASSIFIED
AGARD PUBLICATIONS**

AGARD does NOT hold stocks of AGARD publications at the above address for general distribution. Initial distribution of AGARD publications is made to AGARD Member Nations through the following National Distribution Centres. Further copies are sometimes available from these Centres, but if not may be purchased in Microfiche or Photocopy form from the Purchase Agencies listed below.

NATIONAL DISTRIBUTION CENTRES

BELGIUM

Coordonnateur AGARD – VSL
Etat-Major de la Force Aérienne
Quartier Reine Elisabeth
Rue d'Evere, 1140 Bruxelles

CANADA

Defence Scientific Information Services
Dept of National Defence
Ottawa, Ontario K1A 0K2

DENMARK

Danish Defence Research Board
Ved Idraetsparken 4
2100 Copenhagen Ø

FRANCE

O.N.E.R.A. (Direction)
29 Avenue de la Division Leclerc
92320 Châtillon

GERMANY

Fachinformationszentrum Energie,
Physik, Mathematik GmbH
Kernforschungszentrum
D-7514 Eggenstein-Leopoldshafen

GREECE

Hellenic Air Force General Staff
Research and Development Directorate
Holargos, Athens

ICELAND

Director of Aviation
c/o Flugrad
Reyjavik

UNITED STATES

National Aeronautics and Space Administration (NASA)
Langley Research Center
M/S 180
Hampton, Virginia 23665

THE UNITED STATES NATIONAL DISTRIBUTION CENTRE (NASA) DOES NOT HOLD STOCKS OF AGARD PUBLICATIONS, AND APPLICATIONS FOR COPIES SHOULD BE MADE DIRECT TO THE NATIONAL TECHNICAL INFORMATION SERVICE (NTIS) AT THE ADDRESS BELOW.

PURCHASE AGENCIES

National Technical
Information Service (NTIS)
5285 Port Royal Road
Springfield
Virginia 22161, USA

ESA/Information Retrieval Service
European Space Agency
10, rue Mario Nikis
75015 Paris, France

The British Library
Document Supply Division
Boston Spa, Wetherby
West Yorkshire LS23 7BQ
England

Requests for microfiche or photocopies of AGARD documents should include the AGARD serial number, title, author or editor, and publication date. Requests to NTIS should include the NASA accession report number. Full bibliographical references and abstracts of AGARD publications are given in the following journals:

Scientific and Technical Aerospace Reports (STAR)
published by NASA Scientific and Technical
Information Branch
NASA Headquarters (NJT-40)
Washington D.C. 20546, USA

Government Reports Announcements (GRA)
published by the National Technical
Information Services, Springfield
Virginia 22161, USA

Printed by Specialised Printing Services Limited
40 Chigwell Lane, Loughton, Essex IG10 3TZ

ISBN 92-835-0412-7

END

DATE
FILMED

-87